RL-81-040

Rutherford and Appleton Laboratories
CHILTON, DIDCOT, OXON, OX11 0QX

Science and Engineering Research Council Central Laser Facility

Annual Report to the Laser Facility Committee 1981

Laser Division
Rutherford and Appleton Laboratories

RL-81-040

SCIENCE RESEARCH COUNCIL

CENTRAL LASER FACILITY

ANNUAL REPORT TO THE LASER FACILITY COMMITTEE, 1981

Preface

The report covers the work done at, or in association with, the Central Laser Facility during the year April 1980 to March 1981. It follows the same format as last years report and is arranged in seven chapters reflecting the six groups of the Glass Laser Scientific Programme and Scheduling Committee (GLSPSC) together with the gas laser development group. An appendix at the end of the report lists the publications based on the work of the facility which have either appeared or been accepted for publication during the year.

The scientific groups using the glass laser are listed in the accompanying table together with the names of their chairmen and secretaries and the experimental time allocated to them. The latter exceeds 52 weeks because of parallel operation in the single and six beam target areas. In addition the laboratory held a series of "Open Days" during July 1980 which effectively stopped experimental work for 2 weeks.

As will be clear from the table, half the year under review was devoted to a major reconstruction and upgrade of the glass laser. This is described in Chapter 1 of this report. It represents the first and largest phase of a two stage development programme. The primary objective is increased versatility to meet the diverse requirements of the user community. In particular the six beam system can now operate at two wavelengths (1.05μm and 0.53μm) while first, second and third harmonic operation is possible in the single beam target area. It is no longer necessary to constrain the two target areas to use the same pulse duration and, except when X-ray backlighting is required in the six beam area, shots can be fired simultaneously into the two target areas which effectively doubles the available shot rate. Though other laboratories are building or planning multibeam compression facilities using the harmonics of the glass laser frequency our six beam, 0.53μm, facility

is for the moment unique, as are other features of the new system. Consequently it was thought that the laser deserved a name and VULCAN has been chosen. Vulcan was the Roman god of fire and patron of workers with fire, which includes plasma physicists. A latin acronym then seemed appropriate: *Versicolor Ultima Lux Cohaerens pro Academica Nostra* (the latest multicoloured coherent light for our academics).

The considerable time devoted to laser development during the past year has inevitably reduced the amount of experimental work completed. Furthermore the development work was concentrated into the latter half of the year so we have had very little opportunity to exploit the new facilities. We can, however, look forward to a productive period in the coming 12 months. A full understanding of the wavelength scaling of key properties - absorption, ablation pressure, transport inhibition, etc - is vital to the future development of both inertial confinement and the lasers required to achieve it. Much of the work described in this report is pertinent to the question of wavelength scaling and indeed the gas laser development programme is based on the belief that a short wavelength is desirable, if only because of the increased absorption then obtained.

The ratio of allocated to requested laser time, traditionally reported in this preface, has been artificially inflated during the past year due to the large allocation to laser development. It is, however, of interest to report that four new academic groups - from University College, London and Bristol, Loughborough and Bradford Universities - have begun to take an active part in the facility's programme. As a result of these and other changes the registered user community has increased by about 35% over the past two years while the number of in house staff has remained unchanged.

A F Gibson
31 March 1981

GLASS LASER SCIENTIFIC PROGRAMME AND SCHEDULING COMMITTEE

SCIENTIFIC GROUPS

Group Title	Chairman	Secretary	Approx Time Allocated during year (weeks)
Laser Plasma Interactions	Mr T P Hughes * Essex University after 1.1.81 Professor T J M Boyd Univ Coll of North Wales	Dr R G Evans	11
Transport and Particle Emission	Dr J Kilkenny Imperial College	Mr W T Toner	13
Spectroscopy and XUV Lasers	Dr G Pert Hull University	Dr I N Ross	3
Ablative Compression	Professor M G Haines Imperial College after 1.1.81 Dr T A Hall Essex University	Dr P T Rumsby	10
Facility Development	Dr A F Gibson Rutherford Laboratory	Mr J Boon	for development 27 for maintenance 5
Theory and Computational Modelling	Professor T J M Boyd Univ Coll of North Wales after 1.1.81 Professor M G Haines Imperial College	Dr C Webb	-

* Mr Hughes is Chairman of the Programme Advisory Committee

CHAPTER 1 GLASS LASER FACILITY DEVELOPMENT

INDEX

CHAPTER EDITOR: J E Boon

CHAPTER 1 GLASS LASER FACILITY

1.1 Introduction

Since its establishment, the programme of the Central Laser Facility has interleaved periods for facility development with the users experimental activities. The first experiments in 1976 used a single, 100 Gw, beam and the first compression experiments were performed the following year using two beams. The power of these beams was considerably enhanced in 1978 and 1979 by double passing the final disc type amplifiers and changing the whole system over to a phosphate based glass. 1979 also saw the commissioning of a second target area with a six beam target chamber for compression studies, the six beams being derived by simple passive splitting of the original two. By the beginning of 1980, therefore, two target areas were in use and laser shots could be fired alternately into each area so that two user groups could conduct experiments simultaneously. This paralleling of operations has proved easier than anticipated and has worked well, effectively doubling the productivity of the facility.

As the needs of users expand and experiments become more sophisticated progressive development of the facilities is essential. The pattern of previous years has been repeated in 1980/81 though this year has seen the largest step forward in glass laser performance made since the foundation of the CLF. The details are described in later sections. It will, however, be obvious that for our purposes versatility is vital and we can confidently claim that the new structure is the most versatile high power laser in the world. For example the ability to provide pulses of different duration to the two target areas, probably a unique facility, will remove a constraint on experiment scheduling which has proved a serious handicap in the past. Perhaps the most important single feature of the newly reconstructed glass laser is the provision of harmonic generators to provide six second harmonic (green) beams for compression in Target Area I and both second and third harmonics in Target Area II. Fourth harmonic generation will be added to the latter facility in the coming year.

The reconstruction of the glass laser, described in this chapter, was completed towards the end of the year under review so there has been relatively little time to exploit its novel features. Nevertheless the layout of the laser has been designed to allow the next enhancement (the incorporation of three additional disc amplifiers in 18 months time) to be made fairly easily. Thus the recent upgrade, though large, is again only a step in a continuing process. It does, however, represent a sufficiently substantial improvement in the glass laser as to justify following the precedent set by other major laser laboratories by giving the laser a name. The reasoning behind the choice of VULCAN is given in the preface to this annual report.

A F Gibson (RAL)

1.2 Glass Laser Operations

The experimental programme has been severely curtailed this year, to allow time for installation of the redesigned and enhanced laser. The five and a half months before this major shut down saw a successful final period of operations with the old system. Both target areas were run concurrently with laser pulses directed into either area as required. There were periods of long (1 ns) pulses, short (100 ps) pulses and stacked (1 ns) pulses with shot totals equally divided between long and short pulses at approximately 300 apiece. Short pulse powers per beam of more than 0.5 TW and long pulse energies per beam of more than 120 J were supplied regularly.

Experiments have recently restarted using the new system initially firing a single beam long pulse but at the same time gradually commissioning the rest of the laser. All beams are now available for long pulse experiments and the short pulse oscillator together with pulse stacker will shortly be ready for short pulse or short/stacked pulse operation.

This year has seen a general improvement in system reliability which has led to the same number of target shots as the previous year in spite of

the long five month shut down.

I N Ross (RAL)

1.3 Glass Laser Development

1.3.1 Glass Laser Enhancement Programme

1.3.1(a) Introduction

A major fraction of this year has been devoted to the enhancement scheme, including completion of the design and purchasing as well as its implementation. The scheme is illustrated in Figure 1.01. Implementation of this scheme is now complete while, by the end of 1982, a further three disc amplifiers will have been introduced to enhance six beam output by a factor two. Budgetary and space limitations have placed a severe constraint on the present design but in spite of these limitations it has been possible to arrive at a very much improved and more flexible system. The new arrangement can be considered as two separate lasers in parallel forming an inner beam line and an outer beam line with various points of intersection. At these intersections are placed slide mirrors which give rise to various routes for a laser pulse travelling through the system. In this way various modes of operation are possible.

1.3.1(b) Operating Modes

Two oscillators for 'short' and 'long' pulses respectively are available in 'either/or' or 'and' modes to feed pulses into either one or both beam lines. The inner beam line, made up of a primary rod amplifier chain, a double pass 'feeder' disc amplifier and eventually six double pass disc amplifiers in parallel, drives the six beam compression experiments. This inner beam line can also direct pulses into a second target area for single beam interaction experiments since slide mirrors can transfer pulses from inner to outer beam lines either before or after the 'feeder' disc amplifier. Single beam experiments can also be driven from the outer beam line complete, so decoupling operations in the two target areas.

The oscillator table with its two oscillators is so arranged that the inner beam line can be fed with long, short or stacked pulses while either long or short pulses can be sent into the outer beam line. A further output beam option is generated by transferring the single beam output away from the single beam experimental area onto an x-ray backlighting target in the six beam chamber (1.01). This 'backlighting' beam has all the options available to the single beam, although, because it is only used in addition to the six beams, options involving transfer from inner to outer beam lines must employ beamsplitters rather than mirrors to ensure correct output from the six beams and backlighting beam simultaneously. If the entire outer beam line is used to generate the backlighting beam its pulse duration can differ from that of the main six beams. Such an option, in particular to provide a short pulse backlighting beam with a long pulse in the six beams was largely instrumental in determining the current design of laser system. At present we are able to provide short pulse backlighting for stacked pulse experiments, both being derived from the same oscillator pulse. A high priority is being given to early installation of simulataneous short and 'true' long pulse operation.

Several other options are concerned with the provision of beams to the target areas at rates faster than the one hour standard cycle and at reduced power levels. At the least these options save a great deal of time. For many target area setting-up procedures and commissioning of target area diagnostics, it is difficult if not nearly impossible to carry them out effectively without higher repetition rate pulses. Thus we can provide a beam to the single beam area which by-passes the disc amplifiers and can be run for example up to 20 joules in long pulses on a five minute cycle. An additional benefit is the high quality of this beam, since it does not acquire the beam distortions present in the disc amplifiers.

A further high repetition rate option is available through the outer beam line. A feature of this beam line is the ϕ 9 mm glass amplifier which can operate on a 9 second cycle and provide some tens of millijoules at this repetition rate. This beam, which can be further amplified to a few hundred millijoules on a 2 minute cycle, can be directed into the target

areas in two ways. It can form a probe beam for experiments requiring an optical probe (1.02), and for these experiments optical harmonics are usually required and a high repetion rate is necessary to establish the wavelength conversion stages. It can also be directed through the main beam channels into the six beam and single beam areas. Here again it is particularly useful for setting up harmonic crystals as well as for final adjustments on the short wavelength optics in these target areas. Table 1.01 presents the principal modes of operation of the laser currently required by experiments. These requirements formed the basis of the present laser enhancement scheme.

1.3.1(c) Pulse Generation

The layout of the oscillator tables is shown in Figure 1.02. The (remotely controlled) kinematic mirror M_c selects, according to the experimental requirements for a given shot, either a mode locked pulse or a longer pulse sliced from a Q switched oscillator. Dependent on the positions of mirrors M_c and M_s one can select, via the fixed 50 % splitter S, the options long/long; short/short or stacked/short into the inner and outer beamlines respectively. This covers all useful combinations currently required from VULCAN, in the absence of synchronized long and short pulse oscillators, and in particular facilitates experimental scheduling by allowing experiments in the two target areas to use different oscillators during the same experimental session.

The phosphate glass oscillator is mode locked by an acousto-optic loss modulator and Q switched with a saturable absorber dye. Pulse durations in the range 50 to 700 ps are obtained by varying an intra-cavity etalon. A single stage pulse selector with the Pockels cells driven by a krytron is currently in use but a two stage replacement based on a photoconductive silicon switch is being commissioned. Typical variance on the single pulse is 5 % in power and 10 % in pulse duration.

The Q switched oscillator is based on Nd:YAG which for compatibility with phosphate glass amplifiers is tuned to 1.05 μm line by means of Brewster

angle dispersing prisms and a tilted intra-cavity etalon. A two-etalon resonant reflector as output coupler constrains the oscillator to a single longitudinal mode, ensuring a smooth temporal pulse envelope. At present passive Q switching is used to facilitate single longitudinal mode selection but preliminary tests on a feedback triggered Pockels cell Q switched system have given encouraging results, and a YLF system based on this concept will shortly be tested on VULCAN. The 35 ns Q switched pulse is sliced down to around a nanosecond with a double stage Pockels cell switchout driven by a laser triggered spark gap. Durations from 500 ps (FWHM) upwards are attainable, providing a good overlap with the mode locked pulses. The pulse duration is very easily adjustable (and jitter free) since it is fixed only by the length difference between two cables driving the Pockels cells. Typically the variance of the pulse energy is around 6 %.

Pulses from either oscillator are preamplified with 9 mm and 16 mm aperture phosphate glass rod amplifiers before passing through the diffraction limited spatial filters.

1.3.1(d) Staging

The staging design is based on that in use on the previous system. A pulse from the oscillator table passes through a diffraction limited spatial filter which injects an expanding near perfect quasi-Gaussian beam into the amplifier system. The quasi-Gaussian distribution is modified by an apodiser and the radial gain profile in the rod amplifiers to provide as flat a beam as possible at the laser output without severe edge diffraction effects. Improvements in design based on image relaying were considered but not implemented due to their limited cost effectiveness. The design includes vacuum spatial filters in both inner and outer beam lines to minimise nonlinear beam breakup and generally improve beam quality. Modifications to the existing scheme are being considered to include such filters between laser and target areas to improve beam illumination uniformity at the focusing lenses and on target. Such changes await detailed appraisal of the beam distributions present, coupled to further computational studies using our diffraction propagation

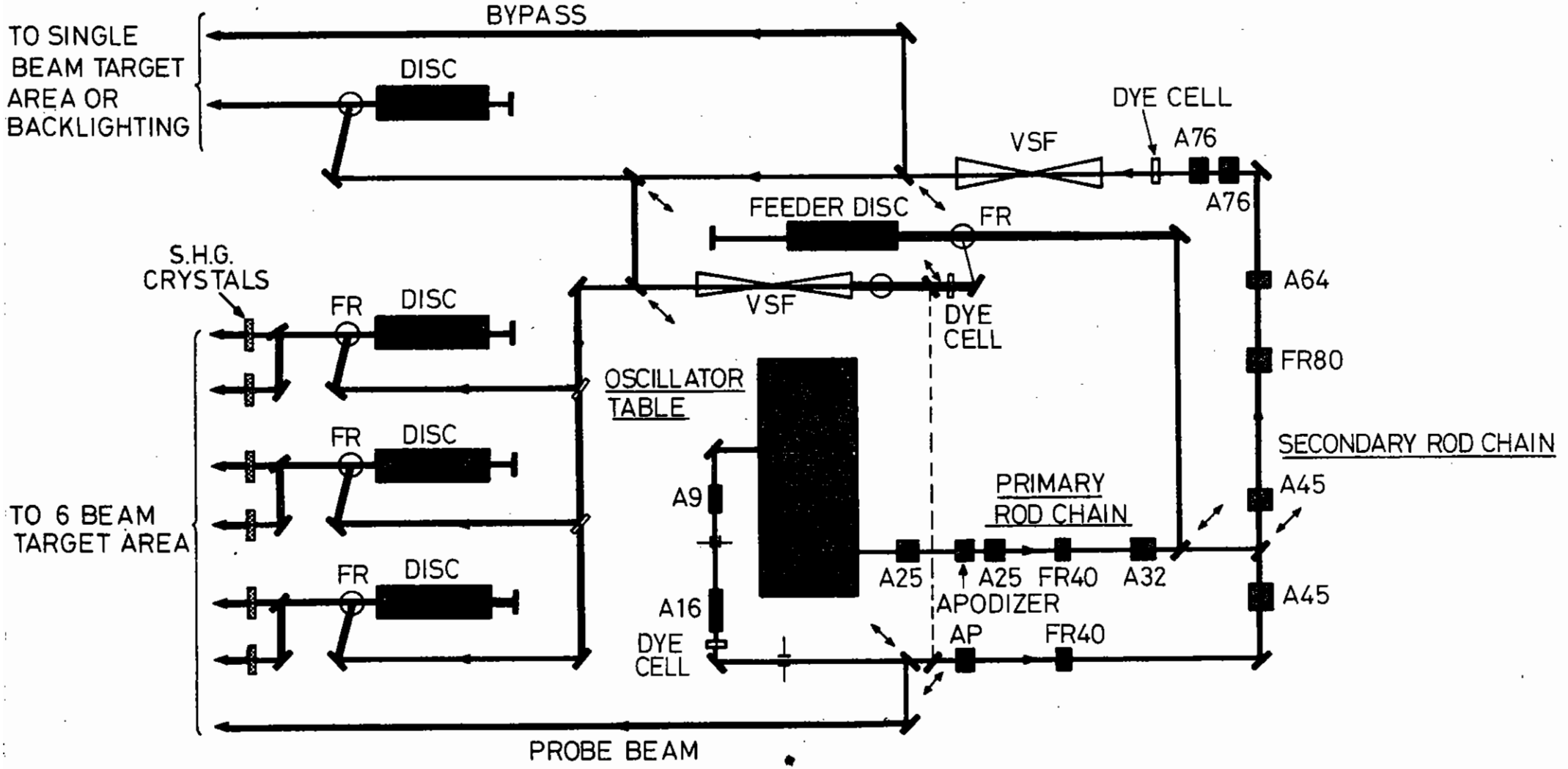

FIG 1.01 Schematic of VULCAN laser system.

TABLE 1.01

PRINCIPAL MODES OF OPERATION OF VULCAN LASER SYSTEM

INNER BEAM LINE → PRIMARY ROD CHAIN I, FEEDER DISC, MAIN DISCS

OUTER BEAM LINE → PRIMARY ROD CHAIN II, SECONDARY ROD CHAIN, SINGLE BEAM DISC

	PRIMARY ROD CHAIN I	FEEDER DISC	MAIN DISCS	PRIMARY ROD CHAIN II	SECONDARY ROD CHAIN	SINGLE BEAM DISC	TIME BETWEEN SHOTS	PULSE	ENERGY PER BEAM (J)
	TARGET AREA ONE								
6 Beams	*	*	*				60 min	Long/Short	200/60
6 Beams	*	*	*				60 min	Stacked	100
+ Backlighting Beam				*	*	*		Short	60
6 Beams	*	*	*				60 min	Long/Short	200/60
+ Backlighting Beam	*	*				*		Long/Short	200/60
	TARGET AREA TWO								
Disc Mode	*	*				*	60 min	Long/Short	200/60
Rod Mode	*				*	*	60 min	Long/Short	200/50
Bypass Mode	*				*	*	5 min	Long/Short	20/5
Probe Beam				*			2 min/5 sec		500mJ/50mJ

NOTES:
(i) Reduce 6 Beam Energy by a factor 2 for interim scheme
(ii) Wavelength - all modes can operate at fundamental or harmonic
(iii) Probe Beam - always available with same options as backlighting beam

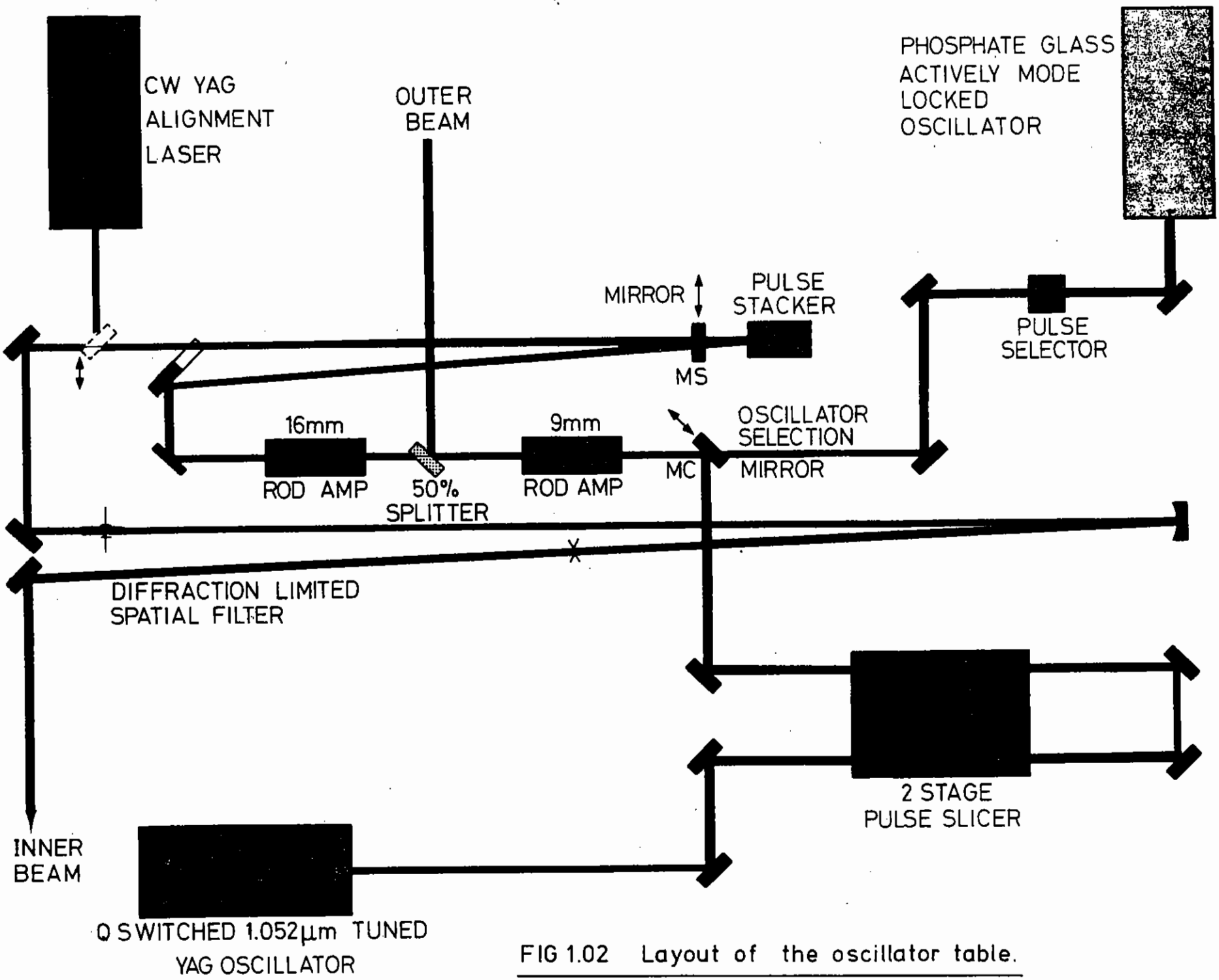

FIG 1.02 Layout of the oscillator table.

code.

Double passing of the disc amplifiers has been retained and extended. Only by so doing was it possible to build with available components a system with two distinct high power beam lines. This technique has now been successfully in operation for three years, and its only limitation, given the high damage levels obtained with commerical polarizers, is some reduction in short pulse power resulting from the nonlinear effects in the Faraday isolator, now the final components of the laser.

1.3.1(e) Beam Intensity Profiles

This is one of the most important considerations in large laser design because it is so closely related to both beam quality on target and to the maximum power and energy from a given laser system. Two aspects of laser design required consideration for their effects on the beam profile and thereby on the beam quality on target and the efficiency of the laser. The first related to the considerable modification to the beam profiles due to the non-uniform radial gain profile in the rod amplifiers. In a single beam line laser the input profile is modified to take this into account and hence optimise the output profile. This was not possible for all modes of operation in VULCAN since the preliminary rod amplifier section can feed either larger rod amplifiers which change the beam profile or a disc amplifier which does not. No input profile is optimum for both options. The solution adopted to overcome this difficulty is to introduce a large aperture rod amplifier fitted with highly doped neodymium glass into the disc beam lines. Adjustment of its pumping level can then be used to compensate for the lack of several rod amplifiers in that beam line.

There are distances up to 30 m between laser and target chamber in the VULCAN laser and there can then be considerable changes and perhaps deterioration in beam profile propagating over this distance. These changes are sensitive to small changes in amplitude and phase at the laser output so that any means of control over these parameters is potentially useful in exerting control over the beam profile at the target chamber.

Such a means is provided by the apodiser. It consists of a cell filled with an absorbing liquid between profiled windows, the liquid being temperature index-matched to the windows. Small changes in temperature result in small phase errors on the beam and provide a useful means of varying the overall profile downstream particularly near its edge.

1.3.1(f) Phase Errors

Some phase errors, largely astigmatic, are introduced onto the beam by the double pass disc amplifiers, the magnitude of this effect being repetition rate dependent. The VULCAN design places two disc amplifiers in series in the main beam lines and ensures that the beam is rotated by 90° between these two amplifiers. By so doing a compensation of small astigmatic phase errors is achieved and higher repetition rates can be used.

1.3.1(g) Harmonic Operation

One of the strengths of VULCAN is its ability to provide several wavelengths for studies of wavelength dependent effects. Together with the fundamental at 1.05 μm, wavelengths at second (0.53 μm) third (0.35 μm) and fourth (0.26 μm) harmonics are available in the single beam target area and six 0.53 μm beams in the six beam target area with appropriate use of large aperture KDP crystals.

Apart from increasing the overall versatility of the laser there are technical advantages to operating at one of the harmonics resulting from the nonlinear response of the conversion process, namely the relaxation of the normally severe requirements on the amplified spontaneous emission and prepulse levels of the laser and reduction in sensitivity of the laser to target back reflections. Saturable dye cells normally inserted to limit these effects may be removed for harmonic experiments resulting in significant increases in achievable power and energy and improvements in beam quality.

1.3.1(h) Electrical Installation

The capacitor banks for the disc amplifiers and Faraday rotators, manufactured by Laser Applications Limited, have been installed and commissioned. Apart from a minor problem with damping resistors the equipment is looking well. The amplifier system now comprises three switching ignitrons each intended to drive two amplifiers while the Faraday system has two ignitrons driving up to six isolators. The amplifier and Faraday systems each have a single charging supply and in order to ensure that each ignitron discharges only its associated capacitor banks isolating diodes and fuses have been connected into the charging lines to prevent any cross coupling. The voltage diodes for sensing capacitor voltage were connected at the output of the power supply. When end of charge was reached the power supply turned off and, due to the isolating diodes, effectively disconnected the sensing circuit from the capacitor bank causing the voltage control to become unstable. To overcome this problem the voltage divider was connected to each capacitor bank using a diode as shown in Figure 1.03. The power supply is switched, using high voltage relays, to provide charge for the PILC capacitors and these too are connected back to the voltage divider using a diode. A similar arrangment is used for the Faraday isolator power supply and satisfactory voltage control is achieved.

The amplifier system uses a single earth point to which all the individual amplifiers are connected. It is possible, therefore, for return current to be conducted not only along the braiding of the cable connecting a set of capacitors to the flash lamps but also by all other parallel paths including the braiding of the charging cable interconnecting the ignitrons. When all amplfiers are in use currents along these spurious paths tend to cancel out but in the new six beam system the number of amplifiers required changes from shot to shot and cancellation is not normally achieved. Currents measured in 1000's of amps flow round the system in an undefined manner. While this cannot be altogether avoided using the present earthing policy, any undesirable effects due to the current loops created have been reduced as much as possible by reducing the current flow between ignitrons to negligible amounts by interposing

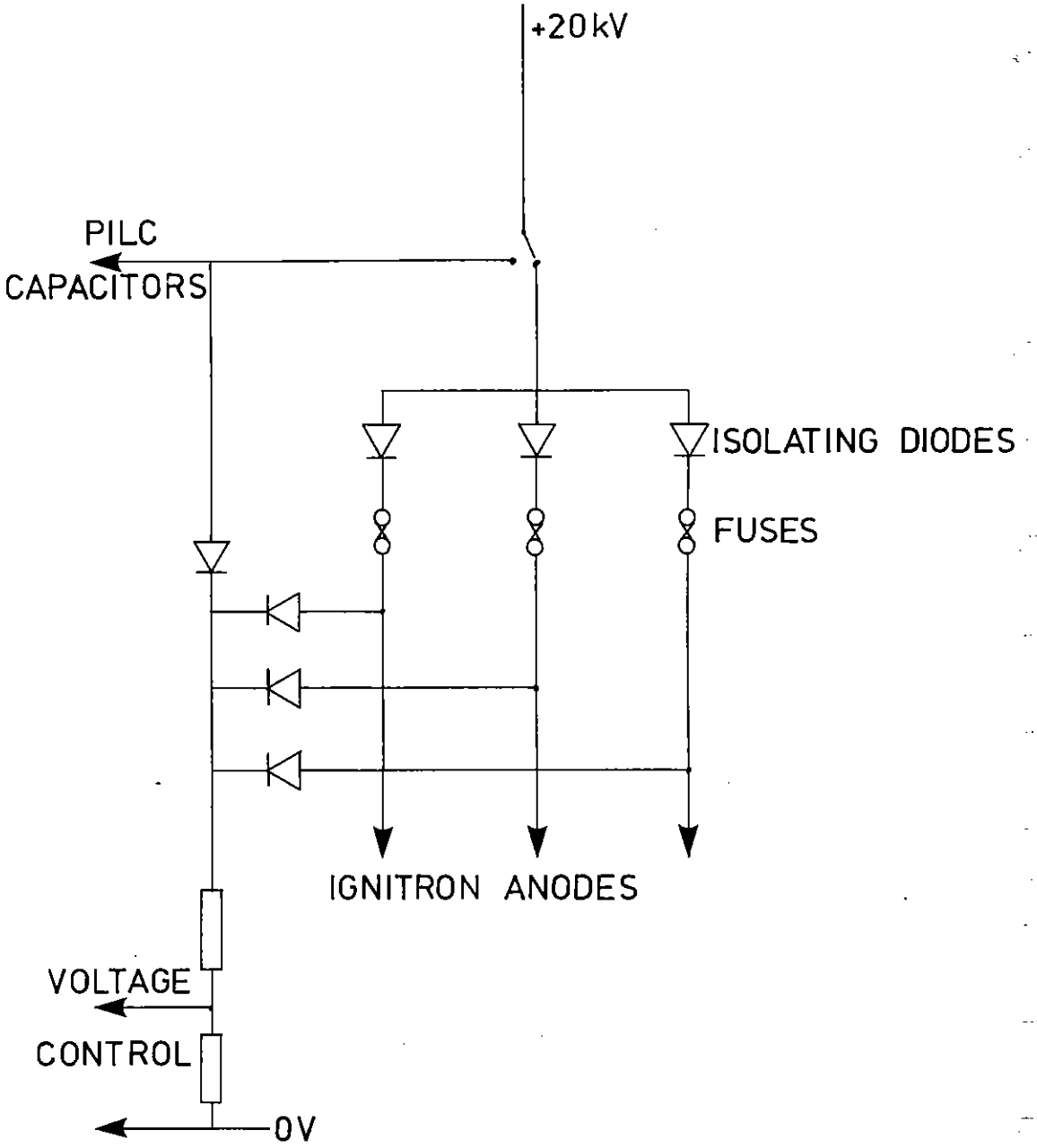

Figure 1.03 Amplifier power supply system

50 Ω resistors in the outer conductors of the charging lines and by ensuring that all high current return paths are channelled along the route of the discharge pulse so as to minimize the area of the current loops.

Additions have been made to the PILC system to allow simultaneous PILC for all five disc amplifiers at present operating. The circuit is shown in figure 1.04. When all amplifiers are in use the total PILC capacitance is 75 μF which is discharged through 50 flash lamp series pairs in parallel. For this to work satisfactorily the triggering characteristics of the flash lamps must be reasonably matched. A recent batch of lamps has characteristics which indicate PILC failure even when a pair of amplifiers connected to a single switching ignitron is subjected to PILC. This configuration has until now always worked. However, by selecting amplifiers in turn the PILC system will operate and the computer control system has been designed to allow for this procedure if required.

1.3.1(j) Computer Operation

To achieve safe and efficient operation of the Laser Facility a mini-computer has been interfaced to the laser itself and to some of the experiments. It consists of a GEC 4080 CPU with 128 K bytes of main memory, 20 M bytes of disk space, fast paper tape, 2 printers, 3 VDU's, 2 graphics terminals and a link to the Laboratory IBM 360 mainframe complex. The laser interface is implemented in CAMAC and gives the operator the facility to check the settings on the laser, the interlocks, the voltages on the capacitor banks and the position of various movable items of equipment (mirrors, beam stops, dye cells etc). The information is displayed on a VDU and on a colour graphics diagram of the laser layout (see Figure 1.05). Once the operator is satisfied that the laser configuration is as required and that all the running conditions are correctly specified, the shot is initiated and the computer checks the interlocks and runs the sequence automatically. The diagnostics from the shot are displayed and a log is printed on a hard copy unit via one of the graphics terminals. The data, which includes energies, voltage levels, switchout and prepulse waveforms etc are archived for future reference. Work is in hand to monitor beam quality automatically via TV cameras and a

video disc interfaced in to the computer.

As part of the above shot sequence, experimenters equipment can be initialised before the shot and the data can be read, analysed, displayed and archived after the shot. Because of the link, it can also be sent to a more powerful computer system for further analysis if required. Currently, point readings can be taken using ADC's, waveforms can be acquired using various waveform analysers and pictures can be digitised using an optical multi-channel analyser. An online graphics input tablet and microdensitometer provide local data analyses between shots for line data and film and the computer operating system allows new programs to be edited, built and tested during operation periods. A more detailed description of the system can be found in (1.03).

I N Ross, M S White, J E Boon, D Craddock, A R Damerell, R J Day, A F Gibson, P Gottfeldt, D J Nicholas and C J Reason (RAL)

1.3.2 Pulse Generator Development

The pulse generator development work during this reporting year has been largely concerned with the designing and commissioning of the new front end of VULCAN. In addition a mode locked pulse selector based on a photoconductive silicon switch was fully commissioned early in the year (but not installed on VULCAN due to lack of funds) and promising preliminary results have been obtained from a Pockels cell Q switched single longitudinal mode oscillator.

M S White (RAL)

1.3.2(a) VULCAN Front End

The new front end system for VULCAN is shown in figure 1.02 and briefly described in section 1.3.1(c). Although there are similarities with the old system from which it derived, there are many changes and improvements. The whole layout has been expanded to occupy about twice as much optical table area, allowing enerineering improvements in some critical mirror and

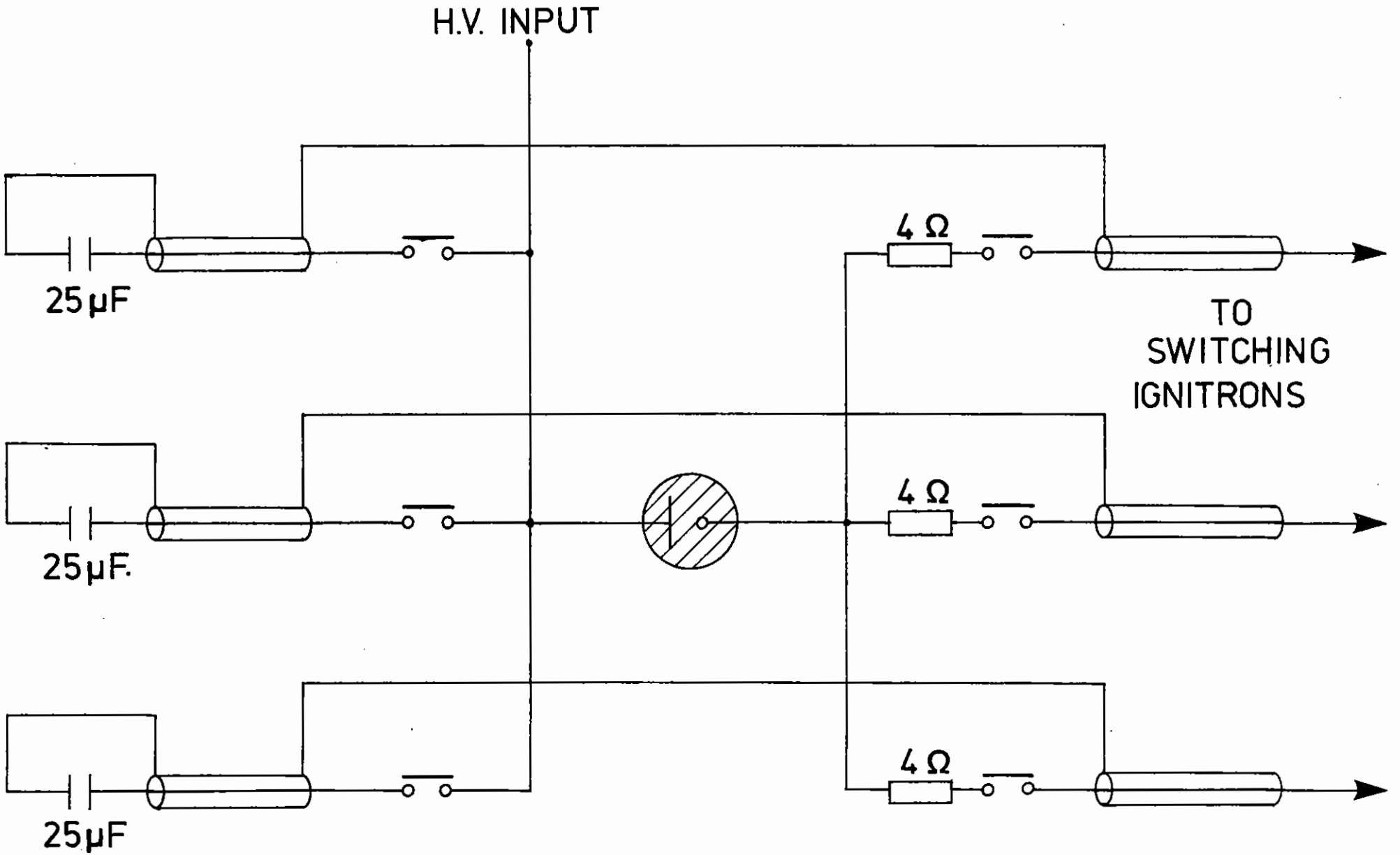

Figure 1.04 P.I.L.C. system

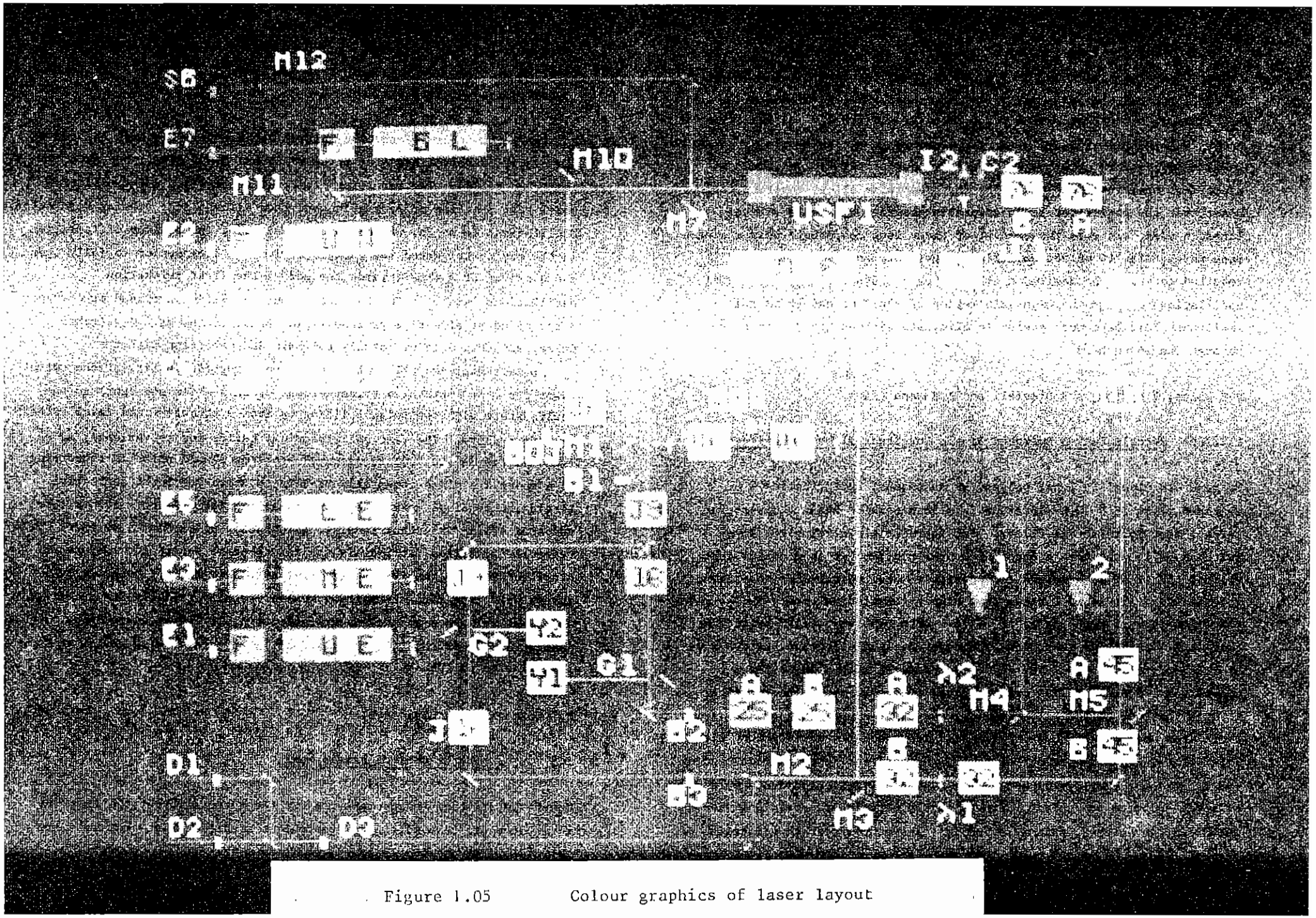

Figure 1.05 Colour graphics of laser layout

component mountings. The long pulse slicer, which selects a variable (∿ 1 ns) pulse from the Q switched oscillator, has been converted to a two-stage system giving an improvement in power contrast ratio from 10 up to 10 . Its Pockels cells, which had previously been DC biased at ∿ 6.5 KV, are now pulse charged for ≃ 50 μs around the time of the laser pulse, and the reduction in electrical duty cycle has shown great benefit in terms of Pockels cell longevity and freedom of the system from electrical breakdown problems. The improved pulse slicer contrast ratio meant that the oscillator bench saturable absorber dye cells were no longer needed, and with the removal of these long components only a single pass through the 16 mm rod amplifier (previously double passed) was required to reach the desired oscillator bench output energy. Parasitic oscillations through the high gain region of the 9 mm and 16 mm rod amplifiers have been much easier to eliminate without the second pass through the 16 mm head.

M S White, I N Ross, A R Damerell and J E Boon (RAL)

1.3.2(b) Pockels Cell Q Switched Single Longitudinal Mode Oscillator

To generate 'long' (≃ 1 ns) pulses for subsequent amplification a Q switched pulse of ∿ 30 ns duration is sliced down to about a nanosecond using a fast Pockels cell slicer. For reproducible slicing the input Q switched pulse must have a smooth temporal profile, which dictates that the oscillator be constrained to run single longitudinal mode to prevent mode beating. It is well known that single longitudinal mode (SLM) operation is very much easier to achieve with passive (dye) Q switching than with most active techniques, because the long effective buildup time of passively Q switched pulse (∿ 0.5 μs compared with ∿ 50 ns for a conventional Pockels cell Q switch) gives the pulse many more transits through the mode selecting etalons. The current VULCAN long pulse oscillator uses passive Q switching, and is reasonably satisfactory with ∿ 7 % fluctuations in the output power and ∿ 1 % incidence of mode beating shots. However the intelligent active Q switch (IAQS) provides a more reliable and more convenient approach to SLM oscillator operation. The technique, in which a prelase period is followed by feedback triggering of

the Q switch, was first proposed by Hanna et al in 1972 (1.04). A test oscillator has been built and operated where this idea was extended and combined with the long-resonant reflector method of SLM selection already in use on the VULCAN oscillator.

In the IAQS test oscillator the initial Pockels cell bias was set not to the quarter wave voltage (as in conventional Q switching) but at slightly less than V(λ/4). The resulting 'leaky' Q switch held off oscillation until near the time of peak gain, but then allowed free running relaxation oscillations to begin. A photodiode monitoring the buildup of radiation in the cavity triggered the Pockels cell drive electronics to fully open the Q switch at a time towards the end of the first relaxation oscillations 'spike'. So the relaxation oscillation provided more than a microsecond of effective prelase period prior to the main Q switched pulse, and this allowed totally reliable SLM selection with the appropriate etalons. Also the shot to shot reproducibility of the output power was most impressive (fluctuations of only a few per cent) as one would expect with the pulse building up from a predetermined level rather than from noise. The test oscillator was built, for convenience, as a 1.064 μm YAG device. No fundamental problems should arise in converting to a phosphate glass comparible wavelength where YLF looks attractive. Single longitudinal mode selection was accomplished using a 100 mm thick uncoated etalon as output coupler, in conjunction with a 15 mm thick 75 % reflectivity tilted intracavity etalon. Because no eltalon temperature stabilization was possible on the test system it was not possible to investigate long term stability. However totally reliable SLM selection and remarkable shot to shot power reproducibility were convincingly demonstrated, and the IAQS oscillator will be pursued with a view to installation on VULCAN.

M S White and I N Ross (RAL)

1.3.3 Computer Control Development

Under the six beam enhancement project the versatility of the laser in terms of rapid beam switching from target area to target area and beam

configurations for different experiments has been greatly extended. To this end a significant number of remotely operated mirrors and other devices have been incorporated. While these are not controlled by the computer, positional information is relayed back. The original computer operating system allowed a number of 'modes' of operation to be selected and the computer would check that the laser was currently set up for the shot defined by the mode.

It was considered that an extension of this system for the upgraded laser would have become rather cumbersome and inflexible in view of the large number of possible operating modes. Alternatively the modes would have had to be defined so loosely as to make them largely meaningless. This scheme was, therefore, abandoned in favour of allowing the operator to set up the laser in any desired configuration using standard manual switching controls. All relevent information on settings is fed back to the computer and is used to up-date a mimic diagram produced on a colour graphics terminal which has been added to the system and is central to the new control philosophy. The display indicates the selected beam paths and which amplifiers and pulse generators have been switched on; it allows the operator to see exactly how the laser is intended to perform. The charging and firing sequence is under computer control and is initiated by pressing a single button. The computer checks that the selected laser configuration is permissible and issues appropriate warnings if any abnormal or unusual situation is detected; such as a dye cell left out or a beam expander in the beam path. Certain situations can be bypassed by pressing the button a second time but anything considered unacceptable must be put right before the button is pressed again. The computer then checks all interlocks before proceeding with the firing sequence. Capacitor charging may be observed from a bar chart, where the height of each bar indicates the state of charge of a particular amplifier or Faraday isolator, produced on the colour graphics terminal. After the shot, beam energies are read and presented on a recently added large screen monitor and a log is produced. Other diagnostic and experimenters programmes are run as selected by the laser operator in a way similar to that of the previous operating system.

The changes described above have necessitated a complete re-write of the laser program which currently takes up 45 K bytes of memory (ie some 5000 lines of Babbage high level assembler code). The local colour graphics system now allows colour contour maps to be produced locally but hard copy is only available using the main laboratory facilities.

P Gottfeldt (RAL)

1.3.4 Computational Studies

A number of beam propagation studies have been carried out using our diffraction propagation code (1.05). This code has recently been modified, the quasi-optical equation being solved on a variable mesh geometry specified by a geometrical ray trace. This has several advantages when dealing with focusing beams, spacial filters and in treating the analysis of beam filamentation. We outline in this section some beam propagation studies carried out on our two beam system (1.06).

Once this particular laser system has been programmed into the code it is possible to analyse its performance by changing any one of the many laser design parameters. The examples given here demonstrate various ways that information extracted from the code can give us a greater insight into the performance of the laser system. We have used two variable input parameters to map out this performance. One is the input power; the other is the spatial noise intensity on the input beam ($\varepsilon = (I_{max} - Imin)/Irms$). This attempts to model the stochastic noise, both in amplitude and phase, generated by the system.

The effect of varying this noise and hence the degree of small scale beam break-up can be seen in Figure 1.06. The value of having the facility of turning off the nonlinearity and diffraction can also be seen by comparing the nondiffraction distribution with, for example, the low noise diffraction case. The effect of diffraction can be seen to give a somewhat larger beam at 25 m downstream (diameter increased by 3½ %). The degree of enhancement of spatial noise is very evident from these distributions. Thus we can see for example from the second distribution

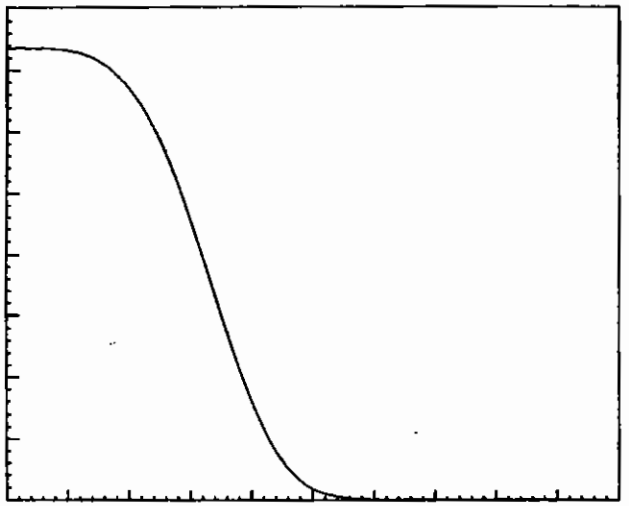

No diffraction: $\varepsilon=0$

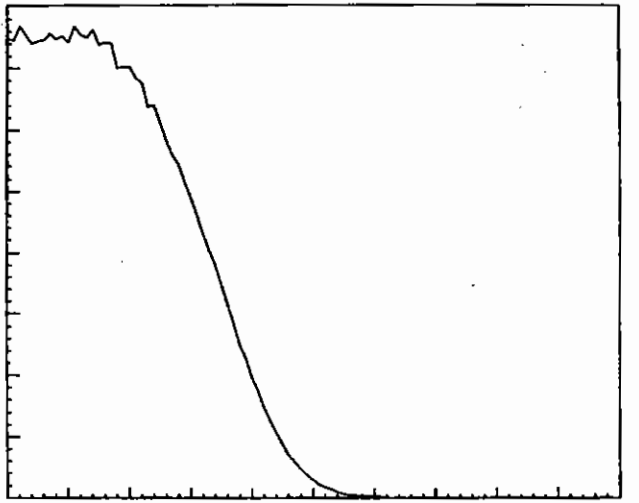

Diffraction: $\varepsilon = 10^{-4}$

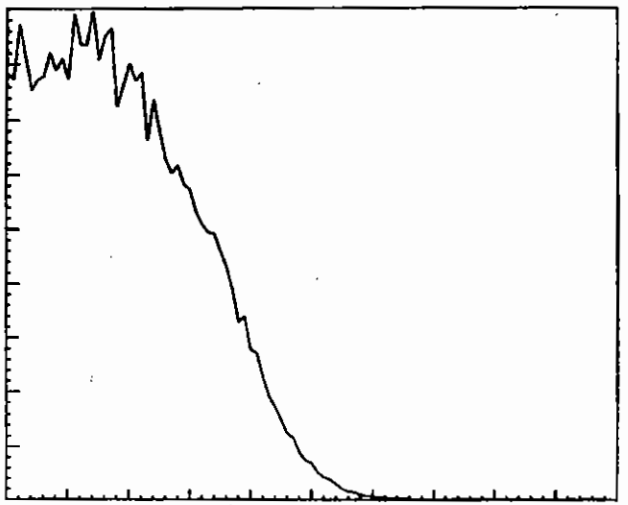

Diffraction : $\varepsilon = 10^{-3}$

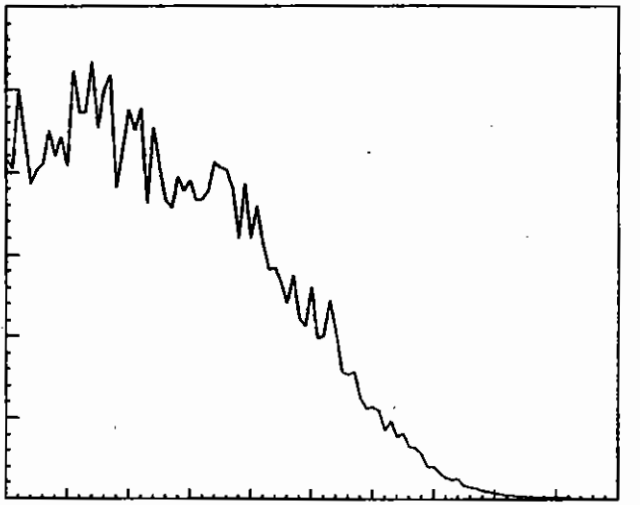

Diffraction : $\varepsilon = 10^{-2}$

Fig 1.06 Beam intensity distributions at 25m for different input intensity noise factors

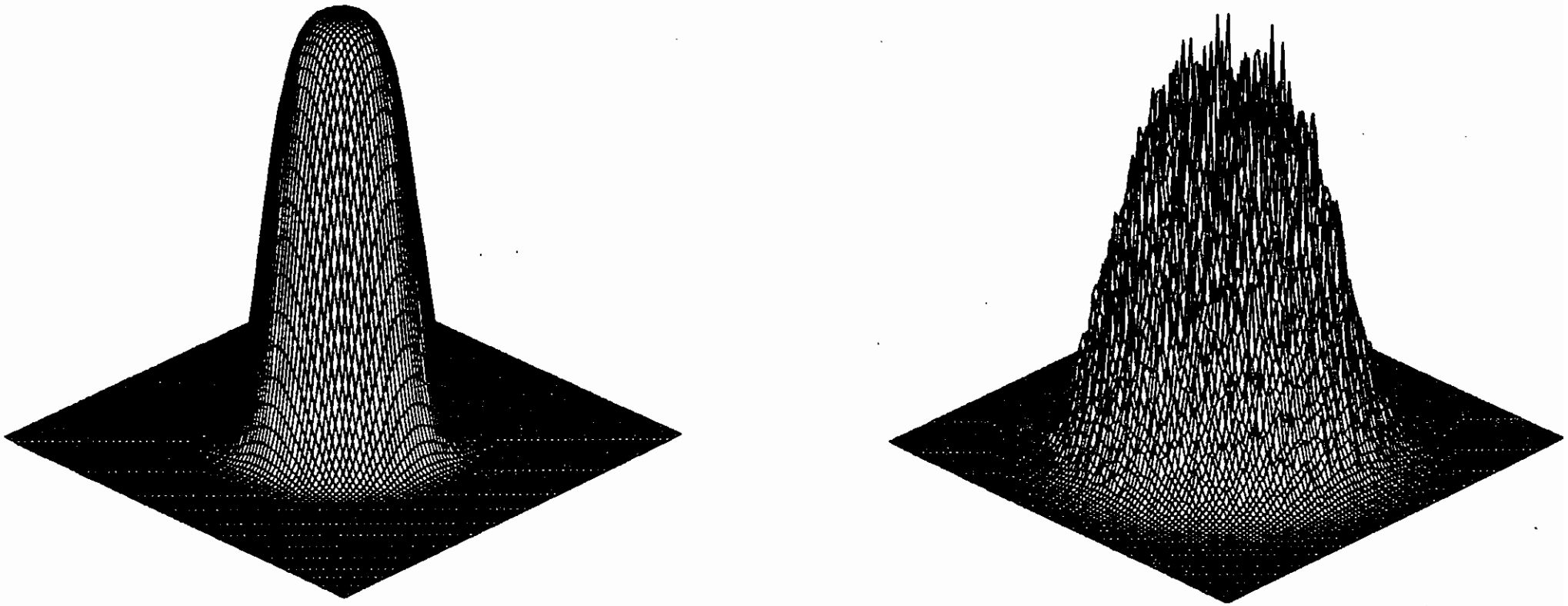

$\varepsilon = 0$ $\varepsilon = 10^{-2}$

Fig 1.07 Beam intensity distributions at 25m for zero and high input intensity noise

that an input noise modulation of 0.01 % is enhanced to 8 % by the nonlinearity, and from the third distribution that the input noise modulation of 0.1 % reaches 34 % at the output of the laser.

Figure 1.07 shows the first and last examples of Figure 1.06 plotted in 3D. Of particular note is the large increase in beam divergence at the high input noise level depicted here; leading to a considerable reduction, caused by nonlinear effects, in the focussable power achievable in practice with the laser.

It has been observed experimentally that not only does the laser system itself greatly enhance the noise modulation on the beam but this modulation can be further enhanced when the beam propagates large distances beyond the laser to the target chamber. This distance can be as large as 70 m for the Rutherford Facility. So it is important for our system to assess the importance of this distance to the beam characteristics. Figure 1.08 shows the computer prediction in a preliminary survey. The variation of noise modulation with distance away from the laser is plotted for different input noise modulations. We can see that, as observed elsewhere and also at Rutherford Laboratory, the beam is predicted to deteriorate so far as noise modulation is concerned. Thus even for low input noise at 0.01 %, the output beam noise modulation increases from 1 % at the laser output to 19 % at the 50 m downstream.

One of the principal reasons for concerning ourselves with this aspect of the beam propagation is in connection with damage to the expensive focusing lenses and other optics in the vicinity of the target chamber. However for this consideration it is the peak intensity in the beam which determines the onset of damage. Figure 1.09 shows how the peak intensity changes when the beam propagates away from the laser. Although Figure 1.08 showed large increases in the noise modulation Figure 1.09 shows that this does not automatically mean high peak intensity and hence a greater damage to components sited there. This apparent anomaly is due to there being a reduction in average beam breaking up in this way. It is worth noting also that for high levels (and also for high input beam intensities) there is an optimum plane downstream at which peak intensity

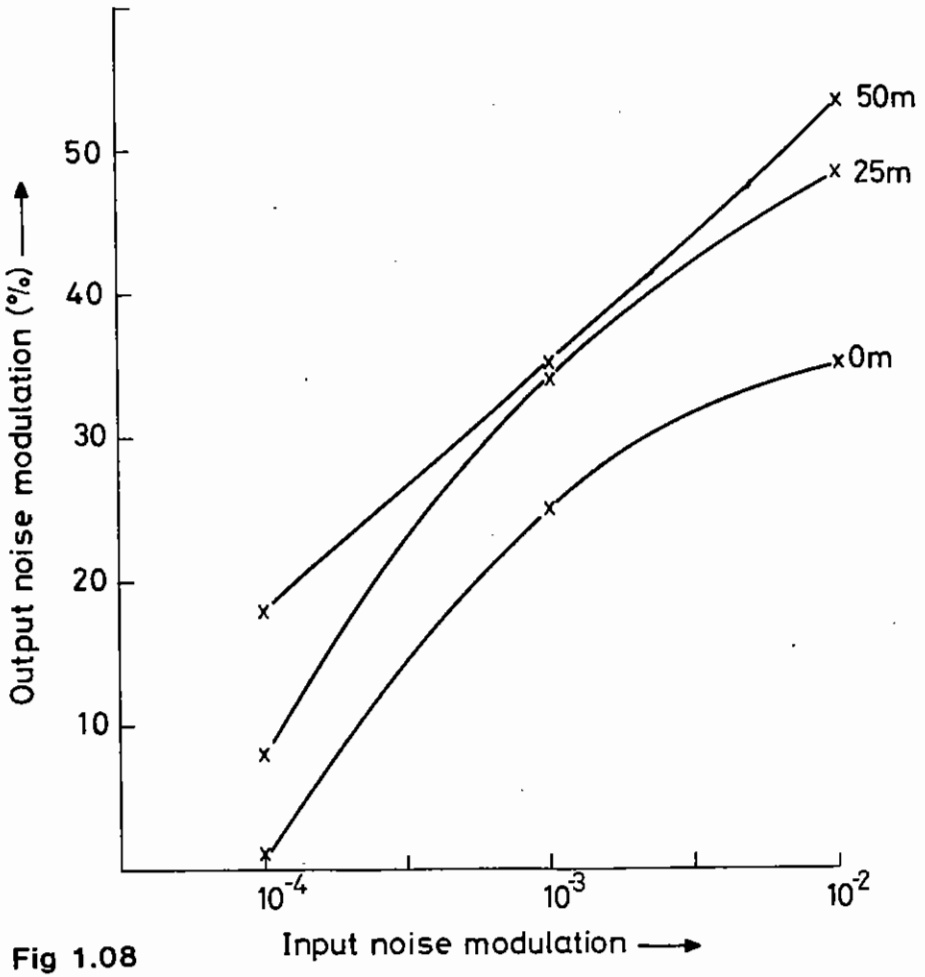

Fig 1.08

Nonlinear enhancement of spatial intensity noise in a laser and the effect on subsequent beam propagation in air

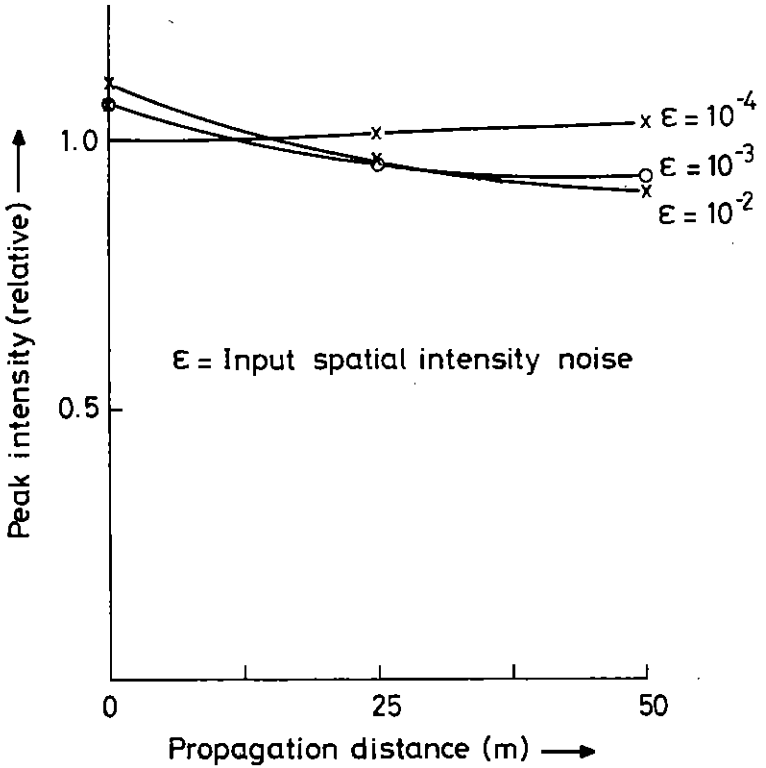

Fig 1.09

Variation of peak intensity at focussing lens with distance of lens from laser

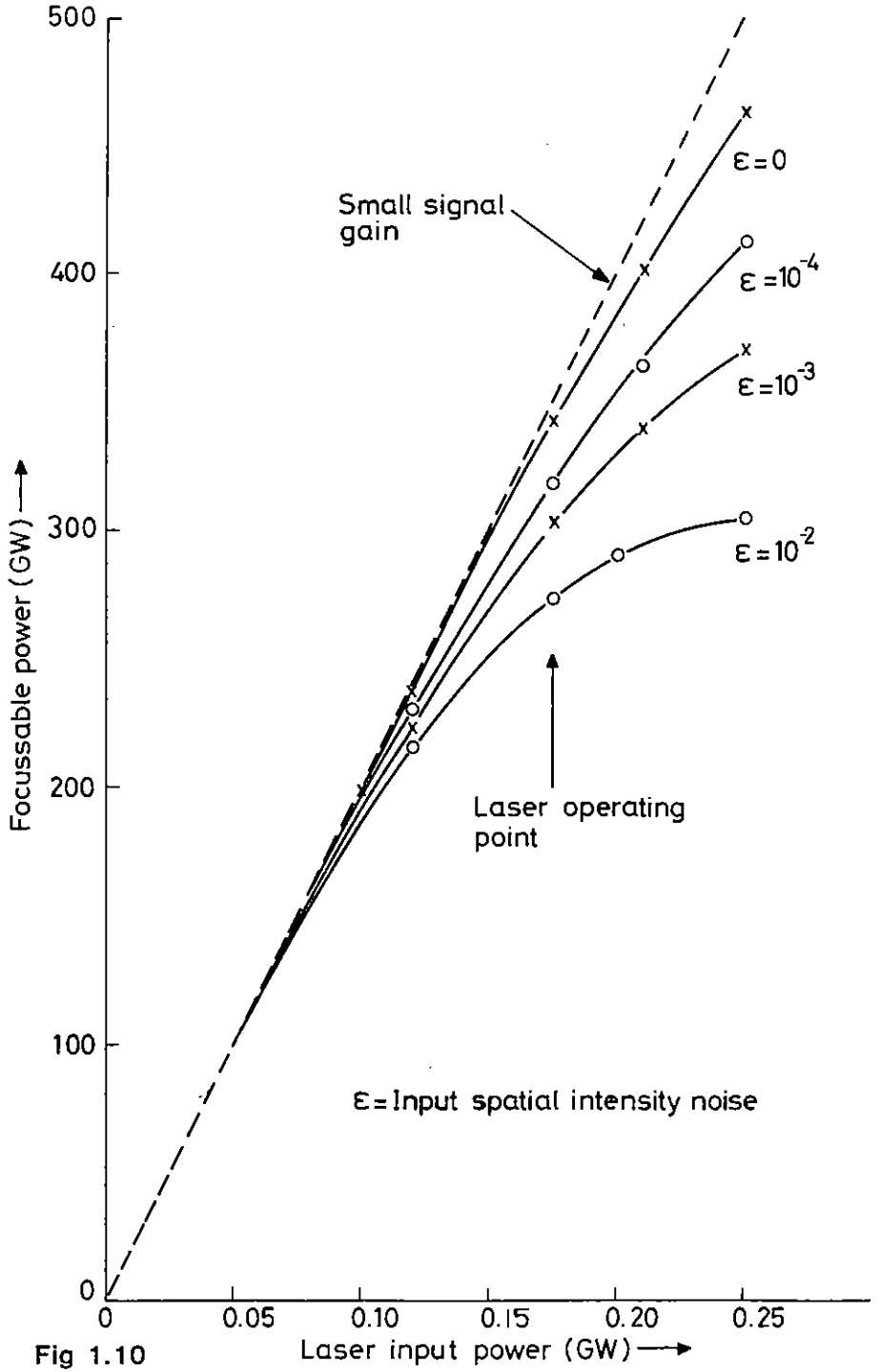

Fig 1.10

Effect on focussable power on nonlinear beam breakup

is a minimum. However this effect is not very marked.

Finally, and perhaps of greatest importance, is the fraction of the laser power focusable on target or the peak intensity achievable in the beam focus. Many experiments are of the former type in which it is important to couple as high a power as possible onto a particular target. A typical experiment at the Rutherford Laboratory uses a 100 μm diameter spherical microballoon target at the focus of an F/1 doublet focusing lens. The power of the propagation code in also modelling the beam focusing enables us to calculate the coupling efficiency onto the target. Figure 1.10 shows some examples of how the focusable power increases with input power at various levels of input spatial intensity noise. The effect of the nonlinearity is clearly demonstrated for the curve at an input noise modulation of 1 %. The focusable power is severely reduced below the laser output power to the point where there is a maximum. Beyond this maximum an increase of input power to the laser results in a decrease of power focusable on target and the laser has exceeded its power limit for one particular lens - target configuration.

D J Nicholas (RAL)

1.4 Target Areas

1.4.1 Target Area TAI

Compression experiments with infra-red irradiation of targets have been carried out in the area up to September 1980. During this period a new vacuum lock target insertion mechanism (section 1.4.3) was installed on the chamber and the new minature X-ray streak camera (section 1.6.1) successfully commissioned and operated experimentally with both spectrometer and pinhole front ends. Experimental operation with the vacuum lock proved extremely successful allowing the target chamber (and streak camera) to remain evacuated for lengthy periods and reducing considerably the time between compression shots. A second vacuum lock, for the insertion of X-ray backlighting targets, has been assembled and is waiting to be installed on the chamber, and in addition new pinhole

cameras incorporating vacuum locks for film removal are being designed.

Arrays of 10 plasma calorimeters and 5 Faraday cup ion detectors have been installed permanently in the target chamber and used to monitor all compression experiments. The output from all these devices is fed direct to the computer monitoring system allowing immediate post-shot indication of absorbed energy, ion velocities and plasma expansion isotropy.

Since September 1980 work has taken place in the experimental area to convert it to operation with six frequency doubled (green) beams for compression experiments. Full aperture (110 mm diameter) type II KDP harmonic generator crystals have been installed on a space frame in the laser amplifier room at the end of the six beam lines just before they enter the target area. A quartz half-wave plate in front of each crystal is used to rotate the input infra-red beam polarization so that the output green beams have polarization directions compatible with the optics in the target area. These waveplates are also used to balance the energies in the six green beams.

All main turning mirrors in the target area have been replaced and the three level reference and alignment platform optics extensively modified. The three small 100 mW Nd YAG alignment lasers (one for each platform level) have been replaced with an argon-ion laser which delivers over 500 mW at λ = 528 nm. The output from this laser is split, expanded to full beam diameter and injected into each of the six main beams for target alignment purposes. Referencing of these green alignment beams to the CW infra-red beams from the main laser system is accomplished as before using telemicroscopes coupled to silicon targeted television cameras. To facilitate this process f/5 telemicroscope lenses having the same focal length at λ = 1.054 μm and 0.527 μm have been designed (section 1.4.4) and installed. Six f/1 doublet lenses optimized for green operation have been installed in the target chamber.

Calorimetry of the energies in each of the six green beams is performed in the target area while incident infra-red beam energies are monitored in the laser area. Both outputs are fed directly to the computer monitoring

system allowing rapid indication of shot conversion efficiencies.

Crystal tuning has been carried out using the high repetition rate, small diameter alignment beam system (section 1.3.1) which delivers pulses of about 100 MW every 9 seconds down each of the six beam lines. Each crystal has been rapidly optimized in angle by monitoring the incident infra-red and generated green energies using silicon diodes and displaying the two signals on a storage scope operating in X-Y mode. An EPL streak camera has been used to monitor the arrival time at the centre of the target chamber of these low power high repetition rate green pulses and allow beam path equalization to be carried out.

C Hooker, S Knight and P T Rumsby (RAL)

1.4.2 Target Area TAII

The major development in TAII during the past year was the conversion of the primary laser beam to its third harmonic. The Rochester high efficiency polarisation mismatch scheme (1.07) (1.08) was used. A successful series of irradiations was carried out with more than 100 third harmonic shots on target (see sections 3.6 and 4.4). The preparatory work and the blue beam system are described here.

Phase matching angles for $\omega_o^o + \omega_o^e \rightarrow 2\omega^e$ and $\omega_o^e + 2\omega_o^o \rightarrow 3\omega_o^e$ were measured at low power at two wavelengths and various temperatures. The results are summarised in Figure 1.11. A programme was written to compute phase matching angles from published data (1.09) (1.10). The results, in particular the strong wavelength dependence of the phase matching angle for type II tripling, are in agreement with the measurements and with similar calculations by Craxton (1.11) although, as he observes, such details as the wavelength at which the angles for type II doubling and tripling become equal are sensitive to the method used to fit Zernike's data and must therefore be measured directly.

An angle tuning curve for the tripling crystal is shown in Figure 1.12. We have found it adequate to compensate for temperature variations of up

to 5° by adjusting the tilt of the crystal in accordance with our measured temperature dependence.

Programmes were written to compute harmonic conversion efficiencies (1.12) for arbitrary beam pulse shapes and spatial distributions. All reflection losses are included, and the small absorption at 1.06 μm is dealt with approximately. Our results are in good agreement with those of Craxton (1.08). The computed second harmonic efficiency is shown in Figure 1.13 for several beam distributions. In converting from intensity to energy the full width at half maximum should be used for the pulse length and twice the area which contains half the beam energy should be used for the effective area.

In the polarisation mismatch scheme for third harmonic generation, the second harmonic is produced in a type II crystal with the o-axis at 35° to the polarisation of the fundamental. The effect of this mismatch on the second harmonic is shown in figure 1.13: there is a broad maximum in the efficiency and the ratio of the power in the harmonic to that in the fundamental is close to 2:1 for a wide range of incoming power, which is the optimum condition for summing. The third harmonic conversion efficiency is shown in Figure 1.14 for our combination of a 12 mm doubling crystal and a 9 mm tripling crystal. The very rapid drop in the single ray conversion efficiency for powers above 3.2 GW/cm^2 is due to the extreme sensitivity of the conversion to the relative amounts of fundamental and second harmonic. The smoothing seen in the curves for non-uniform beam intensity is to some extent illusory since at high average power the conversion efficiency at the peak of the pulse in the centre of the spatial distribution is very low. This effect is illustrated in Figure 1.15.

The arrangement used for target irradiations with the third harmonic is shown in Figure 1.16. The second harmonic crystal is mounted in a cell containing index matching fluid. The third harmonic crystal is also mounted in an unmatched cell. In previous experiments with the second harmonic we found the anti-reflection coatings prone to damage, so all eight surfaces are uncoated. Tuning optimisation was done at low power at

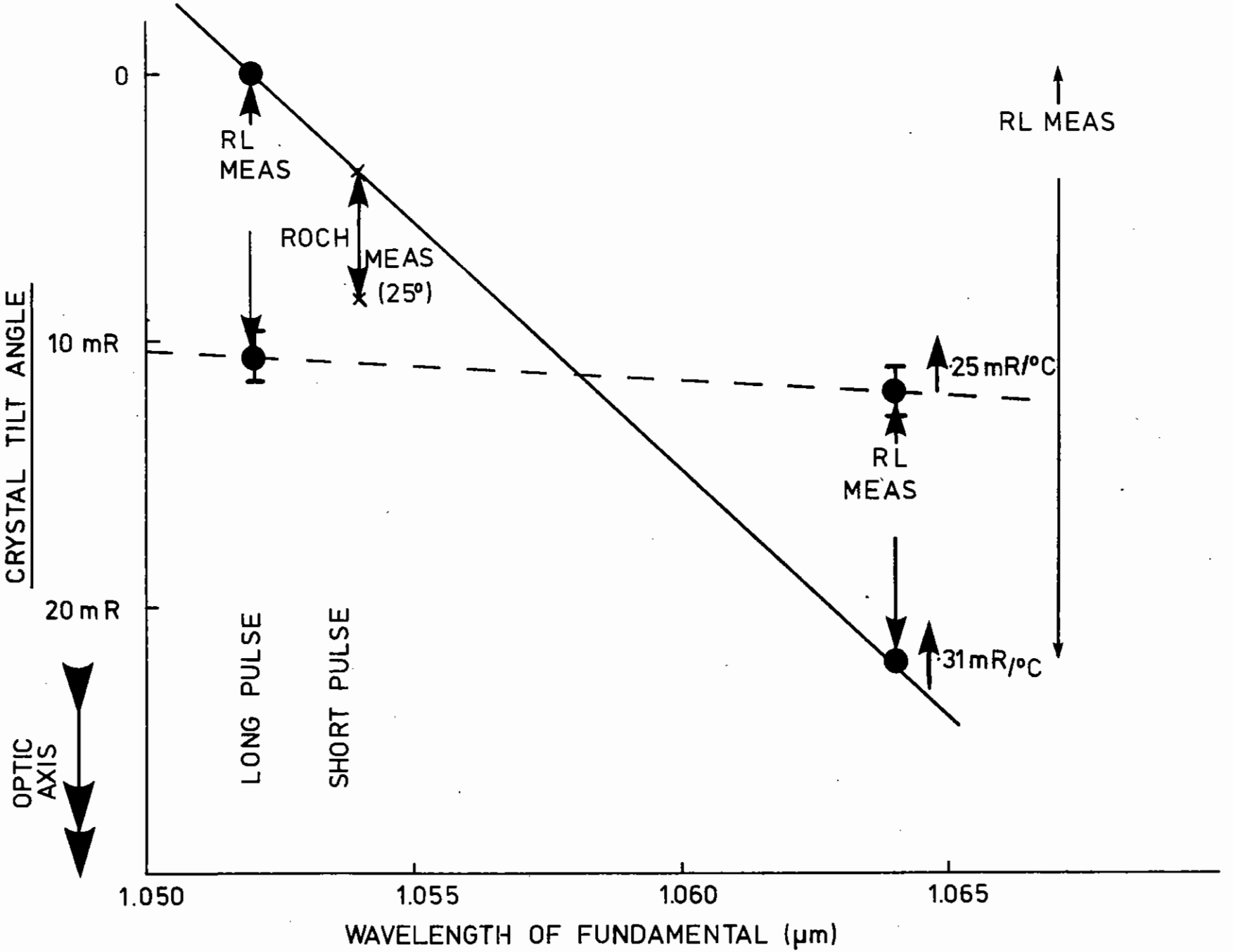

Figure 1.11 Phase matching angles as a function of wavelength for type II doubling and tripling ($\omega_o^e + 2\omega_o^o \rightarrow 3\omega_o^e$) in KDP.

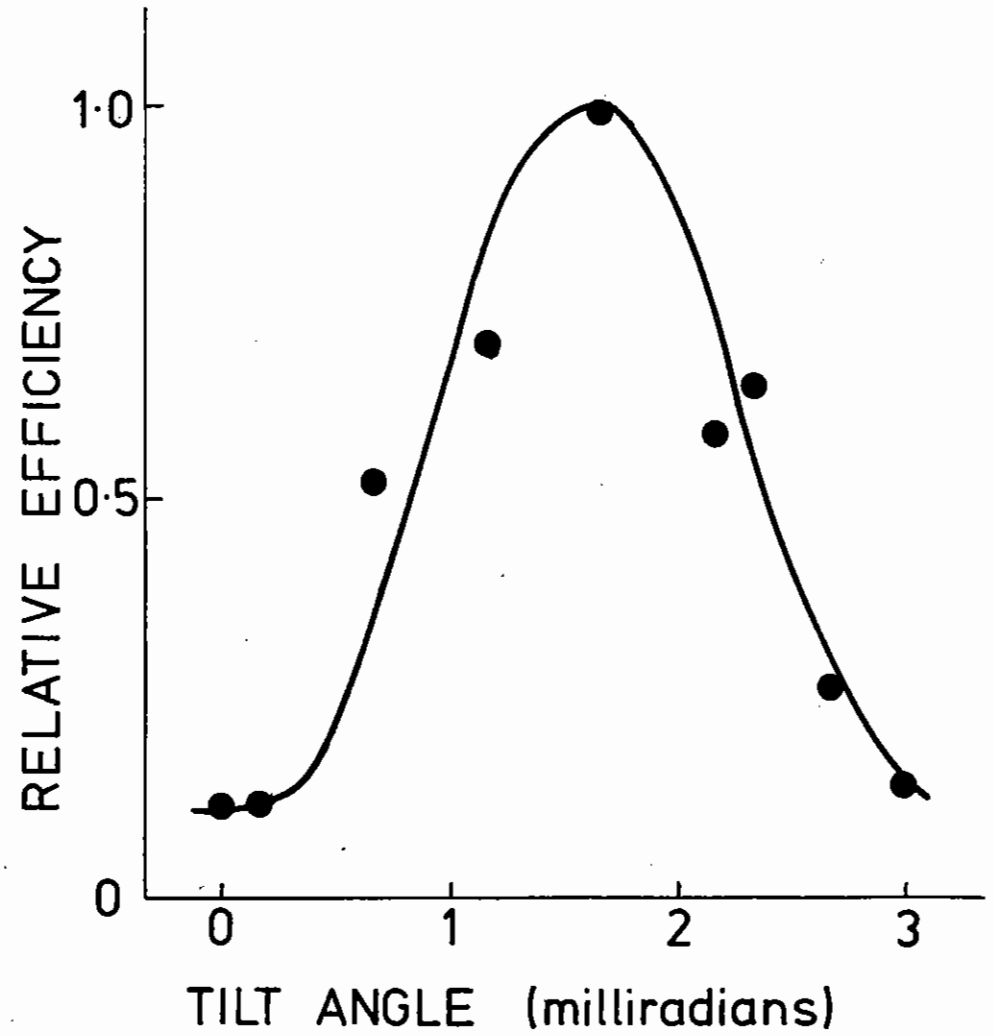

Figure 1.12 Angle tuning curve for third harmonic generation by summing in a 9mm crystal.

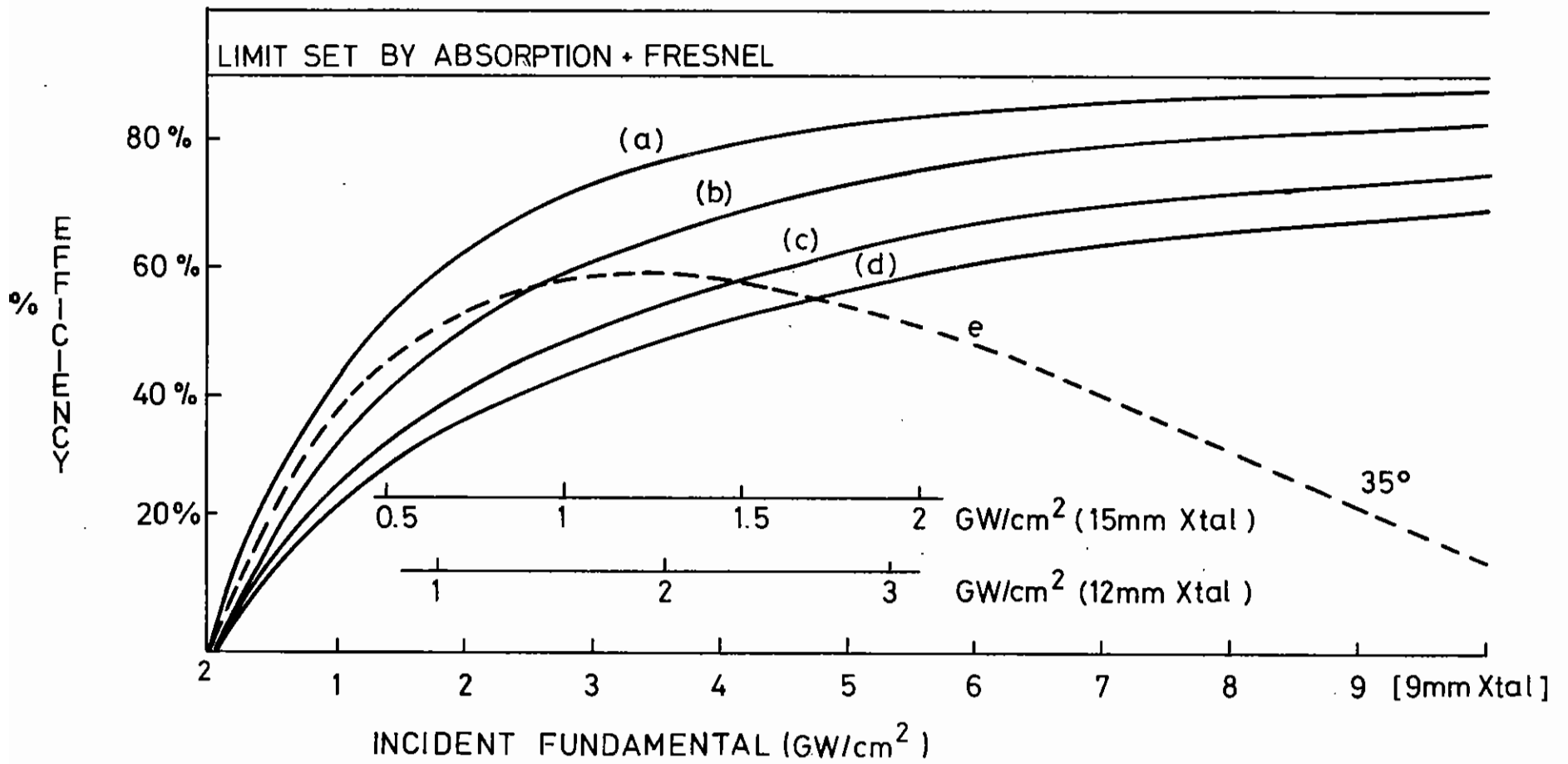

Figure 1.13 Second harmonic generation efficiency for various beam distributions. The dashed line is for a single ray polarised at 35° to the O-axis.

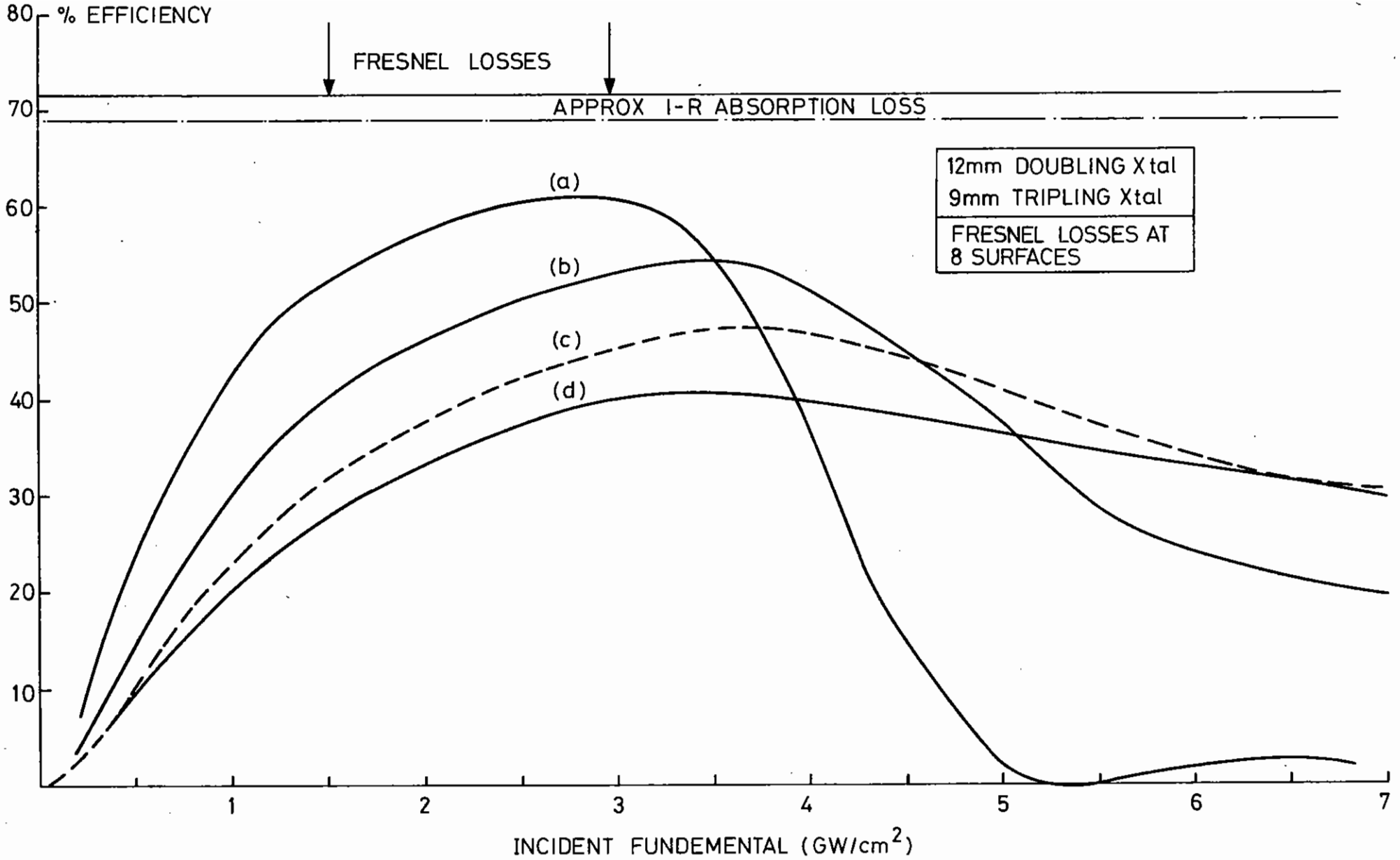

Figure 1.14 Third harmonic generation efficiency for various beam distributions, using the polarisation mis-match scheme. The second harmonic crystal is 12mm thick and the summing crystal is 9mm thick.

TIME FROM PEAK →

DISTANCE FROM CENTRE ↓

47	45	41	33	13
41	39	34	26	9
31	29	25	18	6
18	17	14	9	3
4	4	3	2	0

(a) MEAN INTENSITY 1 GW cm^{-2}

TIME FROM PEAK →

DISTANCE FROM CENTRE ↓

11	21	45	60	44
48	54	60	58	38
61	60	58	53	30
53	51	48	40	18
24	22	19	13	4

(b) MEAN INTENSITY 4 GW cm^{-2}

FIG.1.15 Spatial and temporal distribution of third harmonic generation efficiency for a beam gaussian in space and time.
The grid spacing is such that each square contains the same incident infrared energy.
Reflection and absorbtion losses total approximately 30%.

the beginning of an experimental run spread over five weeks and was not subsequently repeated. All high power measurements of the beam properties were made on target shots.

Blue conversion efficiencies are shown plotted against laser energy in Figure 1.17. Several factors are believed to contribute to the scatter of the data: random and quasi-random monitoring fluctuations, changes in the beam shape and pulse shape and errors in setting the crystal angles. An approximate theoretical efficiency curve for a beam which is gaussian in space and time is shown as a dashed line. It is not known whether the tendency of points at high laser energy to lie below the curve is an intrinsic problem, an effect due to a change in beam quality or the result of a systematic angular tuning error coupled with the reduction in the width of the tuning curve to be expected at high power. A systematic error in the tuning would also give rise to large variations in efficiency for small additional random tuning errors.

It should be noted that the blue conversion efficiency at the peak of the pulse in the centre of the beam distribution, corrected for reflection losses, is in excess of 80 % for those shots lying within 10 % of the theoretical curve.

The pulse length of the blue beam was measured routinely with an S1 streak camera coupled to a 2D OMA (1.13), and the infra-red beam pulse shape was measured shortly after the end of the run. Typical pulse shapes are shown in Figure 1.18.

A near field picture of the blue beam is shown in Figure 1.19. The dip in the intensity in the centre of the distribution is due to a similar dip in the distribution of the infrared beam and not to the effect shown in Figure 1.15. An air-spaced spherical doublet lens of fused silica with an aperture of f:2.5 was used to focus the beam on target. Ray tracing programmes (1.14) were used to design a lens which could also be used at the second and fourth harmonics, with a different spacing of the

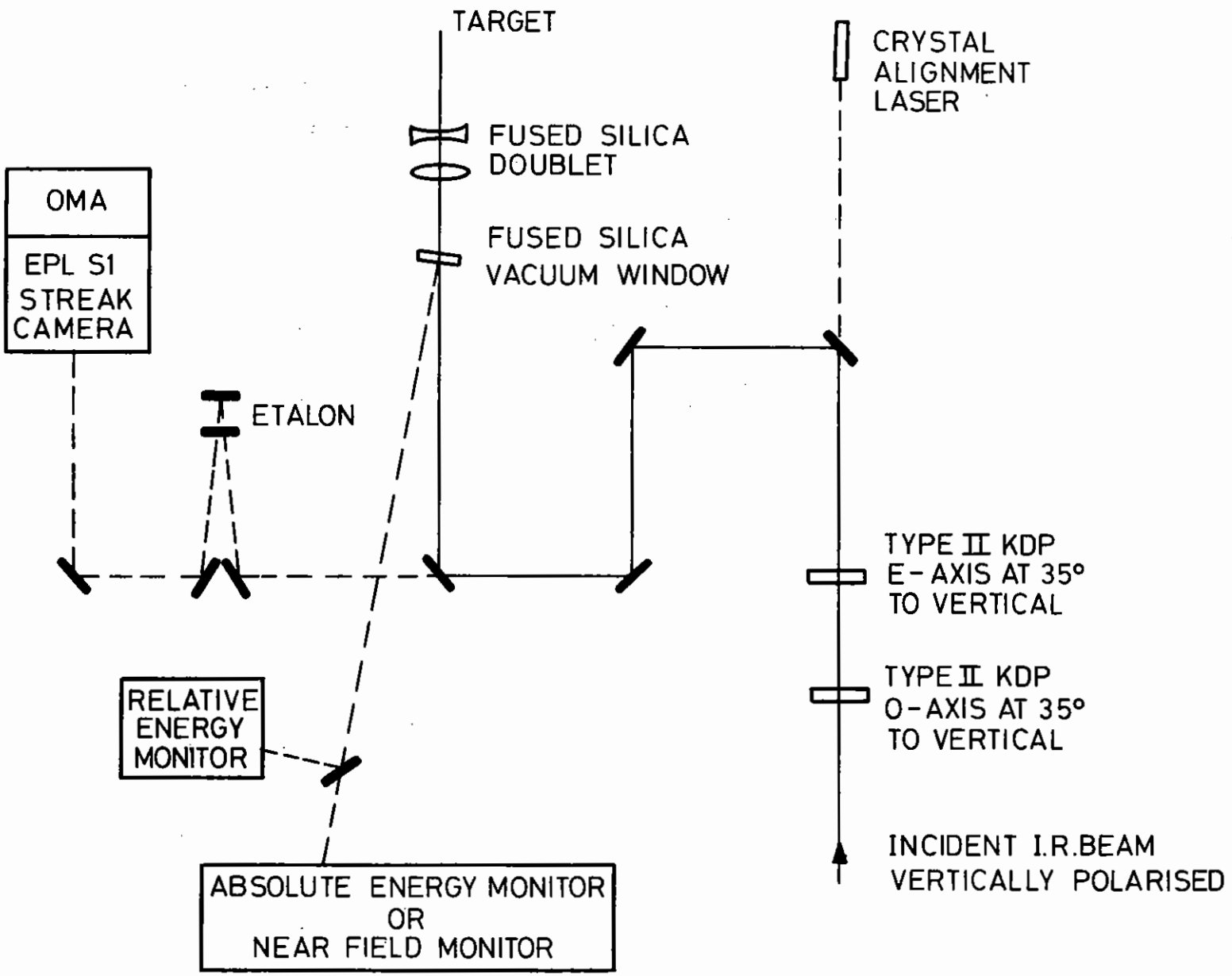

Figure 1.16 Arrangement for target irradiation at the third harmonic.

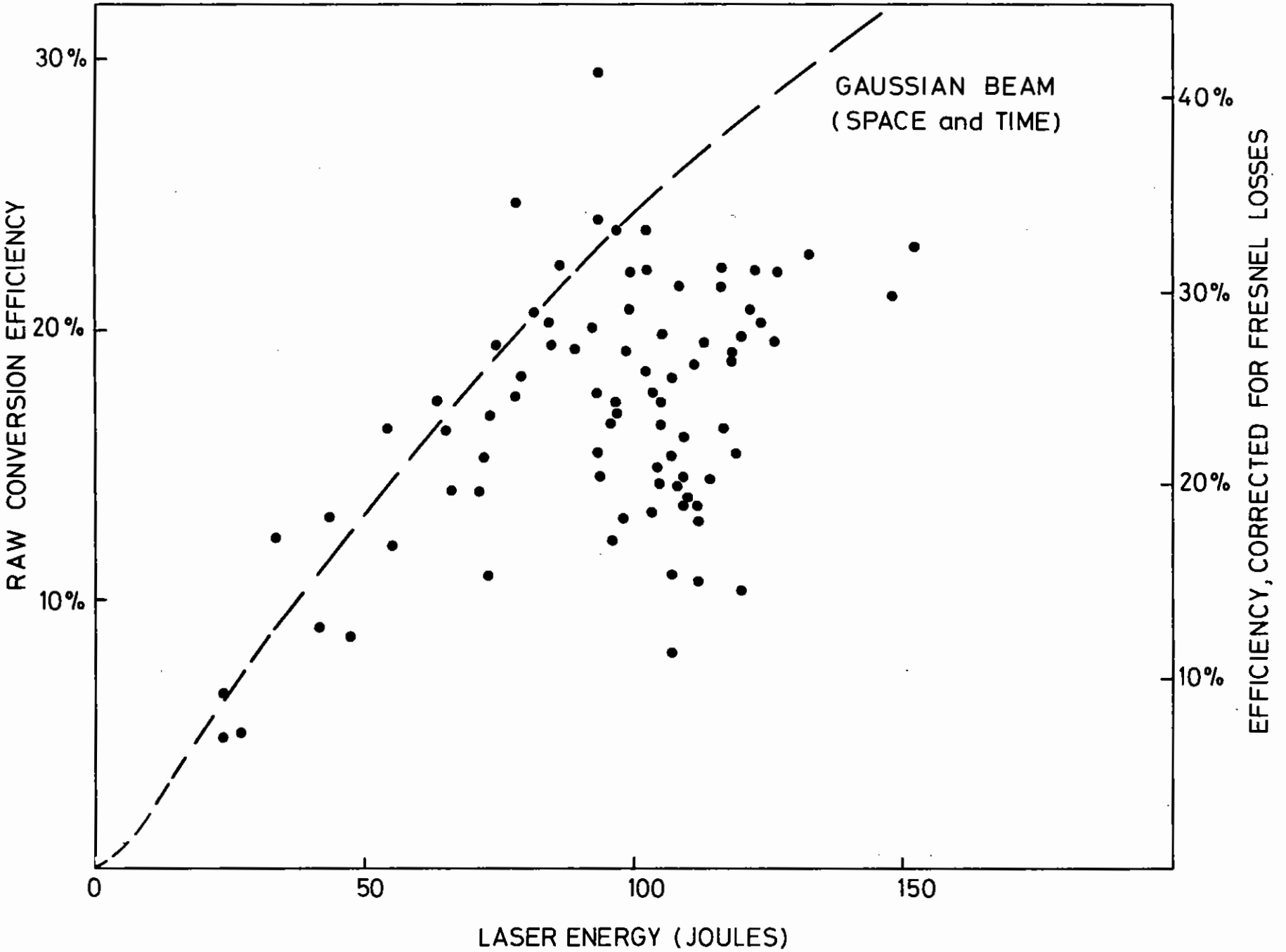

Figure 1.17 Third harmonic conversion efficiencies recorded on target shots.

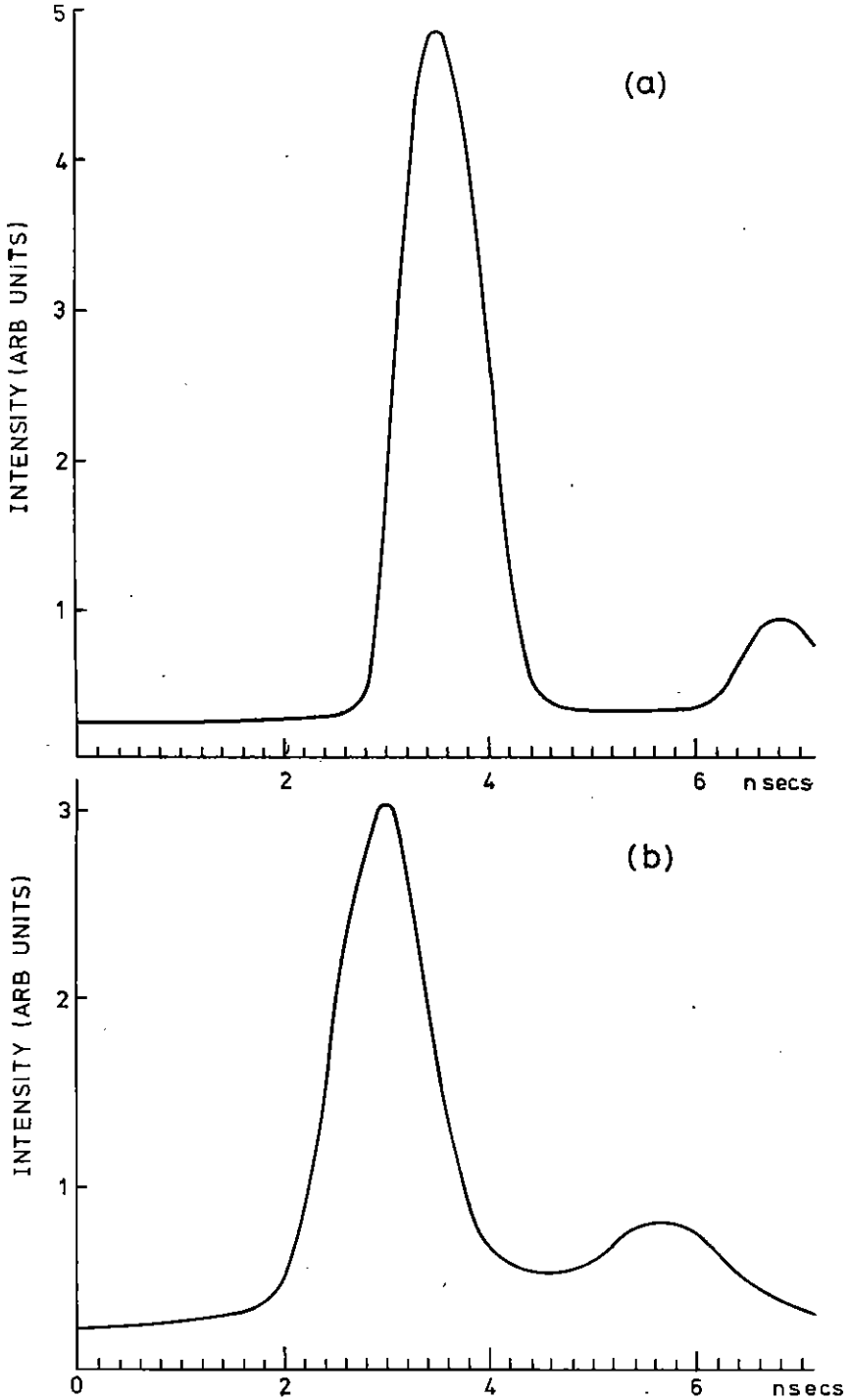

Figure 1.18 Pulse shapes (a) Third harmonic (b) Fundamental. (a) and (b) were not taken on the same shot.

elements.

D Pepler, J Szechi and W T Toner (RAL)

1.4.3 Vacuum Airlocked Target Positioning Mechanism

A new target insertion system has been installed in the six beam chamber to enable the target to be changed whilst the chamber is under vacuum. This facility has improved the stability of the optics, the cleanliness of the chamber and improved the vacuum pressure within the chamber during experimental programmes. Typical operating pressure is of the order of 1×10^{-5} Torr.

The microballoon targets are pre-aligned during preparation with reference to a standard fixed datum target. This is achieved by potting the target mounting stem in cold curing silicon rubber in a mount, whilst the targets are held at the datum position in a special alignment jig (section 1.5). This enables a replacement target to be put into the chamber to a position within 200 μm of the previous target - well within the optical alignment system's field of view.

To replace a target the used target mount is withdrawn into an airlock chamber then an internal trap door is closed at the inner end of the airlock. Air is now admitted to the airlock so that the target insertion rod may be withdrawn and the target replaced. The new target is pushed into the airlock which is then evacuated, allowing the internal trap door to be opened and completing the insertion cycle. The insertion/removal cycle is automatically controlled using an electro-pneumatic system.

Perhaps the most novel feature of this design is the flexible target holder on the insertion rod which enables the target to be effectively transferred to the three axes translation motion yet still be physically attached to the target insertion rod - see Figures 1.20 and 1.21.

The flexible mount holds the target central in the airlock stage of the insertion cycle but after the evacuation of the airlock and opening of the

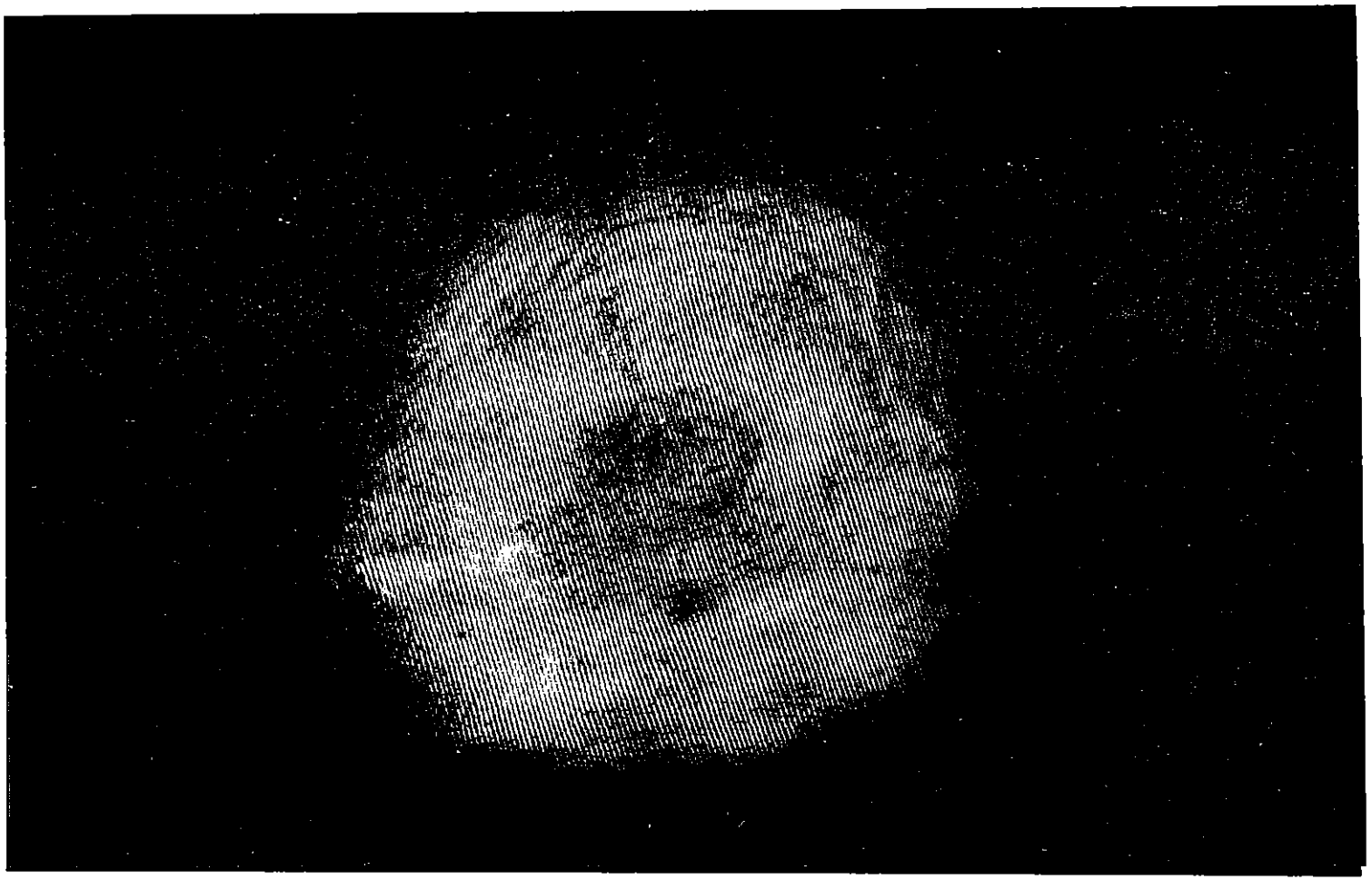

Figure 1.19 Near field distribution of third harmonic beam recorded on type 57 polaroid.

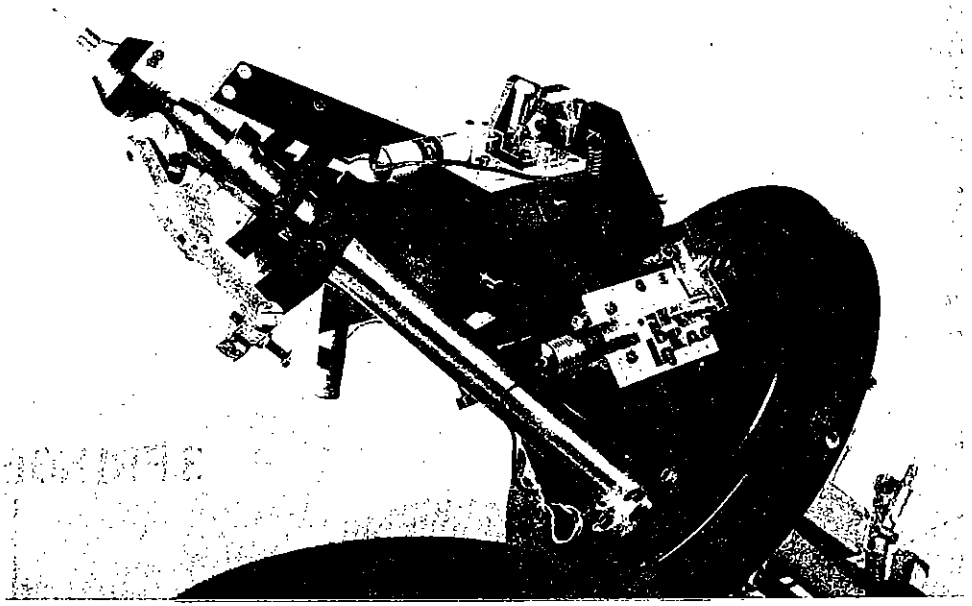

Figure 1.20 Vacuum airlocked target positioning mechanism

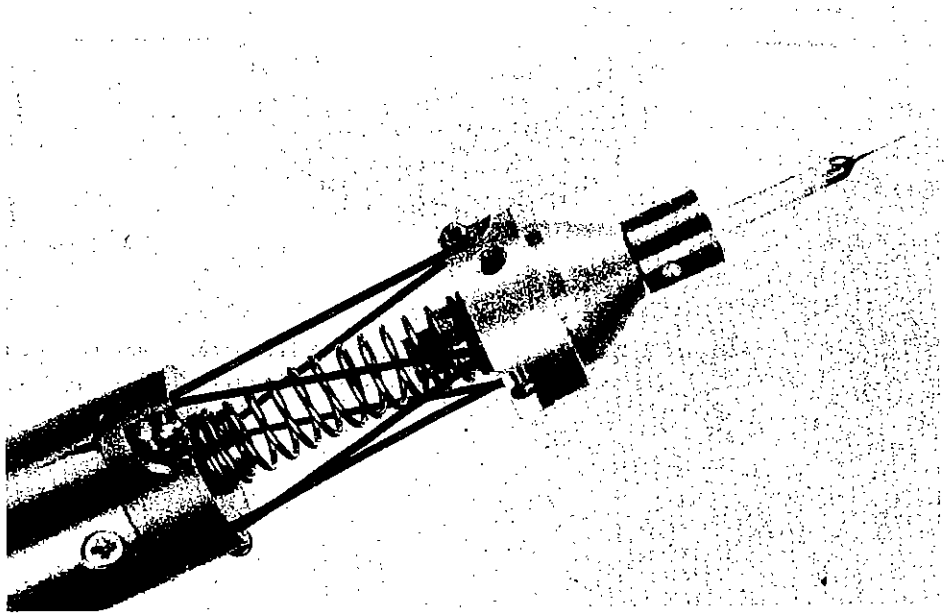

Figure 1.21 Flexible target mounting arrangement

internal trap door, the mount enables the target to align itself on the conical portion of the translation unit finishing in a location diameter. Is is kept in this location by pressure from the spring on the target insertion rod, but is able to move up to ± 3 mm in any of three orthogonal directions remotely positioned by DC driven motorised micrometers to obtain the final alignment. The translation unit is capable of positioning the target to an accuracy of better than 5 μm.

A R Damerell (RAL)

1.4.4 Automated Methods for Production of f/1 Aspheric Lenses

The demand for fast, f/1 aspheric focusing lenses for our six beam system is currently outstripping supply by conventional optical techniques. In this section we describe our attempts to semi-automate this process using conventional CNC jig grinding machines (type G18N) found in manufacturing industry.

The production of the aspheric components by standard optical methods involves a number of stages all of which take a considerable time and require a high degree of skill and experience. First, a best fit spherical surface is formed on to one surface of a prepared blank. Then the spherical radius is roughly shaped to the aspheric profile by rotating the blank about its axis of symmetry, and plunge grinding using hand-set X and Y coordinates calculated to suit the diameter of the grinding wheel. This leaves the surface with a series of ridges or cusps between each coordinate. The profile is then smoothed using polishing pads and a coarse grinding slurry. As the profile becomes smooth it must be continuously measured, using a precision rotating micrometer, until the correct aspheric profile is obtained. A light polish is then placed on each surface.

As soon as the aspheric component is transparent it is removed from the polishing spindle and mounted, with its spherical component, in an

interferometer and null tested. This lengthy polishing and testing procedure is then repeated until a satisfactory performance is obtained from the lens (see Figure 1.22).

Because of the time scales involved in carrying out these operations it takes in general over six months to produced a finished aspheric by these conventional techniques.

To produce an aspheric profile by a CNC machine, it is convenient to start with a grey blank of final thickness, with a best spherical surface on one face, and a flat face which has already been polished.

Grinding is carried out by rotating the lens at approximately 200 rpm and traversing the grinding head across the horizontal centre line, with the tool spindle at an angle to the vertical plane so that the tool contacts at the bottom corner, whilst rotating at approximately 30,000 rpm. The glass surface is cooled by a high pressure spray of water. The machine operates from an X, Y, θ, command; the X and Y coordinates are the true coordinates of the aspheric profile, θ is the so-called 'C' axis, the angle that the head has to be to the surface to be at a constant tangent.

At any time during the grinding process the shape of the profile can be checked by fitting a stylus to the tool spindle and scanning the surface. A typical surface measurement is shown in Figure 1.23. Over the 55 mm radius of the lens there is a gross deviation from the true aspheric profile of around 2 μm. However, the point-to-point variation is approximately half of this. There is also a high spatial frequency $\sim$ 0.2 μm in amplitude which can be attributed to grain boundaries.

The surface structure after grinding is of utmost importance to successful polishing of the lens. The microsurface produced by CNC grinding is much finer than the grey-finish surface obtained by conventional optical techniques. An example of both surface finishes is shown in the microgrammes of Figures 1.24(a) and 1.24(b): both have a magnification of x 270. The surface represented in Figure 1.24(a) is a conventionally produced grey-finish surface and has grain features, typically 20 μm,

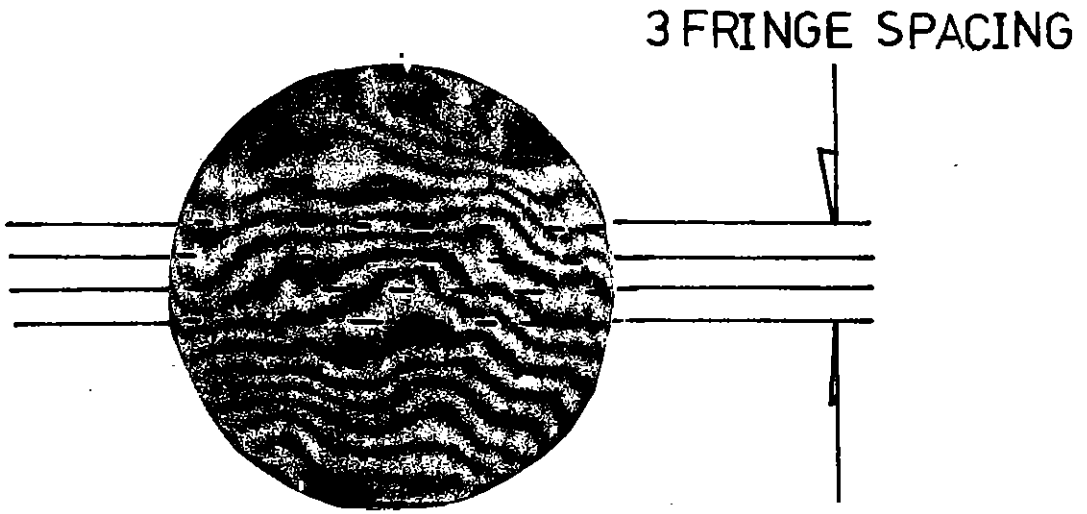

Figure 1.22 Interferogram (Twymann-Green) showing optical performance of a hand finished lens at λ = 456 nm.

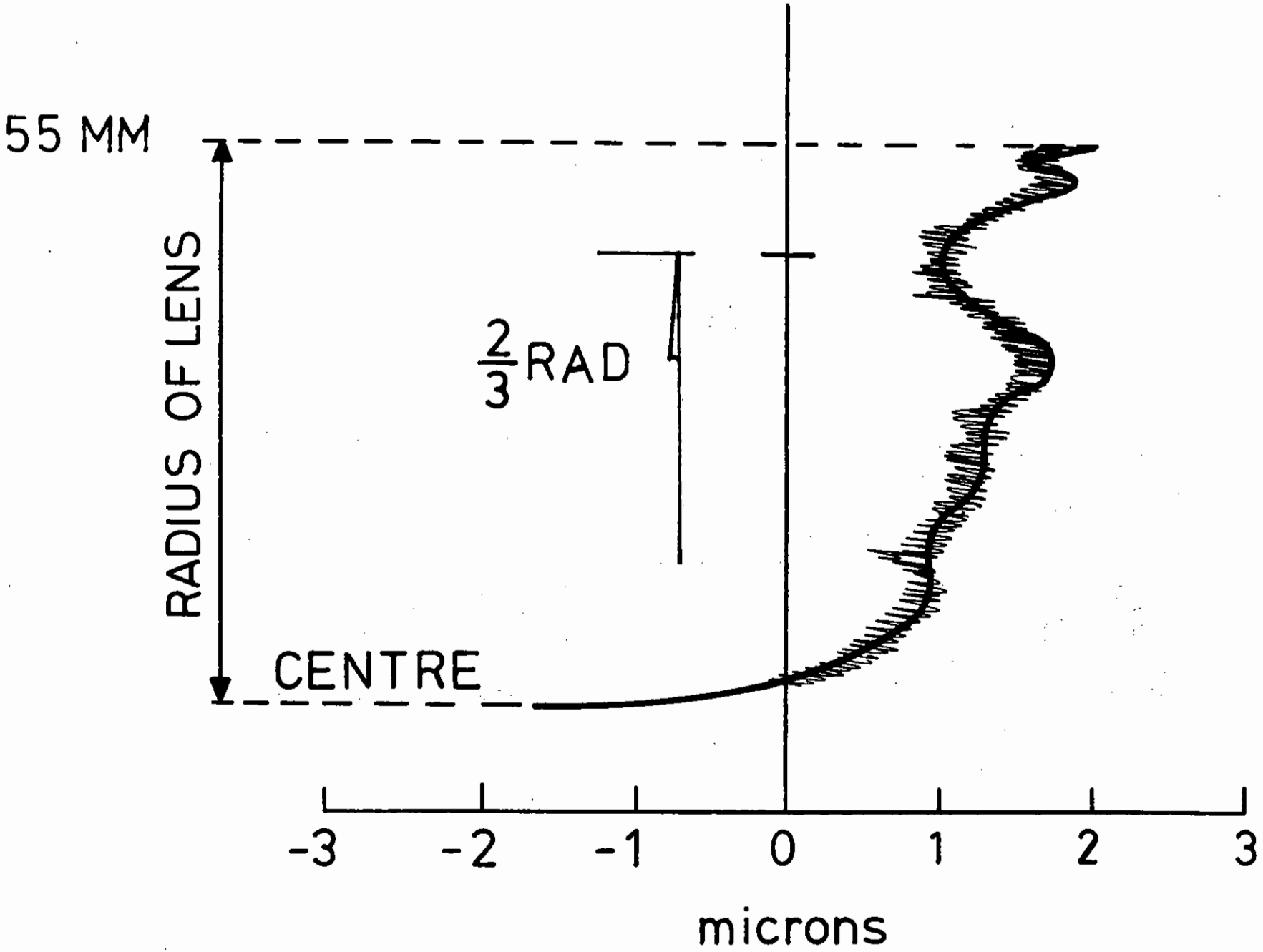

Figure 1.23 Contact stylus measurement of deviation from true surface profile after grinding.

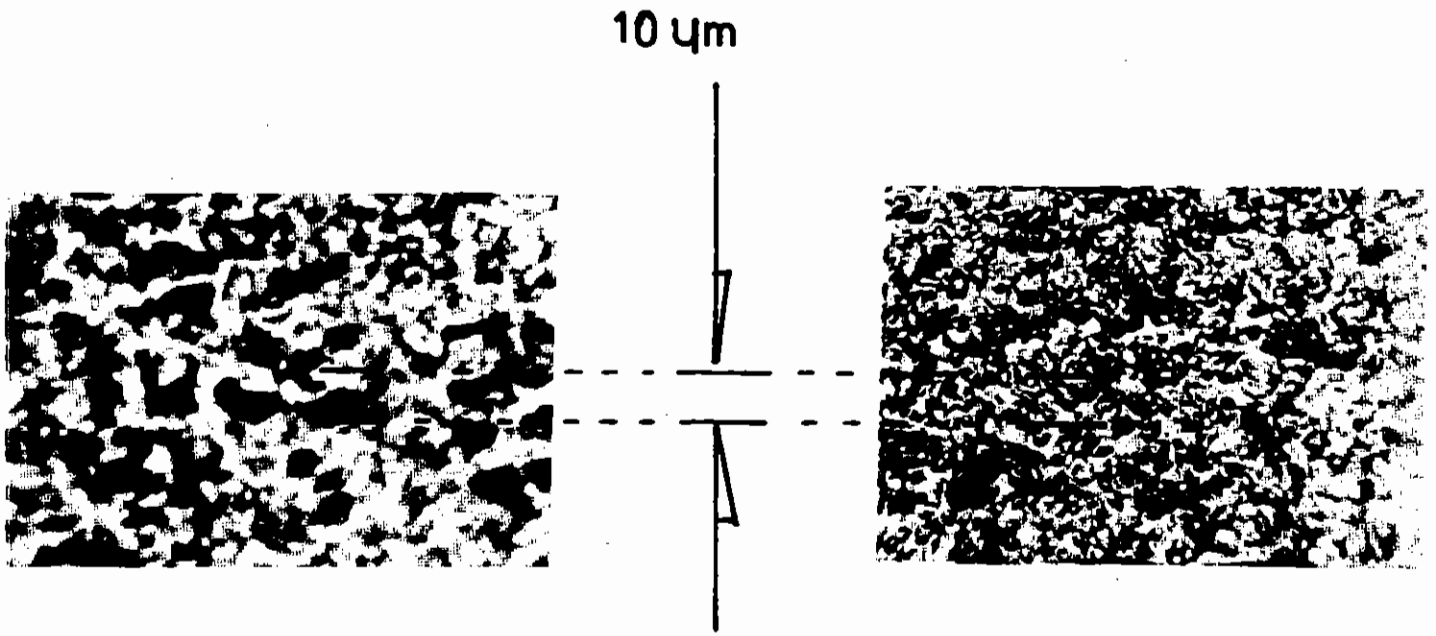

Figure 1.24 (a) Microstructure of conventional grey surface (x 270)
(b) Surface produced on a CNC grinding machine (x 270)

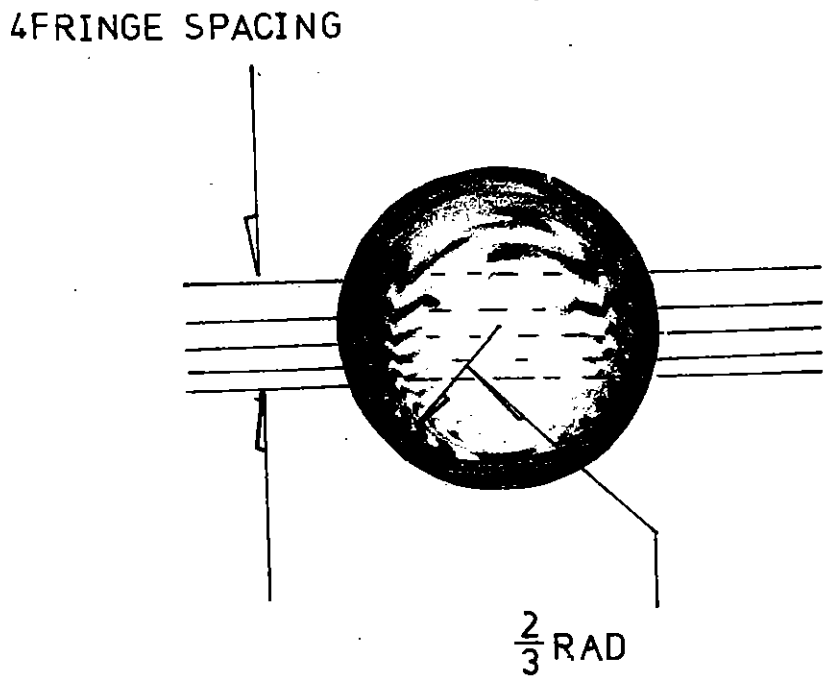

Figure 1.25 Interferogram of partially polished lens (λ = 632.8 nm)

shown prominently on it. This compares with the CNC surface finish shown in Figure 1.24(b) where the grain size is approximately an order of magnitude less than this. This simplifies considerably the final polishing stage.

Using the same arrangement previously described, the diamond tool is replaced by a hard feld mop, and the tool spindle raised and placed vertical such that the mop traverses the lens on the same radial profile. A slurry of 5 µm alumina powder and water is applied to the lens with a soft brush. The machine is set to make continuous passes across the radius, and after some 20 passes, about 1 hour of polishing, a sufficiently polished surface was achieved to obtain the interferogram (Figure 1.25) on a Zygo interferometer at a wavelength of 632.8 nm. Again, superimposed on the interferogram is the mean fringe separation of the central portion of the field of view. At no place is there an overlap of more than four fringes. Taking the wavelength into account this compares very favourably with the hand-polished, near diffraction-limited lens, whose interferogram is shown in Figure 1.22. However a large zonal feature can be seen in the interferogram at approximately 2/3 radius. This feature shows itself again in Figure 1.23 and has to be polished out of the final lens. This lens was successfully finished by hand polishing in a total manufacturing time of around three weeks - a considerable saving in time and effort on a conventionally produced aspheric lens. There still remains, however, the final stage of polishing to be attempted by the CNC machine. This will require, by trial and error, choice of polishing speeds, polishing compounds and mops and operating sequences.

D J Nicholas and J E Boon (RAL)

1.5 Target Fabrication

During the last year the experimental programme has called for targets in considerably larger numbers and of much greater complexity and quality than in previous years. The enhanced demand has arisen partly because of the introduction of parallel operation of the two experimental target areas and partly because of the increasing number of experiments being

conducted involving X-radiography techniques. Such experiments require the preparation of two targets (a microsphere and a suitable x-ray producing source) for each laser shot.

Additional equipment has been obtained to enable the target preparation group to cope adequately with this increased load. Several extra microscopes and manipulators have been installed so that two separate work stations for the selection, characterization and mounting of microsphere targets are now in operation. A jig with orthogonal reference miscroscopes has been set up in order to prealign all microsphere targets in special bases before transfer to the experimental compression area for insertion in the target chamber via the new air lock mechanism (section 1.4.3). Four vacuum plants are now in use, enabling the range of target coating techniques to be extended to include rf, dc and ion beam sputtering, electron beam and resistive evaporation, ion plating and plasma and vapour phase polymerization.

In the past it had been found that microsphere targets frequently became contaminated with small dust particles during measurement and mounting processes and hence became useless for experimental purposes. To overcome this problem high efficiency air filtering equipment has been installed and consequently all target handling and storage now takes place under clean conditions.

Considerable effort has been devoted to improving the surface quality of plastic coatings applied to microspheres. Previously all such coatings have been applied by ac plasma discharge polymerization of various monomers onto spheres kept moving on the surface of one of the discharge electrodes by the alternating field. This technique is easy to carry out and produces large numbers of coated targets but unfortunately the coatings have imperfections on a micron scale size arising from particles picked up from the electrode and incorporated into the coating. To avoid this effect coatings have been applied to targets already mounted on their support fibres by both vapour phase and ac plasma polymerization techniques. Both methods give rise to coatings of greatly superior quality due to the absense of particulate inclusions. As well as improved

surface finish, coating onto mounted targets has the added advantage that microspheres can be measured interterometrically both before and after coating thus allowing accurate independent determination of both the glass shell and plastic coating thickness. A disadvantage of this coating method is that the support stalk also acquires a coating and become thicker and consequently the method is only suitable for plastic layers up to a few microns thick.

Additional work has been carried out to develop new techniques for the fabrication of patterned lolipop targets for planar Rayleigh-Taylor instability experiments. Previously arrays of 2-dimensional perturbations have been applied to targets by mask coating techniques. This work has been extended to make targets with 1-dimensional patterns (which are more suitable for streaked, time-resolved, X-radiography experiments) by coating through a microwave wire grid polarizer onto punched 250 μm diameter lolipops of various materials. Line perturbations with heights up to a few microns and penodicities of 20 μm have been produced. Alternatively, corrugated lolipop targets have been produced by coating through 250 μm diameter apertures onto Moiré fringe gratings which have previously been coated with a release agent. Gratings have been obtained which consist of deposited chrome stripes of height 0.5 μm and periodicity from 20 to 100 μm, and consequently lolipops are produced which replicate these profiles with thicknesses up to several microns.

Characterization of opaque microsphere targets by contact X-radiography has always been a very lengthy procedure as arrays of shells must be prepared, exposures taken, films developed and measured and finally useful targets retrieved. To overcome this limitation, work has been carried out to modify the target fabrication group's scanning electron microscope to enable it to be operated as a scanning X-ray microscope with TV rate display. The electron beam is focused onto the front side of a thin metal foil on the rear of which is placed an array of shells for examination. The characteristic X-radiation generated is transmitted by the foil and passes through the shells to a scintillator/photomultiplier detector placed sufficiently far away and suitably apertured that an essentially collimated beam is observed. The resolution of the system is thus close

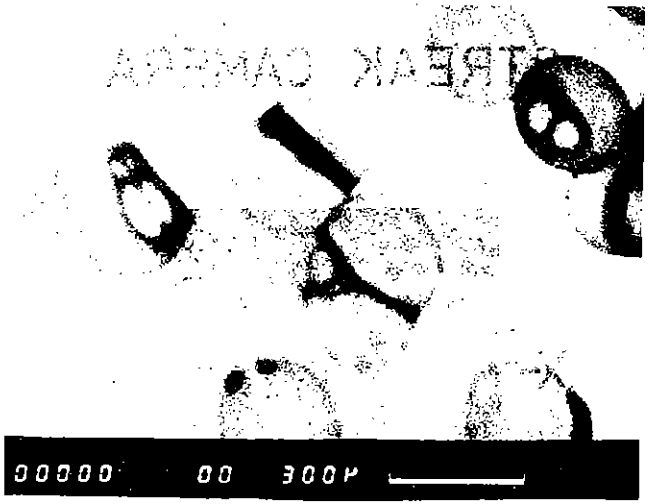

Figure 1.26 X-radiograph of nickel/manganese shells taken with Cu Kα radiation (8.04 KeV) in a scanning X-ray microscope

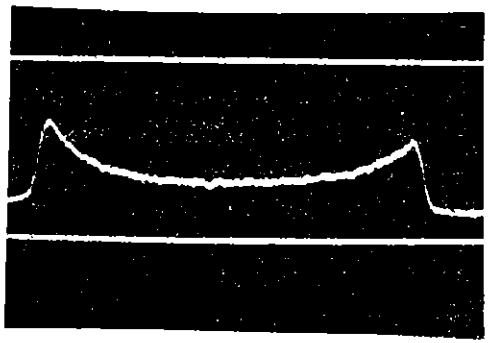

Figure 1.27 Line scan of relative opacity across the diameter of a glass shell taken with Al Kα radiation in a scanning X-ray microscope.

to the diameter of the X-ray emitting spot (0.2 - 1 μm depending on beam voltage and foil material). With sufficient current in the beam a TV rate X-radiograph of the shell array is seen with all normal SEM functions such as intensity and contrast of the image available. The array of shells can be moved mechanically during observation allowing an operator to rapidly detect the useful ones. These can then be studied at high magnification and line scans of opacity obtained. Aluminium, titanium and copper foils (Kα energies 1.49, 4.51 and 8.04 KeV respectively) have been used to examine targets of widely different areal density. Figure 1.26 shows a radiograph (as would be seen on the SEM TV screen) of a group of hollow shells (Solacells) made of nickel/manganese alloy taken with Cu Kα radiation while Figure 1.27 is a line scan of relative opacity across the diameter of a hollow glass target obtained with Al Kα radiation. Work is continuing to improve the resolution of the system (at present 1 - 2 μm) by improving the detection efficiency and thus allowing the beam spot size and detector solid angle to be reduced.

G Arthur, C Brown, B Child, S Hallewell and P Rumsby (RAL)

1.6 Diagnostic Development

1.6.1 Miniature X-ray Streak Camera and Photocathodes

The new compact X-ray streak camera (1.13) has been tested and used in the six beam area (TA1). Results include measurements of six beam infrared mass ablation rates and time-resolved spectroscopy of Al XIII 1 S - 2 P , Al XIII Ly , Si XIII 1 S - 2 P , and Si XIV Ly with their respective satellites (Figure 1.28). The camera is currently being used in six beam $2\omega_0$ time-resolved spectroscopic measurements to determine mass ablation rates and ablation pressures.

The new microfocus X-ray (Rockett) source (1.13) has made it possible to measure the static resolution and sensitivity of the camera (ie without streaking the image). Because the camera photocathodes are readily interchangeable, a comparative study of cathode responses for different types of cathode can be made. A preliminary comparison of photocathodes

Fig 1.28

TIME RESOLVED SPECTROSCOPY OF SILICON

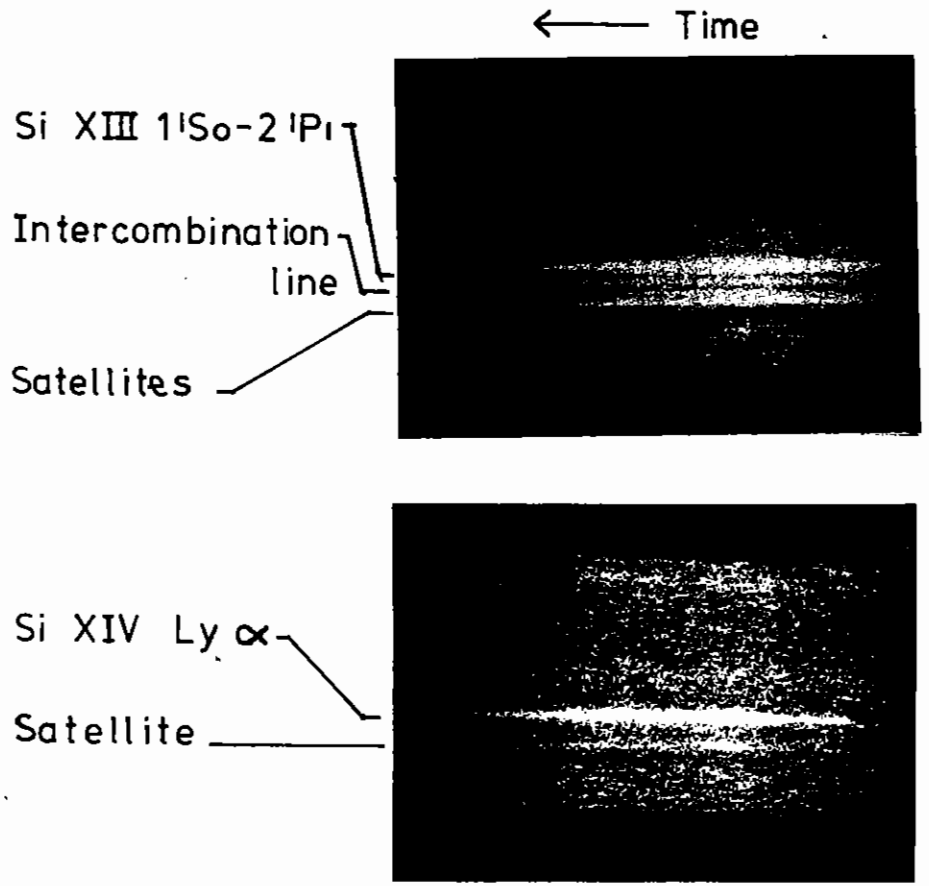

Fig 1.29

STATIC RESOLUTION OF X-RAY STREAK CAMERA

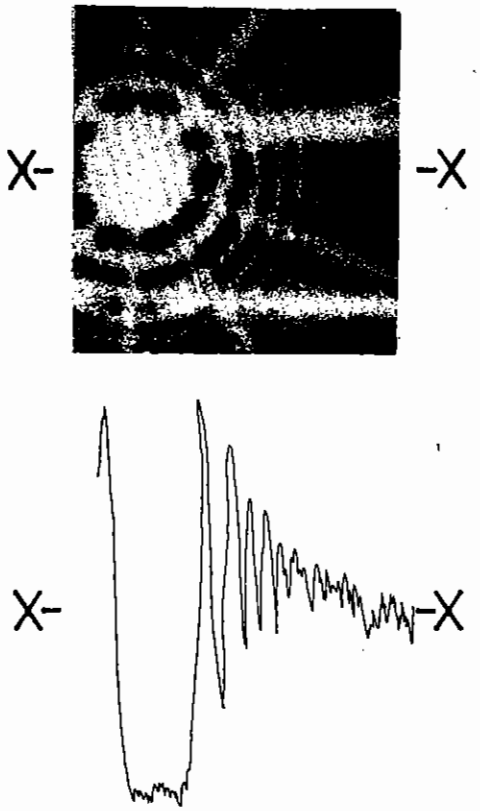

Densitometry of zone plate image, reveals a resolution of 50μm on the photocathode.

formed from a thin layer of gold, solid-density caesium iodide (CsI), or low density CsI (∿ 5 % of solid density), deposited on beryllium foil 15 μm thick, was carried out as follows.

The streak camera was mounted on the X-ray source with its photocathode about 18 cm from the X-ray spot. An etched copper free-standing zone plate (1.13) was suspended about 15 mm in front of the cathode. For a small enough X-ray spot (< 0.50 mm), the zone plate provided a convenient symmetrical shadow of varying spatial frequency. The X-ray targets used were either copper (giving Cu Kα at 8.04 keV), or aluminium (giving Al Kα at 1.49 keV). With the streak camera and image intensifier in focus mode, the image of the zone plate shadow was recorded on Ilford HP5 or FP4 film. Densitometry of the images provided information on the resolution of the camera-photocathode combination, as well as approximate relative cathode sensitivities.

The static spatial resolution of the system with the low density CsI photocathode turned out to be of order 20 line pairs mm (50 μm) on the cathode, a good result (Figure 1.29). The measured static resolution for the gold and solid CsI cathodes was also 50 μm. The spatial resolution in the dynamic mode of the solid CsI photocathode was estimated from the streaked shadows of pulse-backlighted static wires to be 60 μm. Combined with the maximum streak speed of ∿ 50 ps mm^{-1} this implies a temporal resolution of 3 ps, but the energy spread of the secondary electrons from the photocathode will limit this resolution to 40-90 ps, depending on the thickness. Experimental results for low-density CsI indicate 40 ps resolution (1.15).

The preliminary measurements of relative cathode sensitivity indicate that freshly made low-density CsI photocathodes are of order 300 times more sensitive than gold cathodes, and about a factor of 150 more sensitive than the single (rather poor) solid-density CsI cathode tested. Several low-density CsI cathodes were made for these experiments and for use in laser experiments (1.16).

The best of these is currently in use in the camera on the six beam target

chamber. It has been carefully looked after, being usually kept under vacuum, or temporarily in a sealed container with desiccant. The experimental results (figure 1.28) show very significant improvements over those from cathodes treated with less respect, ie exposed regularly to air and water vapour, and used over periods of three months or more. It is concluded that best results will be obtained only by making fresh cathodes for each series of experiments and if possible keeping them under vacuum.

A study has been started of the variation of sensitivity of low-density CsI photocathodes with the thickness of the CsI layer. It indicates that excellent results can be obtained with a thickness (determined from scanning electron micrographs) of not less than 20 μm, but an optimum thickness has not yet been determined.

We gratefully acknowledge the extensive help and guidance given over the last three years by Dr J E Bateman and R J Apsimon of the Physics Apparatus Group of RAL Instrumentation Division, who have made most of the low-density CsI photocathodes used by the Laser Division and have recently given us much valuable assistance to make our own.

J M Ward, P F Cunningham, M J Lamb (QUB) and P M Rockett (Oxford Applied Research Limited)

1.6.2 Gated Micro-channel Plate X-ray Intensifier

Ablatively accelerated ICF targets display implosion times of the order of 1 - 3 ns, principally depending upon the power distribution within the laser pulse. Traditional techniques for obtaining time-resolved data on these time scales, have made use of streak cameras. These devices enable time resolutions of better than 100 ps to be achieved, at the expense of loosing one spatial dimension (see section 5.2). This is not a serious drawback for measurements such as implosion times, burn rates etc; but for observing the symmetry of the implosion or examining X-ray filaments in the under dense plasma (see section 3.2), resolution in two spatial dimensions is essential. The device described below is designed to achieve this end.

Earlier work (1.17) had demonstrated the feasibility of building a high gain X-ray intensifier using a Caesium iodide (CsI) photocathode and a proximity focused micro-channel plate as the intensifying elements. The current design is based upon this configuration. Two dimensional imaging is achieved using a conventional X-ray pinhole. The intensifier has been designed to achieve a gating time of < 150 ps.

A photocathode is made of CsI, evaporated onto a substrate of beryllium or, alternatively, thin (3 - 5μ m) mylar film. The latter needs a thin coating (50 nm) of aluminium in order to make it conducting. The process of coating CsI onto a substrate to form a photocathode can be varied to produce either a deposition of normal, solid density CsI (4.5 gm cm^{-3}) or low density coatings. The exact density depending upon the environmental conditions during the coating (1.18). Preliminary measurements indicate that solid density CsI is comparable to low density CsI in sensitivity to X-rays of around 1 - 2 keV. Solid density CsI is easier to make and is structurally stronger than low density CsI. It is also less affected by moisture in the atmosphere. Because of these advantages most of the work outlined below was performed using photocathodes made of solid density CsI.

The gating operating is achieved by pulsing the extraction field between the cathode and an anode grid. It was therefore important to know how the photocurrent varied as the extraction field was increased. A small DC X-ray source was used to illuminate a test photocathode and anode assembly, and the current measured with a picoammeter as the field was varied. The result is shown in Figure 1.30. It can be seen that to achieve efficient gating operation, ie a large on/off contrast ratio, the cathode should be positively biased to +20 v DC and the switch on pulse should be negative with a magnitude of at least -50 v. This ensures that the photocurrent is independent of the gating pulse magnitude and depends only on the incident X-ray flux.

The sensitivity of a photocathode depends principally upon two factors, the efficiency of absorption of incident X-rays, and the ability of the generated secondary electrons to escape from the solid and be collected by

Fig 1.30 PHOTOCURRENT AS A FUNCTION OF EXTRACTION FIELD.

CsI photocathode illuminated with Ti characteristic X-rays ≈ 10^8 photons str^{-1} s^{-1}

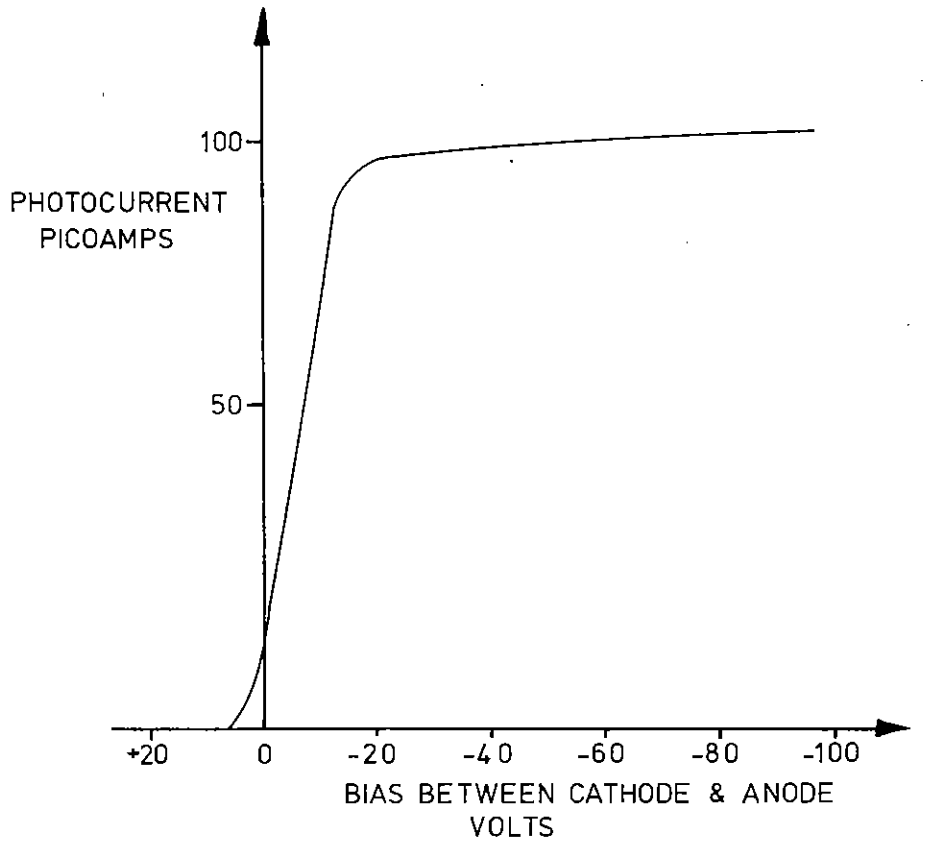

the extraction field. Maximum quantum efficiency is achieved when most of the X-ray absorption - and hence secondary electron generation occurs within an electron escape depth of the cathode surface. Experiments were performed varying the photocathode thickness for different wavelengths of incident X-rays. The results are summarised in Figure 1.31. As can be seen for aluminium Kα X-rays, λ = 8.34 Å, the optimum thickness of solid density CsI was found to be 150 nm.

The spatial resolution of a cathode of this thickness was determined by means of shadowing a resolution grid placed close to the cathode, see Figure 1.32 and can be seen to be of order 80 μm.

The gating pulse is fed to the cathode by incorporating it and the anode grid into a 50 ohm microstrip transmission line. In order to minimise reflections from impedance mis-matches the cathode geometry was carefully designed to maintain the 50 ohm impedance of the microstrip, see Figure 1.33.

The microstrip consists of a piece of copper clad printed circuit board, this provides structural rigidity and a conducting ground plane. Onto the copper is placed a strip of dielectric and onto this is placed a thin strip of copper to form the signal line of the microstrip. The dielectric chosen is polythene because of its relatively low loss-tangent in the gigahertz frequency range. The dimensions of the dielectric and signal line were calculated to produced a line impedance of 50 ohms. The microstrip is carefully joined to a coaxial cable to allow ease of input of the gating pulse. Low inductance capacitors capable of passing high frequencies are employed to isolate the cathode from extraneous DC voltages. A separate line to the cathode region allows the positive bias, necessary to turn the cathode current off, to be applied.

The assembled microstrip and cathode was tested on a sampling oscilloscope using time domain reflectometry (TDR) techniques. This allowed accurate impedance matching of the various sections to be achieved. It was also possible using TDR to measure the rise-time of the system. This was found to be about 140 ps, future work may allow this figure to be further

improved.

In order to obtain the very short 'on' time required it is intended to inject into the microstrip-cathode system a voltage pulse of as large a magnitude as possible (at least 50 v) and as fast a rising edge as possible. This pulse is then reflected from a shorting stub further down the microstrip. The reflected edge of the pulse then chops off the remainder of the incoming pulse and thus turns the cathode off again. Therefore the period of time for which the cathode is gated on will be determined by the separation of the cathode and the shorting stub, this is of the order of a few centimetres for the gating times required.

The fast rising pulse can be generated by a photodiode illuminated by a split off from the main laser. Various types of photodiode were tested: vacuum photodiodes, silicon avalanche photodiodes, silicon PIN photodiodes. Their response times were measured using a real time Thomson high speed oscilloscope at AWRE Aldermaston. The most suitable proved to be PIN diode mounted in a matched holder as described by McCall (1.19). This is capable of delivering a 100 v pulse into 50 ohms with a rise time of 100 ps.

The remainder of the intensifier consists of a proximity focused micro-channel plate and a P11 phosphor. This is coupled to recording film via a fibre optic face plate.

The assembled intensifier has been tested out on the X-ray microfocus and is now ready for testing with a pulsed X-ray source from a laser produced plasma. This will allow the gating operation to be examined.

Future developments envisaged are the incorporation of the intensifier into a target chamber flange to allow operation without breaking vacuum. Also the construction of an evacuated, sealed tube version which will permit the use of a low density CsI photocathode, and make the device independant of the target chamber pressure.

A J Cole, A Dymoke-Bradshaw, J D Kilkenny and J Westlake (Imp Coll)

Fig 1.31

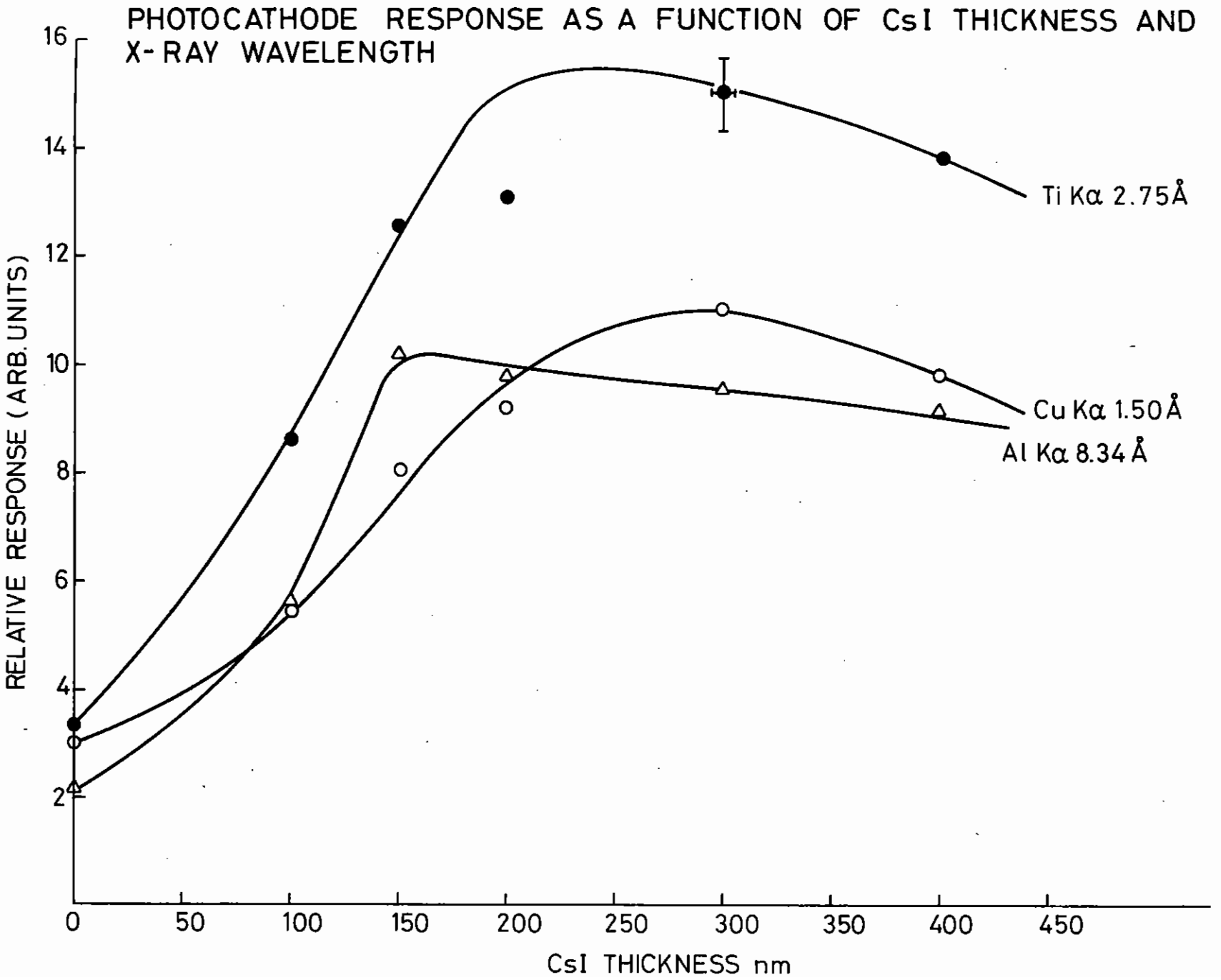
PHOTOCATHODE RESPONSE AS A FUNCTION OF CsI THICKNESS AND X-RAY WAVELENGTH
RELATIVE RESPONSE (ARB.UNITS)
16
14
12
10
8
6
4
2
0
50
100
150
200
250
300
350
400
450
CsI THICKNESS nm
Ti Kα 2.75Å
Cu Kα 1.50Å
Al Kα 8.34Å

Fig 1.32

DENSITOMETER TRACING OF X-RAY INTENSIFIER IMAGE OF RESOLUTION GRID

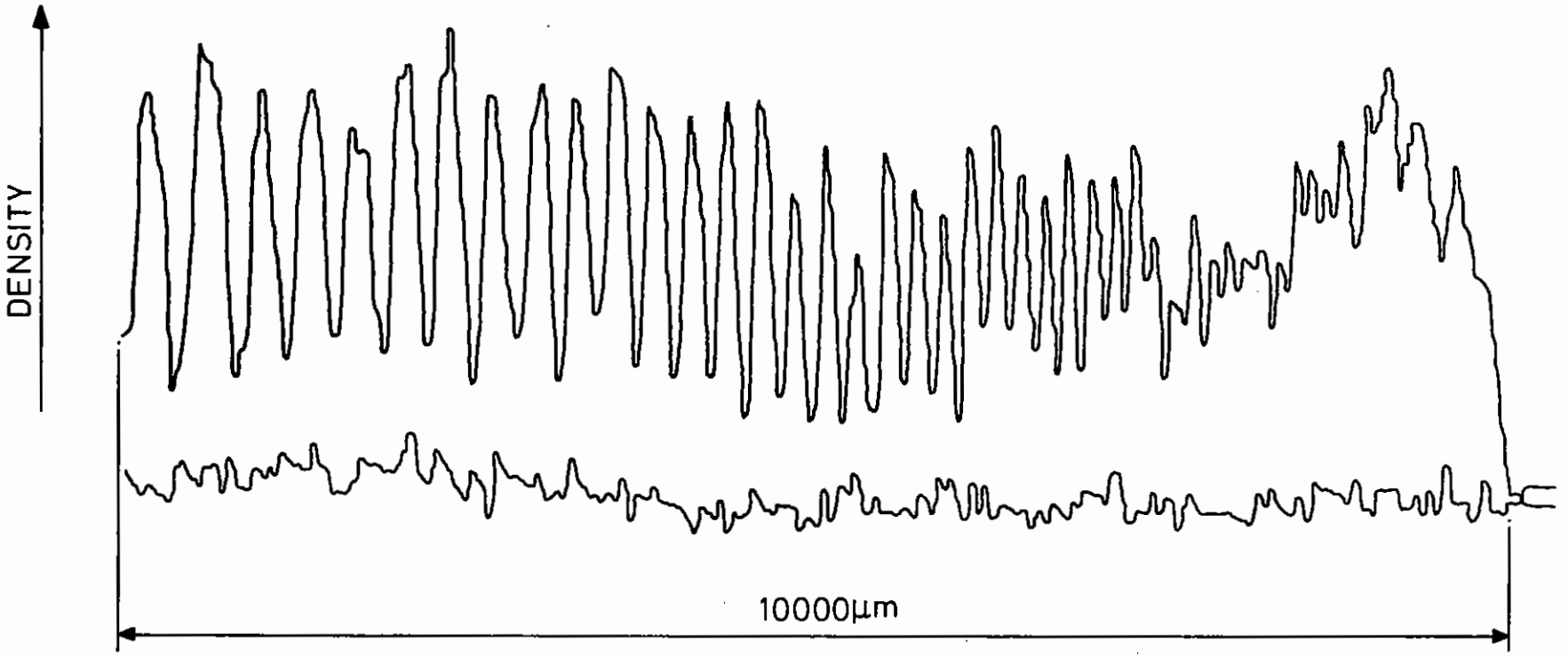

Fig 1.33 GATED MICRO-CHANNEL PLATE X-RAY INTENSIFIER

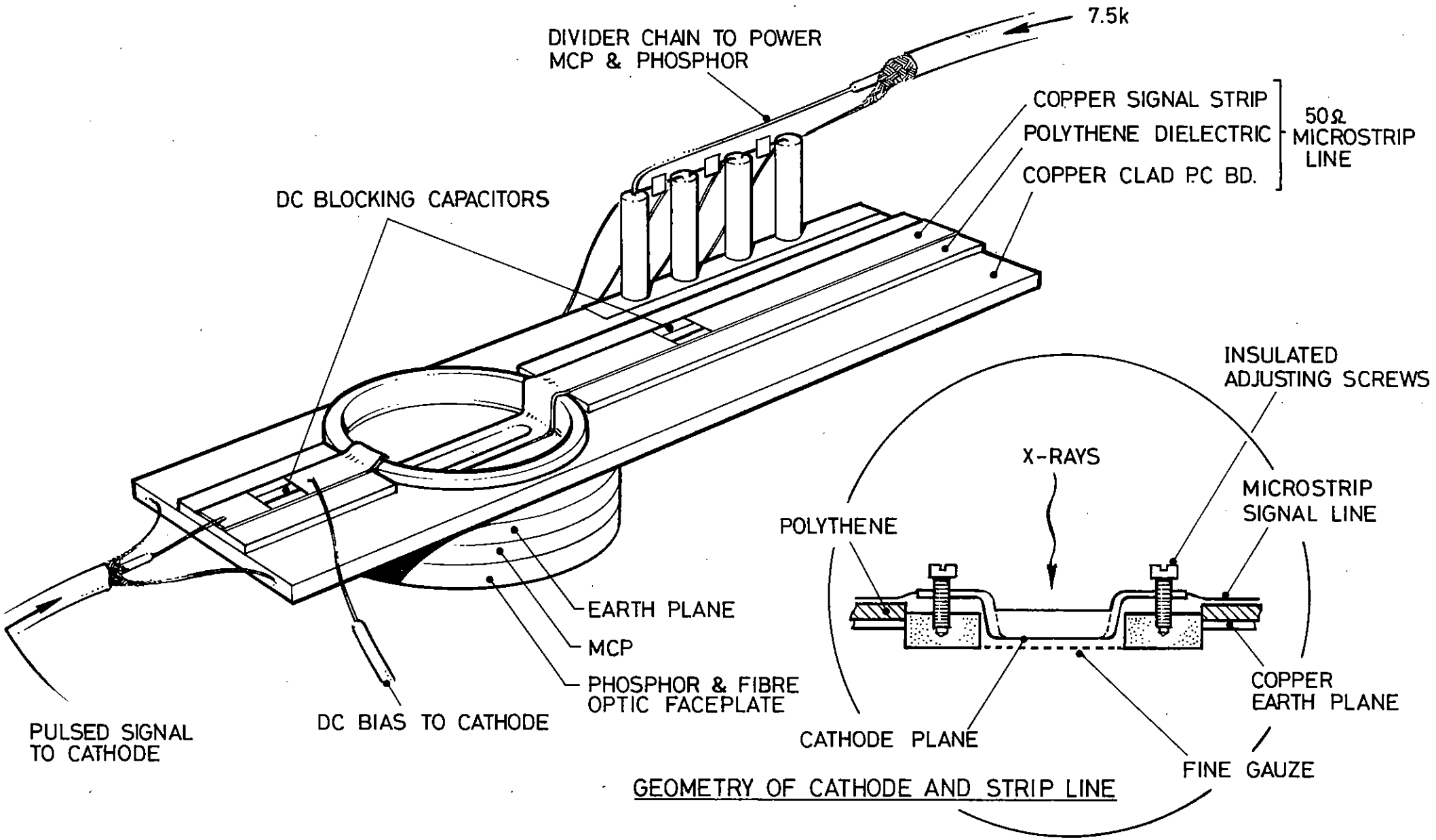

1.6.3 X-ray Diode Array

The mode of operation of the eight channel PIN diode array which is used to measure x-ray continuum emission from laser produced plasmas has already been described (1.13). Recently modifications have been made to the software used to interpret the detector signals. A two temperature, two percentage fit is now used to obtain the total integrated response for various foil-detector combinations.

The problems associated with a simplistic treatment which relies on an assumed and invariant cut-off energy for each foil have been recognised for some time (1.20). If the contribution from hot electrons is sufficiently small then relatively narrow spectral slices, bounded by a low energy cut-off and the K absorption edge of the foil material, can be arranged for each foil-detector combination. If this is not true however, then the signal recorded for some of the softer channels will contain a significant contribution due to the x-ray spectrum above the K-edge, where the foil transmission increases again.

To be useful in routine calculation of hot and cold electron temperatures the software must be capable of deriving meaningful values with the minimum of operator support, using an acceptably small amount of computer time. To this end several iterative unfolding routines have been tried which extract the true x-ray spectrum from the measured diode signals and the known response function matrix. Discontinuities and oscillatory behaviour that sometimes occur in the calculated spectrum mean that smoothing is usually necessary before each iteration, making the technique somewhat cumbersome.

Several minimisation routines have been developed which search for a minimum value of chi-squared in fitting the four parameters, hot temperature, cold temperature, ratio of hot to cold electrons, and a normalisation factor between calculated signal and experimental counts. A quite general routine has been written which calculates a best guess to to the four variables by a progressively narrowing grid technique. This method avoids the problems often encountered in minimisation routines

which arrive at a local minimum in n-parameter space rather than the desired global minimum. An initially coarse grid allows rapid homing in on the best fit parameters, which a subsequent finer grid then optimises.

The routine appears very flexible and does not object to the ill-conditioning which is a characteristic of this problem. Typical run times are less than 40 sec on an IBM 361/195.

An example of the output produced appears in Table 1.02. Diode signals have been calculated for the values of the four parameters shown in column 2, using a typical set of foils. These signals have then had varying amounts of random noise superimposed and been used as input to the minimisation routine. The calculated best fit results for the four parameters are shown, indicating that apart from a single value of T_{COLD}, they all fall within the range of random error introduced.

R Eason (RAL) and A A Pugatschew (Univ of Essex)

1.6.4 Zone Plate Imaging (Coded Apertures)

Preliminary experiments have shown that coded aperture imaging using zone plates is an ideal method for obtaining 2-D X-ray images of imploding targets at energies above a few keV. Images of both the X-ray emission from, and transmission through ablatively imploded targets have been obtained.

During the past year there have been developments in both the experimental and theoretical aspects of this work. New zone plates fabricated in 5 μm thick gold have been obtained for use with X-rays having energies above 4 keV. They have 280 zones with a minimum zone width of 5 μm which is limited by the onset of unwanted diffraction effects in the encoding stage. They are intended for use at low magnification ($\sim$ 2 x) and have a resolution of approximately 8 μm).

The first experiment in which these zone plates were used was the implosion radiography experiment described in section 5.3. The images

TABLE 1.02 Output from Fitting Program

Fitted Parameters	Input Values used to Calculate Diode Signals	Output Values from Minimisation Routine Random errors of up to ± X% superimposed			
		X = 0%	X = 5%	X = 10%	X = 25%
T_{HOT}(KEV)	10.0	10.0	10.4	10.8	12.3
T_{COLD}(KEV)	0.50	0.49	0.46	0.45	0.55
% HOT	5.0	5.0	4.8	4.9	4.7
Normalisation Factor	100,000	99,900	104.000	98,600	96,300

obtained in this experiment were of much higher quality than those obtained with the earlier 120 zone apertures but the signal to noise ratio in reconstruction was not greatly improved.

The zone plates have also been used with the X-ray microfocus source in experiments comparing X-ray pinhole camera images of the X-ray emitting spot with zone plate reconstructions. A simple model of the encoding and reconstruction processes was used to calculate relative X-ray intensities in the source from the reconstructed image. A linear approximation to film response was used, which was reasonable for the range of densities concerned. The resulting relative intensities were found to agree quite well with the relative X-ray intensities calculated from the pinhole camera image. A further experiment is planned in which a glass microsphere will be radiographed using the microfocus source, to test whether X-ray abosrptions can also be obtained from zone plate reconstructions using this model.

C Duncan (Oxford) and P T Rumsby (RAL)

1.6.5 Microfocus X-ray Facility

A new high-performance X-ray source of unusual design was commissioned early in 1980. It was intended for X-ray experiments ancillary to the laser experiments. Since its installation it has been in continual use, to the extent that an operating schedule allotting time on it has had to be established.

A full description of the device can be found in the 1980 Rutherford Laboratory Annual Report to the Laser Facility Committee (1.13). Its performance capabilities are much superior to any similar instrument. A high current electron beam (typically 0.5 - 1.0 mA at 15 kV) can be focused by a single magnetic lens into an external spot on a water cooled target anode selected by means of a rotating turret from one of the following materials: copper, aluminium, molybdenum, titanium or silver. The focal spot diameter can be varied from 0.5 - 1.0 mm down to 3 μm or less, depending on the choice of electron beam aperture. Figure 1.34

X-Ray Microfocus Source

Grid Radiography

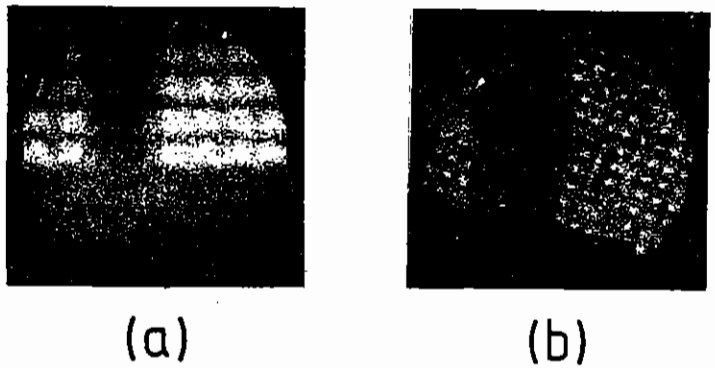

Figure 1.34 Radiographs of silver grids of (a) 1000 and (b) 2000 lines per inch (grid spacing 25 μm and 13 μm). The grid bars are of approximate thickness (a) 9 μm and (b) 6 μm.

shows radiographs of silver grids of (a) 1000 and (b) 2000 lines per inch (grid spacing ∿ 25 μm and ∿ 13 μm) placed 1 cm from the focal spot. The magnification onto the radiograph was x 20, the accelerating voltage 15 kV and the apertured beam current 80 μA in case (a) and 40 μA in case (b). The electron beam was focused for the radiographs with the use of an auxiliary grid casting a shadow onto an X-ray vidicon tube, the image from which was viewed on a TV screen. The resolution of the grids indicates a focal spot size of ∿ 3 μm. The chamber housing the device has four standard ports at the same distance from the chamber centre (and X-ray spot) as are the ports on the laser target chambers from the target.

The flexibility of the facility has made it very useful in a variety of applications. Its ability to produced a finely-focused spot has been exploited in the magnification radiography of specially-structured laser targets to determine the precise density to X-rays of given wavelength. The performance of Fresnel zone plates in X-ray coded imaging (1.13) has also been assessed using this property. A small X-ray spot was also used for testing and cross-calibrating different crystals in a space-resolving Bragg crystal spectrograph.

With a lesser degree of focusing, the source has been used to produce a shadow of a copper zone plate on the cathode of an X-ray streak camera in order to determine the resolution and sensitivity of the camera system (section 1.6.1) on X-ray streak camera and cathodes. Both the X-ray streak cameras in use at the CLF have now been tested in this way, and the system has proved invaluable in the convenient diagnosis of camera faults, and the evaluation of relative cathode sensitivities (section 1.6.1). The development of a fast gated X-ray intensifier system (X-ray framing camera) has also taken place mainly on the X-ray source. The defocused electron beam has been used to produced a high-intensity uniform extended source for radiography of microballoons using an X-ray pinhole camera.

On a simpler level, the source has made possible the comparison of the sensitivities of different types of X-ray film in the CLF experiments. With the development of an absolutely-calibrated reference detection system for the device, the absolute calibration of X-ray film and

instruments will become possible.

A new project which has recently begun on this facility relies heavily on the stability, small spot size and high flux production of the source, as well as on precise and stable engineering, for its success. This is the grazing-incidence imaging and spectroscopy project described below.

The X-ray facility has proved to be reliable and convenient in use. It is an investment which is rapidly paying for itself in terms of saved laser 'test shot' time, reduction of experimental setting-up time, and the ability to rapidly develop new X-ray diagnostics.

1.6.6 Grazing-Incidence XUV Imaging and Spectroscopy

There is considerable interest in the spectroscopy of laser plasmas in the far vacuum ultraviolet region (∿ 20 Å - 300 Å), both because of the potential new physics open to spectroscopic investigation in the region (1.21, 1.22) and because of the diagnostic possibilities of spatially-resolved measurements of line shifts, widths and intensities (1.23).

This wavelength range is technically difficult to investigate, since it lies between the long wavelength limit of Bragg reflection crystal spectroscopy (∿ 25 Å) and the short wavelength limit of conventional near-normal-incidence spectrographs. To obtain appreciable reflection from an optical surface it is necessary that the radiation should be incident at a small grazing angle. In a spectrograph only one reflection should take place, that from the diffraction grating. To achieve good spectroscopic resolution the slit, concave grating, and plate must lie accurately on the Rowland circle of the grating, with a tolerance in radial position of order 20 μm or less. Further difficulties are caused by the small aperture of the instrument (typically f/120 for a 5 m instrument) and the frequently strong variations in grating reflection coefficient with incident wavelength. Lenses cannot be used to focus light into a grazing-incidence instrument, which generally means that it must be placed as close as possible to the emitting source. The restrictions on occupation of solid angle in a crowded laser target

chamber usually make close proximity to the target impossible, so that the necessary single-shot spectrum recording cannot be made.

Some of these problems - those involving high-tolerance alignment of spectrograph components, and grating reflection problems - have been essentially solved (by the devising of the GML5M spectrograph) by Speer and Turner at Imperial College (1.24), who have also suggested a solution to the problem of filling the instrument aperture (1.25). This involves the use of a grazing incidence concave toroidal mirror (1.24) having radii of curvature 25 mm and 5000 mm. The mirror will image radiation incident at an angle of 4° from a point 375 mm from its pole, and on its Rowland circle, at the conjugate focus 375 mm away on the otherside, with a resolution of order 10 μm. The aperture of the mirror is slightly greater than that of the spectrograph, so that the mirror can be used as a collection 'lens' to fill the spectrograph aperture with the slit a convenient 750 mm from the target.

The GML5M spectrograph at the CLF has been used fairly successfully in conjunction with a toroidal mirror with the above characteristics (1.26), but it was clear from that experience that high precision of alignment and mechanical stability would be needed to produce good results. An adaptable system has therefore been devised, based on a rigid bar, by which the toroidal mirror can be positioned accurately and held stably with respect to the X-ray source and the GML5M spectrograph. The first stage in the development of this system, that of investigating the detailed imaging properties of the mirror, is shown in Figure 1.35. The toroidal mirror is supported in the adjustable mount just inside the port, and an X-ray film camera is mounted in the eventual position of the GML5M slit. Preliminary results have just been obtained using this system to image the X-ray source spot onto Kodak No-Screen X-ray film. The basic adaptable mechanical system has already been found useful in unrelated other work.

When the toroidal mirror properties have been fully evaluated, it is proposed to extend the system, as shown in Figure 1.36, to include the GML5M with its slit in the image position. It is hoped that it will be

Grazing-Incidence Imaging

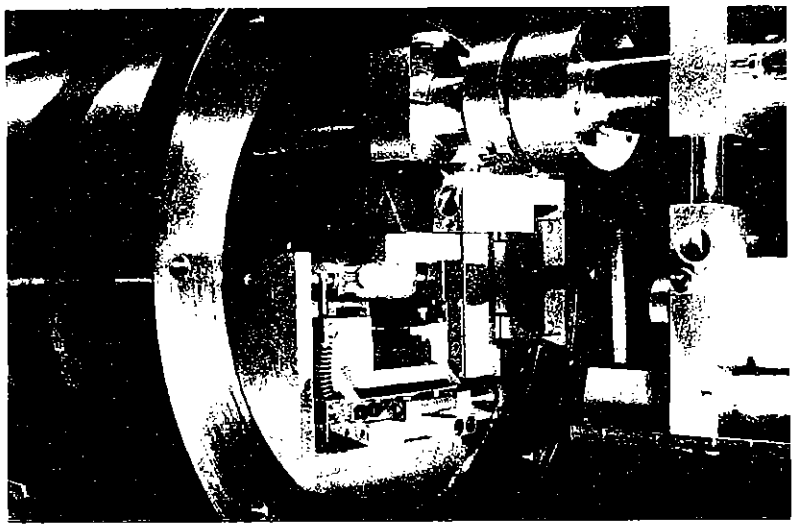

Figure 1.35 A part of the microfocus x-ray source chamber, showing the mounting bar supporting the toroidal mirror mount assembly just inside the port. The end of the horizontal grazing-incidence mirror (major radius 5m, minor radius 25.07 mm) can just be seen in its cradle next to the engraved millimetre scale. The X-ray camera assembly is on the extreme right of the picture

Fig 1.36 GML5 GRAZING INCIDENCE SPECTROGRAPH

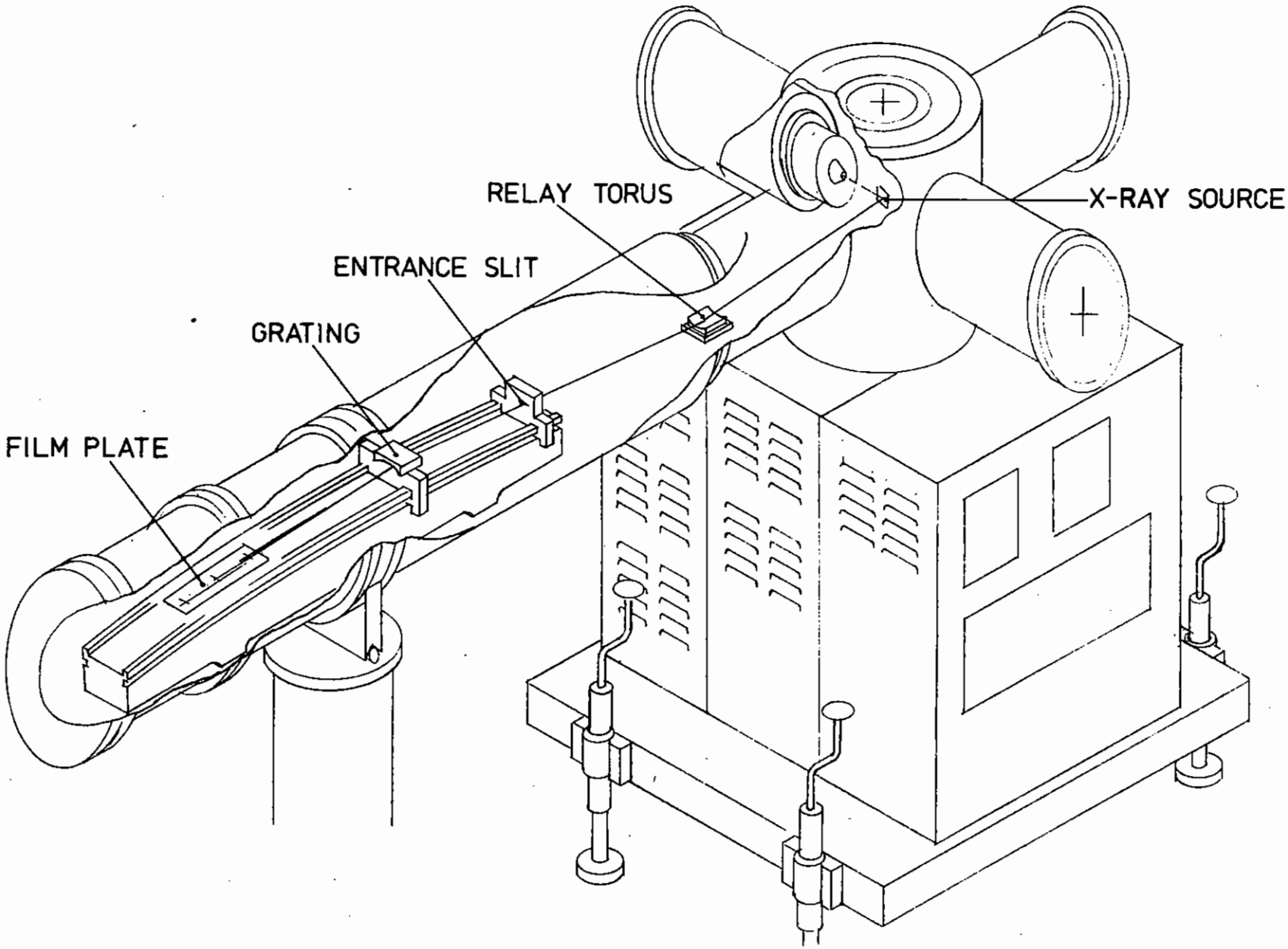

possible to align the combination on the target to a precision of about 20 μm. The final stage in the development will be to fit the GML5M with a toroidal grating (1.24) in cooperation with Dr R J Speer at Imperial College, with the aim of producing stigmatic imaging over a selected range of wavelengths. It should then become possible to produce space-resolved grazing incidence spectra with a spatial resolution of order 10 μm. The system is so designed that it s compatible with the laser target chamber . and can be readily transferred onto a laser experiment.

P M Rockett (Oxford Applied Research Ltd) and J M Ward (QUB)

CHAPTER 1 REFERENCES

1.01 M H Key et al, Phys Rev Lett, 45, 1801 (1980)

1.02 O Willi et al, "Optical probe observations of non uniformities in Laser Plasma Coronas", submitted to IEEE, Jour Quant Elect

1.03 C J Reason, P Gottfeldt and J G Watson, "Control and Data Acquisition at the Rutherford Laboratory Laser Facility", Proc Real Time Data 1979, North Holland (1979)

1.04 D C Hanna, B Luther-Davies and R C Smith, Electronic Letters, 8, 369 (1972)

1.05 Annual Report to the LFC, RL-79-036, 8.52 (1979)

1.06 Annual Report to the LFC, RL-80-026, Figure 1.01 (1980)

1.07 W Seka et al, Optics Comm, 34, 469 (1980)

1.08 R S Craxton, Optics Comm, 34, 474 (1980)

1.09 F Zernike, J Opt Soc Amer, 54, 1215 (1964)

1.10 R A Phillips, J Opt Soc Amer, 56, 629 (1966)

1.11 R S Craxton, private communication

1.12 J A Armstrong et al, Phys Rev, 127, 1918 (1961)

1.13 Annual Report to the LFC, RL-80-026, Section 1.6 (1980)

1.14 D J Nicholas and K P Duffey, Rutherford Laboratory Report RL-80-075 (1980)

1.15 Annual Report to the LFC, RL-80-026, Section 6.1 (1980)

1.16 J E Bateman and R J Apsimon, Adv Elec Phys, 52, 189 (1979)

1.17 Annual Report to the LFC, RL-79-036, 145 (1979)

1.18 J E Bateman, R J Apsimon, Rutherford Laboratory Report RL-79-087 (1979)

1.19 G H McCall, Rev Sci Inst, 43, 865 (1972)

1.20 H N Kornblum et al, Lawrence Livermore Laboratory, UCRL-81471 (1978)

1.21 Rutherford CLF Annual Report, RL-80-026, section 6.4 (1980)

1.22 Rutherford CLF Annual Report, RL-80-026, section 6.5 (1980)

1.23 P Jaeglé et al, Journal de Physique Lettres, 40, L-551 (1979)

1.24 R J Speer, Space Science Instrumentation, 2, 463 (1976)

1.25 R J Speer and D Turner, Annual Report to the CLF (1978)

1.26 Annual Report to the CLF, RL-79-036, section 7 (1979)

CHAPTER 2 GAS LASER DEVELOPMENT

INDEX

CHAPTER EDITOR: F O'Neill

CHAPTER 2 GAS LASER DEVELOPMENT

2.1 Introduction

During the past year gas laser work has concentrated on the development of e-beam-pumped and discharge-pumped KrF lasers. This direction of effort is due to the belief that a high power (~1 KJ, ~1 ns), multibeam (~20) laser system for compression studies could be constructed using KrF as the active medium. Our main effort has gone into the design and construction of the 200 J, 60 ns KrF laser SPRITE and into experiments using ELF to provide physics and engineering information to aid SPRITE's design.

On the physics side we have used the ELF e-beam-pumped laser to investigate the characteristics (gain, absorbing species, etc) of the KrF gain medium under conditions of pump rate and pressure appropriate to the planned operating regime of SPRITE. A computer model of the kinetics of the KrF laser has been developed using the experimental results from this investigation and this model is now being used to optimise the laser aspects of the SPRITE design.

On the engineering side ELF has been used to test a half-size SPRITE e-beam diode to investigate emitter design, and to measure the profile of large area e-beam energy deposition in high density gas. It is important to know the profile so that the diameter of the SPRITE laser cell can be properly chosen in relation to the diode voltage and laser gas pressure. ELF has also been used to test one of the 5 Ω SPRITE pulse forming lines. As can be seen from Figure 2.01 a 1 MV change-over switch has been installed in the ELF Marx bank so that the Marx can eventually be used to pulse charge either the ELF oil Blumlein or SPRITE via a water capacitor. In the meantime a prototype 5 Ω line has been fitted directly to the Marx so that the critical aspects (eg line output gap, e-beam diode insulator, etc) of the SPRITE design can be tested. When these tests are successfully completed we will then order all the SPRITE pulse power components, ie 4 lines, 4 output gaps, 8 diode insulators, etc. Design work on the laser cell is now underway.

This work is discussed in more detail below along with work on discharge lasers and on various aspects of KrF short pulse amplification and generation.

F O'Neill

2.2 KrF Laser Development

2.2.1 Computer Modelling of E-beam-pumped KrF Lasers

During the past year, a computer model of the kinetics of the electron-beam-pumped krypton fluoride laser has been developed and is now running on the IBM 360 computer system at the Rutherford Laboratory. The code was intended primarily to further the understanding of the most important kinetic channels of the KrF laser system and to compare its theoretical predictions with the results of experiments at RAL and elsewhere. The agreement with published results has been excellent, and the code has been used to optimise the design of SPRITE and predict its efficency, and to complement the analysis of experimental measurements of optical gain and loss in KrF* (2.01) in both oscillator and amplifier configurations.

Fourteen species are incorporated in the model including the usual atomic and molecular ions, the rare gas metastables Ar* and Kr*, and the triatomic excimers Kr_2F^*, KrArF*, and Ar_2F^*. In all some fifty processes are treated, including the primary formation kinetics of KrF*, quenching, radiation, and absorption of all species where appropriate, and the metastable reactions. Reaction rates and cross sections are taken from the literature (2.02). The rate equations for the population densities of the atomic and molecular species are solved in steady state by the Gauss elimination method, using a matrix formulation for ease of computation (2.03). The use of a steady-state approach, justified since the kinetics at the normal laser working pressures are rapid compared to the pumping time, greatly reduces the amount of computer time taken for a calculation. This is an important consideration since several of the rate equations solved are non-linear to second order in the chosen variables. In consequence the population density of KrF*, F , F^-, the electron

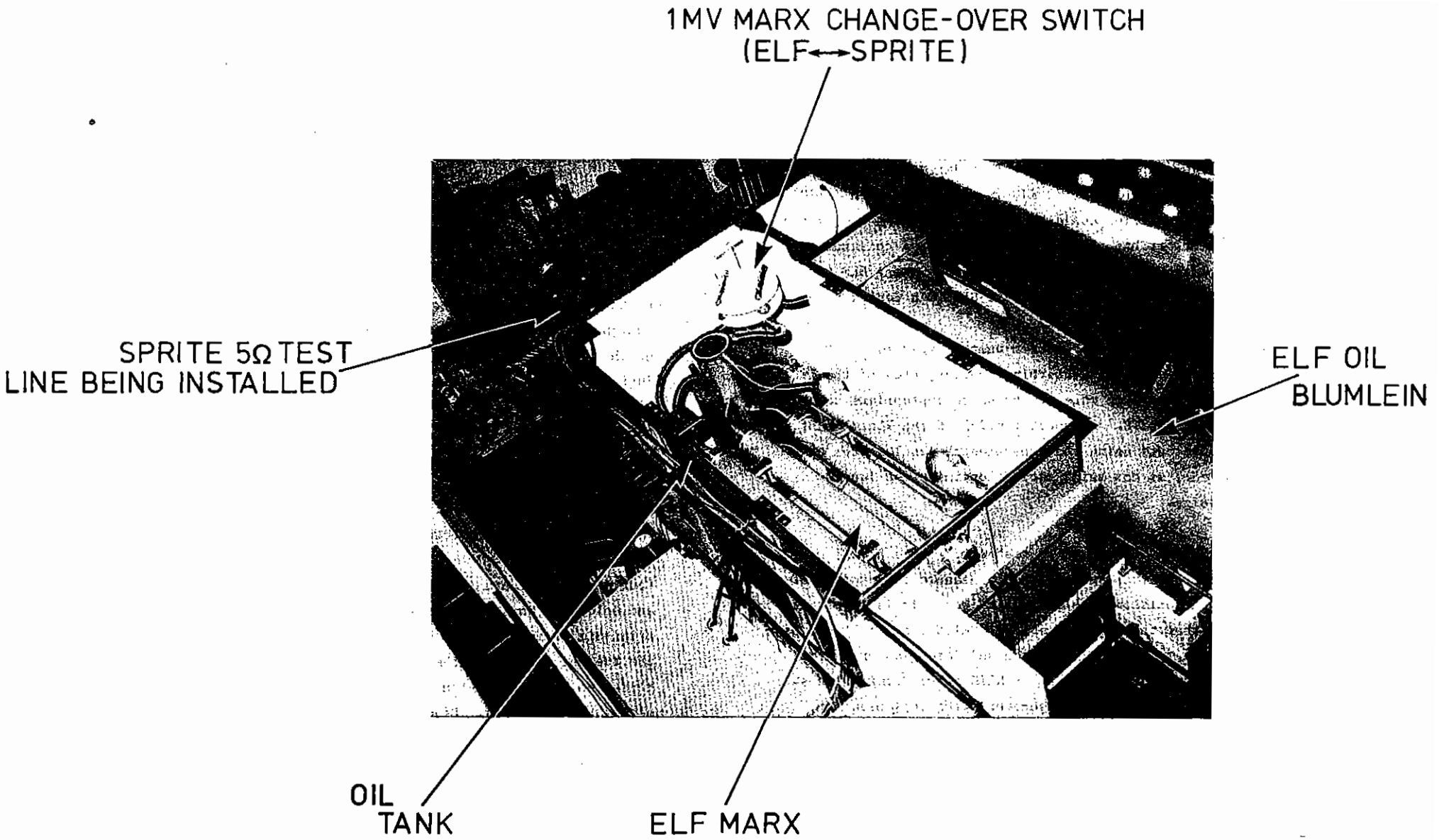

Figure 2.01 The Elf electron beam machine viewed from above

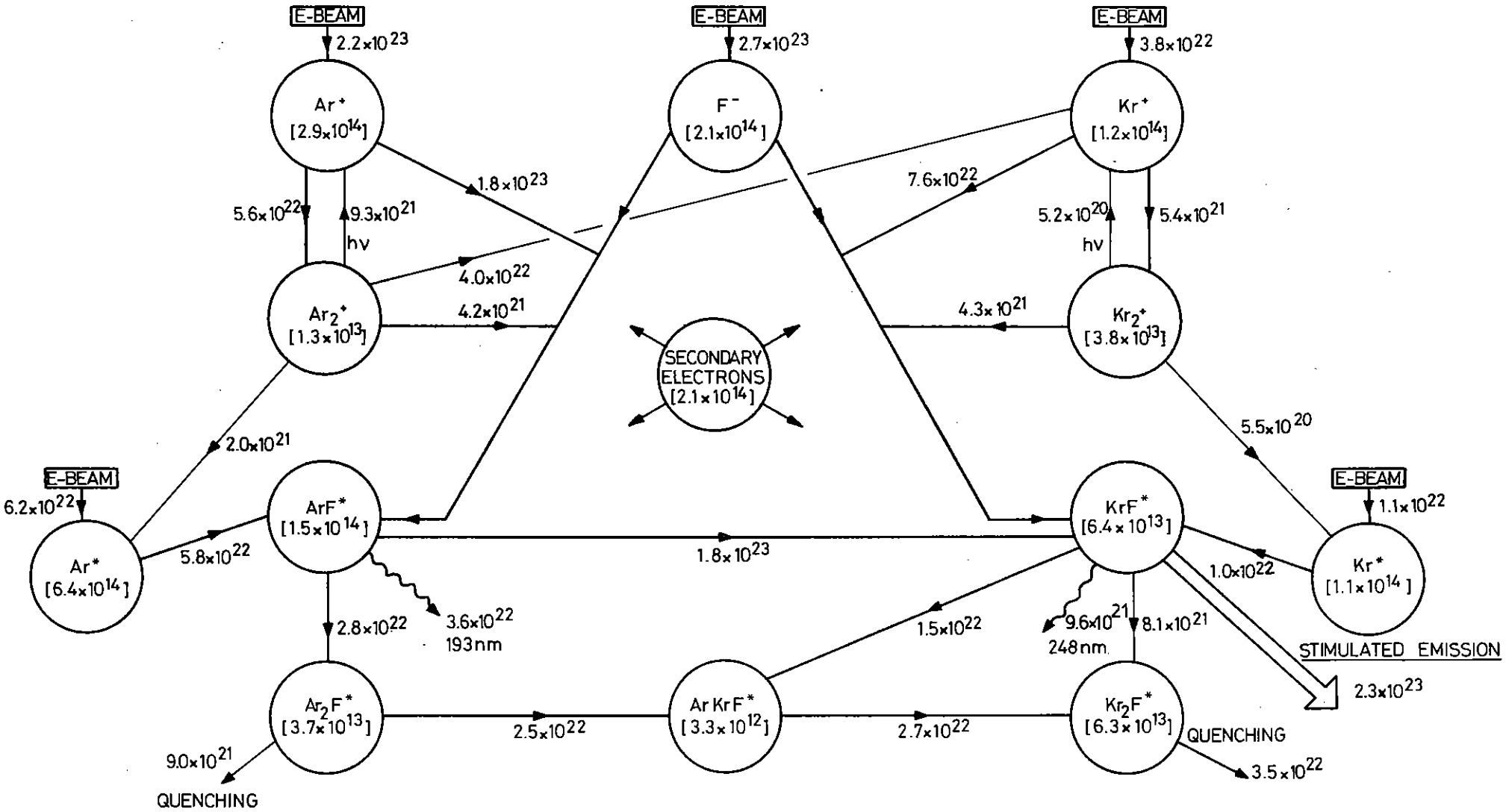

Figure 2.02 Summary of KrF* laser kinetics

density, and the intracavity photon flux in the case of laser action, are calculated to arbitrary accuracy by nested iterations, and each solution takes a substantial amount of processor time. The model treats the case of steady state laser action using the laser threshold equation $R_1R_2 \exp(2g\ell) = 1$ where R_1 and R_2 are the mirror reflectivities, and g is the threshold value of the net gain coefficent of the medium of length ℓ, given by the equation $g = \sigma_s[KrF^*] - \left[\sum_i \sigma_a(i)[i]\right.$ where σ_s is the stimulated emission cross section, quantities in square brackets refer to number density of species, $\sigma_a(i)$ is the absorption cross section of species (i) at the laser wavelength, and the summation is performed over all species. The intracavity laser intensity is determined from the value of the photon flux required to maintain the KrF laser gain at the value defined by the above threshold equation. Laser action may be excluded by the removal of appropriate terms in the rate equations and the code then yields the steady state populations in the approximation of zero intracavity flux. Amplified spontaneous emission is not treated. Thus the model can be used to predict laser output, small signal gain and loss, and the effects of saturable gain and loss as a function of intracavity flux (the amplifier mode).

The dominant kiretic processes are shown schematically in Figure 2.02 where rates (s^{-1}) refer to a 1 MW cm^{-3} pump rate and a gas mixture of F_2:Kr:Ar = 4 torr:125 torr:1371 torr and quantities in square brackets are population densities (cm^{-3}). The code has been used to predict the intrinsic laser efficiency of the ELF KrF laser system (2.04) to within 10 % of measured values at pump rates up to 2 MW cm^{-3}. It also agrees to within 5 % with experimental results obtained by Jacob et al (2.05) at pump rates of 0.1 to 0.25 MW cm^{-3}.

Small signal gain and loss, and saturable absorption have been predicted in extremely good agreement with measurements at the Rutherford Laboratory (see section 2.2.2). In addition, at pump rates of 4 MW cm^{-3}, an experimental measurement of gain of 24 % has been observed by Bradford et al (2.06) while the code predicts 22 % under similar conditions. At lower pump rates, (1.8 MW cm^{-3}) Rice et al (2.07) obtained gain and loss coefficients of 17 % ± 1 % cm^{-1} and 0.8 % ± 0.25 % cm^{-1} while the code predicts 15.5 % and 0.7 % respectively. From these results it would

appear that the code correctly handles the dominant processes in the KrF* laser since good agreement with experiment is exhibited over a wide range of pump rates and gas mixtures. It is therefore possible to use the code as an aid to the design of the SPRITE laser system (see section 2.4.4) and to predict the performance of the KrF laser over a wide range of operating parameters.

Though the steady state approximation is extremely useful in a number of cases, it is planned to extend the code to a fully time dependent solution using a routine which solves the first order equations by a difference formulation of Gear's method. This will still require an iterative approach to the non-linear terms, but will enable optical pulse shapes to be obtained, and saturation effects of gain and loss to be studied more fully.

C B Edwards and F O'Neill (RAL)

2.2.2 Gain and Loss Measurements in E-beam-pumped KrF

One of the requirements for obtaining high efficiency and high output intensity from KrF lasers is that the ratio of gain to non-saturable loss in the laser medium should be as high as possible (2.08, 2.09). In general it is desirable to achieve a gain to loss ratio of > 10. We have carried out measurements to determine the gain and loss characteristics of a KrF laser using 60 ns e-beam excitation at pump rates up to 4 MW/cm^{-3}. These experiments were performed to provide information for the design of the SPRITE high power KrF laser and for checking the computer model described in section 2.2.1.

In the present experiments losses have been measured at pump rates up to 4 MW/cm^{-3} and gas pressures up to 3000 torr and net gain has been measured in a 1500 torr gas mix at pump rates up to 3MW/cm^{-3}. KrF net gain at 248.2 nm has been measured using the single pass/double pass amplified spontaneous emission (ASE) technique (2.10). Transient loss in the laser medium has been measured at 257.2 nm using a 0.5 mW probe beam obtained by second harmonic generation of a 514.5 nm argon ion laser. The absorptions

in the region of KrF gain peak are broadband (2.11, 2.12) and the absorption coefficient at the KrF laser wavelength (248.2 nm) can be assumed to be equal to that measured at the probe wavelength (257.2 nm). Kr_2F^* is a main contributor to the loss in the laser medium (2.13, 2.14). This loss should be saturable (or interceptible) since Kr_2F^* is formed predominately from KrF* which is itself saturated at high intracavity laser fluxes. Evidence for this saturable absorption effect has been observed directly as a reduction of optical loss in the laser medium in the presence of lasing.

The lay-out of the experimental apparatus is shown in Figure 2.03. The e-beam machine and laser cell have been described previously (2.04) but for the present experiments tantalum baffles have been fitted to the gas cell to define the pumped length, ℓ, more accurately. At low pump rates ℓ = 30 cm was used and at high pump rates ℓ = 15 cm was used to avoid gain depletion effects due to axial ASE. The quartz gas cell windows were angled at 5° to the cell axis to prevent gain depletion due to optical feed-back. The detector system for both gain and loss measurements comprised a monochromator (bandpass = 0.06 nm), a fast photomultiplier (response time < 5 ns) and a Tektronix type 7844 oscilloscope. The overall response time of this system was fast enough to resolve the variation of gain and absorption throughout the 60 ns e-beam pump pulse and in the discussion below the values of net gain, absorption and pump rate referred to, will be those measured at the peak of the pump pulse. To avoid saturation of the photomultiplier when taking loss measurements, the 257.2 nm probe laser was pulsed on for 20 μs using a chopper wheel and fast shutter and the e-beam was fired half way through the probe pulse. Absorption measurements in the presence of lasing were carried out using a 30 cm pumped length and a laser cavity formed with R = 100 % and R = 50 % dielectric coated mirrors. Oscilloscope records of some typical absorption results are shown in figure 2.04.

The net gain coefficient, g_o, in the pumped laser gas was calculated using the equation:

$$g_o = \frac{1}{\ell} \ln \left\{ \frac{(I_{DP}/I_{SP})-1}{RT^2} \right\}$$

where g_o = gross gain − loss. Here ℓ is the pumped length, I_{SP} and I_{DP} are the intensities of single pass and double pass ASE from the cell, R is the reflectivity of the mirror placed at the back of the cell to measure I_{DP}, and T is the transmission of the back window of the cell. It has been shown (2.15) that the ASE technique can give erroneous results for net gain measurements. In our case however the results should be accurate since we have used a large cell-detector separation (600 cm), and 2 mm diameter apertures were placed along the optical path to the detector to define a small solid angle (~0.1 μSTER) from which ASE was collected. This minimised errors due to geometric effects. Also since the e-beam driver was extremely reproducible between shots (± 5 % variation in energy deposited in the laser cell) it was possible to make single and double pass ASE measurements on separate shots without introducing large errors. Finally, optical alignment of the apparatus for ASE gain measurements was performed using a frequency doubled 496.5 nm argon ion laser which gives a calibration wavelength exactly at the peak of the KrF* fluorescence profile. This was particularly important for accurate setting of the monochromator.

Figure 2.05 shows a set of measurements of loss as a function of e-beam pump power. For these results the e-beam current density was kept constant at ~300 A/cm^2 (peak) and the pump power was varied by changing the laser gas pressure. The upper results were taken with no laser mirrors on the gain cell and the lower set of results were taken with the laser oscillating at high flux levels. Typically the intracavity laser intensity was 2 to 5 times greater than the KrF* saturation intensity. These measurements clearly demonstrate the reduction of medium loss in the presence of lasing. If we assume that the reduction of absorption is due to the interception of the Kr_2F^* formation channel by the lasing process then the computer model described in section 2.2.1 can be used to calculate the change of Kr_2F^* population brought about by allowing the laser to oscillate and thus give a value for the absorption cross-section of Kr_2F^* at 257.2 nm. Using these calculated values of the Kr_2F^* density and the absorption data of Figure 2.05 we estimate the absorption cross-section to be:

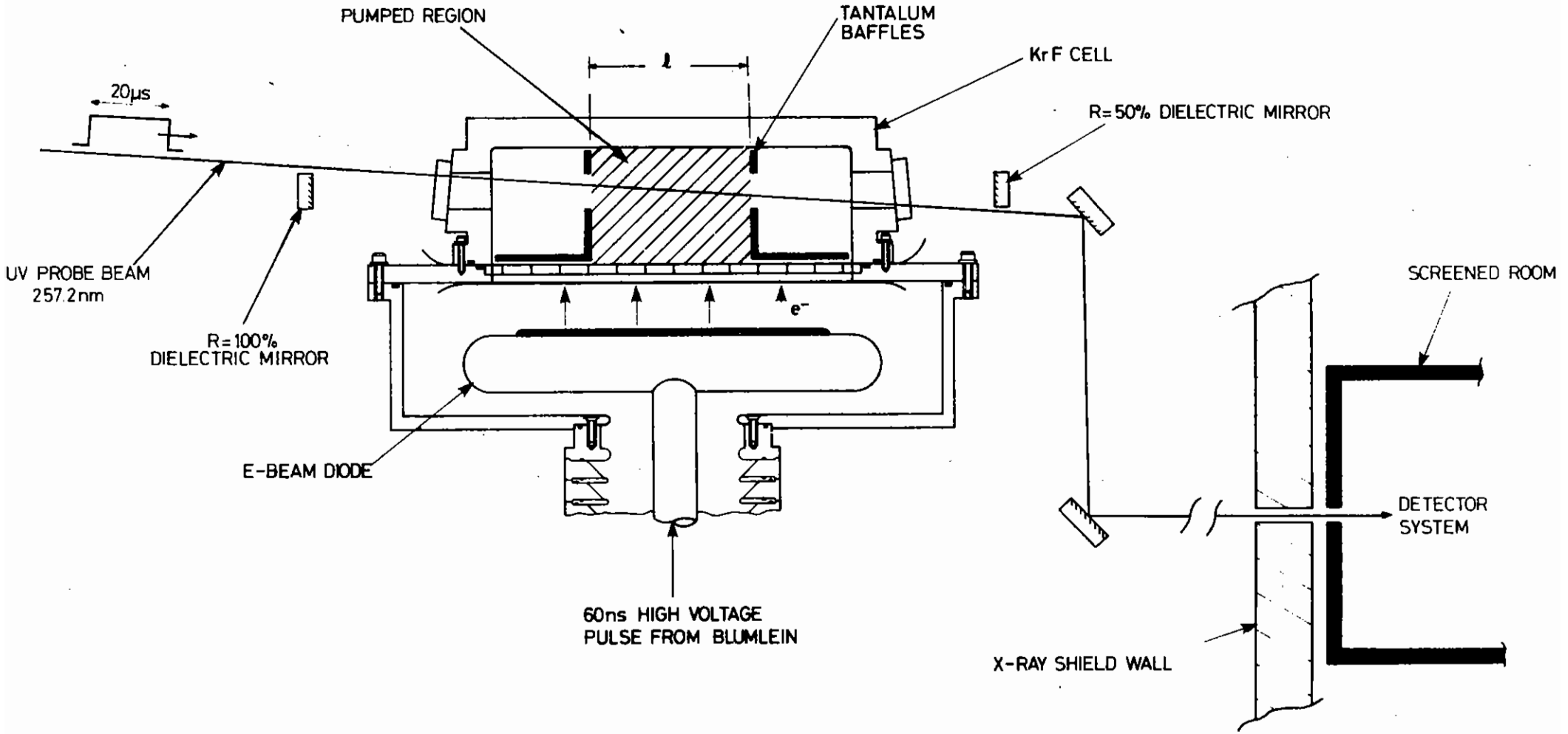

Figure 2.03 Experimental lay-out of apparatus used for absorption and gain measurements

LENGTH OF PUMPED REGION	=	30cm
CW PROBE LASER WAVELENGTH	=	λ = 257.2nm
PEAK E-BEAM PUMP POWER	=	2.1MW/cm^3 (60ns FWHM PULSE)
GAS MIX	=	4 torr F_2/125 torr Kr/1371 torr Ar

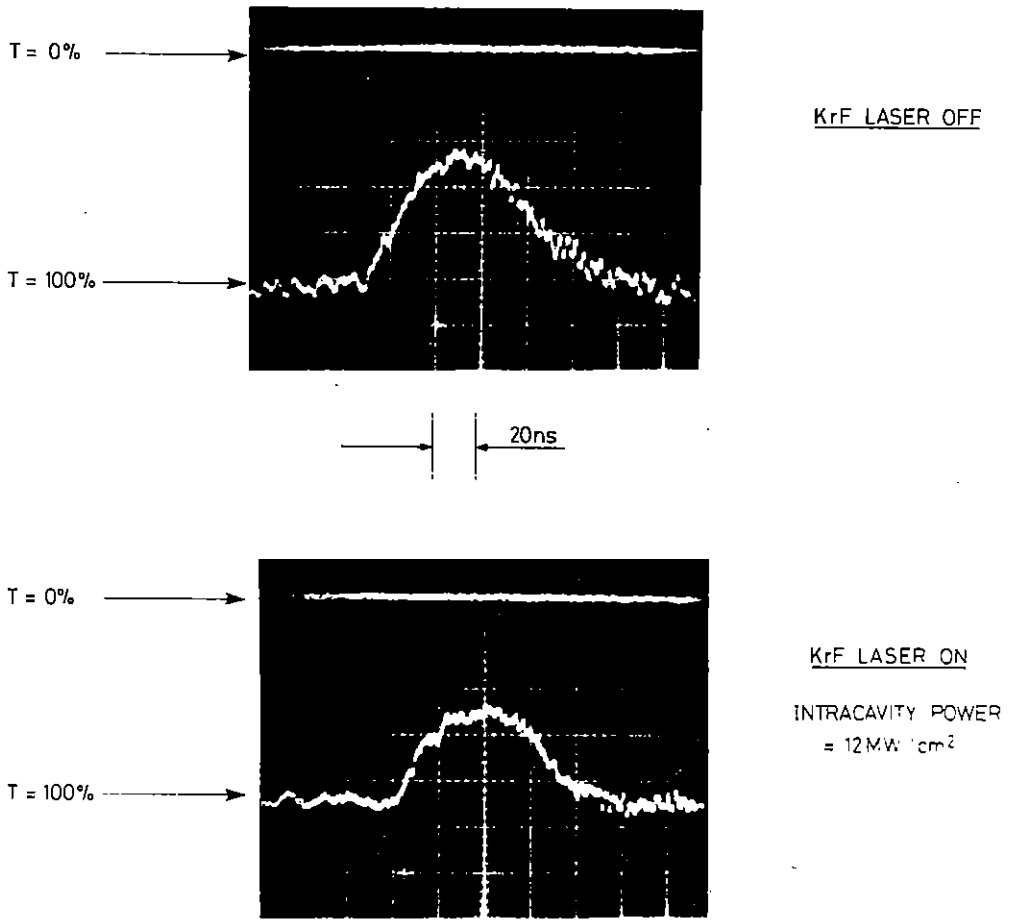

Figure 2.04 Typical oscilloscope records of transient intracavity absorption in E-beam-pumped KrF. Note reduced absorption and absence of decay tail in lower trace due to Kr_2F^* saturation. The Kr_2F^* formation channel has been intercepted by the intracavity laser flux

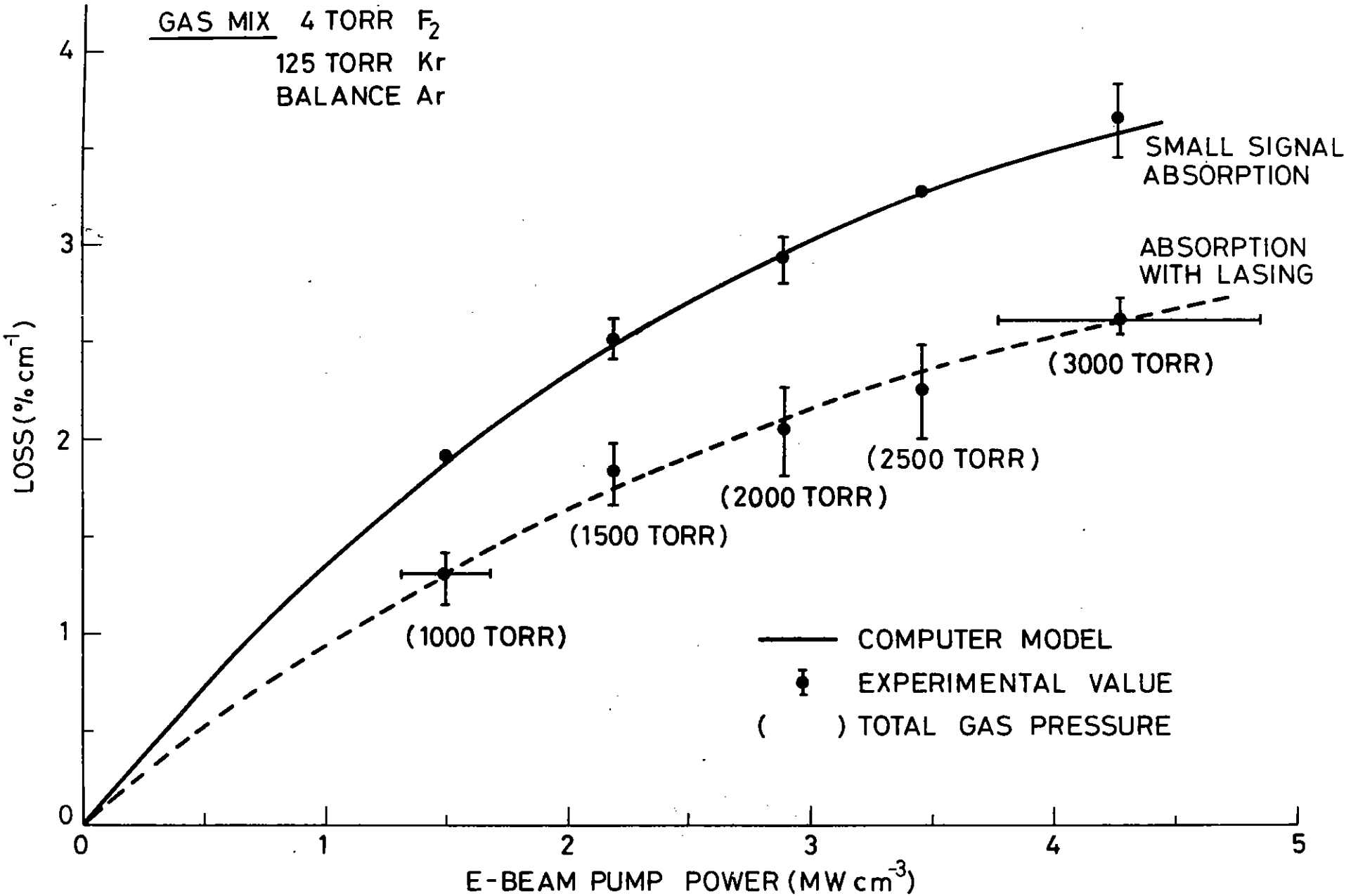

Figure 2.05 Loss at 257.2 nm as a function of E-beam pump rate and gas pressure. Vertical error bars are shown where more than one experimental measurement was taken, and represent one standard deviation

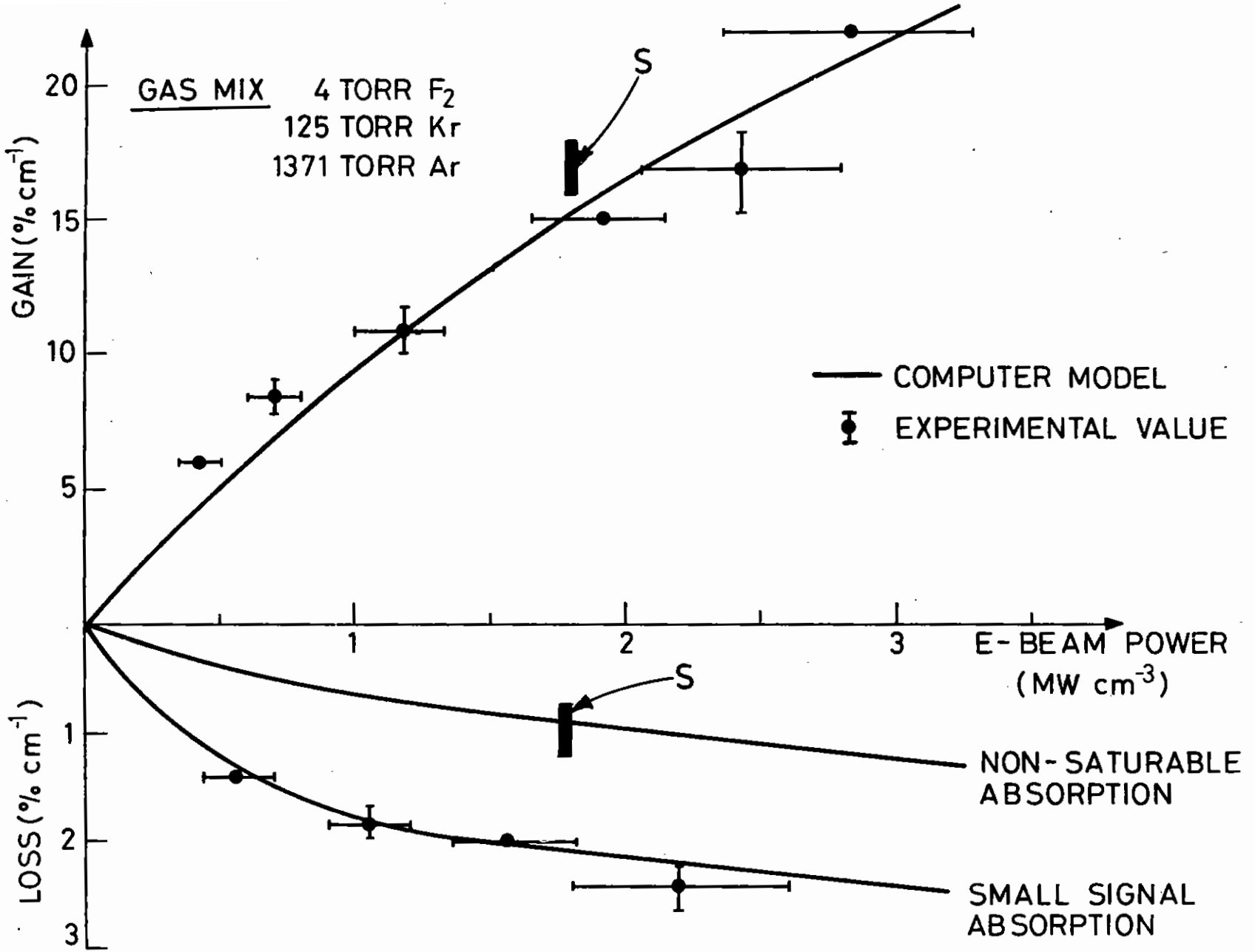

Figure 2.06 Gain and loss in 1500 Torr KrF laser gas mixture. Error bars represent one standard deviation. S = Measurement of net gain and non-saturable loss. Ref. 2.07

$$\sigma_a = 1.8\ (\pm 1.1) \times 10^{-17}\ cm^2$$

This is approximately an order of magnitude greater than the value previously predicted theoretically (2.14, 2.16). The solid line in Figure 2.05 is a computer prediction of small-signal absorption for these experimental conditions and it can be seen that there is good agreement between experiment and theory. The details of the absorber species treated in the model have been described in section 2.2.1.

Figure 2.06 shows the variation of net gain and absorption with e-beam pump rate for the 1500 torr gas mixture which has previously been found to give the highest output efficiency from this laser system. The points are experimental results and the solid lines are computer predictions. The vertical bars labelled S are Sandia Laboratory's measurements (2.07) of net gain and non-saturable loss taken for a gas pressure of 1000 torr and the agreement with the present experimental results is excellent. This comparison of data is reasonable because our computer model predicts that gain and loss do not vary rapidly with gas mixture and pressure at a fixed pump rate. It can be seen from Figure 2.06 that a gain to non-saturable loss ratio >10 is obtained over the full pump range studied here and a ratio ~20 is achieved at the highest pump rate of 3 MW/cm^3. High efficiency performance of the KrF laser can therefore be expected in this operating regime and indeed this has previously been demonstrated (2.04).

From these experiments we come to the following conclusions:

(a) The absorption cross section of Kr_2F^* at 257.2 nm is estimated to be $1.8\ (\pm 1.1) \times 10^{-17}$ cm^2.

(b) Our computer model predicts gain and loss in good agreement with our experimental results and with measurements previously made at Sandia Laboratories.

(c) A high gain to loss ratio (>10) is achieved over the full pump range used here for the 1500 torr gas mix. The computer model can now be used with confidence to predict KrF gain and loss characteristics under operating conditions more appropriate to SPRITE.

C B Edwards, F O'Neill and M J Shaw (RAL)

2.2.3 Wideband, High Resolution, Time-Resolved Absorption Spectroscopy of E-beam Pumped Rare Gases

The rare-gas excimer and exciplex lasers are potentially capable of very high powers and high efficiences. However, the adjustment of conditions necessary to achieve optimum performance requires a detailed understanding of the complex system of interacting species present within the laser mixture. A typical reaction kinetics code (2.02) might involve eighty different processes, for each of which a rate constant or cross section must be determined. In an attempt to check the accuracy of existing data and to illuminate certain more obscure parts of this system it was decided to investigate absorption spectra in e-beam pumped rare gases. This report describes some preliminary work, carried out on the Rutherford Laboratory's E-beam Laser Facility (ELF) in which we probed e-beam excited Argon in the spectral region 500-550 nm, and a detailed study was performed around 510 nm.

The set-up we used allows us to look at a complete region more than 10 nm wide with a resolution of better than 0.1 nm on each shot. This greatly increases the amount of information gathered per shot compared with previous work (2.17). Furthermore the probe beam could be delayed with respect ot the e-beam pulse allowing us to probe both during the excitation pulse and in the afterglow. Delays of up to 1 μs were achievable.

The experimental set-up is shown in Figure 2.07. The gas in the absorption cell is probed with broadband fluorescence from a laser-pumped dye solution, the pump laser being triggered via a variable-length cable

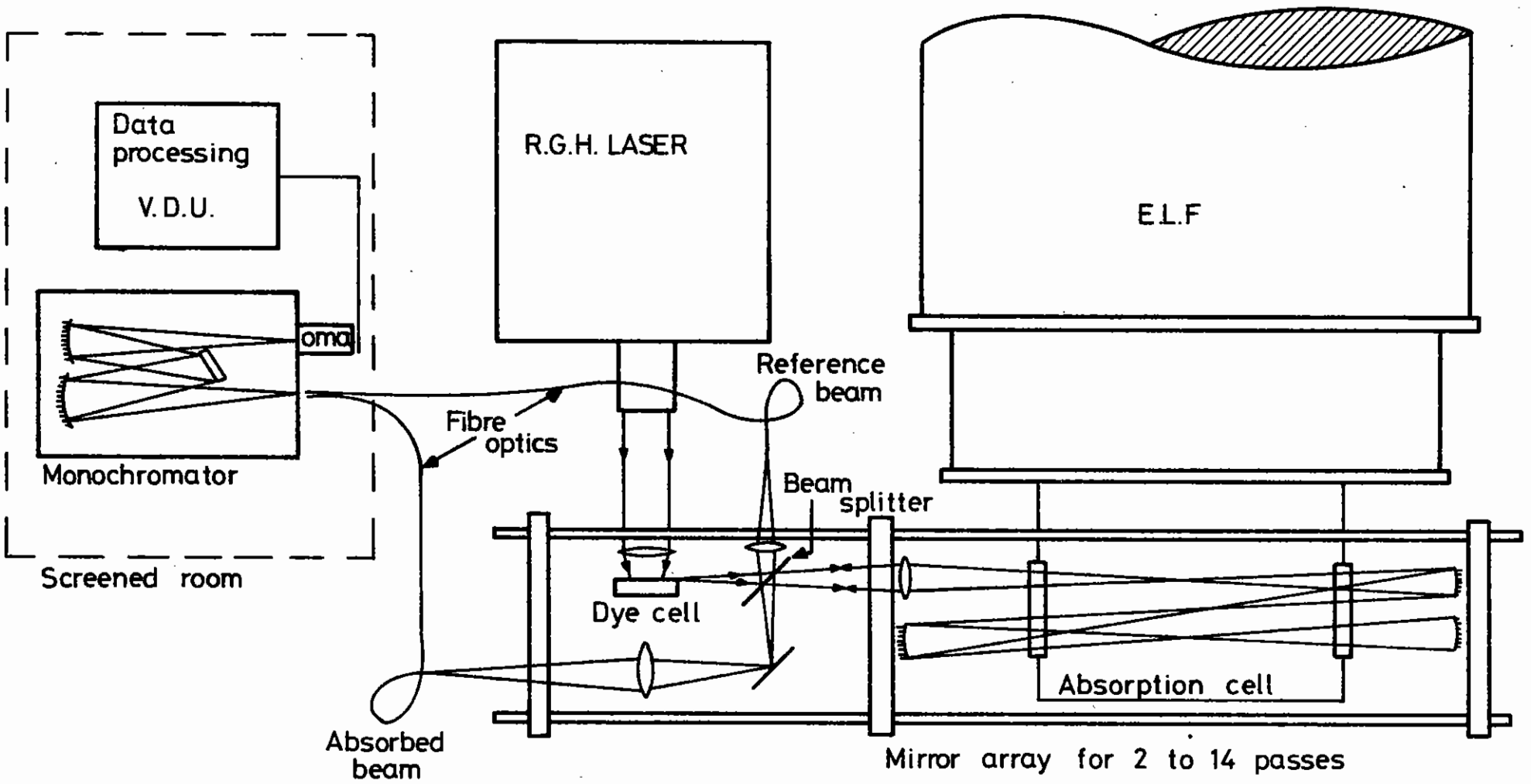

Figure 2.07 Apparatus used for wideband high resolution, time-resolved absorption spectroscopy of E-beam-pumped rare gases

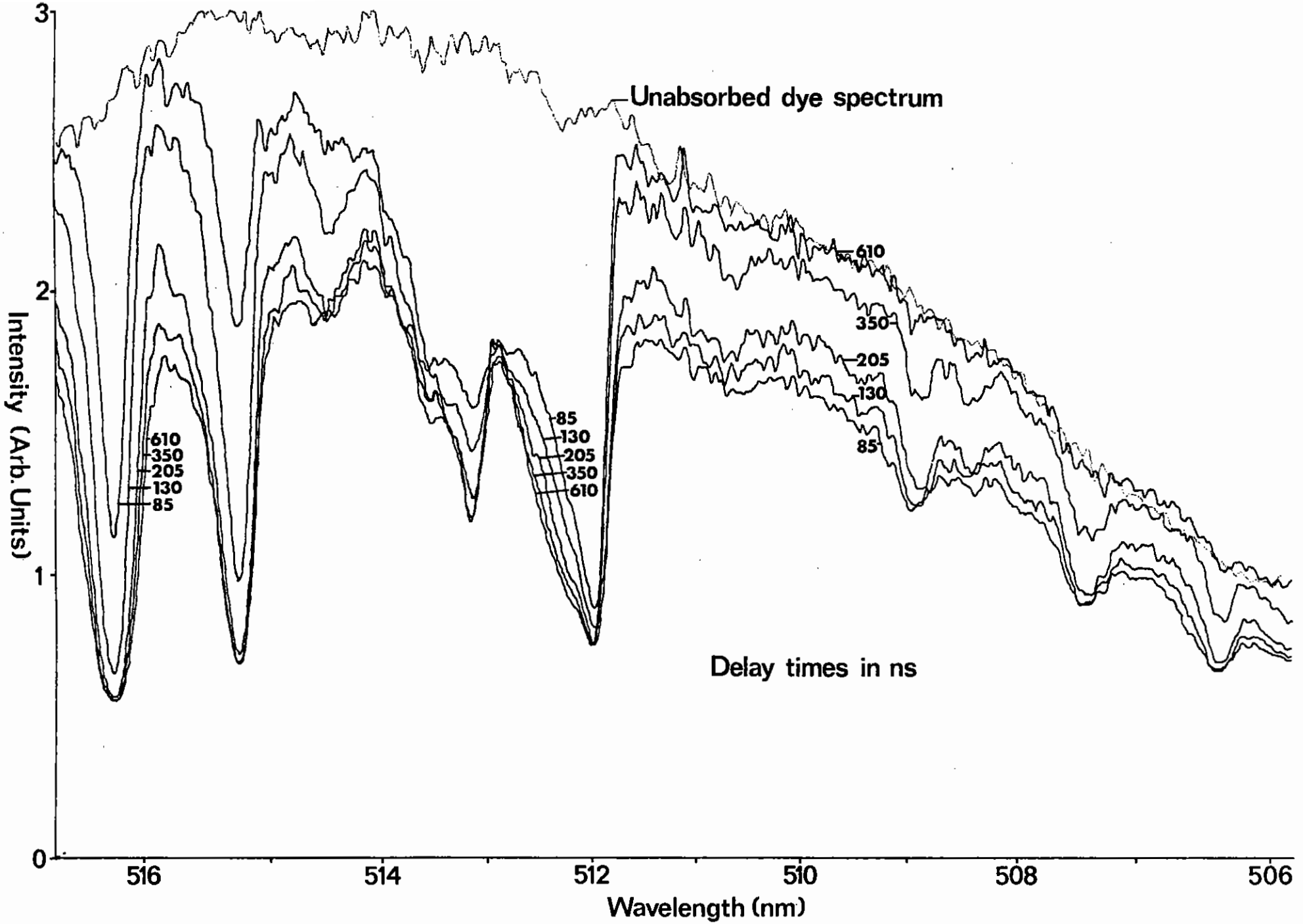

Figure 2.08 Comparison of unabsorbed dye spectrum with absorption spectra taken at various times after the E-beam pulse

delay-line which introduces the delay between the e-beam excitation pulse and the probe pulse. Light from the dye solution is split, half being piped to the top of the spectrometer entrance slit and half passing through the absorption cell before entering the bottom. The two spectra of the unabsorbed (reference) and the absorbed fluorescence fall onto the vidicon detector head of an optical multichannel analyser (OMA) system. This records the intensity (integrated over the 20 ns probe pulse) as a function of position on the head, in digital form. The results discussed in detail below were produced with 500 torr of Argon in the absorption cell and fluorescence from Coumarin 6 dye dissolved in ethanol. Delay times varied between 85 ns and 610 ns and the total absorption length was 70 cm (corresponding to two passes through the pumped Argon). The spectra were calibrated using reference lines from a neon lamp and a polynomial (degree 4) calibration programme in the OMA.

The spectra of the dye fluorescence with absorption imposed are compared, in Figure 2.08 with the unabsorbed spectrum. To compensate for the effects of the different optical paths followed by the absorbed and reference beams and to remove the background intensity introduced by the vidicon we took several spectra with an empty absorption cell and several more with no pump laser pulse. The absorption coefficient is related to the reference intensity I_{ref} and the absorbed intensity I_{abs} by the relation:

$$K_\lambda = \frac{1}{L} \ell n \left\{ \frac{I_{ref} - I_{BGD}}{I_{abs} - I_{BGD}} \cdot \frac{I_{abs.\ empty} - I_{BGD}}{I_{ref.\ empty} - I_{BGD}} \right\}$$

where L is the absorption length, and I_{BGD} is the background intensity. This calculation was carried out using the OMA data processor and the results are shown in Figure 2.09.

The absorption features shown fall into three classes: those due to excitation of atomic Argon, those due to the molecular dimer Ar_2 and a broadband background absorption whose cause is not yet definitely identified. The peaks in Figure 2.09 are assigned to transitions in Table 2.01, the bracketed lines being unresolved.

The areas under the atomic peaks are related to N_j, the number density of atoms in the lower state of the transition by (2.19):

$$\int_{line} K_\lambda d\lambda = \left[\frac{e^2 \lambda^2 f_{ij}}{4 \varepsilon_o m c^2} N_j \right]$$

The OMA was used to calculate the areas under the peaks and the values of N_j (measured 85 ns after the end of the excitation pulse) were 9×10^{19} m^{-3}, 6×10^{19} m^{-3} and 9×10^{19} m^{-3} for the 4p $[\frac{1}{2}]_1$, $[\frac{5}{2}]_2$ and $[\frac{5}{2}]_3$ levels respectively. These are in broad agreement with previous work by Kearsley (2.20).

The time dependence of $\int K_\lambda \, d\lambda$ is plotted in Figure 2.10 for a typical atomic transition (that at 516.2 nm) a molecular transition (at 512.0 nm) and for a region around 510 nm where the dominant absorption is the broadband background.

Reactions such as:

$$Ar^{**} + 2Ar \rightarrow Ar_2^{**} + Ar$$

$$Ar_2^{**} + (Ar) \rightarrow Ar^* + Ar + (Ar)$$

and the superelastic $e + Ar^{**} \rightarrow e + Ar^*$ cause the doubly excited atomic species to relax to the singly-excited state from which they proceed to the excimer level:

$$Ar^* + 2Ar \rightarrow Ar_2^* + Ar$$

Thus as the atomic population falls the excimer population rises and the temporal behaviour of the absorption curves allows us to ascribe the features to one or other of these species.

It has been suggested that the broadband background absorption might be due to photodissociation of a molecular ion, either Ar_2^+ (2.17) or perhaps Ar_3^+ (2.21). The dimer has the larger cross section but would require a highly non-Maxwellian distribution over vibrational states (2.22) to

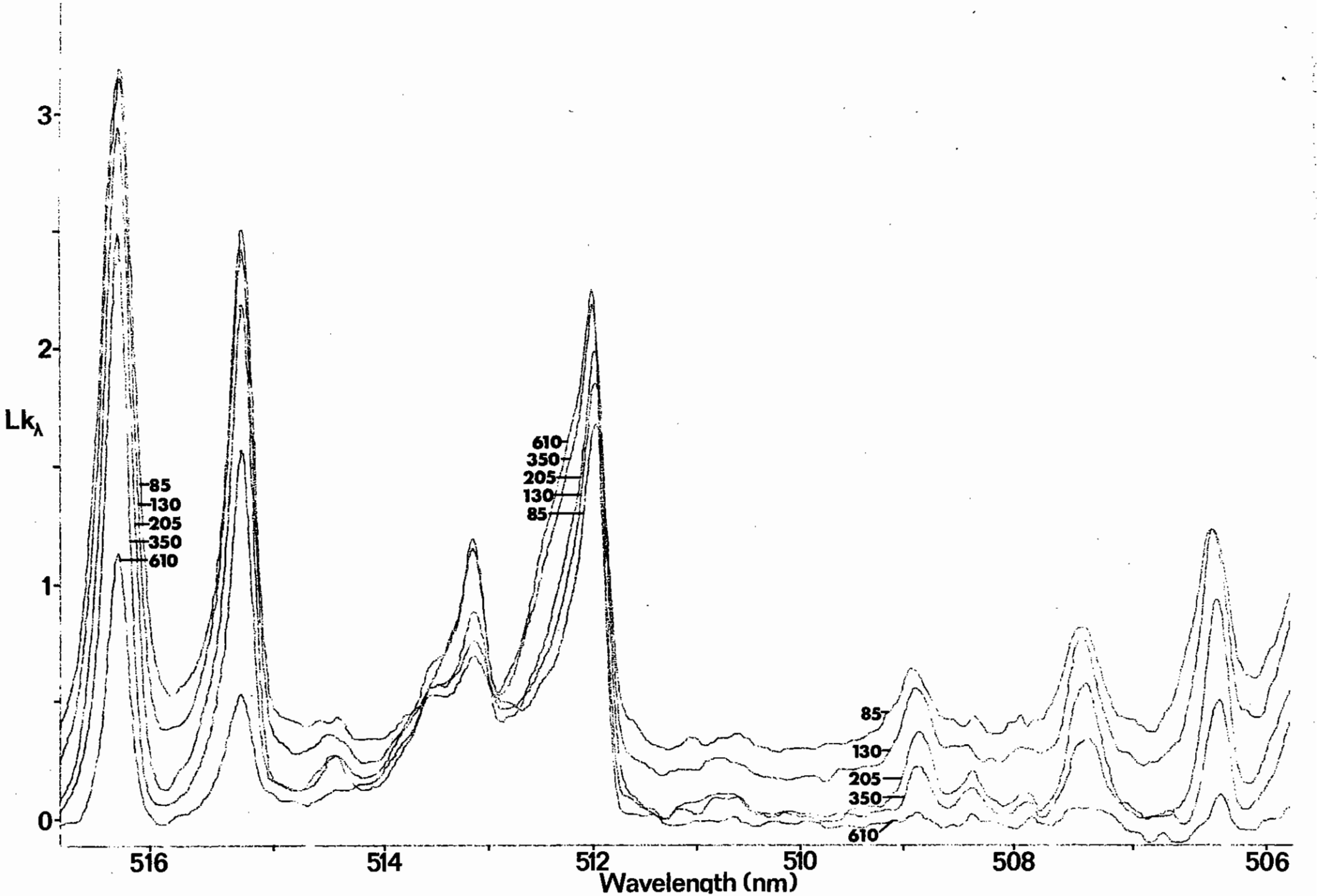

Figure 2.09 Absorption coefficient versus wavelength curves as calculated from the raw spectra of Figure 2.08

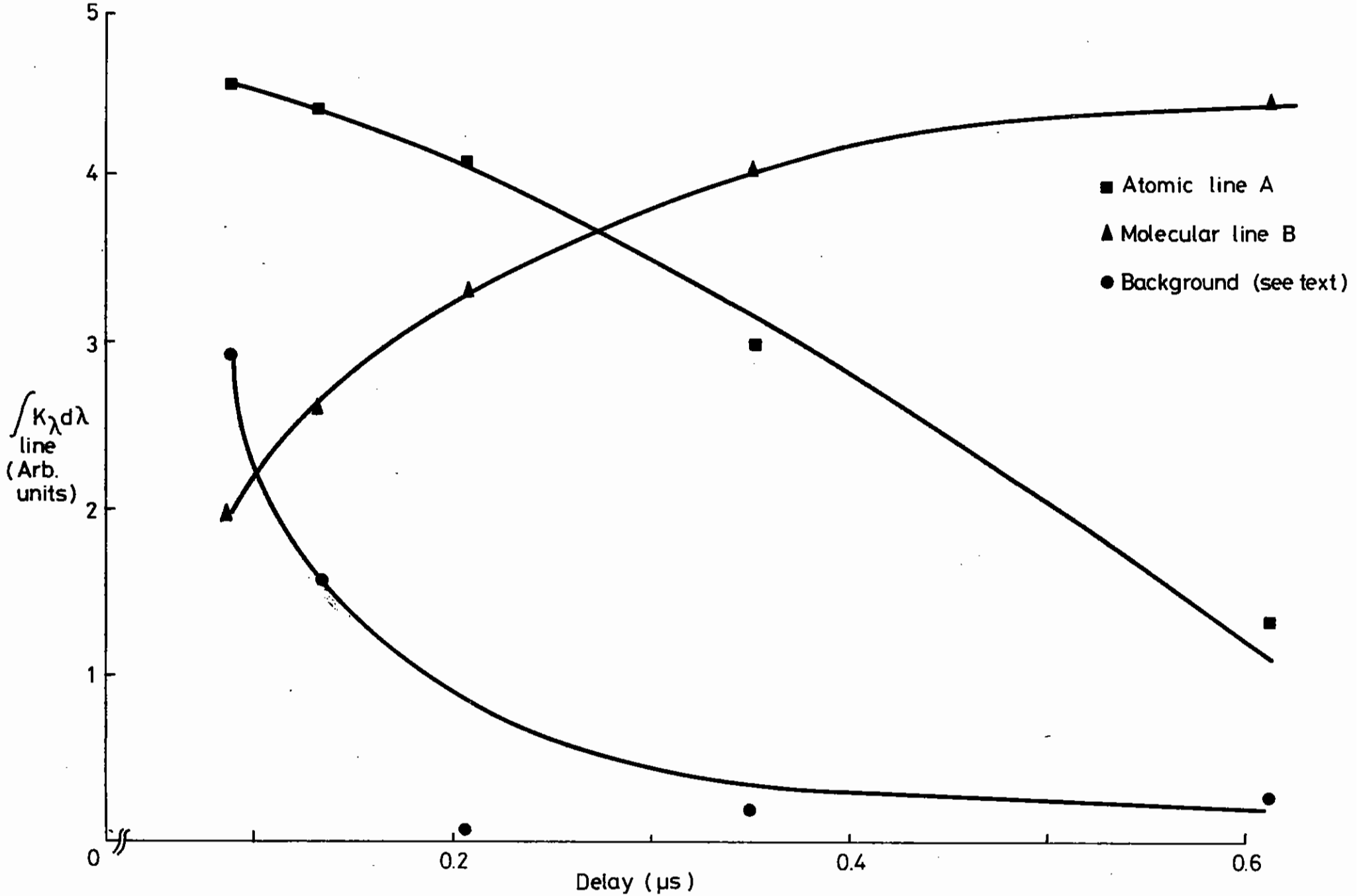

Figure 2.10 Variation of the contribution of the different absorption features with time after the E-beam pulse

TABLE 2.01

Measured Wavelength (nm)	Transition	Species	$f_{ij} \times 10^3$	Ref.
516.2	$3p^5(^2P^o_{3/2})4p[\frac{1}{2}]_1 - 3p^5(^2P^o_{3/2})6d[\frac{1}{2}]^o_1$	ArI	7.09	2.18
515.2	" $4p[\frac{1}{2}]_1 - 3p^5(^2P^o_{\frac{1}{2}})5d^1[5/2]^o_2$	ArI	0.72	2.18
515.1	" $4p[\frac{1}{2}]_1 - 3p^5(^2P_{3/2})6d[\frac{1}{2}]^o_o$	ArI	3.30	2.18
513.1	$4s\,^3\Sigma^+_u - 5p\,^3\Pi_g$ †	Ar_2^*		2.17
512.8 ††	$3p^5(^2P^o_{3/2})4p[5/2]_2 - 3p^5(^2P^o_{\frac{1}{2}})6d^1[5/2]^o_2$	ArI	0.13	2.18
512.0	$4s\,^3\Sigma^+_u - 5p\,^3\Pi_g$ †	Ar_2^*		2.17
508.7	$3p^5(^2P^o_{3/2})4p[5/2]_2 - 3p^5(^2P^o_{3/2})8d[7/2]^o_3$	ArI	0.94	2.18
507.3	" $4p[\frac{1}{2}]_1 - 3p^5(^2P^o_{3/2})6d[3/2]^o_2$	ArI	0.39	2.18
507.1	" $4p[5/2]_2 - 3p^5(^2P^o_{3/2})10s[3/2]^o_1$	ArI	0.63	2.18
506.0	" $4p[5/2]_3 - 3p^5(^2P^o_{3/2})8d[7/2]^o_4$	ArI	1.9	2.18

† The 42 cm^{-1} splitting between these two lines is tentatively ascribed to vibrational splitting of the $5p\,^3\Pi_g$ state.

†† This transition was completely obscured by the molecular features.

achieve the required spectral shape. The trimer is a much broader absorber and may fit the observed shape rather better. Dissociative recombination of these ions is initially so rapid (because n_e is so high) that the ion populations fall very swiftly and rather more passes through the Argon will be necessary if we hope to see the background absorption in the late afterglow.

In conclusion the wide bandwidth and high resolution of our detection system allows us to examine the rare-gas absorption spectra in greater detail than has been achieved before. The time-resolution facility leads to easy identification of the different absorbing species and should, in the future, allow us to produce more precise information about the background absorption spectrum with a view to establishing its cause.

A J Andrews, G Hirst, A J Kearsley and C E Webb (Clarendon Lab)

2.2.4 Discharge Excited KrF Laser with an Unstable Resonator

As a result of high gain causing multimode and parasitic oscillation, the spatial beam quality obtained from discharge excited rare gas halide lasers using stable resonators is poor (a beam divergence of ~5 mrad is typical). The need to amplify and propagate these beams over large distances and to focus them to small spot sizes for target irradiation applications requires a much smaller beam divergence. It has been known for several years that for many high gain lasers the use of unstable resonators can considerably improve the beam quality (2.23). Indeed, for discharge excited KrF lasers there have been several reports of unstable resonator operation (2.24-2.27) and we decided to carry out experiments on such a device. In choosing the optimum resonator configuration it is necessary to match the magnification of the system with the single pass gain of the medium (2.28). In order to avoid intracavity gas breakdown (2.29) we chose to use a positive-branch unstable resonator.

The laser used for this study was a discharge excited KrF laser using automatic preionisation (2.30). The discharge dimensions were 45 x 2x0.6 cm. Once the resonator magnification, aperture and length are

specified then the focal lengths and the aperture of the optics becomes fixed. The laser is shown in Figure 2.11. Lens L_1, which had a 96 %, high reflectivity (HR) dielectric coating at 248 nm on the back plane surface, acted as a mirror of focal length = 67.75 cm at 248 nm. Output coupling was effected via lens L_2 which was coated with a HR 0.07 cm diameter dot on its plane surface so that it behaved as a diverging mirror of focal length = 2.26 cm at 248 nm. This combination then gave an overall resonator magnification of 30. Lens L_3 renders the output beam parallel. Pinhole measurements at the focus of a 175 cm lens indicated that the 2 x 0.7 cm beam had a divergence of ~0.5 mrad in a 10 nsec FWHM pulse of ~150 mJ of energy. This compares favourably with the negative-branch unstable resonator reported by James et al (2.27) without suffering from the problem of gas breakdown.

M C Gower (RAL)

2.2.5 Short pulse probing of E-beam-pumped KrF

Studies of laser produced plasmas generated with 0.53 μm and 0.35 μm radiation have indicated that there will be a need for a short wavelength driver laser such as KrF* (λ = 0.249 μm) capable of producing nanosecond pulses with energies of up to ~1 KJ. Because the storage time of KrF* is only a few nanoseconds, whereas the most efficient KrF amplifiers require pumping pulses of ~100 ns or more, amplification of single pulses is inefficient. This problem may be overcome however by amplifying a sequence of pulses which are then made to strike the target simultaneously (2.31). In such a scheme, it is important to know the time taken for the gain of the amplifying medium to recover, since, if the spacing of the pulses is too short, they will not experience maximum gain and if too long fluorescence, quenching and amplified spontaneous emission will decrease the amplifier efficiency.

When pumped by an electron-beam, KrF* is formed in vibrationally excited states. As shown in Figure 2.12, collisionally induced vibrational relaxation must take place to populate the lowest vibrational states from which laser action occurs. This relaxation rate (τ_v^{-1}) imposes a

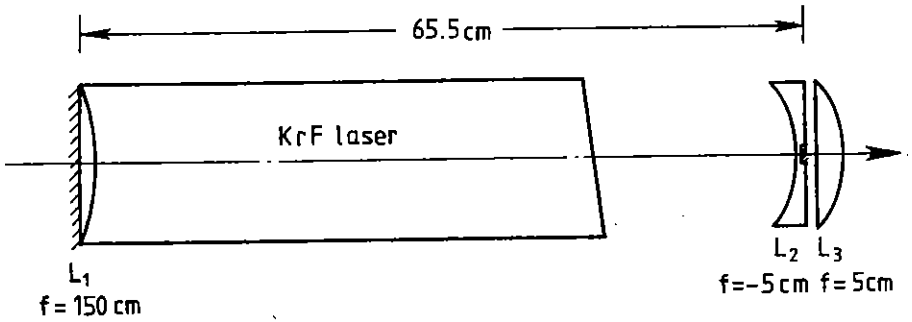

Figure 2.11 Schematic showing positive-branch unstable resonance. Focal lengths of all lenses are specified at the Na 589 nm D-line wavelength

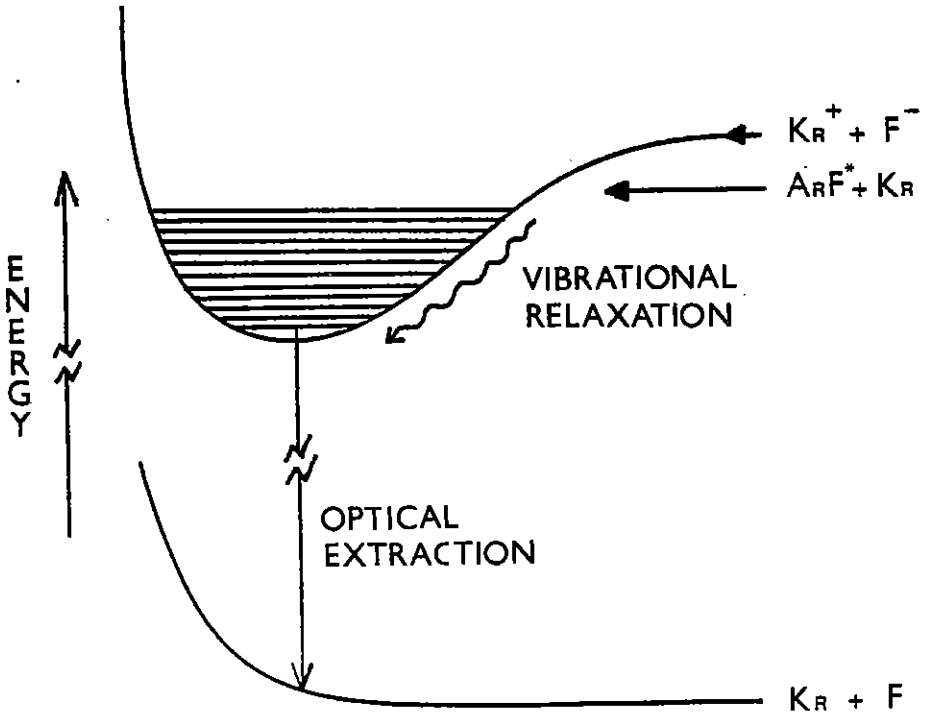

Figure 2.12 Potential energy curves for KrF*

limit on the efficiency of extracting energy from the manifold in a short pulse (2.32) and on the recovery time (τ_r) of the gain following amplification of the pulses. Because of the poor agreement between the values of τ_v suggested by previous work (2.32 - 2.35), a direct measurement of τ_r has been undertaken.

In the experimental arrangement shown in Figure 2.13, a 6 ns pulse from a discharge-pumped KrF laser is focused into a cell containing a suitable mixture of F_2, Kr and Ar which is excited by a 50 ns long pulse of 2 MeV electrons from a Febetron 705 generator. The power density of the focussed KrF laser is considerably greater than the saturation power requirement of ~1 MW cm^{-2}. Synchronism of the outputs of the laser and electron beam has been achieved to within ±10 ns. The intense laser pulse can deplete the population of the lowest vibrational state of KrF* and the rate of recovery of gain (τ_r^{-1}) can be measured by the rate of increase in the fluorescence intensity.

The beam is passed axially along a tube within the gas cell and the interaction region is defined by an aperture which admits electrons only to a small volume of gas. The fluorescence from this volume is monitored by imaging on an aperture placed in front of a photodiode PD1, taking care to exclude fluorescence from regions outside the interaction volume. The undepleted fluorescence is monitored by PD2 for use as a reference.

Under normal laser conditions, the decay time of the excited state due to fluorescence and quenching is ~2 ns, and the vibrational relaxation time is expected to have a similar value (2.33). This is shorter than the trailing edge of the saturating laser pulse being used at present. Preliminary experiments have confirmed that the gain recovers in a time which is comparable to the pulse duration of the laser and indicates that the actual recovery lifetime is very short (< 3 ns).

Further studies will be carried out using a laser pulse with a very fast (< 1 ns) trailing edge. The variation of τ_r with gas pressure and

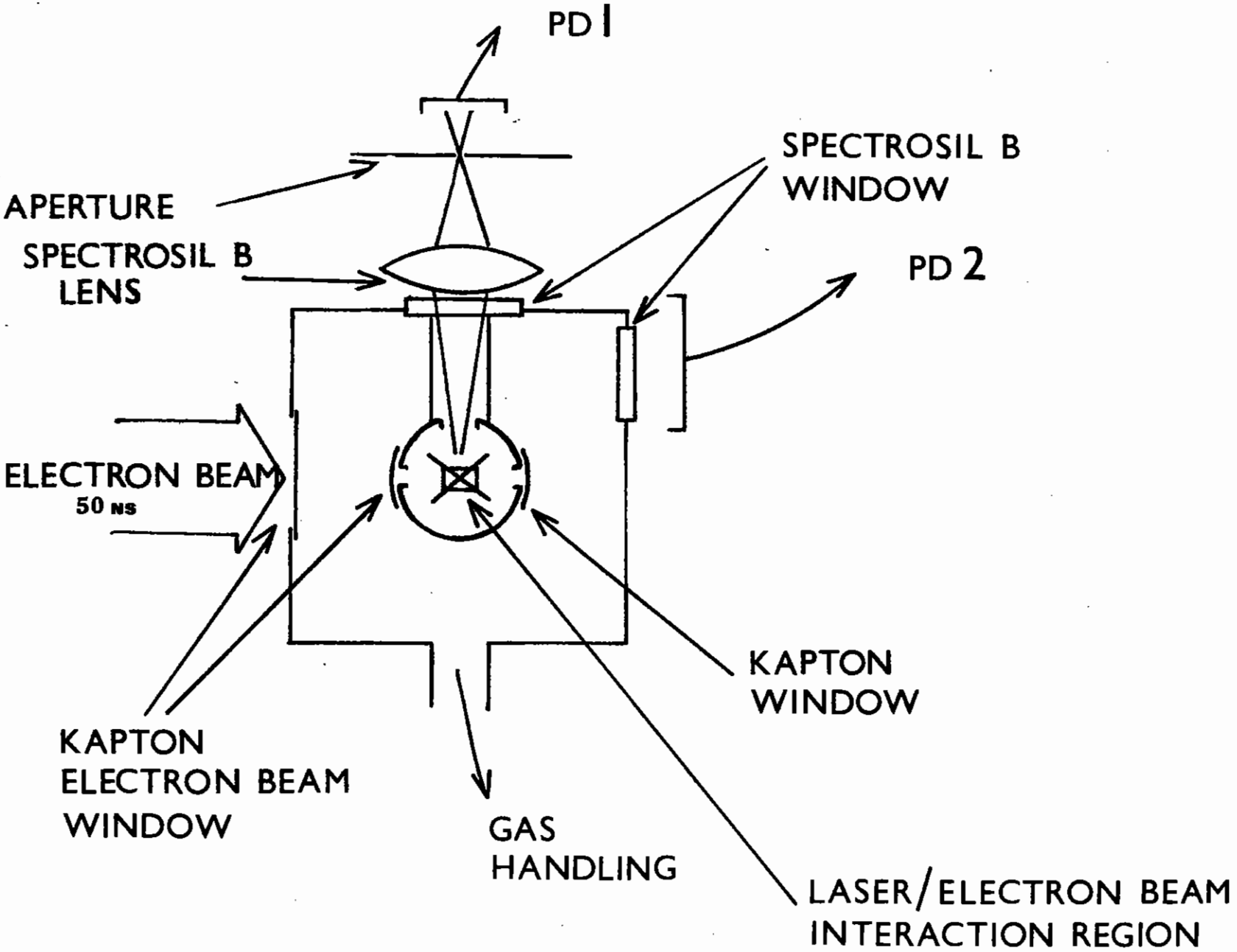

Figure 2.13 Schematic experimental arrangements

electron beam current will then be investigated.

K T V Grattan and M H R Hutchinson (Imp Coll)

2.3 Applications of Rare Gas Halide Lasers

2.3.1 KrF Laser-induced Breakdown of Gases

Using the unstable resonator laser described in section 2.2.4, we measured the threshold laser breakdown intensity for a variety of gases (2.36).

Figure (2.14) shows the results obtained for the threshold intensities for breakdown in the rare gases, air and the Raman scattering gases H_2 and CH_4 as a function of gas pressure. The largest error in the intensity measurements is undoubtedly due to the uncertainty in determining the beam area at focus using the measured laser beam divergence. We estimate this error to be better than ± 60 %, while the relative thresholds for different gases are better than ± 10 %. All measurements are in the region $p\tau >> 10^{-7}$ sec torr, (p = pressure, τ = pulse length) a regime where theory predicts inverse bremsstrahlung absorption (cascade ionisation is responsible for breakdown (2.37). This theory predicts the functional dependence $I_{th} \propto \frac{1}{p\lambda^2}$. Although this relationship seems to be followed in the infrared, in the visible and uv spectral regions the threshold is observed to actually decrease with shorter wavelengths (2.38-2.40). Clearly cascade ionisation theory is an inadequate description of the breakdown process in this spectral region. Unfortunately, multiphoton ionisation theory, which does predict a decrease in I_{th} with decreasing wavelength, also predicts a very weak pressure dependence: $I_{th} \propto p^{-1/n}$ (n is the non-linearity of the multiphoton absorption process and varies between 3-5 for the gases and wavelength in our experiment). Clearly, a much stronger pressure dependence is observed in Figure 2.14 and in references (2.38) and (2.40). Our results at 248 nm shown in Figure 2.14 may be most meaningfully compared with those obtained at 347 nm by Buscher et al (2.38) and Alcock et al (2.40). While the thresholds at both of these wavelengths are of a comparable magnitude, H_2, CH_4, and Xe shows a general decrease while Ne,

Ar and Air an increase in their thresholds at the shorter wavelength. However, it should be pointed out that such comparisons between different experiments can at best be only tentative because of the relatively large errors involved in measuring absolute intensities. The logarithmic plot of the data as shown in Figure 2.14 appears not to lie on a straight line as did such plots of the results of references (2.38) and (2.40) and 5. As mentioned by Alcock et al (2.40) the departure from a straight line for H_2 and CH_4 may be due to the onset of stimulated Raman scattering causing laser pump depletion. Indeed, at the higher pressures used and just below the breakdown threshold intensities, we observed that at least four stimulated Stokes components were generated in H_2. In the rare gases, on the other hand, we note that there exist two and three-photon absorption resonances in Xe and Ar respectively, so that for these gases multi-photon absorptions at the higher intensities may perhaps lead to a departure from a straight line in Figure 2.14.

Murray et al (2.15) have also measured the breakdown intensity (or more specifically the intensity for transmitted laser pulse distortion) at 248 nm in both Xe and CH_4 at $p \geq 10^3$ mbar. In the regime of 10^3 mbar where both our data overlap, our results agree to within $\lesssim$ 35 %.

In figure 2.15(b) we show the temporal behaviour of the transmitted pulse after gas breakdown compared to the normal laser pulse shown in figure 2.15(a) (the oscillations in figure 2.15(a) are discussed in section 2.3.5). It can be seen that the pulse is shortened to ~ 2 nsec due to scattering by the laser produced plasma. The relative magnitude of the background radiation remaining in the tail of the pulse depends strongly on the astigmatism of the breakdown focusing optics, being larger for highly astigmatic systems. However, this scattered radition can never be completely eliminated (2.41). This behaviour contrasts with the plasma shutter effect observed in breakdown using CO_2 lasers. At 10.6 μm the laser frequency is comparable to the plasma frequency at an electron density of ~ $10^{19}/cm^3$ so that, once breakdown occurs, the pulse is completely absorbed in ~30 psec (2.42) resulting in a rapid cut off of the transmitted pulse. Clearly the cut off in Figure 2.15(b) is much

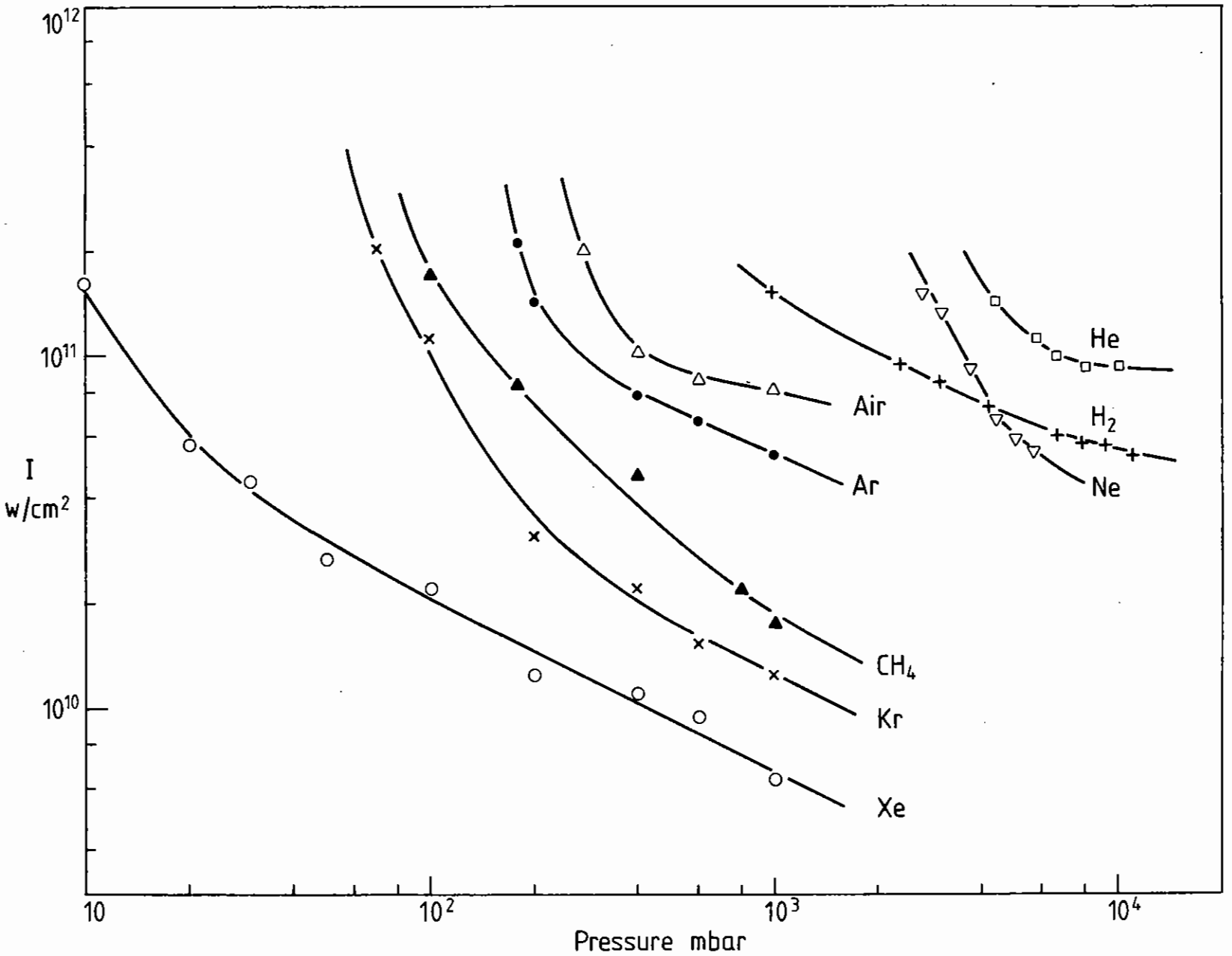

Figure 2.14 KrF laser breakdown threshold intensity as a function of pressure for the gases shown

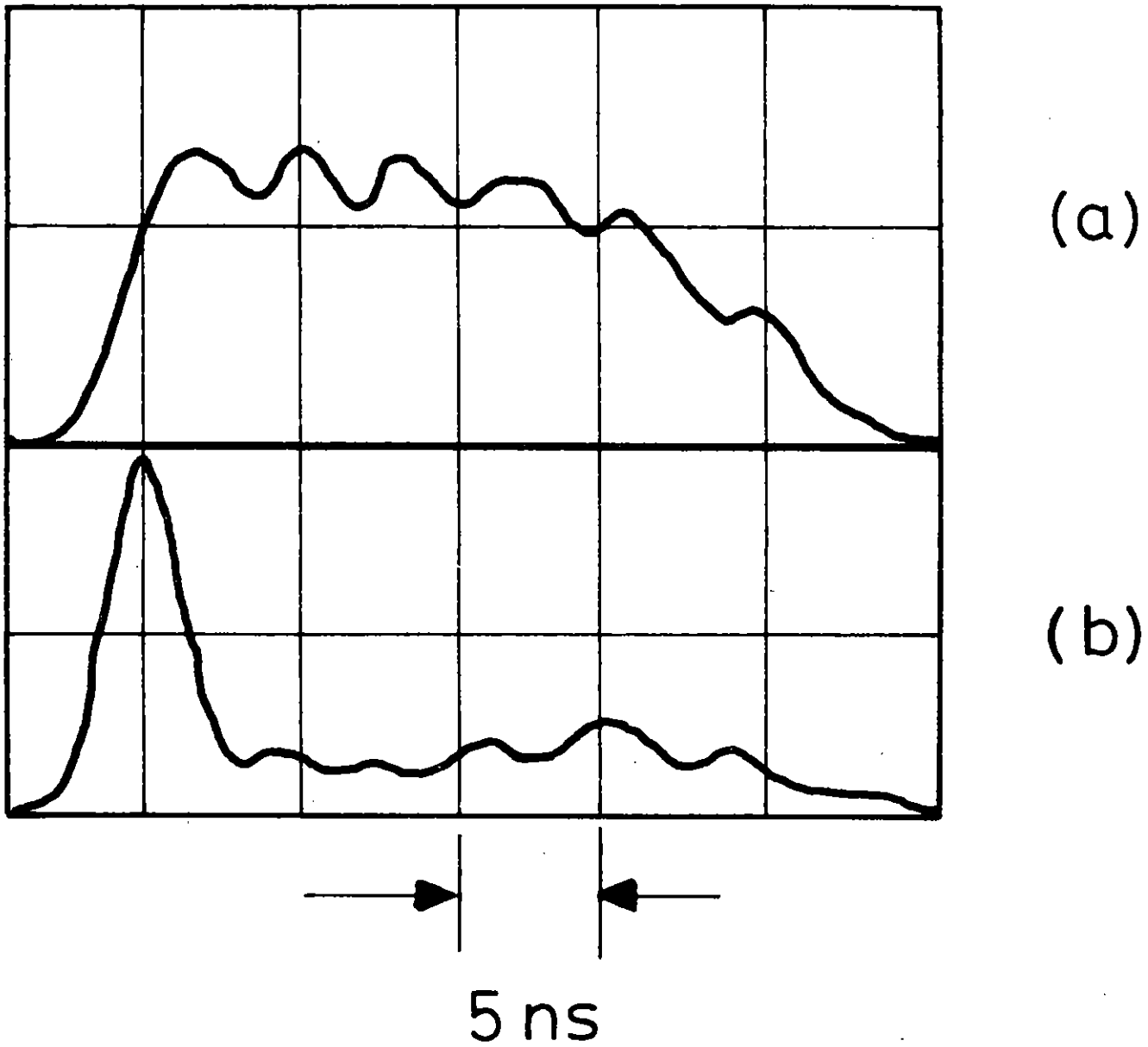

Figure 2.15 (a) Unstable resonator KrF laser output

(b) Transmitted laser pulse after passing through a focus in atmospheric air at which plasma breakdown occurred

slower (the response time of the detection system is $\lesssim$ 0.5 nsec).

M C Gower (RAL)

2.3.2 KrF Laser pumping of C_6D_6

The attraction of medium lifetime energy storage lasers pumped by rare gas halide lasers was discussed in last year's annual report and illustrated with reference to the ArF-pumped I_2 laser. Unfortunately the lifetime of this system (~ 2 ns) was much too short for efficient energy storage from a 50 ns e-beam-pumped RGH laser. Another candidate with a more promising lifetime (~100 ns) is KrF-pumped Benzene vapour and several properties of this system have been investigated in the past year.

Initial experiments showed that fluorescence at around 280 nm was easily excited by KrF pumping of C_6H_6 but that the fluorescene intensity was very much higher (by a factor of seven) when using C_6D_6. Figure (2.16) shows the fluorescence and absorption spectrum obtained with the OMA of the partially forbidden $^1B_{2u} - {}^1A_{1g}$ system of C_6D_6. The KrF wavelength lies close to a peak in the absorption spectrum of C_6D_6 but near a trough in C_6H_6. This fact accounts for the majority of the increased fluorescence intensity in C_6D_6. Measurements of the quantum yield of KrF-pumped benzene were made by comparing the relative yield with that of ArF-pumped I_2 which was assumed to have near 100 % yield in a one atmosphere Ar buffer. The yields obtained at low pressures (< 10 torr) were as follows:

$$C_6H_6 - 0.16 \pm 0.05$$

$$C_6D_6 - 0.20 \pm 0.05$$

in fairly close agreement with previously published data (2.43) using Hg lamp pumping (λ = 253.7 nm). The quantum yields were measured as a function of argon buffer gas pressure. They were found to fall to about one half of the low pressure yield with 100 torr of added argon and then increase slightly at higher pressures (up 20 % at 2 atms). The quenching

may have been due to impurities in the argon since only commercial purity grade was used.

Attempts were made to measure gain and loss in KrF-pumped C_6D_6 using a laser produced plasma as a light source synchronized with the pump beam. These measurements indicated that gain of several % per cm existed at 280 nm. On the basis of these results an oscillator experiment was tried using the 10 J KrF output available from ELF for pumping and using high reflectivity mirrors for the benzene vapour cavity. No laser action was observed. It is now believed that the gain measurements were in error due to non-linearity on the OMA vidicon which was used as a detector for these experiments since the measurement involved subtracting two large fluorescence signals to extract the required gain signal. It now looks increasingly unlikely that laser action in benzene vapour can be realized.

M J Shaw (RAL), R J Donovan and C Fotakis (Edinburgh Univ)

2.3.3 XeCl Laser Annealing of Semi-conductors

Thin films of II - VI semi-conductors, particularly ZnS, are promising materials for electroluminescent devices covering the entire visible range. In the fabrication of these devices it is necessary to introduce various dopants into the films. Ion beam implantation is one method of doing this in a controlled and reproducible manner. However ion-implantation produces considerable structural damage in the material; consequently the implanted specimens have to be annealed to remove this damage and also to redistribute the dopant ions to substitutional lattice sites in order to activate them. Conventionally the annealing is carried out by heating the entire specimen to high temperatures, often with undesirable consequences such as dopant segregation and only partial removal of lattice damage. Such effects have, in fact, been observed recently in thermally annealed Al implanted ZnS films.

In the last few years considerable interest has been generated in using high-power laser radiation as a more effective means of annealing ion-

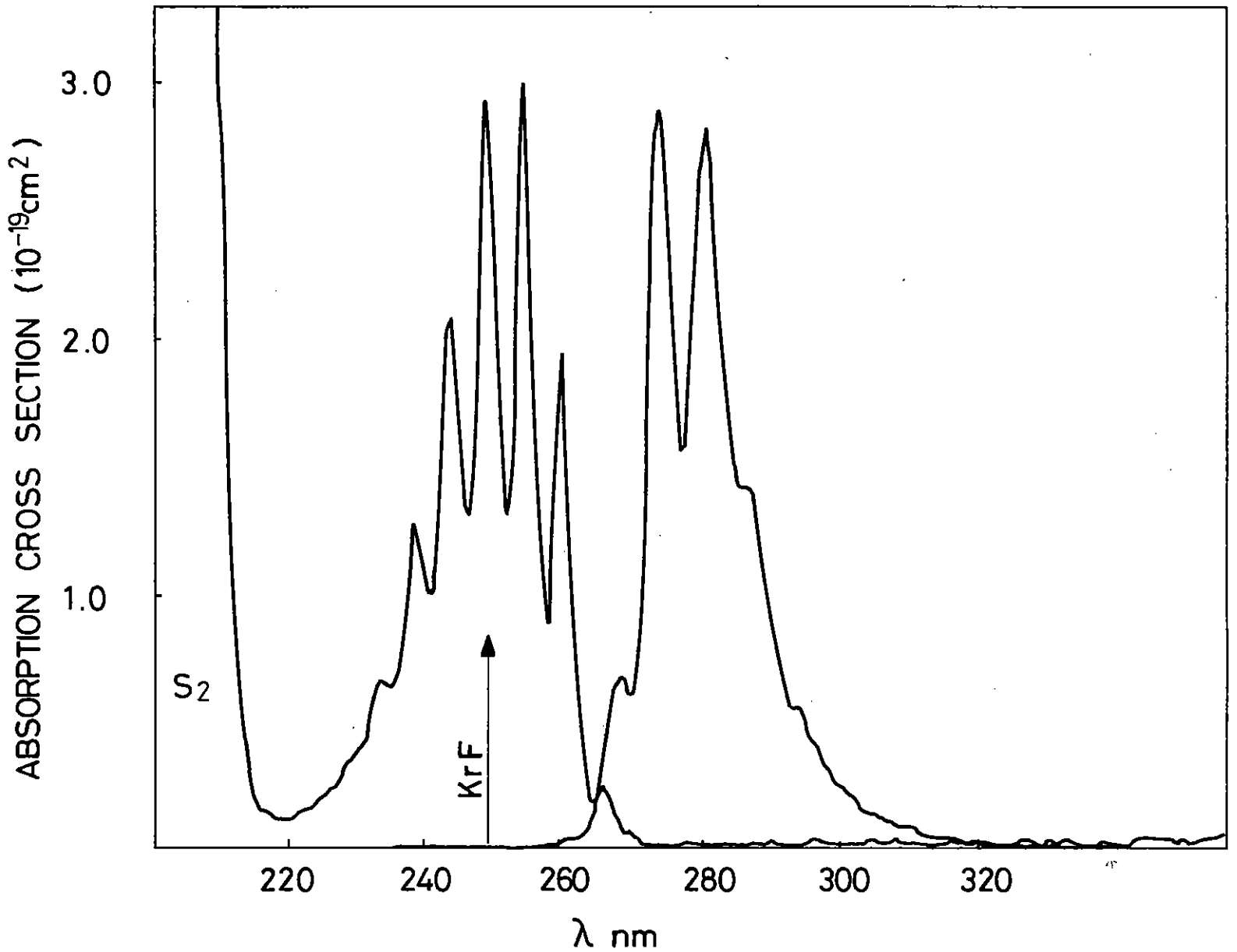

Figure 2.16 Absorption and fluorescence in C_6D_6 vapour

implanted materials. Two distinctly different annealing mechanisms, distinguished by the duration of the laser exposure, have been identified. For relatively long exposure times, the annealing proceeds by a solid-phase process. However for short exposures (typically 1 - 100 ns range) a liquid-phase process, associated with melting and subsequent re-growth of the material, takes place. Although very promising results have been obtained with liquid-phase processing of ion-implanted Si, work on other semi-conductors, particularly the II - VI family is at a less advanced stage.

A programme of research on pulsed laser annealing of ZnS films has been initiated using the electron beam pumped excimer laser system 'ELF' at the Rutherford Laboratory. In order to achieve efficient absorption of radiation in the sample it is necessary to irradiate with photons of energy greater than the band gap, since at longer wavelengths the sample becomes optically thin. The band gap of ZnS is large (~ 3.7 eV) and consequently XeCl laser radiation at 308 nm (4.025 eV) was chosen for the experiments. For the preliminary work ZnS films, grown as either single silicon crystals or Corning type 7059 glass substrates and implanted with Mn and/or Al ions, were irradiated with single laser pulses of 30 ns duration at a range of energy densities between 40 mJ cm^{-2} and 450 mJ cm^{-2}. Preliminary results indicate that pulsed laser annealing shows promise for annealing ZnS films grown on to single crystal Si substrates. Films deposited on to glass suffer visible damage at illumination energy densities of ~ 0.1 - 0.4 J cm^{-2} depending on the film growth conditions. Scanning electron microscopy and electron probe microanalysis have shown the absence of any gross topographical or compositional changes after ~ 0.4 J cm^{-2} illumination of the films grown on to Si. For these films, work is in hand to assess the crystallinity, doping profiles and the electrical and luminescent properties as a function of annealing energy density using densities of up to ~ 2 - 3 J cm^{-2}. Similar measurements on thermally annealed films are being carried out for comparison.

C B Edwards (RAL) and H Reehal (Univ of Bradford)

2.3.4 Laser-Switched Collisions

As discussed in last year's report, the phenomenon of laser switched collisions of the type:

$$A^* + B + \hbar\omega \rightarrow A + B^* \qquad (1)$$

in which the energy of atom A* is transformed to atom B in the presence of a photon field at frequency ω, can be used to invert media and produce new lasers. We also presented experimental evidence of the process of 'pair-absorption'.

In this report we discuss an extension of the diagrammatic technique recently developed for density matrix operator calculations in non-linear optics (2.44, 2.45) to the case of laser-switched collisions. This diagrammatical approach has the distinct advantage of being able to more clearly visualise the interaction than would otherwise be possible using simple energy level diagrams. In addition, one is able to immediately write integral expressions for the density operator describing the interaction which involve a considerable simplification of the algebra. These expressions may then be integrated either numerically or analytically to obtain transition probabilities. As a first example, we consider the process described by equation (1) and the energy level diagram of Figure 2.17(a). The system is initially in the state $|1\rangle \equiv |a_1 b_0\rangle$ (atom A in level a_1 and B in b_0). During the course of a collision between A* and B, the system is transferred to state $|2\rangle \equiv |a_0 b_i\rangle$, whereafter the absorption of a photon at frequency ω puts the system in the final state $|3\rangle \equiv |a_0 b_2\rangle$. The diagrams which explicitly describe this interaction are shown in figures (b) - (d) and depict the time-ordered evolution (vertically) of the system wave function (LHS of the figure), and its complex conjugate (RHS), according to the general perturbation solution of the density operator, ρ_{33}. The complete expression for ρ_{33} is the sum of all three diagrams and their complex conjugates (reflection in the time axis). The contribution of Figure 2.17(b) is given by (2.44):

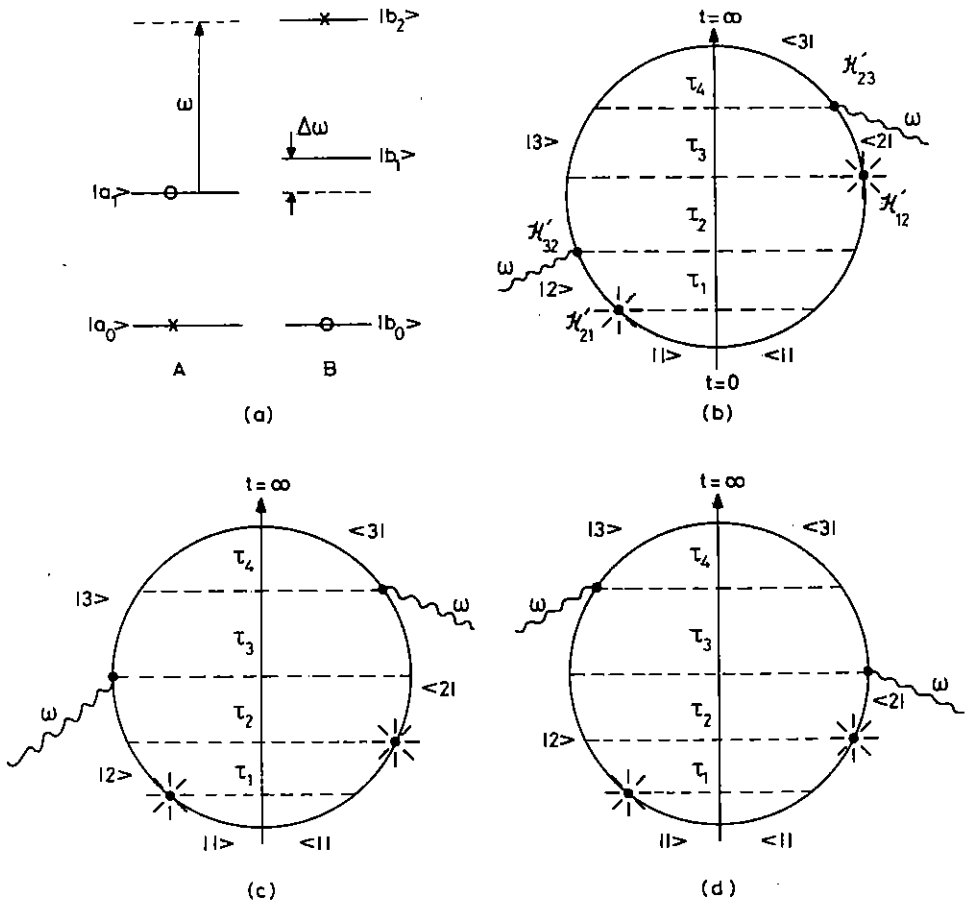

Figure 2.17

(a) Energy level diagram describing equation 1. The atoms are initially in states marked 0 and after the interaction in those marked X

(b) Diagram describing the time evolution (vertically) of the wavefunction (LHS) and its complex conjugate (RHS). Photon absorptions (and emissions) are denoted by rising (and descending) wiggley lines, while collisions are depicted as . The states into which the interactions put the system are also shown

(c) and (d) Other time orderings of the interaction in (a) and (b)

$$\rho^{(b)}_{33} = \int_0^\infty\int\int\int\int H'_{23}(t-\tau_4)A_{32}(\tau_3)H'_{12}(t-\tau_4-\tau_3)A_{31}(\tau_2)\,H'_{32}(t-\tau-\tau_3-\tau_2)A_{21}(\tau_1)H'_{21}(t-\tau_4-\tau_3-\tau_2-\tau_1)\,d\tau_1 d\tau_2 d\tau_3 d\tau_4 \tag{2}$$

where the τ's are the times between the collisions and the photon absorptions as shown in figure 2.17(b). The perturbational Hamiltonians are given by:

$$H'_{32}(t) = H'^{*}_{23}(t) = \langle 3|\,-\frac{\mu^B_{12}E}{2i\hbar}\quad 2\rangle\, e^{-i\omega t} \tag{3}$$

for dipole absorption (with moment μ^B_{12}) between states $|b_1\rangle$ and $|b_2\rangle$ of atom B from the classical photon field $\tilde{E} = E\cos\omega t$, and

$$H'_{21}(t) = H'^{*}_{12}(t) = \langle 2|\,-\frac{\mu^A_{10}\mu^B_{01}}{i\hbar}\,|1\rangle\,\frac{1}{R^3(t)} \tag{4}$$

for dipole-dipole collisions between atoms A and B with an internuclear separation R(t). The dipole transition moments μ^A_{10} and μ^B_{01} refer to transitions $|a_1\rangle \to |a_0\rangle$ in A and $|b_0\rangle \to |b_1\rangle$ in B respectively. For laser-switched dipole-quadrupole collisions such as those observed by Green et al (2.46) then

$$H'_{21}(t) = \langle 2|\,\frac{-\mu^A_{10}q^B_{01}}{i\hbar}\,|1\rangle\,\frac{1}{R^4(t)} \tag{5}$$

where q^B_{01} is the quadrupole moment for the $|b_0\rangle \to |b_1\rangle$ transition in atom B.

The diagonal operators (in the isolated - line approximation), $A_{ij}(t)$, in equation (2) are statistically averaged operators given by (2.44):

$$A_{ij}(t) = \langle\langle ij|\,A(t)\,|ij\rangle\rangle_{ave} = e^{-(\omega_{ij}+\phi_{ij})t} \tag{6}$$

where $\hbar\omega_{ij} = \hbar(\omega_i - \omega_j)$ is the system energy change associated with the transition from the ket state $|i\rangle$ to the bra state $\langle j|$. ϕ_{ij} is the radiative and collisional damping parameter defined in (2.44).

Once one is faimilar with these diagrams, following the time evolution of

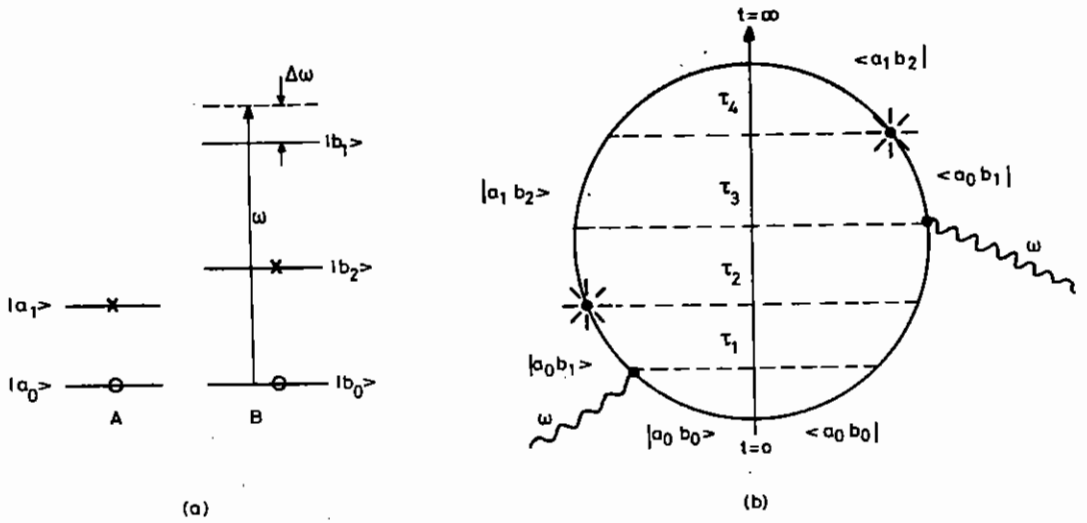

Figure 2.18 Diagrams describing the process of pair absorption

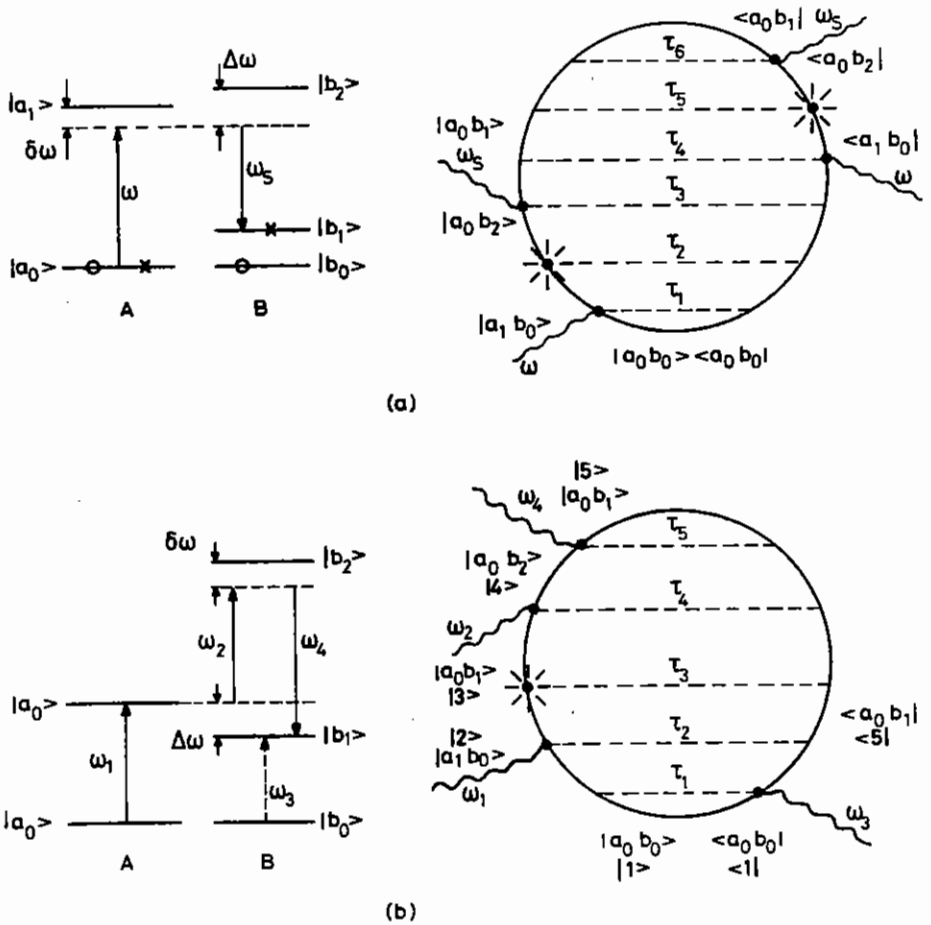

Figure 2.19 (a) Laser-switched (on-resonance) Raman effect with ω_s the scattered frequency

(b) Laser-switched four-wave mixing. Photon ω_3, is absorbed on the bra side, while ω_1 and ω_2 are absorbed and ω_4 emitted on the ket side of the diagram

the system wave function and its complex conjugate enables one to immediately write down expressions similar to equation (2) by writing down the operators H_{ij} and propagators A_{ij} as they occur in the diagram.

Ignoring damping effects and assuming a dipole-dipole collision then substitution of equations (3), (4) and (6) into equation (2) yields the equation:

$$\rho_{33}^{(b)} = C\int_0^\infty\int\int\int\exp\{i[\omega(t-\tau_4)-\omega_{32}\tau_3-\omega_{31}\tau_2-\omega(t-\tau_4-\tau_3-\tau_2)-\omega_{21}\tau_1]\}d\tau_4 d\tau_3 d\tau_2 d\tau_1 \quad (7)$$
$$\frac{}{R^3(t-\tau_4-\tau_3)R^3(t-\tau_4-\tau_3-\tau_2-\tau_1)}$$

where $C = \left(\frac{\mu_{10}^A \mu_{01}^A}{h}\right)^2 \left(\frac{\mu_{12}^B E}{2h}\right)^2$.

For the on-resonance case ($\omega = \omega_{31}$, $\Delta\omega = \omega_{21} = \omega - \omega_{32}$) shown in figure 2.17(a), then equation (7) becomes:

$$\rho_{33}^{(b)} = C\int_0^\infty\cdots\cdots\int \frac{e^{i\Delta\omega(\tau_3-\tau_1)}d\tau_4\cdots\cdots d\tau_1}{R^3(t-\tau_4-\tau_3)R^3(t-\tau_4-\tau_3-\tau_2-\tau_1)} \quad (8)$$

With a straight line classical trajectory such that $R^2(t) = \rho^2 + \bar{v}^2t^2$ ($\bar{v}$ is the mean collision velcoity and ρ the impact parameter), after performing the integrals in equation (8) we obtain:

$$\rho_{33}^{(b)} = 2C\left(\frac{1}{\rho^2\bar{v}\Delta\omega}\right)^2 \quad (9)$$

In deriving equation (9) we have further assumed that changes in $1/R^3(t)$ occur much slower than the oscillations in $e^{-i\Delta\omega t}$ (which is true for $|\Delta\omega| > \bar{v}/\rho \sim$ (collision duration)$^{-1}$).

An identical expression to equation (9) is obtained for the complex conjugate diagram of Figure 2.17(b). In a similar fashion the contributions from the diagrams shown in Figure 2.17(c) and (d) must be calculated. However, under the above assumptions, the contribution from figure 2.17(c) exactly cancels that from Figure 2.17(d) (this is only true in the case of no damping effects - inclusion of damping results in additional terms). Thus the total density matrix for the process described by Figures 2.17(b) - (d) is:

$$\rho_{33} = \rho_{33}^{(b)} + \rho_{33}^{(b)*} + \rho_{33}^{(c)} + \rho_{33}^{(c)*} + \rho_{33}^{(d)} + \rho_{33}^{(d)*} = 2\rho_{33}^{(b)}$$

$$= \left(\frac{\mu_{10}^A \mu_{01}^B}{\hbar\bar{v}\rho^2}\right)^2 \left(\frac{\mu_{12}^B E}{\hbar\Delta\omega}\right)^2 \quad (10)$$

which is identical to the expression for the transition probability derived by Harris et al (2.47) using standard perturbation theory.

By interchanging the photon absorptions with the collisions in Figures 2.17(b) - (d) one obtains the process of pair-absorption (2.48) shown in Figure 2.18. Keeping the propagators A_{ij} identical to those for Figure 2.17, it is easily shown that, with the same assumptions discussed above, the expression for the density matrix for on-resonance ($\omega = \omega_{31}$) pair-absorption is identical to equation (10) (with the energies $h\omega_{21}$ and $h\omega_{32}$ interchanged.

Using these diagrams not only is it much easier to included damping and off-resonance cases in the calculations, it is also very straightforward to write down expressions for higher-order processes than have been considered thus far. Indeed, all non-linear optical interactions occuring in gases may in principle be enhanced by laser-switched collisions. Examples of such higher-order cases are the laser-switched Raman scattering and four-wave mixing effects for which in Figure 2.19 one diagram is shown in each case. By following the interactions of the wave function and its complex conjugate as a function of time, integral equations for , similar to equations (2) and (8), may be written down (2.50).

M C Gower (RAL)

2.3.5 Passive Mode-locking of KrF Lasers

Because of their large gain bandwidth ($\sim 10^{13}$ Hz) it should in principle be possible to produced picosecond pulses in the UV by mode locking of rare gas halide lasers. However, reports of both active (2.51) and passive (2.52) mode locking of rare gas halide discharge lasers have only

produced pulses of nanosecond duration. An insufficient number of cavity passes to establish complete mode-locking during the gain time in these short pulse (~20 nsec) discharge lasers is thought to be the reason for the lack of appreciable pulse shortening. In order to fulfil our requirement for short KrF laser pulses for amplification and kinetic studies, we decided to try to generate subnanosecond pulses by passively mode-locking both ELF (gain pulse duration 60 nsec) and a short (60 cm) cavity discharge laser.

The saturable absorbers p-terphenyl, 7 - diethylamino - 4 - methylcomarin and benzophenone dissolved in ethanol were contained in a 5 mm thick cell and placed in the laser cavities.

2.3.5(a) ELF experiments

With a cavity length of 120 cm, a variety of mirrors ranging from a low to a high cavity Q and varying degrees of resonator stability were used. The saturable absorber concentration in the intracavity dye cell was varied such that its single pass transmission at 248 nm was between 0.05 % and 50 %. Apertures were also placed in the cavity in an attempt to restrict oscillation to a single axial mode. However, all attempts to observe any modulation of the laser output were unsuccessful. In an attempt to more readily saturate the absorbers (which had measured saturation fluences of between 10 - 30 mJ cm^{-2}), we placed the cell at the focus of a one-to-one telescope inside the resonator. Only very slight (<10 % depth) modulation of the output was observed.

2.3.5(b) Discharge Laser Experiments

The laser used for this study was the discharge excited KrF laser using automatic preionisation described in section 2.2.4. The discharge dimensions were 45 x 2 x 0.6 cm. An 85 % reflectivity internal plane aluminium coated mirror was used at one end of the cavity, while variable reflectivity dielectrically -coated external plane output couplers were used at the other end. At the output end the laser cell was terminated by a Spectrosil B quartz window tilted at 3° to prevent unwanted

feedback into the laser.

In the series of photographs in Figure 2.20(a) we show the laser output for different reflectivity output couplers with no dye cell in the cavity. As can be seen even with no output mirror the laser radiation is heavily modulated in a series of gain-switched spikes. As well as varying the modulation depth of the output, changing the Q of the cavity also changes the frequency of oscillation. If the oscillation were caused by partial self mode-locking of the laser then the modulation frequency should be independent of the cavity Q and determined solely by the cavity round trip time. On the other hand, relaxation oscillations (2.53) have been observed in many types of lasers for which the decay time, $\tau = \gamma^{-1}$, of the upper laser level is greater than the cavity decay time, $\tau_c = \gamma_c^{-1} = \frac{t}{\delta}$ (δ is the loss/cavity pass and t the time for a cavity pass). Oscillation is caused by the build up of stimulated emission in the laser cavity which reduces the gain which in turn reduces the stimulated emission. For relaxation oscillations in a homogeneously broadened medium with a step-wise pump rate, (rise time $\tau_p < \tau_c$), the spiking frequency is given by (2.53)

$$f = \frac{1}{2\Pi} \sqrt{\gamma\gamma_c(r-1)} \qquad (1)$$

where $r = \frac{R}{R_t}$ is the degree that the laser is pumped above the threshold pumping rate, R_t. Since $R_t = \frac{\gamma\gamma_c}{K}$, where the stimulated transition rate constant, $K = \frac{\sigma c}{n}$ (σ is the stimulated emission cross section and n the refractive index), then

$$f = \frac{1}{2\Pi} \sqrt{KR - \gamma\gamma_c} \qquad (2)$$

Thus we see that increasing the cavity Q decreases the cavity decay rate, γ_c, and increases f as observed in Figure 2.20(a). Also, as seen in Figure 2.21(a), decreasing the pump rate of the laser (by reducing the charging voltage of the storage capacitor from 45 kV to 25 kV) also decreased f as expected from equation (2). Relaxation oscillations are absent when (2.53)

$$\left(\frac{r\gamma}{2}\right)^2 \geq \gamma\gamma_c(r-1) \qquad (3)$$

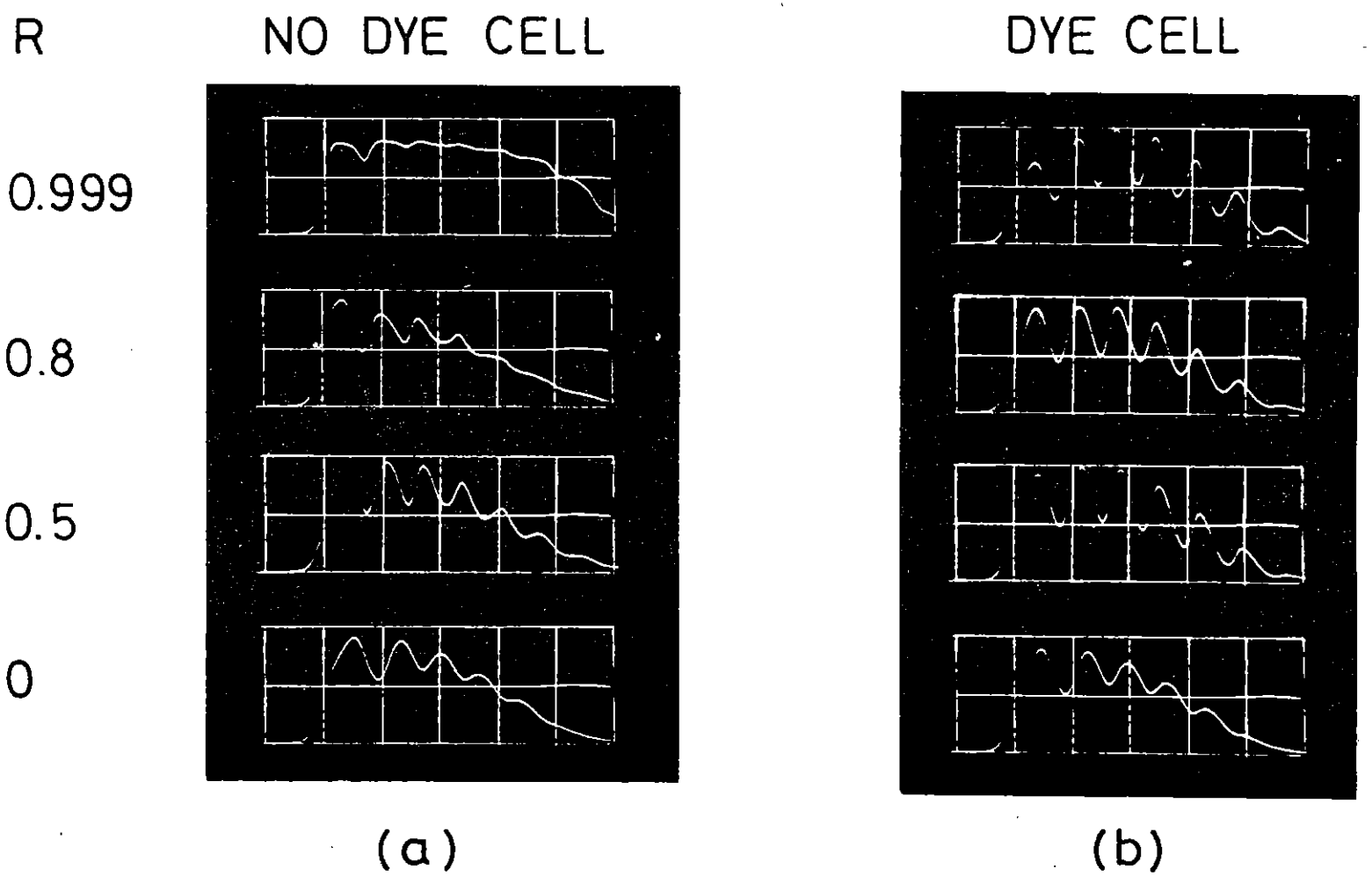

Figure 2.20 (a) KrF laser output for the output coupler reflectivities shown. The energy storage capacitor was charged to 45 kV. Sweep speed = 5 nsec/div

(b) As (a), but with a dye cell containing p-terphenyl in ethanol solution (13% small-signal transmission at 248 mm) placed in front of the output mirror

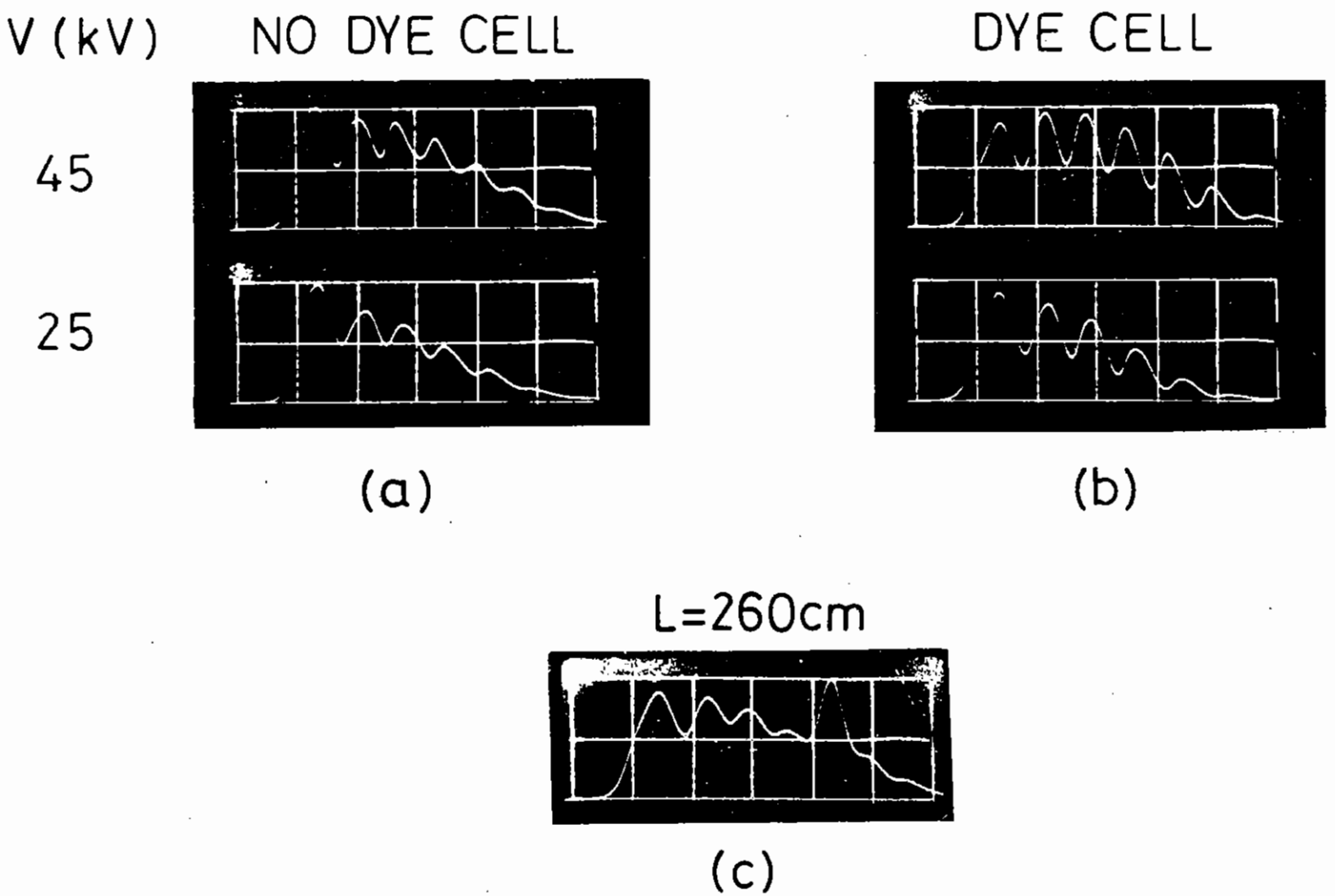

Figure 2.21

(a) KrF laser output as a function of laser pump rate. The energy storage capacitor was charged to the voltages, V, shown. Output mirror R = 0.5. Sweep speed = 5 nsec/div

(b) As (a) with the cell containing the 13% transmitting solution of p-terphenyl in place

(c) Laser output for a 260 cm cavity length with R = 0.5 and V = 45 kV. Sweep speed = 5 nsec/div

which is the case when $\gamma_c \ll \gamma$ and is probably the reason for their almost complete disappearance under high cavity Q conditions (R = 99.9 % in Figure 2.20(a)). From the measured frequency of oscillation, and assuming a distributed non-saturable loss at 248 nm in the discharge of $\alpha = 0.02/cm$, and a 3 nsec total lifetime of the KrF B-state with a B-X stimulated emission cross section $\sigma = 2.5 \times 10^{-16} cm$ (2.54), then equation (2) gives a value of $R = 6.0 \times 10^{23}$ molecules/cm^3/sec. To calculate γ_c we have assumed that the loaded gain $\simeq$ system losses so that $\delta = (\alpha\ell - \ell n \sqrt{R_1 R_2})$. With a 70 % extraction efficiency of KrF B-state molecules to laser photons (2.32), this value of R agrees well with the energy obtained from the laser using optimum coupling conditions (200 mJ).

In attempts to passively mode-lock this laser we inserted the dye cell in front of the output coupling mirror. The absorber concentrations were varied for maximum modulation of the laser output. Typical results are shown in Figures 2.20(b) and 2.21(b) for the same reflectivity output couplings as in Figure 2.20(a) and 2.21(a) respectively. For the cases shown, the single pass small-signal transmission at 248 nm of the p-terphenyl dye solution was measured to be 13 %. As can be seen, the insertion of the dye cell into the cavity does increase the modulation depth and indeed induces oscillation for the R = 99.99 % case in Figure 2.20(b). However, it can also be seen that changing both the cavity Q and the pump rate causes the oscillation frequency to change. As discussed previously, we can therefore preclude the possiblity that the laser is passively mode-locking.

In figure 2.21(c) we show the output when the cavity length is increased to 260 cm. The further amplification of the initial spike after reflection from the output mirror is clearly seen in the tail of the pulse envelope. We also performed experiments on an identical laser having half the discharge and cavity length of the 40 cm device. However, no spiking or passive mode-locking was observed for the different output couplers tested previously - presumably because τ_c has changed such that the

condition $\tau_p < \tau_c < \tau$ is no longer satisfied.

M C Gower (RAL)

2.4 SPRITE - A 200 J KrF Laser

2.4.1 Electrical Design

During the past year the entire pulsed power system for SPRITE has been designed. Many major components have been delivered and some of them have been installed and tested. The status of the major components is as shown in Table 2.02. The majority of the design work can be undertaken using the simple empirical formulae for water breakdown developed by the AWRE group (2.55). However in certain areas, especially those involving large dielectric discontinuities, a fairly accurate knowledge of electric field strength is necessary to ensure that insulators do not become over stressed. The main items of concern were on the oil/water interface, the pulse forming line gaps and the vacuum feed-through tubes.

The aid of the computer applications group at RAL was sought and they supplied a program called PE 2D which solves the Laplace equation in 2D or cylindrical symmetry (2.56).

As an example of the applicability of the program, the design of the vacuum insulator is described here. Figure 2.22 shows the actual final design arrived at. The electric field problem is complex since five dielectrics are involved viz: water, polythene, oil, perspex and vacuum. The main design aim is to reduced the size and hence inductance of the insulator to a minimum. The weakest point is the perspex/vacuum interface. Grading rings are necessary to maintain the field angle to the insulators at 45° which gives the highest breakdown field. The sign of the angle is such that electrons emitted from the plastic do not re-enter the plastic which would cause electron multiplication. For a correctly graded tube the breakdown field, F in kV/cm is given by:

$$F t^{1/6} d^{1/10} \simeq 80$$

TABLE 2.02

	Item	Qty Required	Qty Delivered	Installed & tested
1	Marx change-over switch	1	1	Yes
2	Oil/water interface	1	1	Yes
3	Water capacitor	1	1	No
4	Main spark gap	1	1	No
5	5Ω pulse-forming line	4	1	Yes
6	Vacuum feed through tubes	8	1	No
7	Deionized water system	1	1	Yes

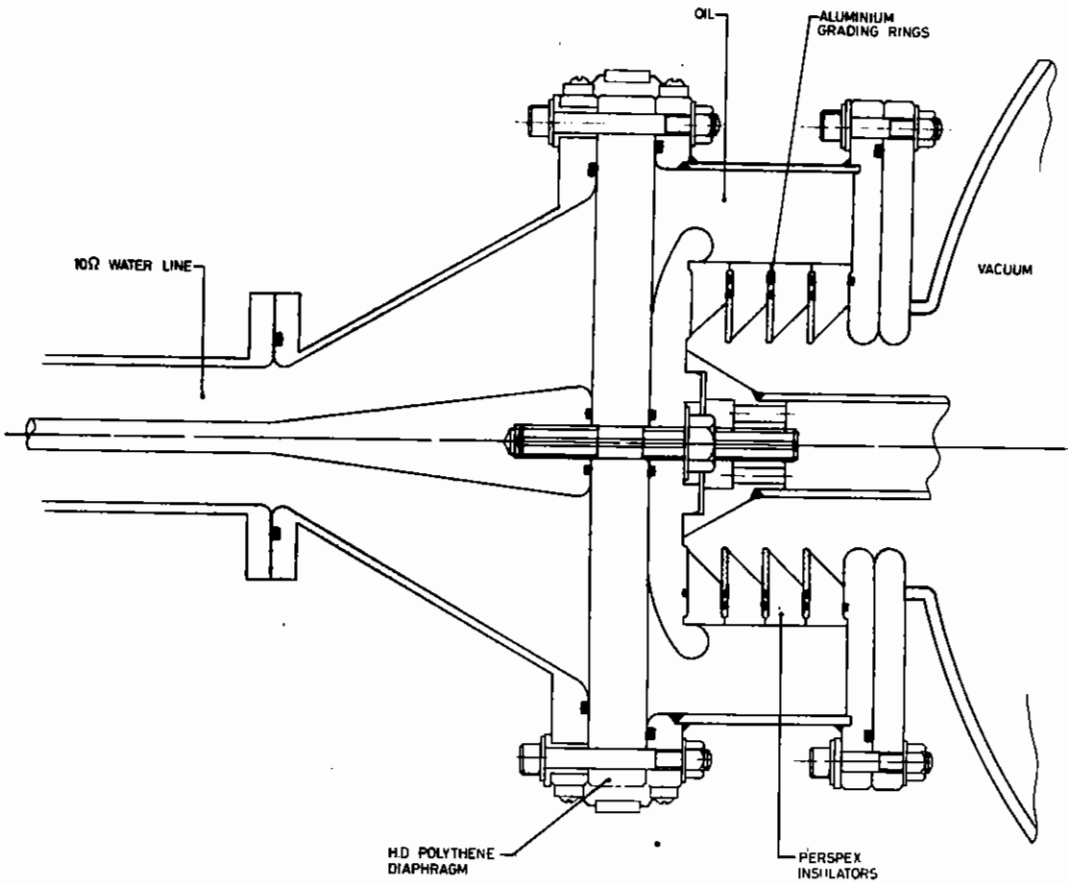

Figure 2.22 Sprite vacuum insulator

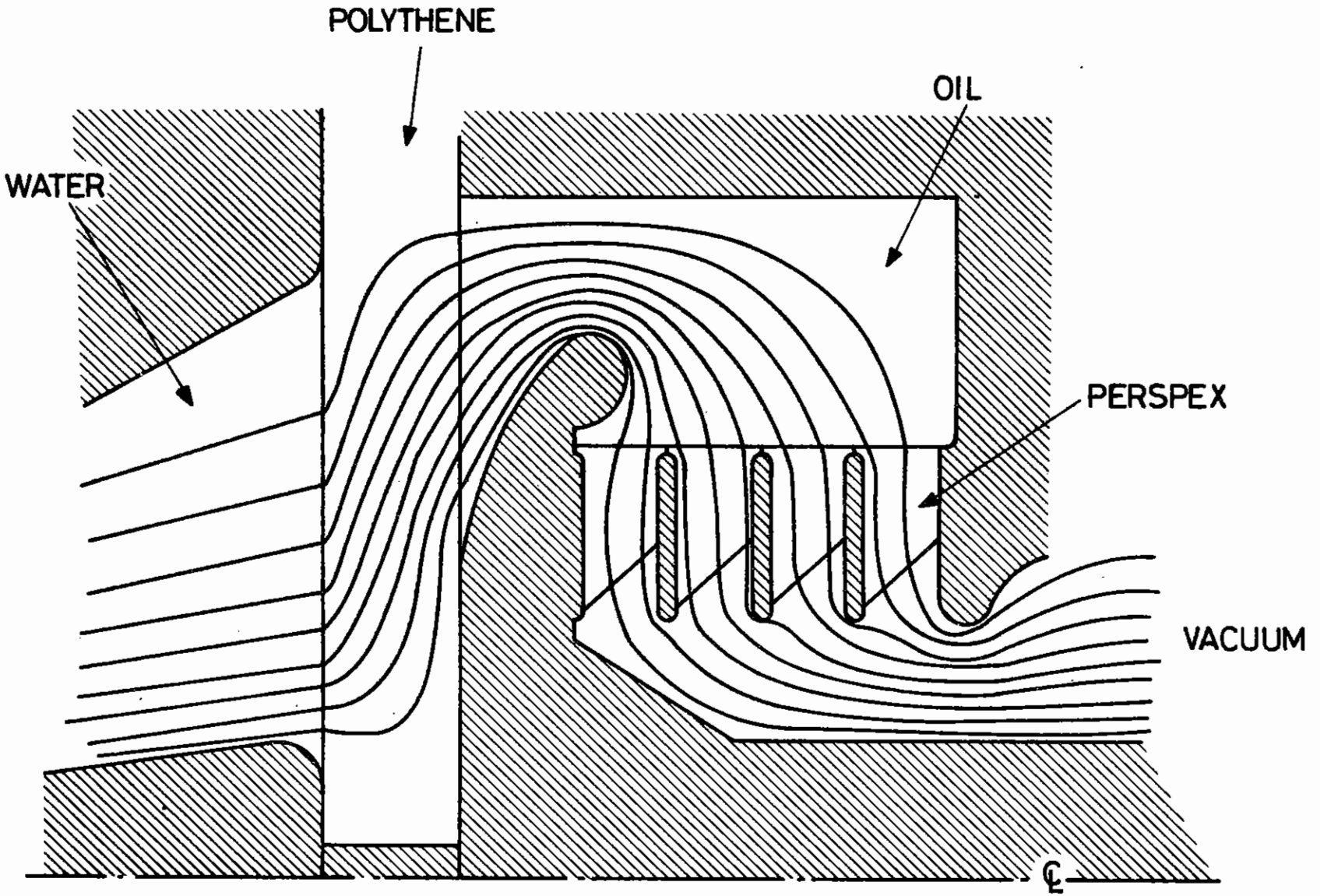

Figure 2.23 Equipotentials in the Sprite vacuum tube

where t is the pulse duration in μs and d is the tube diameter in cm. For our dimensions this gives approximately 100 kV/cm as the breakdown field. A four stage insulator of 2 cm per stage was chosen thus giving a breakdown field ≈ 800 kV. The normal operating voltage of 500 kV is thus ≈ 60 % of breakdown which is a reasonable figure for safe operation of a single shot device.

It is very important however to ensure that this voltage is uniformly graded along the insulator otherwise breakdown can stil occur even when the overall voltage applied is considerably less than the uniform field breakdown voltage. This is where the computer solution is very valuable. The shaping on the insulator backing plate and the diode stem were optimized by the computer to give the best field uniformity along the insulator stack. Figure 2.23 shows computer derived equipotentials in the feedthrough. One interesting point concerning this particular solution is the treatment of the grading rings in the insulator stack which are allowed to float and find their own potential. The program however could only cope with conductors which had defined potentials. The problem was overcome in the calculations by treating the rings as insulators with an exceedingly high dielectric constant. This has the effect of excluding field lines and hence the rings behave as though they were floating conductors. The total inductance of the tube is calculated to be about 25 nH, and thus its contribution to the system rise time amounts to not much more than 1 ns. Since eight vacuum feed throughs are required for SPRITE it is important that the design is absolutely safe and so just one has been ordered at the present time and this will be tested in the near future.

C B Edwards and M J Shaw (RAL)

2.4.2 5 Ohm Pulse Forming Line

Since the operation of the water pulse forming lines is the major determinant of the overall performance of SPRITE, it was decided to build

just one of the four lines and extensively test it before proceeding with the manufacture of the others. The aim of the test was to investigate the electrical and mechanical strength of the sytem, to laser trigger the line output gap and measure its jitter and in general to gain experience with the water dielectric, since this was a new medium to the group.

The line was charged directly from the Marx, as shown in Figures 2.01 and 2.24, rather than via the water capacitor which meant that the charge time was nearer 600 ns rather than 200 ns as it will be in SPRITE. The line was tested to the same voltage as required in the final design (1 MV) which implies an approximately 40 % overvoltage test since breakdown fields generally scale as $t^{1/3}$.

All the metal parts of the line were made from aluminium alloy which was surface treated with Alochrom 1200 (ICI) to prevent corrosion in the deionized water. One untreated part which was installed was found to corrode badly. During operation, water is continuously recirculated through the line via an Elga de-ionizer and oxygen removal system. This worked well giving typical resistivities of 10-20 MΩcm and reducing bubbles in the system by removing dissolved oxygen.

The spark gap body shown in Figure 2.25 was machined from polycarbonate plastic and pressure tested to 300 psi before installation. The normal maximum operating pressure is 150 psi of SF_6.

The electrical tests were conducted by firing the line into a matched 5Ω $Al_2(SO_4)_3$ liquid resistor. Current in the matched load was monitored as well as the charge voltage on the line. The line voltage was gradually increased by increasing the spark gap spacing and SF_6 pressure. The breakdown voltage of the gap was found to be quite linear in SF_6 pressure and very reproducible at pressures up to 100 psia. Above this, however, the breakdown voltage increased more slowly and reproducibility (or jitter) of the gap became quite severe. The variation of the self breakdown voltage at 150 psia was ± 100 kV. However the maximum working voltage (1 MV) was obtained at 150 psi with a 25 mm gap setting. No surface flashover was observed. During these tests it was found that the

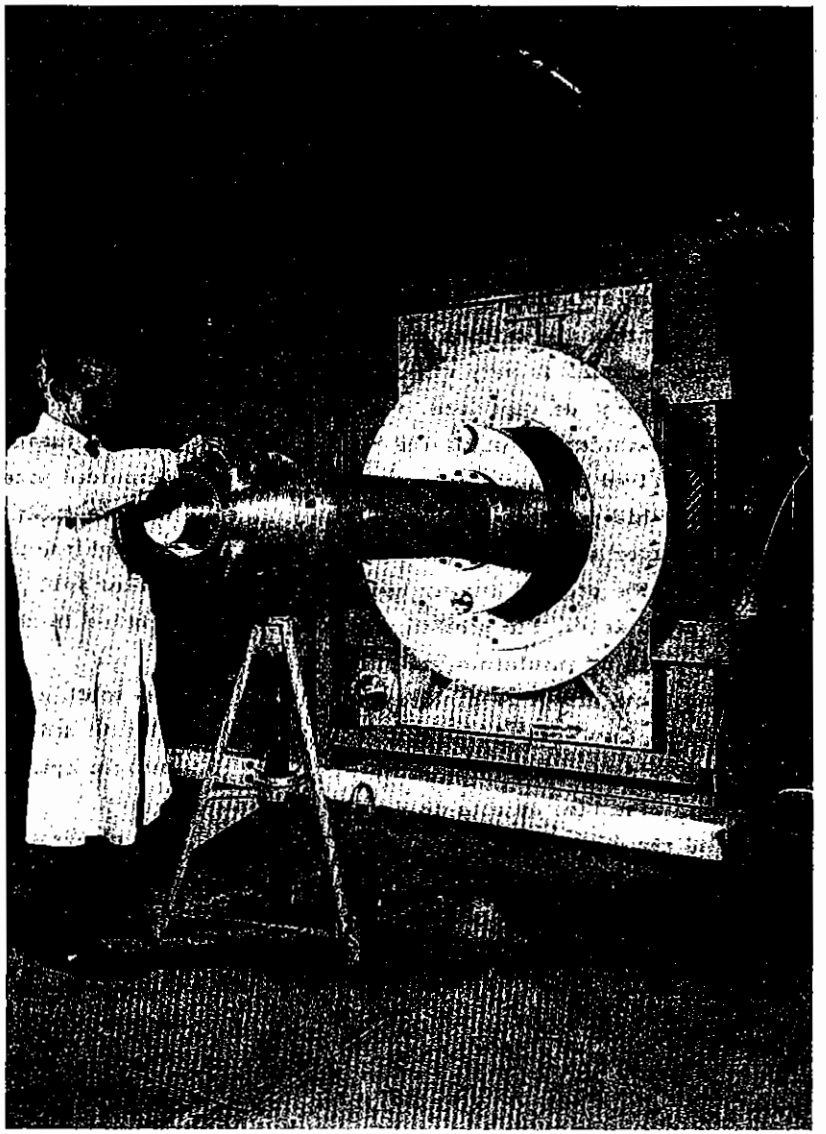

Figure 2.24 Photograph of the test 5 ohm pulse forming line fitted to the back of the Elf marx. The line is pulse-charged from the marx via the 1 MV change-over switch shown in Fig 2.01

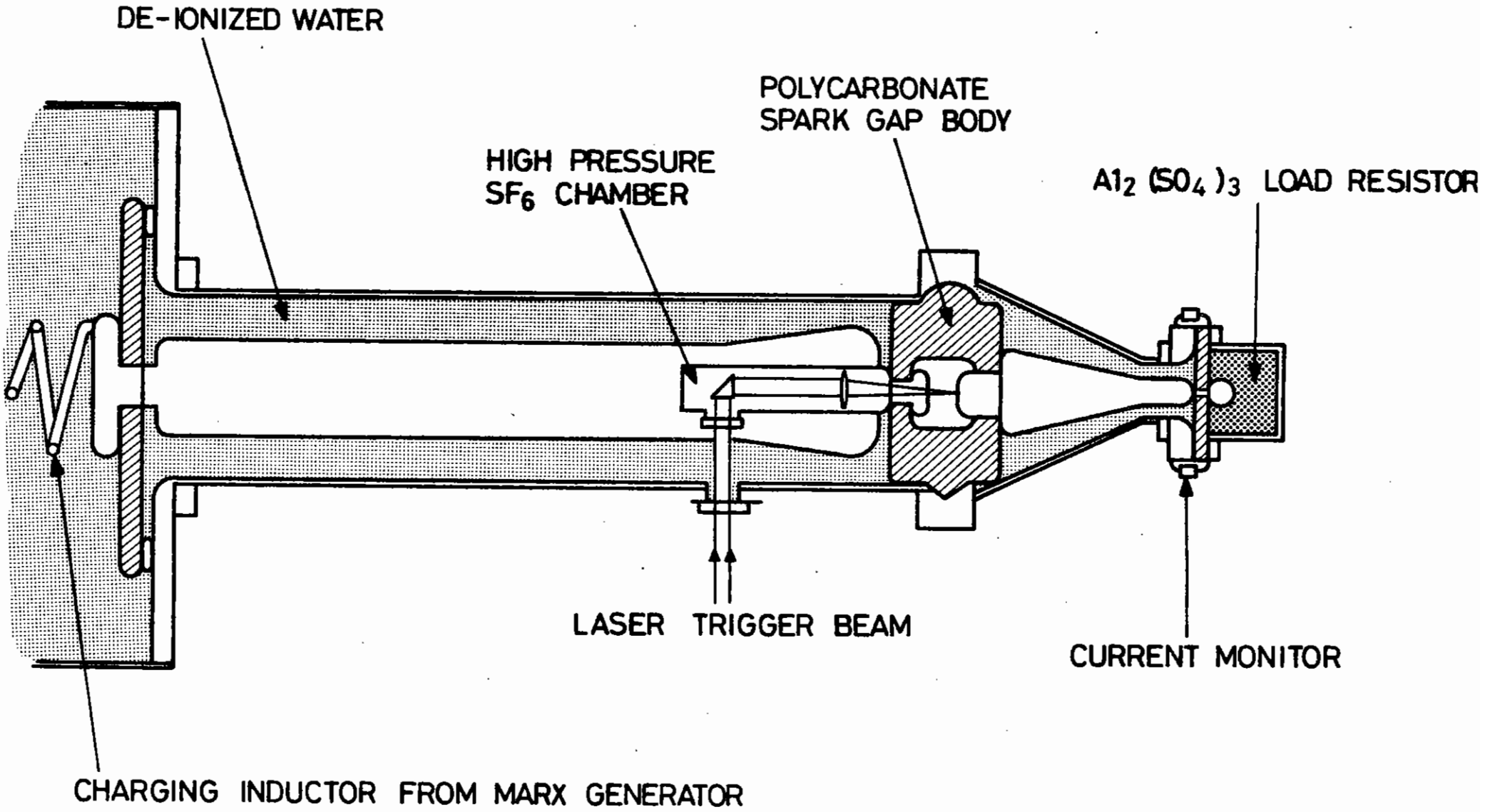

Figure 2.25 5 ohm laser triggered water line

field shaper at the spark gap end of the line had become deformed. This was thought to be due to shock impluses transmitted to the field shaper from the spark gap. The shaper was thus partially filled with high density epoxy to strengthen it and the Marx end of the line was allowed to slide freely in its supporting diaphragm. With these modifications further deformation has been prevented.

The gap was laser triggered using an unstable resonator discharge KrF laser giving about 50 mJ output energy. The optical system shown in figure 2.25 was used which focuses the beam into the centre of the gap. The laser intensity is sufficiently high to cause visible gas breakdown at the focus of the beam. In case gas breakdown does not occur the beam also falls on the opposite electrode where plasma emission is observed at laser intensities much less than the gas breakdown threshold. The laser is triggered by a delayed pulse which occurs at the beginning of the Marx erection. The laser pulse and current pulse were recorded on a dual beam oscilloscope. The gap was found to laser trigger down to 50 % of its self breakdown voltage. The jitter (as measured by only a small number of shots to date) appears to be less than 2 ns.

Whilst jitters of this order imply that the effects on laser pump pulse risetime in SPRITE will be small, it was found that the current risetime from the test line itself was somewhat greater than originally hoped for (20 ns for 10 % - 90 %). This is due mainly to spark gap inductance, the major source of which is the single plasma channel. In order to reduce the risetime further, multichannel operation will be necessary and we are proposing to look at ways of achieving this, either optically or electrically, in the near future.

M J Shaw (RAL)

2.4.3 Large Area Diode Experiments

In this section we describe experiments which were undertaken to answer some of the key questions concerning electron beam generation and energy deposition in SPRITE. The main questions to be answered are:

(a) What is the best emitter for large area cathodes?

(b) What is the best hibachi structure?

(c) What foil transmission is attainable at 500 keV?

(d) What is the deposition profile in the gas?

(e) Can high efficiency, uniform excitation be achieved using four-sided pumping?

Since SPRITE is pumped by four 5Ω diodes, a single half length diode would have an impedance of 10Ω which is close to the line impedance of ELF (15Ω). The ELF diode chamber was thus modified as shown in Figure 2.26 to take a 20 cm diameter cathode holder which could accommodate an emitting area up to (40 x 15) cm^2 which simulates a half-size SPRITE diode. The anode foil and pressure foils (25 μm Ti) were mounted either side of the closure plate. An hibachi with removable vanes was used so that different vane depths could be tried. The electron window height was 15 cm and the vane spacing 3 cm. Bursting pressures of such an aperture closed by a 25 μm titanium foil were measured and found to be ~ 150 psi (considerably in excess of the working pressure - 15 psi for these tests and 30 psi for SPRITE - and incidently implying a foil strength orders of magnitude greater than the ultimate tensile strength of bulk titanium).

The main diagnostics of the beam, in addition to the normal current and voltage measurements, involved firing the electrons into a large (30 x 30 x 60) cm^3 perspex box which could be filled and sealed off with various gases at around atmospheric pressure. The total energy deposited in the gas was obtained from pressure jump measurements and the spatial deposition profile by photographing side fluorescence from the excited gas.

Three different cathode types were investigated viz: multiple blades, carbon felt and multi-point (cheese grater) emitters. Visual inspection of the anode foil gave a crude indication of beam uniformity since highly

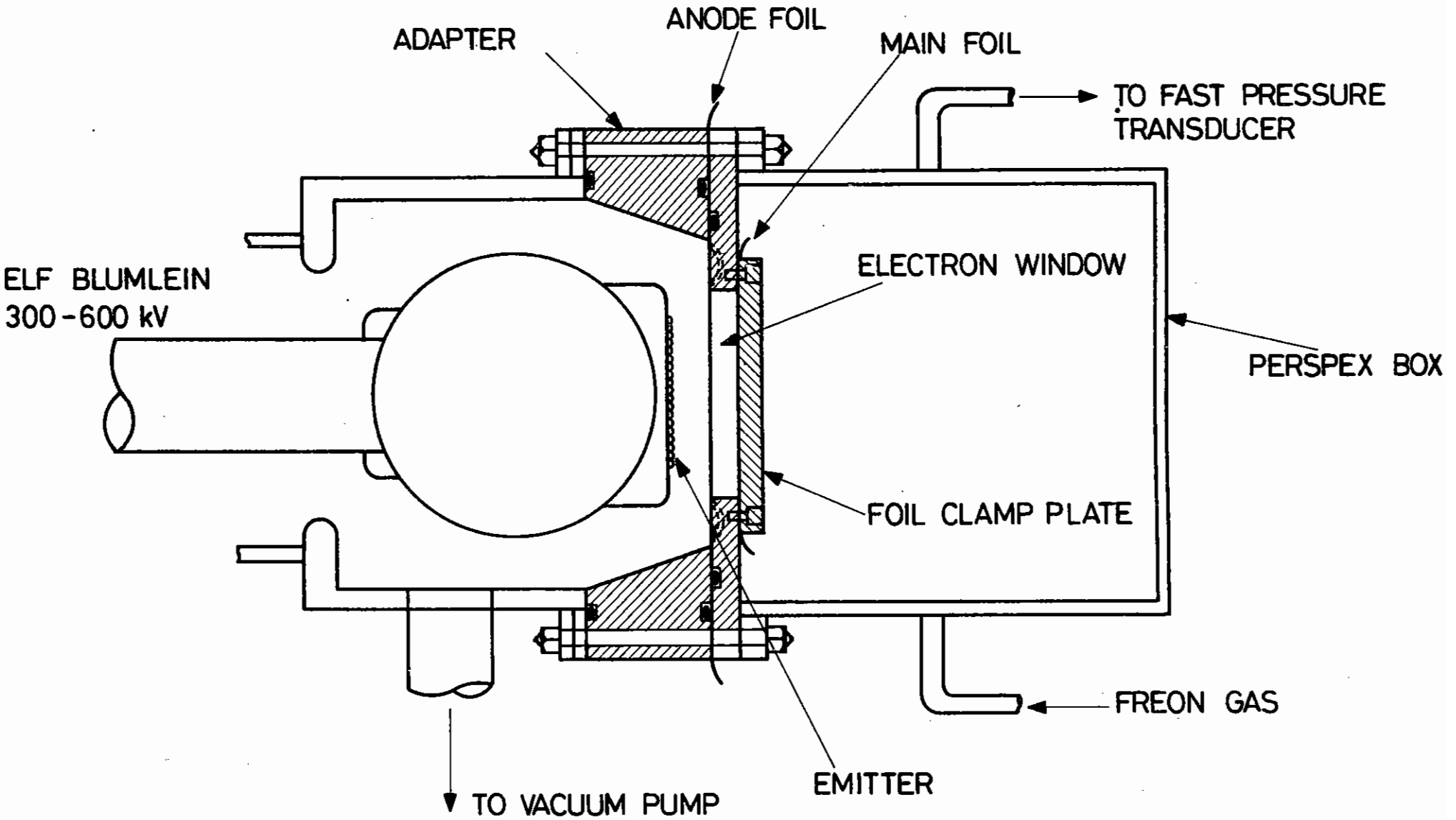

Figure 2.26 Large area diode test apparatus

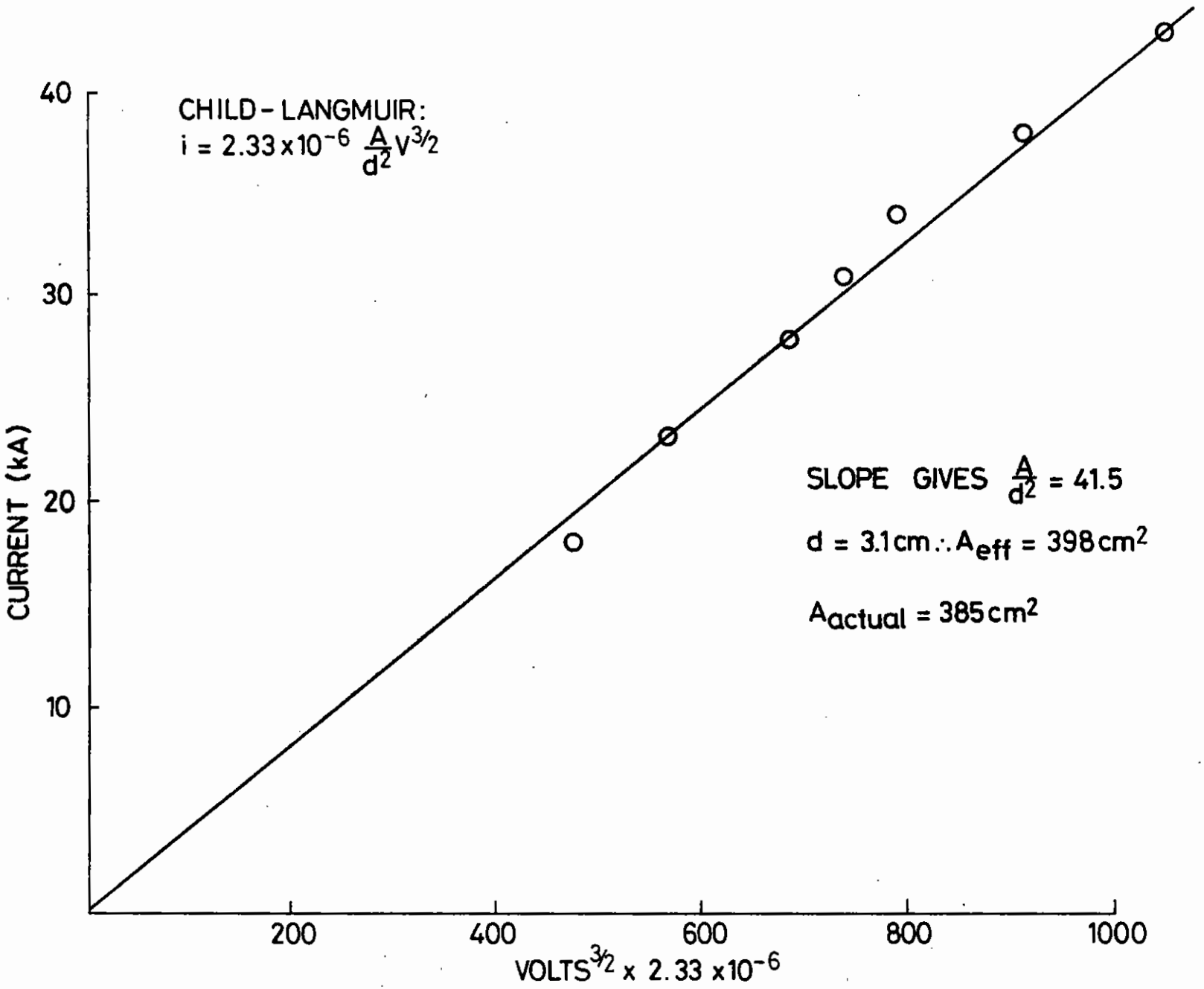

Figure 2.27 Diode perveance plot

non-uniform beams produced post pulse arcing to the anode. Current and voltage traces were used to compute diode perveance and "switch-on" time.

Vertical blades spaced at 30 mm were first tried and found to produced serious non-uniformities which resulted in severe damage to the anode foil. On the other hand carbon felt produced exceptionally uniform beams but suffered from excessively long (~ 20 ns) switch-on times. The cheese grater type was found to be by far the best. The cathode was punched from 150 μm tantalum foil. Triangular spikes 3 mm above the backing plane were spaced at 5 mm intervals covering a total area (10.5 x 34) cm^2. Switch-on time was shorter than could be measured (<2 ns) and no anode foil damage was observed.

Blue cellophane placed behind the anode foil showed uniform emission over the full area but, as expected, with a central magnetic pinch. Figure 2.27 shows a constant diode perveance ($i/v^{3/2}$) over the full voltage range (300 - 600 kv) tested. The slope gives an effective beam area in close agreement with the measured area (mean of anode and cathode areas) and indicates that spurious emission from cathode holder was negligibly small.

The deposition efficiency (energy deposited in gas ÷ diode energy [iVt]) was measured by filling the perspex box with Freon 22 ($CHClF_2$) gas at 800 torr and measuring the pressure jump produced on firing the beam into the box.

The electron range in Freon 22 from 300 - 600 keV is such that the vast majority of the electrons deposit their energy in the gas apart from the unavoidable fraction that are back-scattered to the foil wall. In addition 800 torr of Freon 22 has the same stopping power as 1700 torr of Ar which is around the proposed operating pressure in SPRITE. Thus without requiring a large volume pressure vessel, the energy deposition from a single SPRITE-type diode could be well simulated.

Figure 2.28 shows the deposition efficiency as a function of diode voltage

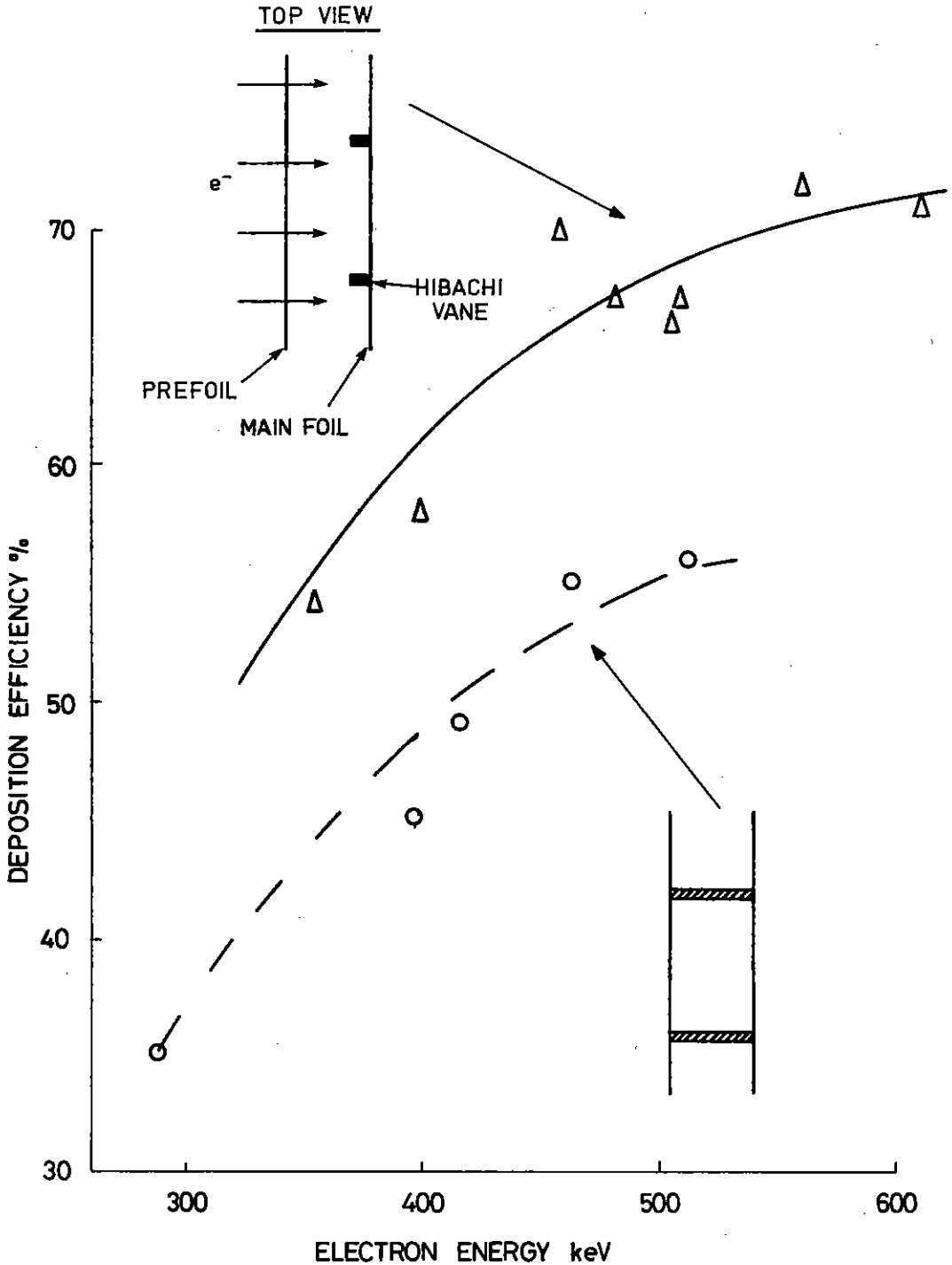

Figure 2.28 Deposition efficiency

for two different hibachi structures. For the curve with lower efficiency the hibachi vanes were 2 mm wide and 18 mm deep spaced at 30 mm and for the higher efficiency the same spacing and width was used but the depth was reduced to 3 mm. The difference in efficiencies is largely due to scattering in the prefoil which increases the emittance of the beam. A fraction of the beam is thus lost on the hibachi which acts as a collimator. At 500 keV the mean projected scattering angle from a 25 μm Ti foil is 28° (2.57) and the calculated geometric transmissions of the two hibachis are 60 % and 88 % respectively. The deposition efficiency is less than this due to two other factors: firstly energy loss in the foils which amounts to about 25 keV per foil thus giving a further 10 % loss at 500 keV, and secondly, back-scattering from the gas itself. The 2D deposition code described below shows that 15 % of the total energy is back-scattered to the foil wall at 500 keV. The deposition efficency is thus given by

$$\eta_{dep} = T\left(1 - \frac{e}{E}\right)(1-f_b)$$

where T is the hibachi transmission, e the energy loss in the foil, E the beam energy and f_b the back-scattered fraction. Numerically at 500 keV the caluculated efficiencies for the two hibachis are:

$$\eta_1 = 0.88 \times 0.9 \times 0.85 = 0.67$$

$$\eta_2 = 0.6 \times 0.9 \times 0.85 = 0.46$$

in good agreement with the measurements shown in Figure 2.28.

The measurement of deposition profile in the gas from a single electron beam is of importance since it allows the determination of the profile to be expected in SPRITE which is pumped from four sides by four identical beams. The extrapolation from one to four beams is only justified if the beams are non-interacting. However in our conditions beam transport is dominated by gas scattering rather than by the beam's self-electric and magnetic fields and the result of multi-sided pumping is assumed to be purely additive. The design objective is to achieve uniform pumping

across the aperture to preserve good laser beam quality. This is particularly important where angular optical multiplexing is contemplated since different pumped regions are extracted by different beams.

In these experiments visible fluorescence from dense gases was used as a monitor of energy deposition based on the reasonable assumptions that the integrated fluorescence intensity from a given region of pumped volume is proportional to the energy deposited and that transport of excited molecules may be neglected on a time scale in the order of the fluorescence liftime. It is thus not necessary to know the detailed mechanisms producing the fluorescence. Freon gas was chosen since densities at one atmosphere are equivalent (in electron stopping power) to higher pressures of argon. For example Freon 12 (CCl_2F_2, MW 121) is equivalent to three atmospheres of argon (MW 40) and Freon 22 ($CHClF_2$, MW 86.5) is equivalent to just over two atmospheres of argon. Most of the measurements were taken on Freon 22. Fluorescence from a single shot was photographed through the perspex side wall along what would be the laser axis using a 4" x 5" plate camera and Polaroid type 57 film (3000 ASA). A typical result is shown in Figure 2.29. The film response and range of fluorescence intensity is such that at any given aperture setting the range of intensities between under and over-exposure are quite localized and quite easily plotted in the x-y plane. Reducing or increasing the aperture by one stop produces another locus of points corresponding to regions where the fluorescence intensity is respectively twice or one half as great as the previous plot. It is thus a simple matter to produce contours of constant fluorescence intensity as shown in Figure 2.30. The intervals between contours correspond to 3 dB in fluorescence intensity. For comparison the results of the 2D e-beam energy deposition code are shown in Figure 2.31. The curve marked 0dB was fixed to cross the axis of symmetry at the same point as the f/11 fluorescence curve so that the experiment and theory could be compared directly. Apart from very near to the foil the agreement between the two is remarkably good. This lends confidence in using the code to predict the deposition profiles for four-sided pumping at different pressures and with different e-beam parameters from those compared here.

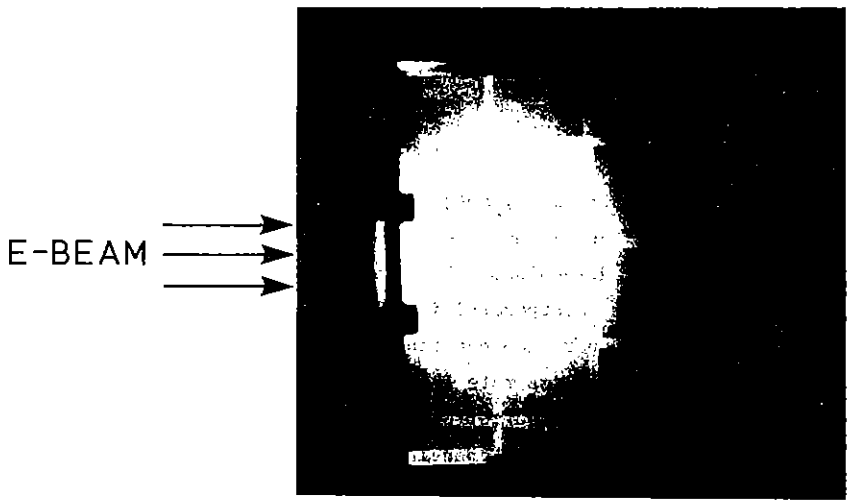

Figure 2.29 Side view of E.beam-excited Freon 22. Fluorescence from the perspex box. Grid spacing = 10 cm. E-beam voltage = 500 Kv. Gas pressure = 1 ATM

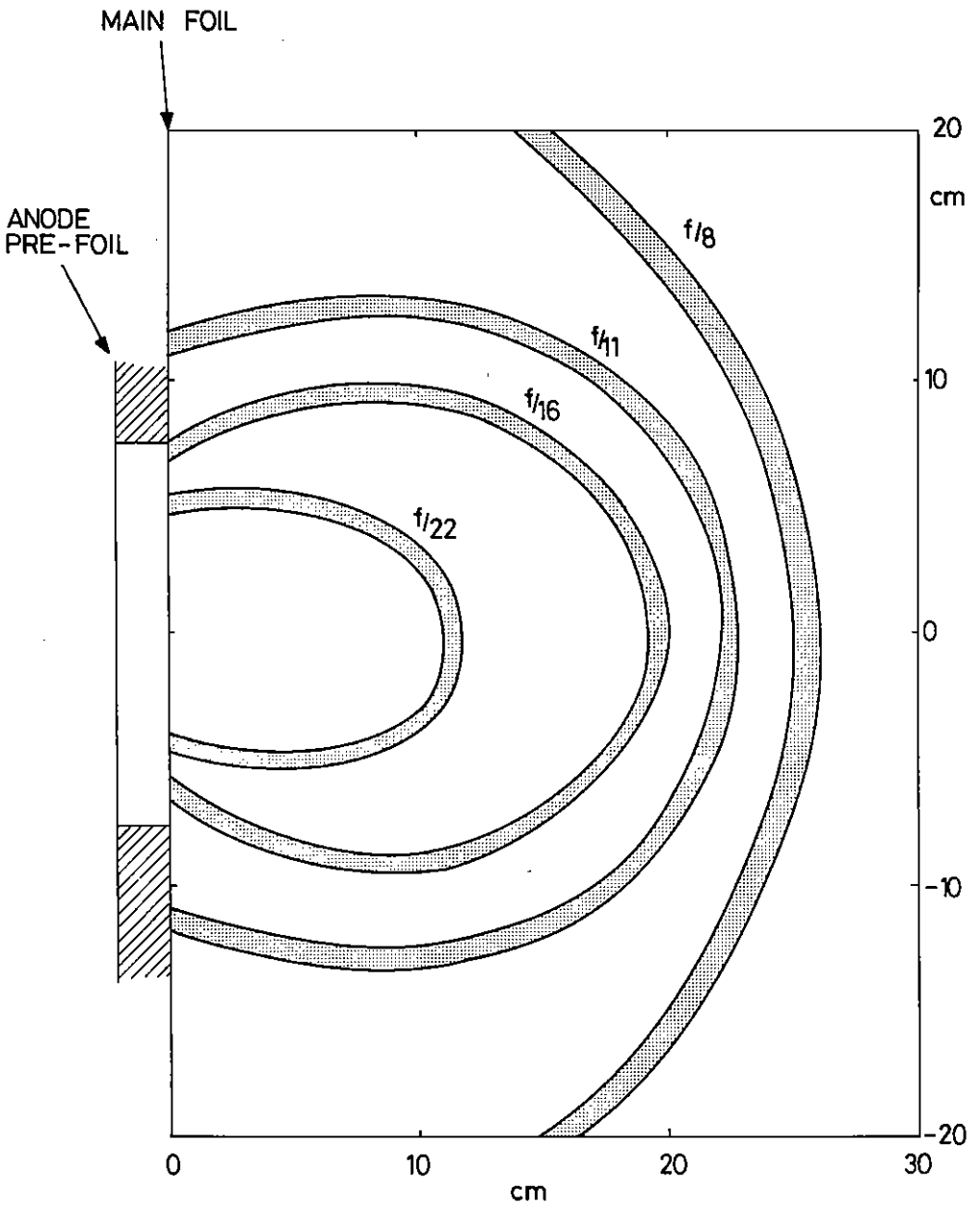

Figure 2.30 Fluoresecence intensity contours

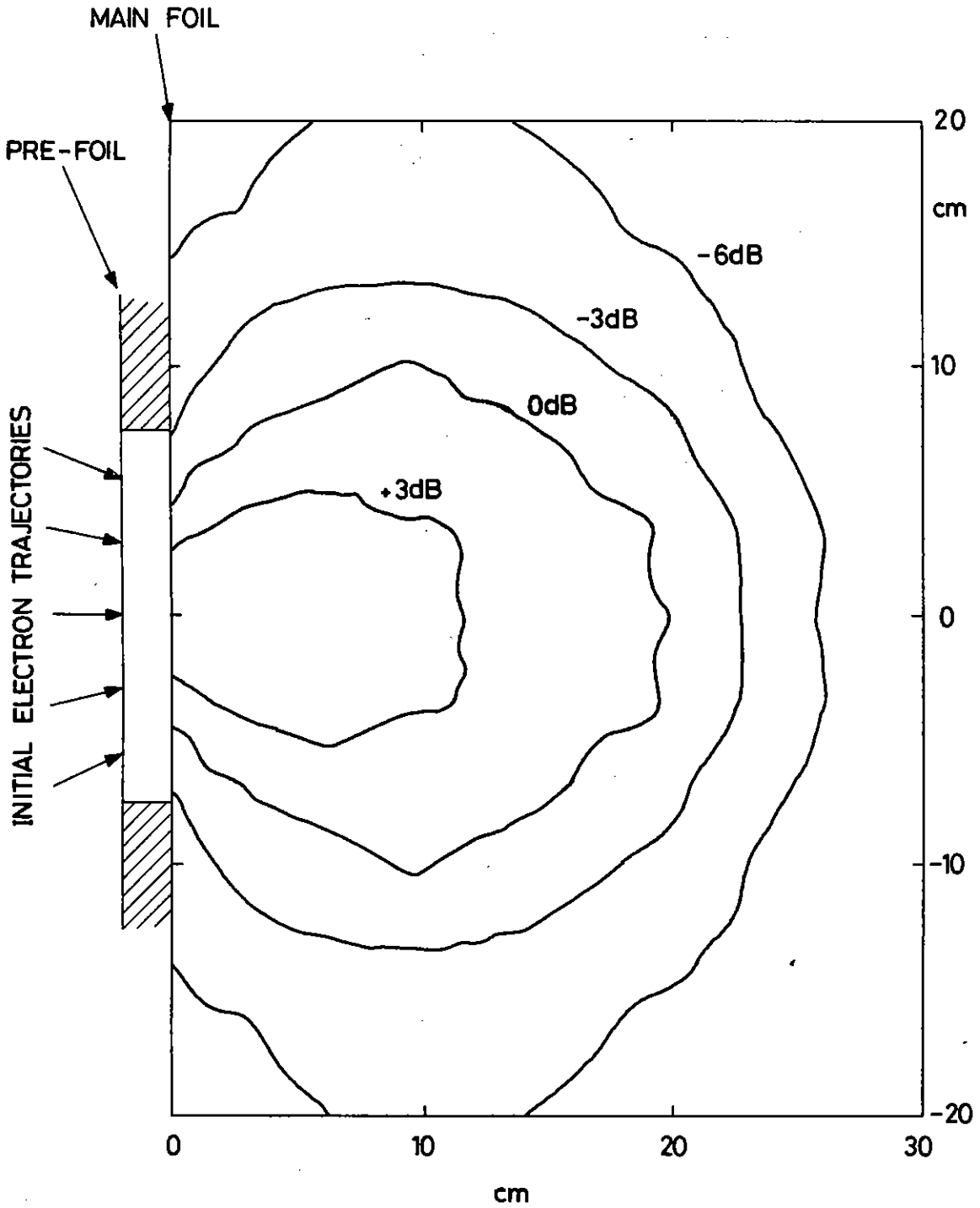

Figure 2.31 Computed energy deposition contours

The e-beam energy deposition code has been extensively modified over the last year to solve the basic transport equation:

$$\underline{v} \cdot \nabla_k f_k + \frac{e_k}{m_k}\left\{\underline{E} + \frac{1}{C}(\underline{v} \wedge \underline{B})\right\} \cdot \nabla_v f_k = \frac{df_k}{dt}\Big|_{coll}$$

in two dimensions for a number of gas species k in the diffusion approximation. Some account of the self pinching in the diode can be taken by allowing a θ dependence of the initial electron distribution f_∞. The energy loss within the prefoil and main foil are calculated within the code as well as the fraction of back-scattered electrons which reach the foil wall and their energy spectrum. The limitations of the diffusion theory in describing correctly the scattering and energy straggling is corrected for by making use of a Monte-Carlo routine. This worked well in the previous 1D version of this code.

The effects of four-fold symmetric pumping of the SPRITE laser cell can be readily simulated using the code. The main adjustable parameters are gas pressure and cell dimensions. For this problem use is made of the variable mesh size incorporated in the code so that effective adjustment of the cell wall separation can readily be made. Figure 2.32 shows contours of constant pump rate (now with linear intervals) for four-sided pumping of Freon 22 at 800 torr and 500 keV with cell dimensions 30 x 30 cm. The effects of changing nothing other than cell dimensions is shown in Figure 2.33 with the cell size reduced to 24 x 24 cm, showing much improved uniformity of deposition.

An exhaustive investigation of the pressure/cell size parameter space is now underway with a view to optimizing the pumping configuration in SPRITE before the start of construction and experimentation.

M J Shaw and D J Nicholas (RAL)

2.4.4 Computer Predictions of SPRITE Laser Performance

The computer modelling of the krypton fluoride e-beam-pumped laser (section 2.2.1) has been extended to predict laser performance and

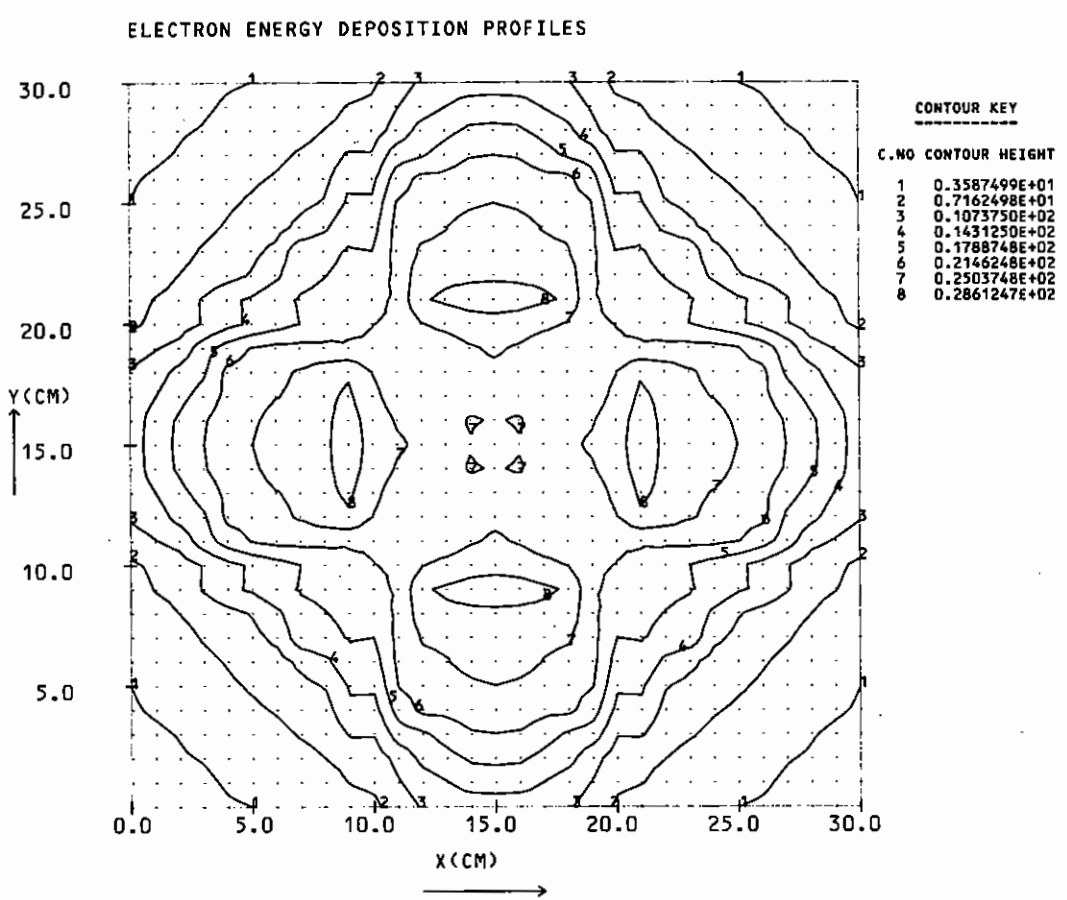

Figure 2.32 Computed E-beam pumping of Freon 22.
Cell size = 30 x 30 cm

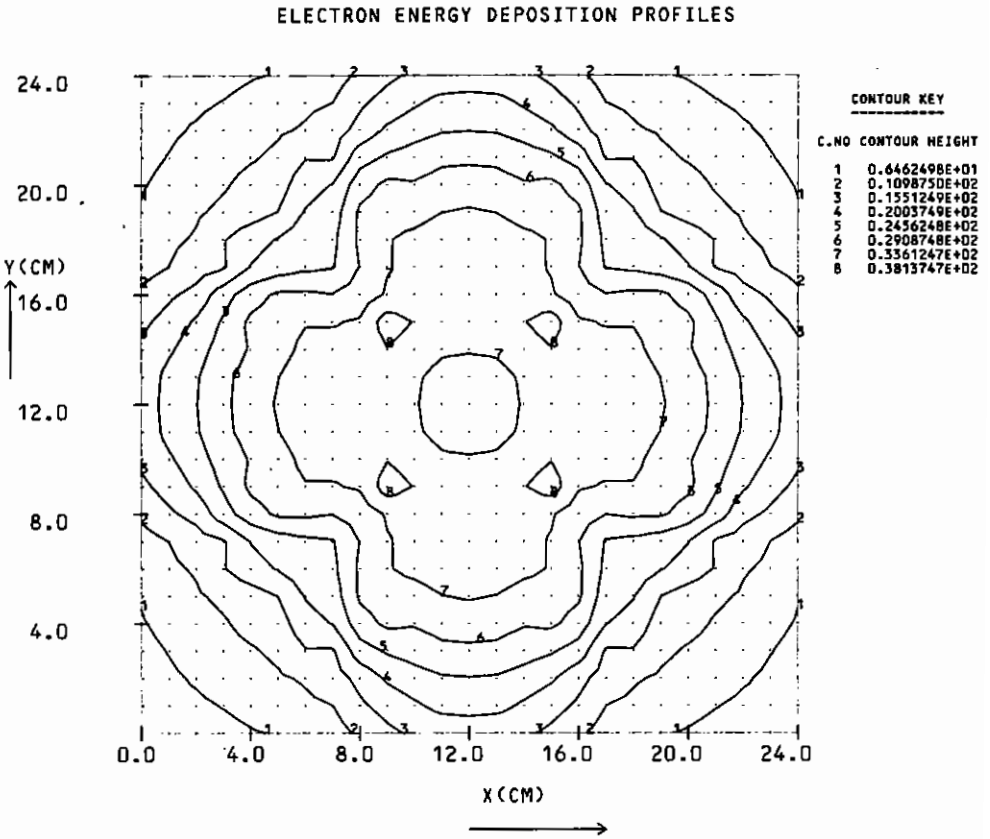

Figure 2.33 Computed E-beam. Pumping of Freon 22.
Cell size = 24 x 24 cm

optimise the optical design of the SPRITE system. With the total input energy, pulse duration, and stopping power of the laser fill determined, the code has been used to optimise the pumping geometry. The effect of varying the pumped length while keeping the (pump power x length) product constant is shown in Figure 2.34. Though the efficiency is higher for shorter lengths, due to the higher intracavity photon flux which extracts laser energy more efficiently, the variation is small over the lengths of interest (50 -150 cm). This implies that optimisation of other parameters, eg e-beam diode size, can be accomplished without great loss of overall efficiency.

Figure 2.34 also shows the effect of varying the fluorine concentration. The higher pressures of fluorine cause loss of laser output due to photoabsorption by F_2 molecules, whilst below 3 torr the burn-up of fluorine during the pumping pulse severely reduces output. The code has also been used to optimise the cavity reflectivity at ~ 20 %.

It is planned to use the time dependent version of the code to model the short-pulse extraction efficiency of a system using SPRITE in an amplifier mode, and to compare with the experimental values when available.

C B Edwards and F O'Neill (RAL)

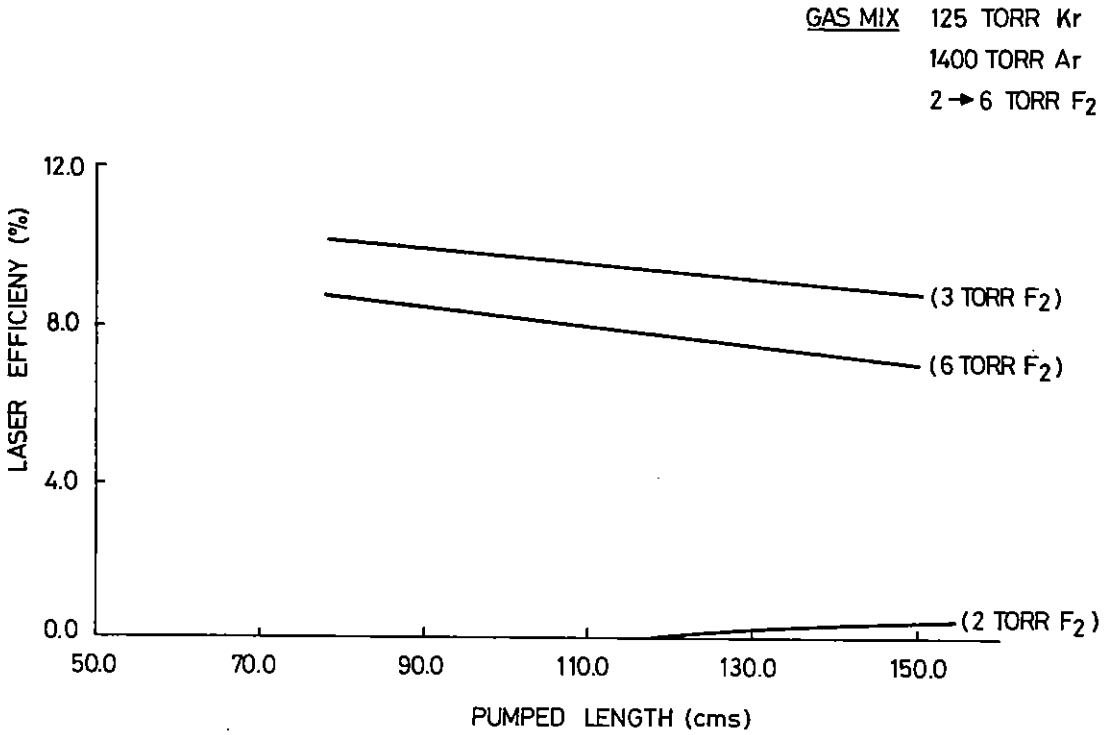

Figure 2.34 Computer optimisation of SPRITE

CHAPTER 2 REFERENCES

2.01 C B Edwards, F O'Neill and M J Shaw, Appl Phys Lett (in press)

2.02 See for example T H Johnson and A M Hunter, J Appl Phys, 51, 2406 (1980)

2.03 D Potter, Computational Physics, Published by John Wiley, Interscience

2.04 C B Edwards, F O'Neill and M J Shaw, Appl Phys Lett, 36, 617 (1980)

2.05 J H Jacob, J C Hsia, J A Mangano and M Rokni, J Appl Phys, 50, 5130 (1979)

2.06 R S Bradford, W B Lacina, E R Ault and M L Bhaumik,Electronic Transition Lasers II, edited by L E Wilson, S N Suchard and J I Steinfeld, Proc 3rd Summer Colloquium on Electronic Transition Lasers, Snowmass, Sept 1976

2.07 J K Rice, G C Tisone and E L Patterson, IEEE J Quantum Electron, QE-16, 1315 (1980)

2.08 D Eimerl, J Appl Phys, 51, 3008 (1980)

2.09 G H Schindler, IEEE J Quantum Electron, QE-16, 546 (1980)

2.10 G Marowsky, F K Tittel, W L Wilson and E Frenkel, Appl Opt, 19, 138 (1980)

2.11 A H Hawryluk, J A Mangano and J H Jacob, Appl Phys Lett, 31, 164 (1977)

2.12 L F Champagne, L J Palumbo and R S F Chang, Paper LB-4 33rd Gaseous Electronics Conference, Norman, Oklahoma (1980) (unpublished)

2.13 M Rokni, J H Jacob and J A Mangano, Phys Rev A, 16, 2216 (1977)

2.14 W R Wadt and P J Hay, J Chem Phys, 68, 3850 (1978)

2.15 W E Ernst and F K Tittel, IEEE J Quantum Electron, QE-16, 945 (1980)

2.16 W R Wadt, D C Cartwright and J S Cohen, Appl Phys Lett, 31, 672 (1977)

2.17 E Zamir, D L Huestis, H H Nakano, R M Hill and D C Lorents, IEEE J Quantum Electron, QE-15, 281 (1979)

2.18 W L Wiese, M W Smith and B M Miles, 'Atomic Transition Probabilities', II, US Dept of Commerce, National Bureau of Standards, NSRDS-NBS 22

2.19 A P Thorne 'Spectrophysics', Chapman and Hall, 298 (1974)

2.20 A J Kearsley, Doctoral thesis (1980)

2.21 H H Michels, R H Hobbs and L A Wright, Appl Phys Lett, 35, 153 (1979)

2.22 T L Rose, D H Katayama, J A Welsh and J F Paulson, J Chem Phys, 70, 4542 (1979)

2.23 A E Siegman, Appl Opt, 13, 353 (1974)

2.24 D L Barker and T R Loree, Appl Opt, 16, 1792 (1977)

2.25 T J McKee, B P Stoicheff and S C Wallace, Appl Phys Letts, 30, 278, (1977)

2.26 J Goldhar and J R Murray, Opt Lett, 1, 199 (1977)

2.27 D James, T J McKee and W Skrlac, IEEE J Quantum Electron, 15, 335 (1979)

2.28 A A Isaev, M A Kazaryan, G G Petrash, S S Rautian and A M Shalagin, Sov J Quant Elect, 7, 746 (1977)

2.29 M C Gower, Opt Comm, 36, 43 (1981)

2.30 A J Kearsley, A J Andrews and C E Webb, Opt Comm, 31, 181 (1979)

2.31 J J Ewing, R A Haas, J C Swingle, E V George and W F Krupke, IEEE J Quantum Electron, QE-15, 368 (1979)

2.32 J H Jacob, D W Trainor, M Rokni and J C Hsia, Appl Phys Letts, 37, 522, (1980)

2.33 H Pummer, K Hohla and F Rebentrost, Appl Phys, 20, 129 (1979)

2.34 M R Flannery, Int J Quant Chem Symp 13, 501 (1979)

2.35 K C Kulander and N W Winter, Private communication, Lawrence Livermore Laboratory

2.36 M C Gower, Opt Commun, 36, 43 (1981)

2.37 C Grey-Morgan, Sci Prog Oxf, 65, 31 (1978)

2.38 H T Buscher, R G Tomlinson and E K Damon, Phys Rev Letts, 15, 847 (1965)

2.39 A J Alcock, C DeMichelis and M C Richardson, App Phys Letts 15, 72 (1969)

2.40 A J Alcock, K Kato and M C Richardson, Opt Comm, 6, 342 (1972)

2.41 J Murray, J Goldhar and A Szöke, Laser Program Report, Lawrence Livermore Laboratories, 7-103, UCRL-50021-77 (1979)

2.42 E Yablonovitch, Phys Rev Letts, 31, 877 (1973)

2.43 J A Poole, J Phys Chem, 69, 1343 (1965)

2.44 T K Yee and T K Gustafson, Phys Rev A, 18, 1597 (1978)

2.45 T K Yee, T K Gustafson, S A J Druet and J-P E Taran, Optics Comm, 23, 1 (1977)

2.46 W R Green, M D Wright, J Lukasik, J F Young and S E Harris, Optics Letts, 4, 265 (1979)

2.47 S E Harris, R W Falcone, W R Green, D B Lidow, J C White and J F Young, 'Tunable Lasers and Applications', Eds A Mooradian, T Jaeger and P Stokseth, Springer-Verlag (1976)

2.48 L I Gudzenko and S I Yakovlenko, Phys Lett A, 46, 475 (1974)

2.49 J C White, G A Zdasiuk, J F Young and S E Harris, Optics Letts, 4,137 (1979)

2.50 M C Gower, 'Atomic and Molecular Physics Conference', Oxford, England, Paper P17 (1980)
T K Yee and M C Gower, to be published (1981)

2.51 C P Christensen, L W Braverman, W H Steier and C Wittig, Appl Phys Letts, 29, 424 (1976)

2.52 T E Efthimiopoulos, J Banic and B P Stoicheff, Can J Phys, 57, 1437 (1979)

2.53 A Yariv, 'Quantum Electronics', 2nd edition, John Wiley and Sons Inc (1975)

2.54 M Rokni, J A Mangano, J H Jacob and J C Hsia, IEEE J Quant Elect, QE-14, 464 (1978)

2.55 It is a pleasure to acknowledge the advice of J C Martin and D W Forster of AWRE Aldermaston on many areas of the electrical design of SPRITE.

2.56 C S Biddlecombe and J Simkin, Technology Division, Rutherford and Appleton Laboratories Report, RL-79-089/Rev 2

2.57 K Siegbahn, "Alpha, Beta and Gamma Ray Spectroscopy", N Holland, (1965)

CHAPTER 3 LASER PLASMA INTERACTIONS

INDEX

CHAPTOR EDITOR: R G Evans

CHAPTER 3 LASER PLASMA INTERACTIONS

3.1 Introduction

During this last year the laser plasma interaction group has continued to investigate the processes occurring in the low density coronal plasma. Processes occurring near quarter critical density, ie two plasmon decay and stimulated Raman scattering, have been investigated by collective scattering and by direct plasma emission. During this period we have obtained the first results anywhere of time and spectrally resolved $\omega_0/2$ emission, described in section 3.5.

As well as the excitation of plasma waves, the generation of low frequency density perturbations in optical filaments has been observed for the first time by a variety of diagnostic methods. Together with the optical filaments there appear spectacular plasma jets, persisting after the laser pulse and probably associated with small scale magnetic fields. The role of magneto thermal instabilities in producing these plasma jets has been investigated and could have a deleterious effect in determining the uniformity of ablation pressure generated by any driver system, laser or particle beam.

3.2 Non-uniformities in the Plasma Corona

Experiments have been carried out to investigate the uniformity of the plasma corona of plane and spherical targets irradiated ablatively with a long (1.5 nsec) laser pulse and probed with a short (50 ps) Raman shifted second harmonic diagnostic pulse. Small scale density non-uniformities (laser beam filamentation and plasma jet formations) and self generated micromagnetic fields have been observed for the first time with good space and time resolution.

At this laboratory optical probing measurements are carried out on both plane and spherical targets using one or four beams of the six beam laser compression facility. The four laser beams are situated normal to each

other in a plane and are focussed onto the targets by f/1.5 lenses. For spherical irradiation the lenses are focussed beyond the target centre by 4.5 target radii in order to achieve as uniform illumination as possible. The direction of the probe beam is perpendicular to the plane of the four heating beams as shown in Figure 3.01.

The laser oscillator generates a short 100 psec (FWHM) Gaussian pulse which is split into two. To generate the heating pulse one of these fractions is passed through a pulse stacker which divides it into ten similar pulses, and introduces a time-delay of 150 psec between each pulse giving an overall pulselength of 1.5 nsec. The peak intensities of the individual pulses vary by less than ±30 %. With this pulse shape energies over the range of 50 to 120 Joules in the four laser beams can be delivered to the target. The second split-off portion is directed through a separate amplifier chain to generate the diagnostic pulse. The layout of the probe beam system is shown in Figure 3.02 and described in reference (3.01).

For plane target studies the target was imaged by an f/1.4 microscope objective with a 40 times overall magnification, whereas spherical targets irradiated with four beams were imaged by an f/3.3 microscope objective with 27 times overall magnification. The microscope objectives were protected from the target debris and scattered 1.05 μm light by the use of a 100 μm thick quartz pellicle with a dielectric mirror coating on the front surface. A spatial resolution of 2-3 μm was obtained with these systems.

For density profile measurments and studies of uniformity of illumination, a Nomarski type of interferometer (3.02) was used. Observations of irregularities in the blow off plasma such as small scale structures were made with a Schlieren system consisting of a microscope objective as described above and a 200 μm diameter needle. The needle was placed in the back focal plane of the microscope objective in order to block the undeflected probe light. For Faraday rotation measurements a sheet polarizer served as analyser. To prevent the film from being exposed by plasma emission, a narrow band pass interference filter (50-100 Å

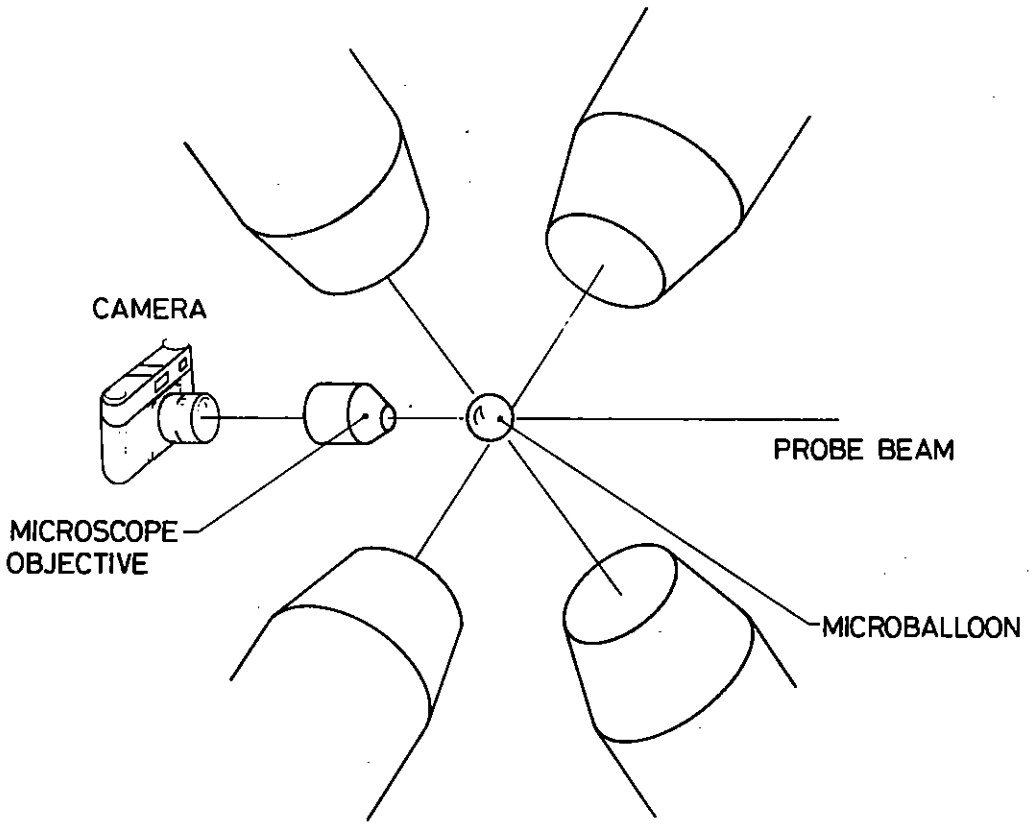

Figure 3.01 Schematic of the experimental arrangement.

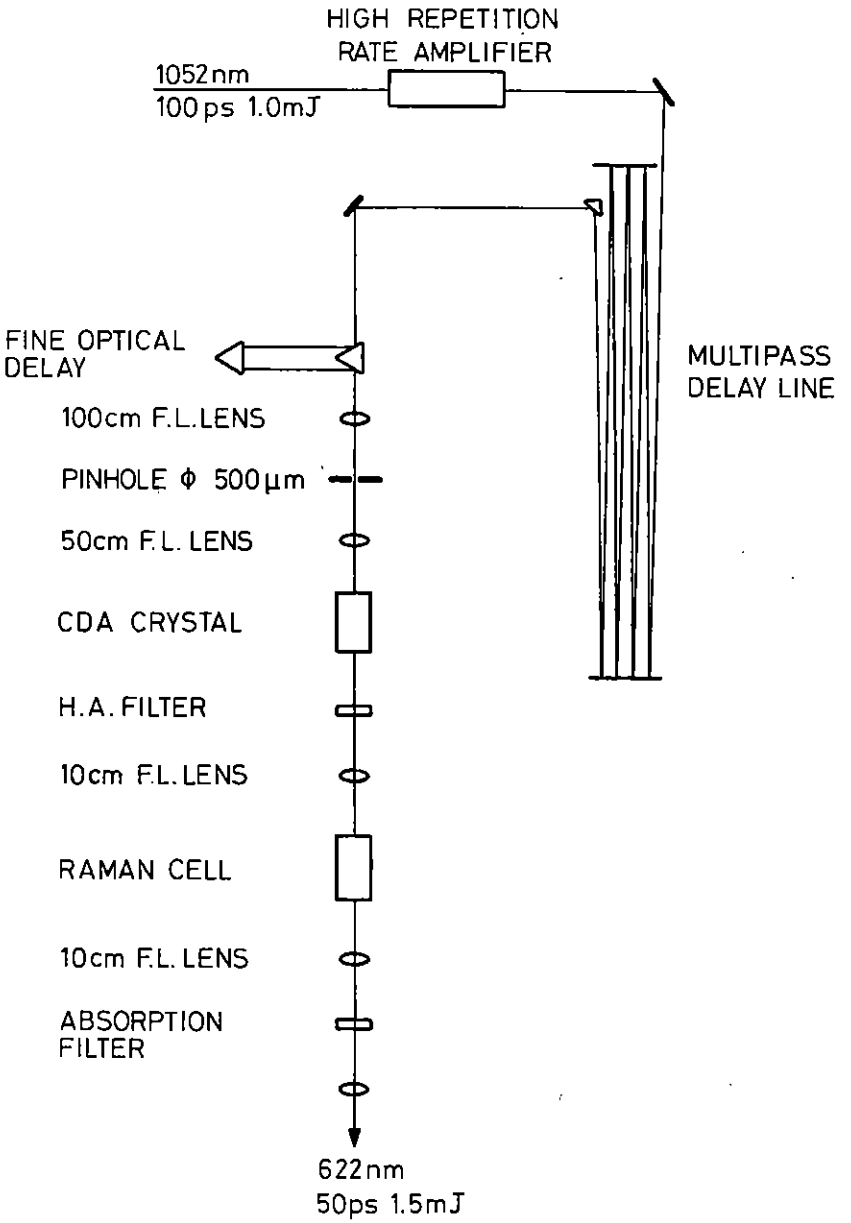

Figure 3.02 Schematic of the optical probe beam system.

bandwidth) and a 3 mm thick heat absorbing glass filter were placed in front of the camera. On each shot the temporal profile of the main laser pulse was recorded on an EPL streak camera.

3.2.1 Density Profile and Coronal Uniformity measurements

The uniformity of illumination of ablatively driven spherical targets has been studied interferometrically for different laser focal conditions. The targets were illuminated with four laser beams placed in a plane and probed normally to this plane. Figure 3.03 shows two interferograms of glass microballoons irradiated with focussing conditions of d/R = 1.7 and 4.5 respectively where d is the distance beyond the target centre at which the beams focus and R is the target radius. Both targets were irradiated at an intensity of 4×10^{13} W cm^{-2} and the interferograms were recorded 0.96 nsec after the beginning of the laser pulse. The overlaid circles indicate the original target positions and the arrows the directions of the incident laser beams. The double image formed is due to the type of interferometer set-up used and consequently some information is lost when their images overlap. As can be seen in Figure 3.03(a) with a focussing condition of d/R = 1.7 the plasma expands grossly non-uniformly. Even with a focussing condition of d/R = 4.5 where the beams overlap and the illumination pattern is consequently more uniform (±30 %), the blow off plasma is still not spherical. At the probe beam cut off a fuzzy surface with a jet-like structure can be seen in both interferograms. In addition some evidence for rippling of the density contours in the underdense plasma region is observable. More details of small scale non-uniformities are given in the following sections. Density scale lengths obtained from these interferograms indicate values of ≃ 50 μm. Such density scale lengths are characteristic of the ablative mode of irradiation rather than the high intensity exploding pusher mode where scale lengths of only a few μm are obtained.

3.2.2 Laser Beam Self-focusing and Filamentation

A spatially modulated laser beam incident onto a plasma may break up into small filaments of light. The plasma density is depressed in the high

intensity regions due to thermal expansion or the ponderomotive force. The refractive index in this region is raised and self-focussing of either the whole or part of the laser beam can occur. In high intensity short pulse (100 psec) experiments the electron density scalelength of the underdense plasma is of the order of a few μm which is short enough to suppress the spatial amplification of filamentation. A large underdense plasma cloud, however, is created on targets irradiated with long laser pulses (1 nsec or longer) allowing filamentation to grow.

Experiments were carried out using gold coated plane targets which were set at 45 degrees to the laser beam axis in order to distinguish between the direction of the incident laser beam and the plasma flow direction which is normal to the target surface. Figure 3.04 shows two Faraday rotation images (analyser set at 80 degrees to the probe beam polarization) and a Schlieren image; all taken 1 nsec after the beginning of the stacked laser pulse. Long bright filaments can be seen along the direction of the incident laser beam (45 degrees to the target surface) in all the images and consequently these filaments can be associated with the break-up of the incident laser beam. The filaments look similar in the Faraday rotation as well as in the Schlieren images and an explanation for this similarity will be given below. Detailed examination of these and other similar results showed that as the irradiance is increased the filament separation decreased.

Similar filamentary structures have been observed on spherical targets irradiated with four laser beams. Narrow filaments are seen along the laser beam directions and not normal to the target surface. Figure 3.05 shows a Schlieren image of a 215 μm diameter plastic coated target taken 1 nsec after the beginning of the laser radiation. The target was illuminated at an irradiance of 3×10^{13} W cm^{-2}. Results from many similar shots irradiated at 3×10^{13} W cm^{-2} showed that for plastic targets the light filaments are separated transversely by 10 to 18 μm whereas 9 to 12 μm is the transverse scalelength for the filaments on gold coated targets. The observed width of the filamentary structures is in both cases about 7 μm but as discussed below the actual light trapping filaments may have somewhat larger diameters.

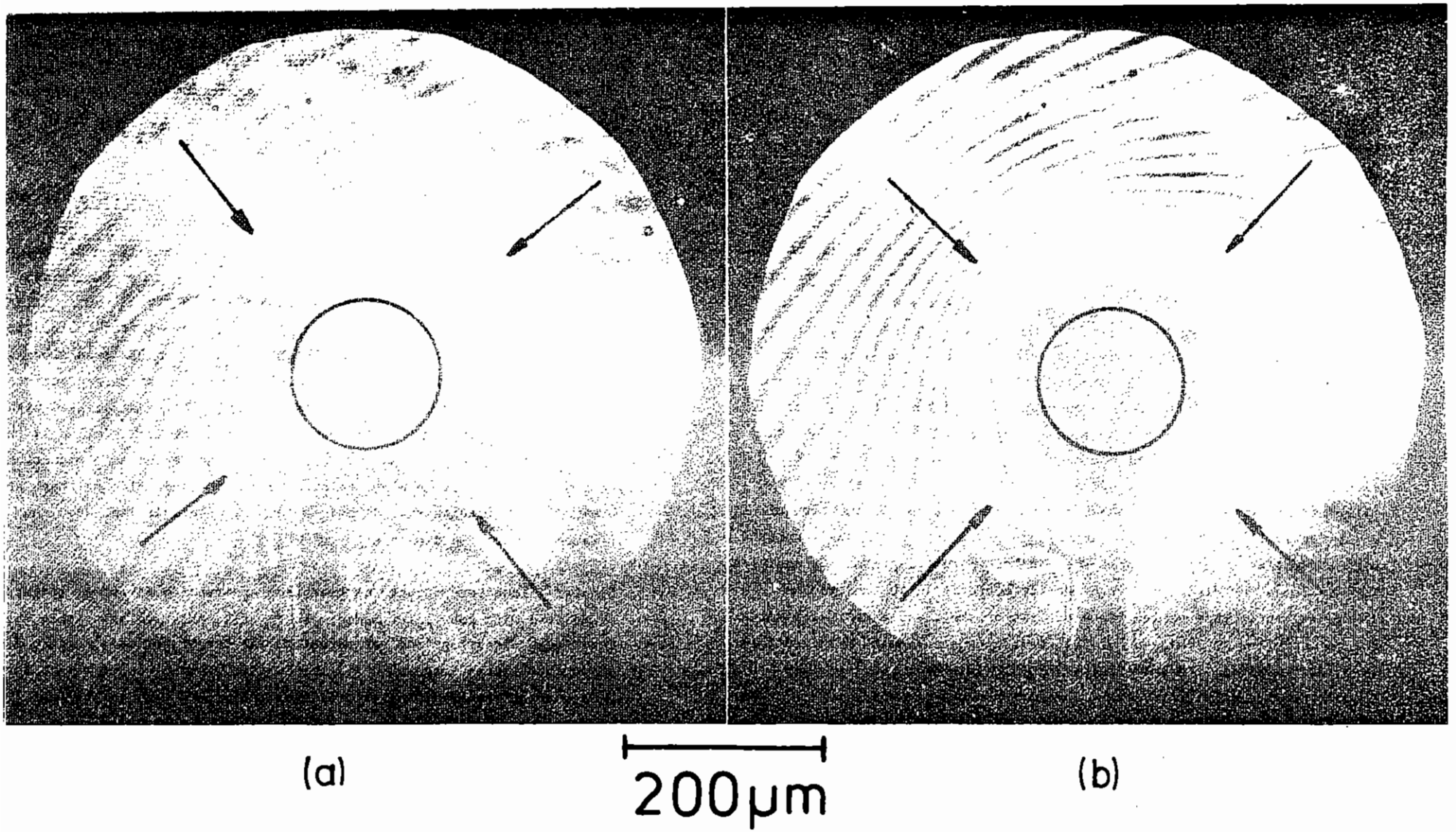

Figure 3.03 Interferograms of a 147 μm diameter (a) and a 146 μm diameter microballoon (b) irradiated with four laser beams (arrows) and recorded during the laser pulse.

Faraday rotation

$I = 2.0 \times 10^{13} Wcm^{-2}$

Faraday rotation

$I = 8.0 \times 10^{13} Wcm^{-2}$

Schlieren image

$I = 5.0 \times 10^{13} Wcm^{-2}$

Figure 3.04 Faraday rotation and Schlieren images for gold coated wire targets showing striations along the incident laser beam (aligned at 45° to target surface).

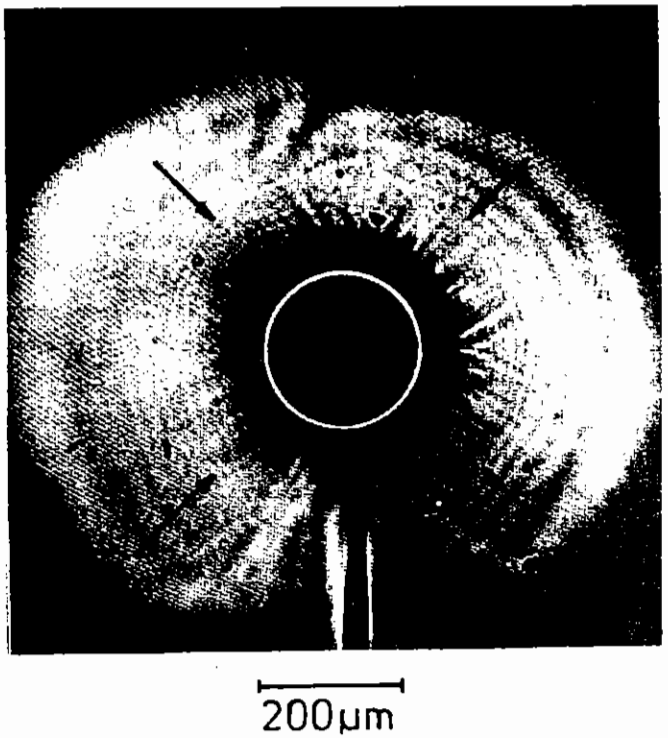

Figure 3.05 A Schlieren image for a plastic coated microballoon irradiated with four laser beams at an intensity of 3×10^{13} W cm^{-2} showing bright striation along the directions of the main laser beams.

In order to find out the reason for the similarity of the observations of filamentary structures in shadowgrams and Schlieren and Faraday rotation images a three dimensional ray tracing routine was adapted to investigate the refractive effects of the probe beam in a plasma with density discontinuities and with channels of lower local plasma density. A spherical plasma with a critical density radius of 50 μm and an exponentially decaying electron density profile of scalelength 50 μm was simulated in the code. Normal to the probe beam direction a channel of lower plasma density was modelled to simulate a filament. Ray traces were performed in either two or three dimensions and a result of a two dimensional run is shown in Figure 3.06. The probe rays have a wavelength of 622 nm (as used in the experiment) and propagate in the y-direction. The filament, with a diameter of 20 μm, is aligned along the x-direction and has a Gaussian density profile with zero plasma density on axis. For the figure shown the background plasma density at the boundary of the filament is 0.25 n_c. As can be seen the probe rays are strongly focused in the filament ie the filament acts as a positive lens.

In three dimensional simulations the full experimental arrangement for Schlieren imaging was modelled in the code. A spherical plasma surrounding a microballoon target with filaments on opposite sides (in the positive and negative x-directions) was relayed by an f/3.3 lens onto the film plane as in the experimental set-up. The imaging plane of the lens was set 80 μm back from the target centre (y axis) to coincide roughly with the focused bundle of rays in Figure 3.07. A needle 200 μm in diameter was placed in the back focal plane of the lens to simulate a Schlieren stop.

Figure 3.07 shows an example of one of the ray traces. The dots represent rays hitting the film plane. As can be seen, due to focusing effects of the probe rays in the filaments, a local concentration and depletion of the rays landing on the film occurs, indicating the presence of the filaments. In addition rays are lost due to the Schlieren edge as can be seen. The inner area where no dots appear represents the area where rays are refracted out at large angles missing the collection optics (ie the cut off boundary). The ray trace result shown in Figure 3.07 shows

features very similar to the experimental observations seen in Figure 3.05.

Detailed examinations of many similar ray tracing runs indicate that the bright striations seen in the experimental observations are not actual filaments but are due to focusing effects of the probe beam. Consequently no differences will be observed between the various recording techniques. The degree of focusing occurring within the filaments depended strongly on the density profiles in the filaments and background plasma as well as on the probe beam wavelength. Optimum observation of filamentary structures occurs when the imaging lens is focused on a plane between 20 and 100 μm from the filament plane.

Further clear evidence for laser beam filamentation was obtained from time integrated photography of the $(3/2)\omega_o$ harmonic emission from spherical targets irradiated with six overlapping beams. The targets were imaged in two perpendicular directions, one channel using the central portion of one of the main f/1 focusing lenses to image the target while the other used a separate f/8 microscope objective mounted inside the target chamber.

Examples of some of the photographs obtained are shown in Figures 3.08(a) and (b) where the original target sizes and incident beam directions are indicated. Figure 3.08(a) is recorded via the microscope objective mounted in the plane of four of the lenses and consequently views in a direction at 45° to these four incident beams and at 90° to the other two. The target is 187 μm in diameter while the average incident irradiance is 9×10^{13} W cm^{-2}. Figure 3.08(b), on the other hand, is recorded via the main lens and so views in a direction parallel to two of the beams and perpendicular to the rest. In this case the target is 252 μm in diameter while the irradiance is 3×10^{13} W cm^{-2}. As can be seen, on this shot observation of part of the target was prevented by the presence of an X-ray backlighting target near the main target. Both photographs show many extended filamentary $(3/2)\omega_o$ emission structures aligned along the direction of the incident beams. A particularly clear group of filaments is seen in Figure 3.08(a) along one of the beams viewed at 90°. It should be noted that initially all the lenses are focused well beyond the target

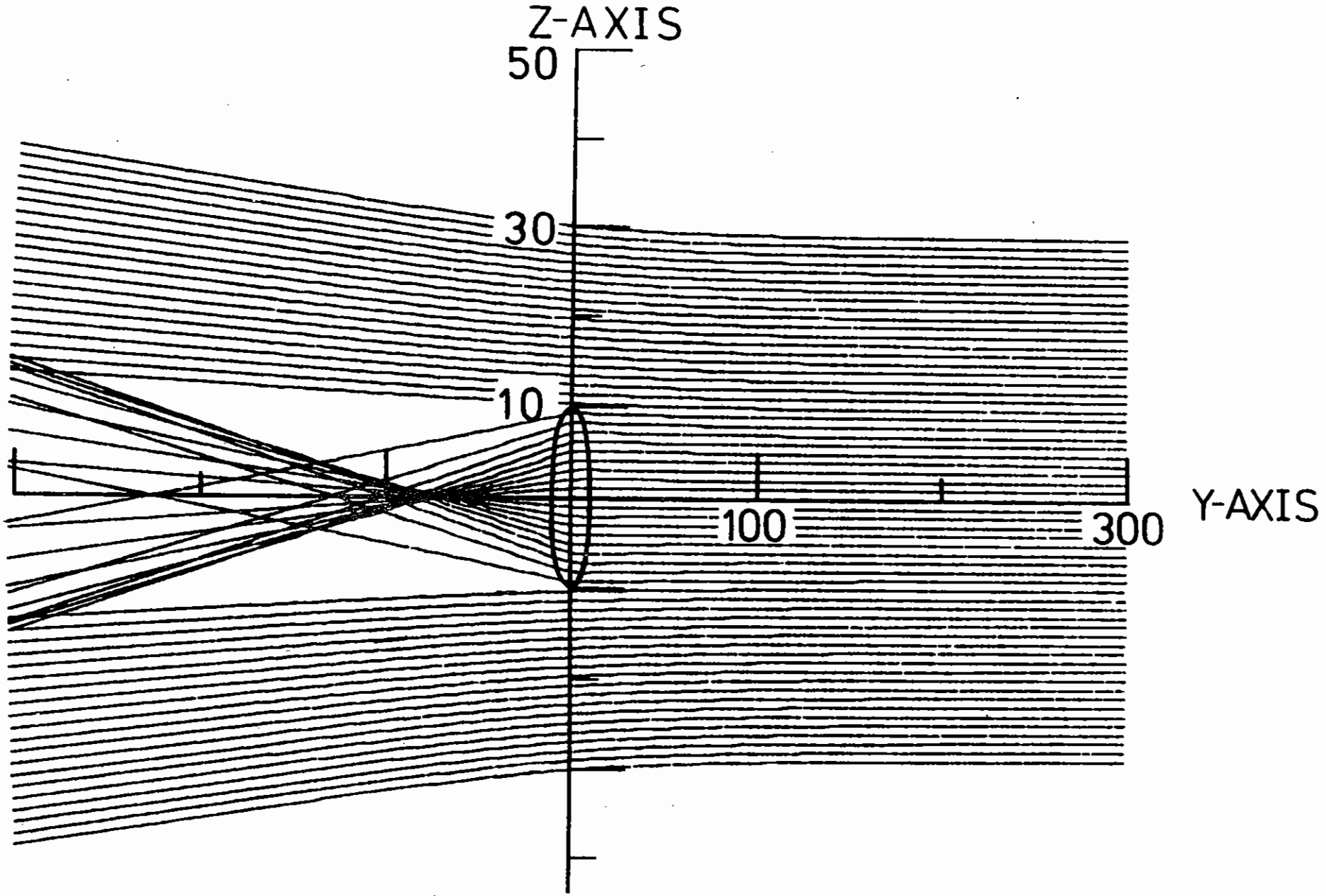

Figure 3.06 A spherical plasma with a cylindrical filament (x-direction) simulated and ray traced in the y-z plane showing focusing effects of the probe rays within the filament.

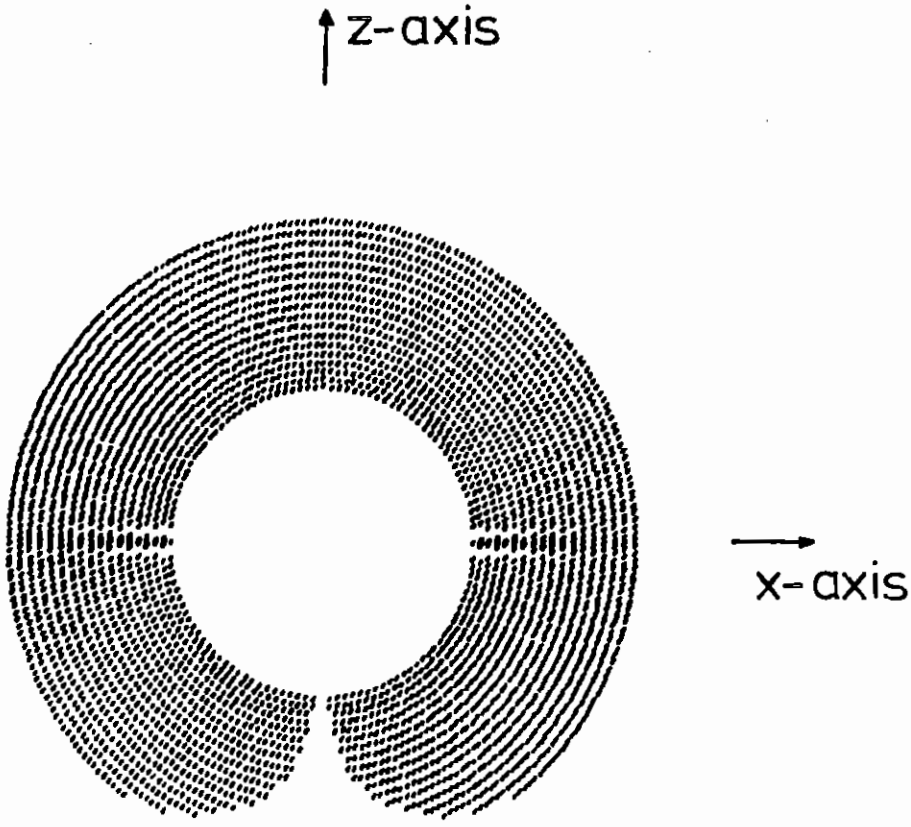

Figure 3.07 Modelling of the experimental arrangement for Schlieren imaging for a spherical plasma with filaments on opposite sides.

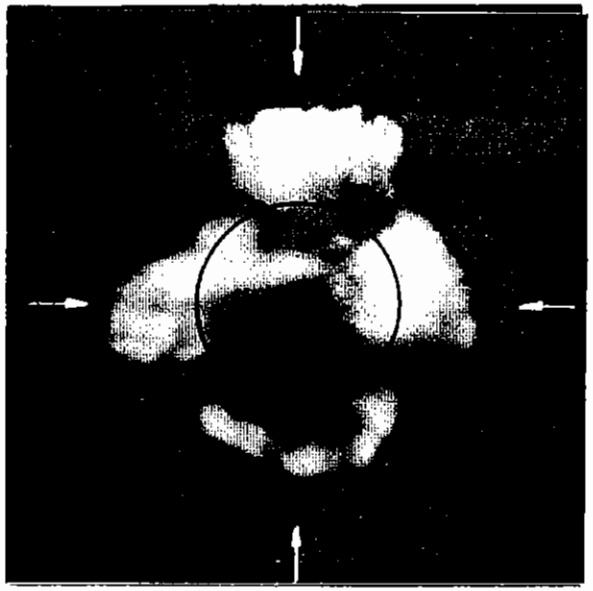

(a)

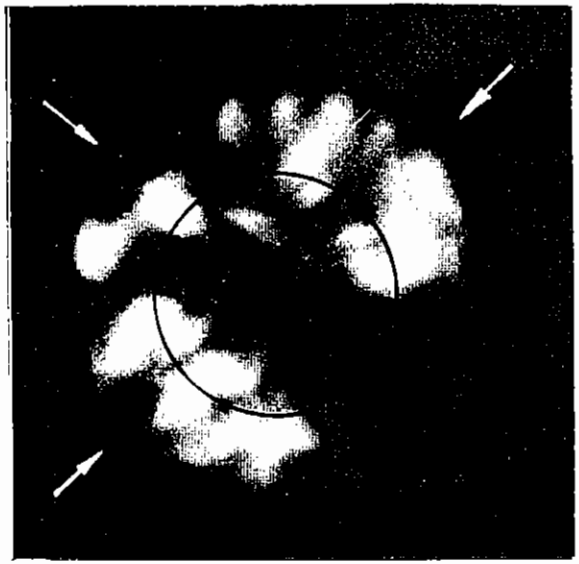

(b)

Figure 3.08 Photographs of the $(3/2)\omega_o$ harmonic emission from six beam irradiated spherical targets taken from two perpendicular directions.

centre such that a fraction of each beam passes round the target edge. As a consequence, when the plasma forms on the target surface and expands to fill the irradiated volume, the outer regions of each beam will pass tangentially through the subcritical density coronal plasma. Some filamentary $(3/2)\omega_o$ emission structures associated with such tangential rays can be clearly seen in Figure 3.03(b).

According to theoretical predictions (3.03), (3.04), the growth rate for filamentation should be low at laser intensities of a few times 10^{13} W cm^{-2}. Thus in our experiments, filaments have grown from initial hot spots in the laser beams. Measurements of the spatial distribution of the laser beams showed a ± 20 % intensity variation with a range of spatial wavelengths between a few and 20 μm in the target plane. These measured spatial periodicities are close to the spatial scalelengths of the theoretically predicted most unstable modes (3.04) and consequently the observed separation of the filaments is on a similar scale.

3.2.3 Plasma Jet Formation

Further non-uniformities have been observed in the form of short plasma jets expanding normal to the target surface which appear during the laser pulse and continue to grow with time. They become much more pronounced after the end of the heating laser pulse.

Figure 3.09 shows the time evolution of the non-uniformities in the corona for gold coated targets irradiated at 2×10^{13} W cm^{-2}. Up to 0.25 nsec after the beginning of the laser pulse no non-uniformities are visible. At 0.5 nsec a filamentary structure can be observed along the directions of the laser beams. At 1 nsec striations along the laser beams can still be seen but other kinds of non-uniformities, namely short plasma jets become visible normal to the target surface and are growing with time. After the laser pulse, at 2 and 3 nsec, the underdense plasma is broken up into a great number of jets with spatial scalelengths between a few and 20 μm. Due to probe beam refraction these jets could only be observed up to the quarter critical density region and consequently the source of these jets is not yet known. From interferograms in which the plasma jets

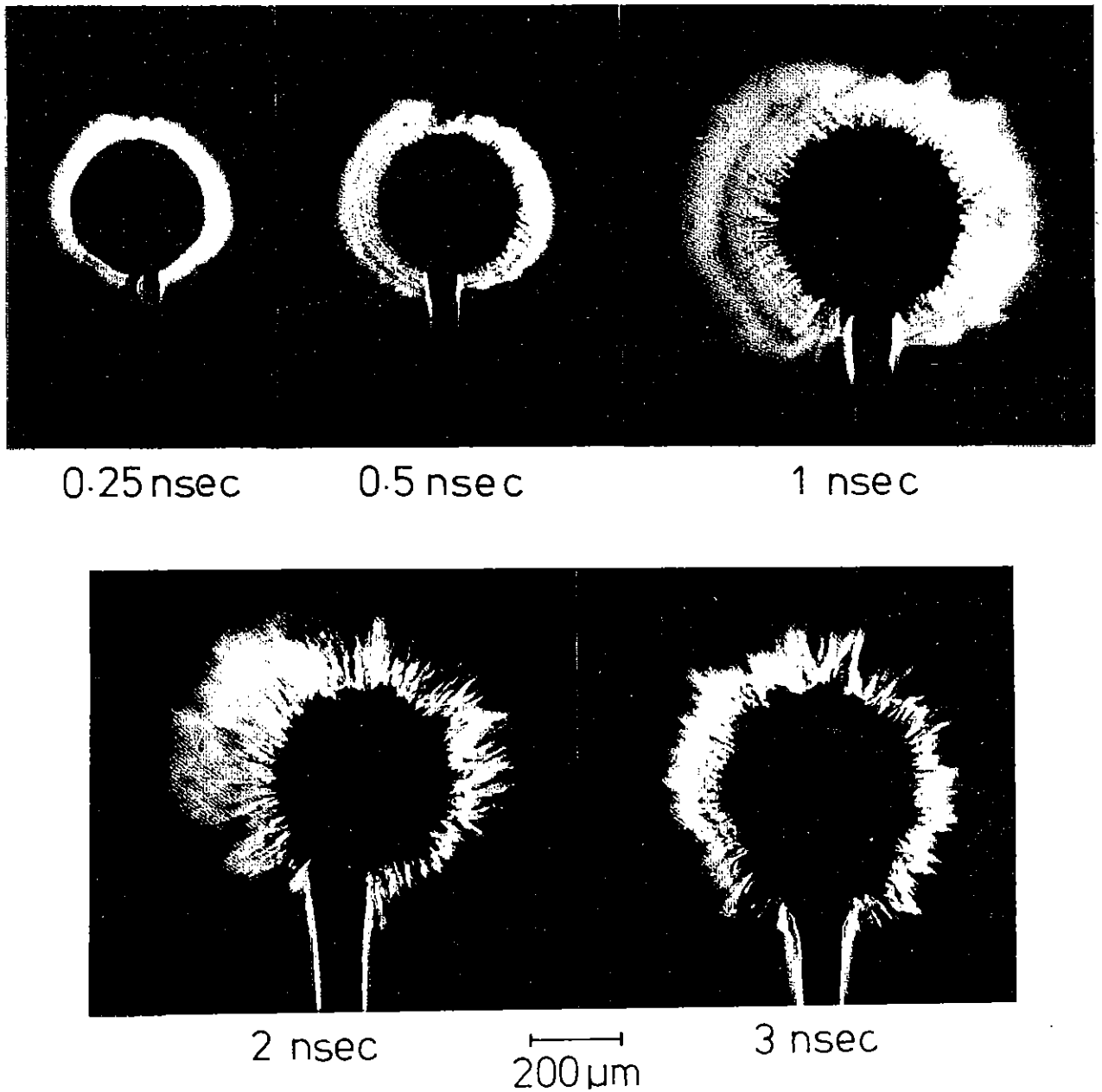

Figure 3.09 A sequence of Schlieren images for gold coated sperical targets showing the time evolution of the plasma jets.

are surrounded by interference fringes it can be deduced that the electron density in the plasma jets is higher than the background plasma density.

Results taken on plastic targets showed a much less pronounced jet-like structure at the cut off region of the probe beam than on gold coated targets. Figure 3.10 shows a Schlieren image taken on plastic targets at 3 nsec (1.5 nsec after the end of the heating pulse). This should be compared with the 3 nsec exposure on a gold target of Figure 3.09.

X-ray pinhole camera images ($\sim$ 1 keV energy band, 7 μm resolution) taken on targets irradiated with six overlapping laser beams showed the presence of short jets and intense spotty structures. The pinhole camera was situated on one of the diagonal axes of the six beam cubical irradiation system and hence viewed a side of the target irradiated predominantly by three of the beams. Figure 3.11 shows X-ray images for a plastic and a gold coated target both irradiated at an intensity of 2×10^{13} W cm^{-2}. As can be seen in Figure 3.11 the small scale structure is much more pronounced for gold than for low Z-targets such as plastic and glass.

Simultaneously with optical probe measurements ion signals were recorded by using Faraday cups. For gold coated targets where a strong plasma jet formation was observed, energetic ions (10 % of the total number of ablated ions) with a velocity of $1\text{-}2 \times 10^{8}$ cmsec^{-1} at intensities as low as 10^{13} W cm^{-2} were recorded whereas no ions (< 0.5 %) of comparable velocity were seen at similar intensities for plastic targets. Figure 3.12 shows ion signals for plastic and gold coated targets. This data, the X-ray images and the optical probe results suggest that plasma jetting is a phenomenon that is strongly linked to the target atomic number.

A sequence of Schlieren images showing the intensity dependence of the plasma jet formation for gold coated targets is seen in Figure 3.13. All the images are taken at 0.5 nsec after the end of the laser pulse and so no light filamentation can occur. As can be seen, some bubbles occur in the underdense plasma (0.1-0.25 n_c) even at intensities as low as 3×10^{12} W cm^{-2}. An increase in the laser intensity causes a more pronounced jet-like structure. A limitation in the available laser power

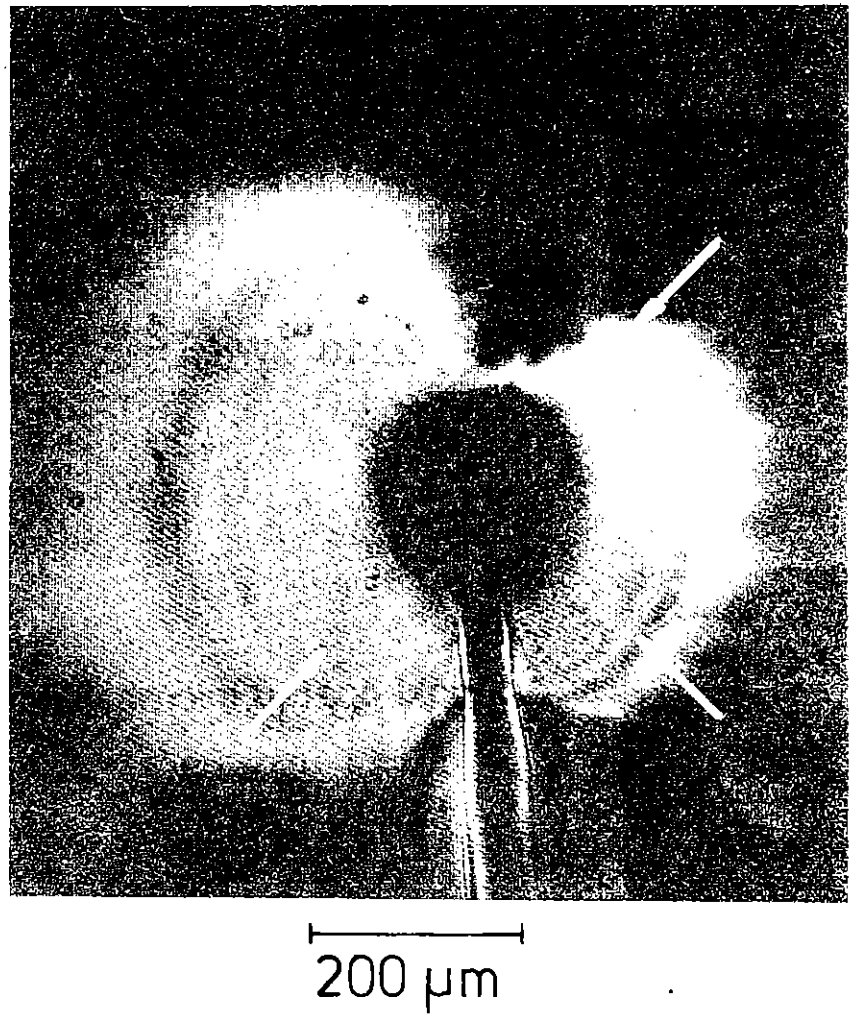

Figure 3.10 A Schlieren image for a plastic coated microballoon irradiated at an intensity of 3.5×10^{13} W cm^{-2} and recorded 3 nsec after the beginning of the laser pulse.

pinhole camera images

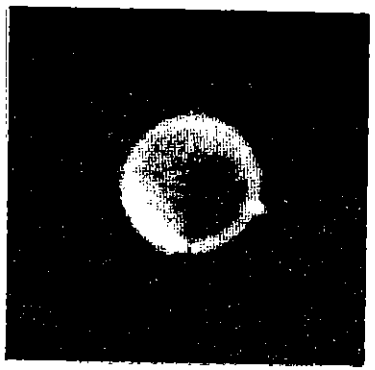

plastic coated microballoon

$I = 2 \times 10^{13}\ W cm^{-2}$

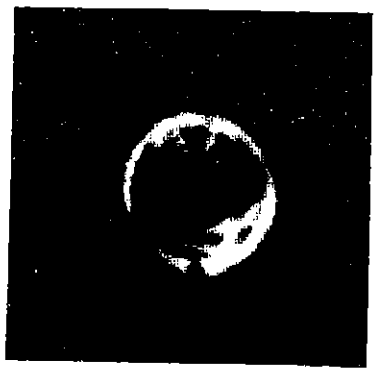

gold coated microballoon

$I = 2 \times 10^{13}\ W cm^{-2}$

Figure 3.11 X-ray pinhole camera images (filtered with 25 μm beryllium) for six beam irradiated plastic and gold coated targets showing small scale non-uniformities.

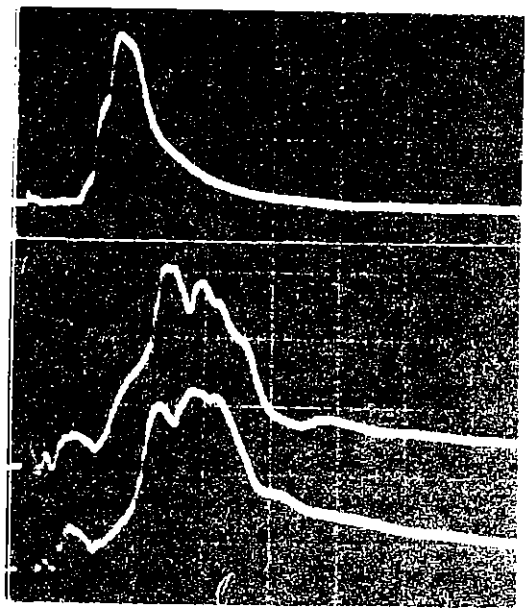

Figure 3.12 Ion signals from plastic and gold targets irradiated with four laser beams at an intensity of $2\ 10^{13}\ W\ cm^{-2}$ showing a large fraction of fast ions only for the gold targets (detection distance 38 cm, time base 500 nsec/div, vertic: sensitivity for gold targets 25 times that for plastic).

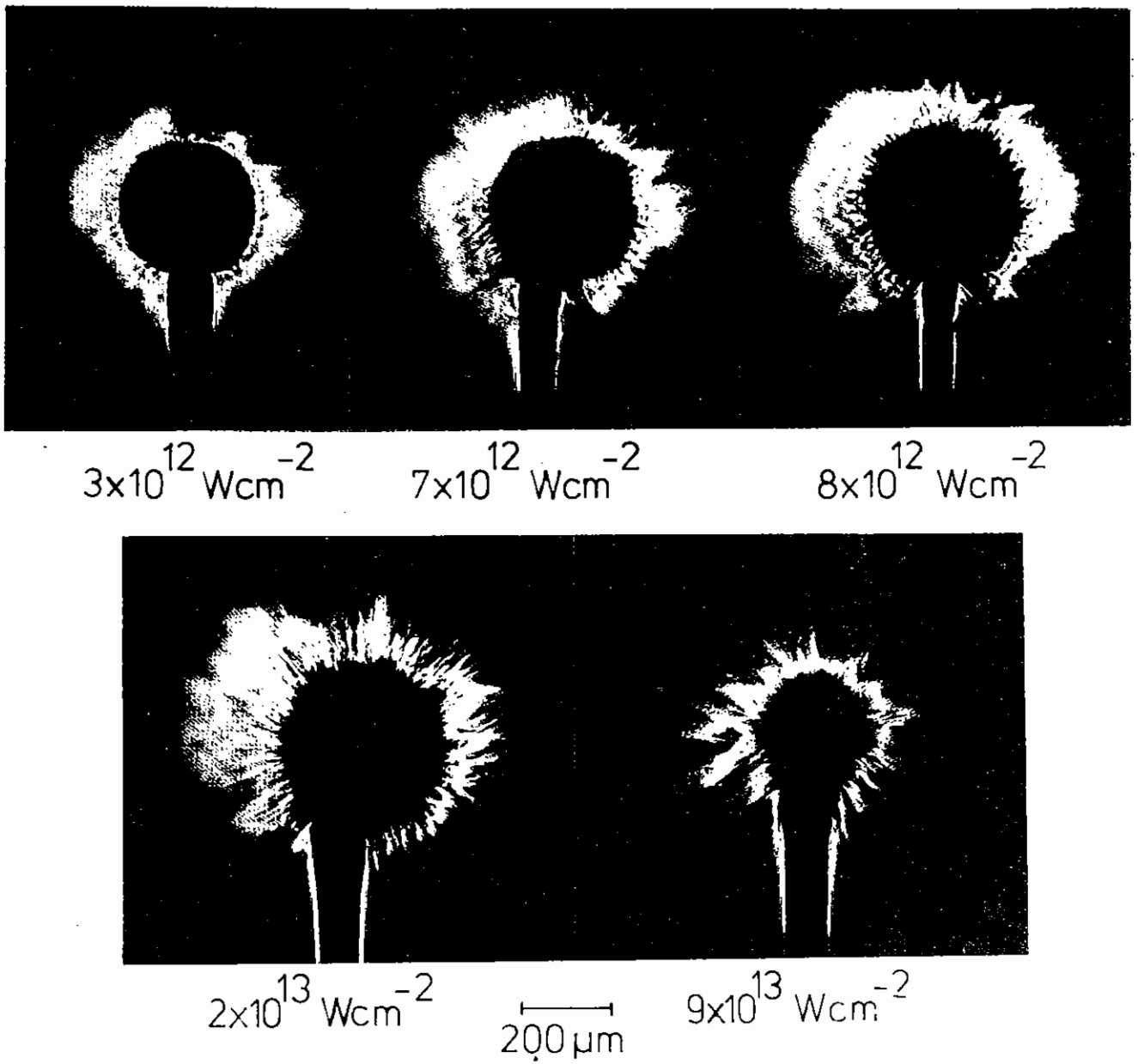

Figure 3.13 Schlieren images showing the intensity dependence of the plasma jets for gold coated microballoon targets all recorded 0.5 nsec after the end of the laser pulse.

at an intensity of 9 x 10^{13} W cm^{-2} made it necessary to use a smaller sized target.

Various generation mechanisms may be responsible for the occurrence of plasma jets. Filamentation of the laser beams might for example cause localised hot spots from which hot plasma is expelled. This might be a reason for the plasma jet formation, particularly because in high Z-plasmas where plasma jets have been observed most strongly the thermal smoothing effects are poorest. There are however several other processes such as Weibel (3.05), thermoelectric (3.06), (3.07) and heat flow (see section 3.3) instabilities, which might create plasma jets with associated magnetic fields (as observed and described in section 3.2.4). Theories suggest that these processes become more important for high atomic number targets. Accelerational Raleigh-Taylor type instabilities can be excluded because similar jet like structures were seen on solid spheres as well as on hollow shell targets.

3.2.4 Small Scale Magnetic Field Structures

Self-generated magnetic fields with a magnitude of a few Megagauss have been observed so far only around the focal spot of the laser beam of non-uniformly irradiated targets. Several theoretical models predict however magnetic fields on a small scale caused by temperature perturbations along the critical surface. These may occur even on uniformly illuminated pellets and may break up the spherical implosion. Experiments were carried out to look for the presence of these small scale fields using Faraday rotation techniques. On both plane and spherical ablatively irradiated targets micromagnetic field structures were observed.

Figure 3.14 shows a Faraday rotation image for an aluminium wire target taken 0.96 nsec after the beginning of the stacked pulse. The analyser was set at 85 degrees to the probe beam polarization. The initial bright spot in the photograph is due to scattered 1.05 μm radiation and provides the reference focal spot position. A global dark-bright pattern can be seen which indicates a toroidal magnetic field ringing the focal spot of

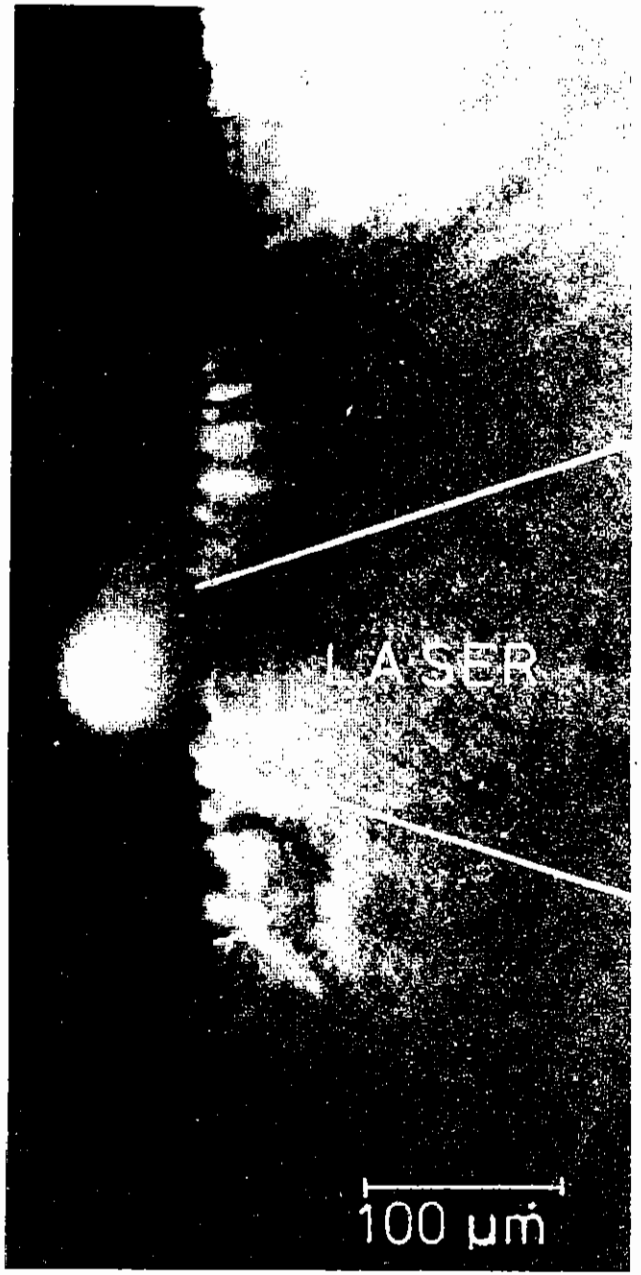

Figure 3.14 A Faraday rotation image for an aluminium wire target irradiated at 3.5 x 10^{13} W cm^{-2} and recorded 0.96 nsec after the beginning of the laser pulse showing small scale magnetic field structures.

the laser beam (see section 4.6). In addition a small scale dark-bright structure with a spatial scalelength of 8-18 μm is visible in the photograph indicating small scale magnetic fields. These dark bright patterns follow the plasma flow and occur well outside the cone of the incident laser beam.

Small scale magnetic fields are also observed on spherical targets. Figure 3.15 shows a Faraday rotation image of a glass microballoon irradiated at 3 x 10^{13} W cm^{-2} and taken 0.96 nsec after the beginning of the laser pulse. The analyser was set at 80 degrees. A series of clear dark bright patterns can be observed in the photograph which, together with results taken with crossed polarizers showing double bright structures, indicate that the magnetic fields are toroidal. These magnetic fields extend far into the underdense plasma. It is difficult to establish with certainty if the small scale magnetic fields on the spherical targets follow along the direction of the laser beams or are normal to the target surface.

It is interesting to note that results taken with crossed polarizers showed a bright region on each side of the target mounting stalk while a dark and a bright region can be seen in Figure 3.15 where the analysing polarizer was set at 80 degrees to the probe beam polarization. The dark bright pattern indicates the presence of a toroidal magnetic field surrounding the stalk and its orientation implies than an electron current is flowing up the stalk towards the target.

There are several mechanisms such as heat flow, Weibel and thermoelectric instabilities which may be responsible for the generation of the observed magnetic fields. They are based on a temperature perturbation in the critical density region which may be induced by localised heat absorption. Such field generation processes will inevitably give rise to strong density inhomogeneities or jets and consequently the results shown in the last two sections are clearly linked. Experimental observations of both jets and fields are probably two methods by which information about these small scale field generating mechanisms may be obtained. Another source for magnetic fields may be filamentation itself where a light filament of

small scale magnetic fields on spherical targets

$I = 3 \times 10^{13} W cm^{-2}$

$\emptyset = 282.5\ \mu m$

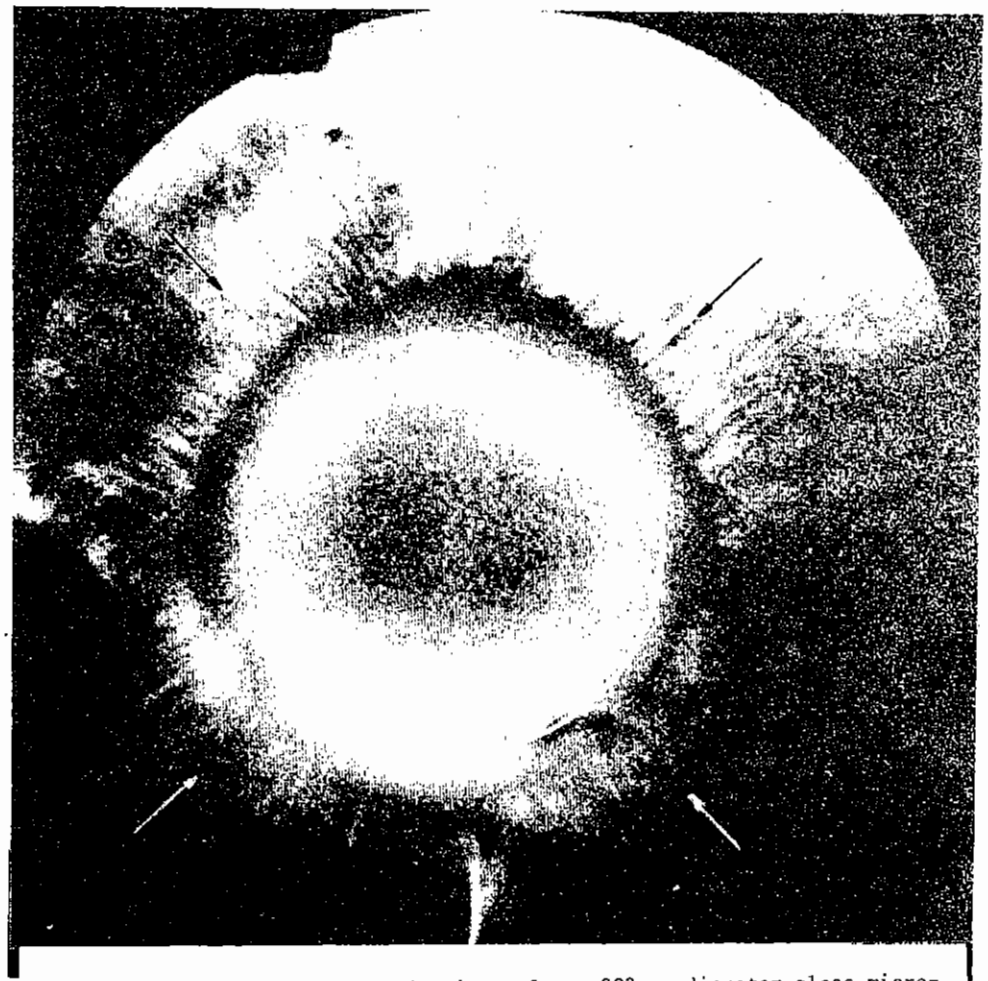

Figure 3.15 Faraday rotation image for a 282 μm diameter glass microballoon illuminated at an irradiance of 3 x 10^{13} W cm^{-2}.

lower density may be surrounded by a $\nabla n_e \times \nabla T$ magnetic field with a density gradient across the filament and a temperature gradient along the filament. This mechanism may explain the occurrence of magnetic fields on spherical targets only, not those on plane targets (seen in Figure 3.14) where the magnetic fields are seen far outside the cone of the laser beam and consequently cannot be associated with filamentation.

Z Q Lin (Shanghai), P T Rumsby, O Willi (RAL) and S Sartang (Westfield Coll)

3.3 Thermomagnetic Instabilities

When a large heat flow exists in a laser-irradiated plasma we have found that it can be unstable. This instability has a wave number orthogonal to the heat flow and might be the explanation of the filamentary structures described in section 3.2. Two models have been studied. The first describes the heat flow as a collisionless flow of hot electrons counter-streaming against a collisional flow of cold electrons, and the instability results from a thermal instability associated with the Ohmic heating. The second model employs the full set of linear transport terms of Braginskii together with plasma flow and unequal temperatures and also predicts criteria for the growth of a thermomagnetic instability. Further details are in section 7.4.4.

M G Haines and E M Epperlein (Imp Coll)

3.4 Thomson Scattering

In a laser-produced plasma, instabilities exist in the underdense region. In particular, electron plasma waves are produced in the quarter critical density region due to the two plasmon decay instability (3.08) and Raman scattering (3.09).

Until recently there has been no direct observation of these plasma waves. Evidence for their existence has depended mainly on the observation of the $3\omega_0/2$ harmonic emission (3.10) - (3.13). Recently, however, these waves

have been observed directly in an experiment carried out by Baldis et al (3.14) using Thomson scattering techniques.

Thomson scattering is a well known diagnostic technique (3.15), (3.16). The most important experimental parameter is

$$\alpha = \frac{1}{k\lambda_D}$$

where k is the scattering vector

$$|\underline{k}| = \frac{4\pi}{\lambda} \sin\frac{\theta}{2}$$

θ is the scattering angle and λ_D is the Debye length hence numerically

$$\alpha = \frac{1.08 \times 10^{-4} \lambda\ (\text{cm})}{\sin \theta/2} \quad \frac{\sqrt{n_e\ (\text{cm}^{-3})}}{T_e\ (\text{eV})} \qquad (1)$$

The value of α in a given experiment determines the shape of the scattered spectra. For $\alpha \gg 1$, the spectrum consists of a broad central feature determined by the ion motion and two satellites determined by the electrons. These peaks are displaced from the centre by a frequency $\Delta\omega$ where

$$(\Delta\omega)^2 = \omega_p^2 + 3\,k^2\,v_e^2 \qquad (2)$$

is given by the Bohm Gross dispersion relation.

It is these satellites that must be investigated in order to see the presence of electron plasma waves.

The scattering angle was chosen to be 180°. The probe beam was formed by splitting off part of the incident beam and frequency doubling it. This fixed λ at 5260 Å. The region to be investigated is the quarter critical density region so ne is fixed. With these parameters chosen, the value of α depends only on the electron temperature T_e. Typically T_e is in the region of 700 - 800 eV, giving a value of α of $\sim$ 3-4.

From equation 2 this gives the shift of the satellites to be

$$\Delta \omega = \pm \omega_0/2$$

where ω_0 is the frequency of the incident wavelength. Hence the satellites occur at the harmonic frequencies of 3/2 ω_0 and 5/2 ω_0.

It was decided to look at the satellite at 5/2 ω_0, since the harmonic emission at this frequency is expected to be less intense than that of 3/2 ω_0.

Figure 3.16 shows the experimental arrangement of the probe and incident beams. Timing of the beams was such that the probe could arive co-incidently with the main beam or up to 600 ps after the peak.

The probe was focussed by an f/5 doublet lens with a focal spot size of $\simeq$ 60 μm. Up to 10 J in 2 ns was available in the probe.

The incident beam energy was about 40 J on target in 2.2 ns. This was focussed by an f/1 doublet lens to a focal spot size of $\simeq$ 40 μm.

The targets consisted of plastic coated microballoons of 90 - 120 μm diameter. These were coated with a 25 nm layer of aluminium to assist alignment.

Since the scattering angle was 180°, the f/5 lens acts as the collecting lens for the Thomson scattered signal. Figure 3.17 shows the schematic layout of the detection system.

A grating spectrometer with a 600 lines per mm grating was used. The output plane of the spectrometer was the imaged onto a 520 Imacon streak camera, giving a spectral 'window' at the camera of $\simeq$ 400 Å. The camera operated at a streak speed of 3 ns per cm without any slits. This reduced the temporal resolution to $\simeq$ 0.6 ns.

It is essential to ensure that the probe beam 'sees' the correct region of

the plasma, and that the light detected comes from this region. This was done by backlighting the target in blue light and imaging the balloon onto the 3 mm wide spectrometer slits (the image of the balloon at the spectrometer had a x 50 magnification). The balloon was then moved back in the incident beam plane until the edge of the balloon was 1 mm from the edge of the slit. Hence the area 'seen' by the detection system was the under-dense region 10-70 μm out from the critical surface (Figure 3.18). The quarter critical density should be somewhere in this region.

The spectral resolution of the system was poor, $\simeq$ 30 Å, limited by the 3 mm width of the spectrometer slits.

The spectrum observed with no probe beam present is shown in Figure 3.19. It consists of a single broad peak slightly shifted to the blue. This is probably due to 5/2 ω_0 harmonic emission.

A λ/2 waveplate was introduced into the main beam to see if rotation of the polarisation of the incident beams (and hence rotation of the direction of the plasma waves at quarter critical (3.17)) would have any effect. No noticeable change in the signal was observed.

Figure 3.20 shows the spectrum obtained when the probe beam was present. In this case the probe beam was delayed by $\simeq$ 450 ps relative to the main beam. It can be seen that the spectrum observed is broader with the probe present, and shows no observable shift to the red or blue.

From these results it is difficult to be certain that Thomson scattering has actually been observed. What has been observed is an enhancement of the emission coming from this region. This could be simply enhancement of the 5/2 ω_0 harmonic since the probe frequency is twice the incident frequency, or it could be combination of both 5/2 ω_0 emission and Thomson scattering, both occur separately, but indistinguishably from each other. Further experiments are necessary to resolve this problem perhaps where the probe beam frequency is shifted away from 2 ω_0.

T P Hughes, E McGoldrick and S M L Sim (University of Essex)

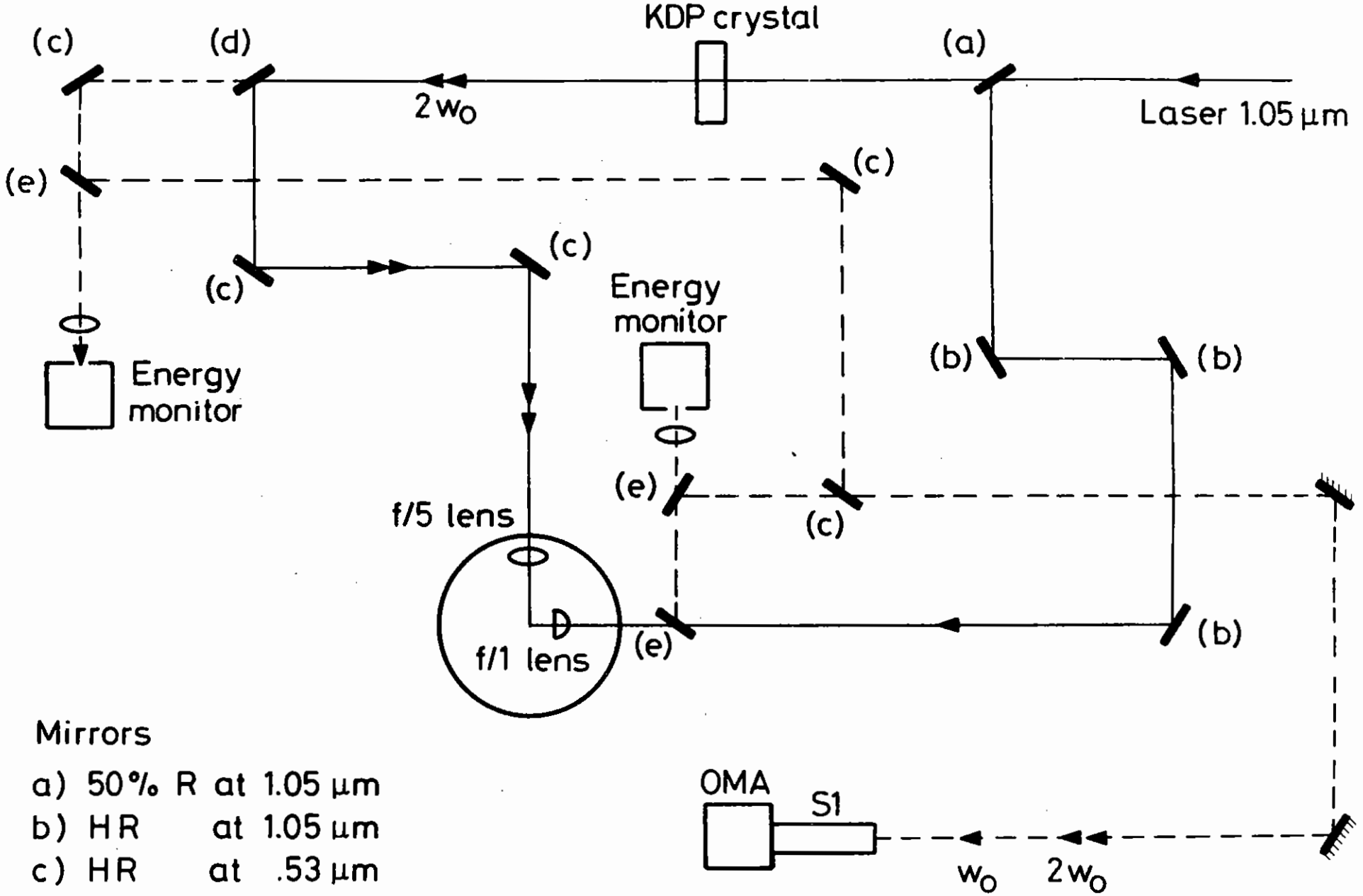

Figure 3.16 Schematic of the experimental arrangement.

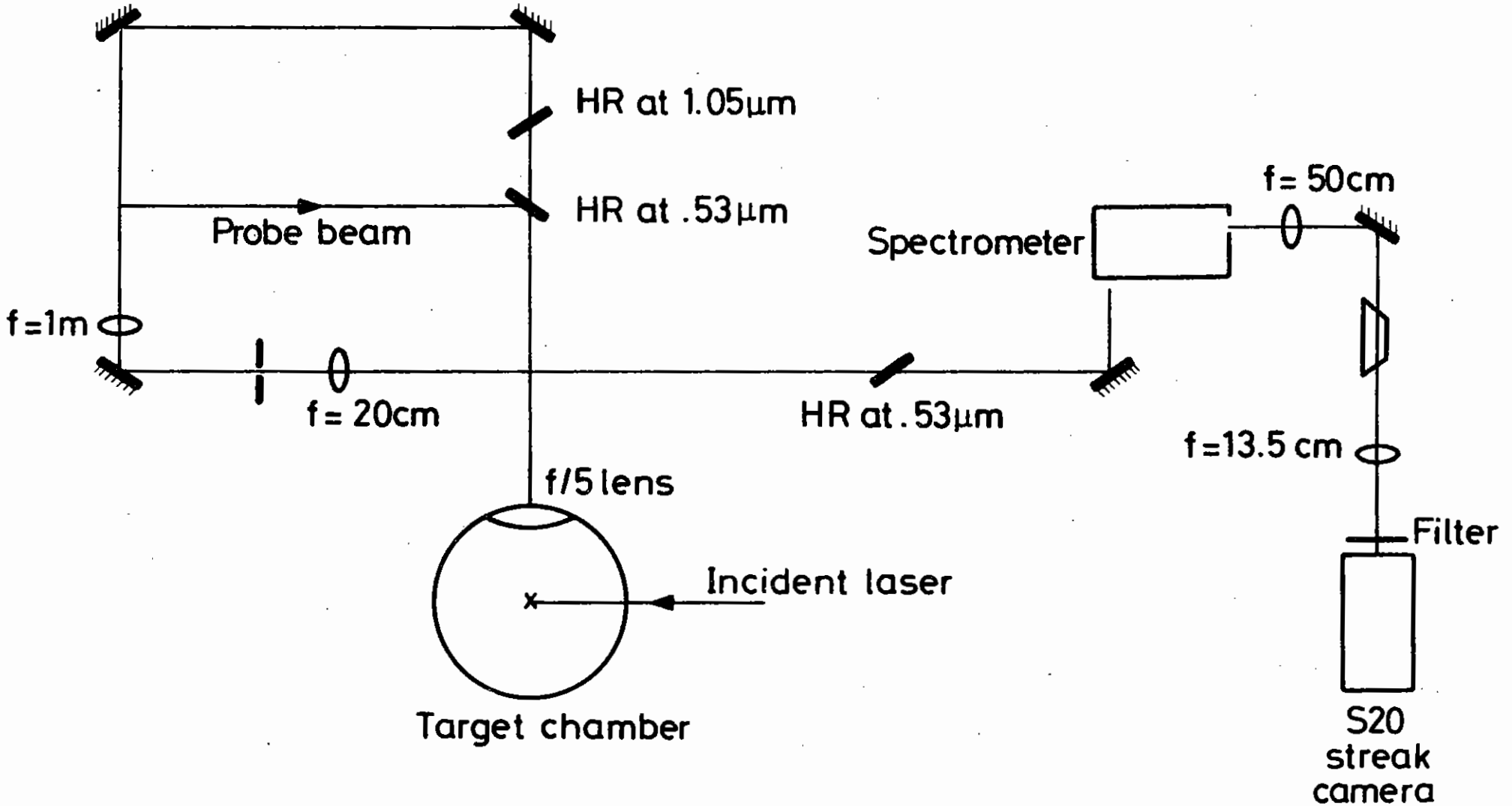

Figure 3.17 Schematic of the detection system.

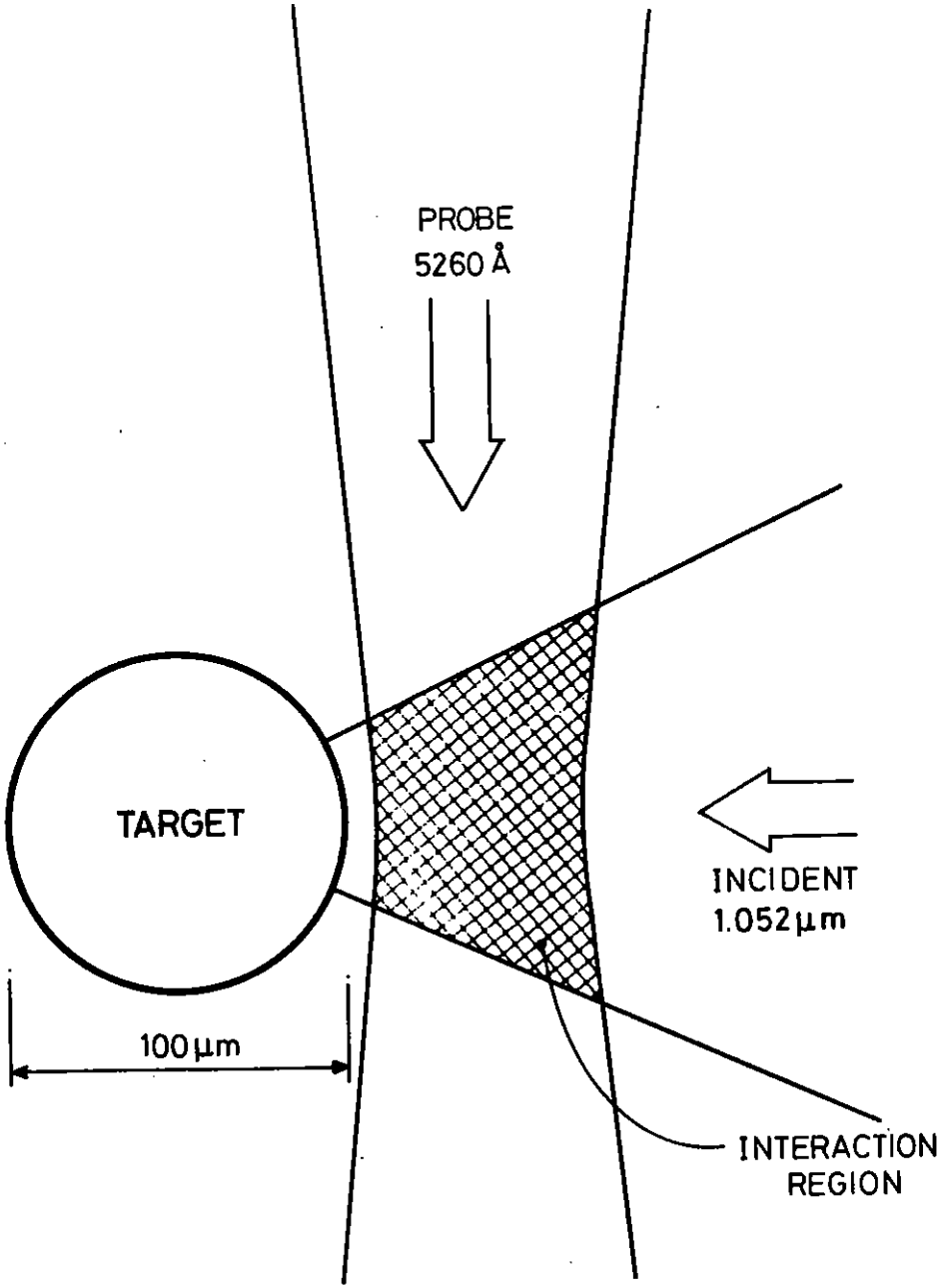

Figure 3.18 Scale diagram of the relative positions of the incident and probe beams at the target.

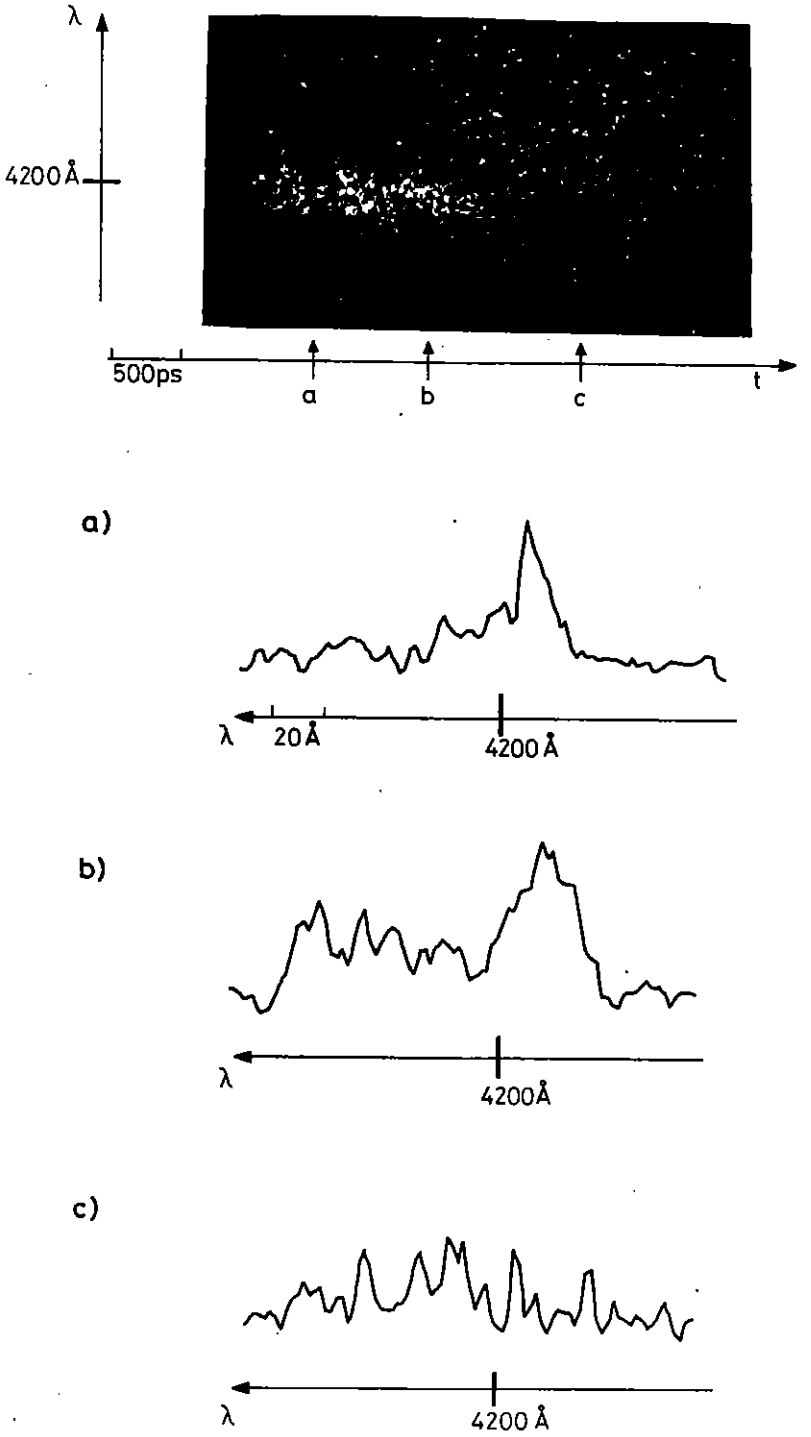

Figure 3.19 Spectrum observed with no probe beam.

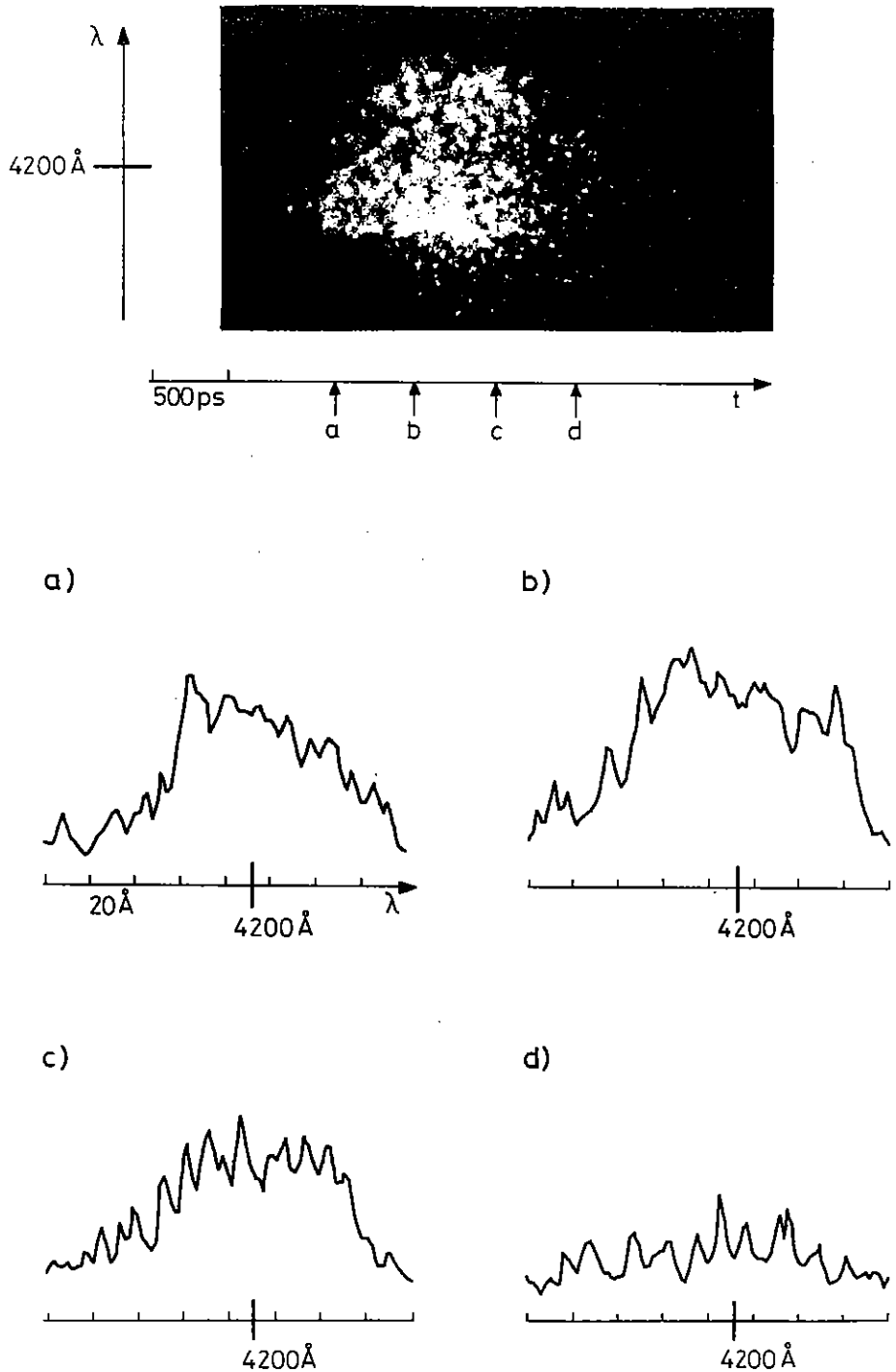

Figure 3.20 Spectrum observed with probe beam on, delayed 450 ps after main beam.

3.5 $\omega_0/2$ Harmonic Emission

The observation of scattered light at the $\omega_0/2$ frequency can be evidence of either the stimulated Raman scattering instability (3.09) or linear mode conversion of the $\omega_0/2$ electron plasma waves arising from the two plasmon decay instability, or Raman down scattering of the incident pump wave off these plasmons. Each of these generation mechanisms occur at the quarter critical density surface.

The earliest report of the experimental observation of light at $\omega_0/2$ was by Bobin et al (3.18). A line spectrum centred at $2\omega_0$ with 60 Å FWHM (compared with 30 Å for the incident light) was seen, which could be due to either stimulated Raman scattering or linear mode conversion of electron plasma waves. More recently, Phillion (3.19) has reported observations of $\omega_0/2$ emission from Nd/glass laser irradiated solid targets at irradiances = 5×10^{14} W cm^{-2} using InAs detectors cooled to 77° K. A spectrum extending from 1.6 μm to 2.2 μm was measured by means of different interference filters on a multishot experiment. These results were interpreted as evidence for stimulated Raman scattering in very underdense plasma ($< 0.1\ n_c$). Electron plasma waves at $\omega_0/2$ have been directly observed by Baldis et al (3.14) in a CO_2 irradiated plasma using Thomson scattering diagnostics.

We would like to present here the first report of temporally and spectrally resolved observations of the $\omega_0/2$ harmonic emission. The data was obtained from a range of targets irradiated by the third harmonic (0.35 μm) of the Nd/glass laser. There are two main advantages of using the third harmonic: (a) the $\omega_0/2$ emission is produced at the convenient wavelength of 0.7013 μm and (b) the $\omega_0/2$ signal cannot be confused with unconverted 1.05 μm or 0.5260 μm light.

The experimental layout is shown in figure 3.21. The generation of the third harmonic incident beam is described in section 1.4.2 of this report. The incident UV light (λ = 0.35 μm, FWHM = 800 ps) is focussed onto the target by the f/2.5 doublet lens. The $\omega_0/2$ harmonic emission backscattered through the lens was collected by a dichroic mirror

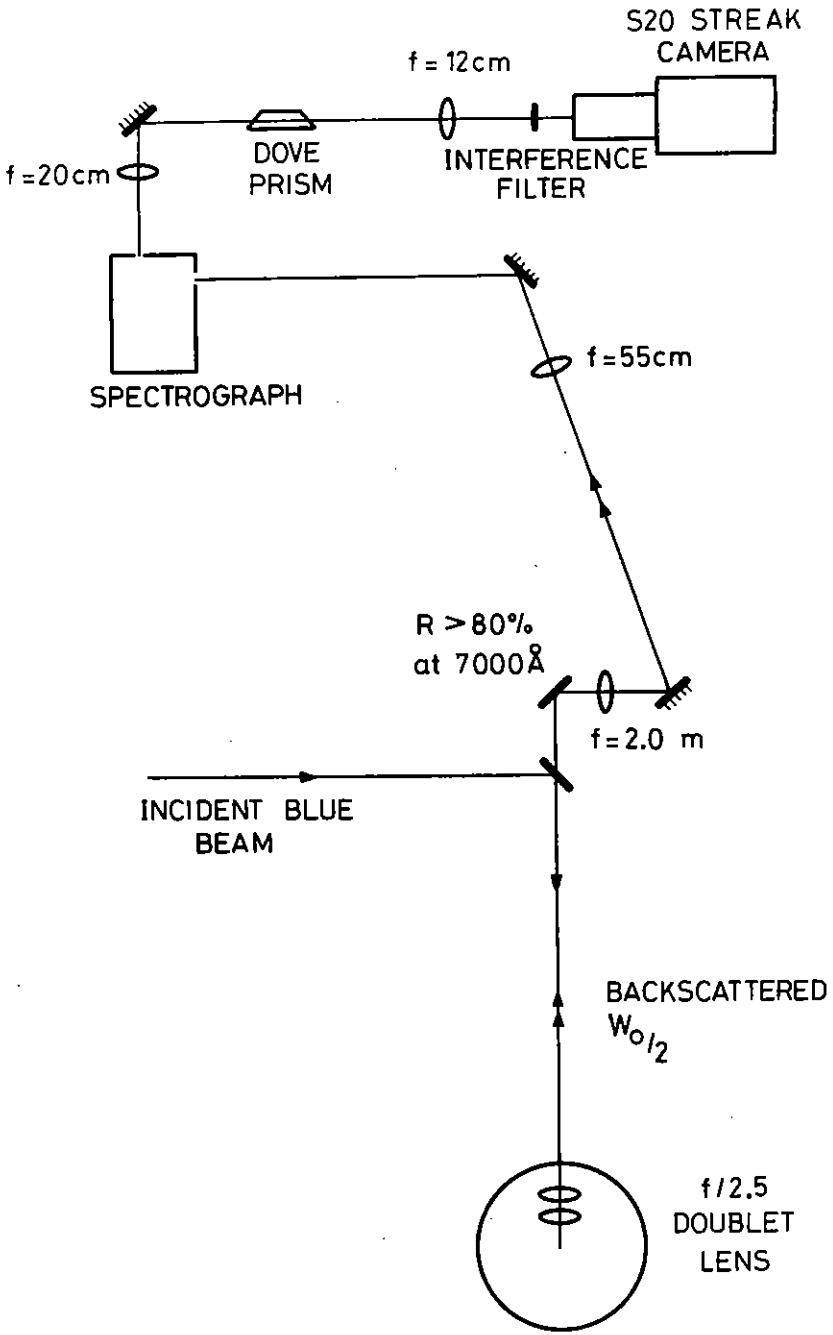

Figure 3.21 Experimental layout for time resolved observations of $\omega_0/2$ harmonic emission.

(R ≈ 80 % for 0.7 μm, T ≈ 80 % for 0.5 μm) and imaged with two relay lenses onto the slit of a grating spectrograph (1200 lines mm^{-1} grating). The dispersed output was then rotated by the dove prism so that wavelength lay along the slit of the S-20 streak camera. A broadband transmission interference filter (≈ 200 Å centred at 7013 Å) was placed in front of the streak camera slit and the input optics arranged so that the spectral window at the streak camera was ≈ 200 Å.

Calibration marks were obtained after every shot by streaking part of the second harmonic incident beam produced by a subsequent low energy shot, with the wavelength setting of the spectrograph at 5260 Å and appropriate adjustment to the trigger delay cable. Although this method relied on the linearity and reproducibility of the grating drive mechanism, it was sufficiently accurate for our purposes since the instrumental error was smaller than our spectral resolution of ∿ 16 Å.

Figure 3.22 shows the result of a moderate irradiance ($\phi \approx 7 \times 10^{14}$ W cm^{-2}) shot on a gold coated microballoon which is typical of our data. The $\omega_0/2$ harmonic spectrum consists of two peaks symmetrically shifted to the blue and the red of the nominal $\omega_0/2$ position, where the separation between the two peaks is ≈ 105 Å. The emission also has a pulsed nature, where the duration of each pulse is limited by the time resolution (≈ 20 ps) of the system and separated by ≈ 90 ps. As such it bears a striking resemblance to our previous observations of $(3/2)\omega_0$ harmonic emission obtained with 1.05 μm incident light (3.13).

Although the stimulated Raman scattering instability produces $\omega_0/2$ harmonic light directly, we do not believe that this is the mechanism responsible in this experiment since our irradiance did not exceed the theoretical threshold for this instability. Instead, we attribute the mechanism for the $\omega_0/2$ harmonic emission in our observations to the two plasmon decay, which has a lower threshold. This may be followed either by linear mode conversion or by Raman down scattering of the pump wave. The $\omega_0/2$ harmonic emission spectrum thus provides a direct measurement of the dispersion of the $\omega_0/2$ electron plasma waves and can be used to

estimate the electron temperature at quarter critical density in the underdense plasma at about 800 eV.

E McGoldrick and S M L Sim (University of Essex)

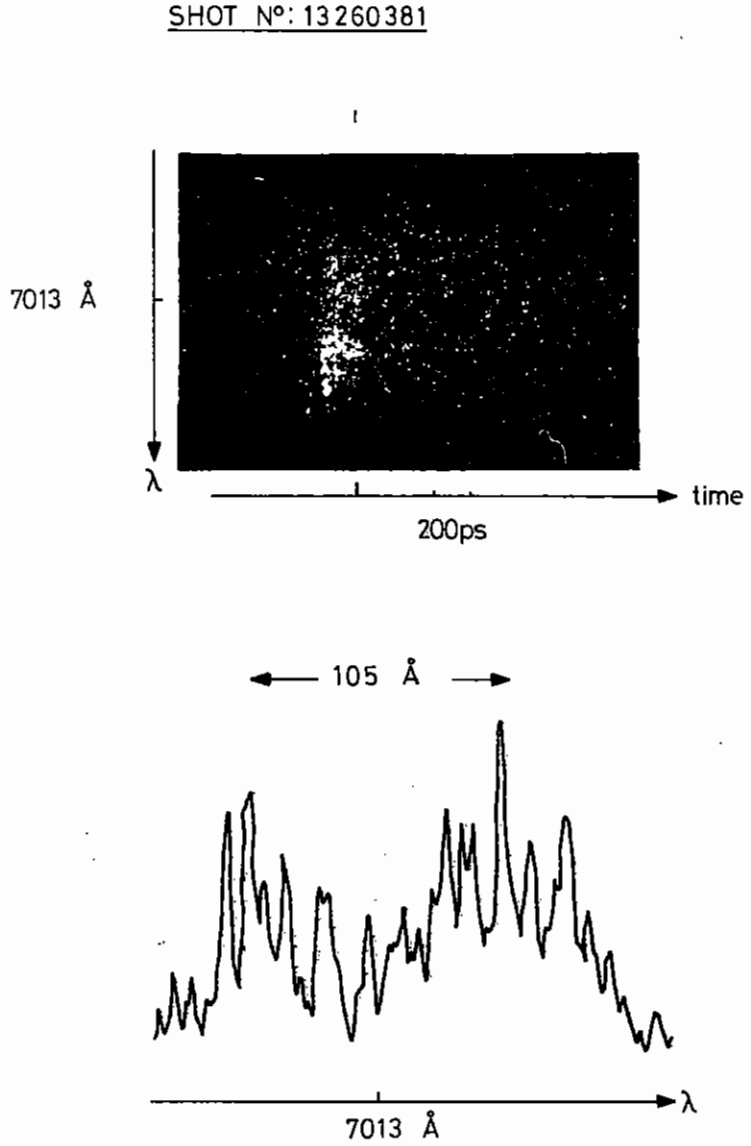

Figure 3.22 Time Resolved $\omega_o/2$ harmonic emission spectrum $\phi \simeq 7 \times 10^{14}$ W cm $^{-2}$.

CHAPTER 3 REFERENCES

3.01 Rutherford Laboratory Central Laser Facility Annual Report 1980, RL-80-026, Chapter 1 (1980)

3.02 R Benattar, C Popovics and R Sigel, Rev Sci Instrum, 50, 1583 (1979)

3.03 V K Tripathi and L A Pitale, Jour Appl Phys, 48, 3288 (1977)

3.04 B I Cohen and C E Max, Phys Fluids, 22, 1115 (1979)

3.05 E S Weibel, Phys Rev Lett, 2, 83 (1959)

3.06 D A Tidman and R A Shanny, Phys Fluids, 17, 1207 (1974)

3.07 M Ogasawara, A Hirao and H Ohkubo, Jour Phys Soc Jap, 49, 322 (1980)

3.08 C S Liu and M N Rosenbluth, Phys Fluids, 19, 967 (1976)

3.09 C S Liu et al, Phys Fluids, 17, 1211 (1974)

3.10 S Jackel et al, Phys Rev Lett, 37, 95 (1976)

3.11 V V Aleksandrov et al, Soviet Phys JETP Lett, 24, 508 (1976)

3.12 A I Avrov et al, Soviet Phys JETP, 45, 507 (1977)

3.13 P D Carter et al, Phys Rev Lett, 44, 1407 (1980)

3.14 H A Baldis et al, Phys Rev Lett, 41, 1719 (1978)

3.15 D E Evans et al, Rep Prog Phys, 32, 207 (1969)

3.16 J Sheffield, 'Plasma Scattering and Electromagnetic Radiation', Academic Press (1975)

3.17 N A Ebrahim et al, Phys Rev Lett, 45, 1179 (1980)

3.18 J L Bobin et al, Phys Rev Lett, 3, 594 (1974)

3.19 D W Phillion, Lawrence Livermore Laboratory Report, UCRL 84148 (1980)

CHAPTER 4 TRANSPORT AND PARTICLE EMISSION STUDIES

INDEX

CHAPTER 4 TRANSPORT AND PARTICLE EMISSION STUDIES

4.1 Introduction

The main emphasis in the work of the Transport and Particle Emission group in the past year has been on the study of processes which are important in the long pulse ablative regime and on wavelength scaling effects. In addition, work on preheat inhibition has continued and it is shown in Section 4.2 that the effect is larger than can be accounted for in a homogeneous low-density medium.

Section 4.3 is devoted to the pulse length dependence of preheat. A very substantial decrease in preheat has been observed for pulses longer than 150 picoseconds at 1.05 μm, in plane geometry. Evidence that this may be due to lateral spreading of the fast electrons was seen in a collaborative experiment carried out at Garching and later confirmed at the Central Laser Facility. A decrease in the amount of resonance absorption may also contribute.

The major part of this chapter is a discussion in Section 4.4 of our data on mass ablation and ablation pressure. Plane target mass ablation rates have now been measured by X-ray spectroscopy at 1.05, 0.53 and 0.35 μm under directly comparable conditions. A substantial increase in the ablation rate is obtained by going to short wavelengths and remains even after account is taken of changes in the absorbed fraction. The dependence of the ablation rate on absorbed irradiance is not strong. The difficulty of deducing an ablation pressure is discussed and further evidence is presented for the importance of lateral energy transport in long pulse irradiations. The spot size and irradiance dependence of ion data was investigated in complementary experiments carried out on the Nd laser at Queen's University Belfast.

Data on mass ablation rates and pressures in spherical geometry were obtained for a more limited range of irradiance at 1.05 and 0.53 μm by both spectroscopic and ion measurement techniques. The mass ablation rate shows a pronounced scaling with absorbed intensity. The interpretation of

ablation pressure in spherical geometry is discussed and values are obtained which show a similar and almost linear dependence on absorbed irradiance at the two wavelengths. Ablation pressures at high incident irradiance are thus higher the shorter is the wavelength and even more pronounced pressure enhancement could be obtained at short wavelength by working at constant $I\lambda^2$.

In the course of this work a possible disadvantage to working at short wavelength was observed: hot spots in the X-ray emission for large focal spot sizes appear to be formed more readily at short wavelengths. (See also Section 3.2 of this report.)

In our report last year we noted that although an improvement in symmetry could be seen in pinhole photographs of our first six-beam implosions, there was no significant increase in the yield of neutrons from exploding pusher targets. A later set of implosions which is discussed briefly in Section 4.5 gave much enhanced yields which are attributed to further improvements in symmetry due to experience in setting up, although no obvious effect is seen in the pinhole pictures.

The observation and interpretation of magagauss fields in long pulse irradiations of both plane and spherical targets is described in Sections 4.6 and 4.7. It was demonstrated experimentally that any large scale fields generated when spherical targets are irradiated uniformly are less than 100 kilogauss. Simulations reproduce well the large fields and density profile structures seen under non-uniform conditions.

4.2 A Measurement of the Reduction of the Range of Fast Electrons from Laser Irradiated Targets due to Density Structure in Low Density Gold Substrates

In a previous paper (4.01) an experiment showing a reduction of the fast electron preheating range (4.02) in low density gold substrates was reported. This effect arises because a return current balancing the current of fast electrons into the target must be set up. The electric field required to drive this return current can significantly impede the

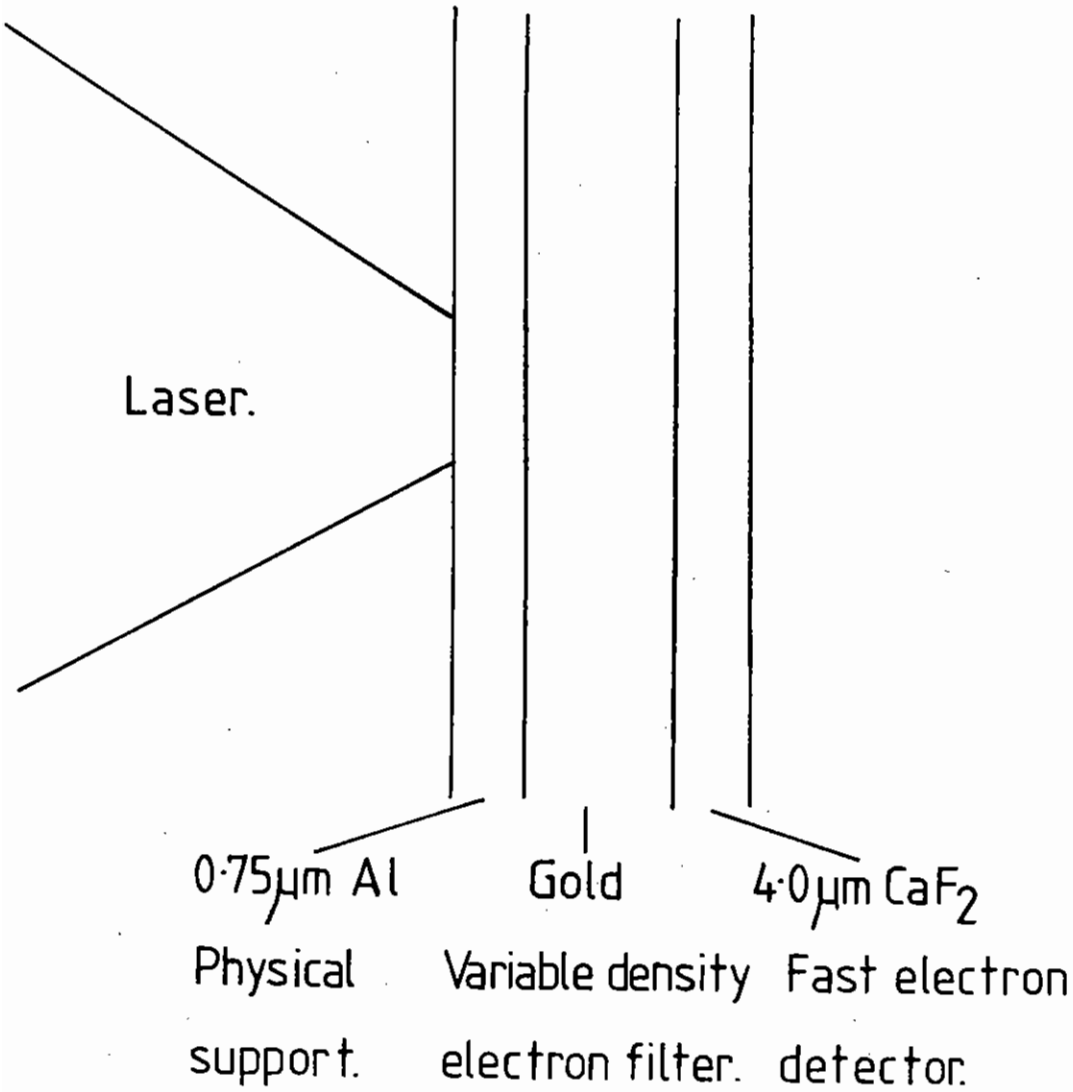

Figure 4.01 Details of the layered fluor targets containing low and solid density gold layers.

fast electrons if the target substrate is made from low density gold. The presence of fast electrons at various depths in a target was monitored by K_α fluorescing tracer layers (4.02, 4.03) placed beneath the gold layer. However the use of a front fluor layer to normalise the electron flux into the target reduced the flux into the low density gold, decreasing the effect of resistive inhibition. Nevertheless no fast electrons were detected from the rear fluor with a low density gold substrate, compared with a significant signal with a high density gold substrate of the same areal density. Thus an upper limit to the range of this large current density of fast electrons in low density gold was found. Comparison with a one dimensional Monte Carlo simulation indicated that the coefficient of resistivity of the low density gold might be increased by a factor of 3 from the Spitzer resistivity (4.04).

In this paper we report a series of experiments in which targets with a single rear fluor layer were used to measure the fast electron preheating range in low and solid density gold layers.

Targets as shown in Fig 4.01 were irradiated on the aluminium side. The 0.75 μm aluminium, which was also the support for the target, was thick enough not to burn through during the laser pulse; however it was thin compared with the fast electron range (4.02) and so did not significantly reduce the electron flux. The low density gold was produced by evaporation in an argon atmosphere (4.01) and the areal density of the layers was determined both by weighing and by radiography. The density of the gold was then determined from the thickness measured with a scanning electron microscope. The rear layer of CaF_2 detected fast electrons reaching it by emitting Ca K_α radiation.

The targets were irradiated with 1.05 μm, 25 J laser pulses of 150 ps FWHM duration. A focal spot size of 80 μm was used, measured by the amount of defocus of the F/1 focusing lens, or the 2 keV pinhole camera. The intensity on target was 3×10^{15} W cm^{-2}.

The K_α yields from the rear fluor of the targets were measured by a calibrated X-ray crystal spectrometer and Kodirex X-ray film, and the

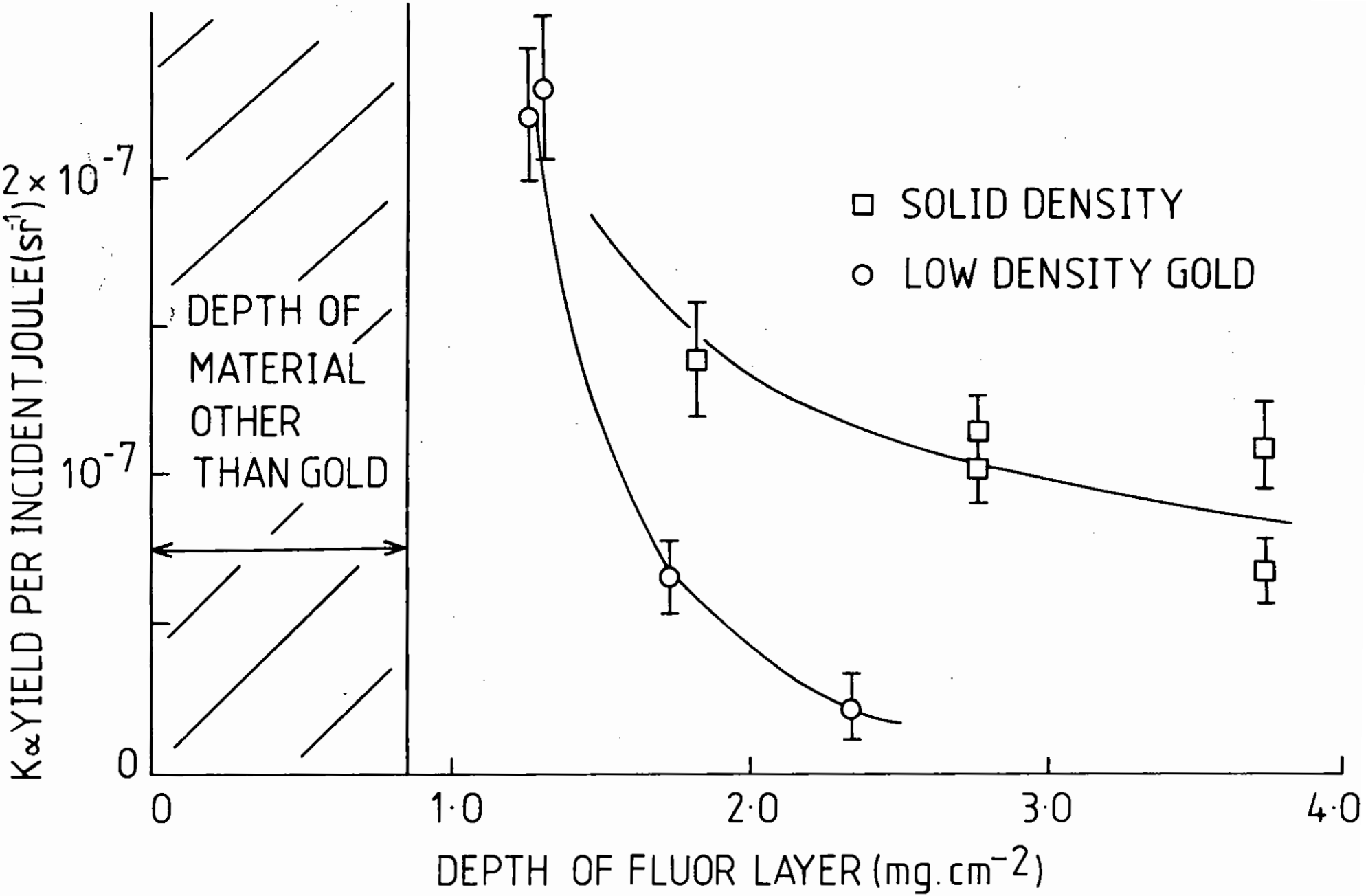

Figure 4.02 The Kα yield per incident joule of laser energy as a function of the areal density from the target surface to the centre of the fluor layer for targets containing solid density and low density gold layers.

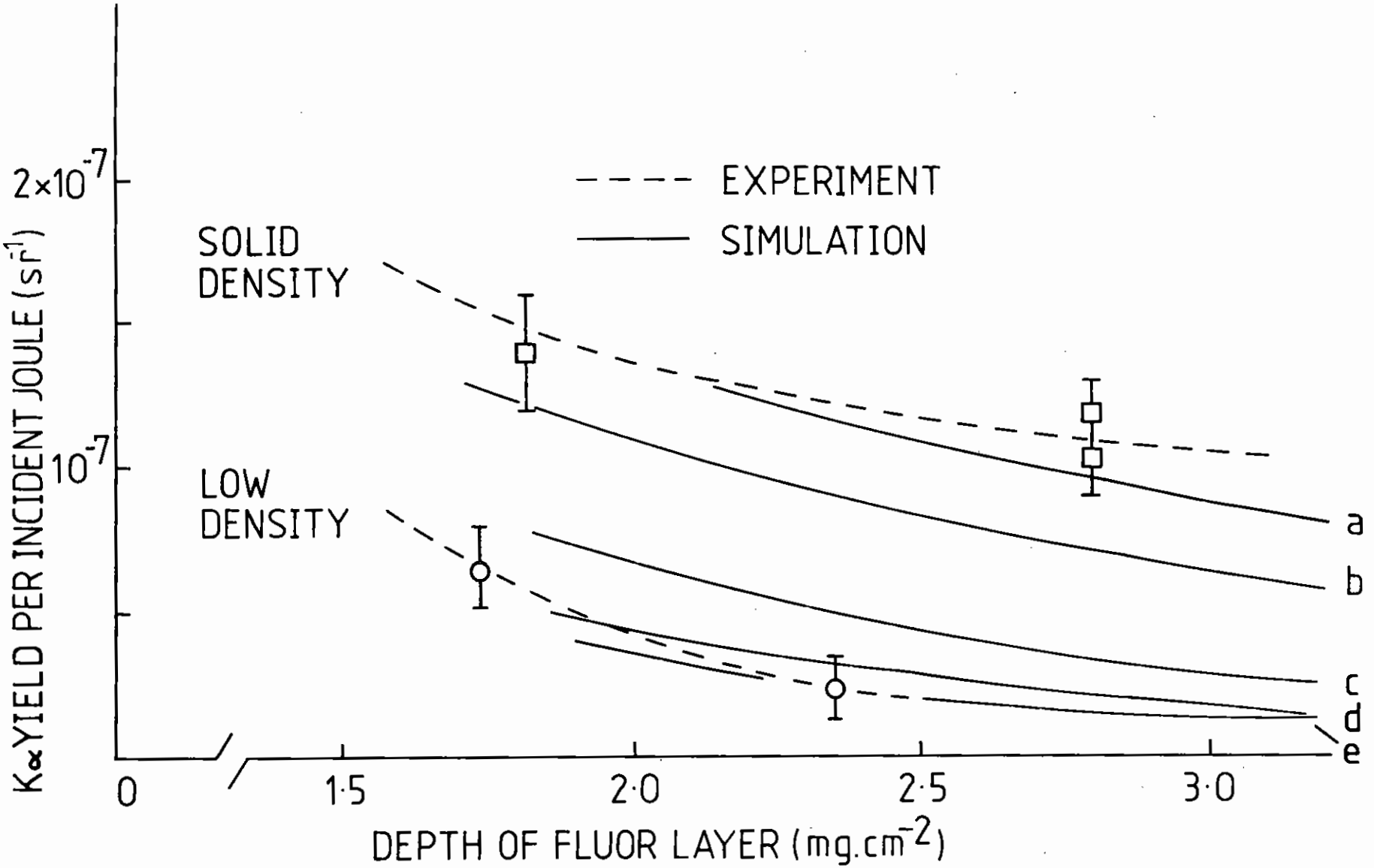

Figure 4.03 A comparison of various simulations with the experimental yields for low and high density targets. In the simulations the fast electron distribution referred to in the text was incident in a 80 μm diameter spot and was deposited over 150 ps. Simulation (a) was for a solid gold layer and resistive effects were negligible. The other simulations were for a 0.6 % solid density gold layers. In (b) and (e) no density structure was assumed and Spitzer and 10X Spitzer resistivity were used respectively. In (c) and (d) a 2 μm gold strand separation was included with Spitzer and 2X Spitzer resistivity respectively.

absolute K_α yields per incident joule of laser energy are shown in Fig 4.02 from shots with both solid and low density gold. The K_α yield is approximately proportional to the energy deposition by fast electrons (4.02) and as can be seen in Fig 4.02 the preheat range is reduced by a factor of 2 - 3 in low density gold over the range in high density gold.

The fast electron energy spectrum for the above conditions was measured by two fluor targets as in (4.02), and was of the form

$$f(E) = AE^{3/2} \exp\left(-E/kT_H\right)$$

with $kT_H = 12 \pm 2$ keV and a total energy content of 1 J. The energy content of this distribution is lower than in (4.02) due to a greater pulse length (4.05).

This distribution function was used in simulations of the target experiments. In the simulation the fast electron scattering cross-section was calculated using a combination of Fermi and Debye shielding of the nuclear charge. A continuous slowing down approximation was used for energy deposition, accounting for energy loss to bound (4.06) and plasma (4.07) electrons.

Fig 4.03 shows a simulation result with Spitzer resistivity and an LTE ionisation model (4.08) for both low and high density gold layers. The predicted inhibition with a low density gold layer is insufficient to match the experiment. For agreement the resistivity must be increased by a factor of 10, which is also shown in Fig 4.02.

An increase of resistivity by a factor 10 is not expected. The value of V_{th}/V_{ia} in a simulation is less than unity so no streaming instability should be excited. A more likely explanation is that the apparent resistivity might be increased by persistent structure in the low density gold. Fig 4.04 shows a scanning electron micrograph of a low density gold layer. Density structure on the scale of a few μm is evident. The gold consists of many filaments, and resembles cottonwool. Assuming the return current is restricted to the filaments, the effective

area through which the current passes is reduced, leading to a high initial apparent resistivity. As thermal expansion of the filaments homogenises the density structure the apparent resistivity will decrease to the Spitzer value.

Account of this is taken in the simulations by considering the low density gold to consist of strands, initially at solid density. These strands expand at the local ion thermal velocity until the voids between the strands are filled. The current is assumed to flow uniformly within the expanding strands.

Taking the density scale length to be 2 μm and assuming Spitzer resistivity still gives too little inhibition. A combination of density structure and 2 x Spitzer resistivity gives good agreement with experiment. These two simulations are shown in Fig 4.03. It is not unreasonable that Spitzer resistivity should be incorrect by a factor of two since $\ln\Lambda$ in the relatively high density and cool gold is very low. In conclusion we have measured a reduction in range of fast electrons by a factor of 2 - 3 in low density gold. The reduction is larger than expected if the target substrate were homogeneous, but can be accounted for by density structures in the substrate.

D J Bond, J D Hares and J D Kilkenny (Imp Coll)

4.3 A Demonstration of the Decrease of Fast Electron Preheat from Laser Produced Plasmas with Increasing Pulse Length

It is widely believed that short pulse, high intensity laser interactions are dominated by fast electron preheat. The so called exploding pusher experiments indicate that a large fraction of the absorbed energy is coupled into preheat (4.09). Manifestations of the fast electrons are hard X-ray continuum production, fast ion production and K_α emission. Measurements of the temperature of these electrons have been made by several groups (4.10) and it is found that T_H is a function of $I\lambda^2$, although T_H is virtually independent of pulse length from 80 ps to 2 ns (4.11).

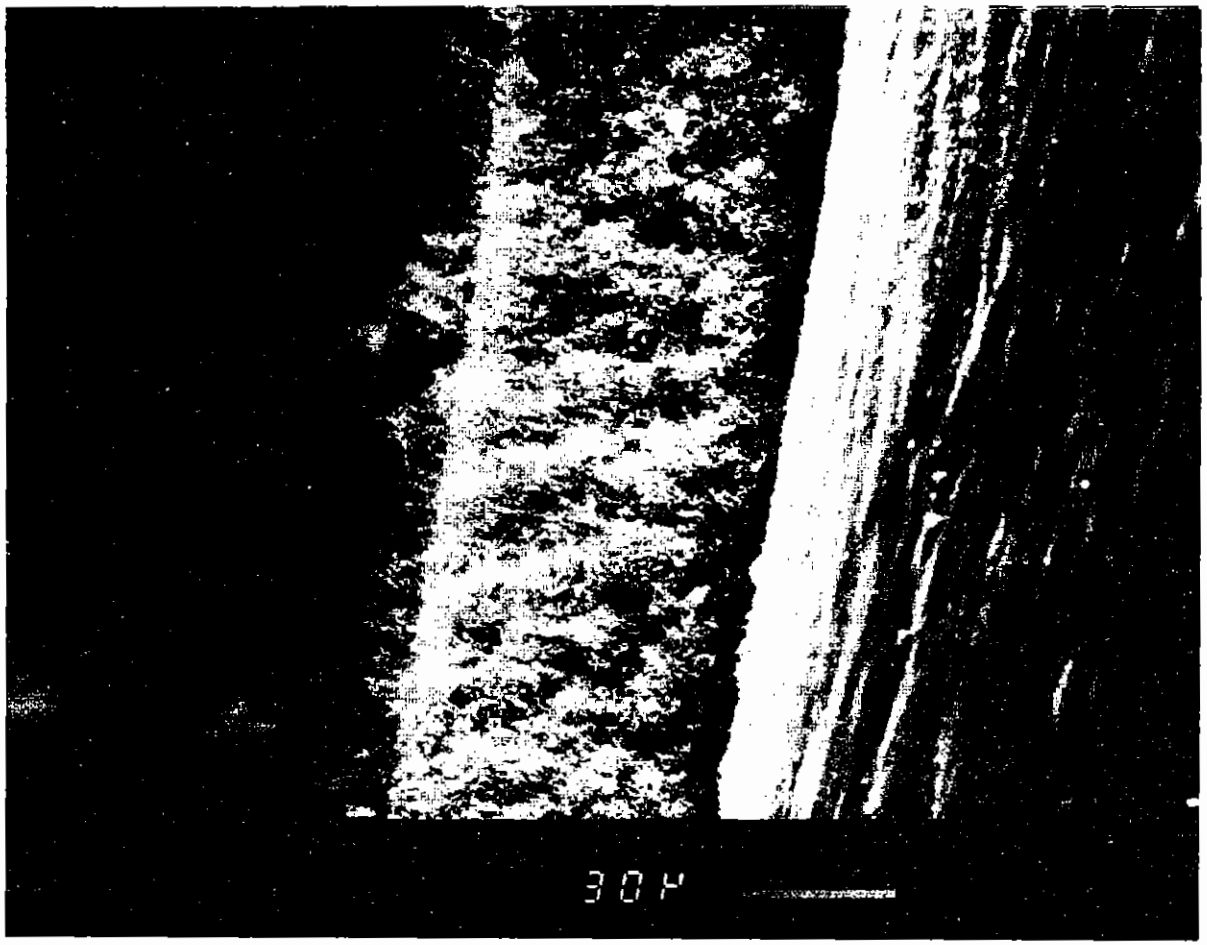

Figure 4.04 A scanning electron micrograph of a 0.6 % solid density gold layer. The layer has been deliberately torn to enable it to be viewed edge-on. The material to the right is the underlying aluminium support. There is no fluor layer present.

Measurements of E_F, the fraction of the incident energy that appears as preheat in the target, are not so definitive. Estimates of E_F can be made from the implosion dynamics of exploding pushers (4.09, 4.12), the absolute intensity of the hard X-ray continuum emission (4.13, 4.14) and the fast ion emission (4.15). Analysis of exploding pusher experiments (4.09) with 30 ps pulses shows that a large fraction of the absorbed energy is coupled via fast electrons to the shell.

Analysis (4.13) based on the hard X-ray continuum is sensitive to the form of the assumed fast electron velocity spectrum, but shows that approximately 10 % of the incident energy is converted into fast electrons for short pulses.

Measurements of E_F using X-ray fluorescent layers (4.01, 4.02) are less dependent on the fast electron velocity spectrum. The fast electron induced characteristic X-ray emission indicates quite accurately the fast electron energy deposited in the fluor. The K_α yield from layered targets has been measured and calculated for various incident energies of electrons (4.02), but essentially, if the electron energy is greater than $2 \times E_{KI}$, twice the K shell ionisation energy, then the ratio of energy loss into K ionisation to the total rate of energy loss by fast electrons, R, is approximately constant. The energy deposited into any element of the target whose fluorescence yield is ω, is simply $U_{K_\alpha}/(\omega \times R \times E_{K_\alpha}/E_{KI})$, where U_{K_α} is the energy emitted in the K_α line. Typically this method shows that E_F is 7 % at 2×10^{15} W cm^{-2} for 100 ps, 1.06 μm pulses.

With long pulses, ie about 1 ns, there is good evidence (4.11) from the slope of the hard X-ray continuum emission that T_H is the same as for short pulses at the same intensity. However there is evidence that E_F is considerably lower than it is for short pulses. It can be inferred from the absolute levels of the hard X-ray continuum that the fractional coupling into fast electrons, E_F, is less (4.14, 4.16) giving values of 5 - 17 % for short pulses and $\lesssim$ 2 % for long pulses. The hydrodynamic behaviour of thin foils suggests that for 300 ps pulses, at 1.3 μm and 2×10^{14} W cm^{-2}, $E_F \sim 2$ % (4.17). Exploding pusher experiments with

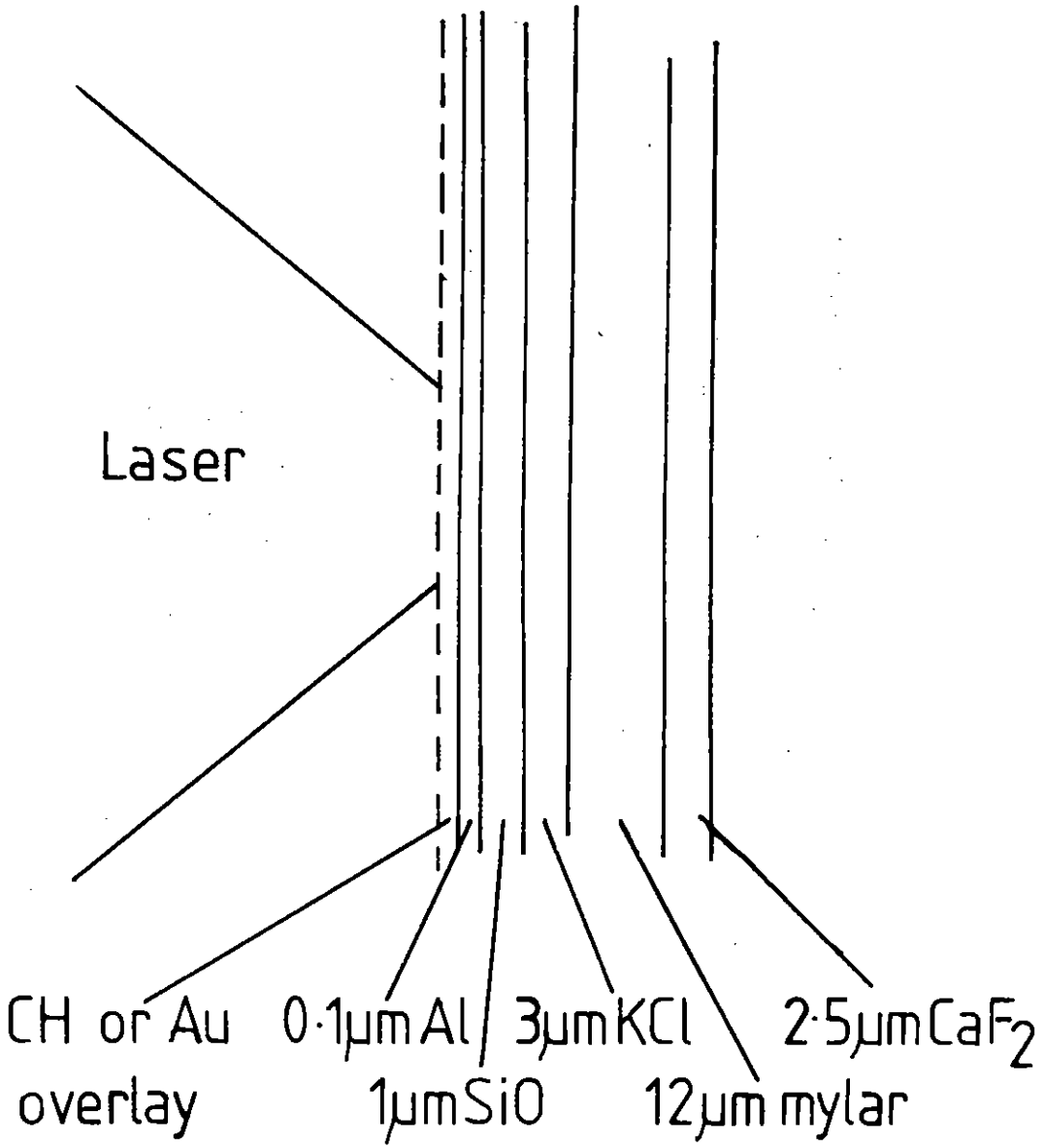

Figure 4.05 The multilayered Kα fluor targets. For the longer pulse lengths solid titanium foils were used for increased sensitivity.

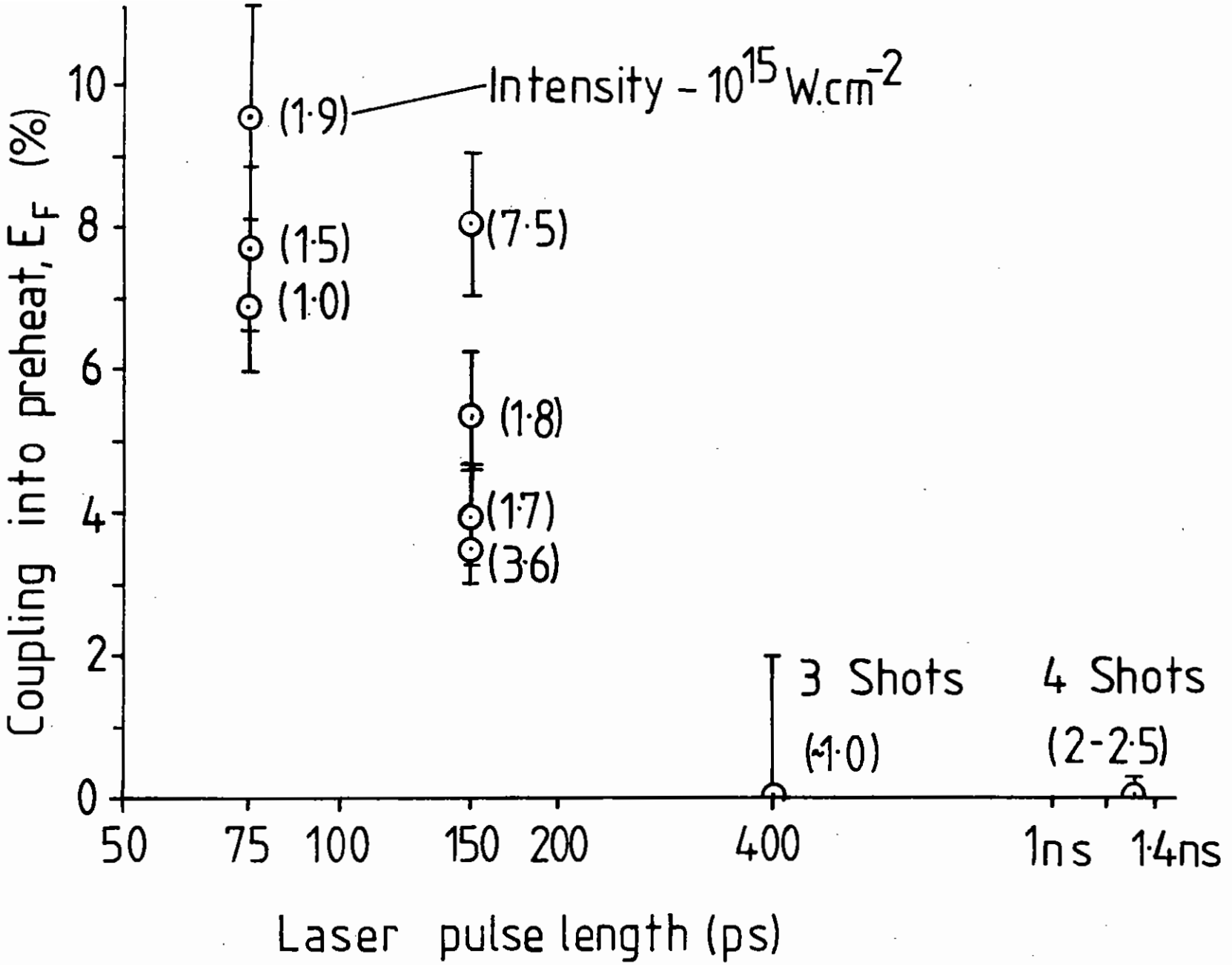

Figure 4.06 The fractional coupling into preheat, E_F, as a function of pulse length. The yields for 400 ps and 1.3 ns pulses were experimentally zero within error bars set by film noise.

250 ps pulses (4.12) indicate that $E_F \sim 3$ %. Finally, target recoil measurements (4.18) have been used to investigate resonance absorption by varying the angle of incidence. With long pulses no difference was found between s and p polarisation, implying that the resonance absorption which was observed with short pulses, was not significant for long pulses.

In this experiment E_F has been measured using K_α emission with four different pulse lengths. A mode-locked YAG oscillator was used to produced pulses of 80 ps or 150 ps FWHM as measured by an optical streak camera. These were focused onto K_α fluor targets (4.02) with a surface layer of Al. The targets are illustrated in Fig 4.05. Pulses of 400 ps duration were obtained by stacking five 100 ps pulses. Finally 1.3 ns pulses were obtained by optical chopping from a single mode Q switched oscillator. For the latter pulse lengths the targets were solid titanium which is a more sensitive indicator of fast electrons. The intensity on target was calculated both from the measured defocus of the target and from the size of X-ray pinhole camera images. For irradiances of $2 \pm 1 \times 10^{15}$ W cm^{-2} and 7.5×10^{15} W cm^{-2}, E_F is shown in Fig 4.06. For the short pulses, Kα emission was observed from both fluors in the targets and E_F and T_H could be measured. For the two longer pulse lengths, and despite the use of more sensitive solid fluor targets, no K_α emission was detected. Thus an upper limit on E_F is shown in Fig 4.06 set by the background noise on the spectrometer film. As shown in Fig 4.06 increasing the intensity with 150 ps pulses increased E_F, however this was not possible for longer pulses since the intensity was already at a maximum. Fig 4.06 shows a pronounced decrease in E_F as the pulse length increases.

With 150 ps pulses the atomic number of the surface plasma was also varied, using the K_α fluor targets. The targets shown in Fig 4.05 were either left with an aluminium surface or were overcoated with plastic (CH) or gold. The thickness of these overlays was much less than the fast electron range. Results are shown in Fig 4.07 for an intensity of $1.8 \pm 0.8 \times 10^{15}$ W cm^{-2} and a pulse length of 150 ps. The fast electron temperature T_H was measured from the ratio of the potassium to calcium Kα emission, and was found to be 7 ± 2 keV independent of Z. It is

apparent that E_F increases with increasing Z although there were large and unexplained shot to shot variations.

A possible explanation for both Figs 4.06 and 4.07 is that the density scale length is increasing as either the pulse length increases, or the atomic number decreases, thus making resonance absorption less effective. In linear resonance absorption theory the fractional absorption depends on $(K_oL)^{2/3} \sin^2\theta$, maximising at approximately 50 % absorption for $(K_oL)^{2/3} \sin^2\theta = 0.6$ (4.19). With an average value for $\sin^2\theta = 0.12$, appropriate to our f/1 focusing optics, the resonance absorption peaks when $L/\lambda = 4$.

If we neglect profile steepening by the ponderomotive force then a simple estimate for the density scale length is

$$L \sim \left(\frac{ZkT}{m_i}\right)^{\frac{1}{2}} \tau_p$$

where τ_p is the laser pulse length and $\left(\frac{ZkT}{m_i}\right)^{\frac{1}{2}}$ is the expansion velocity. This implies that for efficient resonance absorption by fully ionised Al at 500 eV,

$$\tau_p \lesssim 27\text{ps}.$$

Thus for pulses longer than 27 ps we expect the coupling into fast electrons to drop and for higher m_i/Z we would expect the coupling to increase. This behaviour is seen in Figs 4.06 and 4.07. The value of L and hence τ_p assumed a planar absorption region. Any rippling or curvature would increase the value of L for maximum resonance absorption.

Our results imply that the resonance absorption is falling with increasing pulse length. This is not inconsistent with other observations that the total absorption does not decrease with increasing pulse length (4.16), because the resonance absorption fraction we are measuring is small compared with the total absorption. We also note that we expect E_F to be dependent on the pulse shape, with a fast rising pulse favouring good coupling into preheat.

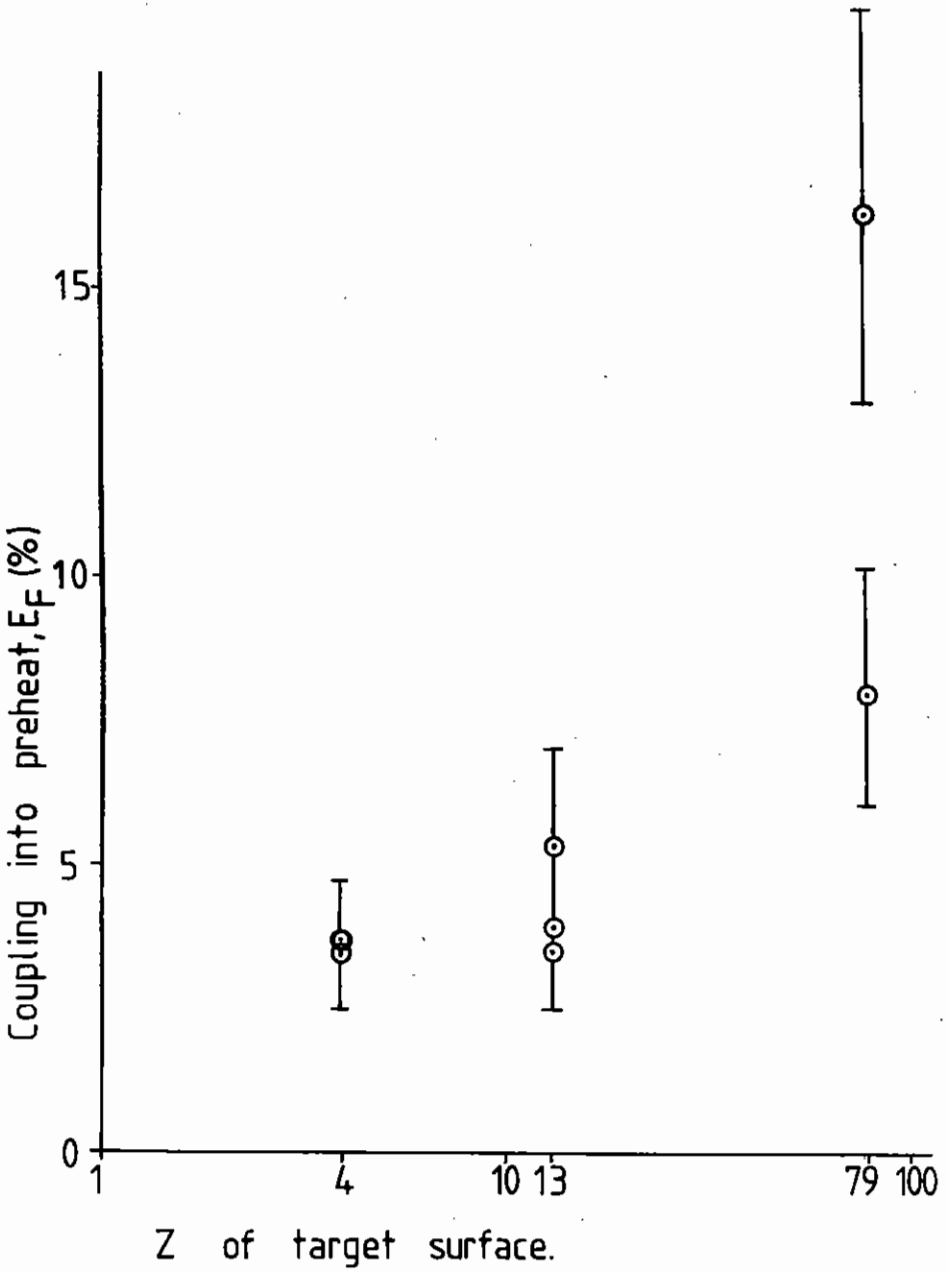

Figure 4.07 The fractional coupling into preheat for 150 ps pulses at ~2 x 10^{15} W cm^{-2} as a function of Z of the target surface.

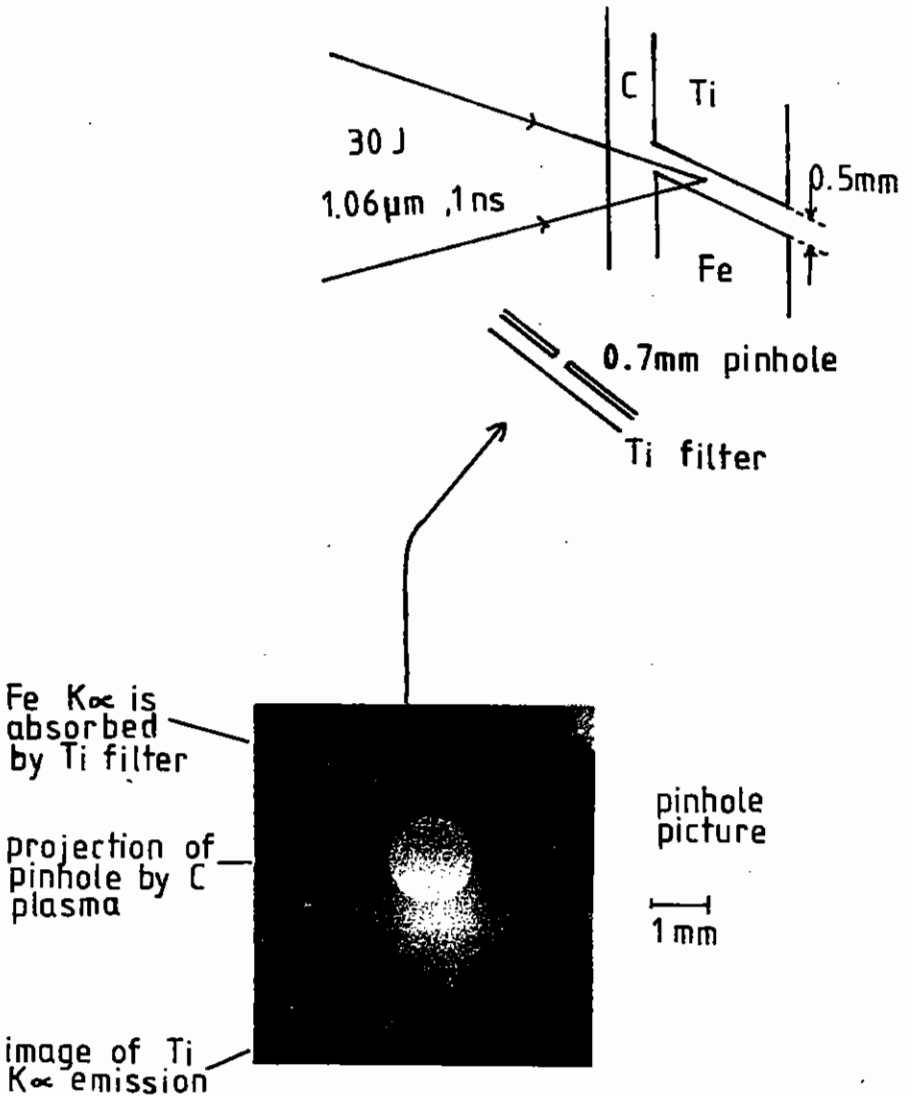

Figure 4.08 Illustration of lateral spread of past electrons in long pulse irradiation.

An alternative way to explain the data of Figure 4.06 is by radial spreading of the fast electrons. This effect was first noticed in a joint experiment at Garching (4.20) with 300 psec pulses at a wavelength of 1.3 μm and subsequently confirmed at the Central Laser Facility with 1.2 nsec pulses at a wavelength of 1.05 μm. It can be seen by irradiating a carbon target with foils of Ti and Fe either side of the focal spot, as illustrated in Figure 4.08. The X-ray emission was viewed through a large pinhole filtered by 10 μm of Ti. Thus Fe K_α emission would be strongly absorbed by the Ti filter, whereas Ti K_α would not be strongly attenuated. Continuum emission in the region of 2.5 Å would be similar from both the Ti and Fe. The emission up to 2 mm away from the focal spot, as shown in Figure 4.08, is therefore due to Ti K_α, or just possibly Ti XXI $1^1S_0 - 2^1P_1$. The second explanation is unlikely because the Ti was about 500 m away from the focal spot and the high temperature necessary to excite the $1^1S_0 - 2^1P_1$ is not expected that far away.

Since the ratio of K_α emission to fast electron energy deposition is virtually constant above the K shell excitation threshold the fast electron energy can be accurately measured from the K_α emission. From a few preliminary experiments, assuming azimuthal symmetry, we estimate there is at least 1 J of energy associated with this K_α emission for 30 J on target in 1 ns. The energy may be higher than this, as the K_α emission far from the target could be significant because of radial scale factors.

The reason for radial spreading might be that the electrons are effectively channelled along the surface, being unable to move away from the surface plasma because of their space charge, and being reflected from the solid surface. This effect would be expected to be greater for longer pulses as the surface plasma would take time to develop.

The achievement of a high density compression requires a preheat level comparable to or less than the Fermi energy (ie ~ 5 eV for solid DT). The preheat level at fixed I, and hence T_H (4.11) is a function of the product $\tau_p E_F$. Measurements with 100 ps 1.06 μm pulses (4.02, 4.13, 4.14) indicate that target preheating is high for I ~ 10^{15} W cm^{-2}. The longer pulses required for an ablative compression make the situation

worse since τ_p is larger. The poorer coupling into preheat with long pulses is important since it relaxes the constraints on intensity and target thickness (4.21) for Fermi degenerate compression.

In conclusion we have measured a decrease in the fast electron preheat with increasing pulse length, and discussed two possible mechanisms to account for this decrease.

J D Hares and J D Kilkenny (Imp Coll)

4.4 Measurements of Mass Ablation Rates and Ablation Pressure

4.4.1 Introduction

This section describes and discusses a series of experiments in which the process of ablation by laser pulses of 1 ns duration at irradiances ranging from 10^{13} to 10^{15} W cm^{-2} was studied at wavelengths of 1.05 μm, 0.53 μm and 0.35 μm on plane targets and 1.05 μm and 0.53 μm on spherical targets. Measurements of the mass ablation rate and ablated ion velocity were made and the data are discussed in relation to analytic and numerical models. Attention is given to the deduction of ablation pressure from the data in view of the importance of ablation pressure in laser driven compression of matter and in laser fusion.

The plane target data at 1.05 μm were described in last year's Annual Report (4.22) together with a restricted set of experiments at 0.53 μm. A more complete set of data at 0.53 μm was obtained before the laser upgrade together with some 1.05 μm data for spherical targets. New experiments using the upgraded laser facility (chapter 1) have been carried out recently and have given plane target data at 0.35 μm and spherical target data at 0.53 μm. Additional data on the focal spot size dependence of ablated ion velocity from plane targets irradiated at 1.05 μm were obtained using the glass laser facility at Queen's University Belfast.

Improved analysis of all these results has led us to revise our initial conclusions on ablation pressure based on the early plane target data as a

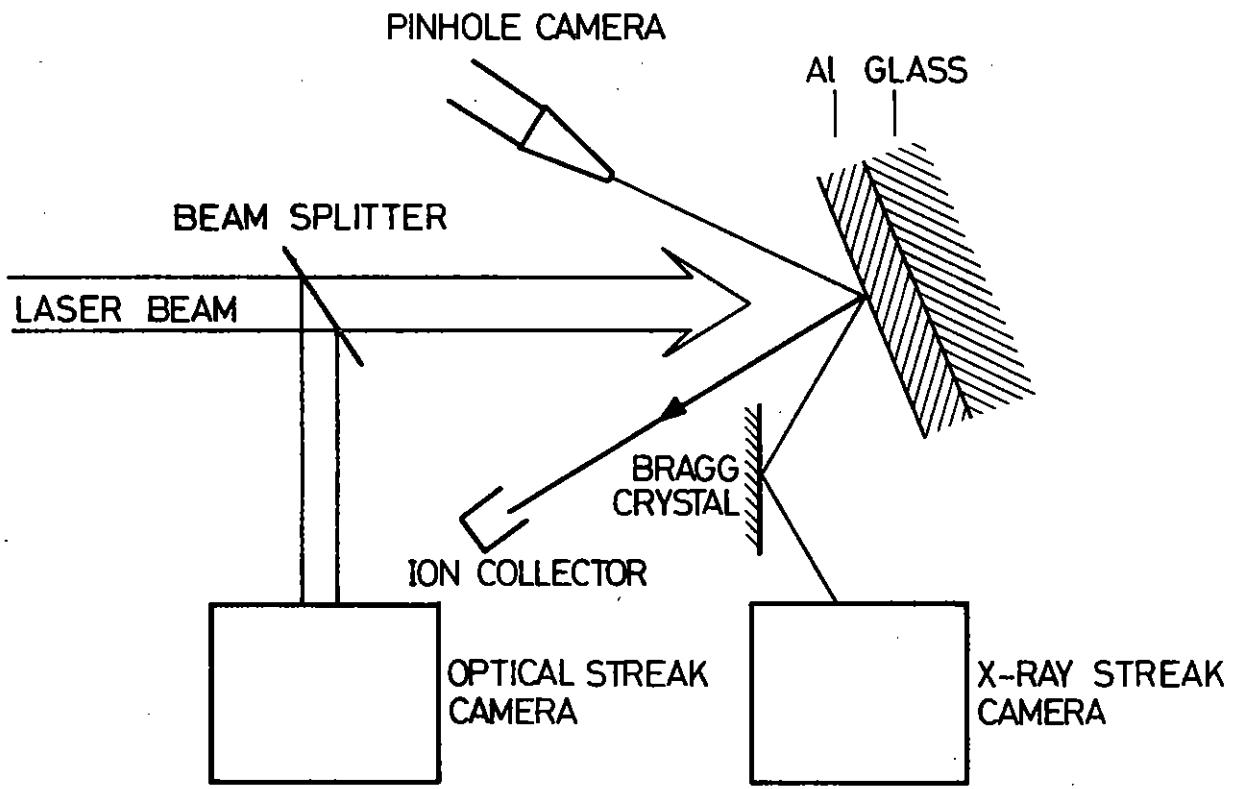

Figure 4.09 Schematic diagram of experiments to measure ablation from plane targets.

result of more careful consideration of the effects of lateral transport of energy from small focal spots on plane targets.

Sections 4.4.2 to 4.4.4 present the experimental results for plane targets which are discussed in 4.4.5, while spherical target data are presented in 4.4.6 and 4.4.7 and discussed in 4.4.8.

4.4.2 Spectroscopic Measurements of the Mass Ablation Rates from Planar Targets at 1.05 μm, 0.53 μm and 0.35 μm

Time resolved X-ray spectroscopy was used to measure the rate at which matter is ablated away from a solid target irradiated at 1.06 μm, 0.53 μm or 0.35 μm and a variety of intensities. In this technique, the delay in emission between certain resonance lines of different elements in a layered target gives a burn time and the thickness of material in the top layer gives the area mass density. The intensity of the laser beam was varied by defocusing at constant energy.

For this experiment the laser was used in its long pulse mode. For 1.05 μm irradiation the pulse length was 1.5 ns with typically 50 J on target. For 0.53 μm the pulse length was 0.6 ns with typically 20 J on target as described in (4.22). For 0.35 μm the pulse length was 0.7 ns with typically 8 J on target as described in Section 1.4 of this report. For 1.05 μm and 0.53 μm an f/1 glass doublet was used to focus the beam whereas at 0.35 μm an f/2.5 fused silica doublet was used. The targets usually consisted of an aluminium layer deposited onto a glass microscope slide. The thickness of the aluminium layer was measured during deposition by a film thickness monitor and after use by a scanning electron microscope. Thicknesses between 0.1 μm and 2.0 μm were used. The target normal was angled 7° away from the laser beam axis (Figure 4.09).

The main diagnostic was an x-ray streak camera set up in a spectroscopic mode with a TlAP crystal producing a spectrum of the Al and Si resonance lines from 6.7 Å to 5.5 Å with a time resolution of better than 100 ps.

Some typical streaks are shown in Figure 4.10(a). Three pairs of lines were used for measurement of the burnthrough time. The dielectronic satellites of Al XII $1^1S_0 - 3^1P_1$ and of Si XIII $1^1S_0 - 2^1P_1$ are spectrally distinct and the delayed Si emission can be seen on Figure 4.10. The Al XII $1^1S_0 - 5^1P_1$ line of Al XII and the L_α line of Si XIV are not spectrally resolved but an increase in brightness at this wavelength due to the start of the silicon emission can be seen. Finally, the Si XIII $1^1S_0 - 3^1P_1$ line is spectrally distinct from the neighbouring Al XIII L_γ and L_δ lines and a time delay can be measured. As shown in Figure 4.10(a) the time delay from these three methods agreed well.

An alternative target was used for some of the 0.35 μm experiments. This consisted of SiO coated on Al, which allowed the resonance lines of He like Silicon and He and H like aluminium to be used for the measurement of burn through time. A typical streak from such a target is shown in Figure 4.10 (b).

A pinhole camera with 6 μm platinum pinholes was used to obtain the spot size which was varied between a 'tight' focus (a diameter of 30 μm at 1.06 μm, 50 μm at 0.53 μm and 30 μm at 0.35 μm) and a diameter of about 750 μm. It had two channels, one filtered by 25 μm Be to 1.4 keV and the other by 125 μm Be to 2.4 keV. For 1.05 μm and 0.53 μm irradiation a large focal spot, up to 500 μm could be used before the intensity of the x-ray spectral lines became too low. However at 0.35 μm the x-ray image broke up into discrete hot spots when the focal spot diameter exceeded 100 μm, thus introducing considerable uncertainty in the effective laser beam intensity. The origin of these hot spots is unclear and may be due in part to beam inhomogenities and in part to non linear filamentation of the laser beam and/or thermal instabilities. Data from these shots were therefore not used.

An optical streak camera was used to measure the pulse length and the pulse energy was obtained from a calibrated monitor just outside the vacuum chamber. Ion collectors were placed on the inside of the target chamber wall to measure the ion velocity of the ablating plasma.

FIG 4·10 (a). TWO TYPICAL STREAKED SPECTRA FOR THE 0.53μm EXPT. THE TOP SPECTRUM SHOWS NO BURNTHROUGH (Al SPECTRUM ONLY) WHILST THE BOTTOM SHOWS A BURNTHROUGH TIME OF ABOUT 400ps (Al AND Si SPECTRA COMBINED). THE DENSITOMETER TRACINGS SHOW THE LINE IDENTIFICATIONS.

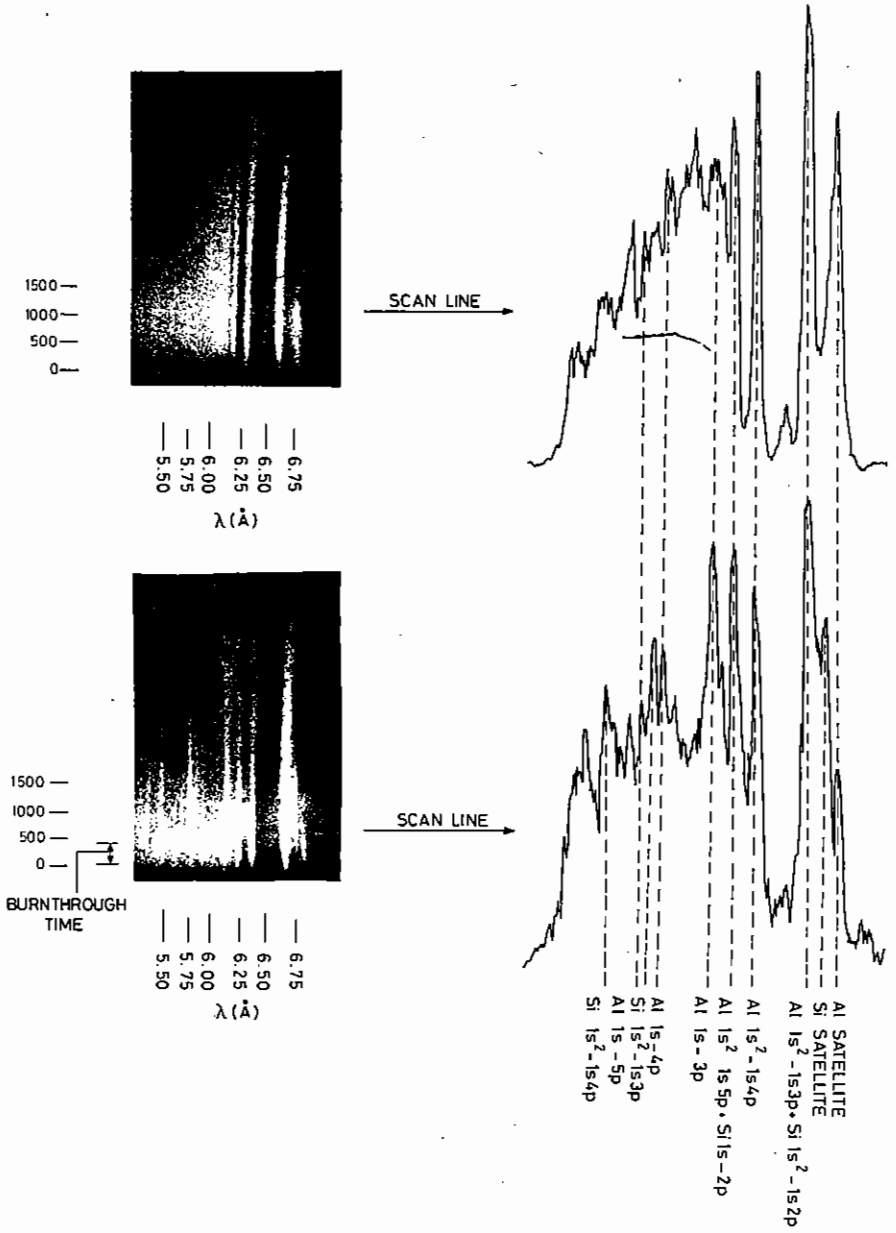

The X-ray streak data were analysed in the following way. To first order the specific mass ablation rate is

$$\dot{M}_s = \rho l / t$$

where ρl is the area density of the aluminium layer and t is the simple burn time, ie the time between the start of the aluminium emission and the start of the Si emission. This would be true if there were a square pulse in time. To correct for the variation of intensity (and hence burn rate) with time we use the laser pulse shape shown in Figure 4.11. The correction factor is

$$C = t / \int_0^t f^{\alpha}(t')dt'$$

where t = 0 is taken at the start of the laser pulse, f(t') is the laser pulse shape and α is the power scaling of a provisional $\dot{m}_s$ against I fit. The correction factors are plotted in Figure 4.12.

Care had to be taken in measuring the burn time. The Al He-like continuum is seen on all these data and was found to be short-lived enough to resemble closely the laser pulse shape (Figure 4.10); this meant that the peak of the laser pulse could be referenced to the peak of the continuum.

The sizes of the focal spots were taken from the x-ray pinhole pictures and plotted against the defocus of the lens so that any spurious variations in the data could be removed (Figure 4.13). For large spot sizes the effective aperture of the lens was f/1.5 at 1.05 μm and 0.53 μm. It is interesting to note that both the 25 μm Be and 125 μm Be images lie on the same line indicating little radial spreading for this high temperature x-ray emission. The FWHM of the spot and the pulse length measurement variation allowed a peak laser flux I_o to be calculated. Graphs of $\dot{m}_s$ as a function of I_o are plotted in Figure 4.14 for 1.06 μm, 0.53 μm and 0.35 μm. It is seen that $\dot{m}_s$ increases as I_o increases and as λ decreases. There is some scatter in the data, even after correcting for the pulse shape variation.

FIG 4·10(b). A TYPICAL STREAK FROM THE 0.35μm EXPT. USING SiO DEPOSITED ON THICK Al SHOWING THE LOW ORDER RESONANCE LINES. THE BURNTHROUGH TIME IS MUCH EASIER TO MEASURE WITH THIS ARRANGEMENT THAN THE ONE USED FOR EARLIER EXPERIMENTS AT 0.53μm AND 1.06μm

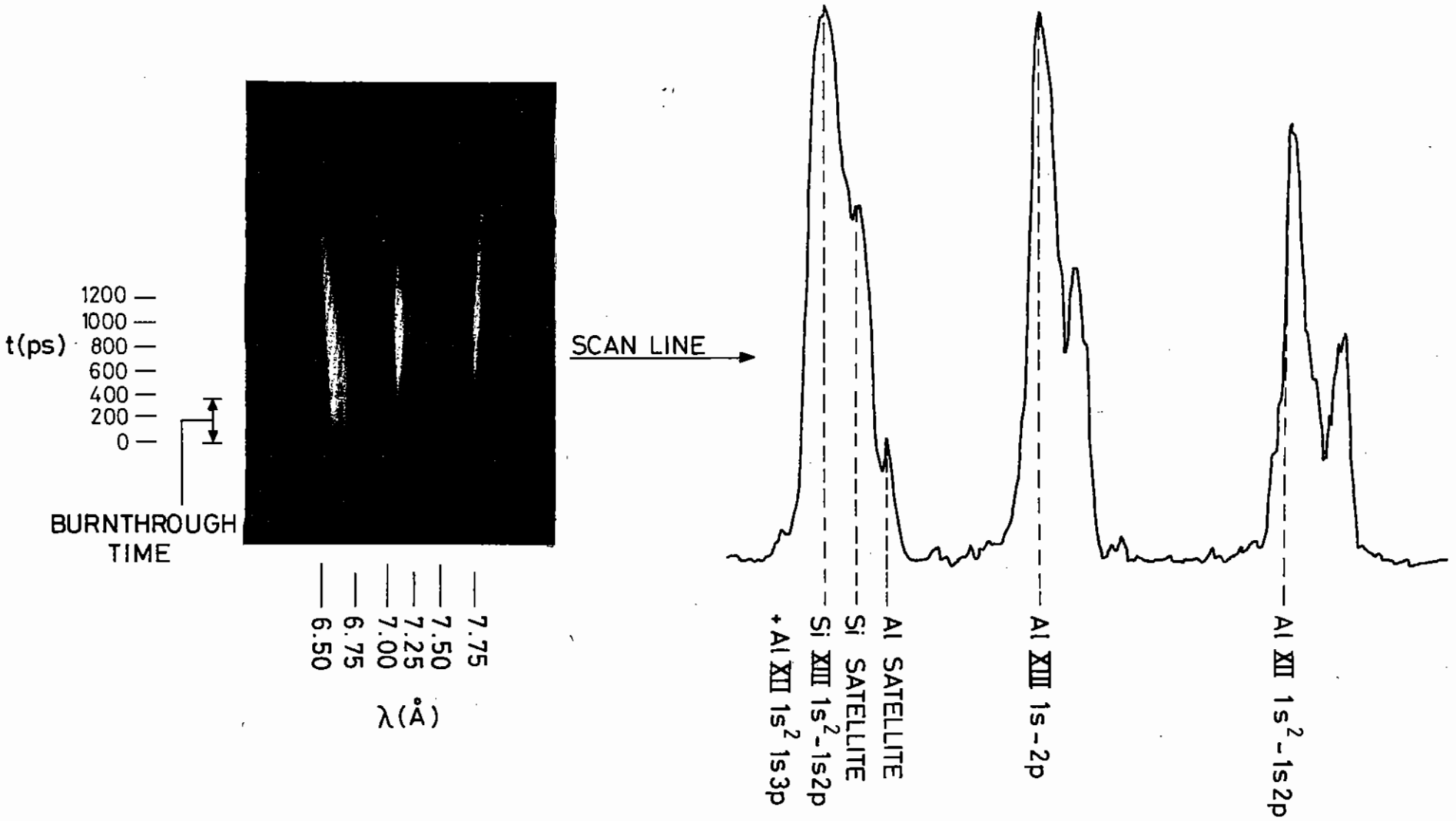

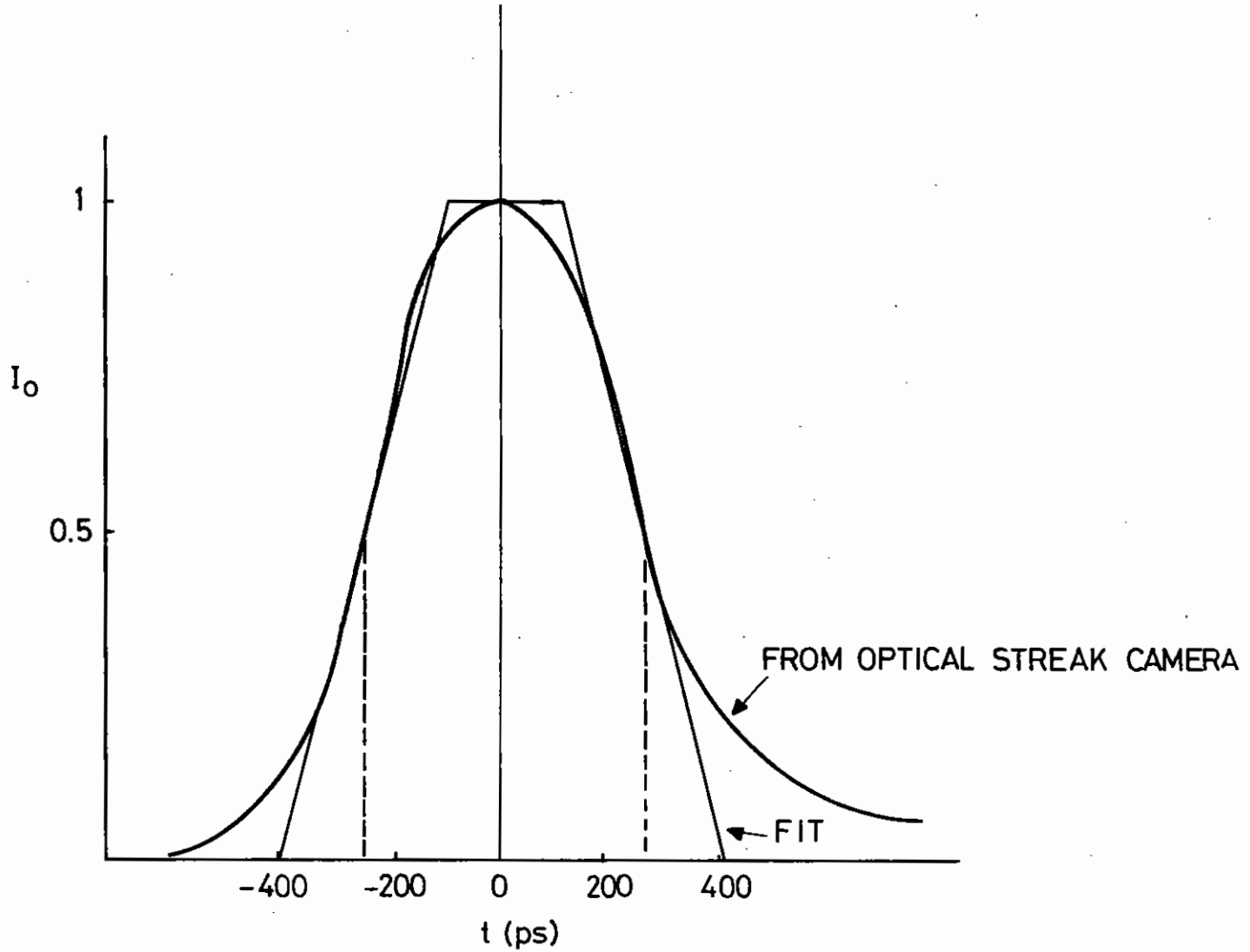

FIG.4.11 0.53 μm LASER PULSE SHAPE

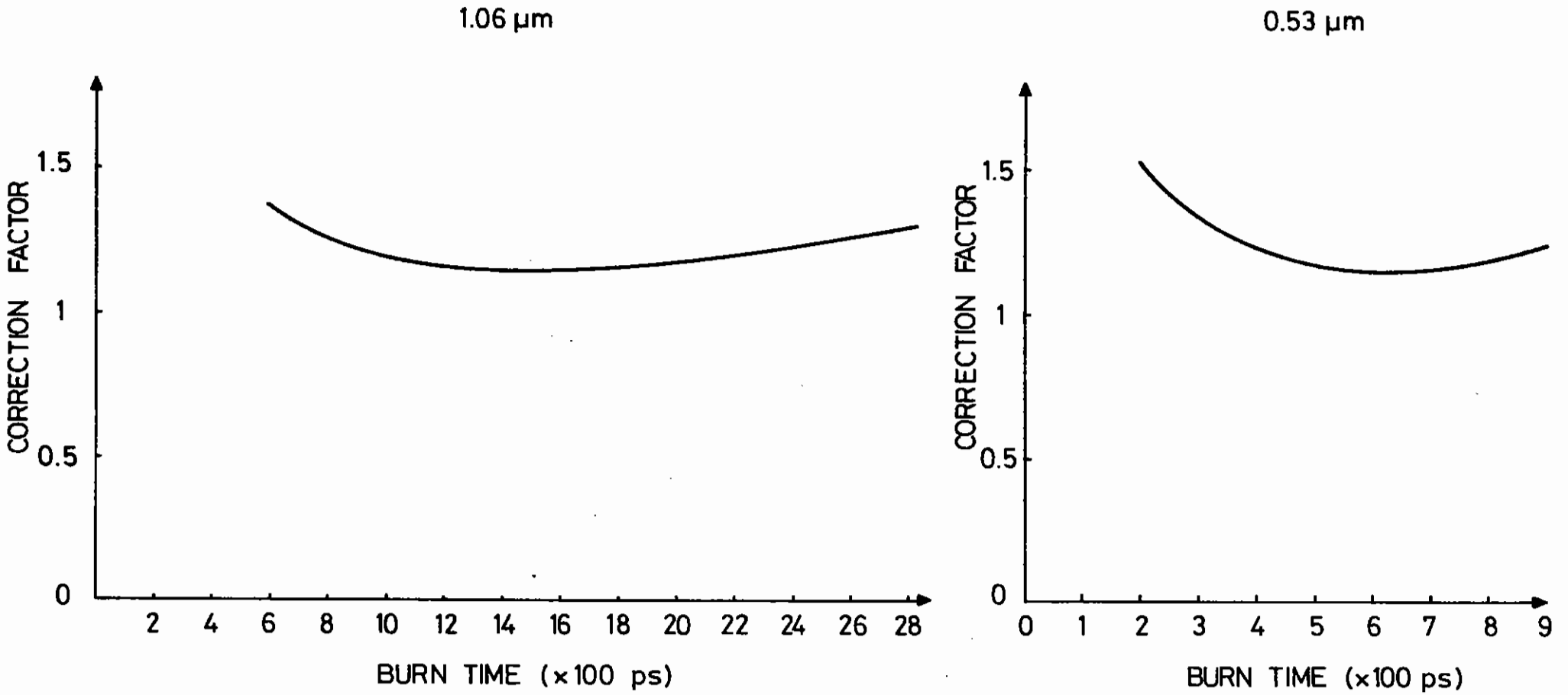

FIG 4.12 $\dot{m}$ CORRECTION FACTORS FOR PULSE SHAPE

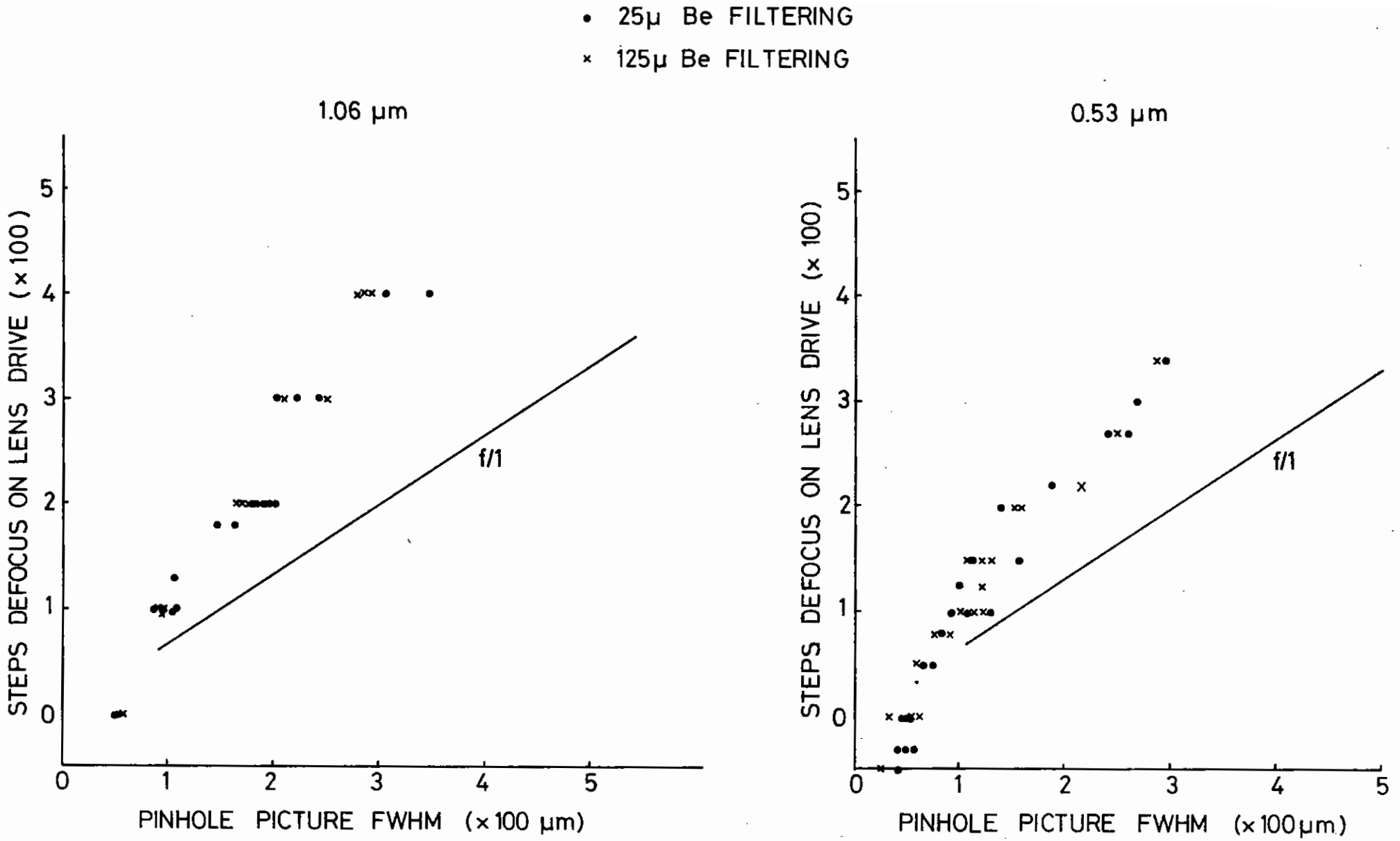

FIG 4·13 DEFOCUS V MEASURED PINHOLE CAMERA PICTURE FWHM

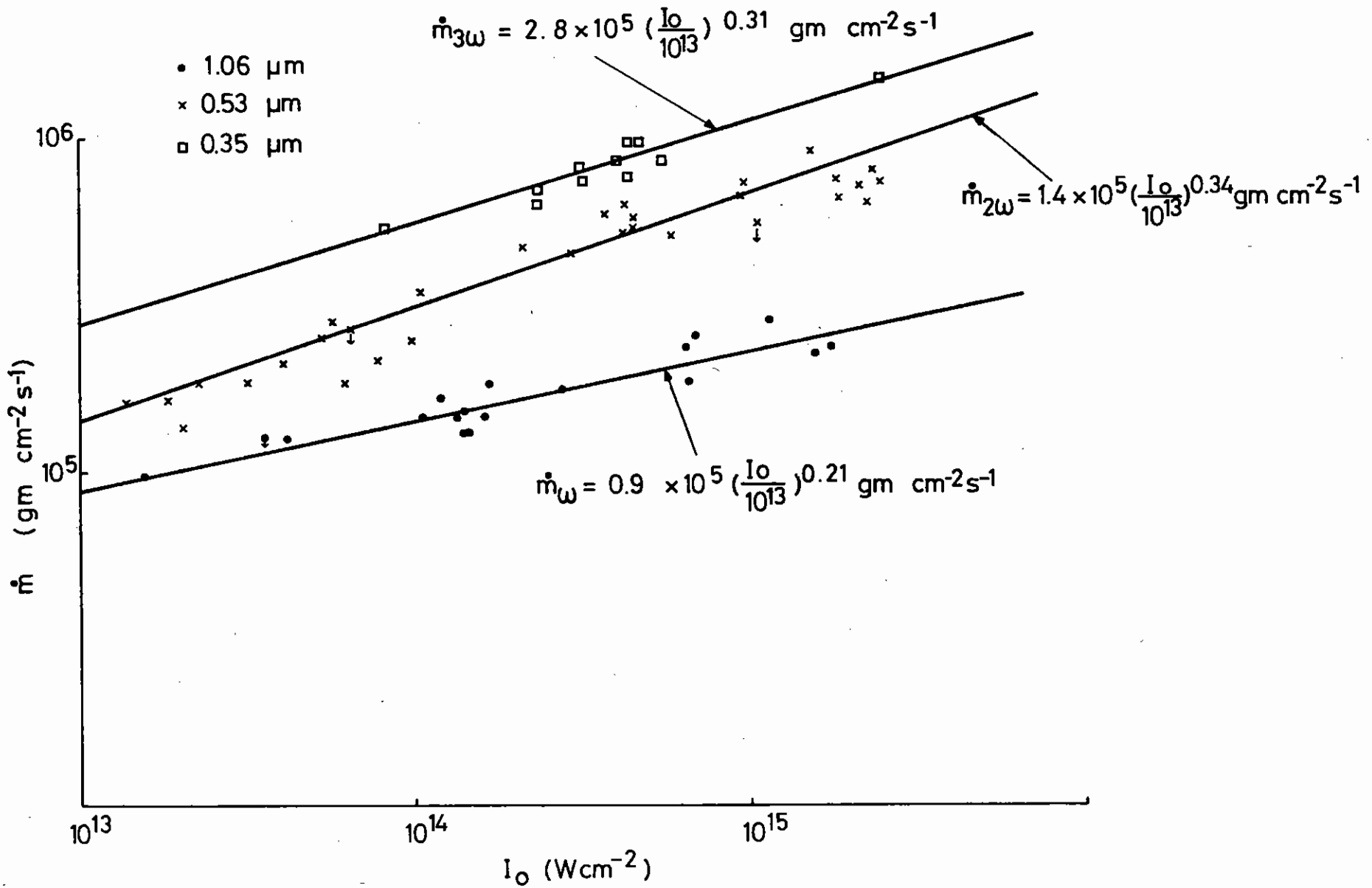

FIG 4.14 $\dot{m}$ V INCIDENT INTENSITY

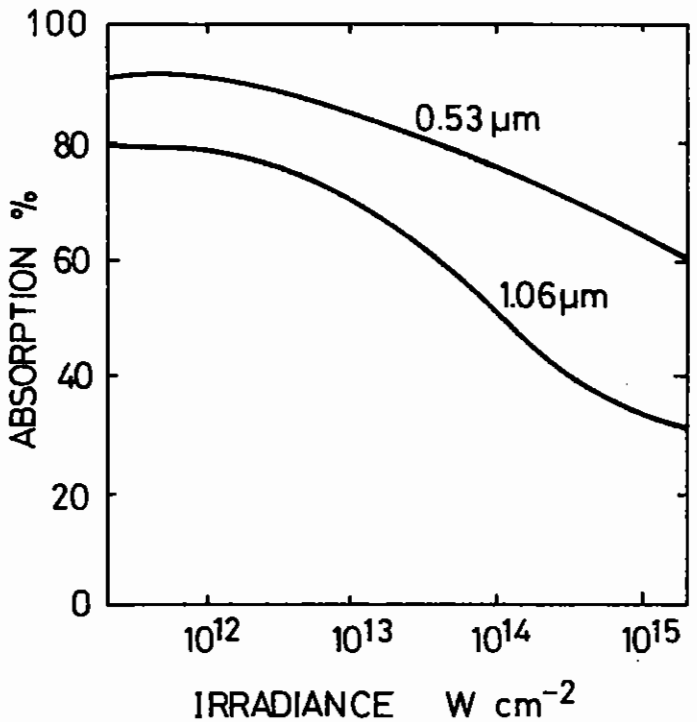

Figure 4.15 Absorption fractions for λ = 1.05 µm and 0.53 µm based on compiled experimental data for plane targets irradiated with nanosecond pulses.

FIG 4.16 SPECIFIC MASS ABLATION RATE Vs ABSORBED INTENSITY

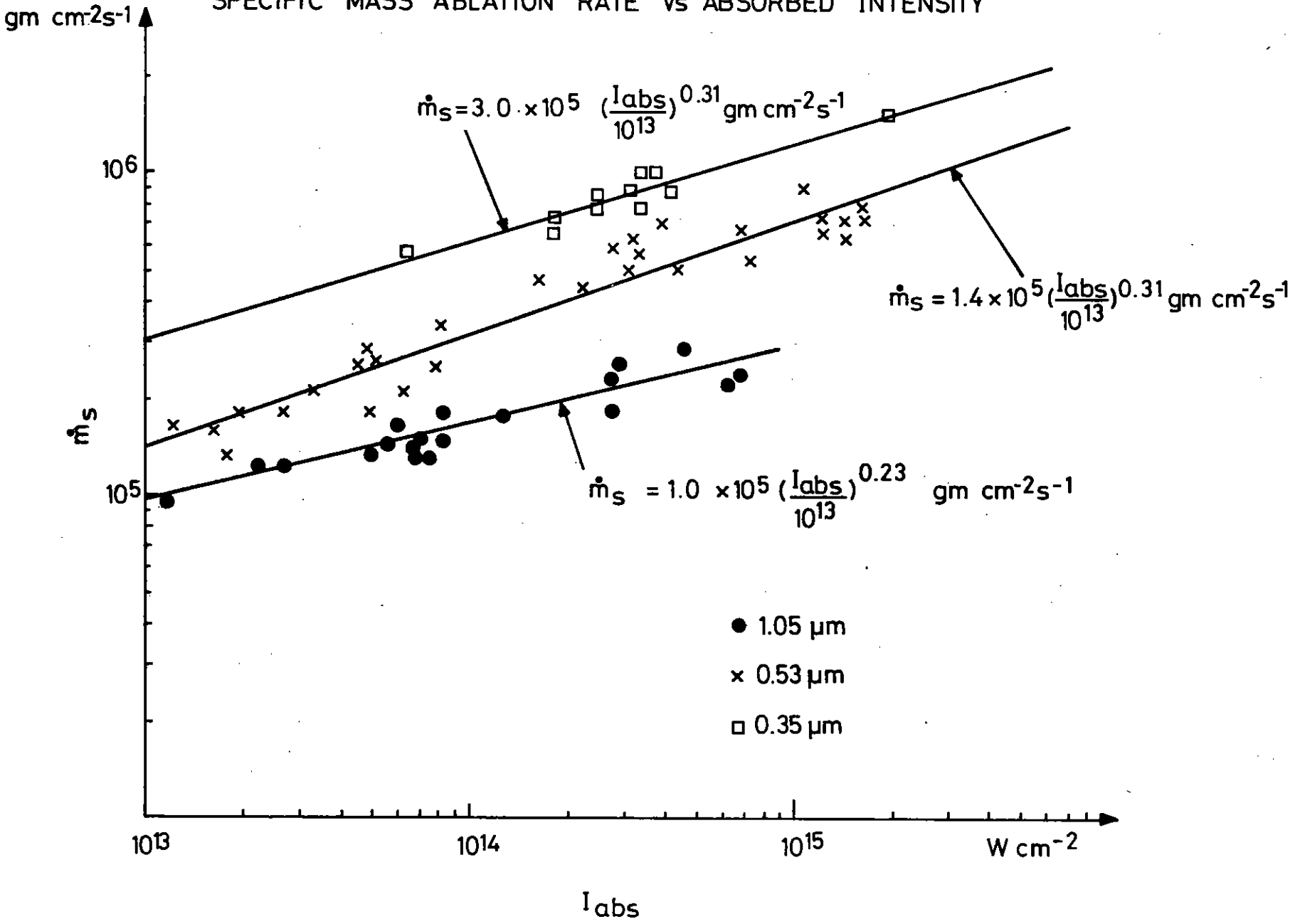

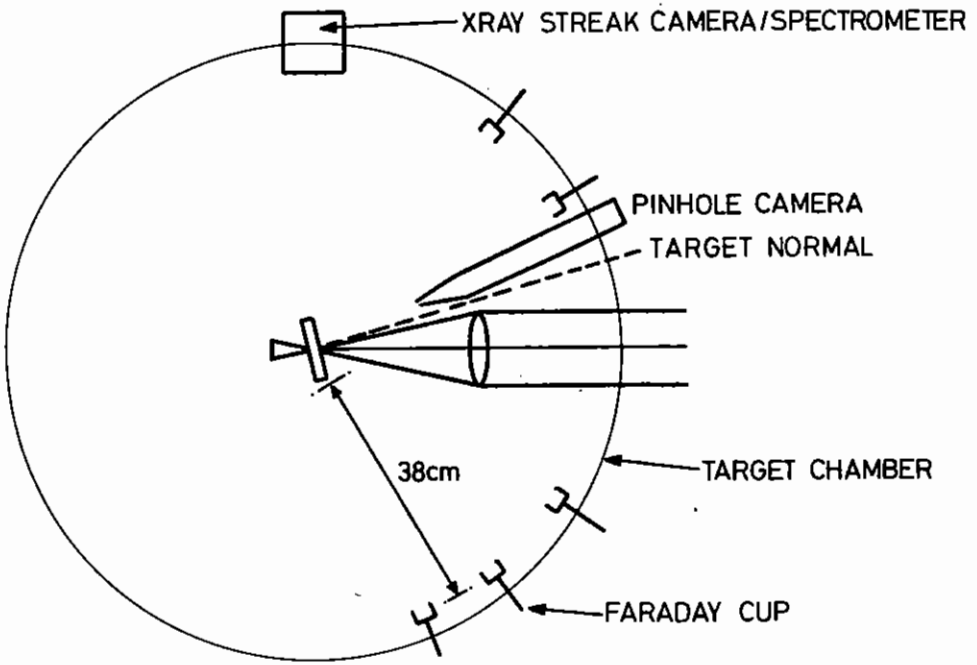

Figure 4.17 Schematic diagram of Faraday cup arrangement.

A least squares fit to the data at 1.06 μm is

$$\dot{m}_s = 0.88 \times 10^5 \left(\frac{I}{10^{13}\ W\ cm^{-2}}\right)^{0.21}\ gm\ cm^{-2}s^{-1}$$

whereas at $\lambda = 0.53$ μm the best fit is

$$\dot{m}_s = 1.4 \times 10^5 \left(\frac{I}{10^{13}\ W\ cm^{-2}}\right)^{0.34}\ gm\ cm^{-2}s^{-1}$$

and at 0.35 μm the best fit is

$$\dot{m}_s = 2.8 \times 10^5 \left(\frac{I}{10^{13}\ W\ cm^{-2}}\right)^{0.31}\ gm\ cm^{-2}s^{-1}$$

For comparison with theoretical models it is necessary to consider the absorbed laser flux. The absorption was not measured during this experiment, but the absorption figures from other laboratories can be used to scale our incident flux to absorbed fluxes as shown in Figure 4.15. The scaled data is shown in Figure 4.16. A least squares fit to the data gives

$$\dot{m}_s = 1.0 \times 10^5 \left(\frac{I_{abs}}{10^{13}\ W\ cm^{-2}}\right)^{0.24}\ gm\ cm^{-2}s^{-1}$$

at 1.06 μm. At 0.53 μm

$$\dot{m}_s = 1.4 \times 10^5 \left(\frac{I_{abs}}{10^{13}\ W\ cm^{-2}}\right)^{0.35}\ gm\ cm^{-2}s^{-1}$$

and at 0.35 μm

$$\dot{m}_s = 3.0 \times 10^5 \left(\frac{I_{abs}}{10^{13}\ W\ cm^{-2}}\right)^{0.31}\ gm\ cm^{-2}s^{-1}$$

4.4.3 Ion Measurements at the Rutherford Laboratory

During the mass ablation rate experiments mentioned above, the ion fluxes were monitored using Faraday Cups placed at a distance of 38 cm from the target at a variety of angles between 0° and 90°, as shown in Figure 4.17. The chamber pressure was typically 8.10^{-5} torr.

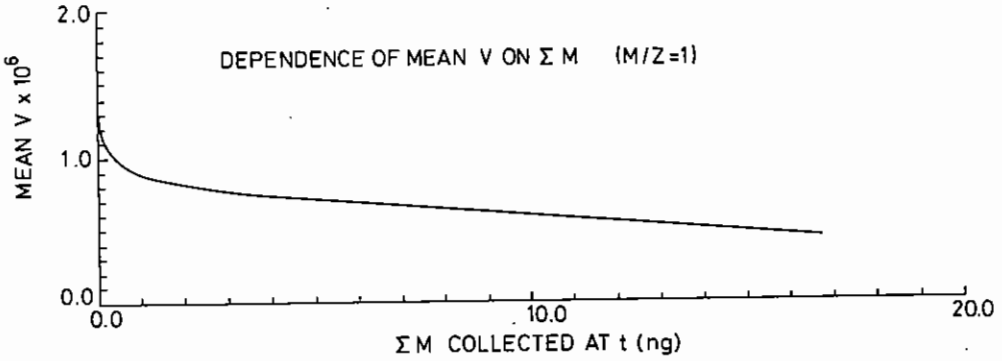

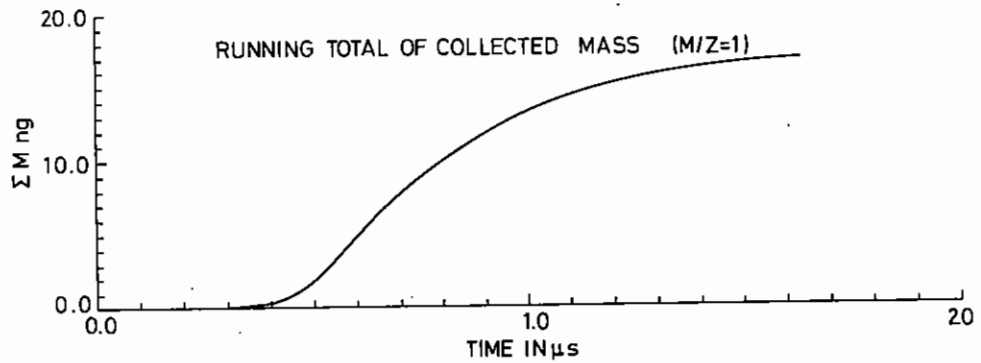

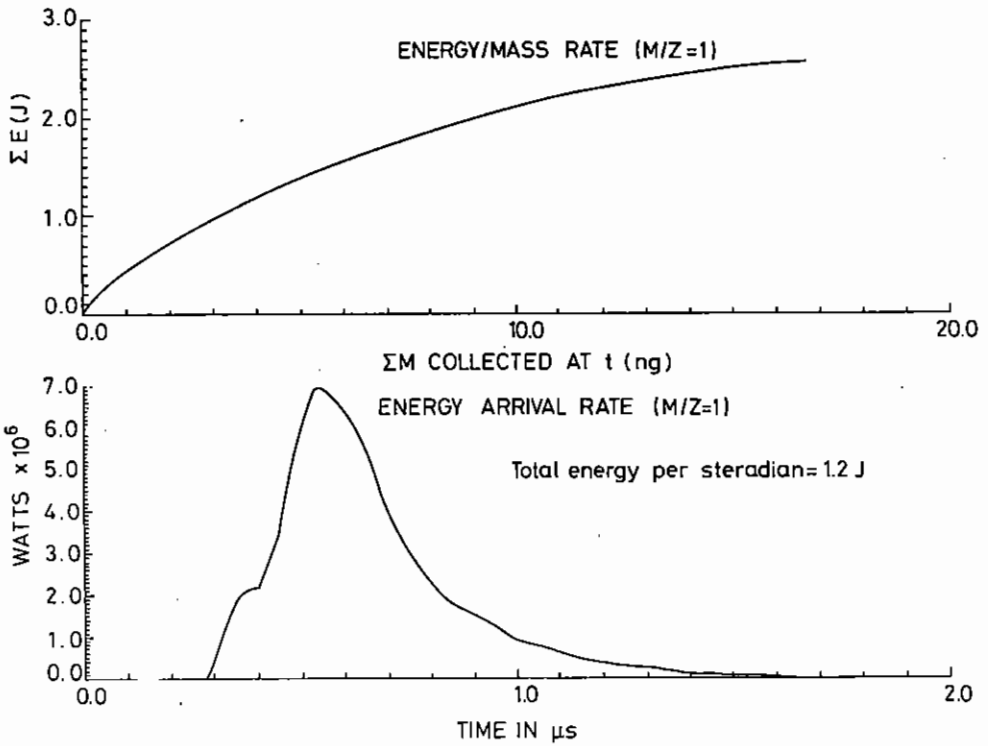

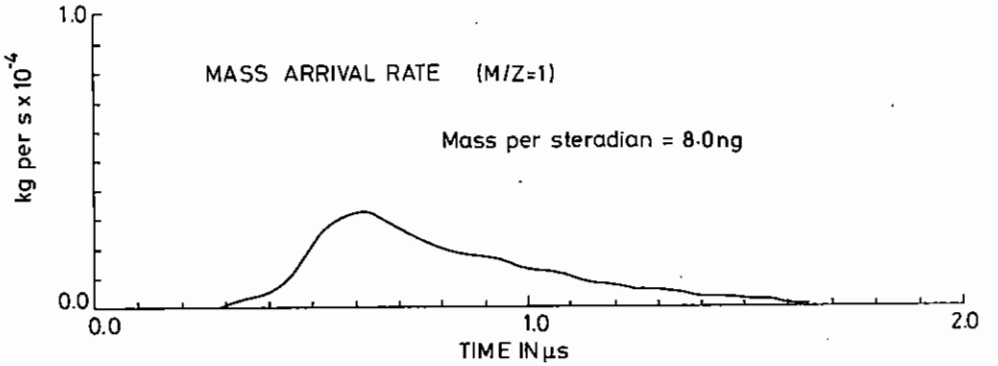

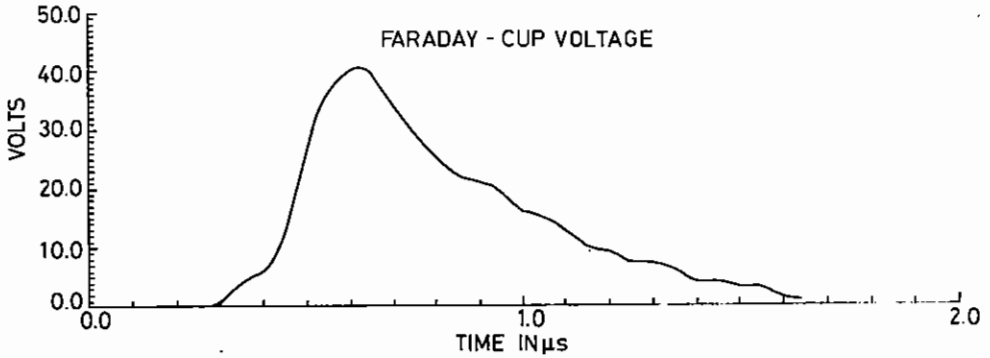

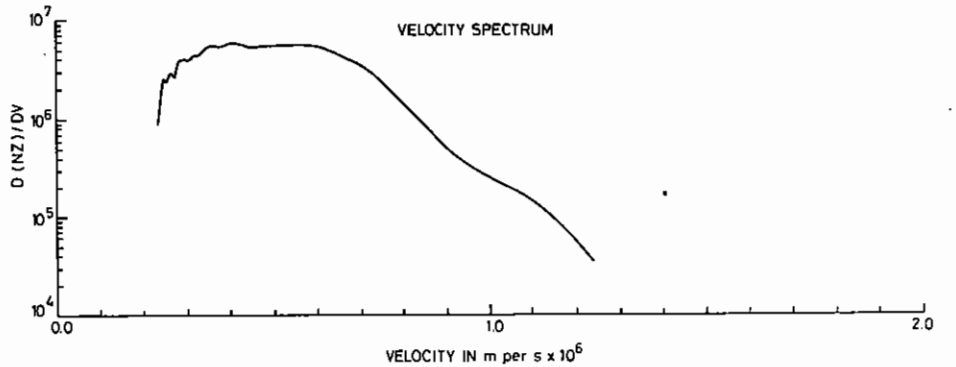

FIG 4.18 Analysis of Faraday cup data.

A typical ion trace and various quantities derived from it on the assumption of a constant mass to charge ratio (taken as 1.0 for convenience) are shown in Figure 4.18.

Ion velocities corresponding to the peak in the cup voltage curve were obtained for the intensity and wavelength parameter scan described above (4.4.2) and the values of V_{peak} are shown plotted against the absorbed intensity in Figures 4.19, 4.20 and 4.21. Least squares fits to the data give

$$V_{peak} = 5.4 \times 10^7 \left(\frac{I_{abs}}{10^{13} \text{ W cm}^{-2}} \right)^{0.0} \text{cm s}^{-1} \qquad (1.05 \ \mu\text{m})$$

$$V_{peak} = 4.5 \times 10^7 \left(\frac{I_{abs}}{10^{13} \text{ W cm}^{-2}} \right)^{0.11} \text{cm s}^{-1} \qquad (0.53 \ \mu\text{m})$$

$$V_{peak} = 4.2 \times 10^7 \left(\frac{I_{abs}}{10^{13} \text{ W cm}^{-2}} \right)^{0.06} \text{cm s}^{-1} \qquad (0.35 \ \mu\text{m})$$

The remarkable feature of these results is the absence of any substantial dependence on intensity. We will see (in 4.4.4 below) that V_{peak} depends on both spot size and intensity in such a way that it is very nearly constant at constant laser power.

In order to get a better understanding of this result we have made a rough comparison of the total mass represented by the ion cup data, M_{FC}, with the ablated mass implied by the X-ray burn-rate results of the previous section, $M_{X\text{-ray}} = \dot{m}_s A\tau$, where A is the area of the focal spot and τ is the laser pulse length. An angular integration must be made. The angular distribution from one shot where the target normal was tilted at 25° to the laser axis is shown in Figure 4.22. Data from other shots in this experiment and from the runs at Belfast (4.4.4) show no strong dependence of the angular distribution on shot parameters and so that ion cup data from the whole experiment can be used we have made all angular integrations using the $\cos^3(1.32\theta)$ distribution suggested by Leppelmeier (4.23). This distribution is also shown in Figure 4.22. The spot size dependence of the ratio $M_{FC}/M_{X\text{-ray}}$ is shown in Figure 4.23, where the mass-to-change ratio is still taken as 1.0. There is clearly a strong dependence on spot size and when allowance is made for a

realistic mass per unit change, the data at small spot size show that the Faraday cups detect much more mass than is ablated fromthe smallest focal spots.

We attribute the variation in the ratio $M_{FC}/M_{X\text{-ray}}$ with spot size to geometrical effects associated with the radial transport of energy from the focal spot. In the limit of large spot sizes, where the irradiance in this experiment is less than 10^{13} W cm^{-2}, directly ablated ions make up the whole signal and V_{peak} is the ablation velocity but, for very small spots, slow ions from a relatively cool annulus around the focal spot dominate the signal and depress the value of V_{peak}. If this is the case (see also section 4.4.5), we can obtain an approximate upper limit for the velocity of the directly ablated ions assuming them to be the fastest and integrating the signals up to the point at which the normalised collected mass equals the ablated mass, $M_{X\text{-ray}}$. These velocities are shown in Figures 4.24 and 4.25 for 1.05 μm and 0.53 μm respectively. Figure 4.24 also shows the ratio of the normalised total collected mass to the mass ablated from the focal spot $M_{FC}^{'}/M_{X\text{-ray}}$.

The scaling is seen to be

$$\overline{V}_{spot} = 5.2 \times 10^7 \left(\frac{I_{abs}}{10^{13} \text{ W cm}^{-2}} \right)^{0.14} \text{cm s}^{-1} \qquad (1.05 \ \mu\text{m})$$

$$\overline{V}_{spot} = 3.6 \times 10^7 \left(\frac{I_{abs}}{10^{13} \text{ W cm}^{-2}} \right)^{0.22} \text{cm s}^{-1} \qquad (0.53 \ \mu\text{m})$$

4.4.4 Ion Velocity Measurements at Queen's University, Belfast

Experiments were carried out at Queen's University, Belfast to resolve some questions arising from ion velocity measurements during mass ablation rate runs at the Central Laser Facility. The latter measurements, made on plane layered targets, indicated a strong saturation of ion velocity at a level of $\sim 5 \times 10^7$ cm sec^{-1} which was apparently independent of irradiance above 10^{13} W cm^{-2} when the spot size was varied at constant laser power.

FIG 4.19
VARIATION IN ION VELOCITY (Vp) WITH ABSORBED IRRADIANCE FOR PLANE TARGETS. 1.05μm LIGHT

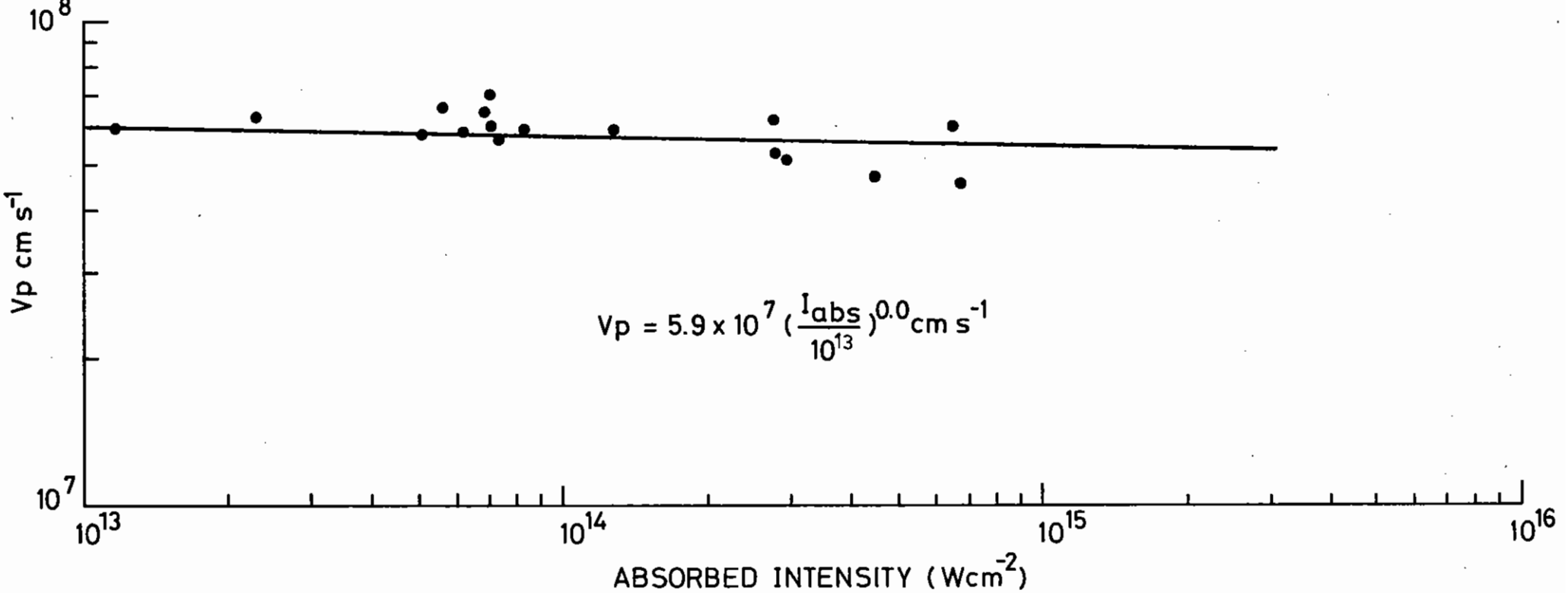

FIG 4.20
VARIATION OF ION VELOCITY (Vp) WITH ABSORBED IRRADIANCE. PLANE TARGET, 0.53μ LIGHT

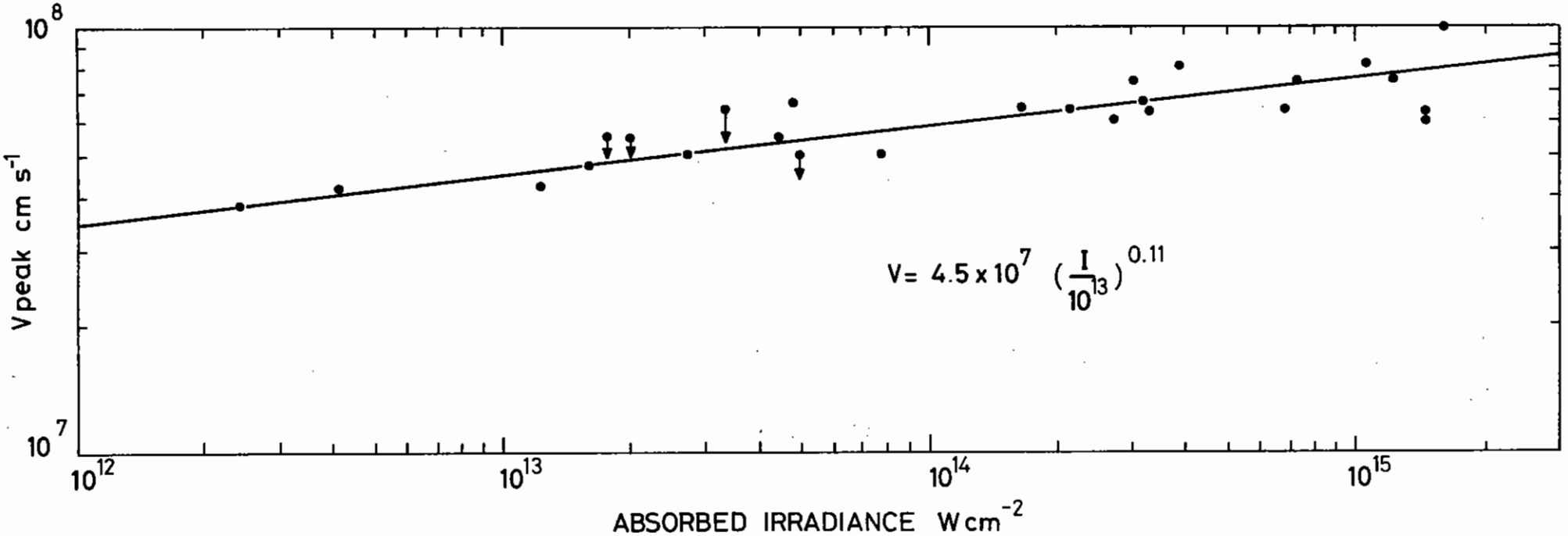

A 10 J, 1.7 nsec (FWHM), 1.06 μm laser pulse was used to irradiate flat targets. Lenses with focal lengths ranging from 75 mm to 2000 mm were used to focus the 50 mm diameter beam on target, to give optical spot diameters from 30 μm to 660 μm. For two shots the 2 metre lens was defocused to give a spot diameter of 3.5 mm. Irradiance on target was varied at constant spot size by inserting calibrated glass filters in the main beam. The incident beam was vertically polarised.

Ion velocities were recorded using six time-of-flight Faraday cup collectors arrayed in the horizontal plane from 10° to 80° to the target normal and at distances of 40 cm from the plasma. The laser was incident normal to the target surface, except for the smallest spot measurements (30 μm) where the target was angled at 45° to the laser allow the cups to record at angles of 0 - 80° from the target normal.

Incident energy on target was measured with an integrating photodiode sampling the main beam which was calibrated against a calorimeter placed inside the target chamber. The focal spot size was measured in an equivalent plane monitor. Direct measurement of the large spots was possible by placing a 1Z plate at the target position.

Ion velocities were calculated from the arrival time of the peak ion current. Polar ion velocity plots were extrapolated to determine the ion velocity normal to the target surface. These ion velocities were then plotted against irradiance for each spot size (Figure 4.26). This data refers to massive specularly reflecting aluminium targets. Occasional shots on plastic (melinex) targets during the parameter scans showed no significant difference in measured velocities. Figure 4.26 shows the normal ion velocity against irradiance. In all cases it scales as $I^{0.2}$ for a fixed spot size. Using these curves and an extrapolation for the ϕ_s = 3.5 mm data assuming the same $I^{0.2}$ scaling it is possible to plot the normal velocity as a function of spot diameter, ϕ_s, for a fixed irradiance. Figure 4.27 shows this for $I = 10^{12}$ W cm^{-2} and it is found that $v \propto \phi_s^{0.25}$. In absolute terms the velocity scaling is

$$v_{peak} = 5 \times 10^7 \left(\frac{I_{abs}}{10^{13}\ \text{W cm}^{-2}}\right)^{0.2} \left(\frac{\phi_s}{200\ \mu\text{m}}\right)^{0.25} \text{cm s}^{-1}$$

which is almost independent of irradiance at constant laser power.

Integrating the quantity $\frac{1}{2}N_i m_i v_i^2$ over solid angle gives the energy content in the ion flow where N_i is the number of ions detected per unit solid angle, m_i is the ion mass, v_i is the ion velocity and N_i and v_i are functions of angle. Evaluation of this integral assuming a M/Z ratio of 2.6 (ie average ion charge of 10) shows agreement with the absorbed laser energy to within 20 % in all cases covered by the present parameter scan. This indicates that for $I < 2 \times 10^{14}$ W cm^{-2} there is no evidence for large energy losses in well defined narrow fast ion jets (4.32) which might have missed the detectors. As a corollary to this observation it is found that the specific ablated mass scales as $I^{0.6}$ for a fixed spot size since $\frac{1}{2} M_{TOT} v_i^2 = E \propto I A\tau_L$. The dependence of ion velocity on optical spot size, apparently without any saturation up to ϕ_s = 3.5 mm, suggests that the ion source area and the optical spot area are not the same (see section 4.4.5). Further analysis of the data should yield the angular spread in the ion flow which should give an indication of the size of the ion source when compared to 2D codes (ie small sources will give a more spherical flow and large sources a more planar flow).

A further feature seen in the ion traces is that cups placed at 70° - 90° from the target normal show a faster group of ions than those discussed above. These ions have velocities typically 2 to 3 times faster than the 'thermal' ions in the same direction. At angles of 70° - 90° the numbers of ions in each group are comparable, but the fast component is rapidly swamped out at smaller angles. For the smallest spot size (30 μm) this fast group of ions carries 10 % of the energy but this fraction reduces rapidly with increasing spot size. It is suggested that these fast ions originate from the central hot region and have a more spherical distribution but that the bulk of the ions are produced in a more planar flow as thermal conduction causes the effective area of the ion source greatly to exceed the area of the focal spot.

4.4.5 Discussion of Plane Target Mass Ablation Data

We begin by reviewing steady state models in section 4.4.5(a) and discuss

FIG 4.21
VARIATION OF ION VELOCITY (Vp) WITH ABSORBED IRRADIANCE. PLANE TARGET, 0.35μ LIGHT

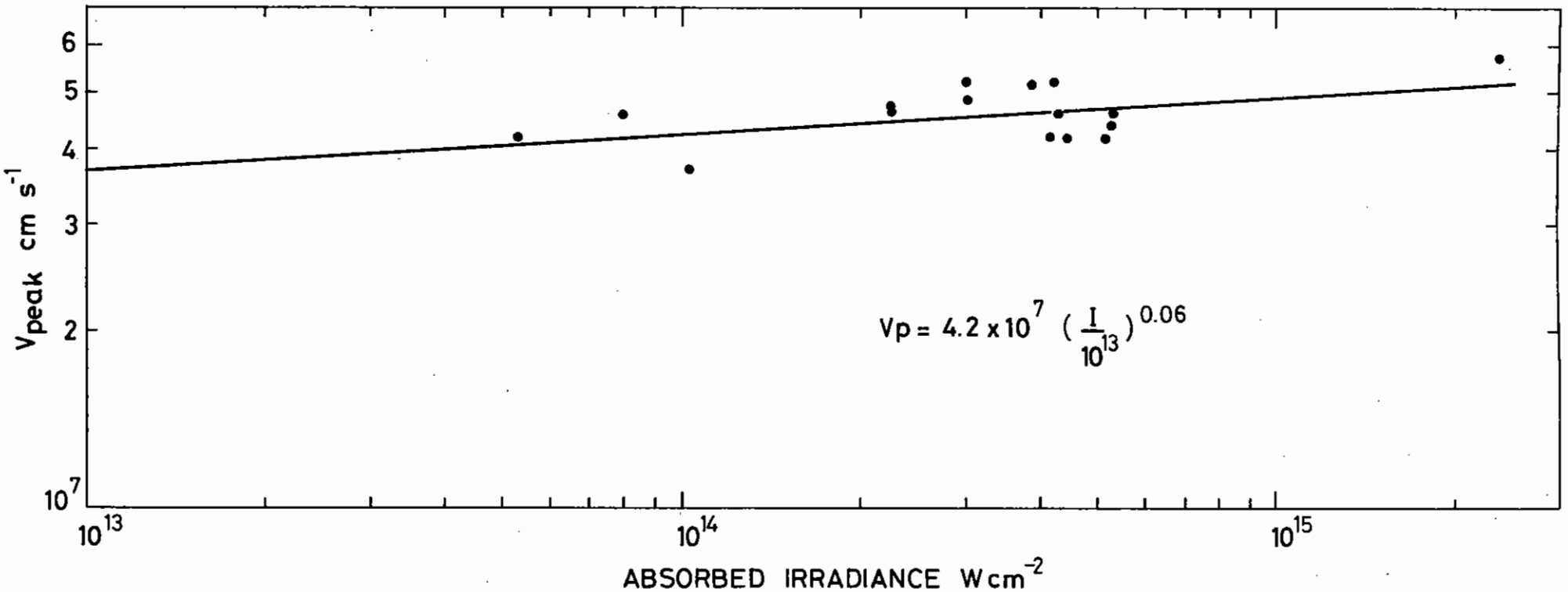

FIG 4.22
VARIATION IN RECOVERED ENERGY PER STERADIAN WITH ANGLE

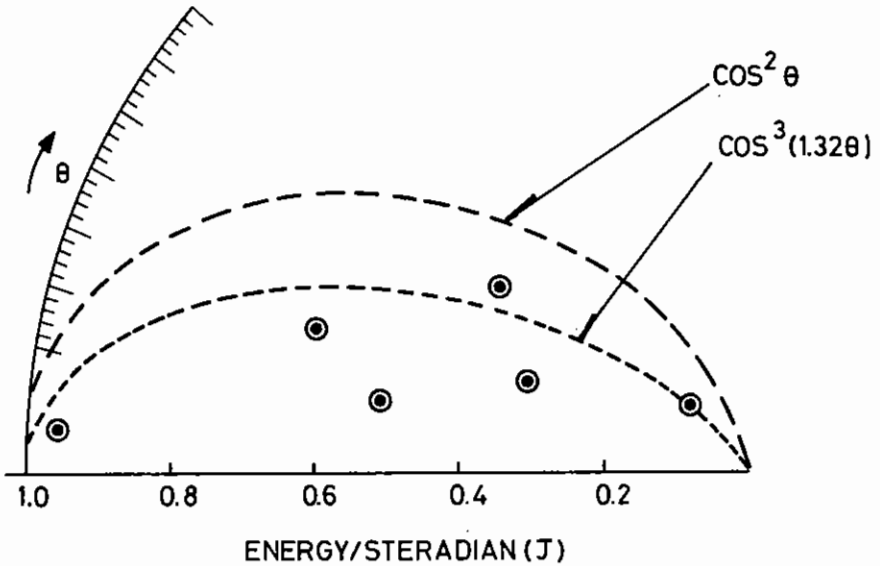

transient effects in 4.4.5(b). Comparison with the plane target data in section 4.4.5(c) shows evidence for lateral spreading of the absorbed energy. Finally, in section 4.4.5(d), various estimates of ablation pressure are made.

4.4.5(a) Scaling Laws for Steady State Ablation

In a simple rocket model in planar geometry when the specific mass ablation rate $\dot{m}_s$ is constant, energy conservation requires

$$\tfrac{1}{2}\,\dot{m}_s\,\bar{v} = I_{abs} \qquad (1)$$

where I_{abs} is the absorbed irradiance. Momentum conservation gives the ablation pressure P_a:

$$P_a = \dot{m}_s\,\bar{v} \qquad (2)$$

or, from equations (1) and (2),

$$P_a = (2\,\dot{m}_s\,I_{abs})^{\frac{1}{2}} \qquad (3)$$

These relationships assume that all absorbed laser energy is transformed into ablation kinetic energy without significant loss to radiation or 'fast' ions and electrons.

In principle, therefore, the ablation pressure can be deduced from momentum conservation given $\dot{m}_s$ and I_{abs}.

The scaling of $\dot{m}_s$, v and P with absorbed irradiance, I_{abs}, and laser wavelength, λ, can be deduced with appropriate assumptions.

If the sonic point in the ablation flow is taken as a point of reference to define ablation velocity, v_a, density, ρ_a, temperature, T_a, and enthalpy, h_a, then conservation of energy, mass and momentum give

FIG 4.23
VARIATION IN MASS RATIO WITH SPOT SIZE
FOR PLANE TARGET AT 0.53μ (M/Z =1)

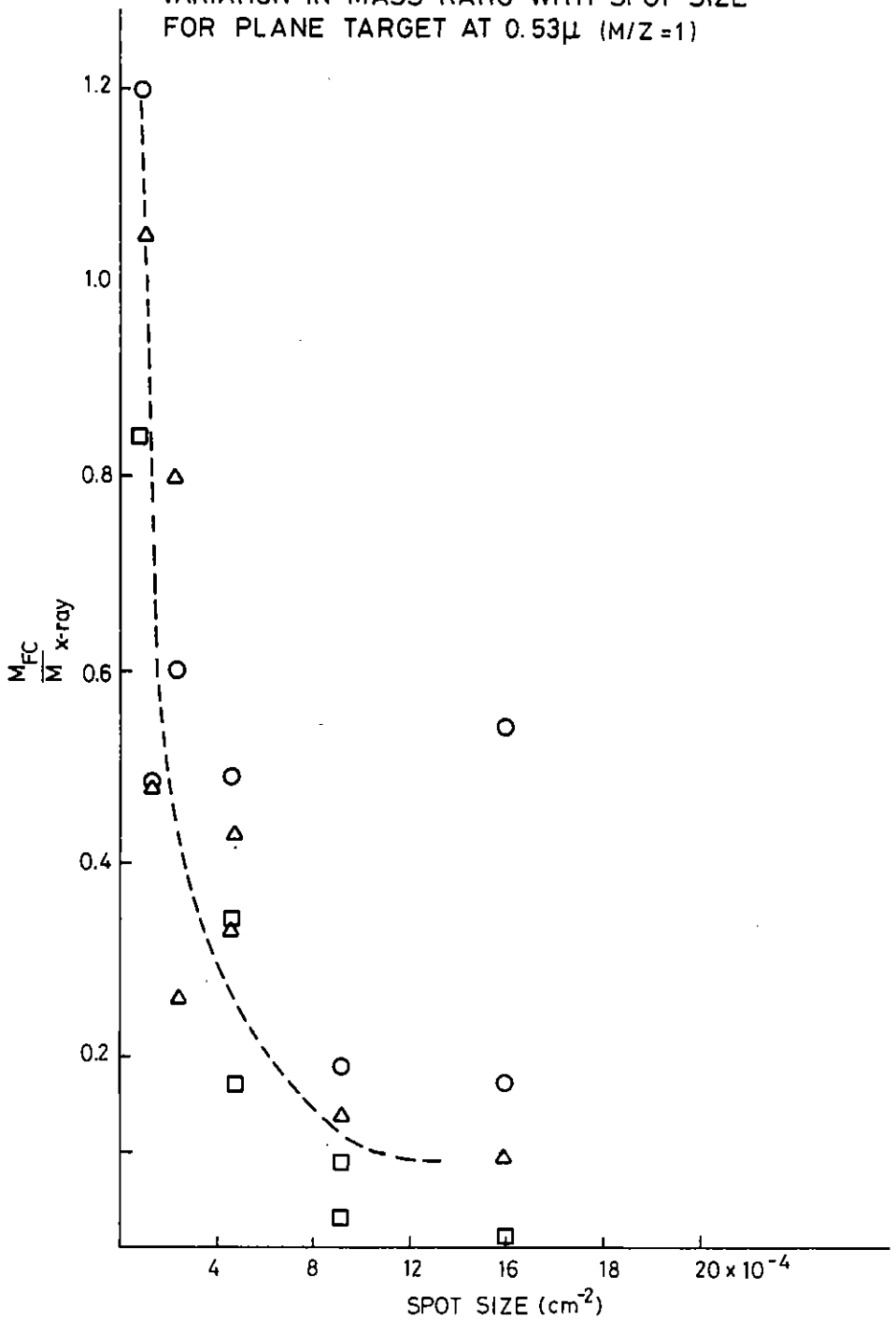

$$\left.\begin{aligned} I_{abs} &= \tfrac{1}{2}\rho_a v_a^2 + h_a \rho_a v_a \\ P &= \rho_a v_a^2 + nkTa \\ \dot{m}_s &= \rho_a v_a \end{aligned}\right\} \quad (4)$$

while from the definition of the sonic point

$$\left.\begin{aligned} v &= \left(\frac{\gamma nkT_a}{\rho_a}\right)^{\frac{1}{2}} \\ h_a &= \left(\frac{\gamma}{\gamma-1}\right)\frac{nkT_a}{\rho_a} \end{aligned}\right\} \quad (5)$$

It follows from equations (4) and (5) that scaling behaviour is of the form

$$\left.\begin{aligned} I_{abs} &\propto \rho_a v_a^3 \\ P_a &\propto \rho_a v_a^2 \\ \dot{m} &\propto \rho_a v_a \end{aligned}\right\} \quad (6)$$

A useful approximation is obtained by assuming that $\rho_a = \rho_c$ where the critical density ρ_c is given by

$$\rho_c = 3.3 \times 10^{-3} \left(\frac{\lambda}{1\mu m}\right)^{-2} \quad (7)$$

This leads to well known results (4.24) for steady state ablation which can be written

$$\left.\begin{aligned} \dot{m} &= 0.8 \times 10^{5} \left(\frac{\lambda}{1\mu m}\right)^{-4/3} \left(\frac{I_{abs}}{10^{13}\ W\ cm^{-2}}\right)^{1/3} && g\ cm^{-2}\ s^{-1} \\ \bar{v} &= 4.1 \times 10^{7} \left(\frac{\lambda}{1\mu m}\right)^{-2/3} \left(\frac{I_{abs}}{10^{13}\ W\ cm^{-2}}\right)^{1/3} && cm\ s^{-1} \\ P_a &= 3.2 \left(\frac{\lambda}{1\mu m}\right)^{-2/3} \left(\frac{I_{abs}}{10^{13}\ W\ cm^{-2}}\right)^{2/3} && M_{bar} \end{aligned}\right\} \quad (8)$$

The density at the sonic point tends to be increased by thermal conduction which becomes more effective at high irradiance and temperature. The effect on scaling behaviour may be assessed qualitatively by assuming that

FIG 4.24
VARIATION IN MASS RATIO AND ION VELOCITY WITH ABSORBED INTENSITY, PLANE TARGETS, 1.05μm LIGHT

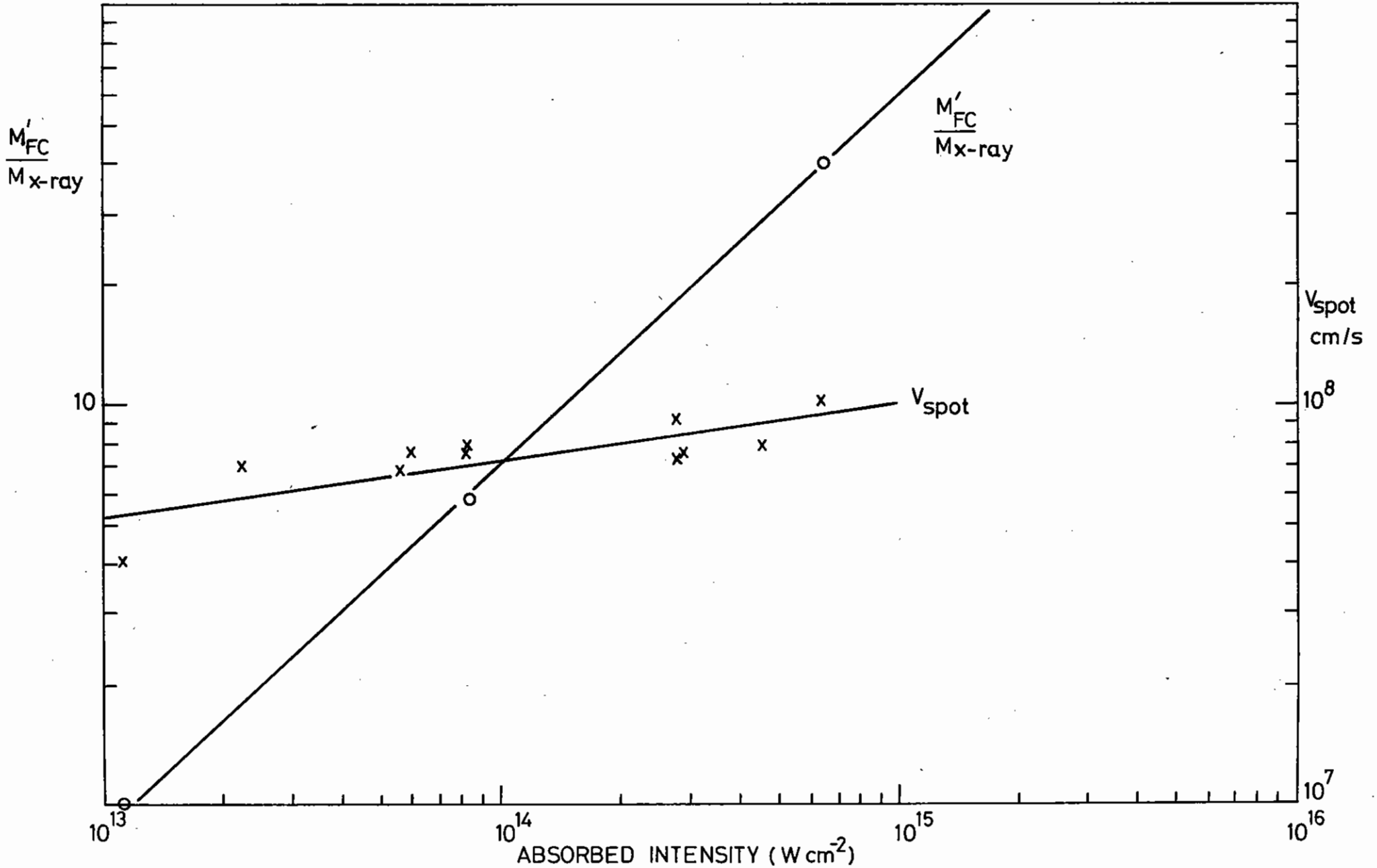

FIG 4.25
VARIATION IN ION VELOCITY WITH ABSORBED INTENSITY. PLANE TARGETS, 0.53μm LIGHT

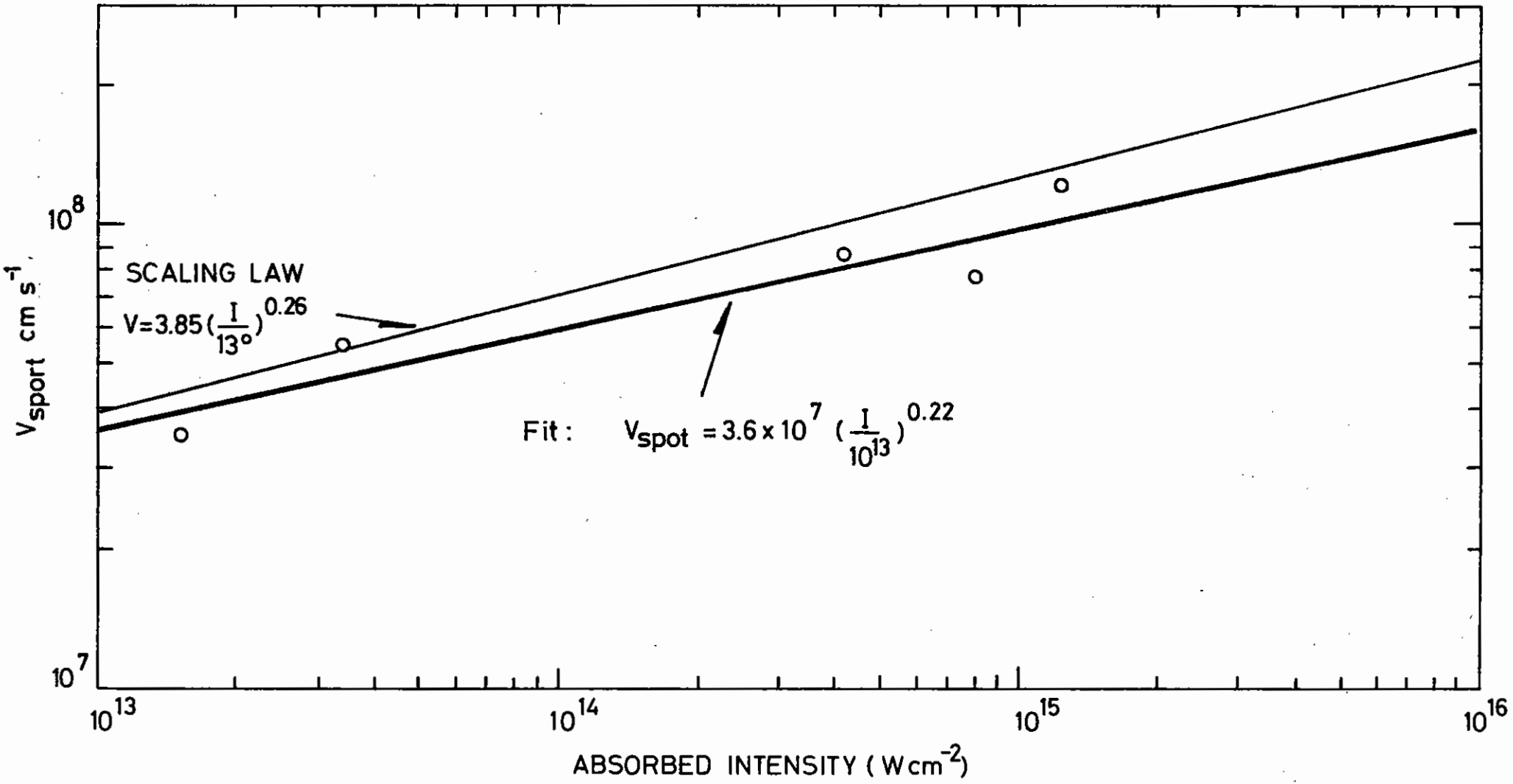

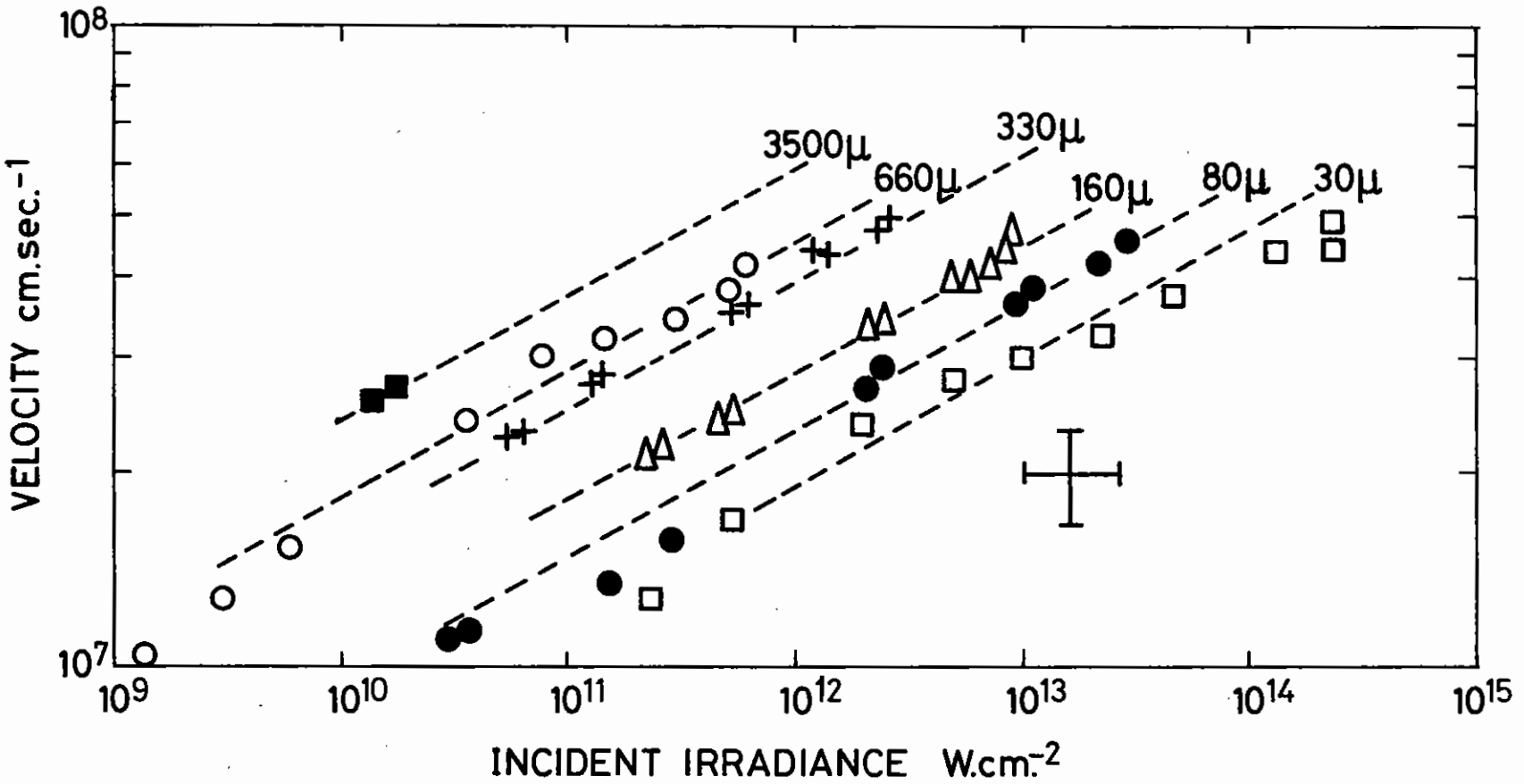

Figure 4.26 Dependence of ion velocity on irradiance and focal spot size.

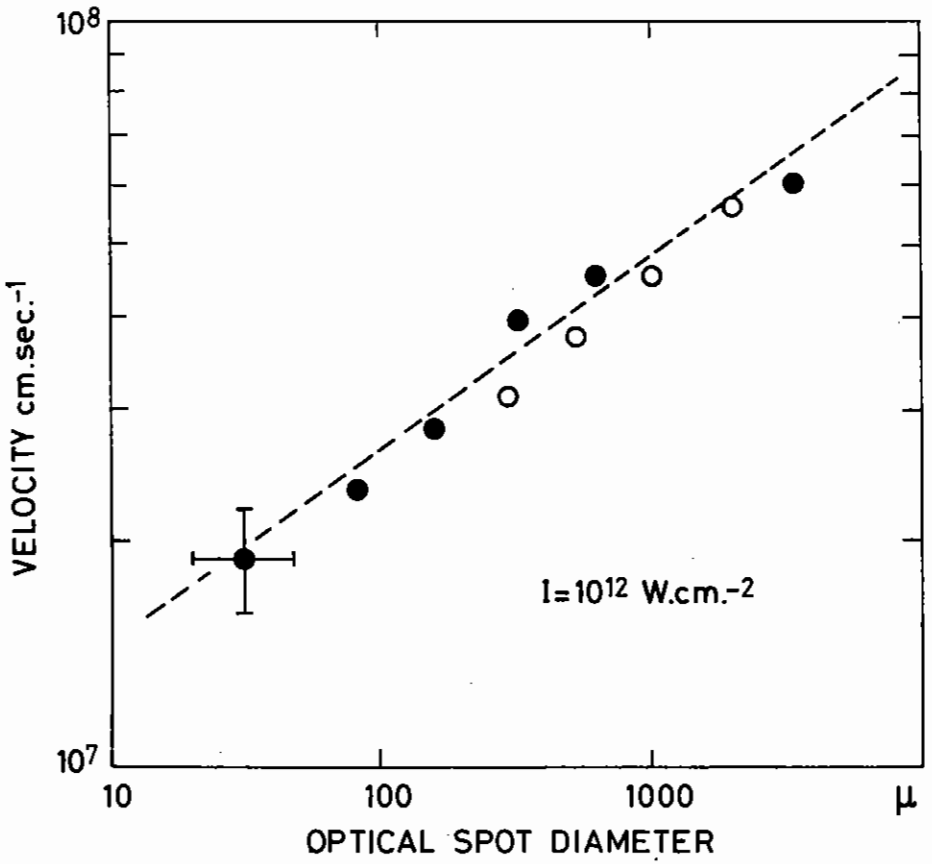

Figure 4.27 Dependence of ion velocity on spot diameter at constant irradiance.

for $I_a = I_{ao}$, $\rho_a = \rho_c (I_{abs}/I_{ao})^x$ which results (cf equations (5) and (8)) in scaling of the form

$$\left.\begin{array}{lcll} \dot{m} & \propto & I_{abs}^{(1+2x)/3} & \lambda^{-4/3} \\ \bar{v} & \propto & I_{abs}^{(1-x)/3} & \lambda^{2/3} \\ P_a & \propto & I_{abs}^{2(1+x)/3} & \lambda^{-2/3} \end{array}\right\} \quad (9)$$

Thus the effect of increasing thermal conduction is to depress the slope exponent of $\bar{v}$ with I_{abs} but conversely to increase the slope of $\dot{m}_s$ with I_{abs} by double the amount.

Such qualitative observations can be compared with a recent analytic treatment of steady state ablation in spherical geometry which includes thermal conduction (4.25). The radius R_a of the target enters the analytic expressions for the total mass ablation rate $\dot{M}$ and for $\bar{v}$ and P_a. For a flux limit of 3 % this model gives

$$\left.\begin{array}{lll} \dot{M} = 0.76 \times 10^4 \left(\frac{\lambda}{1\mu m}\right)^{-0.82} \left(\frac{I_{abs}}{10^{13}\ W\ cm^{-2}}\right)^{0.48} \left(\frac{R_a}{1mm}\right)^{1.89} & g\ s^{-1} \\ \bar{v} = 0.60 \times 10^6 \left(\frac{\lambda}{1\mu m}\right)^{0.41} \left(\frac{I_{abs}}{10^{13}\ W\ cm^{-2}}\right)^{0.26} \left(\frac{R_a}{1mm}\right)^{0.055} & cm\ s^{-1} \\ Pa = 1.9 \left(\frac{\lambda}{1\ m}\right)^{-0.99} \left(\frac{I_{abs}}{10^{13}\ W\ cm^{-2}}\right)^{0.57} \left(\frac{\bar{z}Ra}{1mm}\right) & M_{bar} \end{array}\right\} \quad (10)$$

There is a further complication which enters into the model through its assumption of steady state spherical flow, namely that the radius of the critical density surface, r_c, is a variable and can be significantly greater than R_a. Specifically,

$$r_c = 0.12 \left(\frac{Ra}{1mm}\right) \left(\frac{I_{abs}}{10^{13}\ W\ cm^{-2}}\right)^{0.11} \left(\frac{\lambda}{1mm}\right)^{0.38} \left(\frac{\bar{z}Ra}{1mm}\right)^{-0.08} cm \quad (11)$$

This more sophisticated ablation model can be related to the earlier discussion provided its mass ablation rate and absorbed irradiance are referred to the same area. I_a is defined in equations (10) and (11) by $P_L/4\pi R_a^2$ where P_L is the absorbed laser power. Examination of the

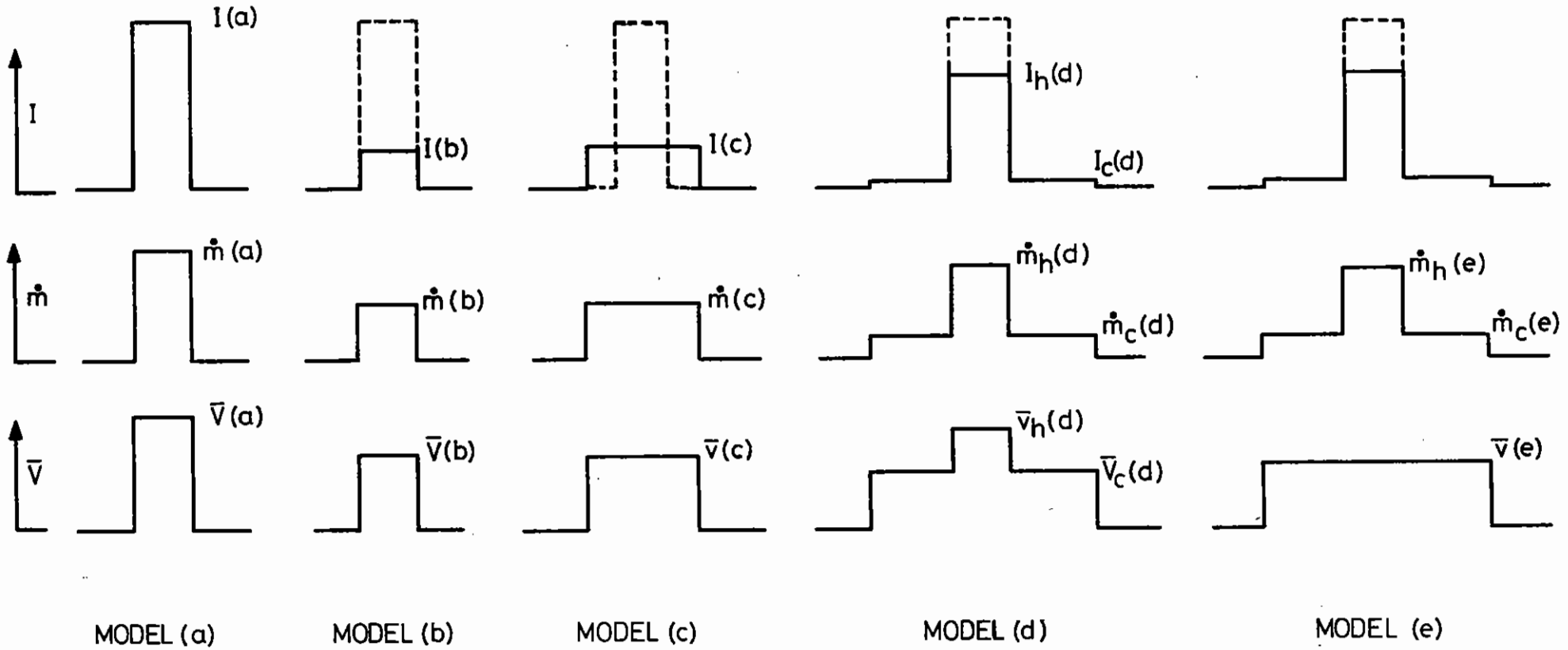

Figure 4.28 Schematic models for the spatial profile of absorbed irradiance, I, mean ablation rate, $\dot{m}$, and average ablated ion velocity, υ.

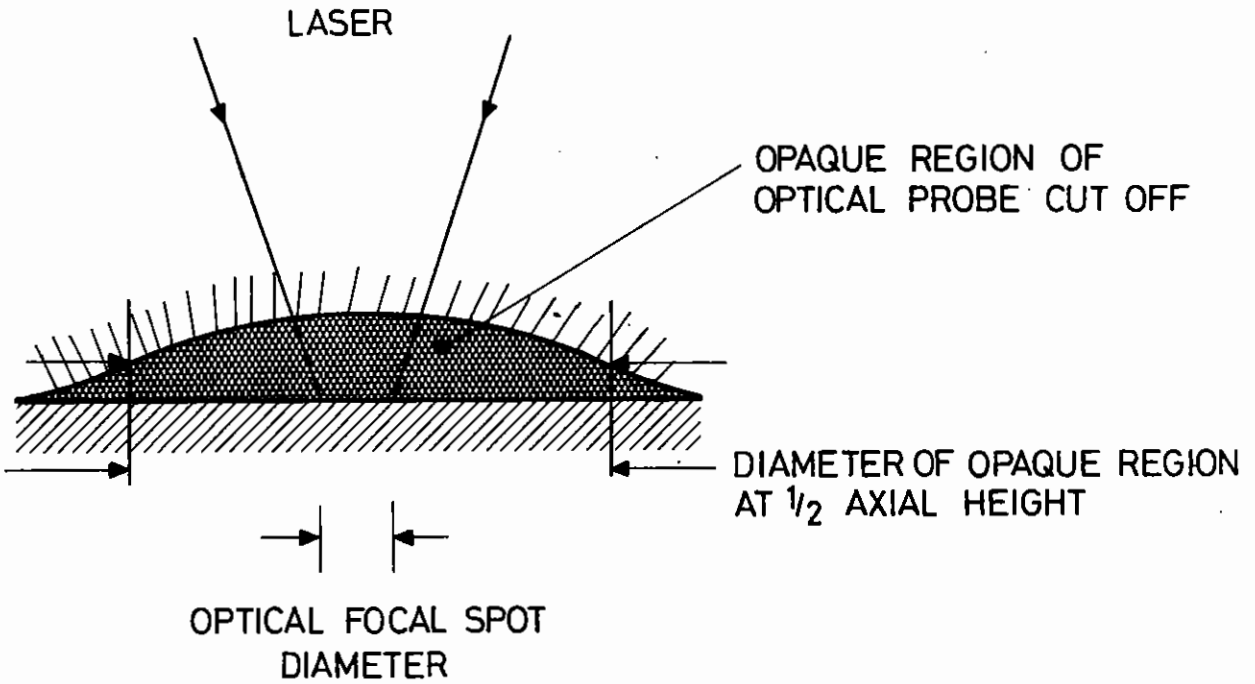

FIG 4.29

SCHEMATIC SHADOW GRAPH OR SCHLIEREN IMAGE

model shows that most of the acceleration of the ablated material occurs at the critical density so that for purposes of assessing momentum conservation the more appropriate definition is $\dot{m}_s = \dot{M}/4\pi r_c^2$. The relationship $P = \dot{m}\,\bar{v}$ is then seen to hold to quite good approximation. (See also Section 4.4.8(a)) Similarly it is necessary to define $I_{abs} = P_L/4\pi r_c^2$ in order to obtain agreement in the expression $P = (2\dot{m}\, I_a)^{\frac{1}{2}}$. The scaling of $\dot{M}$ and $\bar{v}$ in equations (10) suggests $x = 0.22$ in $\rho_a = \rho_c(I_a/I_{ao})^x$ as discussed above.

The effect of increasing density at the ablation front with increasing irradiance is also seen in analytic formulations of the ablation process which use the idea of self regulating absorption (4.26) and include therefore a description of the process of absorption unlike the models described above. Self regulating absorption by inverse Bremsstrahlung in spherical geometry lead to the scaling behaviour

$$\dot{m} \propto I^{0.56} \qquad \bar{v} \propto I^{0.22}$$

and may be expected to occur in the limit of low laser irradiance and short laser wavelength. Self regulating absorption of 'hot' electrons in spherical geometry has been shown to give $\dot{m} \propto I^{0.71}$ and $v \propto I^{0.14}$ and may be expected to occur in the limit of high irradiance and long laser wavelength.

The more rapid rate of increase of $\dot{m}$ with I_{abs} associated with these absorption mechanism based models is of interest for comparison with experimental data on spherical ablation discussed in section 4.4.8 below.

4.4.5(b) Transient Effects in Ablation Flow

Where there is hydrodynamic equilibrium there is a separation between the critical density and the ablation density. If the laser pulse were suddenly switched on a finite time would be required for a thermal wave to diffuse into the solid before the hydrodynamic equilibrium would be set up. Time resolved spectroscopy would measure an anomalously large penetration rate. An estimate of the penetration depth, l, can be

obtained by equating the heat conducted in to the enthalpy flow out, ie setting

$$\frac{KTe}{l} \sim \frac{5}{2}\,\bar{v}\, n_e k T_e$$

where K is the plasma thermal conductivity, and v is the outward flow velocity. Therefore

$$l\, n_e = \frac{2}{5}\,\frac{K}{k}$$

The depth of the penetration is

$$2\, m_p l n_e = \frac{4}{5}\,\frac{K\, mp}{k\, \nu}$$

where $\frac{M}{Z} = 2$. If $v^2 = \frac{ZKTe}{M}$ then for T = 1 keV and Z = 12

$$2\, m_p\, l n_e = 5.4\ \mu g\ cm^{-2} \simeq 0.02\ \mu m \text{ of Al}$$

Although this is a rather crude calculation, it shows that if burn depths of order 0.1 μm or greater of Al are measured then initial transients are unlikely to affect the measurement of burn rate when the thermal conductivity is diffusive.

When the laser pulse switches off, the pressure will remain high for a time approximately equal to $2m_p l n_e/\dot{m}_s$. As typical values of $\dot{m}_s$ are 10^5 gm cm^{-2} s^{-1}, this relaxation time is ~ 50 ps. We are led to the conclusion that the time for which the pressure remains high, Δt_p, is only slightly greater than the laser pulse length, Δt_l, in the absence of fast electrons.

The situation for fast electron driven ablation is quite different. For fast electrons of range λ_e the time for ablation to occur is λ_e/V which could be much longer than Δt_l. Under these conditions, the mass flow in the ablating plasma would be $\dot{m}_s\, \Delta t_p$. Thus ion diagnostics could give too large a value for $\dot{m}_s$ if Δt_p were set equal to Δt_l. However, time resolved spectroscopy would give the correct value for $\dot{m}_s$.

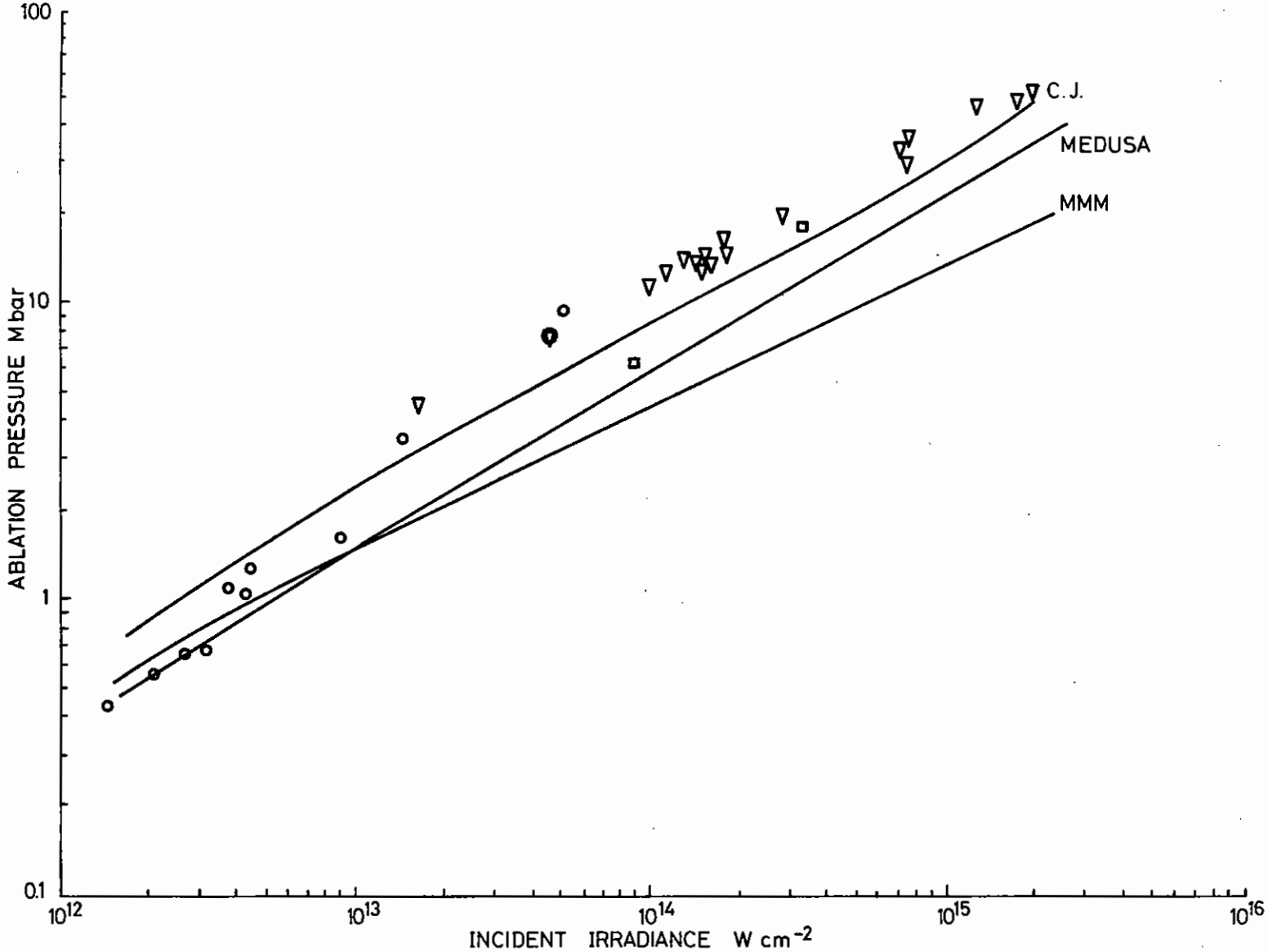

Figure 4.30 Ablation pressure for irradiation at $\lambda = 1.05$ μm. Solid lines are calculated. CJ denotes the critical density ablation model (equation (8)), MMM the steady state model for spherical ablation (equation (10)) and MEDUSA numerical simulations ((18)). The results are expressed in terms of incident irradiance assuming the absorption fractions shown in figure (4.15). The open triangle data points are the present best estimate of pressure in the absence of lateral transport effects derived from mean ablation rate measurements. The open square are from shock velocity measurements (ref (4.40)) and the open circle from ion measurement with large focal spot size (ref (4.33)).

4.4.5(c) Interpretation of Plane Target Data

The experimental results for plane targets described in 4.4.2 above were obtained at essentially constant laser power with irradiance being controlled by varying the focal spot size. They can be summarized by the relationships

$$\dot{m}_s = 1.0 \times 10^5 \left(\frac{I_{abs}}{10^{13}\ W\ cm^{-2}}\right)^{0.23} \quad g\ cm^{-2}\ s^{-1}$$

$$\dot{m}_s = 1.4 \times 10^5 \left(\frac{I_{abs}}{10^{13}\ W\ cm^{-2}}\right)^{0.35} \quad g\ cm^{-2}\ s^{-1} \qquad (12)$$

$$\dot{m}_s = 3.0 \times 10^5 \left(\frac{I_{abs}}{10^{13}\ W\ cm^{-2}}\right)^{0.31} \quad g\ cm^{-2}\ s^{-1}$$

for $\lambda = 1.05$, 0.53 and 0.35 μm respectively.

The ion velocity at the three wavelengths can be represented by

$$\bar{v} = 5.4 \times 10^7 \left(\frac{I_{abs}}{10^{13}\ W\ cm^{-2}}\right)^{0.0} \quad cm\ s^{-1}$$

$$\bar{v} = 4.5 \times 10^7 \left(\frac{I_{abs}}{10^{13}\ W\ cm^{-2}}\right)^{0.11} \quad cm\ s^{-1} \qquad (13)$$

$$\bar{v} = 4.2 \times 10^7 \left(\frac{I_{abs}}{10^{13}\ W\ cm^{-2}}\right)^{0.06} \quad cm\ s^{-1}$$

where $V_{peak} = \bar{v}$ as discussed in 4.4.3 above.

There is evidence that these ion velocities are not representative of the focal spot region. First it was inferred in section 4.4.3 that the mass in the Faraday cups was too large for small spot sizes. Second, the independent study of ion velocity as a function of focal spot size and irradiance at $\lambda = 1.06$ μm described in section 4.4.4 gave the result

$$\bar{v} = 4.9 \times 10^7 \left(\frac{I_{abs}}{10^{13}\ W\ cm^{-2}}\right)^{0.2} \left(\frac{\phi_s}{200\ \mu m}\right)^{0.25} cm\ s^{-1} \qquad (14)$$

which implies that the total mass ablated at constant spot size scales as $I^{0.6}$.

It is first instructive to examine the consistency of equation (14) with the first of equations (13) which applies at a constant laser power. The ion velocity scaling given by equation (14) is

$$\bar{v} = 7 \times 10^7 \left(\frac{I_{abs}}{10^{13}\ W\ cm^{-2}}\right)^{0.075} \quad cm\ s^{-1} \qquad (15)$$

at a power of 5×10^{10} Watts. There is sufficient agreement between equations (15) and (13) to conclude that the essentially irradiance independent velocity at constant laser power is understood in terms of the scaling of velocity with focal spot size.

While this is encouraging it remains to explain the strong focal spot size dependence, which is not contained in any of the simple scaling models discussed earlier.

Finally, energy conservation should be satisfied by the data on mass ablation rate and ion velocity through equation (1) if there is no significant energy flow from the focal region in forms other than ablation kinetic energy. This is readily checked from expressions (12) and (13) for $\dot{m}$ and $\bar{v}$ whence it is seen that the ratio $\alpha = \frac{1}{2}\dot{m}\,\bar{v}^2 / I_a$ is a decreasing fraction which can be expressed as

$$\alpha = \left(\frac{I_{abs}}{I_{ao}}\right)^{-0.76}$$

$$\alpha = \left(\frac{I_{abs}}{I_{ao}}\right)^{-0.42} \qquad (16)$$

$$\alpha = \left(\frac{I_{abs}}{I_{ao}}\right)^{-0.57}$$

where $I_{ao} = 1.6 \times 10^{13}$, 1.6×10^{13} and 5.4×10^{13} for $\lambda = 1.05$, 0.53 and 0.35 μm respectively.

The irradiance below which the ablation from the focal spot accounts for all the absorbed laser energy corresponds to the lower limit of irradiance in the experimental data and to focal spot diameters (at the laser power used) of about 370 μm, 420 μm and 170 μm for $\lambda = 1.05$ μm, 0.53 μm and 0.35 μm respectively. α goes down to 0.08, 0.19 and 0.27 for focal spot

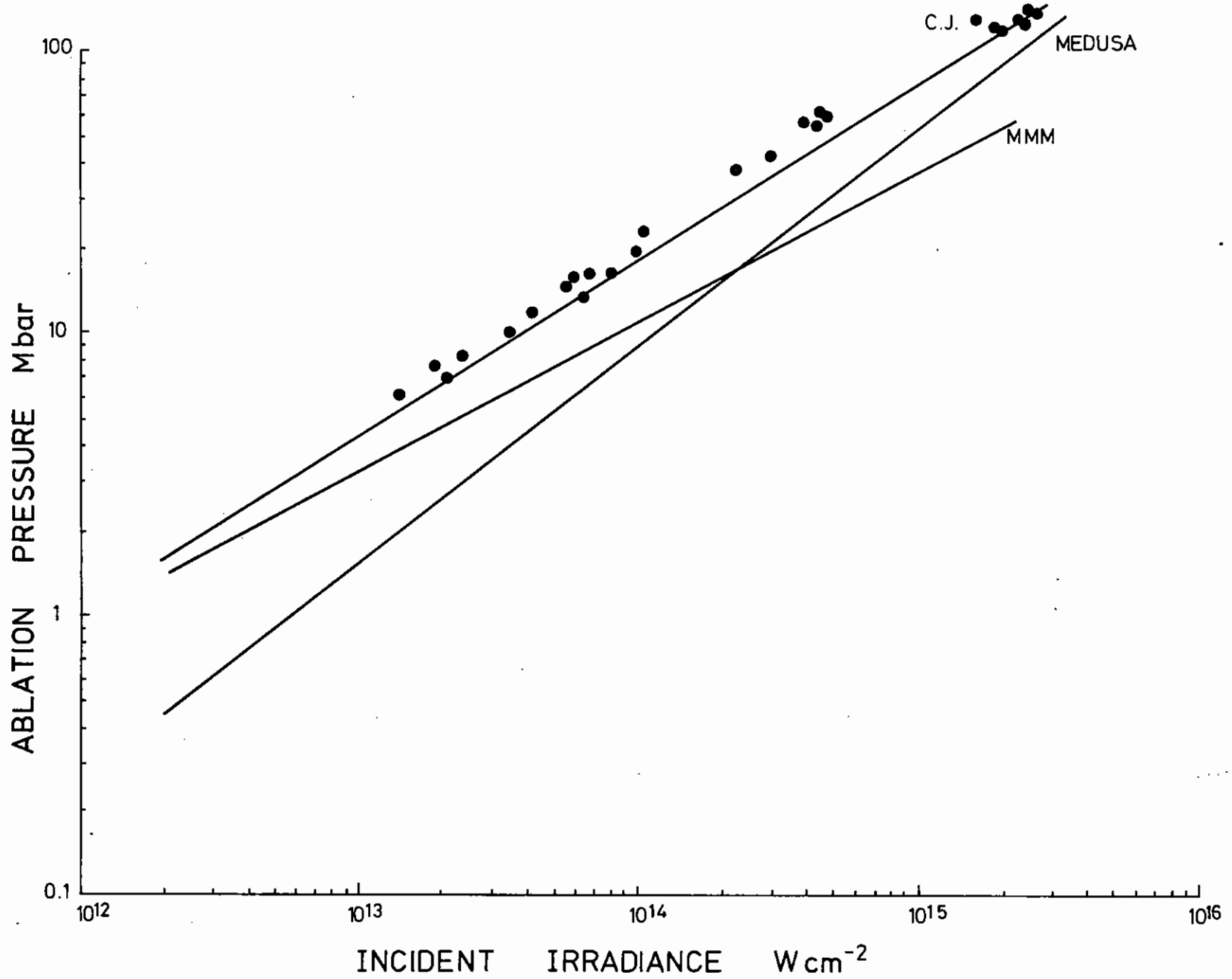

Figure 4.31 As figure 4.30 but for λ = 0.53 μm with data from the present mean ablation rate measurements.

diameters of about 50 μm at the three wavelengths respectively.

Clearly the ablation flow from the optical focal spot accounts for a progressively smaller fraction of the energy absorbed from the laser as the spot size is decreased and the irradiance is increased, namely 13 % and 34 % for 1.05 μm and 0.53 μm respectively at 10^{15} W cm^{-2}.

Equations (16) show that a simple interpretation of the ion data leads to an inconsistency in the energy flows. Either energy is being lost from the focal region, or the values of V_{peak} from the ion cups are unduly low. However the latter possibility was recognised in section 4.4.3 and a corrected velocity, corresponding to the flow velocity for the mass from the focal spot was estimated. The ratio of the energy flows is then

$$\alpha = \left(\frac{I_{abs}}{I_{ao}}\right)^{-0.48}$$

and

$$\alpha = \left(\frac{I_{abs}}{I_{ao}}\right)^{-0.21}$$

where I_{ao} = 1.7 x 10^{13} and 0.6 x 10^{13} for 1.05 μm and 0.53 μm respectively.

Various ways in which this might be explained are illustrated in Figure (4.28) which shows schematically:

(a) The ideal situation where ablation carries all the energy from the optical focal spot.

(b) Ablation from a focal spot of the same area with less energy being carried by the ablation plasma and the remainder being emitted as x-ray radiation, fast ions and hot electrons.

(c) A lateral spreading of the profile of energy deposition to give a reduced effective absorbed irradiance and ablation from a larger area, accounting for all the incident laser energy.

(d) A central 'hot' region of high effective irradiance and dimensions similar to the optical focal spot with a large surrounding 'cold' region with low effective irradiance. There is a different ion flow velocity and mass ablation rate in each region.

(e) As (d) but with thermal conduction causing all the ion flow to have the same average velocity.

These schematic situations can be analysed as follows:

Model (a)

This is obviously invalid in general because of the small fraction of the energy observed to be carried by the ablation flow from the optical focal spot as discussed above. It may be valid for spot sizes > 500 μm and low irradiance < 2 x 10^{13} W cm^{-2} and wavelength < 1 μm.

Model (b)

This has been shown to be valid for 100 ps pulses at λ = 1.06 μm at high irradiance (I = 2 x 10^{15} W cm^{-2}) for small spot sizes on plane targets and small spherical targets. Only a few per cent of the absorbed energy was found to be accounted for by ablation (4.27) with the remainder being accounted for by hot electron preheating and fast ions (4.02)(4.28). It was assumed in our earlier analysis (4.29) that a similar conclusion would be drawn about long (1.5 ns) pulse experiments since hot electron temperature is known to scale with $I\lambda^2$ independent of pulse length (4.30) and the percentage of the energy in the ablation flow from the focal spot for the long pulse data is similar to that for the short pulse data at the same irradiance.

Subsequent work has cast doubt on the validity of such a conclusion. Most long pulse (> 1 ns) experiments have shown a several fold reduction in the fraction of energy associated with fast ions and hot electron preheating (4.31) relative to that for short (< 100 ps) pulses at the same $I\lambda^2$.

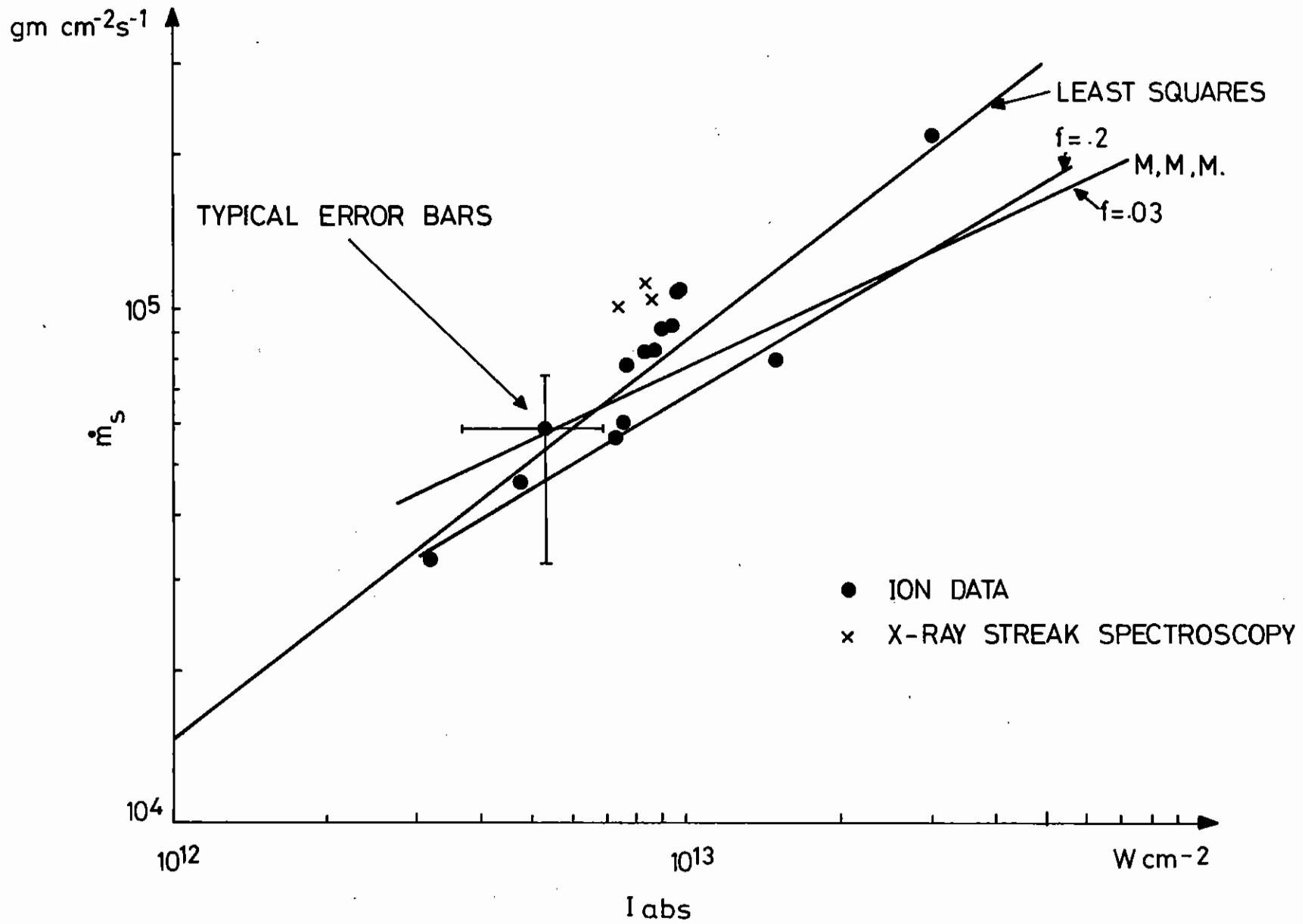

Figure 4.32 Mass ablation rate vs. Absorbed irradiance of 1.05μm.

There is some recent evidence that this could be due in part to the fast ions being emitted in a very narrow angular cone and fast electron preheating extending over a much larger region than the optical focal spot so that a major fraction of the energy in both processes would go undetected (4.32).

Thus apart from the caveat about possible non-detection it is not possible to account for the bulk of the energy in this way. Nor can thermal X-ray emission account for more than 10 % of the energy absorbed in the Al targets used in the present work.

An independent consideration is that the reported spot size dependence of ion velocity at constant irradiance (4.33) confirmed by our data (equation 14) is incompatible with model (b).

A final point is that angular integration of the ion signals indicates that the ratio of total ablated mass to that ablated from the optical focal spot increases as the spot size decreases in such a way that the absorbed energy is close to the total ion kinetic energy. (Section 4.4.4 and Figure 4.24).

On balance therefore it seems that model (b) should be ruled out except in relation to the dissipation of a small (< 20 %) fraction of the energy in the present experiments.

Model (c)

If the effective absorbed irradiance is reduced because lateral thermal conduction spreads the absorbed energy over a larger focal spot, the effect is qualitatively similar to the present observations. We require (see equations 16) $I_a(c) = \alpha I(a) = I_a(a)^{1-x} I_{ao}{}^{x}$ with $x = 0.768$ and 0.488 for $\lambda = 1.06$ and 0.53 μm respectively to account for the energy.

This can be carried through to give a modified form to the scaling laws for the mass ablation rate and ion velocity by substituting $I_a(c)$ for

$I_a(a)$ in equations (8) with the results (for 1.06 μm and 0.53 μm respectively):

$$\begin{aligned} \dot{m}_s &= 0.9 \times 10^5 \, I_a(a)^{0.08} \\ \bar{v} &= 4.0 \times 10^7 \, I_a(a)^{0.08} \\ \dot{m}_s &= 0.85 \times 10^5 \, I_a(a)^{0.19} \\ \bar{v} &= 4.4 \times 10 \, I_a(a)^{0.19} \end{aligned} \qquad (17)$$

where $I_a(a)$ is in units of 10^{13} W cm^{-2}.

It is apparent that equations (12) and (13) are inconsistent with equations (17) and that model (b) in this form has failed to predict the observed low power law scaling of v and higher power law scaling of $\dot{m}$ with I_a.

Use of the spherical ablation model in this context is complicated by the need to obtain $\dot{m}$ from $\dot{M}$. If $\dot{m} = \dot{M}/4\pi r_c^2$ as discussed above the procedure analogous to (17) gives even lower power law scaling of $\dot{m}$ which is at variance with the data. If we assume $\dot{m}_s = \dot{M}/4\pi R_a^2$ the correspondence is better but the justification for the assumption is doubtful.

If the experimental relationships for constant spot size $\bar{v} \propto I^{0.2}$ and $\dot{M} \propto I^{0.6}$ are used and it is assumed in addition that $\dot{m}_s \propto I^{0.6}$, the scaling in equation (17) is modified and is closer to that in equations (12) and (13), but still not consistent.

A further consideration is that model (c) requires the effective focal spot to be up to four times the optical focal spot diameter at the highest irradiance, smallest focal spot, limit of the 1.05 μm data. X-ray images of the focal spot in the range 1 to 2 keV characterise the 500 eV temperature region whose density is several times critical (4.34) ie the ablation front region. These images are seen to be similar in dimensions

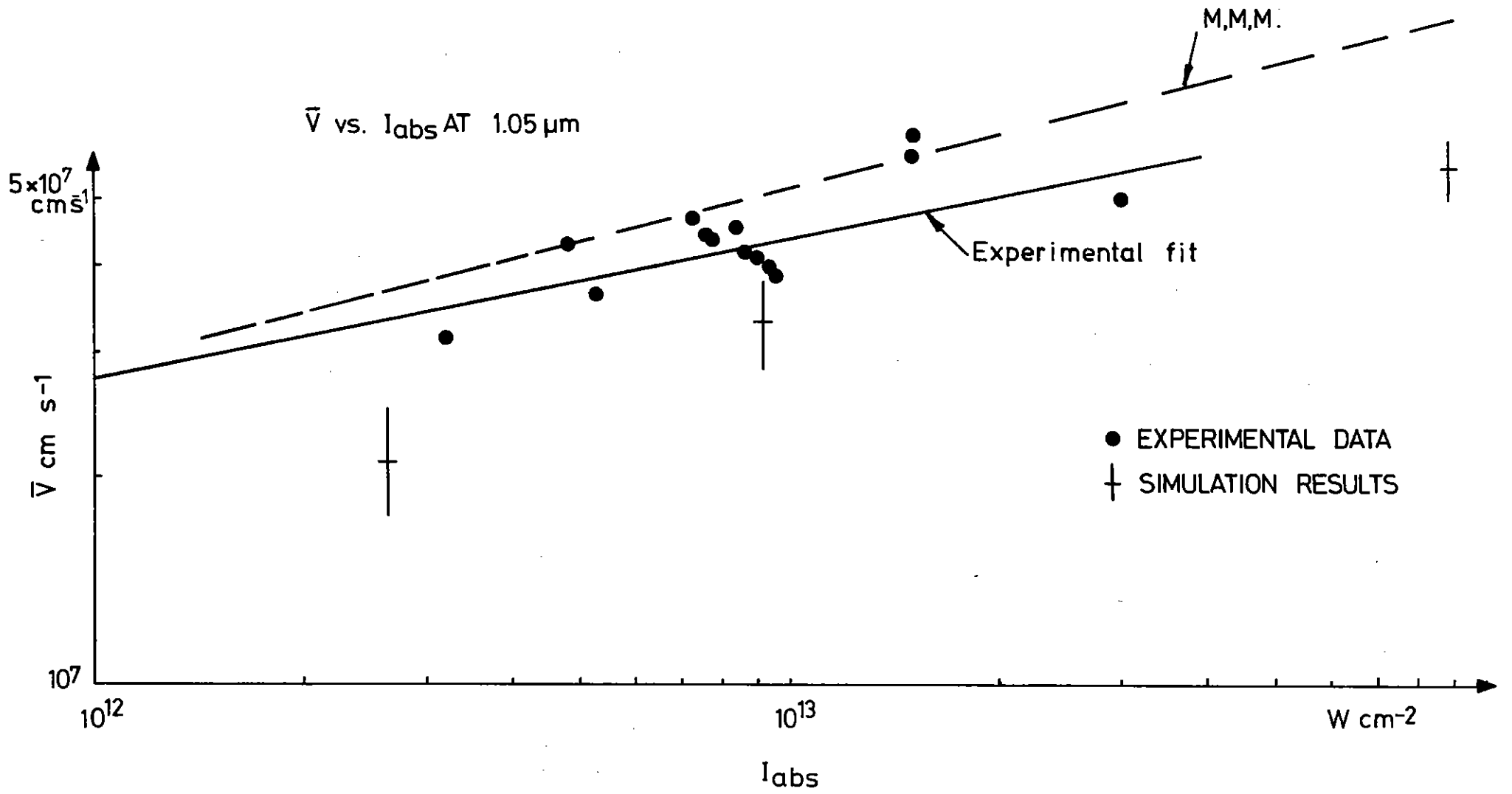

Figure 4.33 Theoretical result from Max McKee Mead is dashed line.
Best fit to experimental results is solid line.

to the optical focal spot (section 4.4.2) and to be 50 μm in diameter in the above worst case, rather than 200 μm diameter as required by model (c).

Conversely, optical probe Schlieren and shadowgraph images recorded transverse to the focal spot under similar long pulse irradiation conditions (4.35) (4.36) have shown a broad plasma plume whose dimensions may be typified by the width at half axial height of the region of optical cut off (see Figure 4.29), which has been seen to be 200 μm. This suggests the hot plasma core seen in the X-ray images may have a cool plasma region around it. The failure of model (c) to fit the observed scaling laws for $\dot{m}$ and $\bar{v}$ also suggests that it is an inappropriate model.

Model (d)

If within the optical focal spot the effective absorbed irradiance and the local ablation temperature are high, this would dominate in the spectroscopic observations of mass ablation rate. If the focal spot is surrounded by a relatively large cool region of low effective absorbed irradiance where the ablation is due to some combination of factors such as thermal x-ray radiation, hot electron energy deposition and radial electron thermal conduction, then the ions from this region may dominate and produce the observed slow ion signals. Since the spatial regions and physical processes determining the behaviour of the mass ablation rate and ion velocity are now separate there is enough freedom in principle to fit the observed flat scaling of $\bar{v}$ and steeper scaling of $\dot{m}$.

There would still have to be a non negligible number of faster ions from the hot region if this model were valid.

The derivation of the velocity v_{spot} discussed in 4.4.3 is an attempt to identify these faster ions. However the ratio $\frac{1}{2}\dot{m}_s v_{spot}/I_{abs}$ falls significantly below unity with increasing irradiance above 10^{13} W cm^{-2}. Therefore either ablation energy flow from the focal spot is indeed a small fraction of the total absorbed energy or the velocity v_{spot} is low for some other reason.

Model (e)

An explanation of the absence of 'fast' ablation ions from the 'hot' core region preceeding the larger 'slow' ion signal can be sought as follows.

Ablation ions acquire their velocity by conversion of thermal energy to kinetic energy in adiabatic expansion. If the plasma flow can lose energy by lateral electron heat conduction, the ablated ions from the hot region may not accelerate to their full terminal velocity while ions from the cold region may experience additional acceleration, so that the resultant ion flow may be at an average velocity characteristic of the total number of ions and the total thermal energy. The feasibility of such a process is determined by whether heat diffusion on the spatial scale required can occur before the hot plasma loses a large fraction of its energy to adiabatic expression.

The scale length of the density gradient is typically 1 μm at ρ_c and 40 μm at $0.1\rho_c$ (4.37) while the electron temperature is about 1 keV. For sonic flow at 1 keV the flow velocity is 3×10^7 cm s^{-1}. Thus the time for thermal diffusion is 3×10^{-12} secs at ρ_c and 1.2×10^{-10} secs at $0.1\rho_c$. The characteristic length for thermal diffusion is $\ell = (4Xt)^{\frac{1}{2}}$. With X taken as the Spitzer thermal diffusivity and λ = 1 μm, the scale lengths for ρ_c and 0.1 ρ_c are 42 μm and 880 μm respectively. It seems possible, therefore, that in the absence of inhibition processes a strong measure of temperature equalisation could occur for $\rho < 0.1\ \rho_c$ and that this might limit the acceleration of the ions in the optical focal spot. Some support for this conjecture is also obtained from 2D numerical simulations of long pulse, spatially non-uniform irradiations (4.38).

There is also a reduction of the ion velocity from the hot region irrespective of the above quenching mechanism since $I_{ac}(e) < I_a(a)$ and we expect $\bar{v} \propto I_a^n$ where n is in the range from 0.2 to 0.33 (experiments at constant spot size and analytic model equations (8)). Taking the 1.05 μm data as the most extreme case we would expect in the ideal situation of case (a) that the velocity would increase from

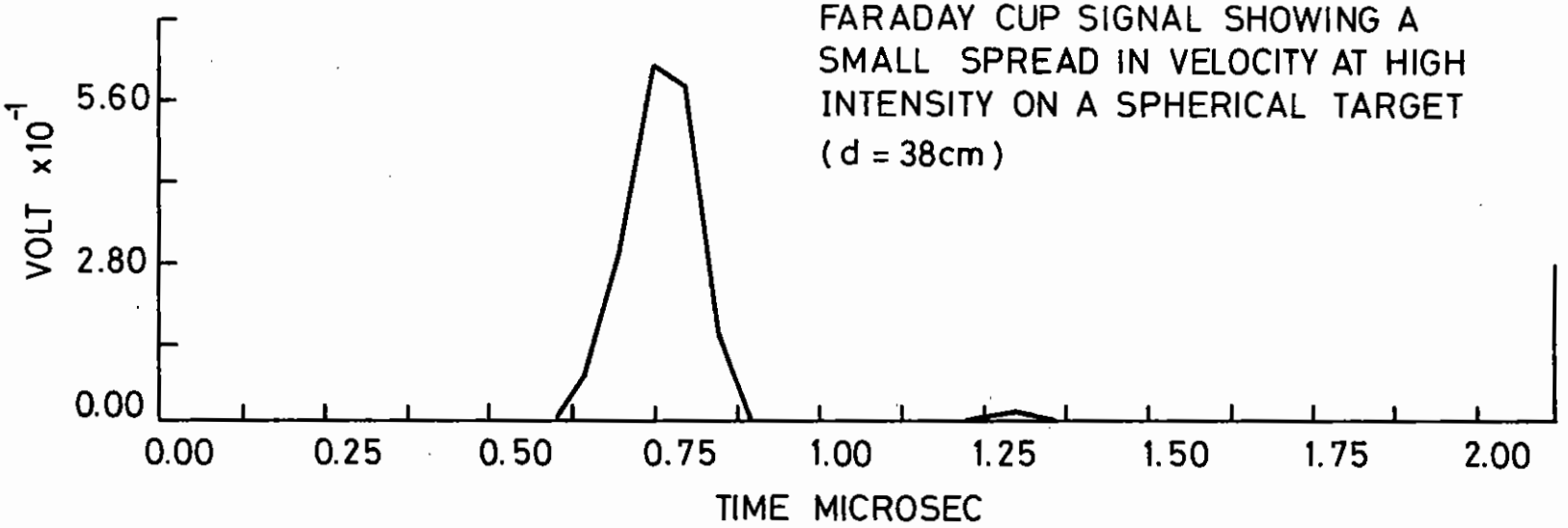

FIG 4.34
FARADAY CUP SIGNAL SHOWING A SMALL SPREAD IN VELOCITY AT HIGH INTENSITY ON A SPHERICAL TARGET
(d = 38cm)

5.8×10^7 to 1.2 to 1.8×10^8 in the absorbed irradiance range 2×10^{13} to 7×10^{14}, whereas in fact the velocity is constant and the mass ablation rate $\dot{m}$ increases by a factor of 2.3. Since $\dot{m}_s \propto I_a^m$ with the extreme possibilities for $\dot{m}$ ranging from 0.6 to 0.33 (experiments at constant spot size and analytic model equations (8)) the implied increase in I_a (e) is between 4.0 and 12 over the experimental range. This implies a reduced rate of increase in the velocity of ions from the hot region giving a possible range of maximum velocities of from 7.4×10^7 to 1.3×10^8. It is this already reduced maximum velocity which must be further reduced by the above quenching process in order to fit the data.

It is interesting to consider how much the observed scaling of $\dot{m}$ with I_a(a) differs from the scaling which would be obtained in the ideal limit. The observed scaling is quite close to the $I^{1/3}$ of the critical density sonic flow model (equations (8)) but at variance with the $I^{0.6}$ scaling of the total mass ablation $\dot{M}$ implied by the experimental data (equation (14)). The local rate $\dot{m}$ must scale in the same way as $\dot{M}$ in the large focal spot limit where effects peripheral to the focal spot are negligible. But data are then only available at very low irradiance (Section4.4.4). The behaviour at high irradiance cannot be determined with certainty since model (e) is qualitatively compatible with scaling of the form $\dot{m} \propto I^m$, with m from 0.33 to 0.6. Resolution of this uncertainty would require either measurement of the energy flow to regions outside the optical focal spot or experiments at large spot size where the effect is negligible.

4.4.5(d) Estimating Ablation Pressure

Experimental data on ablation at high irradiance and with short laser wavelength are of particular interest at the present time since it is important to determine the maximum ablation pressure which can be developed in laser driven implosions without causing degradation of compression due to preheating by hot electrons. Since hot electron preheating becomes important for $I\lambda^2 > 10^{14}$ W cm^{-2}, ablation experiments spanning this value of $I\lambda^2$ are required.

Unfortunately with presently available laser power, experiments in the interesting range of irradiance can only be conducted with small focal spot size and they are beset with the complications discussed above. Nevertheless, since data of this type are available, it is desirable to extract the maximum possible information on ablation pressure.

It is clear from the previous discussion that the spatially integrated ion velocity v measured in plane target experiments at constant laser power and variable focal spot size cannot be used to determine pressure using $P_a = \dot{m}\,\bar{v}$ since it is strongly dependent on effects peripheral to the optical focal spot. The mass ablation rate $\dot{m}$ determined from the burn through of layered targets is on the other hand a parameter characterising pressure within the focal spot. Thus a pressure determined from

$$P_a = (2\dot{m}\, I_{abs})^{\frac{1}{2}} \tag{18}$$

is of more interest.

Ideally we require to know the pressure which would be obtained in the limit of large focal spot size where effects peripheral to the focal spot are negligible or (in terms of Figure 4.28),

$$P_a(a) = (2\dot{m}(a)\, I_{abs}(a))^{\frac{1}{2}}$$

The measured variable is $\dot{m}_h(e)$ which it is physically reasonable to assume is less than or equal to $\dot{m}(a)$. The incident irradiance may be taken to be that given by the laser power and the optical focal spot size. With collated data on the absorption fraction for laser pulses of similar duration spot size and wavelength, incident irradiance can be converted to absorbed irradiance. This gives the value $I_a(a)$. Using $[2\dot{m}_h(e)I_a(a)]^{\frac{1}{2}}$, the pressure scalings obtained from the experimental data are

$$\left.\begin{aligned} P_a &= 4.4 \left(\frac{I_{abs}}{10^{13}\ \text{W cm}^{-2}}\right)^{0.62} \text{Mbar} \\ P_a &= 5.3 \left(\frac{I_{abs}}{10^{13}\ \text{W cm}^{-2}}\right)^{0.68} \text{Mbar} \end{aligned}\right\} \tag{19}$$

FIG 4.35

V_{peak} versus ABSORBED IRRADIANCE FOR 0.53μm SPHERICAL TARGET

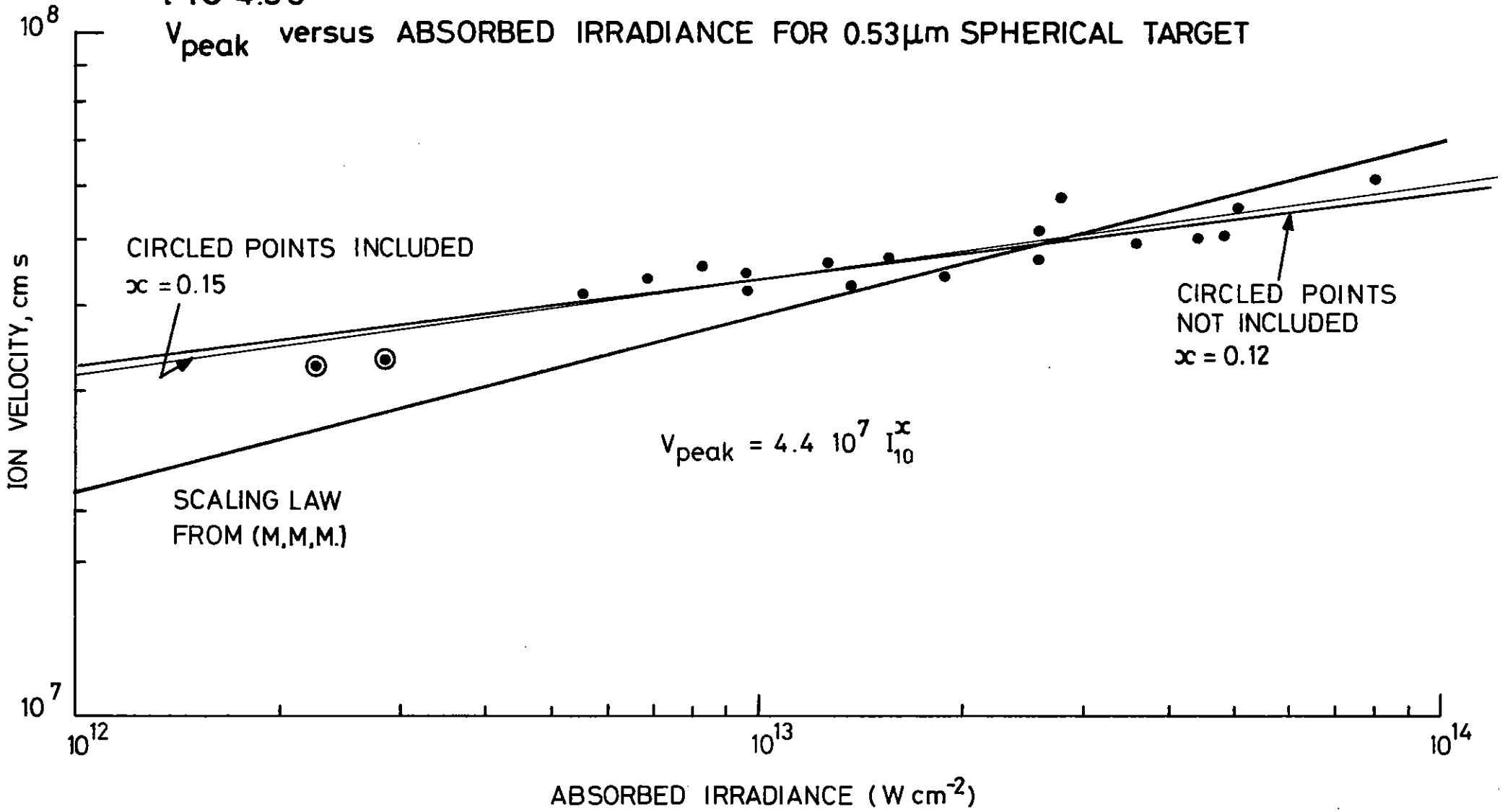

$$P_a = 7.8 \left(\frac{I_{abs}}{10^{13}\ W\ cm^{-2}}\right)^{0.66} Mbar \qquad (19)$$

for 1.05, 0.53 and 0.35 μm respectively. Figures 4.30 and 4.31 show our data treated in this way for 1.06 and 0.53 μm respectively.

Comparison of the 1.05 μm data with data from other sources in Figure 4.30 shows reasonable consistency. There are no comparable data at other wavelengths.

It should be emphasised that the pressures given above are not the actual pressures in the present experiment because of the lateral flow of energy. Values of the pressure in the present experiment can be estimated from $\dot{m}_s\, v_{spot}$. These are

$$Pa = 5.1 \left(\frac{I_{abs}}{10^{13} W\ cm^{-2}}\right)^{0.37} \quad Mbar$$

$$Pa = 5.0 \left(\frac{I_{abs}}{10^{13} W\ cm^{-2}}\right)^{0.57} \quad Mbar$$

for 1.05 μm and 0.53 μm respectively. These pressures are lower than would be obtained in the absence of edge effects.

It is relevant to consider the nature of the errors in the determination of P_a. If $\dot{m}$ (e) is related to I_{abs} (e) (see Figure 4.28(e)) by a relationship of the form $\dot{m}(e) = I_{abs}(e)^n$ with n having a possible range between 0.6 and 0.33 as discussed above, and if there is reduction of the effective absorbed irradiance by a factor of η then

$$(2\dot{m}_h(e)I(a))^{\frac{1}{2}} = \eta^{n/2}\ (2\dot{m}(a)I(a))^{\frac{1}{2}}$$

and P(a) would be underestimated by a factor $\eta^{n/2}$. The error will be relatively unimportant unless η is very small. The worst case in our data is for the smallest focal spot and highest irradiance at λ = 1.05 μm, where only 0.08 of the absorbed energy is found in ablation from the focal spot area. A lower bound on η is 0.07 but other considerations discussed earlier (model (e)) put it higher, with a possible range between 0.1 and 0.3. Thus the possible range of error in P_a lies between 0.5 and 0.8. Since this is the worst underestimate which can be made at the highest irradiance at λ = 1.05 μm all the other

data should be more accurate. The set of data on ablation pressure may thus be considered a useful comparison of the absolute pressure generated in the ideal limit by irradiation at 1.05 μm, 0.53 μm and 0.33 μm.

The experimentally deduced pressure may be compared with theoretical values from numerical simulations with the MEDUSA code (4.39) made for 100 μm radius spherical targets 1 ns after the start of constant power irradiation, as well as with the analytic models discussed earlier.

Agreement with the critical density sonic flow model is good for both the 1.05 and 0.53 μm data (Figures 4.30 and 4.31). The model for spherical ablation with thermal transport agrees less well, predicting lower pressures at both wavelengths than are deduced from the experiments. This may be connected with the steady state assumption which leads to a critical density surface area larger than the target surface area and a corresponding reduction of the pressure. This spherical geometry effect is not present in plane target experiments.

The numerical simulations give pressures quite close to the 1.05 μm data but give substantially (2.5 times) lower values than the 0.53 μm data. This may be connected with the high classical absorption at subcritical density in the simulation which exceeds that in experiments.

Table 4.01 in Section 4.4.9 below compares the pressure generated at the three wavelengths used for the same absorbed irradiance, incident irradiance and for the same values of $I\lambda^2$. The advantages of reduced wavelength are apparent in the table. In particular there is a 5.2:1 ratio of pressure at $I\lambda^2 = 10^{14}$ W cm^{-2} μm^2 between 0.53 μm and 1.05 μm irradiation and the 0.53 μm pressure is 50 Mbar. This suggests that pressures sufficient for laser fusion requirements may be generated with low hot electron preheating at this wavelength and it also implies that very high pressures and densities of considerable general physics interest may be obtained in small scale implosions driven with short wavelength radiation (see section 7.2). The observation noted above of hot spots in X-ray emission from large focal spots in 0.35 μm experiments shows the problem of achieving spatial uniformity of pressure at shorter wavelengths.

FIG 4.36
SPECIFIC MASS ABTATION RATE VS ABSORBED INTENSITY.
SPHERICAL TARGET, 0.53 μm LIGHT

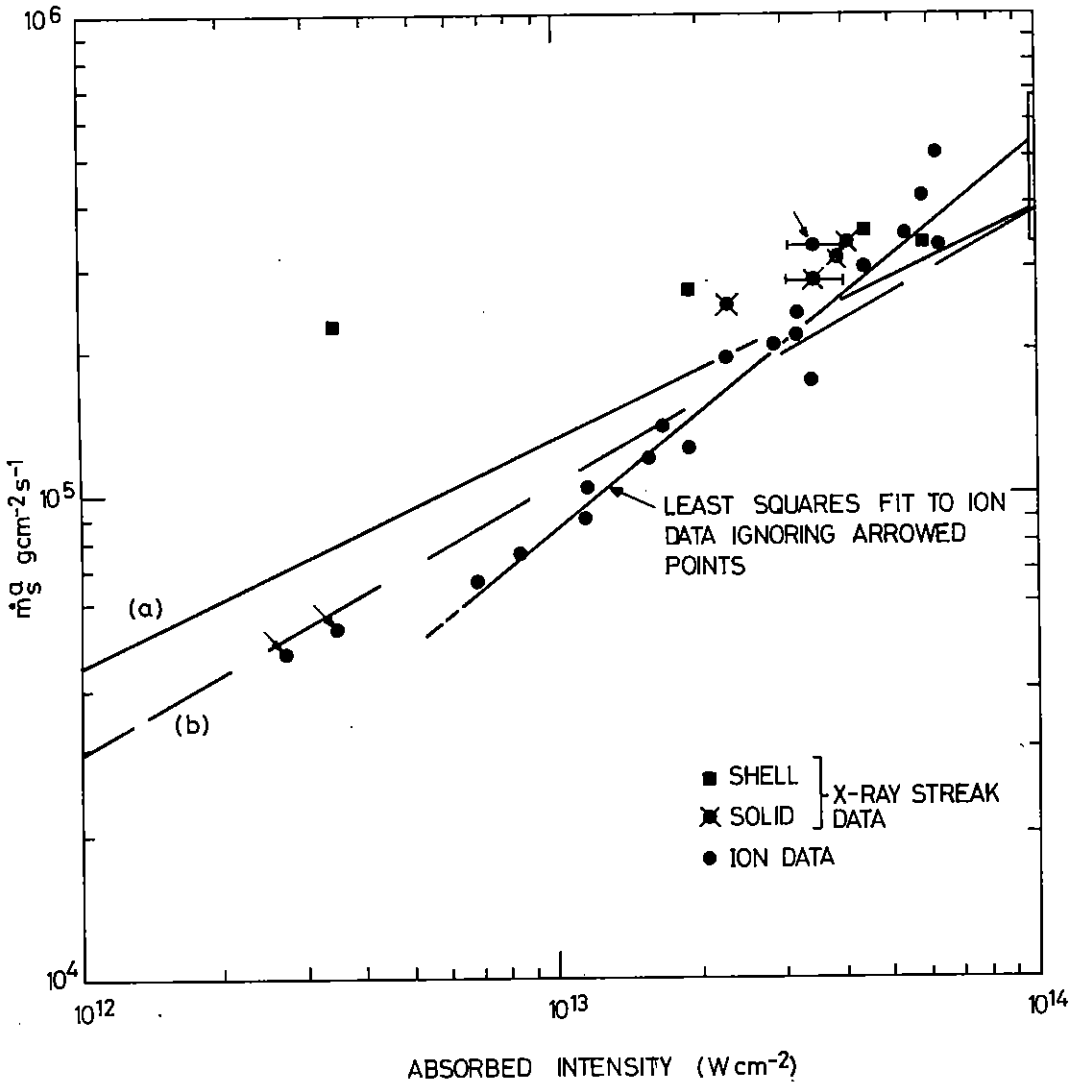

CAPTION

LINE (a) SCALING LAW WITH FLUX - LIMIT OF 3%
(b) AS ABOVE, BUT FLUX-LIMIT 9%

4.4.6 Spherical Target Data at 1.05 μm

4.4.6(a) Ion Data

Measurements of the ion emission have been used for some time as a method of obtaining both qualitative and quantitative information about the plasma ablated from targets irradiated by high power lasers. One simple detector frequently used is the differential ion calorimeter (4.41) (4.42) which, with no assumptions needing to be made about the plasma parameters, enables the time integrated energy in the expanding plasma flow to be determined. Another detector in common use is the ion Faraday cup (4.43) (4.44) which, when correctly constructed to avoid secondary electron emission effects and suitably biased, measures the time resolved ion current density at some distance from the target given by $J(t) = N_i(t)Ze\ v(t)$, where N_i, Ze and v are respectively the number density, charge and velocity of the ions at the detector. If the laser pulse length is much less than the ion flight time to the detector then analysis of Faraday cup signals leads to the determination of several important ion emission parameters. The ion mass flux and energy flux at the detector are given by $m_f(t) = J(t)M/_Z(t)M_p/_e$ and $E_f(t) = \frac{1}{2}\, m_f(t)\bar{v}(t)$ respectively where M_p is the proton mass. If $M/_Z$ is known the total mass and energy in the ion flow to the detector can be calculated by integration of these expressions. If the charge state is assumed to be constant throughout the recorded current signals then ion velocity distributions can readily be calculated from which values of the average ion flow velocity (v) towards the detector can be deduced.

In the past (4.42), (4.45), arrays of both types of detector have been used to obtain information about the total mass (m_{tot}) ablated from plane targets by a laser beam by means of combining the total ion energy values (E) derived from the calorimeters with the average ion velocities ($\bar{v}$) deduced from the Faraday cups to give $M_{tot} = 2E/\bar{v}^2$. This procedure is prone to errors in the two dimensional angular integration of the strongly anisotropic ion emission. Furthermore the spread in velocity, Δv of the detected ions leads to errors of order $(\Delta v/\bar{v})$ in

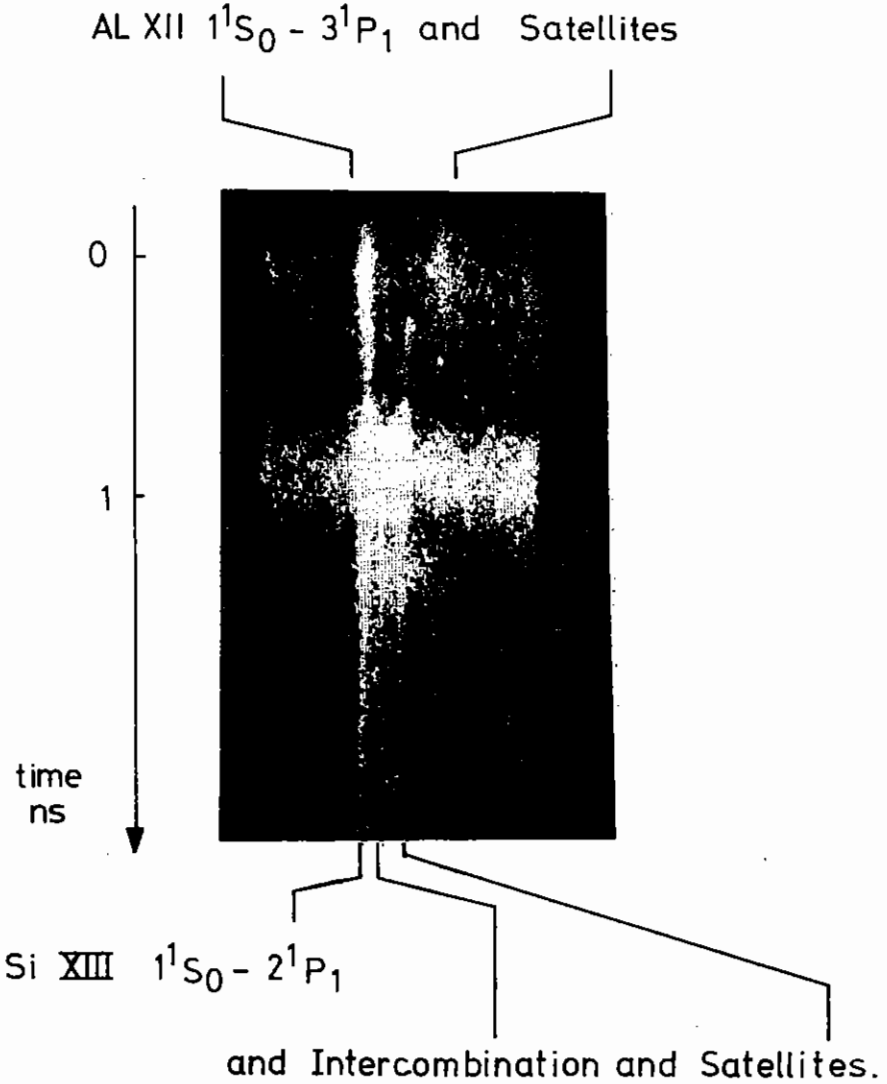

Figure 4.37 X-ray streak of ablation burn through in spherical geometry.

using the average velocity to deduce the ablated mass. Errors of a different kind can arise from assuming that this mass originates from the focal spot. For small spots it is possible that lateral energy transport can make the effective area larger than the focal spot.

In this section we present target mass ablation rate measurements obtained from experiments on symmetrically irradiated spherical targets using arrays of Faraday cups and ion calorimeters. In spherical geometry the initial target surface area is accurately known, edge effects are removed and the angular integration of the signals can be accurately performed as the plasma expansion is symmetric. In addition we have eliminated errors due to the finite spread in ion velocities by analysing the data in the following way. We calculate a mean value of M/Z for each laser shot by equating the total ion flow energy obtained from the calorimeter data with that obtained by numerically integrating data from the Faraday cup currents.

$$E_{cal} = \frac{M}{Z}\left(\frac{M_p}{e}\right) \iint_0^\infty J(t)v^2(t)\ dt\ d\Omega$$

The M/Z value derived from this expression is then used to deduce the total mass ablated (M_{tot}) for each laser shot derived from the Faraday cup signals.

$$M_{TOT} = \frac{M}{Z}\ \frac{1}{e}\ \iint\ J(t)\ dt\ d\Omega$$

Targets were irradiated in the six beam target chamber with up to 110 Joules of energy at a wavelength of 1.054 μm in an approximately triangular laser pulse of 1.5 ns half width. The targets consisted of hollow and solid glass spheres in the diameter range 140-280 μm coated uniformly with either a thin (100 nm) layer of aluminium or with a 1 μm thick layer of polymer. Overlap of the six laser beams on target was adjusted to give best illumination unformity (± 20 %) and incident intensities in the range 5.10^{12} - 10^{14} W cm^{-2}. Target chamber background pressures were between 10^{-4} and 10^{-5} torr.

The spherical ion emission was monitored using five ion Faraday cups and

eight differential ion calorimeters uniformly distributed about the target at distances of 38 and 20 cm respectively. Output from both types of detector was recorded automatically direct to computer store via a multichannel digitizer (4.44) for the Faraday cups and via amplifiers for the calorimeters. This direct recording system allowed rapid processing of the faraday cup data and immediate post shot printout of the total target absorbed energy and irradiance from the calorimeter signals. The plasma expansion on each shot was found to be nearly isotropic with 20 % variations in both total energy and ion currents recorded at different detector positions. In addition to the Faraday cups and calorimeters a Thomson parabola ion analyser with a microchannel plate detector was mounted on the chamber in order to provide an independent measure of the mean plasma M/Z value.

After each laser shot the average plasma M/Z value at the Faraday cups was computed by numerically integrating the data derived from the Faraday cup traces and comparing it with the total energy recorded by the calorimeters as indicated in equation 1. The M/Z values deduced by this method varied between 2 and 4.5 on different shots independent of absorbed intensity. The Thomson parabola analyser gave data which indicated M/Z values on each shot in very close agreement with those obtained from the Faraday cups and calorimeters.

The calculated M/Z values were then used to compute the total target mass ablated for each shot as indicated in equation 2. It should be pointed out that the variations in the amount of ion recombination which take place along the flight path from shot to shot do not cause any errors in the calculation of the ablated mass using the above method as would happen if only Faraday cup detectors were used and M/Z values assumed. This is because the M/Z value of the plasma flow at the entrance to the Faraday cups is the only unknown in equation 2 and this is determined for each shot using the ion calorimeter data. Assuming the measured total mass is ablated from the target during the 1.5 ns of the laser pulse and that the area through which the ablation occurs is the original surface area of the target one can convert the mass data into terms of more useful specific mass ablation rates $\dot{m}_s$ at the original target radius. This data is

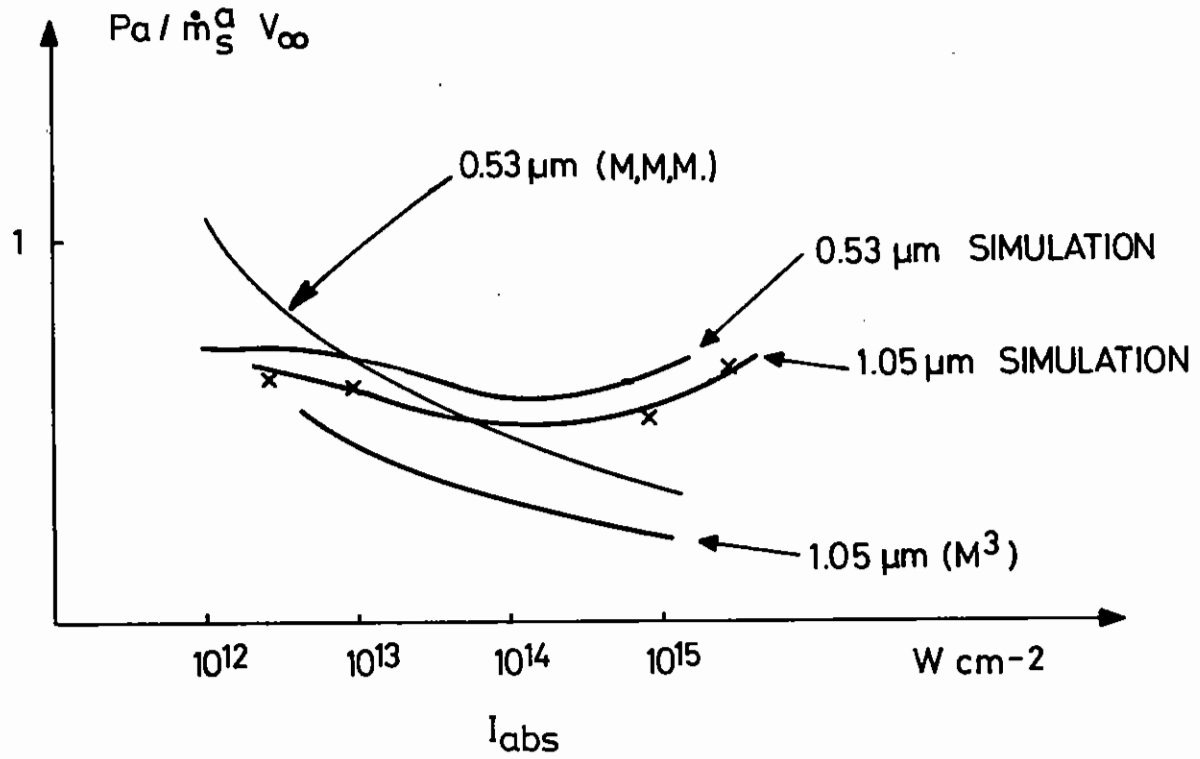

Figure 4.38 Ratio of ablation pressure to $\dot{m}_s^a V_\infty$ from the analytic model MMM and numerical simulations.

plotted in Figure 4.32 as a function of target absorbed irradiance (I_a). A least squares fit to the data is

$$\dot{m}_s = 0.86 \times 10^5 \left(\frac{I_{abs}}{10^{13}\ W\ cm^{-2}}\right)^{0.8} g\ cm^{-2}\ s^{-1} \qquad (20)$$

This in very good agreement with other ion measurements in the same intensity range on spherical targets (4.46).

The variation of the average velocity of the ion emission is shown in Figure 4.33. The observed scaling is $v = 4.4 \times 10^7\ (I_{abs}/10^{13})^{0.2}$ in this intensity range in reasonable agreement with an energy conservation model (4.47). These results should be contrasted with plane target experiments with small focal spots (section 4.4.3) where the velocity scaling appears to be much weaker, probably due to lateral transport of thermal energy.

4.4.6(b) X-ray Streak Spectroscopy at 1.05 μm

On three shots it was possible to obtain mass ablation rates from six beam irradiation of microballoons using the technique of streak x-ray spectroscopy. For this purpose a beryl crystal spectrometer was used and the burn through time was measured from the time delay between the Al and Si satellites. The mass ablation rate was corrected for the pulse shape as described in section 4.4.2. The values of $\dot{m}_s$ are plotted on Figure 4.32 for comparison with the mass ablation rates measured from the Faraday cup. As can be seen the agreement with the ion data is good.

4.4.7 Spherical Target Data at 0.53 μm

The start of experiments with the new laser giving six 2ω beams enabled a similar set of experiments to be performed at 0.53 μm at the end of the period of this report. The laser pulse length was 1 ns and absorbed laser irradiances up to 10^{14} W cm^{-2} were achieved, with typically 50 J past the lenses in the six beams. The target radii ranged from 35 μm to 100 μm and for the purpose of the x-ray streak observations the targets were coated with a variable thickness of plastic and overcoated with a thin

film of Al. A greater range of targets were irradiated at 0.53 μm than at 1.06 μm.

Ion data measurements of $\bar{v}$ and $\dot{m}_s$ were made as described in section 4.4.6. It was noted that at the higher irradiances available the spread in velocity deduced from the Faraday Cup was reduced and as shown in Figure 4.34, $\Delta v/v_{peak} = 17$ %. The variation in v_{peak} with absorbed intensity is shown in Figure 4.35 and a least squares fit to the data gives

$$v_{peak} = 4.4 \times 10^7 \left(\frac{I_{abs}}{10^{13} W\ cm^{-2}}\right)^{0.15} cm\ s^{-1}$$

which is again a stronger variation than was observed in section 4.4.3 presumably because of the absence of edge effects. The mass ablation rate from the ions referred to the intial surface area of the target is shown in Figure 4.36. If the two points at low intensity are ignored the scaling with absorbed irradiance is

$$\dot{m}_s = 0.89 \times 10^5 \frac{I_{abs}}{10^{13} W\ cm^{-2}} \quad g\ cm^{-2}\ s^{-1} \qquad (21)$$

Comparison with theory is discussed in section 4.4.8.

An X-ray streak from this series of experiments is reproduced in Figure 4.37. This streak shows the fiducial X-ray emission from the Al XII $1^1S_0 - 1^1P_1$ and dielectronic satellite which clearly decreases as the thin surface layer of Al is burnt off and the plastic begins to be ablated. At a later time, emission from the underlying Si is seen and a well defined burn time corresponding to the start of the main Si emission can be measured. The X-ray mass ablation rates calculated from the start of the main Si emission and corrected for the pulse shape dependence are shown on Figure 4.36 for both solid and shell targets.

The X-ray streak values of $\dot{m}_s$ show a larger scatter than the values derived from the ions. This is because of the sensitivity of the X-ray streaks to imperfections in the irradiation symmetry, target manufacture or indeed filamentation. However on some shots, particularly at high

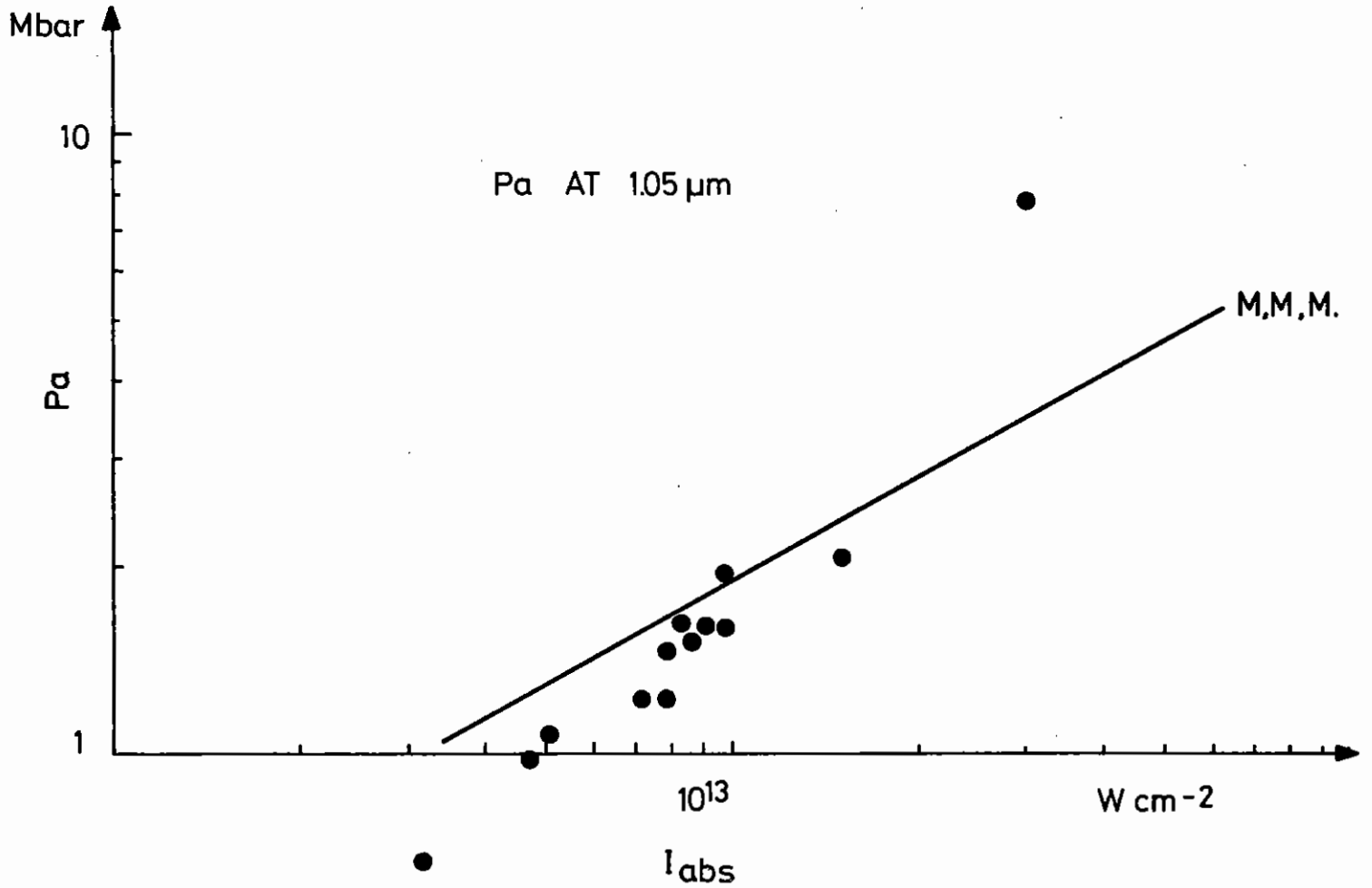

Figure 4.39 Ablation pressure as a function of absorbed irradiance at 1.05 µm.

intensities, there was moderately good agreement between the X-ray and the ion data, with the X-ray mass ablation rates 20-30 % higher than the ion mass ablation rates. If fast electron driven ablation were occuring, values of $\dot{m}_s$ from the ion data might be higher than the values derived from the X-ray data.

One very interesting feature of these streaks is the observation of a precursor to the main Si emission. Figure 4.37 shows this feature although only on the dielectronic satellite of Si XIII $1\,^1S_0 - 2\,^1P_1$ and probably not in the main line. In other shots precursor emission from the satellite was often clearly visible, although it could not be seen whether or not there was emission from the resonance line because the Al emission did not usually decrease so rapidly as in Figure 4.37. There are several possible reasons for this precursor emission. It could be evidence for burn through in a few spots, because of filamentation of the laser beam. Similarly it could be evidence for breakup of the shell, although the precursor emission was seen even when solid spherical targets were used, eliminating the possibility of a simple Rayleigh Taylor instability. It could be evidence for preheating of the Si to a Li like state of ionisation and the line being excited by radiation from the Al. The fact that in Figure 4.37 the intensity of precursor emission decreases as the Al emission decreases would favour this explanation. However at this early stage none of these explanations is conclusive.

4.4.8 Discussion of the Spherical Mass Ablation Rate Data

In planar geometry the quantities $\dot{m}_s$ and $p + \rho v^2 = p + \dot{m}_s v$ are spatially invariant. A measurement of the specific mass ablation rate $\dot{m}_s$ and of the ion velocity at large distance from the target (v_∞) will then give the ablation pressure though $P = \dot{m}_s v$. However in spherical geometry this is not the case - $\dot{m}_s$ is no longer invariant, and is proportional to $1/r^2$. Modification of the discussion in section 4.4.5 is therefore appropriate and a description of models for spherical mass ablation is given here, before a comparison is made with our results.

4.4.8(a) Theoretical and Numerical Models for Spherical Mass Ablation

Max McKee and Mead (4.25) have found analytic equilibrium solutions to mass ablation in spherical geometry with flux limited heat flow. The principle assumptions of the model are energy deposition only at the critical density surface and the absence of energy transport other than by flux limited thermal conduction. Properties of the ablation flow can be determined for a variety of flux limits, but are given below for a flux limit of 3 %.

The mass ablation rate is shown to be

$$\dot{m}_s^a = 6.2 \times 10^4 \left(\frac{\lambda}{1\mu m}\right)^{-0.81} \left(\frac{Ra}{1mm}\right)^{-0.11} \left(\frac{I}{10^{13}\ W\ cm^{-2}}\right)^{0.48} \quad g\ cm^{-2} s^{-1}$$

which differs from the specific mass ablation rate at the radius of the critical surface R_c by $1/y_c = (R_a/R_c)$. From the model $y_c = 1.2(\lambda/1\,\mu m)^{0.38}\ (I_{abs}/10^{13}\ W\ cm^{-2})^{0.11}/(R_a/1\ mm)^{0.08}$. If the flow velocity at $r = \infty$ is v_∞ then from energy conservation

$$v_\infty = 5.7 \times 10^7 \left(\frac{\lambda}{1\mu m}\right)^{0.41} \left(\frac{Ra}{1mm}\right)^{.06} \left(\frac{I}{10^{13}\ W\ cm^{-2}}\right)^{0.26} \quad cm\ s^{-1}$$

In the model the ablation pressure is given by

$$Pa = 2.36 \left(\frac{Ra}{1mm}\right)^{0.07} \left(\frac{\lambda}{1\mu m}\right)^{-0.98} \left(\frac{I}{10^{13}\ W\ cm^{-2}}\right)^{0.58} \quad Mbar$$

In plane geometry the ablation pressure can be obtained from $\dot{m}_s v_\infty$ (section 4.4.5). It can be shown that this is a good approximation for spherical geometry if $\dot{m}_s$ is referred to the critical density surface as the pressure drop is localised to the critical surface. Experimentally $\dot{m}_s$ is measured at the initial target surface ($\dot{m}_s^a$). From the theory

$$\gamma = \frac{Pa}{v_\infty}\left(\frac{4\pi Ra^2}{\dot{M}}\right) = \frac{Pa}{v_\infty \dot{m}_s^a} = .37\left(\frac{Ra}{1mm}\right)^{0.12}\left(\frac{\lambda}{1\mu m}\right)^{-0.57}\left(\frac{I}{10^{13} W\ cm^{-2}}\right)^{-.16}$$

It can be seen that γ is the correction factor by which the experimentally measured quantity $\dot{m}_s v$ should be multiplied to give values of the ablation pressure: it is plotted in Figure 4.38 for the range of our

experiments. For 0.53 μm irradiation γ is close to unity because there is a small separation between R_c and R_a.

Comparison was made with results from the numerical simulation MEDUSA. To simulate the ablation process accurately a variable zone size was used. Values of γ from MEDUSA are also shown in Figure 4.38.

4.4.8(b) Discussion of Experimental Data in Spherical Geometry

The results for $\dot{m}_s$ and $\bar{v}$ show that the ratio $\alpha = \frac{1}{2}\dot{m}_s\bar{v}^2/I_{abs}$ giving the fraction of the absorbed energy reconverted in ablation is close to unity. Specifically $\alpha = 0.83\ (I_{abs}/10^{13}\ W\ cm^{-2})^{0.2}$ for $\lambda = 1.05$ μm and $\alpha = 0.86\ (I_{abs}/10^{13}\ W\ cm^{-2})^{0.1}$ for $\lambda = 0.53$ μm. The advantage of spherical geometry in eliminating energy loss from the focal spot is apparent here. The fact that the exponent of I_{abs} is not zero leading to $\alpha > 1$ for $I_{abs} > 3 \times 10^{13}$ W cm^{-2} indicates a small error in the data.

From Figures 4.32 and 4.36 it is evident that in contrast to plane geometry there is a strong scaling of $\dot{m}_s$ with I_{abs} for both 1.05 μm and 0.53 μm irradiation. Experimentally the values of $\dot{m}_s$ at 0.53 μm are only 20 % greater than at 1.05 μm. Comparisons with the Max McKee and Mead model, for a 3 % flux limit are shown in Figures 4.32 and 4.36. There is some agreement for both wavelengths, with the 1.05 μm experimental points lying above the model's predictions and the 0.53 μm experimental points below the prediction at 10^{13} W cm^{-2}. However the data at 0.53 μm shows that the irradiance scaling from the Max McKee and Mead model is too weak. Increasing the flux limit to 9 % increases the scaling with I_{abs} but gives theoretical results which are slightly too low as shown in Figure 4.36. Simulation results for a flux limit of 10 % are also shown in the figure. Remarkably good agreement is evident. However the simulation shows that $\dot{m}_s$ is not very sensitive to the flux limit below 10^{14} W cm^{-2} because the heat flux is not saturating.

At intensities below about 10^{13} W cm^{-2}, inverse Bremsstrahlung is the dominant absorption mechanism, and little light penetrates to the critical

density surface. The irradiance at the critical density surface is then lower than it would have been without inverse Bremstrahlung absorption; the observed mass ablation rate is thus lower than the MMM model would predict. Indeed, in this intensity region a better model may be that of the self regulating absorption (4.26) and the scaling law found for this model is $I^{0.56}$, which is closer to the experimental scaling of $I^{0.8}$.

At high irradiances the Max, McKee and Mead model predicts too low a scaling in $\dot{m}_s$ with I, and here too an alternative model may be considered. It is known that at these intensities hot electrons are produced, and it is possible that in penetrating the target they increase the specific mass ablation rate above that expected in their absence. The scaling obtained from a model of Kidder which assumes that hot electrons propagate to some distance R_c ahead of the ablation front (4.26) and set up a self regulating ablation is $\dot{m}_s \propto I^{5/7}$.

However at our highest intensities $I_{abs}\ \lambda^2$ is only 2×10^{13} W cm^{-2} μm^2 and fast electron preheat is probably insignificant.

The velocities from the Max, McKee and Mead model with f = 0.03 are compared with the experimental results in Figures 4.35 and 4.33. The experimental scaling is clearly weaker than from the model which reflects the fact that the experimental scaling for $\dot{m}_s$ is stronger than in the model.

Experimental pressures were obtained from $P_a = \gamma\dot{m}_s\bar{v}$ with γ taken from the analytic model. These values of P_a are plotted in Figures 4.39 and 4.40. Good agreement with the analytic model is seen, essentially because $\dot{m}_s$ scales more strongly and $\bar{v}$ scales more weakly with I_{abs} than predicted from the model.

4.4.9 Conclusions

The most general conclusion that can be reached on the basis of the above data and discussion is that a satisfactorily self consistent picture of

FIG 4.40
VARIATION IN ABLATION PRESSURE $P_a = \dot{m}_s^a \gamma \bar{v}$ WITH ABSORBED INTENSITY. SPHERICAL TARGETS, 0.53 μm LIGHT

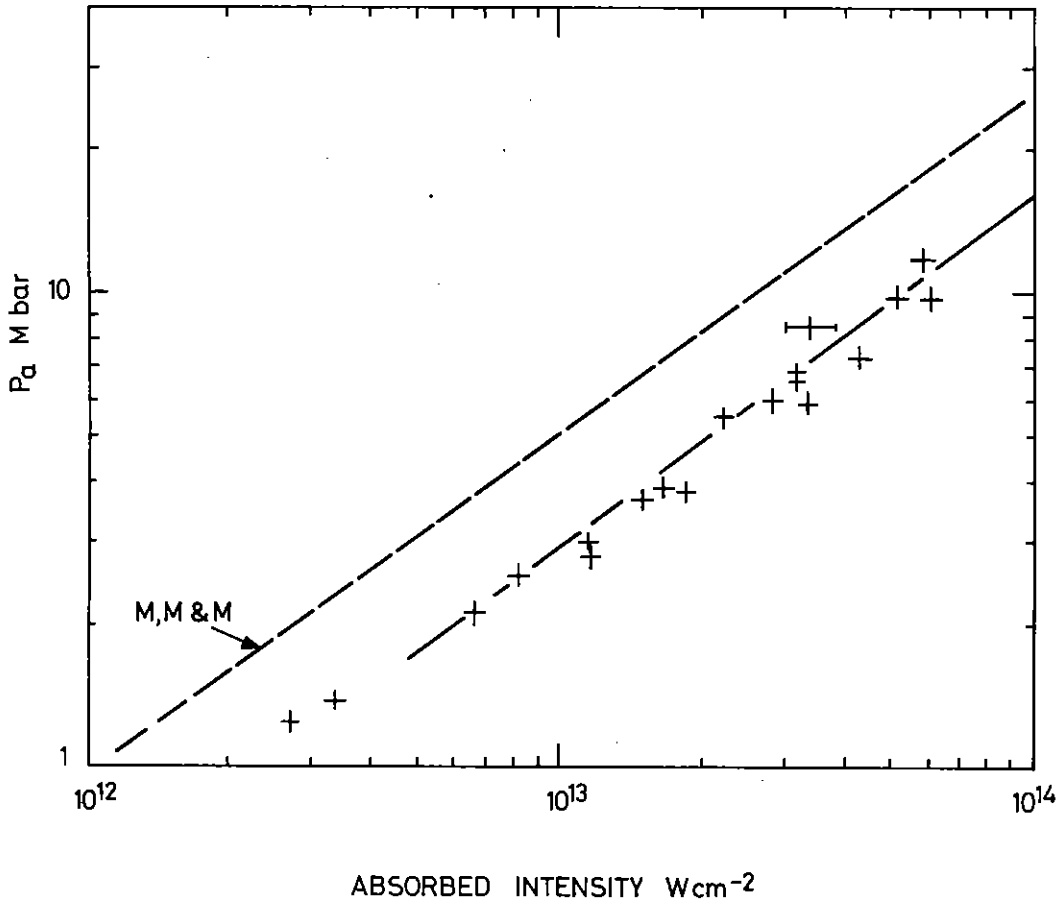

the essential features of the ablation process has been obtained both for plane targets at wavelengths 1,05, 0.53 and 0.35 μm and for spherical targets at 1.05 and 0.53 μm.

It has been clearly seen that where irradiance is varied at constant laser energy by varying spot size on plane targets, lateral flow of energy from the focal spot gives very different behaviour from that observed on spherical targets and also on plane targets at constant spot size. With due appreciation of the nature of the process it was shown how both the actual pressure generated and the pressure that would be generated in the limit of negligible lateral energy flow could be estimated from plane target data to a useful degree of accuracy. The effect of the lateral energy flow is to reduce the exponent of the power laws relating $\dot{m}_s$ and $\bar{v}$ to the absorbed irradiance I_a. There results a sharp contrast between the rate of increase of $\dot{m}_s$ with I_{abs} in spherical geometry and plane geometry at constant laser energy.

The spherical data are clearly simpler to interpret though they are more limited in range of irradiance and wavelength. The strong $I^{0.8}$ scaling of $\dot{m}_s$ with I is interpreted as showing evidence of a progressively increasing density at the ablation front which may be due at low irradiance to decreasing classical absorption at subcritical density and at high irradiance to increasing ablation by either thermal transport or more penetrating 'hot' electrons and/or soft X-ray radiation. This strong scaling is an encouraging feature for attempts to obtain hydrodynamically efficient laser driven compression. The derivation of pressure from the spherical target data is complicated by the need to define the effective surface area for momentum transfer, but apart from this uncertainty involving a factor $\gamma \simeq 0.5$ the results can be summarized by

$$Pa = 4.2\gamma \left(\frac{I_{abs}}{10^{13} \text{ W cm}^{-2}} \right)^{0.9} \quad \text{Mbar}$$

at $\lambda = 1.06$ μm and

$$Pa = 4.2\gamma \left(\frac{I_{abs}}{10^{13} \text{ W cm}^{-2}} \right)^{0.74} \quad \text{Mbar}$$

Table 4.01

	$I_{abs} = 10^{14}$ W cm^{-2}		$I_{inc} = 10^{14}$ W cm^{-2}		$I_{inc}\lambda^2 = 10^{14}$ W cm^{-2} m^2	
1.05 μm	18 Mbar	17	12	9.4	12	9.4
0.53 μm	25	20	21	15	50	48
0.33 μm	36	-	32	-	130	-
	P_a plane	P_a sphere	P_a plane	P_a sphere	P_a plane	P_a sphere

Tabluated values of ablation pressure from the analytic fits to experimental mass ablation rate data. The spherical pressure values are multiplied by the correction factor γ taken from the numerical simulation results in figure 4.38.

at $\lambda = 0.53$ μm, using $P_a = \gamma(2\dot{m}_s I_{abs})^{\frac{1}{2}}$.

These expressions may be compared with those derived from the plane target data in the limit of neglibible lateral energy flow viz

$$Pa = 4.4 \left(\frac{I_{abs}}{10^{13} \text{ W cm}^{-2}}\right)^{0.62}$$

$$Pa = 5.3 \left(\frac{I_{abs}}{10^{13} \text{ W cm}^{-2}}\right)^{0.68}$$

$$Pa = 7.8 \left(\frac{I_{abs}}{10^{13} \text{ W cm}^{-2}}\right)^{0.66}$$

for $\lambda = 1.05$, 0.53 and 0.35 μm respectively.

The wavelength scaling of pressure is seen to be weak when expressed in terms of absorbed irradiance which is qualitatively consistent with significant absorption at subcritical density

Allowance for the wavelength dependent absorption fraction shows however a significant increase in the pressure generated for a given incident irradiance as the wavelength is reduced (see Table 4.01).

The table also compares ablation pressure at the same value of $I\lambda^2$ and thus shows the maximum pressure available for a given level of hot electron preheating. The advantage of shorter wavelength irradiation is very pronounced.

However, there are clearly considerable problems in maintaining spatial uniformity of energy deposition as the laser wavelength is reduced and it remains an important and not fully understood question at what price in loss of spatial uniformity the gain in pressure is obtained.

P Cunningham, C L S Lewis, A K Roy, J M Ward (QUB), T Goldsack, J D Kilkenny, S Veats, B McGowan (Imp Coll), L Pina (Budapest), M H Key, W T Toner and P T Rumsby (RAL)

4.5 Exploding Pushers

Neutron yields were measured from a number of six-beam implosions of exploding pusher targets, with a non-optimal pulse length of 180 psec. Other diagnostics used on these shots were a pinhole camera, X-ray spectrometers and ion calorimeters.

For each shot, an effective absorbed energy was derived by multiplying the absorbed energy given by the ion calorimeters by the fraction of the laser energy deposited before the cut-off time predicted by the Storm model (4.48). The cut-off time depends sensitively on the target mass and size in relation to the laser energy and pulse length, particularly in non-optimal cases. Neutron yields, normalised by a factor $\rho_0^2 R_0^4$ to take account of variations in the initial fuel parameters, are shown in Figure 4.41 plotted against specific effective absorbed energy.

Ion temperatures derived from the data are compared with those predicted by the model in Figure 4.42. In contrast to results from our previous runs (4.22), the experimental temperatures are now substantially higher than those predicted. This may indicate either higher compression or higher temperatures at the centre of the core due to better spherical convergence of the implosion shock wave. Volume compressions of about 300 were seen in three of the sixteen shots for which good pinhole camera data are available. However we have not been able to establish a correlation between core size and neutron yield and some small cores were seen in our previous six beam run. We attribute the presumed improvement in symmetry to better focusing of the six beams on target resulting from experience.

Some Argon-filled microballoons were imploded and analysed spectroscopically using the techniques described in (4.49). The results from one shot where the conditions (apart from pulse length) were similar to those for the core spectrum analysis presented last year (4.22) are shown in Figures 4.43, 4.44 and 4.45. On this occasion, three Argon lines could be fitted and the ground state density resulting from the fit shown in Figure 4.44 is in agreement with the density deduced from the pinhole picture of the core. The very high electron density implies a substantial

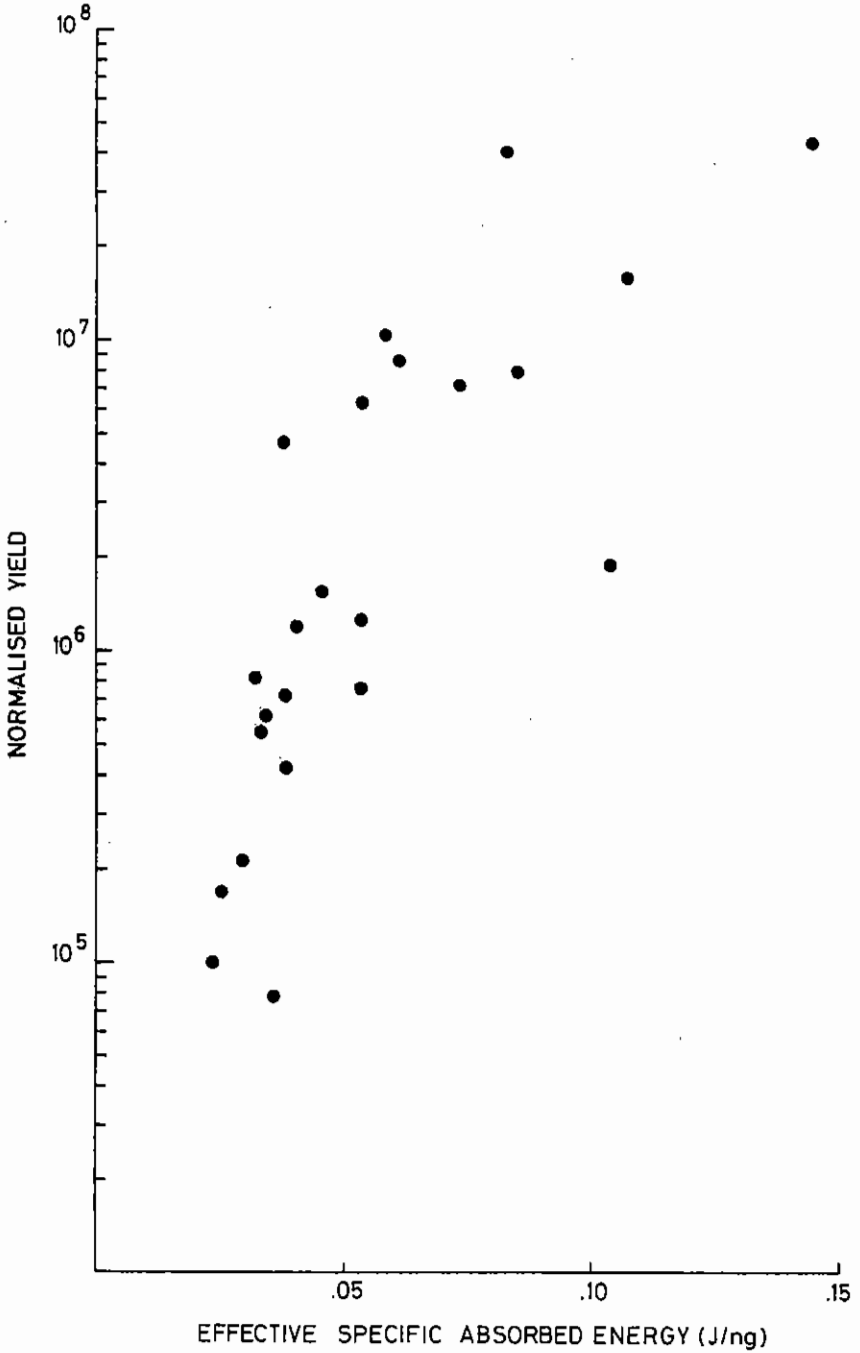

Figure 4.41 Normalised neutron yield vs. effective specific absorbed energy. Normalisation is by a factor fo^2Ro^4 with reference to a 100 μm diameter target filled to 10 atmospheres.

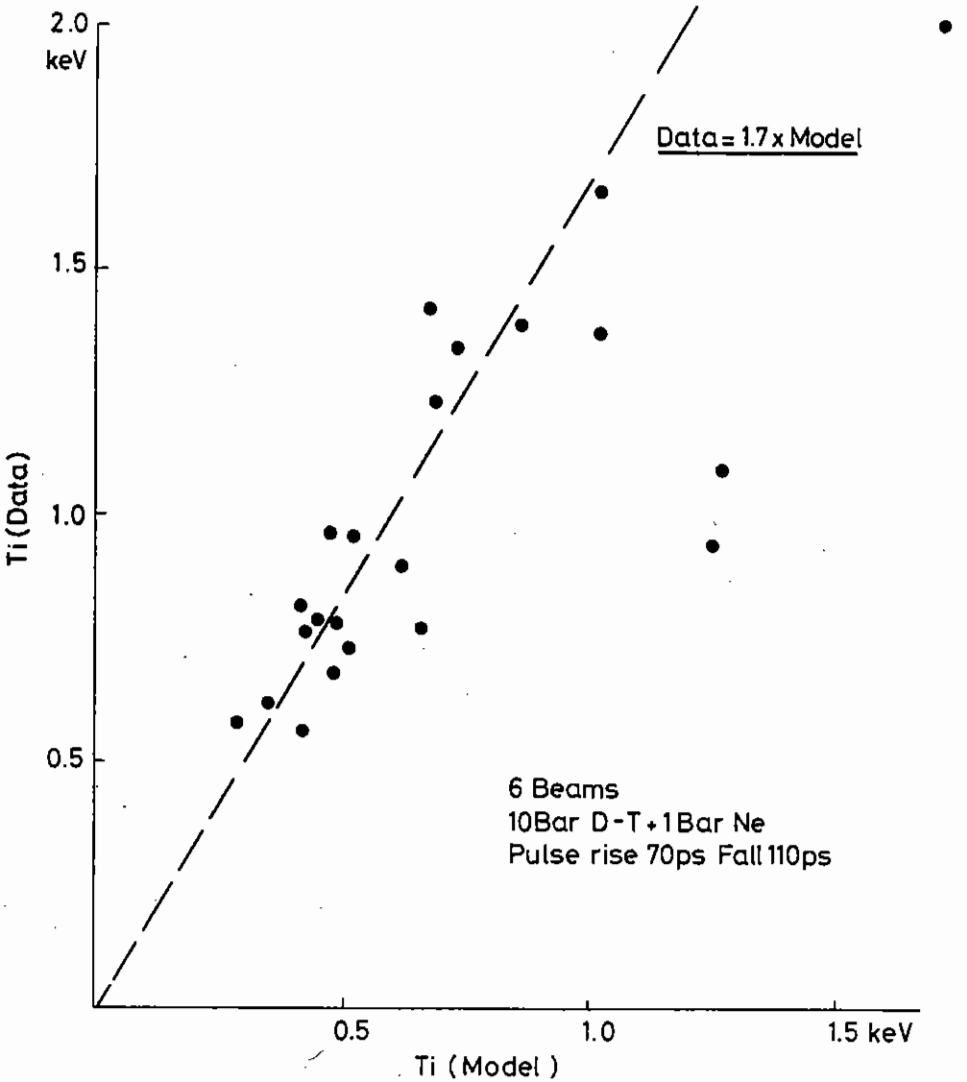

Figure 4.42 Ion temperatures derived from data compared with model predictions.

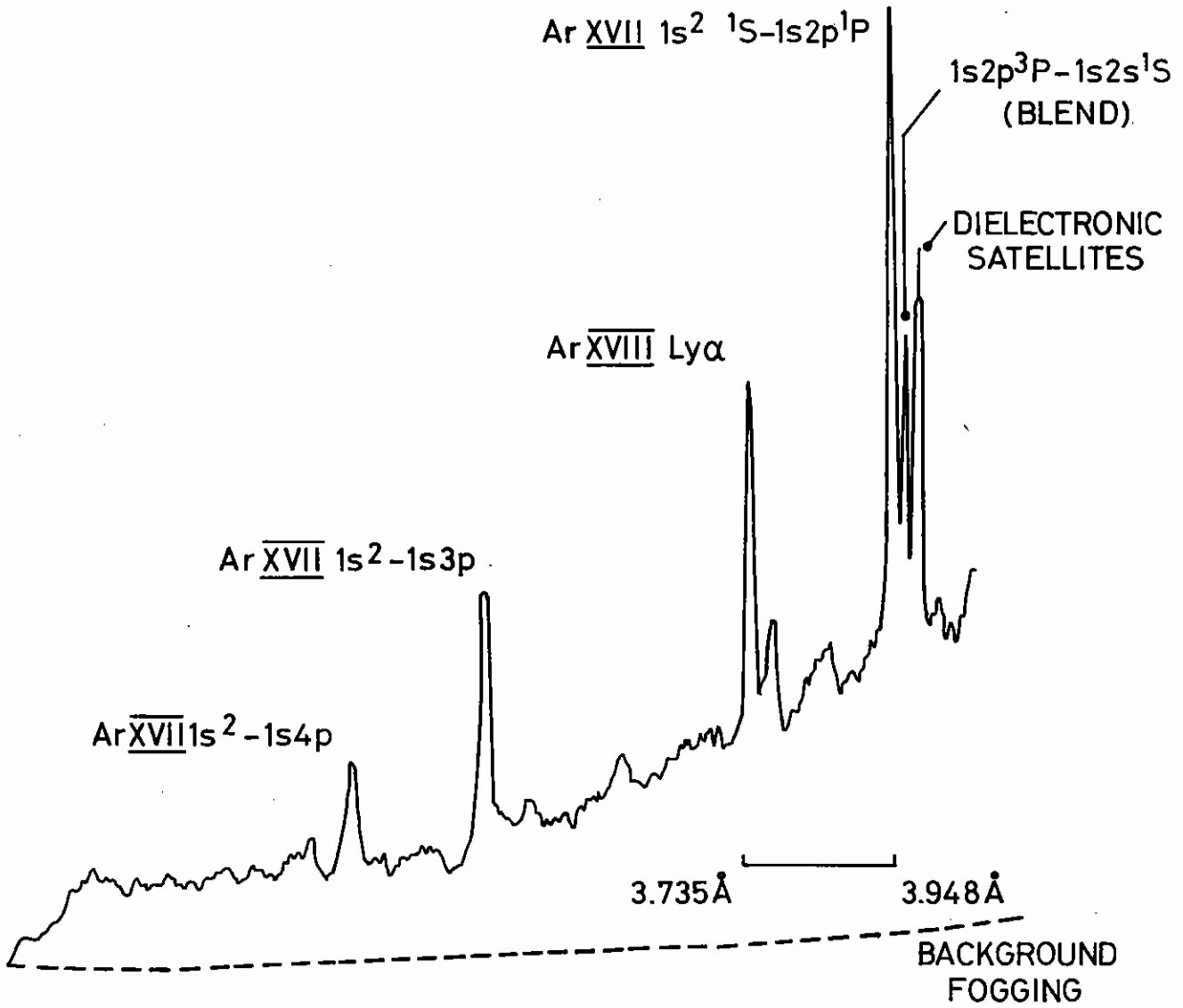

Figure 4.43 The emission spectrum of a 6 Beam implosion of an Argon filled glass microscope. The laser wavelength was 1.06 micron. The hydrogenic and helium like resonance lines are shown.

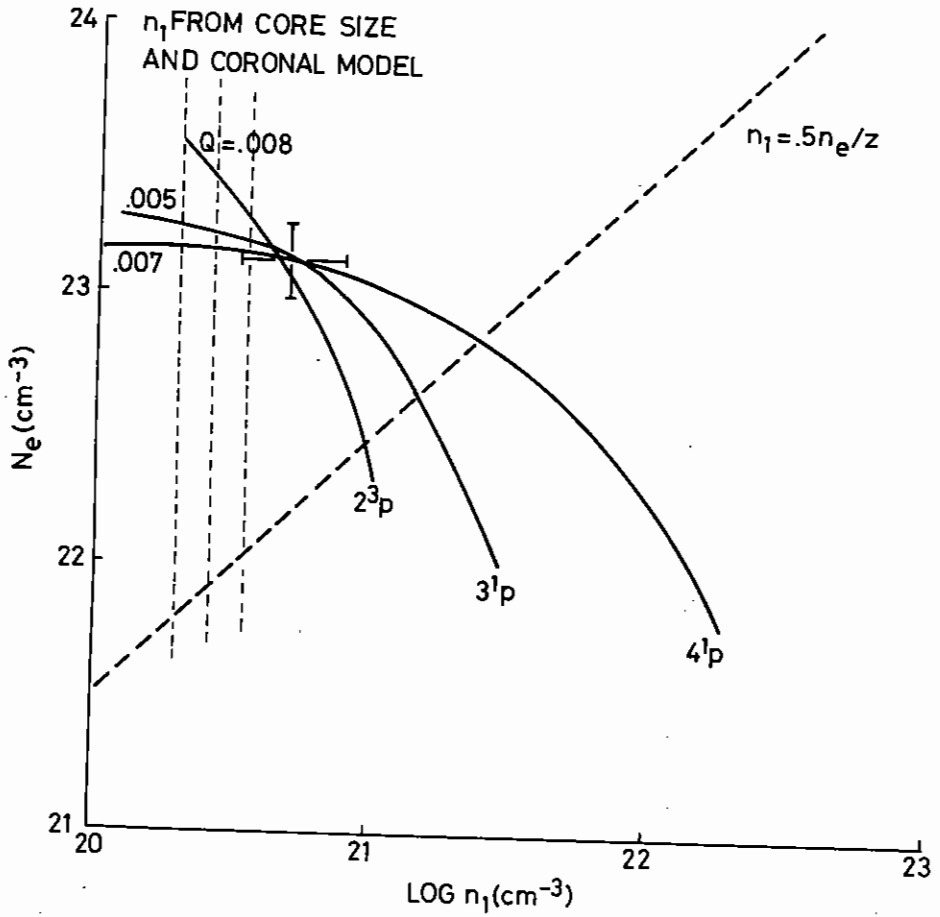

Figure 4.44 The n_e vs. n_1 plot for Argon filled microsphere. Temperature is 6.10^6K.

The solid lines are the line of best fit with the cross the inferred densities. The values of Q obtained is labelled on each transition. The dashed line is the constraint equation given in text.

amount of Silicon in the core.

The satellite to the Argon XVIII Ly_α line is a mixture of dipole forbidden $1\,^1S - 2\,^1S$ and spin forbidden $1\,^1S - 2\,^3P$ transitions. It is possible to obtain an estimate of the contribution of each transition to the satellite by using a fitting procedure similar to that for the main line and get an independent measure of the plasma parameters. Figure 4.45 shows the result of a fit to the Ly_α satellite seen in Figure 4.43. The plasma parameters agree with those deduced from the simultaneous line fit of Figure 4.44. Analysis of the line and its satellite should be possible in streaked spectroscopy and may afford a means of making time resolved density measurements of hot cores.

S Sartang (Westfield Coll), W T Toner (RAL) and S Veats (Imp Coll)

4.6 Self-generated Magnetic Fields

4.6.1 Experimental Investigations

Faraday rotation experiments were carried out on both planar and spherical ablatively driven targets to look for the presence of self-generated magnetic fields. Measurements were taken during and after the laser pulse in the intensity range of 10^{13} to 10^{14} W cm^{-2}.

Targets consisting of 240 to 280 μm diameter empty glass microballoons and 1 mm diameter aluminium wires were irradiated with one or four laser beams. The heating pulse was generated by stacking eight 100 psec (FWHM) Gaussian pulses separated by 150 psec giving an overall pulse length of 1.2 nsec. The peak intensities of the individual pulses varied by less than ± 30 %. The diagnostic beam was a Raman shifted second harmonic beam (622 nm) which was generated by splitting off a fraction of the oscillator pulse before the pulse stacker and passing it through a separate amplifier chain (see chapter 3.2). After conversion to the red the probe beam energy was measured to be 1 mJ in 50 psec. The timing of the probe pulse in relation to the main pulse was carried out using an EPL streak camera and was known within ± 15 psec. The target was imaged by an f/1.4

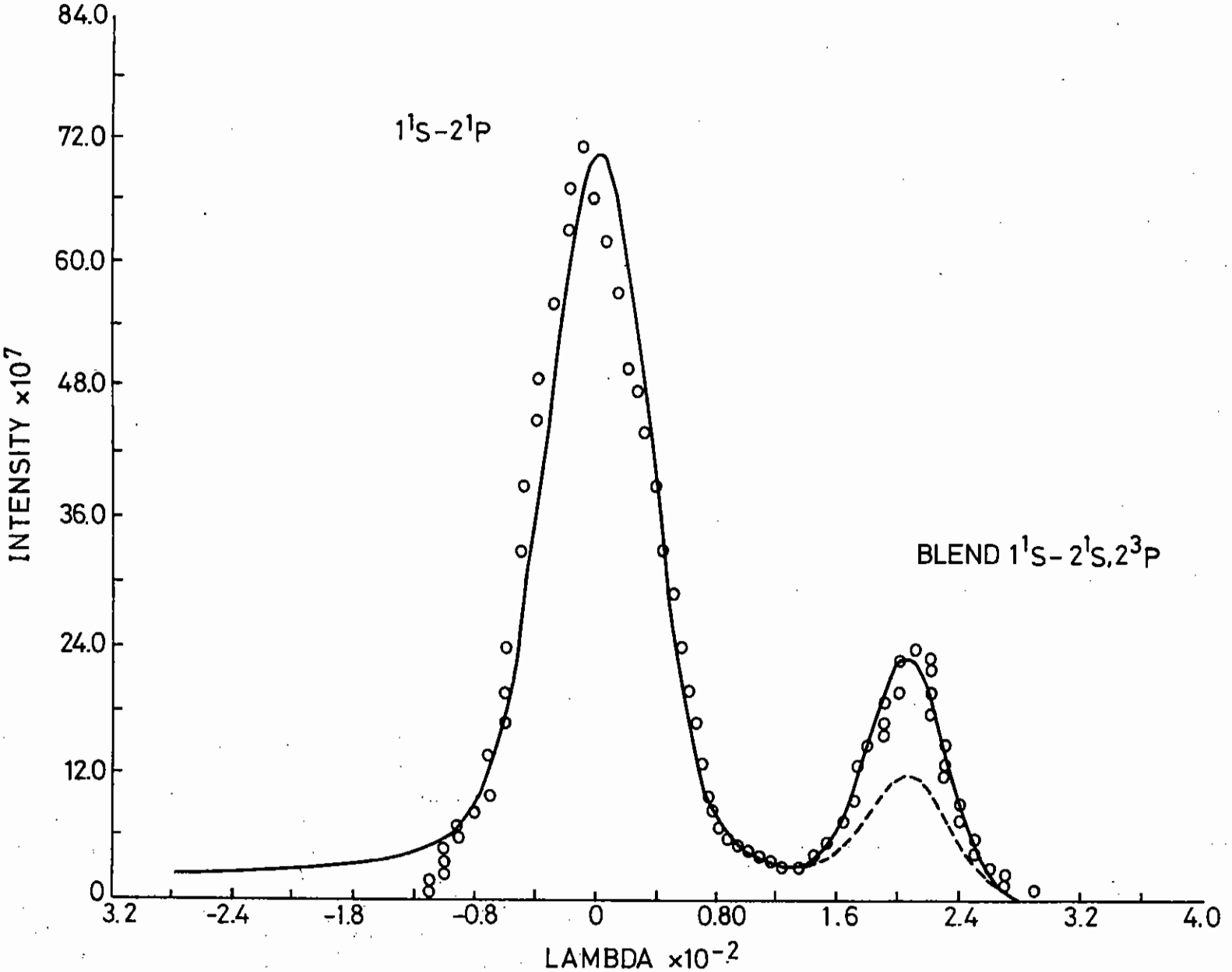

Figure 4.45 The Ar XVII 1^1S-2^1P, and 1^1S-$2^1S,2^3P$ Blend for the plasma diagnosed in Figure 4.43

------- is contribution of 2^1S only
——— is contribution of total profile
ooooooo are experimental points

microscope objective with a 40 times overall magnification. For Faraday rotation measurements a sheet polarizer served as analyser and was set either orthogonal or at 80° to the probe beam polarization, while for density profile measurements a Nomarski type of interferometer was used. Faraday rotation images were recorded on Polaroid type 57, and the interferograms on Polaroid type 55.

4.6.1(a) Planar Targets

Figure 4.46 shows an interferogram (a) and a Faraday rotation image (b) for an aluminium wire target taken 0.96 nsec after the beginning of the main laser pulse. The irradiance on target was 3×10^{13} W cm^{-2}.

The analyser was set at 80° to the probe beam polarization resulting in a dark-bright pattern of the Faraday rotation images. Similar results taken with crossed polarisers showed two bright regions, one above and one below the focal spot indicating the presence of a toroidal self-generated magnetic field.

The Faraday rotation and interferometric data were unfolded by means of an Abel inversion routine which assumed axial symmetry and gave density and magnetic field profiles. Figure 4.47 shows the magnetic field profile obtained from Figure 4.46(b) in the axial and radial directions where Z is in the direction of the heating laser beam and R is normal to it. The peak value of the magnetic field is 1.6 MG and occurs at a radius of about 60 μm ie at the edge of focal spot (the focal spot diameter was 100 μm). The electron density profile for the shot shown in Figure 4.46 is shown in Figure 4.48, where Z is again in the axial direction. A shell structure can be observed in the electron density profile which is probably caused by the magnetic field pressure.

Similar results were obtained at higher irradiance. Figure 4.49 shows an interferogram (a) and a Faraday rotation image (b) taken at 0.96 nsec after the beginning of the laser pulse, (ie at a similar time to the observations in Figure 4.46). The target was irradiated at an intensity of 1.10^{14} W cm^{-2}. Again the analyser was set at 80° to the probe beam

polarization. The Abel inversion analysis of these data are shown in Figure 4.50 and Figure 4.51. The magnetic field has a maximum value of about 3 MG in the quarter critical density region. As at lower irradiance a shell structure is observed in the electron density profile.

Results were also taken 0.27 ns after the end of the laser pulse. Figure 4.52 shows the magnetic field profile and Figure 4.53 the electron density profile. The magnetic field profile is modulated radially probably due to the temporal modulation of the stacked laser pulse. On the symmetry axis a spike is observed in the electron density profile with a dip where the maximum magnetic field is situated. The radial plasma expansion is inhibited by the self-generated magnetic field. A similar electron density profile has been observed before on a plane target irradiated at the much higher intensity of 10^{16} W cm^{-2} (4.50).

4.6.1(b) Spherical Targets

Figure 4.54 shows an interferogram (a) and Faraday rotation image (b) for a 247 μm diameter glass microballoon heated by a single laser beam. This was taken 1.46 nsec after the beginning of the stacked laser pulse. The energy on the target was 5 J and the focal spot 100 μm in diameter which resulted in a peak irradiance of 4×10^{13} W cm^{-2}. The overlaid silhouette on the interferogram marks the original target position. The central bright spot in the Faraday rotation image is due to scattered 1.05 μm radiation and provides the reference focal spot position. In this case the analyser-polarizer was orthogonal to the probe beam polarization and consequently the two bright regions observed above and below the focal spot indicate the presence of a toroidal magnetic field.

Figure 4.55 shows the magnetic field profile (derived from the data of Figure 4.54) in the axial and radial directions where Z is in the direction of the heating laser beam and R is normal to it. The field is seen to be strongly modulated radially and to have a peak value of about 2 MG at a radius of 67 μm. The radial field modulation may be due to the temporal modulation of the heating pulse. In the axial direction the peak magnetic field occurs at 18 μm from the target surface and a fall-off in

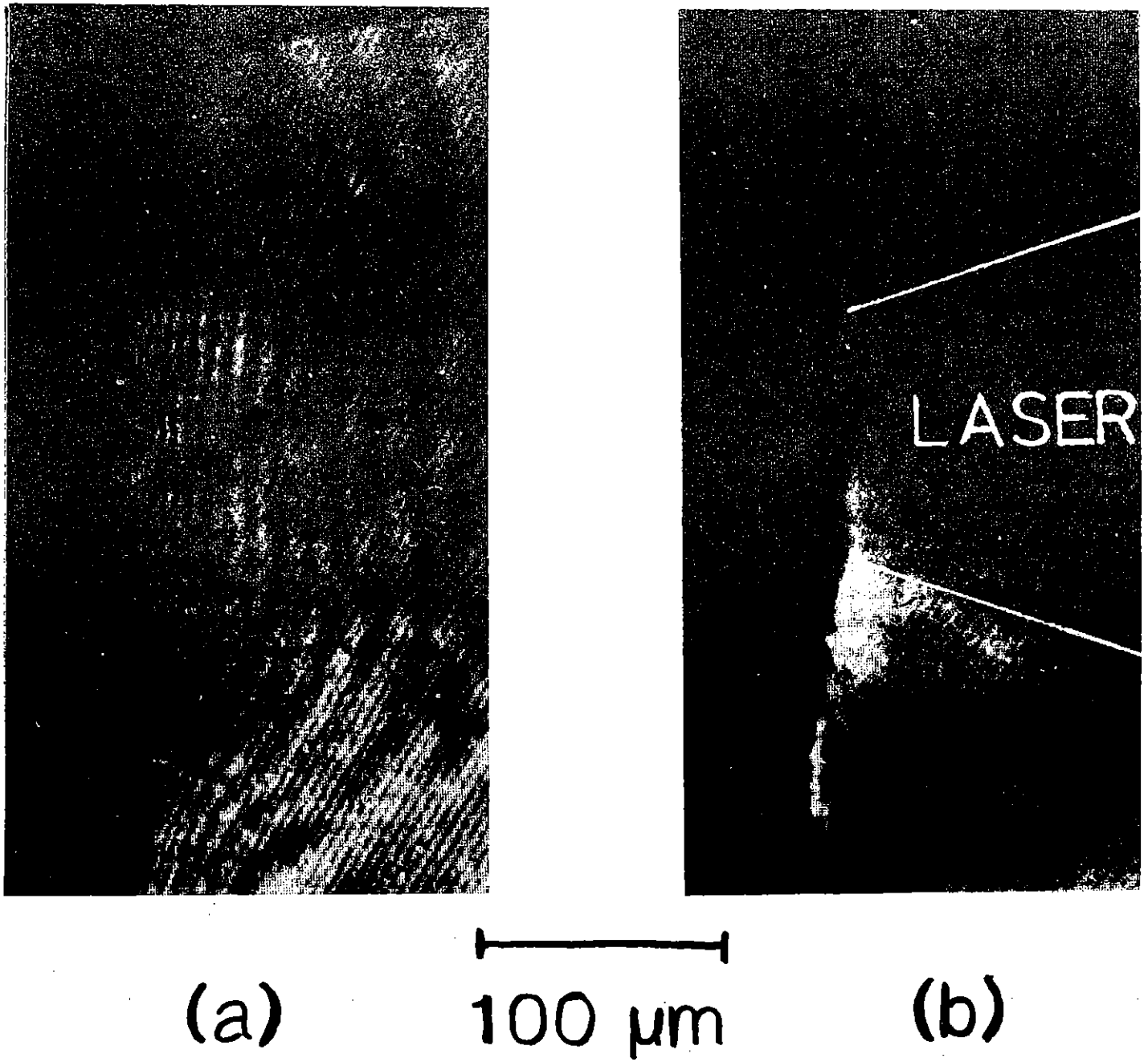

Figure 4.46 Interferogram (a) and Faraday rotation image (b) taken on an aluminium wire target 0.965 nsec after the beginning of the laser pulse. The peak irradiance was 3×10^{13} W cm^{-2}.

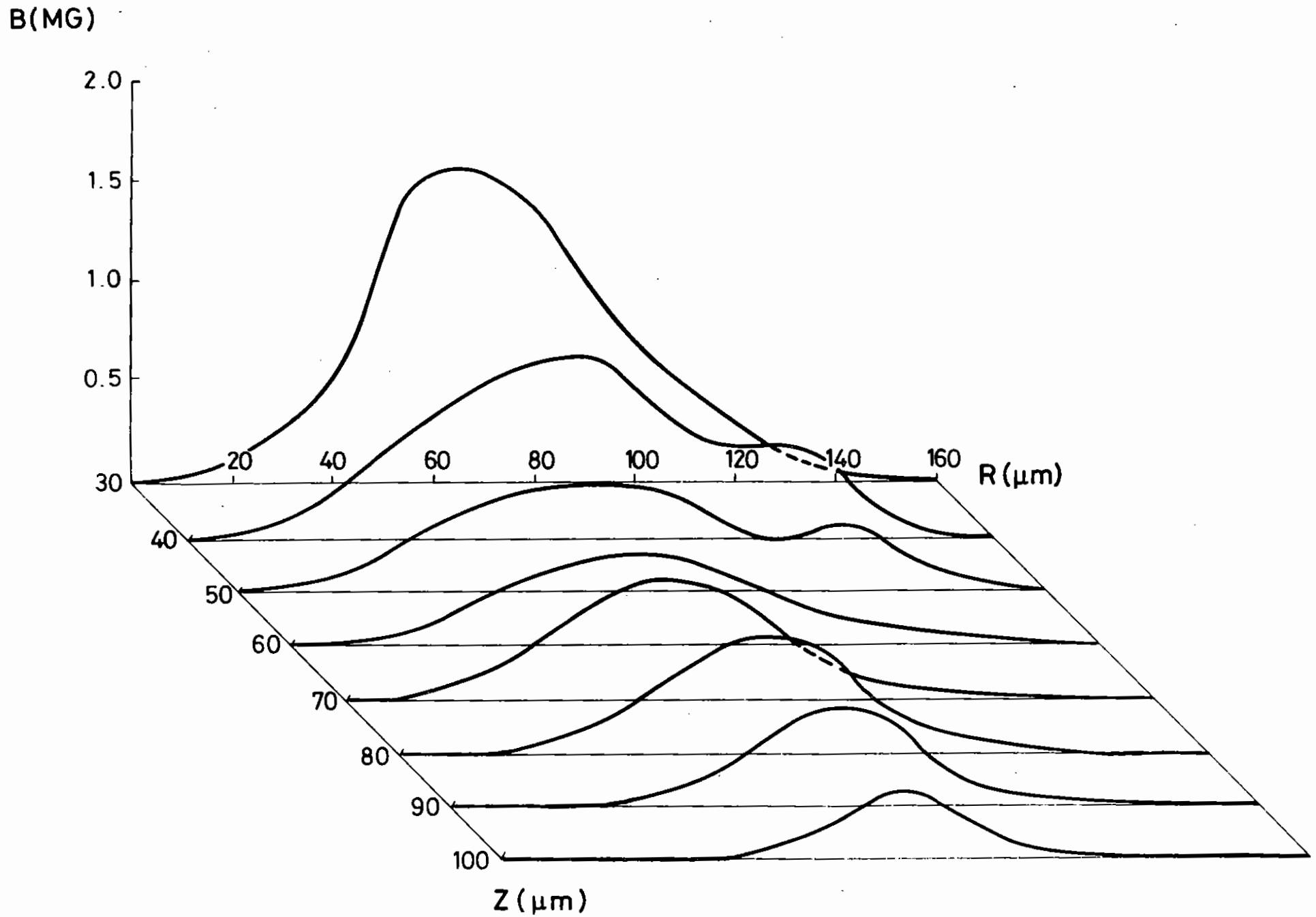

Figure 4.47 Magnetic field profile of Fig 4.46(b)

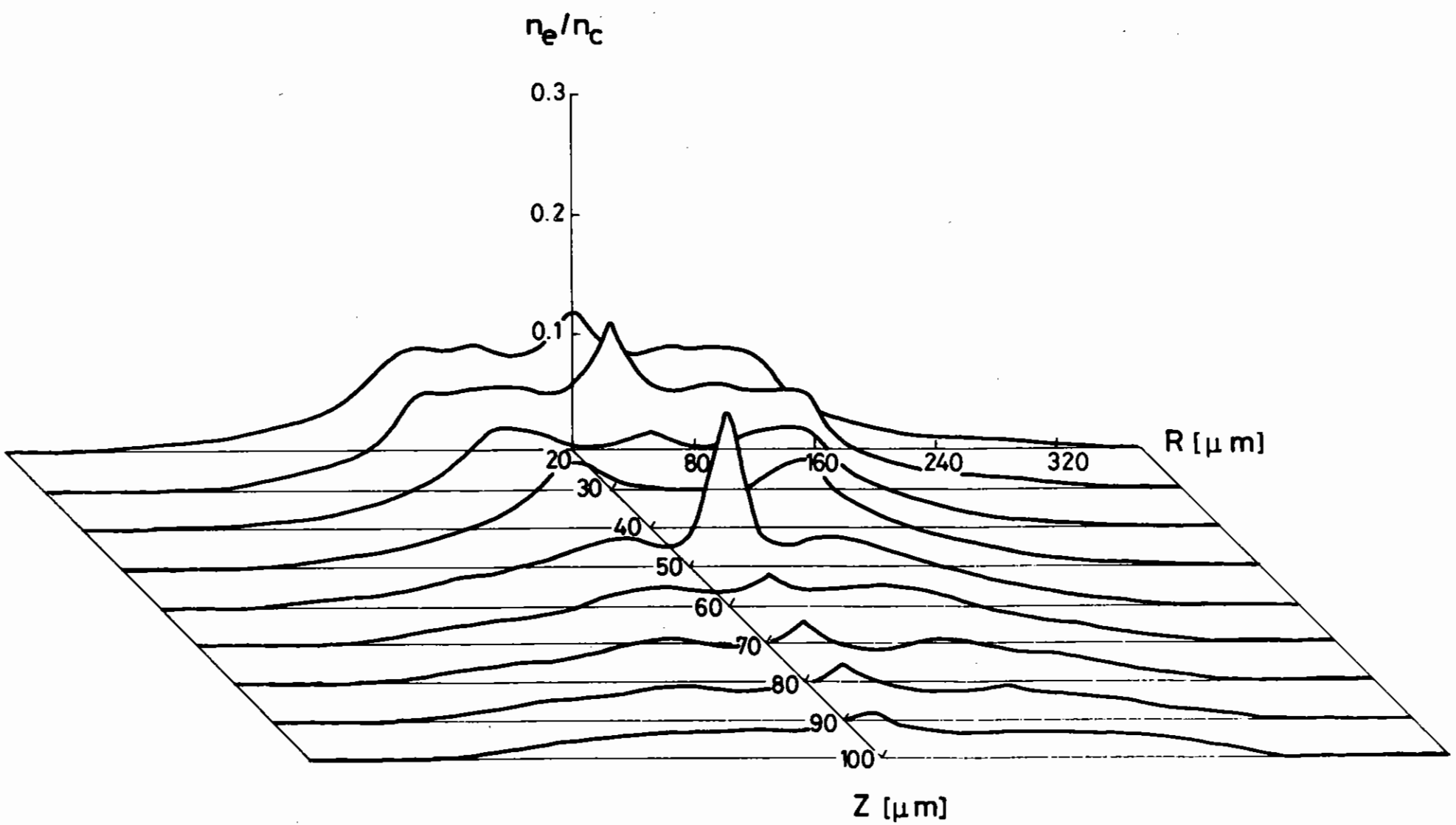

Figure 4.48 Electron density profile of Fig 4.46(a)

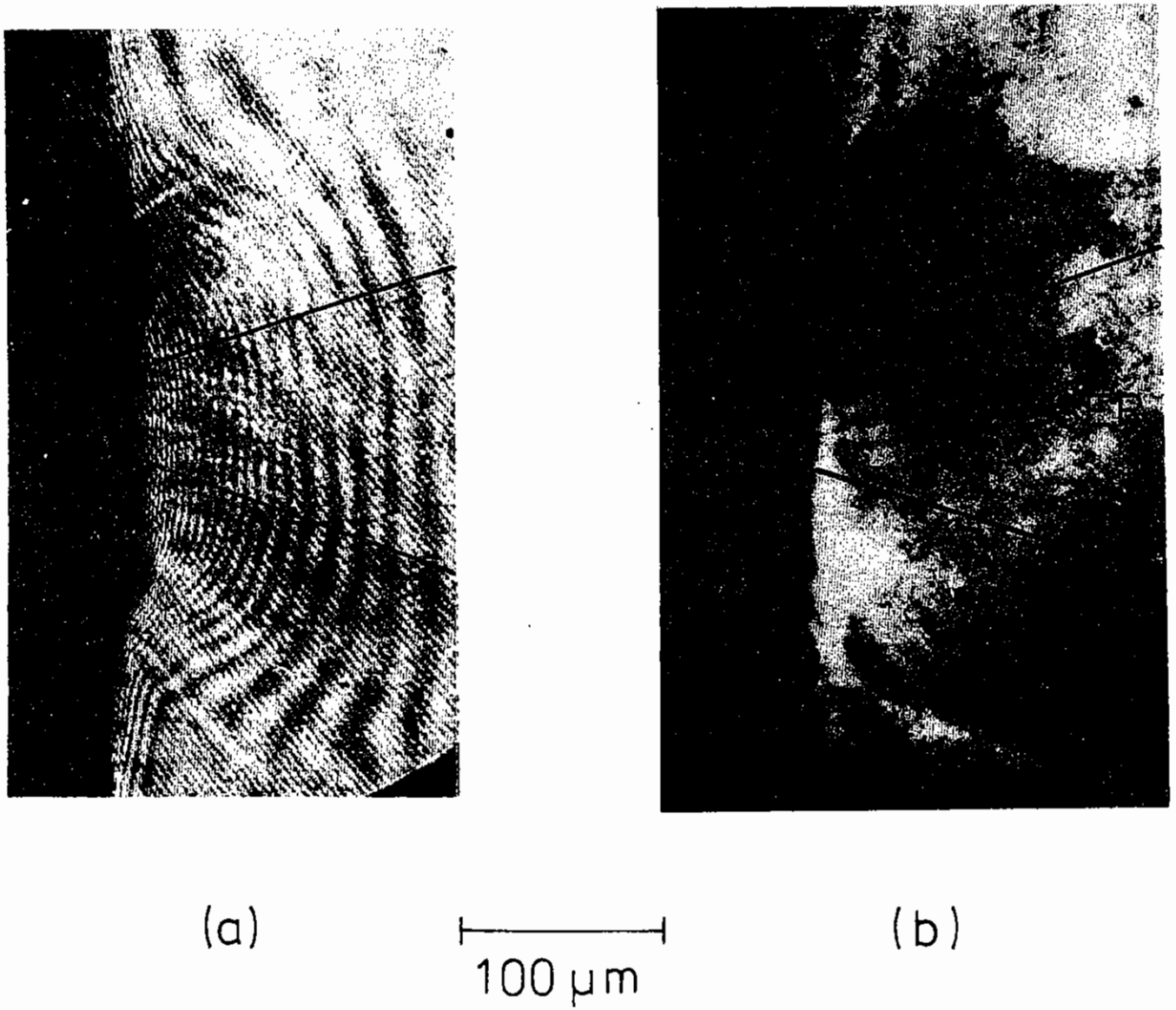

Figure 4.49 Interferogram (a) and Faraday rotation image (b) taken on an aluminium wire target 0.965 nsec after the beginning of the laser pulse. The peak irradiance was 1×10^{14} W cm^{-2}.

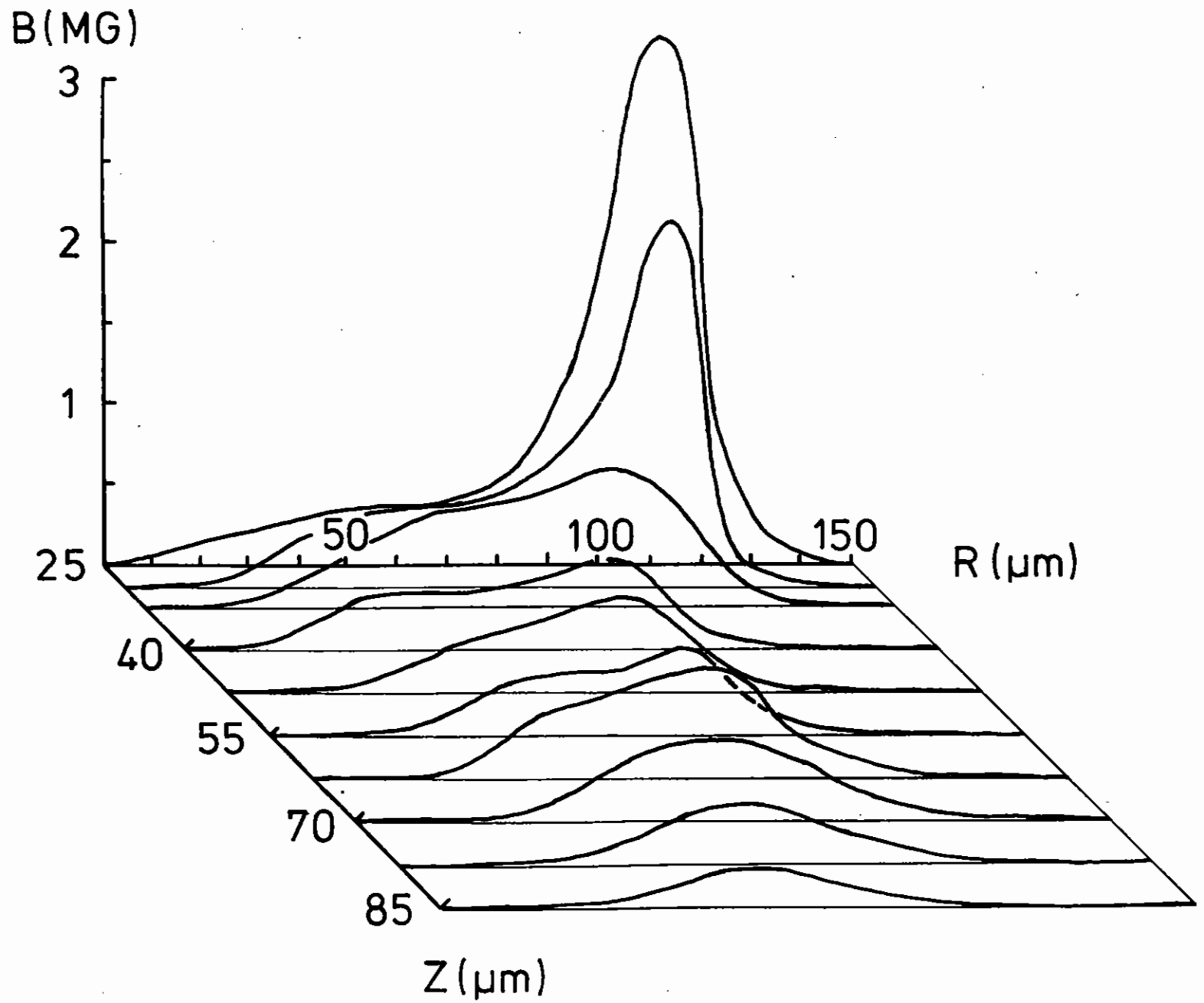

Figure 4.50 Magnetic field profile of Fig 4.49(b)

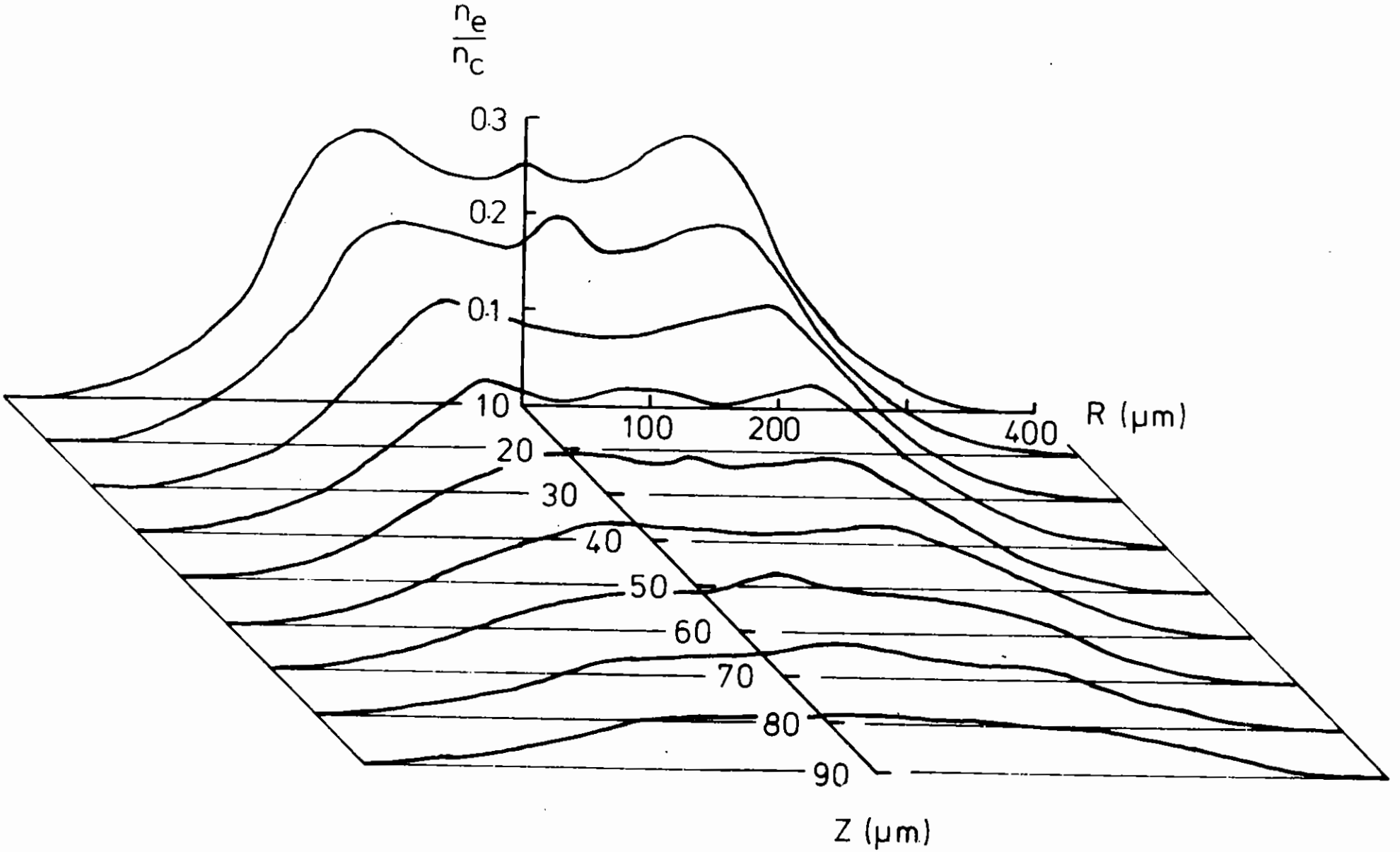

Figure 4.51 Electron density profile of Fig 4.49(a)

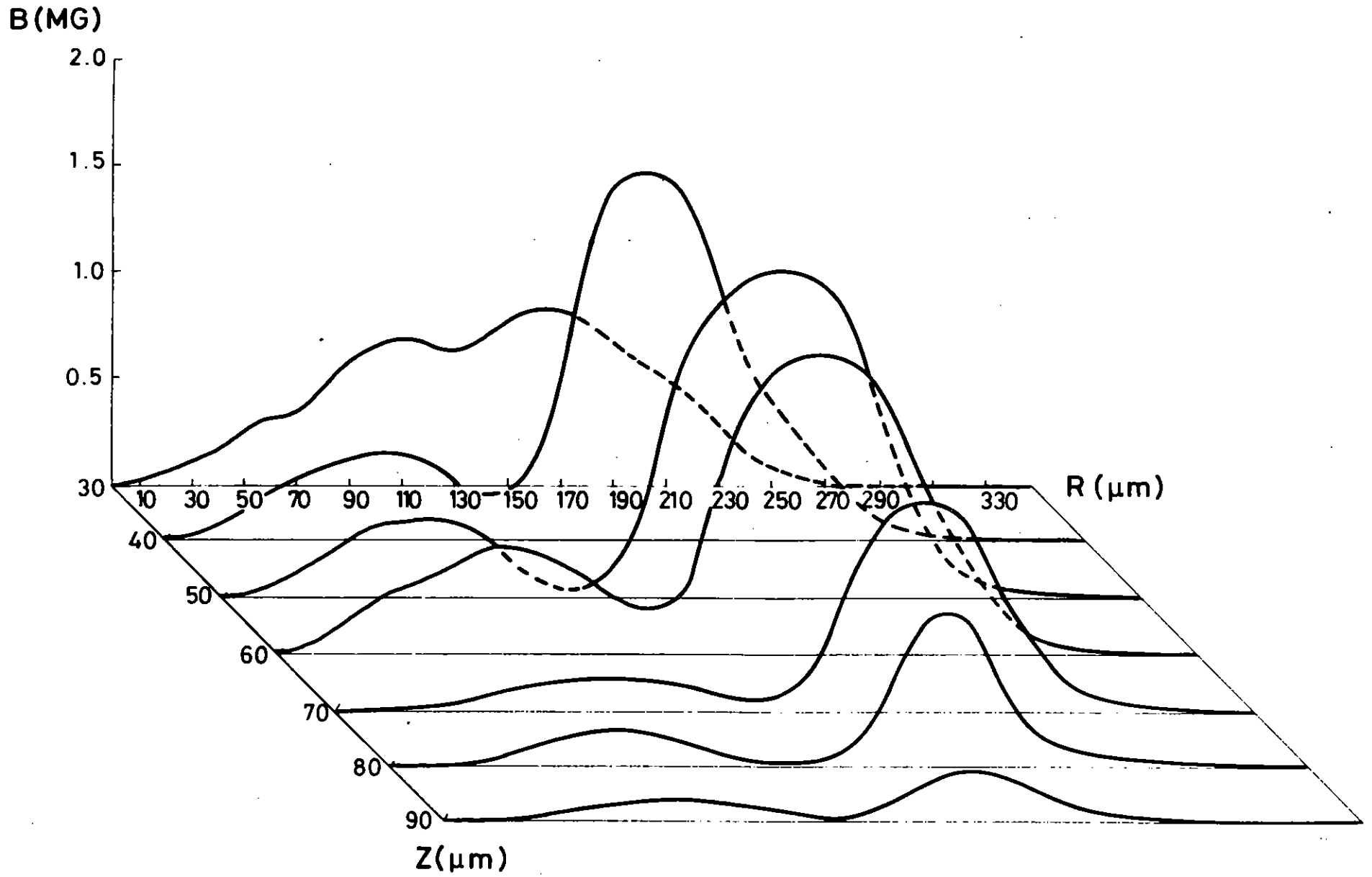

Figure 4.52 Magnetic field profile taken on an aluminium wire target 1.465 nsec after the beginning of the laser pulse. The irradiance was 3×10^{13} W cm^{-2}.

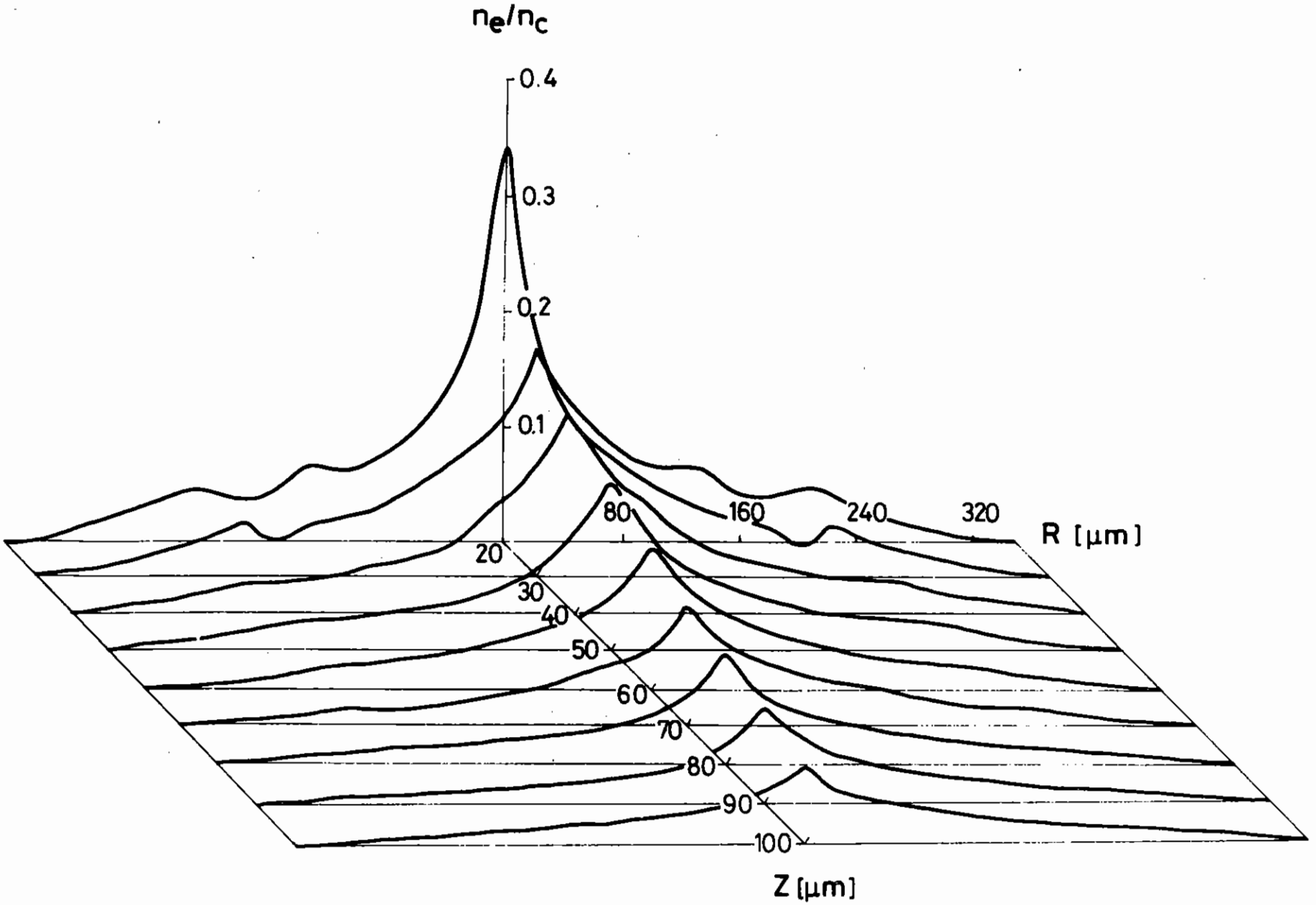

Figure 4.53 Electron density profile taken on an aluminium wire target 1.465 nsec after the beginning of the laser pulse.

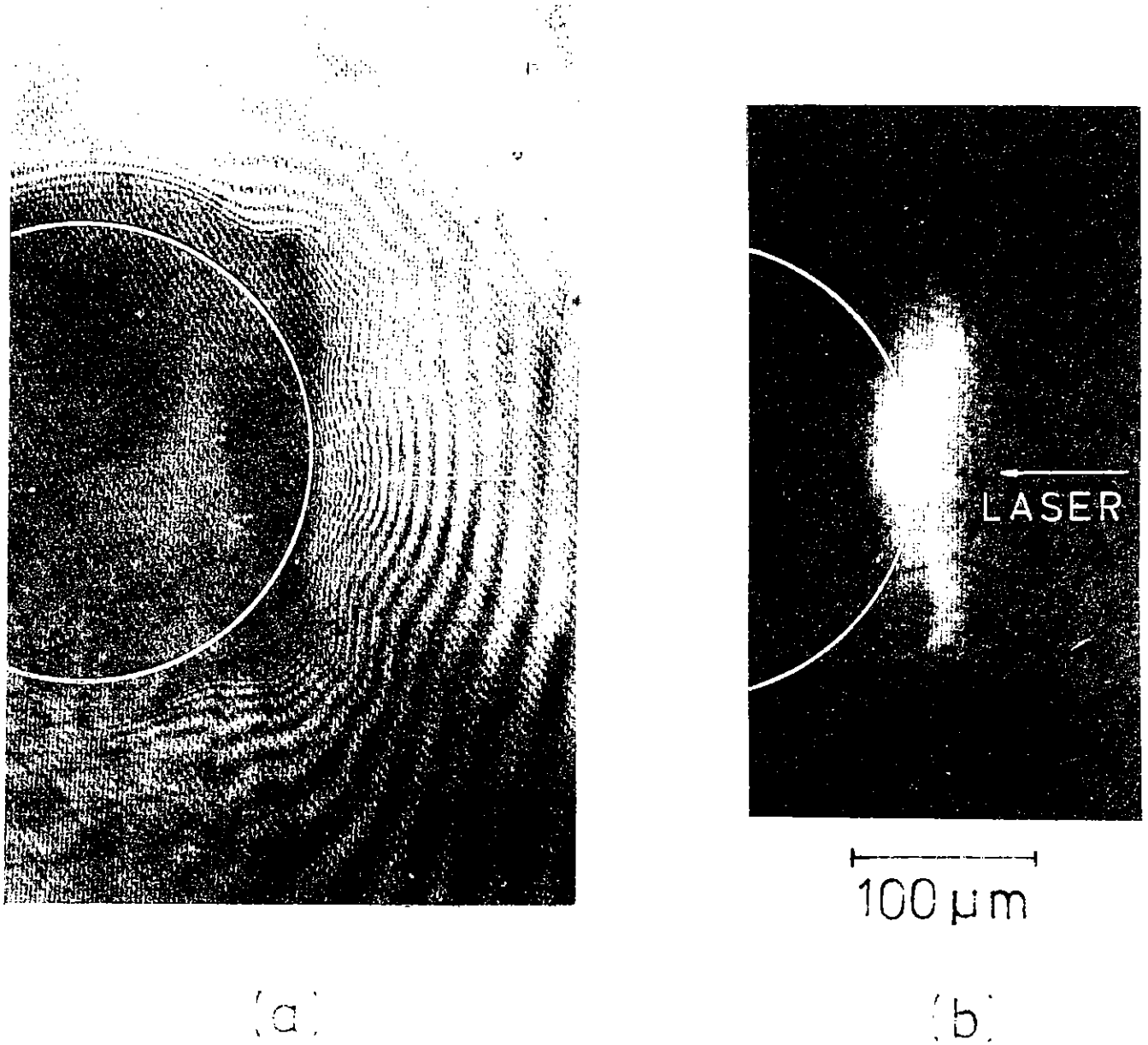

Figure 4.54 Interferogram (a) and Faraday rotation image (b) with the analyser set at 90° to the probe beam polarization. The 247 µm diameter glass microballoon was irradiated by a single laser beam.

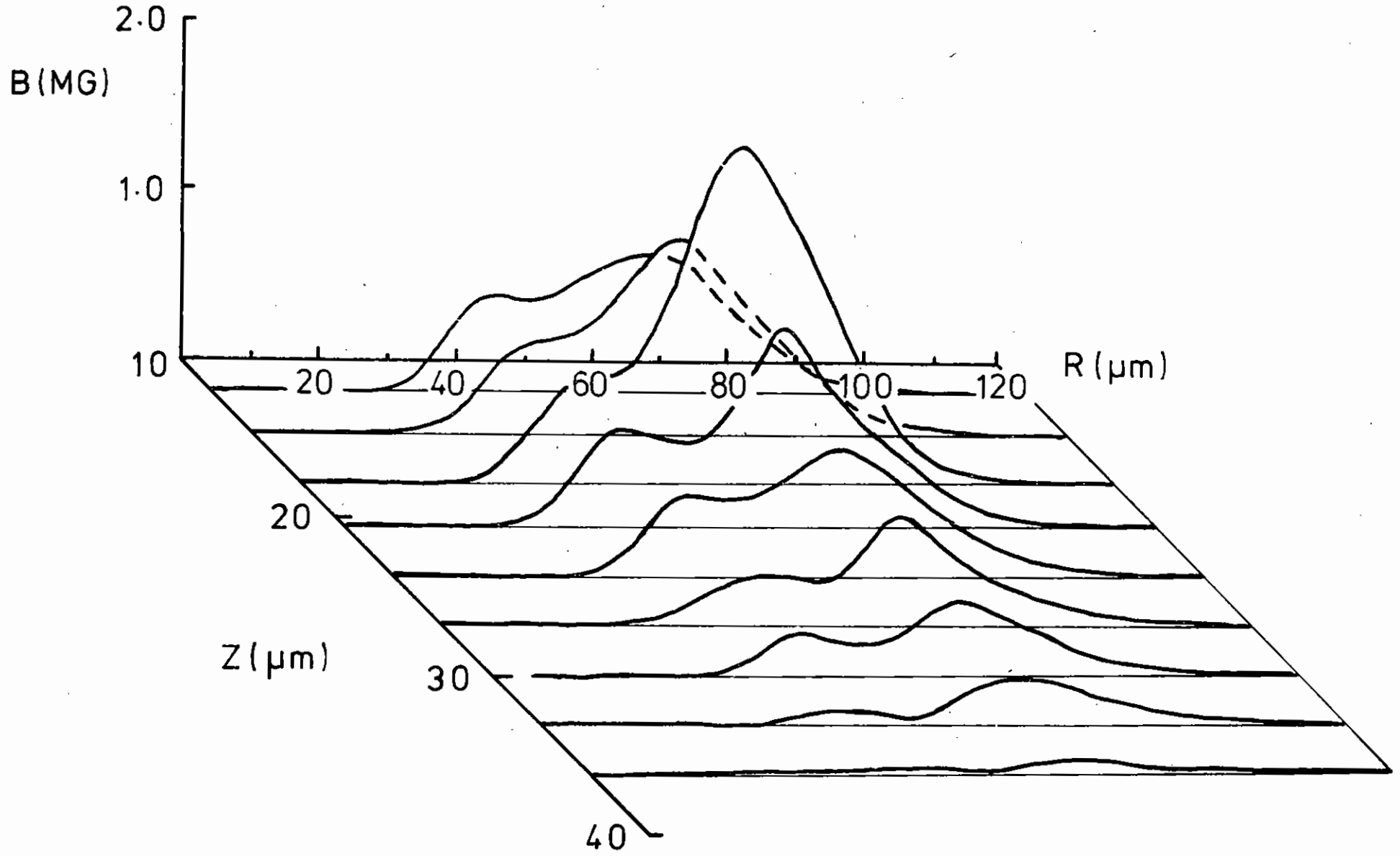

Figure 4.55 Magnetic field profile of Fig 4.54(b)

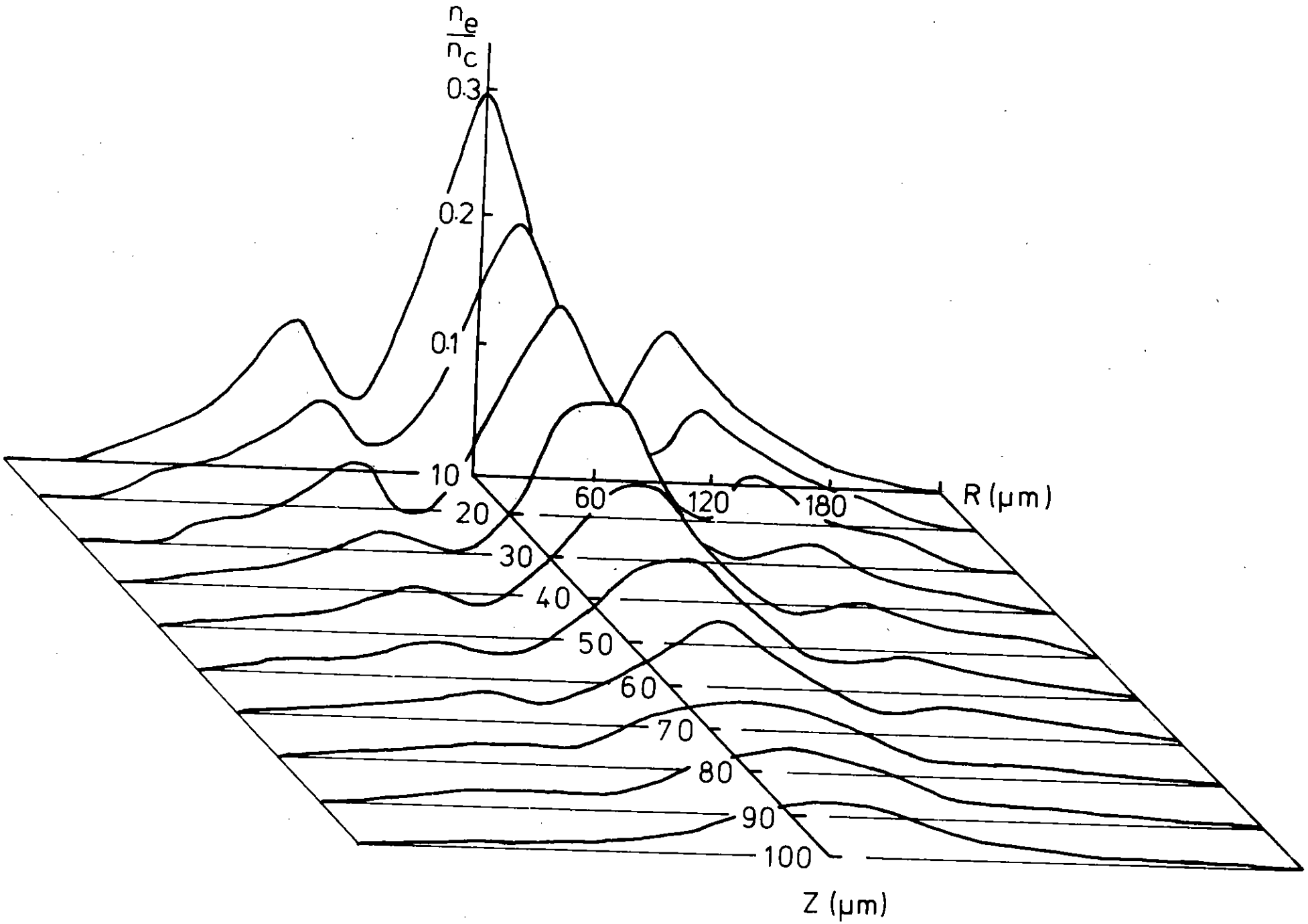

Figure 4.56 Electron density profile of Fig 4.54(a)

the magnitude of the magnetic field towards the target surface is noticeable. The orientation of the field was checked in several similar shots by setting the analyser at 80° (10° off perpendicular to the probe beam polarization). The field was observed to be of toroidal nature and it was consistent with the orientation of a $\nabla n \times \nabla T$ magnetic field. In Figure 4.56 the electron density profile in the axial and radial directions can be seen. Due to refraction, the probe beam has been cut off at 0.3 n_c. A dip in the density profile occurs in the same radial position as the magnetic field. This is due to the magnetic field pressure which pushes the plasma out of this region.

The experimentally observed magnetic fields are in reasonable agreement with those expected theoretically. Simple analytical expressions for the growth rate and saturation level of the thermoelectric magnetic fields considering only the $\nabla n \times \nabla T$ source term and the convection term have been deduced by Max et al (4.51). Using their saturation expression, a magnetic field of about 1 MG is calculated assuming an electron temperature of 400 eV and taking the measured electron density scalelength in the axial direction of 45 μm. For a proper comparison between the experimental results and theory, however, all the magnetic source terms must be considered as pointed out by Colombant and Winsor (4.52).

In order to study the effects of target illumination uniformity on the magnetic fields, spherical targets were illuminated with four laser beams situated normally to each other in a plane perpendicular to the probe beam. Figure 4.57 shows an interferogram and a Faraday rotation image of a 280 μm diameter microballoon taken 0.96 nsec after the beginning of the heating pulse (ie the heating pulse is still on). Each of the four beams was focused at the centre of the microballoon (d/R = 0) giving focal spots 100 μm in diameter (R is the target radius and d is the distance from the target centre to focal plane in the direction of the laser beam). By choosing these focusing conditions the target was not illuminated completely uniformly and therefore magnetic fields still occur which can be observed in the dark-bright pattern of the Faraday rotation image (the analyser was set at 80° to the probe beam polarization). The thermal conductivity was not sufficient to smooth out lateral temperature

gradients. As in Figure 4.54 dips in the interference fringes are observed where the magnetic fields occur as plasma is pushed from these regions due to the pressure. The expanding plasmas interact and collide at the interface between the focal spots giving rise to shock like structures.

By gradually enlarging the focal spots of each of the four beams, however, the magnetic fields gradually decreased. Eventually when d/R was 4.5, the illumination was sufficiently uniform that no large scale magnetic fields greater than 100 kG (the dedection threshold) were observed.

Due to the large f-number imaging lens and the probe beam being polarized either p or s relative to the density gradient, depolarization effects of the probe beam can be neglected in these Faraday rotation observations, according to Lehmberg and Stamper (4.53).

C Duncan, W D Luckin, O Willi (Oxford) and P T Rumsby (RAL)

4.6.2 Numerical Studies

In order to model the self-generated magnetic fields on plane targets the two dimensional Eulerian computer code, CASTOR was used.

Use of the transport coefficient as given by Braginskii gave good agreement with the magnitude and distribution of the field, but density and temperature distributions near the axis (where the field is absent) did not compare well with experimental observations. A much hotter plasma was observed on the axis which resulted in strong axial plasma ejection causing a density depletion to arise in numerical simulations in axial regions at later times whereas the experiments had observed a density enhancement.

The variation of $\omega\tau$ to alter the heat flux away from the axis was explored to simulate turbulent diffusion (4.51), and it was discovered that the code produced good agreement with all the experimentally observed parameters when the transport coefficients were calculated with the

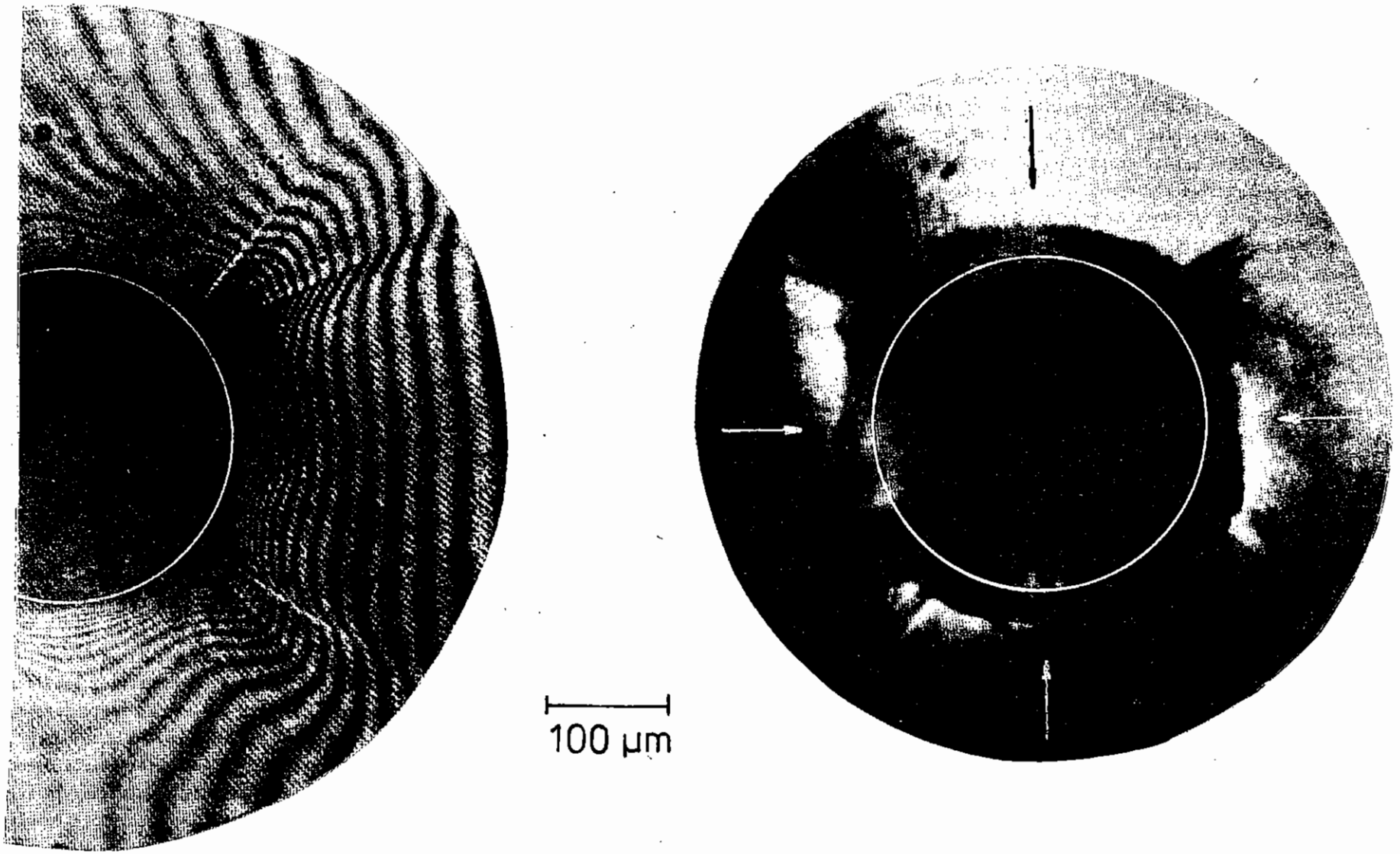

Figure 4.57 Interferogram (a) and Faraday rotation photograph for a 280 µm diameter glass microballoon heated with four laser beams situated orthogonally to each other in a plane. The peak irradiance on target was 8×10^{13} W cm^{-2}.

collision frequency enhanced by 20 %.

We report here a simulation of an Nd glass laser beam incident on a plane aluminium target. The pulse contains a total of 20 J and is Gaussian shaped in space with a beam radius of 30 μm. The pulse is made up by stacking 8 pulses of varying amplitude each of which is a Gaussian with a FWHM of 100 ps. The maximum intensity attained is 10^{14} W cm^{-2}. For the range of intensity considered the absorption is mainly via inverse bremsstrahlung and in our numerical simulations it is assumed that only 5 % of the energy reaching the critical surface is absorbed there.

The growth of the magnetic field, which is azimuthal in direction, is modelled by the equation

$$\frac{\partial \underline{B}}{\partial t} = \nabla x(\underline{v} \times \underline{B}) - \nabla x(\underline{\underline{\eta}}.\underline{J}) - \nabla x\left(\frac{1}{en_e}\,\underline{J} \times \underline{B}\right) - \frac{K}{en_e}\,\nabla n_e \times \nabla T_e - \frac{K}{C}\,x\,(\underline{\beta}.\nabla T_e)$$

The Hall effect and the thermoelectric force terms are included in addition to the usual electron pressure gradient source term.

Figures 4.58, 4.59 and 4.60 show the results obtained when Braginskii coefficients were employed. These diagrams show radial profiles through regions of magnetic field maxima at three different times. The magnetic field arises initially just outside the laser focal spot (~ 50 μm) in the low density corona. It reaches a maximum value of 1.8 MG at around 900 ps where $n_e/n_c \sim 0.4$. With a maximum $\omega\tau \sim 700$ the heat transport is strongly affected and the radial heat flux inhibition gives rise to a hot core of plasma which is accelerated axially by the combined effects of thermal and magnetic pressure. In the coronal plasma β is of order unity and the $\underline{J} \times \underline{B}$ forces are significant. At later times (Figure 4.60) the field maximum is found to exist around the critical density region and well outside the focal region. Significant magnetic fields (0.8 MG) were observable even at 1.6 ns which is the latest in time the simulation has been attempted.

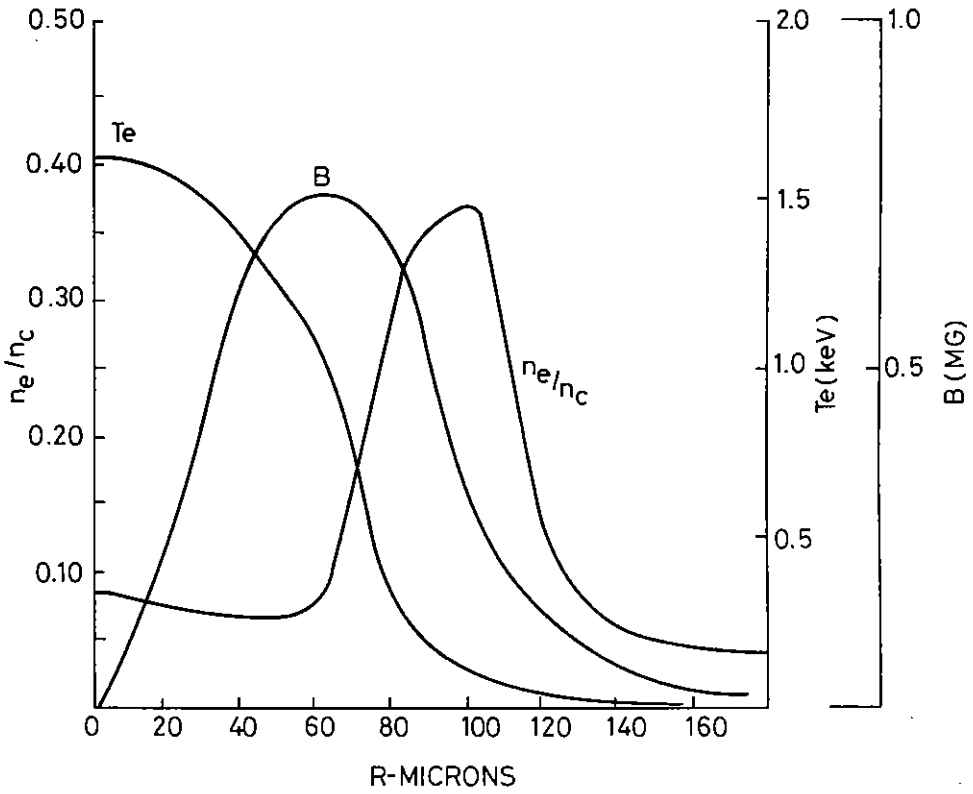

Figure 4.58 Radial profiles through B_{max} at 420 psec.

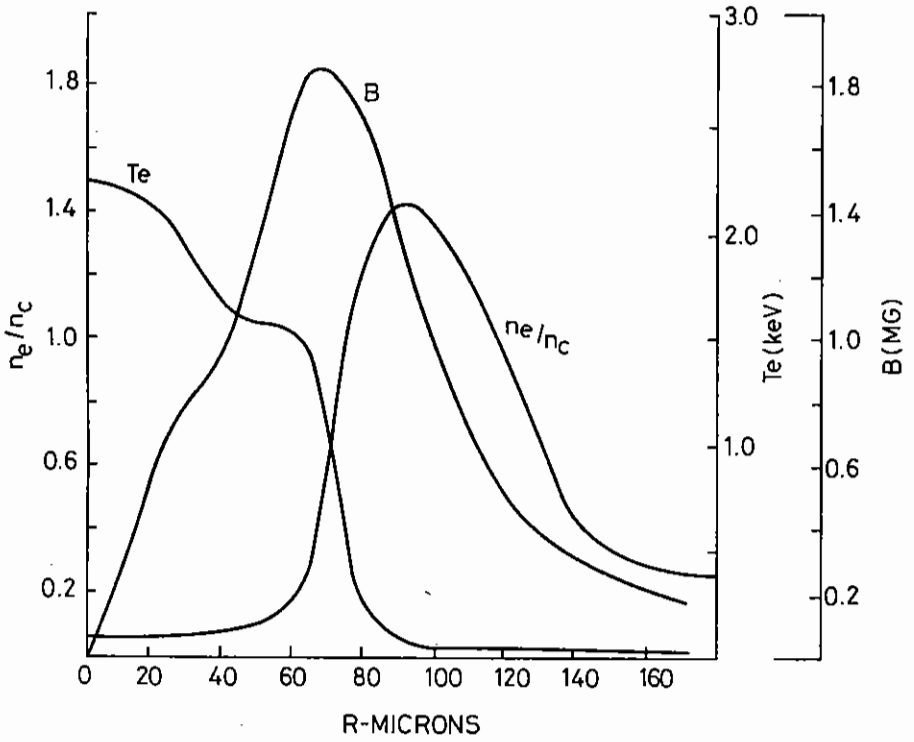

Figure 4.59 Radial profiles through B_{max} at 900 psec.

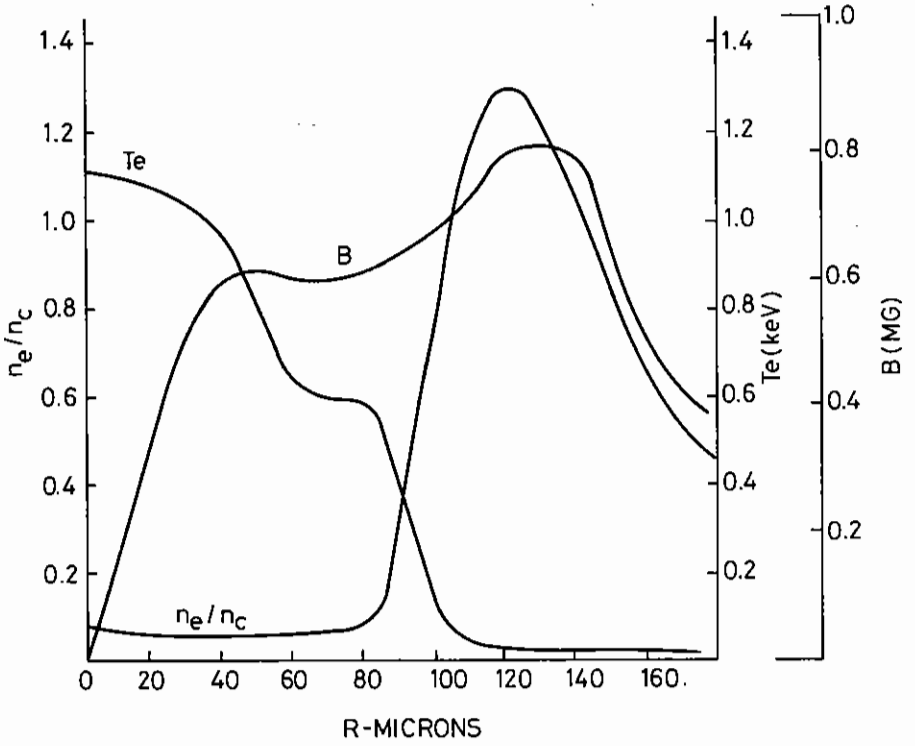

Figure 4.60 Radial profiles through B_{max} at 1.6 nsec.

The severity of heat flux limitation via the $\omega\tau$ effects was explored and as an extreme case we took the thermal conductivity $K = K_{11}$, where K_{11} is the classical field free conductivity. A much more uniform plasma was observed and significantly reduced magnetic field maxima (~ 0.3 MG) arose. A variety of limitations on K have been explored.

Figures 4.61, 4.62 and 4.63 show the results obtained when the collision frequency was enhanced by 20 % and the transport coefficients varied accordingly. Figure 4.61 in comparison with 4.58 shows a broader T_e profile and T_{max} is reduced by a factor of 2. The other parameters are not significantly changed.

The field reaches its maximum around 900 ps, this time being a response to pulse shape and approximately the same in all the runs. The value of the maximum field observed is about 1.6 MG and is found in the region n_e/n_c ~ 0.4. Again in Figure 4.62, T_{max} on the axis has been reduced by a factor of 2. A slight density increase on the axis is visible in Figure 4.62. Comparison of Figure 4.60 and 4.63 shows that whereas the magnetic field profile is only slightly changed and slightly shifted radially, the temperature and density profiles are significantly different. There is now visible a clear density enhancement on the axis.

More detailed analysis of this work will be published elsewhere.

S J Abas (Bangor)

4.7 Numerical Simulations of Magnetic Field Structure

As reported last year (4.54) we have used a numerical model to study the generation and evolution of magnetic fields in plasmas produced by the high intensity irradiation of solid targets and their consequent effect upon the density profile.

Figures 4.64 and 4.65 show the principal results from a simulation corresponding to an experiment reported by Raven and Willi in (4.50). The density profile was measured independently in the experiment enabling us

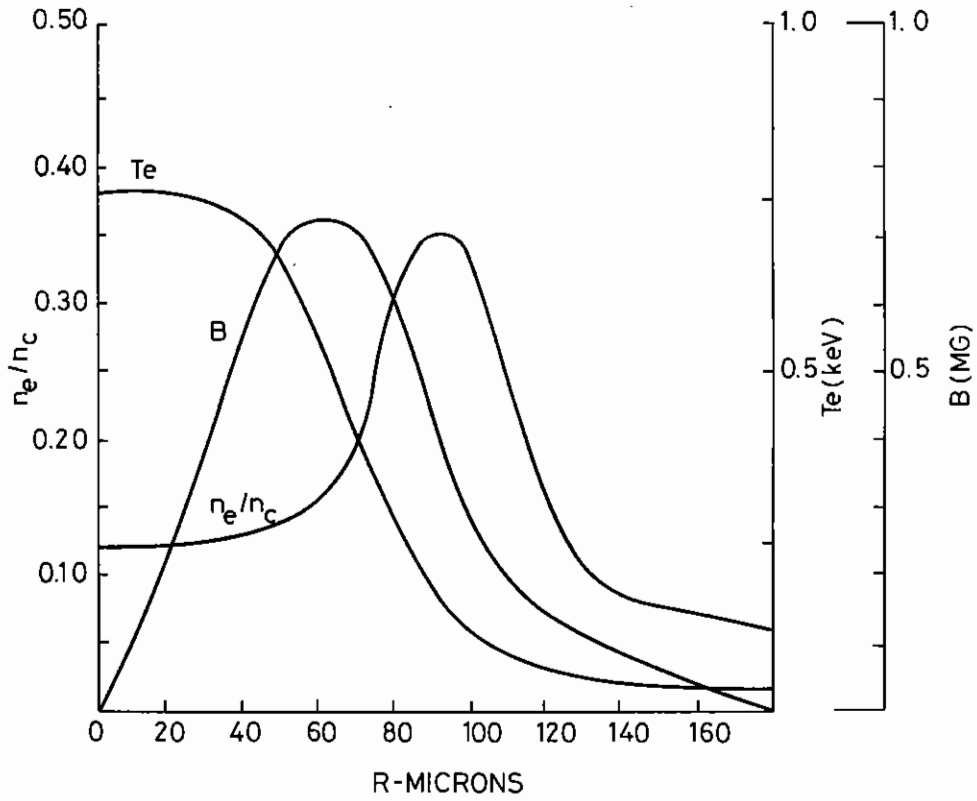

Figure 4.61 Radial profiles through B_{max} at 420 psec with enhanced collision frequency.

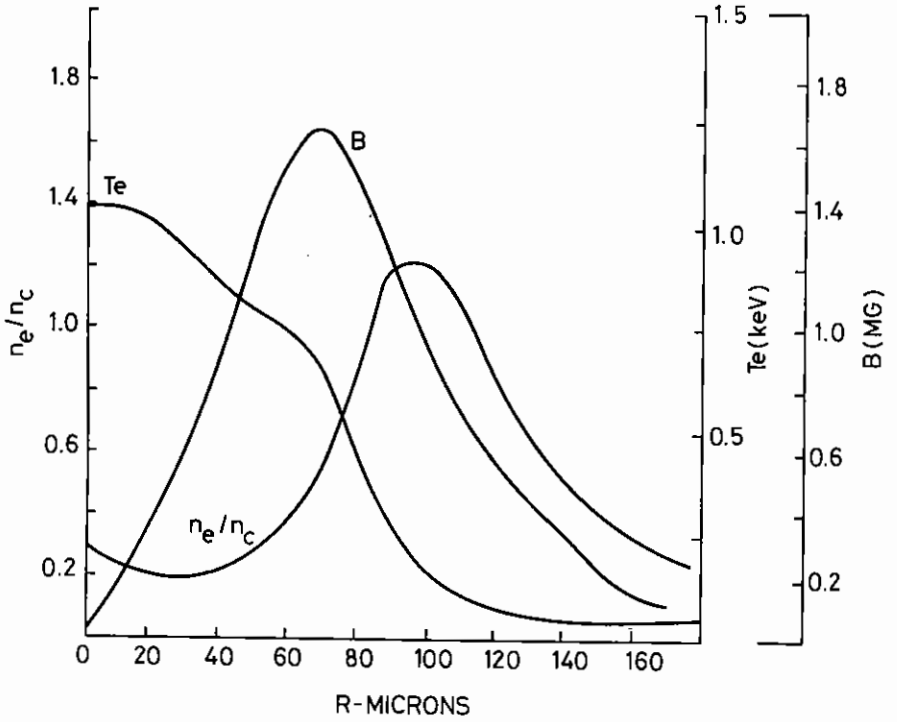

Figure 4.62 Radial profiles through B_{max} at 900 psec with enhanced collision frequency.

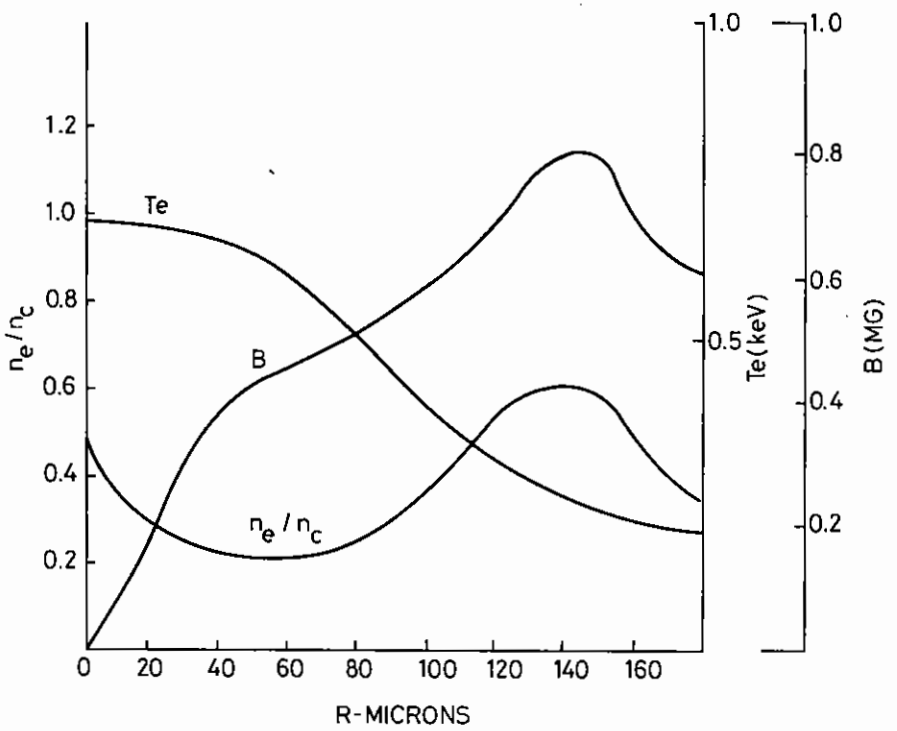

Figure 4.63 Radial profiles through B_{max} at 1.6 nsec with enhanced collision frequency.

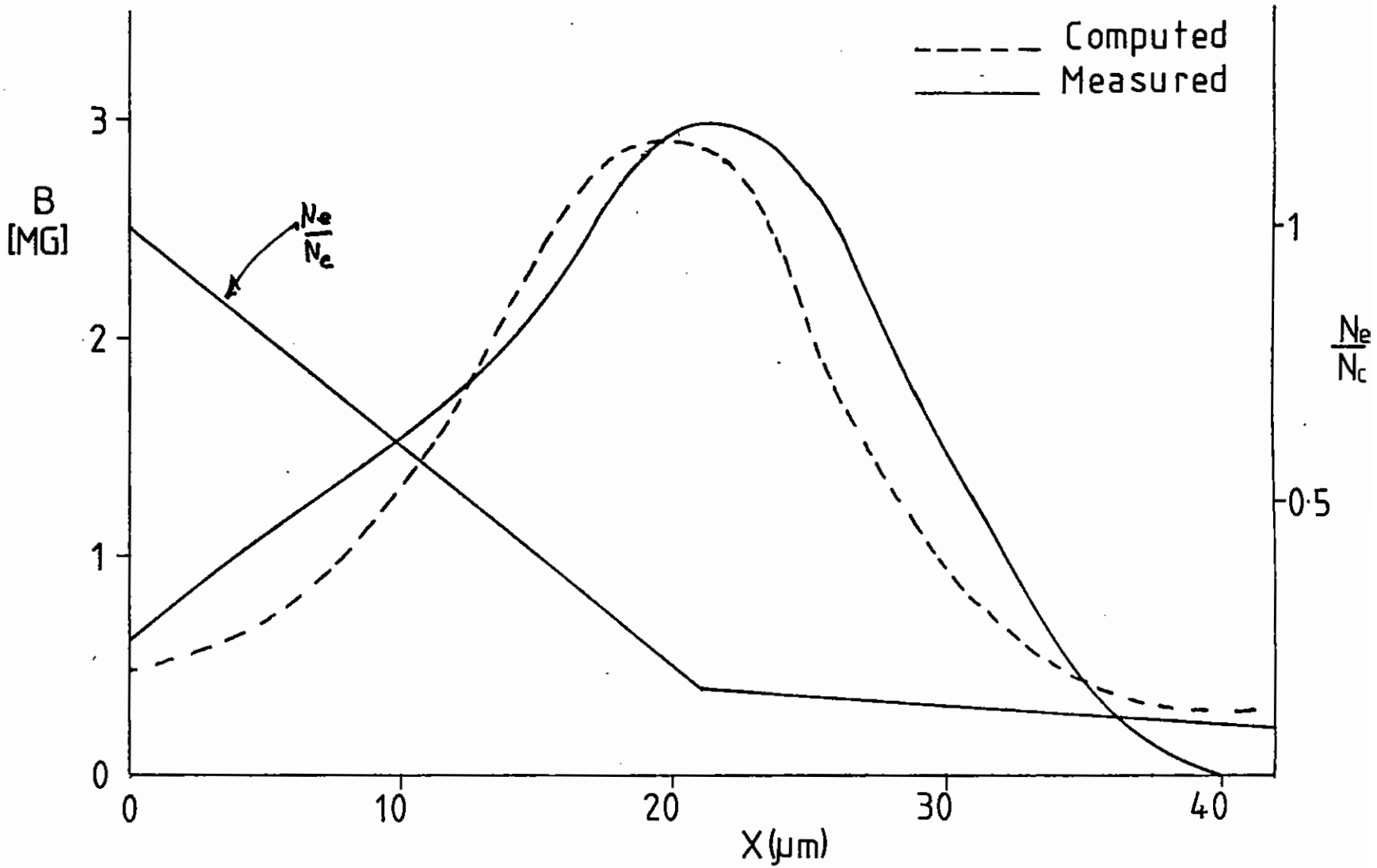

Figure 4.64 Computed magnetic field compared with experimental data for short pulse irradiation. The experimental density profile is also shown.

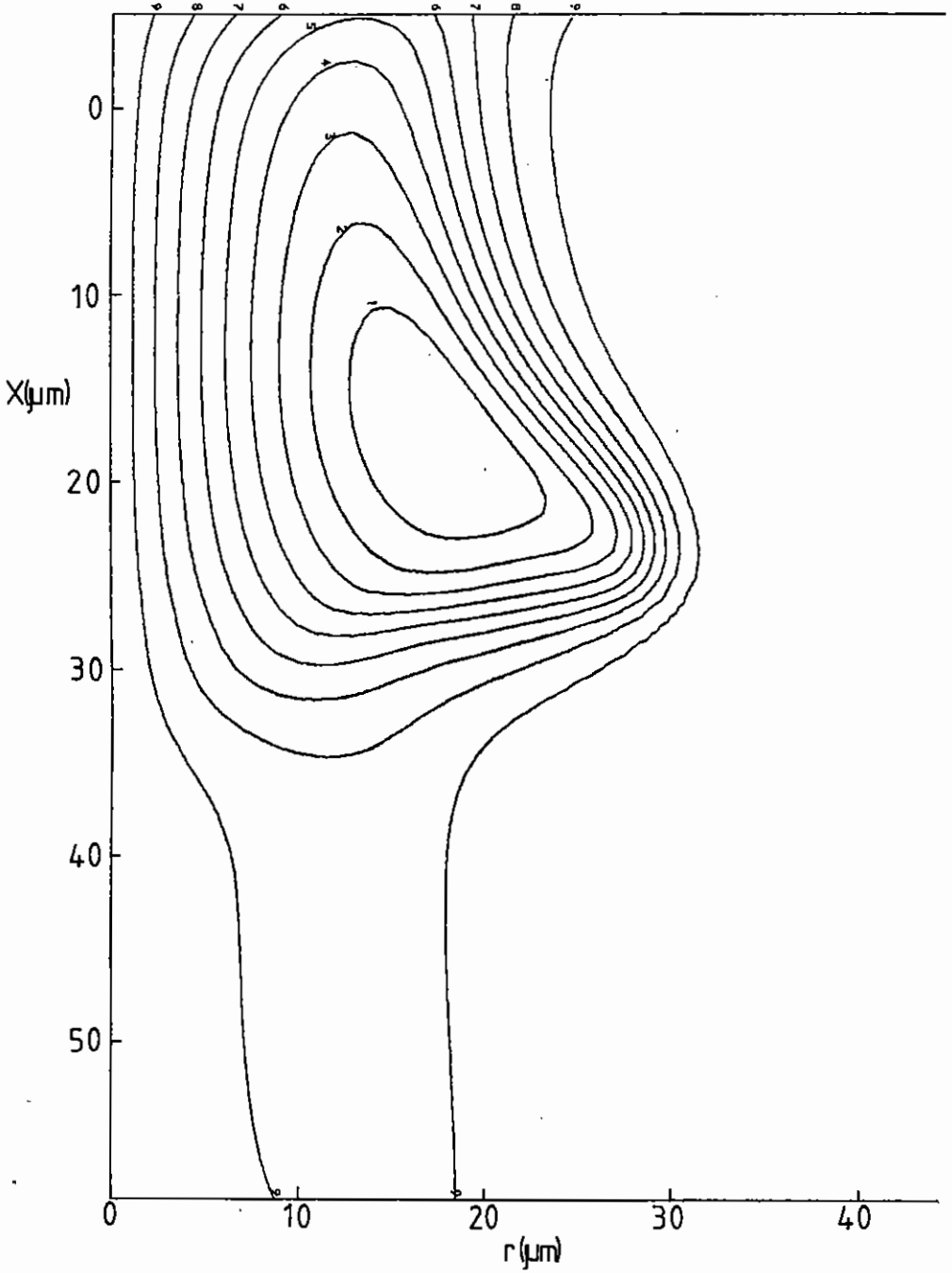

Figure 4.65 Magnetic field contours corresponding to Fig (4.64).

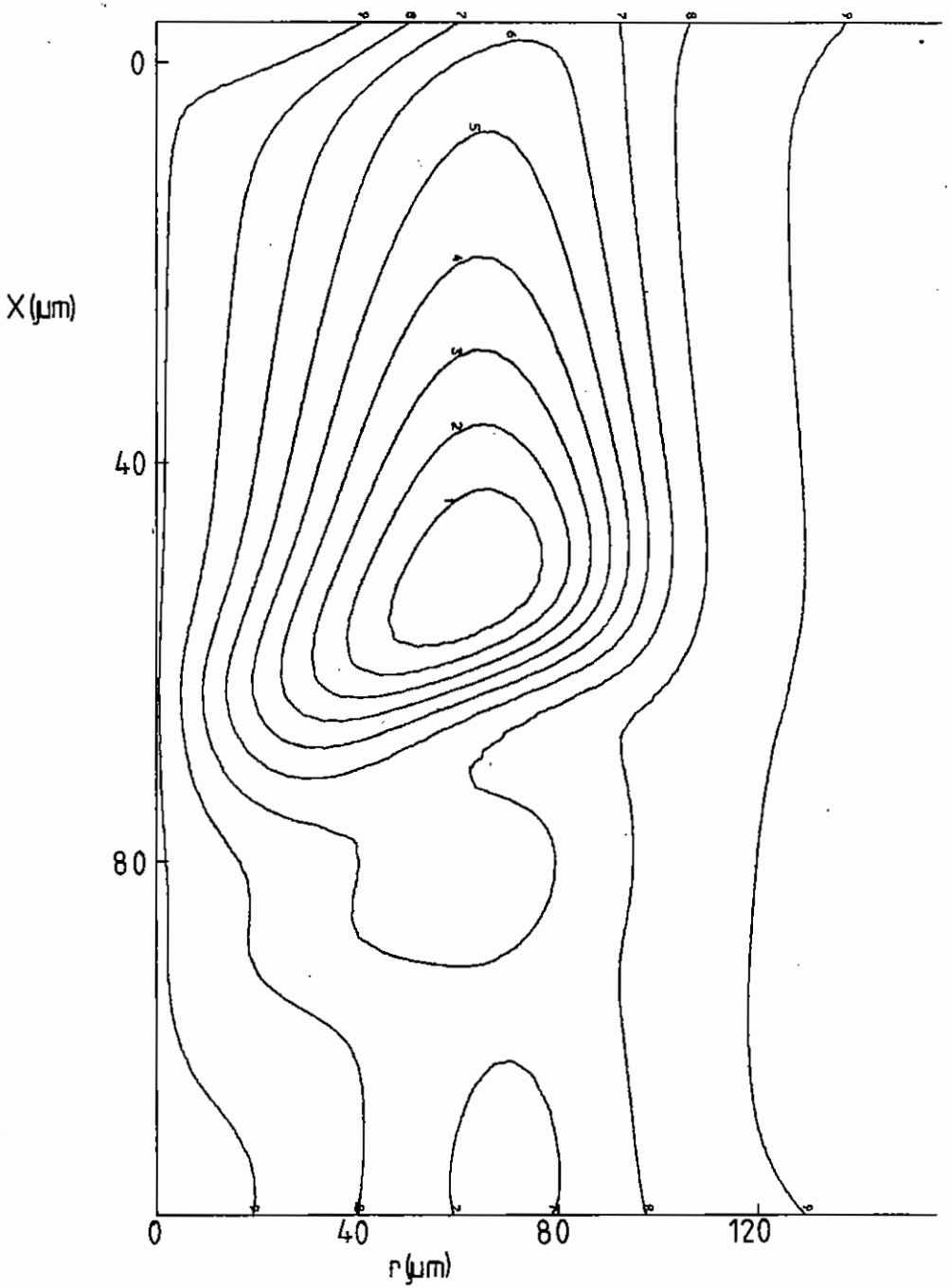

Figure 4.66 Magnetic field contours for a long pulse irradiation.

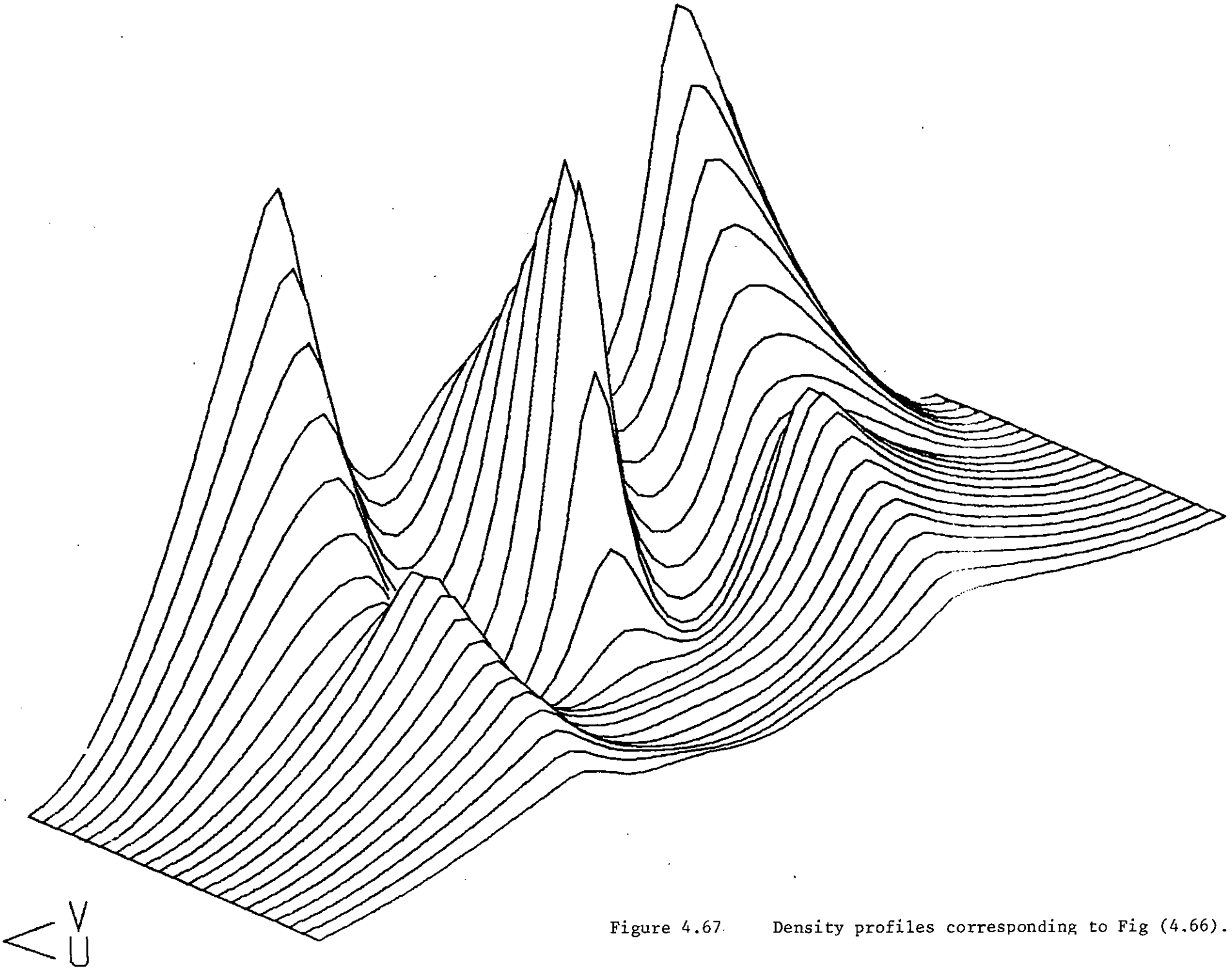

Figure 4.67 Density profiles corresponding to Fig (4.66).

to model it specifically. The temperature on the other hand is not known experimentally. In the result shown here we have modelled the temperature using a gaussian profile with a half width corresponding to that of the incident laser beam, namely 15 μm with maximum temperature 700 ev.

The agreement between the theoretical and measured profiles (Figure 4.64) as far as magnitude and spatial position of the peak magnetic field go and the overall structure of the profile is seen to be satisfactory. Figure 4.65 shows the magnetic field contour plot from this simulation; the peak field contour corresponds to a magnetic field of approximately 3 MG and the contours are evenly spaced at 300 KG intervals.

We have since extended this work to model long pulse experiments. Figures 4.66 and 4.67 show magnetic field contours and density profiles at approximately 1.3 ns with a focal spot diameter of 100 μm and maximum temperature 300 ev. The peak field contour corresponds to a magnetic field of approximately 2.25 MG and the contours are evenly spaced at 225 KG intervals.

Comparing these results with those for short pulses we note the change in the shape of the field which derives from the reduction in the relative size of the field term generated by the magnetic pressure. Similar results have been obtained in the short pulse simulations with this term excluded. Looking axially up the field contours one sees that there is a peak in the field close to the axis which is the cause of the central spike (0.25 N_c) in the density profile. At higher densities the field close on axis is smaller allowing the ponderomotive force to dominate and generate the trough seen in the density profile.

T J M Boyd and D Cooke (Bangor)

CHAPTER 4 REFERENCES

4.01 D J Bond, J D Hares, J D Kilkenny, Phys Rev Lett, 45, 252 (1980)

4.02 J D Hares, J D Kilkenny, M H Key, J G Lunney, Phys Rev Lett, 42, 1216 (1979)

4.03 R Castaing, J Descamps, J Phys Rad, 16, 304 (1955)

4.04 L Spitzer, Physics of Fully Ionised Gases, Interscience (1956)

4.05 J D Hares, J D Kilkenny, submitted to Plasma Physics

4.06 H A Bethe, Ann Phys, Leipzig, 5, 325 (1930)

4.07 D Pines, D Bohm, Phys Rev, 85, 338 (1952)

4.08 Ya B Zel'dovich, Yu P Raizer, Physics of Shock Waves and High Temp Hydro Phenomena, Academic Press, p201 (1966)

4.09 E K Storm et al, Phys Rev Lett, 40, 1570 (1978)

4.10 D W Forslund, J M Kindel, K Lee, Phys Rev Lett, 39, 284 (1977)

4.11 E Fabre et al, Paper IAEA-CN-38/1-4, Brussels (1980)

4.12 E H Goldman, J A Delettrez, E I Thorsos, Nuclear Fusion, 19, 555 (1979)

4.13 K A Brueckner, Yim Tin Lee, Nuclear Fusion, 19, 1431 (1979)

4.14 Rapport d'Activitie 1979, Groupement de Recherches Coordonnees Interaction Laser Matiere, Ecole Polytechnique, 91128 Palaiseau, p80

4.15 L M Wickens, J E Allen, P T Rumsby, Phys Rev Lett, 41, 243 (1978)

4.16 F J Mayer et al, 14th European Conf on Laser Interaction with Matter, Palaiseau 1980, unpublished and PLF Garching report PLF 41 (1980)

4.17 S Witkowski et al, 14th European Conf on Laser Interaction with Matter, Palaiseau 1980, unpublished

4.18 B Arad et al, Phys Rev Lett, 44, 326 (1980)

4.19 D W Forslund, J M Kindel, K Lee, E L Lindman and R L Morse, Physical Review A, 11, 679 (1975)

4.20 K Eidmann, J D Hares and J D Kilkenny, unpublished (1981)

4.21 J Nuckolls, L Wood, A Thiessen, G Zimmerman, Nature, 236, 139 (1972)

4.22 Annual Report to Central Laser Facility, RL-80-026, Chapter 4 (1980)

4.23 G Leppelmeier, Rochester Report LLE 087 (1979)

4.24 C Fauquinon and F Floux, Phys Fluids, 13, 386 (1970)

4.25 C E Max, C F McKee and W C Mead, Phys Fluids, 23, 1620 (1980)

4.26 M H Key, Lectures on the Physics of the Superdense Region, Proc 20th Scottish Universities Summer School on Physics, Eds R A Cairns and J J Sanderson, SUSSP Edin Univ (1979)

4.27 J D Kilkenny et al, Proc Workshop on Laser Interactions and Related Plasma Phenomonena, Plenum Press

4.28 P M Campbell, R R Johnson, F J Mayer, L V Powers and D C Slater, Phys Rev Letts, 39,274 (1977)

4.29 M H Key et al, Rutherford Laboratory Report, RL-80-023 (1980)

4.30 F Amiranoff, E Fabre, R Fabbro, C Garban and M Weinfeld, GRECO Interaction Laser Matière Rapport d'Activité (1979)

4.31 J D Hares, PhD Thesis, University of London (1980) and Section 4.3 of this report.

4.32 K Eidmann et al, paper presented at the Gordon Research Conference unpublished (1979)

4.33 B H Ripin et al, Naval Research Laboratory Mem, Report 4212 (1980)

4.34 M H Key, J G Lunney, J M Ward, R G Evans and P T Rumsby, J Phys B, 12, L213 (1979)

4.35 T P Donaldson, PhD Thesis, Queen's University, Belfast (1973)

4.36 O Willi, P T Rumsby, Z Q Lin and S Sartang, Rutherford Laboratory Report, RL-81-015 (1981); see also Chapter 3

4.37 O Willi, R G Evans and A Raven, Phys Fluids, 23, 2061 (1980)

4.38 R G Evans, Section 7.2 of this report.

4.39 R G Evans and A R Bell, Rutherford Laboratory Report, RL-80-085 (1980)

4.40 P T Trainor, J W Shauer, J M Auerbach and M C Holmes, Phys Rev Lett, 42, 1154 (1979)

4.41 A H Williams, D V Giovanielli and G H McCall, Los Alamos Report, LA-UR-76-1695 (1976)

4.42 B H Ripin, Naval Research Laboratory Report 3890 (1978)

4.43 F J Mayer, C K Cheng and J G Downward, KMSF Report U-192 (1974)

4.44 A Raven, P T Rumsby and J Watson, Rev Sci Instrum, 51, 351 (1980)

4.45 B H Ripin, S E Bodner, S H Gold, R H Lehmberg, E A McLean, J M McMahon, S P Oberschain, J A Stamper, R R Whitlock, F C Young, H R Griem, J Grun and M J Herbst, Naval Research Lab Report, 4212 (1980)

4.46 N G Basov et al, 14th ECLIM, Palaiseau (1980)

4.47 H Puell, Z Naturforsch, 25a, 1807 (1970)

4.48 E K Storm et al, UCRL preprint 79788 (1977)

4.49 Annual Report to the Central Laser Facility, RL-79-036, Chapter 4 (1979)

4.50 A Raven and O Willi, Phys Rev Lett, 43, 278 (1979)

4.51 C E Max, W M Manheimer and J J Thomson, Phys Fluids, 21, 128 (1978)

4.52 D G Colombant and N K Winsor, Phys Rev Lett, 38, 697 (1977)

4.53 R H Lehmberg and J A Stamper, Phys Fluids, 21, 814 (1978)

4.54 T J M Boyd, G J Humphreys-Jones and D Cooke, Annual Report to the Laser Facility Committee, RL-80-026. 7.29 (1980)

CHAPTER 5 ABLATIVE ACCELERATION AND COMPRESSION STUDIES

INDEX

CHAPTER EDITOR P T Rumsby

CHAPTER 5 ABLATIVE ACCELERATION AND COMPRESSION STUDIES

5.1 Introduction

The commissioning of the upgraded laser system together with the installation of frequency doubling crystals has meant that ablative compression experiments have been possible with six, $\lambda = 0.53$ μm wavelength beams from March 1981.

Initial tests were carried out to tune the crystals and to balance the beam energies. Target shots were performed in order to determine the focusing condition necessary to achieve most uniform ablation pressure on the target surface and maximize absorption fraction.

Streaked X-radiography experiments have been carried out using an additional $\lambda = 1.05$ μm beam for backlighting in order to study the dynamics and stability of shell targets imploded by six green beams. Preliminary results from these experiments are reported in section 5.2.

In addition section 5.3 gives details of experiments performed earlier in the year, using $\lambda = 1.05$ μm target irradiation, to test whether Fresnel zone plates can be used for 2-d X-ray imaging in the coded aperture mode for target radiography. These test experiments are a prelude to work to be performed in mid 1981 when a short (100 ps) pulse backlighting beam synchronized with a long (1 ns) main driving pulse will be available for flash 2-d radiography of ablatively imploded targets.

P T Rumsby

5.2 Study of Ablative Implosions Driven by 0.53 μm Irradiation in Six beams

5.2.1 Introduction

The upgraded laser facility has been used to generate six 0.53 μm beams of 1 ns pulse duration and up to 100 J total energy. Spherical shell targets

of typically 180 μm diameter have been irradiated at 5×10^{13} W cm^{-2} to generate ablative implosions.

An independent single beam line has given 100 J 1 ns pulses at 1.05 μm which were used in a seventh beam to provide an X-ray backlighting plasma by irradiating a plane Al target in a 400 μm diameter focal spot.

The objective of the experiment was to study the implosion dynamics of targets driven by 0.53 μm radiation in order to verify predictions of increased driving pressure and hydrodynamic efficiency relative to those obtained with 1.05 μm radiation.

5.2.2 Experimental Method

An X-ray streak camera was used to record time resolved X-ray shadowgraphs. This technique was shown to give direct information on the ablative acceleration of spherical shells and indirect information on any non-uniform break up of the imploding shell in our earlier work (5.01).

The present experimental apparatus is similar to that used previously, (see Figure 5.01), but uses a modified X-ray streak camera and X-ray imaging system to record the streaked X-ray shadowgraphs. The X-ray imaging was via a 6 μm diameter pinhole in a 20 μm thick Pt substrate (5.02). The camera is a more compact version of that used previously (see Section 1.6.1) and gives 50 μm resolution at its photocathode and a static imaging sensitivity 700 times that of direct recording on Noscreen X-ray film when used with a low density C_sI photocathode on a 15 μm Be substrate.

The compact size of the camera permitted location of its photocathode 23 cm from the plasma. The pinhole camera imaging was at 15 times magnification and at the X-ray wavelength used (7.76 Å) gave near optimal resolution with Fresnel number 0.8. The 110 μm magnified size of a resolution element was well matched to the 50 μm resolution at the photocathode of the camera so that there was no significant loss of resolution in the X-ray streak camera.

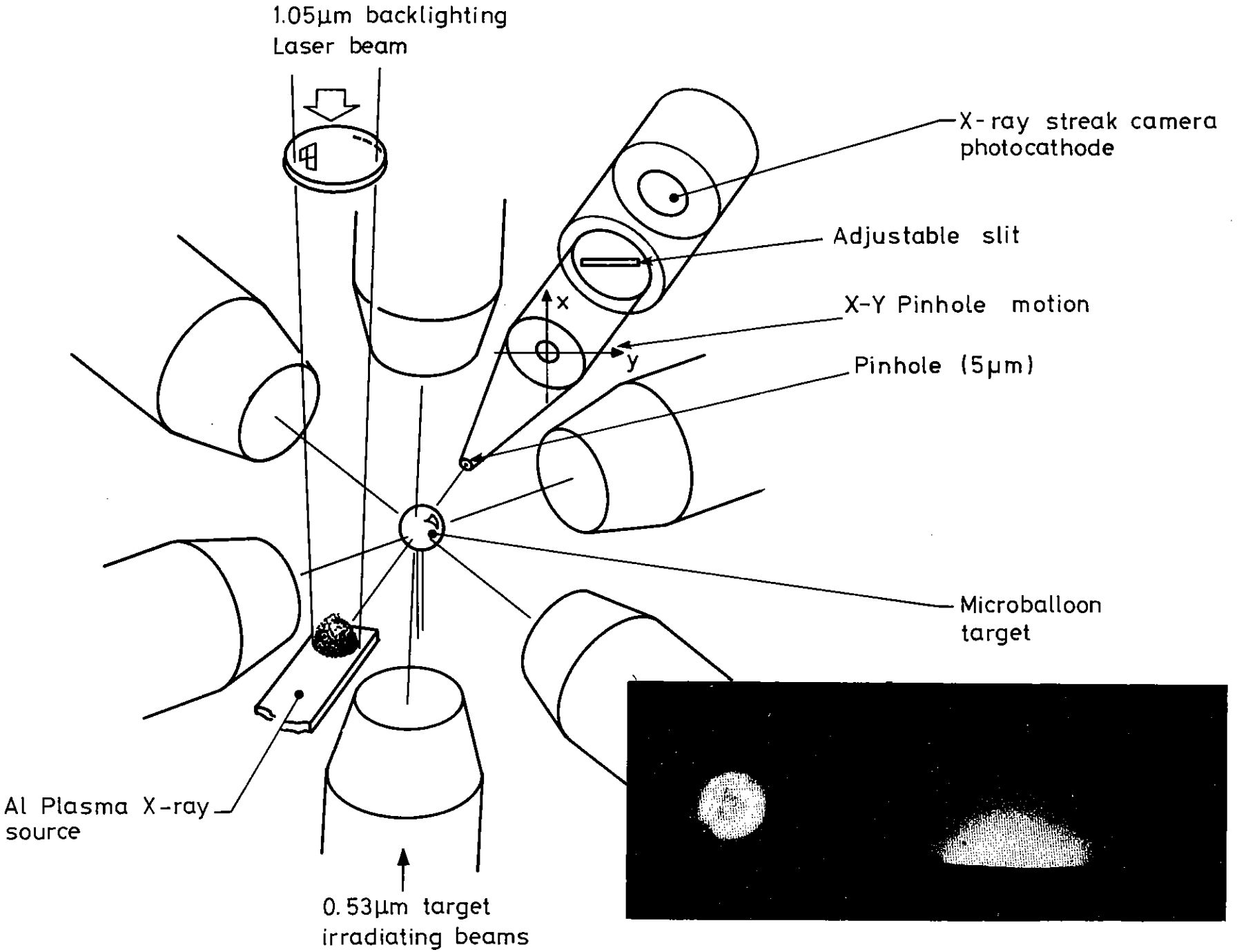

Figure 5.01 Experimental system. The Inset photograph is from an X-ray pinhole camera imaging the microballoon and backlighting plasmas.

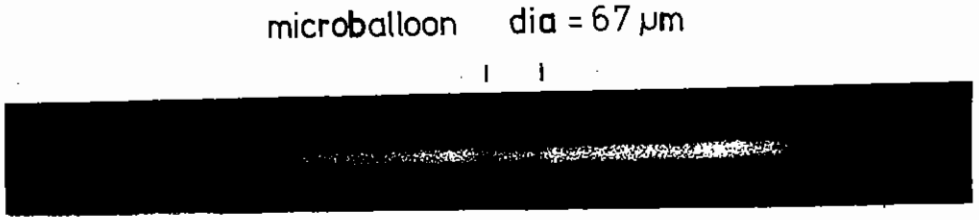

Static image via slit (18 μm wide in object plane)

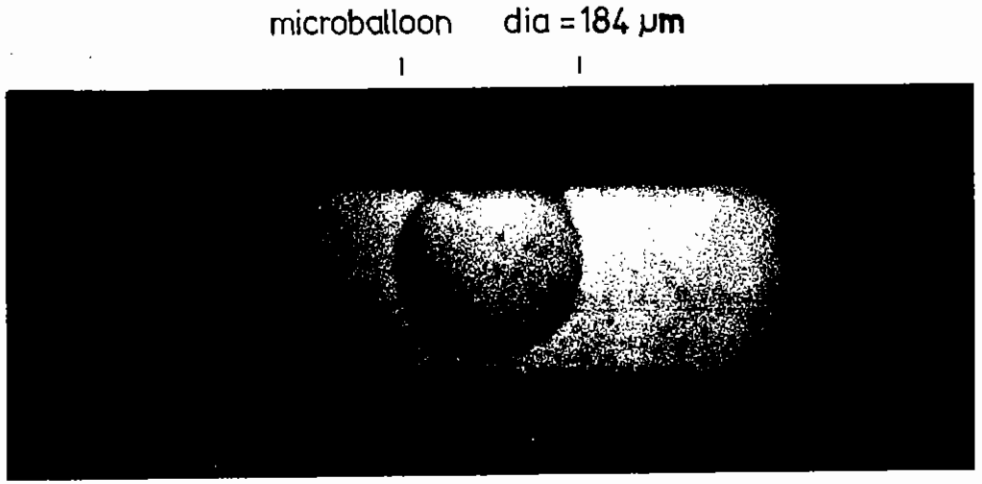

Static image via slit (189 μm wide in object plane)

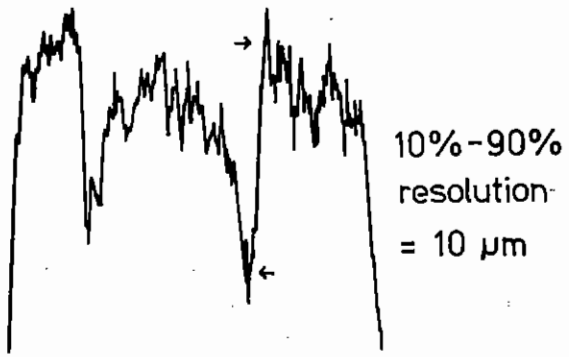

Densitometer tracing across the 184 μm microballoon (1·3 μm glass shell coated with 2 μm of plastic)

Figure 5.02 Static image tests of the X-ray shadowgraphy system.

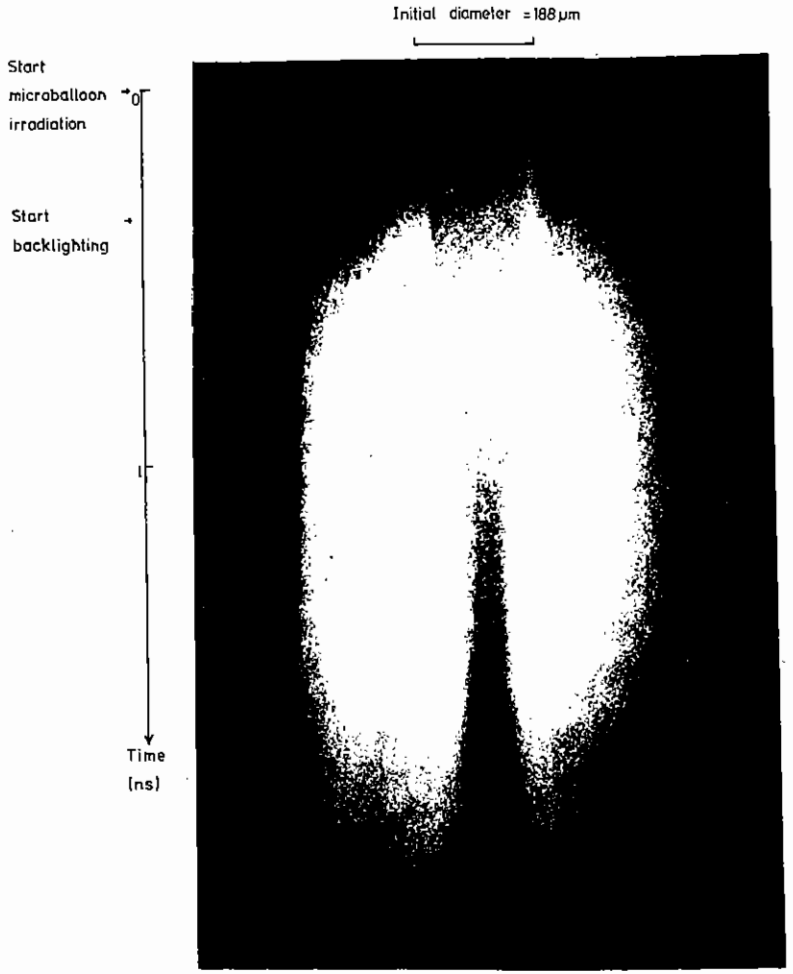

Implosion of microballoon by $1{\cdot}3\times10^{15}$ W cm^{-2} absorbed irradiance at $\lambda = 0{\cdot}53\,\mu m$ (target diameter = 188 μm, Δr glass = 1·28 μm, Δr plastic = 1·94 μm)

Figure 5.03 A streaked X-ray shadowgraph of a microballoon implosion.

The imaging system viewed the microballoon target against backlighting from the plasma produced by the seventh beam as shown in Figure 5.01. The microballoon irradiation was from six f/1 doublet aspheric lenses with their focal points located 4.2 radii behind the centre of the target. The backlighting beam was focused by a f/2.5 lens to a 400 μm focal spot on an Al foil target with the target surface normal along the seventh beam axis. The backlighting plasma was located about 800 μm behind the microballoon with its target surface parallel to the plane defined by the streak camera slit and viewing axis but one radius below the microballoon centre. Both targets were inserted into the chamber via airlock mechanisms.

Initial alignment of the X-ray image was made with continuous low power X-ray emission from a 0.4 mm spherical tungsten anode aligned optically to simulate the microballoon. A tungsten filament delivered 0.5 mA at 5 kV to the anode giving sufficient emission intensity for photographic recording of static images via the streak camera/pinhole camera system.

The laser was used to produce intense Al XII $1^1S_0 - 2^1P_1$ backlighting X-ray emission which (as in our earlier work (5.01)) was filtered by an 8 μm thick SiO filter on a 2.5 μm polymer substrate. The K edge absorption of this filter served to suppress Si XIII emission from the ablation of the glass microballoon and to select Al XII resonance lines from the backlighting source.

Figure 5.02 shows a static shadowgraph of an unirradiated microballoon produced in this way. It was used to centre the streak slit jaws on the microballoon centre. The slit width was then reduced to 18 μm in the object plane as shown in Figure 5.02. 10 μm spatial resolution was obtained as measured by densitometry. (This is a two fold improvement on our earlier system (5.01).) The stability of positioning of the slit relative to the centre of subsequently aligned microballoons was estimated at ± 5 μm by making alignment checks of the above type before and after a series of shots.

The temporal resolution was 30 ps for a streak rate of 100 ps/mm at the output of the camera. A conventional X-ray pinhole camera imaged the

microballoon and backlighting plasmas on an axis perpendicular to that of the X-ray streak camera via 6 μm and 20 μm pinholes giving qualitative information on the uniformity of irradiation of the microballoon. (See inset ot Figure 5.01.)

The laser beams were characterized on each shot by energy monitors on each of the six 0.53 μm beams, and by an equivalent focal plane camera on one beam monitoring the irradiance distribution at a plane equivalent to the surface of the microballoon. The beam balance was typically ± 10 % and the distribution in the equivalent focal plane was on average flat topped with a fill factor of about 0.4 and a profile similar to a super Gaussian. There were also straight fringes in the beam pattern of 2:1 peak to valley intensity ratio and 15 fringes across the beam. This is a temporary defect due to poor anit-reflection coating on a beam splitter. The pulse duration was measured in a separate experiment using a streak camera/OMA system.

5.2.3 Experimental Results

The system described above was used to record streaked X-ray shadowgraphs of the implosion of polymer coated glass microballoons filled with 10^{-2} g cm^{-3} of Neon gas.

The target diameters were typically 180 μm and their aspect ratios $r/\Delta r$ were varied from 17 to 65 by variation of the polymer coating thickness. The smoothness of the target surfaces was ± 0.1 μm and the uniformity of wall thickness ± 1 %.

Figure 5.01 shows an X-ray pinhole camera image of the microballoon plasma and the backlighting plasma illustrating the good overall symmetry of irradiation of the microballoon and showing the conical plasma flare associated with colliding cylindrical and spherical plasma expansions at the point of attachment of the support fibre. Figure 5.03 shows a streaked shadowgraph result (actually the first shot with the system). The backlighting is delayed by 0.3 ns and relatively weak self emission from the target is seen before the backlighting displays the absorption

features of the imploding shell.

Table 5.01 gives a preliminary summary of the initial results from this experiment which is still in progress at the time of writing.

Implosion times can be measured from the shadowgraph records since the timing of the backlighting relative to the microballoon irradiation is known from calibration experiments. Implosion times less than 1 ns have been recorded for some targets where the incident irradiance was 5×10^{13} W cm^{-2}. The absorbed irradiance under these conditions was measured by plasma calorimetry in separate experiments with no backlighting plasma. The absorption fraction was 0.5.

Detailed analysis of these data has not been completed at the time of writing but a preliminary appreciation of the main features can be made using the analytic model of ablative implosions discussed in Section 7.2.3.

The ablation presure is related to the implosion time τ in this model by

$$Pa = \left(1-\left(\frac{\rho_1 \Delta r}{0.5\rho_s r}\right)^{1/3}\right)^2 \quad \frac{3\,\rho_s\, r\, \Delta r}{\tau^2}$$

where ρ_1 is the gas fill density, ρ_s the shell density and Δr the shell thickness.

Checking this relationship against the more detailed analysis of our similar experiments at 1.05 μm (5.01) shows it to give a satisfactory estimate of the pressure in those experiments and Table 5.01 shows pressures ranging from 8 to 18 Mbar deduced in this way.

The mass ablation fraction $\Delta M/M$ is given by $\dot{m}\tau/\rho_s \Delta r$. The mass ablation rate measured from ion emission data is reported in Section 4.4.7 and those results for $\dot{m}$ have been used to compute the values of $\Delta M/M$ shown in Table 5.01. The fraction is significant but still low enough to permit application of the analytic model. The hydrodynamic efficiency ε_h and

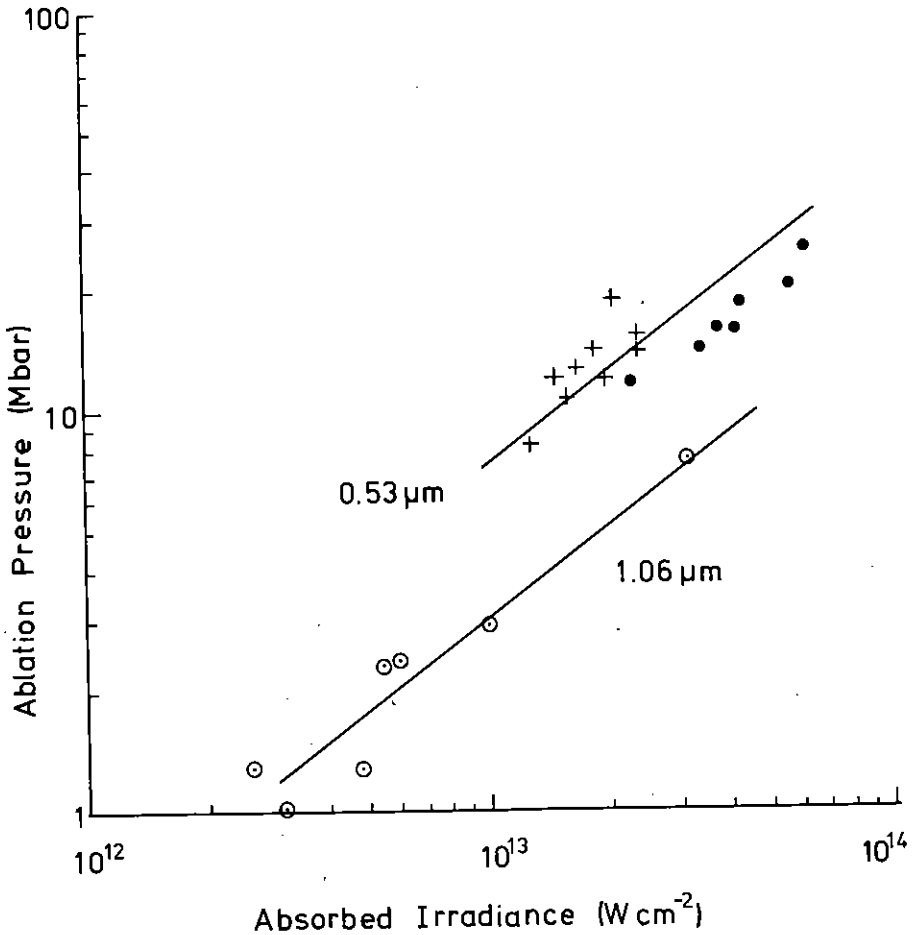

Figure 5.04 Ablation pressure results. Crosses are from the 0.53 μm implosion time measurements. Solid circles are from 0.53 μm X-ray streak spectroscopy measurements of $\dot{m}$ assuming $Pa = (2\,\dot{m}\, I_{abs})^{\frac{1}{2}}$. Open circles are from 1.06 μm implosion time measurements (5.01).

TABLE 5.01

SHOT	2r μm	Δr glass μm	Δr ch μm	$r/\Delta r$	I_{abs} 10^{13} W cm^{-2}	τ ns	P_a Mbar	$\Delta M/M$	ε_h	V_{max} 10^7cms^{-1}
14	188	1.28	1.94	29	1.3	1.3	8.2	0.26	0.51	1.4
16	180	1.49	-	60	2.1	0.7	19	0.31	0.76	2.5
18	177	1.2	1.76	30	2	1.0	12	0.31	0.35	1.7
21	183	1.57	2.72	21	1.7	1.2	13	0.23	0.37	1.5
02	182	1.6	3.2	19	1.9	1.2	14	0.22	0.38	1.5
04	194	1.78	4.6	17	1.6	1.3	11	0.2	0.31	1.2
06	184	1.38	1.16	36	2.4	0.92	14	0.34	0.39	1.9
08	175	1.33	-	65	2.4	0.7	14	0.38	0.50	2.2
10	192	1.33	1.2	38	1.5	1.0	12	0.27	0.49	1.8

Target parameters and absorbed irradiance for implosions recorded by streaked X-ray shadowgraphy. Implosion times τ were measured from the shadowgraph records. Ablation pressure P_a, hydrodynamic efficiency ε_h and maximum implosion velocity V_{max} are derived from τ using an analytic model discussed in the text. The mass ablation fraction $\Delta M/M$ is estimated from τ and separate measurements of mass ablation rate.

peak velocity v_{max} in the implosion can similarly be derived from the implosion time in the forms

$$v^2_{max} = \frac{4}{3}\frac{P_a r}{\rho_s \Delta r}$$

and

$$\epsilon_h = \frac{2}{3}\frac{P_a r}{I_{abs}\tau}$$

and these quantities are also shown in Table 5.01.

For small fractions it is theoretically established that $\epsilon_h = \Delta M/M$. The data in Table 5.01 show values of ϵ_h rather greater than those for $\Delta M/M$. The reason is because $\Delta M/M$ was deduced from data from the separate mass abation experiments from which the inferred pressures were somewhat lower than estimated from the implosion times here. The values of hydrodynamic efficiency are high as a result of the high mass ablation rate obtained at 0.53 μm.

The pressure data are plotted in Figure 5.04 together with results from our earlier similar experiment at 1.05 μm (5.01). Also shown are pressures deduced from mass ablation rates measured by X-ray streak spectroscopy (Section 4.4.7) assuming $P_a = (2\dot{m}I_a)^{\frac{1}{2}}$. The agreement is good without a geometrical correction factor γ (discussed in Section 4.4.8) suggesting that separation of the critical density and ablation surfaces is small. Numerical simulations under these conditions also show a negligible separation of the two surfaces. The uncertainty introduced into the determination of pressure from the ablation data through the γ factor is eliminated here in these direct observations of acceleration.

The rather high ablation pressure and hydrodynamic efficiency observed here are very encouraging for achieving high pressure ablative compression in view of the fact that the irradiance can be further increased to $\sim 2 \times 10^{14}$ W cm^{-2} before hot electron preheating is expected to become dominent.

The limiting factors on the compression achieved are the symmetry of the implosion and any decompression of the imploding shell due to preheating. A preliminary examination of the minimum size of the opaque cores of the implosions with aspect ratio ~ 30 shows them to be about two times greater in diameter (eight times greater in volume) than predicted by 1D simulations. This is a similar discrepancy to that noted in our experiments at 1.05 μm (5.01).

This departure from ideal behaviour gives less compression of the gas and thus lower values of density pressure and temperature than predicted by the analytic model and 1D simulations. An estimate based on the model results can be made by assuming an eight times reduction of density. The Neon would then be compressed to about 5 g cm^{-2} in a 20μ diameter core and its temperature would be adiabatically scaled down by $8^{2/3}$ to about 350 eV and its pressure by $8^{5/3}$ to 1000 Mbars.

The Neon gas would become a strong source of X-ray emission with brightness increasing very rapidly for temperatures above 300 eV and evidence for such emission was sought in pinhole camera images and streak photographs. It was observed that there was a threshold for such emission at about 2×10^{13} W cm^{-2} absorbed irradiance on shells of aspect ratio 30 or greater. Pinhole camera images showed a bright outer ring with a low emission region corresponding to the opaque core of the shadowgraphs and a small emission core of about $1/10$ of the initial target diameter. Streak camera records of the self emission of implosions with no backlighting also showed a core emission feature starting about 0.5 ns before peak compression of duration about 0.5 ns. The X-ray pinhole camera image of the microballoon plasma in Figure 5.01 is for the seventh case listed in Table 5.01 and has an emitting core feature clearly visible in the original photograph and much more pronounced examples have been recorded subsequently.

5.2.4 Conclusion

Preliminary analysis of the implosion of spherical shell targets of moderate aspect ratio by 0.53 μm irradiation shows high ablation pressure

and hydrodynamic efficiency. Implosion velocities sufficient to generate a relatively hot ablative implosion have been obtained and X-ray emission from this implosion core has been observed. The compression shows signs of degraded volumetric compression ratio relative to idealised 1D calcualtions but despite this it seems probable that final presures of the order 1000 Mbar are achieved and that with increased irradiance higher values are possible. Further study of these implosions is in progress.

C L S Lewis, M Lamb, P Cunningham, M Ward (QUB), J D Kilkenny (Imp Coll), M H Key, P T Rumsby, C Hooker and R G Evans (RAL)

5.3 Zone Plate Coded Radiography (ZPCR) of Ablative Implosions

Further experiments have been performed to investigate the use of zone plate coded imaging techniques for X-radiography of ablatively driven implosions. The preliminary results reported previously have been extended using zone plates of improved quality.

Figure 5.05. shows the experimental arrangement used for ZPCR of six beam driven ablative implosions. The laser system delivered pulses of 800 ps duration at λ = 1.052 μm with up to 150 Joules on target via the six beams used to drive the implosions and up to 50 Joules in the backlighting beam. X-ray backlighting targets consisted of 2 μm thick layers of KCl deposited onto 50 μm thick, 1 mm wide mylar strips. Further details of the experimental techniques have been reported previously (5.03)

The zone plates used were made in 5 μm thick gold by electroforming. They had 280 zones , with a minimum zone width of 5 μm, giving a theoretical limit on the resolution of 7 μm. They were placed 3 cm from the target, giving a collection solid angle of 10^{-1}sr. A 125 μm beryllium foil was placed between the zone plate and providing a low energy X-ray filter.

The film pack used to record the images contained two films with a 7 μm aluminised mylar light shield. The first film was Ilford EP4 35 mm film and this recorded an image in a band between 2 and 4 KeV with the main

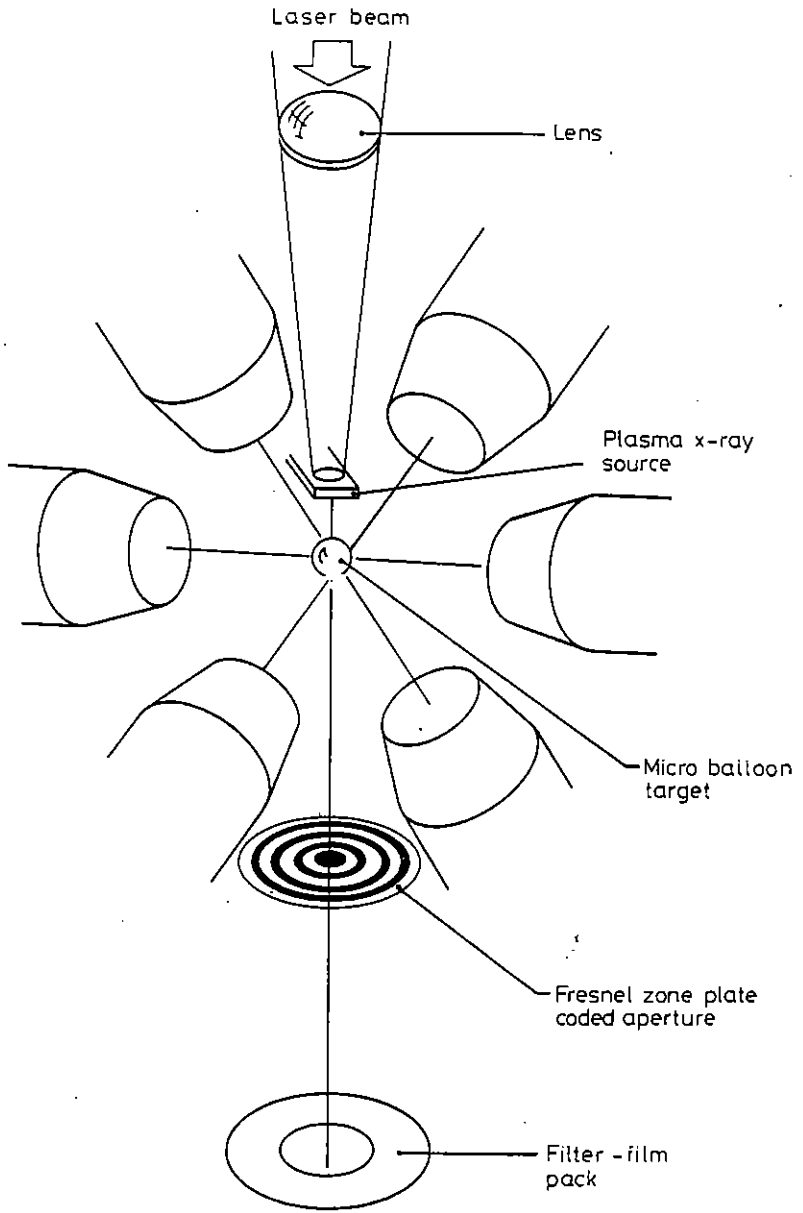

Figure 5.05 Experimental arrangement for zone plate coded radiography of six beam ablatively imploded targets.

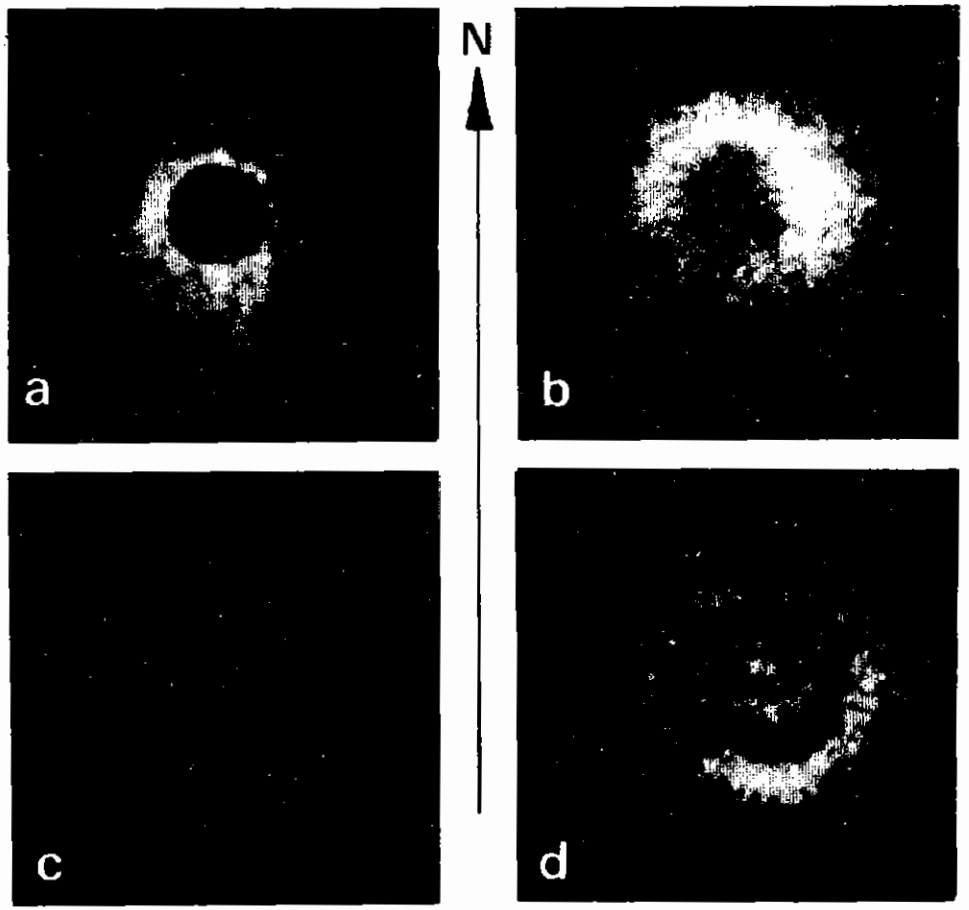

Figure 5.06 X-radiographs obtained by ZPCR. (a) An unirradiated solid uranium target. (b) Implosion core at 2.1 ns time delay. (c) Implosion with low irradiance on NS poles at 1.8 ns delay. (d) Implosion with high irradiance on NS poles at 0.8 ns delay.

contribution coming from the line spectrum of KCl. This film acted as a wider band centred on 5 KeV. The exposed coded images were contact printed onto Kodak High Resolution Plates and reconstructed using a HeNe laser. The bright background of undiffracted light was removed by placing a converging lens in front of the coded images and using a small stop in the Fourier plane of the lens (5.05). All reconstructions were performed in the first order because the signal to noise ratio of third order images was too low.

The system was set up by imaging static targets. This allowed the correct filtering to be found and fixed the plane of reconstruction for subsequent implosion shots. Figure 5.06(a) shows an image of a solid uranium target of 105 μm diameter. A large X-ray emitting region is required for ZPCR unlike emission imaging and since the signal to noise ratio of the reconstruction decreases with the size of the emitting area, it is vital to keep the backlighting source as small as possible. Several shots were used to determine that the optimal size was 300 μm diamter.

For radiography of ablative implosions, large targets coated with layers of polymer were irradiated with the six main laser beams at an intensity off 10^{13} W cm^{-2}. The targets were 1 μm thick glass shells (280 μm diameter) coated with 2 μm of plastic. Such targets gave no significant X-ray emission. These parameters were chosen to give a long implosion time so that the 0.8 ns resolution time of the backlighting pulse would not smear the radiographs too severly. Data from similar implosions obtained from streaked shadowgraphy experiments using a Kirkpatrick-Baez microscope system in the 1.5 - 1.8 KeV X-ray region, showed that such targets imploded to a diameter of about 120 μm at a time about 2 ns after the peak of the main pulse. The data showed that the core diameter did not change greatly over a period of 1 ns which would further mitigate the time smearing inherent in this method.

Coded images of ablative implosions were recorded at several stages in the implosion by varying the time delay of the backlighting beam. The images show the three stages of ablative implosions; the glass shell moving inwards, the compressed core and the final expansion. Time resolution is

not good enough to show any fine structure, but the shape of the dense material can be seen quite plainly. Figure 5.06(b) shows the minimum size implosion core obtained with a backlighting pulse delayed 2.1 ns after the main pulse. The core diameter is about 120 μm which is a little less than half the original target diameter of 260 μm. Since ZPCR is a two dimensional imaging technique, varying focal conditions were applied to observe the effect of the symmetry of the implosion. Figures 5.06(c) and (d) show two results obtained during the shell implosion phase with similar targets and the same incident energy. In Figure 5.06(c) (1.8 ns backlighting delay) the north and south lenses were defocused, compared to the standard position (Figure 5.06(b)) reducing the driving pressure on the north-south axis. The imploded material is oval in cross-section with the long axis in the north-south direction. Figure 5.06(d) shows the result when the pressure on the north and south poles was increased above the standard condition. The imploded material is more symmetric in this case. As the backlighting delay was 0.8 ns for this shot transmission through the centre is visible. There is however a slight flattening in the north-south direction since the focal spots were somewhat smaller than would be used for uniform illumination.

These radiographs clearly demonstrate the usefulness of ZPCR for investigating the dense plasmas which will be generated in future ablative compression experiments. In future experiments, time resolution and high energy X-ray generation efficiency will be improved by using a short pulse (100 ps) beam for backlighting, synchronised to the main long pulse for target irradiation.

C Duncan (Oxford), A Raven and P T Rumsby (RAL)

CHAPTER 5 REFERENCES

5.01 M H Key, P T Rumsby, R G Evans, C L S Lewis, J M Ward and R L Cooke, Phys Rev Letts, 45, 1801 (1980)

5.02 Pinholes were generously made available by LLE Rochester

5.03 Annual Report to the Laser Facility Committee, RL-80-026, Section 5.6 (1980)

5.04 The zone plates were manufactured by Graticules Limited, Tonbridge United Kingdom

5.05 H H Barrett and F A Horrigen, Appl Optics, 12, 2686 (1973)

5.06 M H Key et al, Phys Rev Lett, 45, 1801 (1980)

CHAPTER 6 SPECTROSCOPY AND XUV LASERS

INDEX

CHAPTER EDITOR: I N Ross

CHAPTER 6 SPECTROSCOPY AND XUV LASERS

6.1 Introduction

The ongoing programme of experiments whose objective is a demonstration of laser action in the XUV spectral region, has continued during the year 1980/81. This work represents a continuation of the programmes carried out over the past three years.

The long term aim of this programme is to investigate the feasibility of generating laser action at x-ray wavelengths of less than 10 Å. The present experiments are however, restricted by technological constraints to the less demanding XUV region at around 200 Å. A number of approaches to this problem are being considered, namely, recombination in carbon and aluminium, and electronic collision pumping of an optically forbidden transition in calcium. Of these, however, only the carbon fibre approach has so far been experimentally pursued. In these experiments a population inversion is established between the n = 3 and n = 2 levels of the hydrogen-like carbon ion (CVI) during the expansion of a laser heated carbon fibre. Laser action is expected on the Balmer α line at 182 Å.

The University of Hull, Queen's University, Belfast, and the Rutherford Laboratory are collaborating on this project.

Experimental work on atomic spectroscopy and radiative transport, having been relatively quiet over the past year, is now showing a welcome revival of interest with two new areas of research planned for the coming year. Both of these open new areas of physics and are well suited for inclusion in the programme of the Central Laser Facility, namely studies of line narrowing and spontaneous electron-photon excitation. Over the past year experimental work has principally been carried out in conjunction with the laser compression programme. Of particular importance in this regard has been the continuation of study of spectral line shapes produced from high density plasmas.

G Pert (Hull)

6.2 CVI Experiment

6.2.1 Theoretical Considerations

The recent experiments at Hull, described briefly in the next section have provided important quantitative data on the spectral emission from laser heated fibres which can be compared with data from the codes. It is clear from a cursory study that the gain does not obey the scaling law with fibre diameter given by the uniformly heated model, but rather shows at most only a very weak scaling with fibre diameter. This conclusion is further reinforced by a study of additional data such as the transverse total H α emission which shows a similar behaviour. It is therefore apparent that only a fraction of the fibre is contributing to the plasma, and of magnitude almost independent of fibre diameter.

In order to study this behaviour, the Eulerian code MAGT was modified by including an expanding grid to model fibre heating. The results thus obtained present a consistent picture with the experimental observations, and further enhance our understanding of the interaction physics of these targets. These studies also emphasise the importance of the pre-pulse and the avoidence of 'non-classical' behaviour during heating. It is found that the role of the pre-pulse is to create a relatively tenuous plasma blanket around the fibre, which both enhances the geometrical coupling of the main laser pulse, and also provides a thermal blanket surrounding the fibre core enhancing the heating of the latter, and ensuring a symmetric expansion as is observed experimentally. At the power levels used experimentally the core is not uniformly heated. Due to the strong dependence of thermal conductivity on electron temperature (enhanced by ionisation effects) a reasonably sharp boundary between the heated plasma, and cold residual core is seen. Under experimental conditions a layer of order 1 μm thick is evaporated from the fibre. The conditions in this layer are found to closely resemble those of the uniformly heated fibre of equivalent diameter.

In the experiments it is found that the gain results are independent of diameter over the range of fibre diameter 2.5 ~ 6.0 μm. The MAGT

simulations indicate nearly complete burn-through of fibres of 2.5 μm under the experimental conditions. If we compare the experimental results with those obtained from the uniformly heated model for a 2.5 μm diameter fibre we obtain the following values at peak gain assuming ∿20 % laser absorption in accordance with earlier experiments.

	Expts	Comp
Laser energy (J)	8	8*
Gain (Gl)	5	2
Hα spontaneous emission (ergs)	2×10^3 (±50 %)	2×10^3

* Including 20 % loss in lens and windows

The agreement is remarkably good, and gives confidence in the interpretation of the results in terms of this model.

G J Pert (Hull)

6.2.2 Summary of Experimental Results at Hull

In a series of experiments at Hull reported last year (6.01) the Balmer (Hα, 182 Å) transition in CVI was shown to exhibit gain along the axis of a laser produced carbon fibre plasma. The laser was operated at ∿ 5 - 10 J in 180 ps with a 20 % prepulse ∿200 ps before the main pulse. The laser output was focused to a line ∿50 μm x 2.5 mm using a 2 m concave cylindrical lens in conjunction with a 10.4 cm SORO lens. A carbon fibre ∿2.5 - 5 μm diameter was placed into the focus such that ∿ 1.5 - 2 mm was irradiated ensuring that the free end was efficiently heated and avoiding the development of an absorbing end. Two grazing incidence spectrographs viewed the plasma from different directions and their responses were carefully cross-calibrated using an optically thin source formed by irradiating a carbon fibre with a spot focus (6.02). A 2 m Hilger and Watts E580 viewed the plasma along its axis whilst a 1 m rocket spectrograph (Astrophysics Research Unit, Culham) looked at the

fibre transversely. Figure 6.01 illustrates the experimental configuration described above. Kodak SC5 plates (in the E580) and SC7 film (in the rocket) were employed for recording the emission from the plasma. The emulsions had been carefully calibrated in separate experiments (6.03).

Gain could be inferred directly from an intensity anomaly in the axial Hα signal and the results obtained indicated values of gain-length product of up to ∿5. In addition, the Hα line is made up of 7 transitions which are grouped together to give the appearance of a doublet with the components separated by 0.14 Å (6.04). Because of the different transition probabilities of the two components we would expect the intensity ratio of the peaks to depart from the normal, statistically populated, value of about 1.07:1 (red:blue) in the presence of gain. This behaviour is an extremely sensitive indicator of gain but cannot be considered reliable in predicting the actual magnitude of the gain due to the fact that the assumption of statistical equilibrium between the levels has been made (6.01). Nevertheless, the gain-length products predicted are again up to ∿5. Throughout the experiments a threshold for gain was observed at a laser energy of ∿ 6 J (ie ∿ 3 J mm).

L D Shorrock (University of Hull)

6.2.3 Carbon VI Experiment at the Central Laser Facility

In view of the very promising results obtained at the University of Hull, it was decided to repeat and confirm these measurements (section 6.2.2 above), extending them with the greater power available from the CLF laser, with which gain-length products $\alpha l > 5$ were expected. A direct gain experiment using the methods described in our 1979 Annual Report (6.05) would follow if the initial experiments were successful.

6.2.3(a) Experimental Arrangement

The arrangement of experimental apparatus used is shown in Figure 6.02. The 1.06 μm laser beam was brought to a line focus at a slight angle to

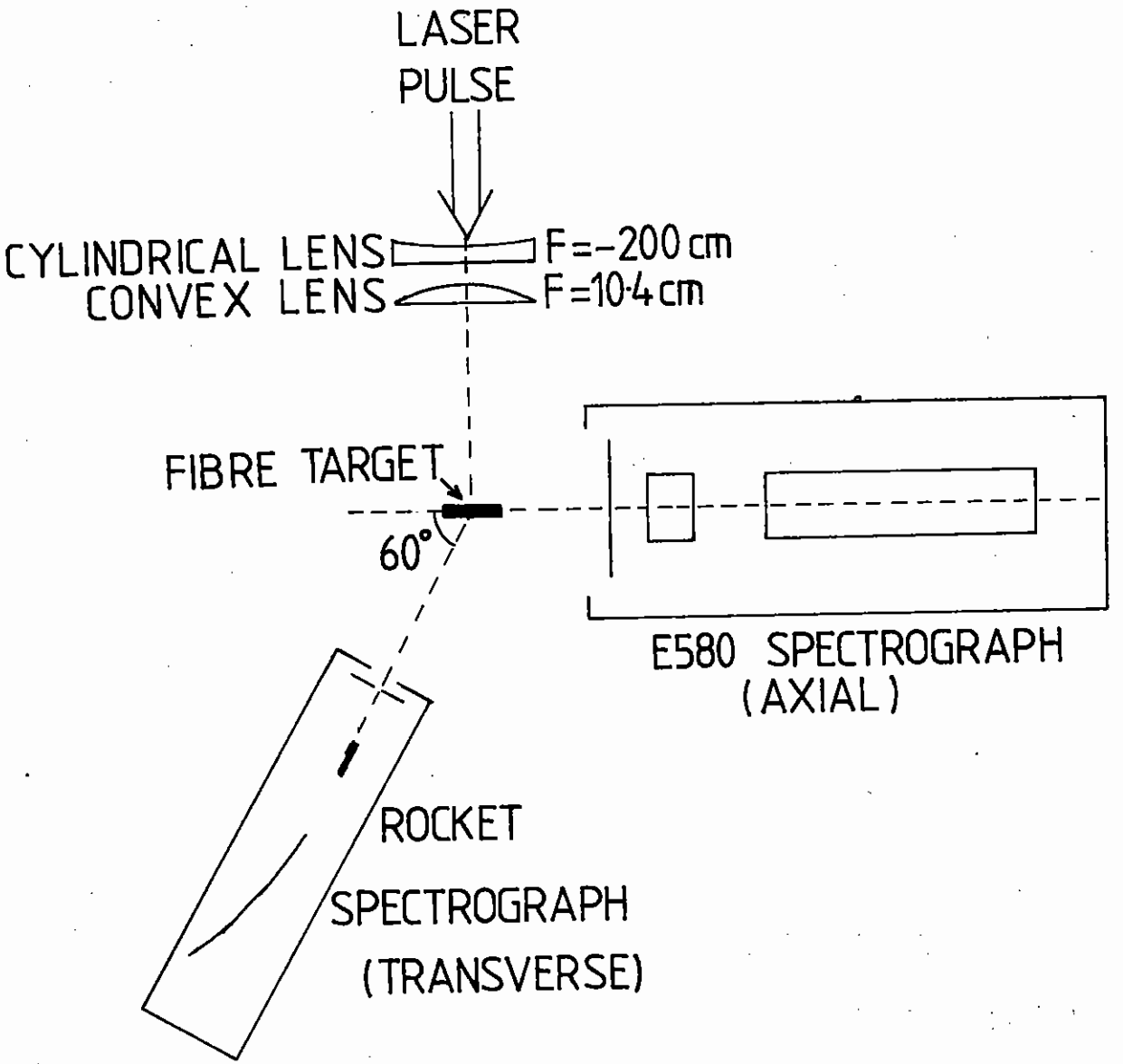

Figure 6.01 Experimental configuration at University of Hull.

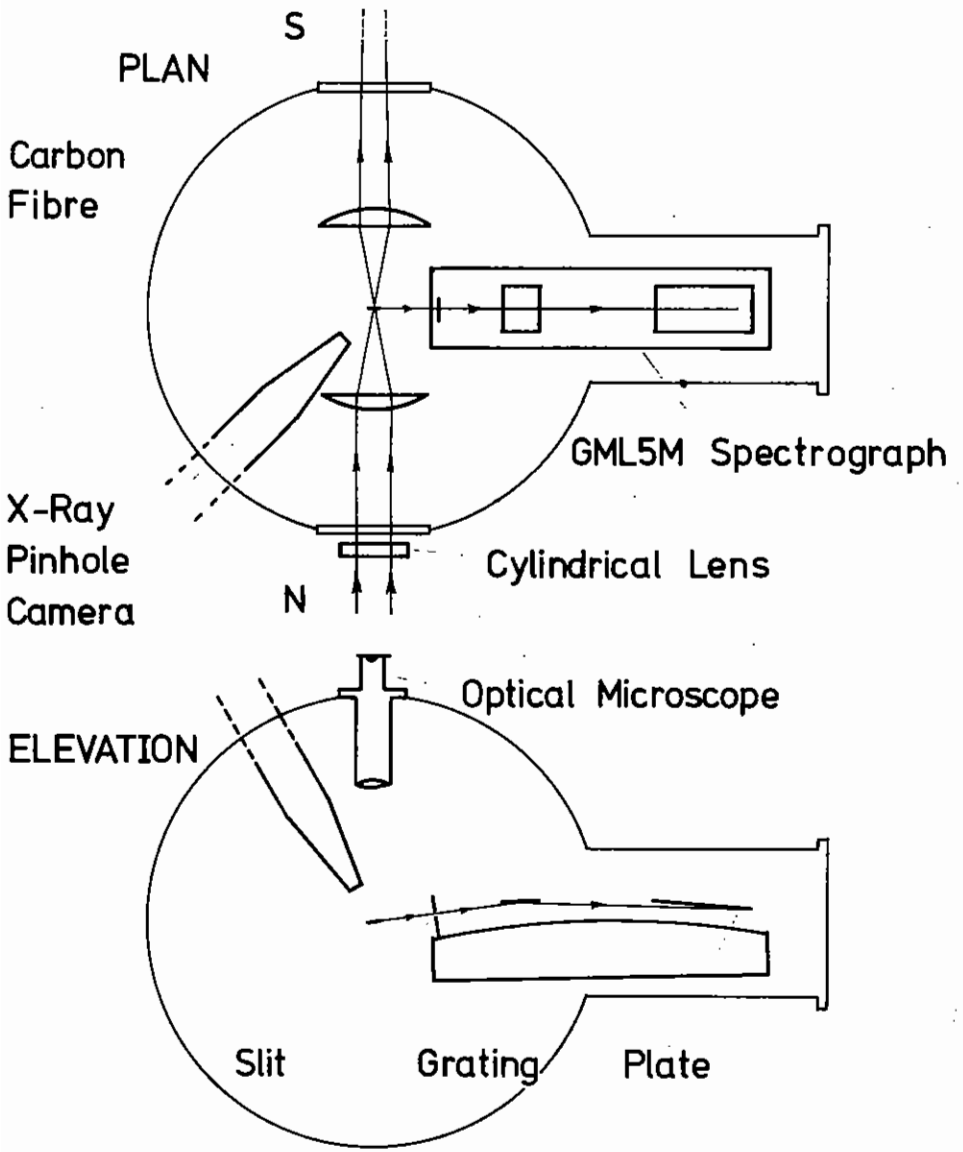

Figure 6.02 Experimental configuration at the C.L.F.

the horizontal plane by passing it first through a cylindrical diverging lens (f = -1.0 m) outside the target chamber, and then through the main f/1 ICOS (North) focusing lens. The cylindrical lens was positioned as close as possible to the ICOS lens to maximize the throughput energy.

The laser pulse length was approximately 200 ps, with a 200 ps prepulse at a level of 10 % of the main pulse arriving 200 ps before it. The beam energy was typically 50 J.

The targets were carbon fibres of diameter 3 - 7 μm, mounted with one end free so that the fibre pointed directly along the slit-grating line of the spectrograph, ie at an angle of about 8° to the horizontal. A glass microballoon was mounted near the secured end of the fibre to aid in positioning the fibre, which was too narrow to give appreciable retro-reflection into the telemicroscope system or even to see easily when viewed as a magnified transmission image.

The main spectrograph for observations down the fibre axis was to be the 5 metre grazing incidence GML5M (6.06) and the spectrograph for transverse (radial) intensity measurements a one metre rocket spectrograph from the Astrophysics Research Unit, Culham Laboratory. Restrictions on space and the decision to attempt to infer the existence of gain by the anomalous Hα doublet ratio method (section 6.2.2) caused the abandonment of the transverse-viewing spectrograph in favour of a white-light miroscope and graticule. These were positioned on top of the target chamber to view the fibre from above, again to ease alignment.

An x-ray pinhole camera was used to produce an image of the plasma at a magnification of x 2.2 on Kodirex film. The pinhole size was either 25 or 50 μm, and the filtering typically 0.75 μm of aluminium.

Two sets of auxiliary detectors were arranged in the chamber to obtain plasma diagnostic information. One was an array of eight x-ray diodes (6.09) to measure the plasma electron temperature, and the other an array of six plasma calorimeters (6.09) to measure the energy in the expanding plasma, and hence the energy absorbed from the laser beam.

6.2.3(b) Alignment Procedure

Accurate alignment of the carbon fibre in the cylindrical laser focus was of the greatest importance, and may well have deleteriously affected the previous experiments. The technique employed in this case was to locate the position of the base of the fibre by viewing the retro-reflected CW YAG laser radiation from the small microballoon attached to the fibre. This defined the position of the fibre on the N-S axis of the lenses (Figure 6.02); if necessary the fibre could now be rotated slightly by turning the target base until the fibre lay normal to the N-S axis.

The fibre position on the optical microscope graticule was then noted for reference; subsequently initial fibre positioning was done using the optical microscope, with the reflection of the target area alignment He-Ne laser being used to help find the (uncoated) microballoon and fibre.

Final focusing was achieved by moving the South (ICOS) lens away from the target to a position known to produce a sharp image (32 x magnified) at a distance of 4.4 m, defocusing the N lens slightly to provide a uniform background illumination, and using an infra-red viewer to observe the movement of the fibre into good focus on reference marks placed where the line focus was known to fall. A subsidiary confirmatory method, similar to the Foucault knife-edge test, involved viewing the near-field of the south lens without defocusing the N lens. When the fibre was accurately in the focal position it obscured the maximum amount of light from the N lens and produced the largest shadow in the near field of the S lens.

Laser burn patterns were taken by putting unused exposed Polaroid negative paper at the S lens image position. Firing a shot produced a burn mark on which the interposed fibre could be seen to absorb a significant fraction of the energy when it was well-aligned in the line focus.

Measurements made from these burn patterns and from direct measurements of the magnified image of the line focus through the S lens, using CW YAG illumination, showed that the line focus was 30-40 μm across and reasonably uniform. The optimum focus was axially displaced by ∿150 μm

from one end to the other of the 6 mm line focus due to curvature of the focal plane, so that the best focusing position was to some extent a compromise. The quality of the line focus was however quite acceptable, and the fibre positioning methods were much better than those previously used. Straight-edged masking plates were used in front of the diverging lens to stop down the beam and hence shorten the line focus if required.

6.2.3(c) Results

Spectra were first obtained using the one metre rocket spectrograph (1200 line mm^{-1} grating) viewing along the fibre axis in what was to be the position of the GML5M (Figure 6.02). Single shot spectra on Kodak-Pathe SC7 film were recorded from carbon fibres of diameter about 6 μm, irradiated at ∿ 5 J mm^{-1} over lengths of ∿ 3-4 mm, but with insufficient resolution to determine the Hα doublet ratio. The brightness of the Hα line was similar to that recorded in multiple exposure spectra transverse to the axis in the experiments at the University of Hull (section 6.2.2).

The GML5M was first set up to view along the fibre axis with a 600 line mm^{-1} grating used at a grazing angle α of 2°. Single shot recording with carbon fibres gave insufficient exposure to record spectra. Weak spectra were observed when sensitive plate (Kodak-Pathe SC5) was used to record five shots on fibres but the Hα line was not observed. On the hypothesis that the grating was inefficient at the particular combination of wavelength and α used, it was changed for one having 300 lines mm^{-1}, chosen with optimisation for this experiment in mind. With this grating the resolution was about 7 mÅ per micron slit width. Using SC5 plate and a 25 μm slit, a good test spectrum, including Hα, was obtained from the plasma produced from a plane carbon target. With a fibre target a shot of 4.2 J mm^{-1} onto a 3.7 μm fibre then produced a very weak spectrum showing CV resonance lines and Ly α in fourth order, but not Hα. This level of exposure was also seen with ∿ 0.2 J incident on a spot focus on a plane solid carbon target. Line focus shots at a flat carbon slab gave a strong spectrum from the GML5M (25 μm slit) on which the Hα doublet was clearly resolved and the 1:1.4 intensity ratio of the peaks appeared to indicate gain on the transitions (Figure 6.03).

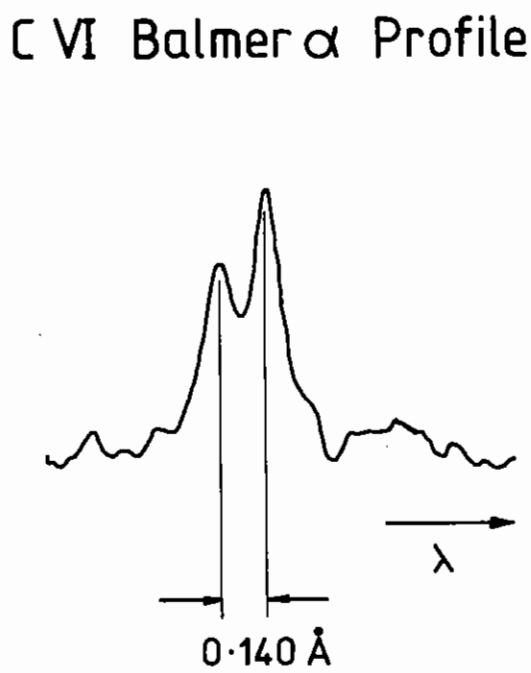

Figure 6.03 Densitometer trace of CVI Hα doublet: ratio of peak heights is ∿ : 1.4 spontaneous ratio is 1:1.07.

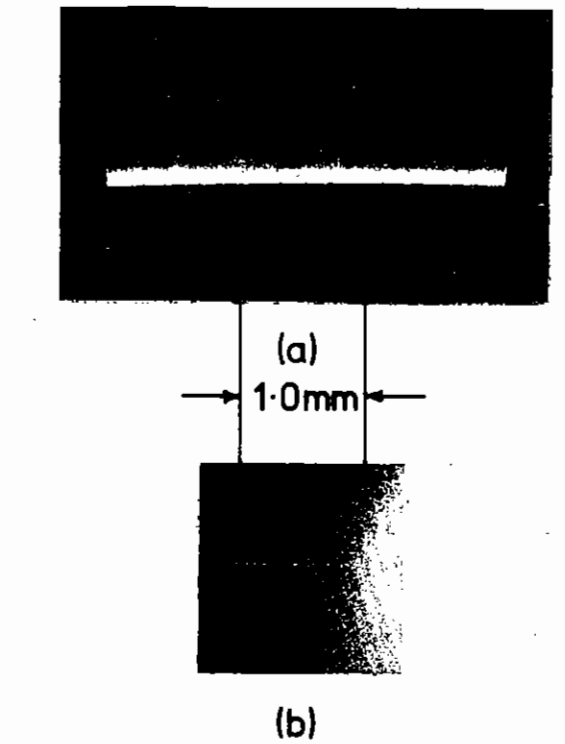

Figure 6.04

a) Line focus on solid carbon target: 5 μm pinhole and 0.7 μm Al filter. Energy on target ∿ 5 J mm^{-1}.

b) Line focus on 6.1μm carbon fibre: 25μ pinhole and no filter. Energy on target ∿ 5 J mm^{-1}.

The experiment was therefore repeated on a polished flat carbon surface. The whole width of the face was irradiated in a 5 mm line focus, the laser pulse including the prepulse used for the fibre experiments. Spectra were obtained in this manner suggesting gain-length products $\alpha\ell$ of order 2-3, as deduced from the ratios of the doublet line intensities (6.02).

However, varying the length of the line focus did not change the gain-length product by the expected amount, and it was concluded that the anomalous line ratio must be due to other causes, in particular perhaps non-statistical sub-level populations (6.07).

On the hypothesis that the observed doublet intensity, being integrated over the distance from the target surface, was superimposed upon some different line structure (eg due to Stark broadening), and that therefore the gain appeared non-linear with length, a spatially-resolved spectrum was obtained with the GML5M by using a 300 μm vertical slit placed between the entrance slit and the grating. The doublet ratio was seen to be invariant with distance from the target surface.

6.2.3(d) X-ray Pinhole Camera Results

Figure 6.04(a) shows the x-ray pinhole photograph obtained using a 50 μm pinhole with a 0.7 μm aluminium filter to view the line focus ($\sim$4 J mm^{-1}) on a solid carbon plane target. It is apparent that the line focus is quite uniform. Such apparent non-uniformities as do occur in the photographs are probably due to irregularities in the target surface. A series of alignment and filtering difficulties meant that few results were obtained from shots onto fibres, but those results which are available indicate that the uniformity of focus on the fibre is also quite good. Figure 6.04(b) shows a photograph of the plasma from a 6.1 μm fibre taken through a 25 μm platinum pinhole without filter. The line energy density was 4 J mm^{-1}.

6.2.3(e) X-ray Diode Results

The x-ray diode array gave results suggesting electron temperatures of

200-300 eV for carbon fibres and 100-200 eV for solid targets, although technical difficulties again precluded many measurements on fibres. The former value is in good agreement with that expected from computer code modelling.

6.2.3(f) Calorimetry Results

Four calorimeters were arranged symmetrically around the target chamber in the N-S vertical plane so as to intercept the expected radial annular flow of the fibre plasma. Two further calorimeters were placed at intervals of a few degrees towards the east on the azimuth of the calorimeter above the S lens, to intercept the flow if it was not in the expected plane.

The calorimeter data showed little consistency or uniformity in either direction or recorded energy from shot to shot on carbon fibres. The total recorded energy also implied coupling into the fibre of 10 % or less, much less than the value of 20 % of the incident laser energy expected from the Hull measurements. However, it is now thought that the plasma flow from the irradiated fibres can be expected to be almost entirely radial; calculations show that the flow of energy at angle θ to the radial flow direction is expected to be given by a function of the form

$$f\left[\cos^2\theta + \left(\frac{v}{u}\sin\theta\right)^2\right]^{-5/2}$$

where v is the radial velocity and u the axial velocity. Since $v >> u$ the $\sin^{-5}\theta$ term dominates, so that the energy flow is a very strong function of angle. It can therefore be expected that slight misalignment of the calorimeters would result in most of the energy flow being missed.

6.2.3(g) Conclusions

The experimental results are unfortunately rather inconclusive. While it initially seemed that gain could be inferred from anomalous values of the line ratio for the Hα doublet from a solid target, more detailed analysis, taking into account the possibility that the sub-levels of the transition

were not statistically populated, indicated that this was not the case. In particular, the fact that the gain-length product inferred did not scale linearly with the length of the line focus on the target led to the conclusion that the anomalous values must have a different cause.

There were some indications that the coupling of laser energy into the fibre was lower than required for gain conditions. The calorimetry indicated a low absorbed energy, although as pointed out above this might have been due to calorimeter misalignment. X-ray pinhole pictures were weak, requiring as little filtering as possible. Axial spectra proved too weak to record on the GML5M, though well-exposed spectra were obtained with the rocket instrument. This may have been due to a combination of misalignment and the inherent loss of a factor of 2.5 in sensitivity compared with the rocket spectrograph, although it was expected that with a 300 line mm^{-1} grating the GML5M would be as sensitive as the E580 spectrograph used in the Hull experiments. Spectra could be recorded from a plane target using energies of the order of 1 J, whereas fibre targets required about six 30 J shots.

These various observations show that large α l gain was not obtained for reasons as yet not fully understood. Possible differences between the experiments at Hull and at the CLF include different pulse duration, prepulse level, and line focus alignment.

The next scheduled experiments will therefore concentrate on resolving these problems, and particularly on measuring the energy coupling more accurately. The latter experiment will also be performed at Hull using a purpose-built calorimeter, in an attempt to find any previously unnoticed differences between the experiments. It is hoped that these experiments will form the basis for a future demonstration of superfluorescent laser action at 182 Å.

G J Pert, L D Shorrock, G J Tallents (Univ of Hull), M H Key (RAL),
C L S Lewis, E Mahoney and J M Ward (QUB)

6.3 Progress on Line Shapes in High Density Matter

The progress of the study of X-ray emission from high density plasmas has followed three lines of research. First, the theory of spectral line broadening in these plasmas has been investigated and extended to new ionic species. Second, simulation of the detailed spectra emitted by the compressed plasmas has been used to study effects of rate equation models, line profile models and gradients on the spectra. Third, progress has been made on using line shapes as diagnostics of the laser compressed plasmas.

6.3.1 Study of Lines at High Densities

Simple scaling laws were employed to illustrate the fact that there are indeed regions of plasma temperature and density which are obtainable in the laser compression plasma regime that can be useful for the study of the details of spectral line profiles. In figure 6.05 the regions which must be obtained for one to derive useful line profiles are shown. Note that the regions will differ for different transitions of the same series in the same ion stage. Further, as indicated in the figure, conditions appropriate to the study of line shapes have been obtained.

To delimit the areas of interest it is informative to analyze, with simple considerations, what we can hope to see experimentally. This will indicate where our main efforts should be. First let us make the statement that line wings, ie the region from about the Weisskopf frequency separation, $\Delta\nu_w$, from line centre and beyond is not of interest to us. This is, of course, in distinction to the work of recent years in which the theory of line broadening has been extended to allow one theoretical treatment to have the correct asymptotic limits in both the line wings and the line core (6.10). The reason that the wings are not of interest is derived from two considerations. First, we can ask where the wing lies relative to the core as we go from the standard sources ($n_e \lesssim 10^{18}$, $z \sim 1$) to the LCP (with $n_e \gtrsim 10^{22}$, $z \gtrsim 10$)? The Weisskopf frequency, as a function of z, scales as z (6.11). Thus for the same hydrogenic transition the Weisskopf frequency goes further out from

line centre. Second, the contribution of the line profile at the Weisskopf frequency ($\Delta\nu_w$) scales as

$$\phi(\Delta\nu_w) \quad \alpha \quad \frac{n_e^{2/3}}{Z^{1}1}$$

and finally, when the emission at $\Delta\nu_w$ is compared to the background arising from either bound-free or free-free emission occurring in the plasma, the ratio of the line to continuum scales as

$$\frac{P_{Line}}{P_{Cont}}\Big|_{\Delta\nu_w} \quad \alpha \quad \frac{n_e^{2/3}}{z^{14}}$$

This ratio proves that for any realistic form of n_e versus z relationship (such as $n_e \alpha\ z^6$) the problem of seeing line wings is insurmountable.

6.3.2 Study of Calculation of Shift of Spectral Lines

Recent attempts at determining the shift of spectral lines has led to a number of single particle propagator (one level) formalisms. It can be shown that there is a direct relationship between the width of a line and the shift of the line. In the case of the width it has been shown by Fano that the contributions of the two levels are not just additive but that the effects interfere (6.12). That is, the Rydberg-Ritz intercombination principle which simply states that if the energies of the upper and lower states of a system are given by E_U and E_L, respectively, then the transition energy is $E_{UL} = E_U - E_L$, does not hold for level widths and shifts. Thus the level propagator (single particle effects) which has a shift and width operator (6.10), Δ, does not produce transitions with shifts and widths which are linear combinations of the level shift and width, ie

$$E_{UL} + i\,\Delta_{UL} \quad \neq \quad (E_U + i\,\Delta_U) - (E_L + i\,\Delta_L)$$

This implies that attempts to calculate transition shifts, induced by plasma perturbations, by solving the appropriate Schroedinger equation for each level and adding the shifts (see the article by Skupsky for an

extremely clear exposition of this method (6.13)) is ill considered. Moreover, the inapplicability of adding widths has been proven for low density line shape by comparison between theory and experiment (6.14).

The problem arises from collisions which can couple the upper and lower levels and can be illustrated in Figures 6.06 and 6.07. In Figure 6.06 we have terms that affect only one level at a time and satisfy the additivity assumption, however those contributions shown in Figure 6.07 couple the levels and interfere, thereby negating the additive nature of the shifts.

6.3.3 Line Profiles of Lithium-like Ions

In the case of the lithium-like structures we do not have a firm grounding in the study of neutral emitters, because neutral lithium-like line profiles from plasmas are difficult to study experimentally and are not nearly so well suited to theoretical calculation as hydrogen or helium which contain most of the features of theoretical interest. Thus the present work on the line profiles of Lithium-like ions in plasmas is motivated largely by experimental data which indicate that it is fruitful to study these lines. Further, there are interesting features which can be useful as diagnostic information. First, the Lithium-like ions will have the isolated lines found in helium, eg the $1s^2\ 2p^2P_{1/2} - 1s^2\ 3d^2D_{3/2}$ in Br XXXIII, and the dipole allowed-forbidden line pairs such as the dipole allowed $1s^2\ 2s^2\ S_{1/2} - 1s^2\ 3d^2\ P_{3/2\ 1/2}$, and the neighbouring dipole forbidden $1s^2\ 2s^2\ S_{\frac{1}{2}} - 1s^2\ 3d^2\ D_{\frac{1}{2}}$. In addition, the possibility arises of having two allowed lines from the same ground state as neighbouring spectral features due to the doublet nature of the spectrum, eg the $1s^22p\ P_{3/2} - 1s^23d^2D_{3/2}$ and $^2D_{5/2}$. These latter features will be resolvable in, eg Br XXXIII.

Finally, it should be noted that Br XXXIII is of special interest for experiments on thick shell targets in laser compression because the Lithium-like Bromine has an ionization potential of approximately 3000 eV, and the $1s^2 2p\ ^2P$ to $1s^23d\ ^2D$ transitions fall below the Silicon edge in a spectral window between low lying Silicon lines of Si XIV and Si XIII. This implies that spectroscopic measurements may be used to estimate

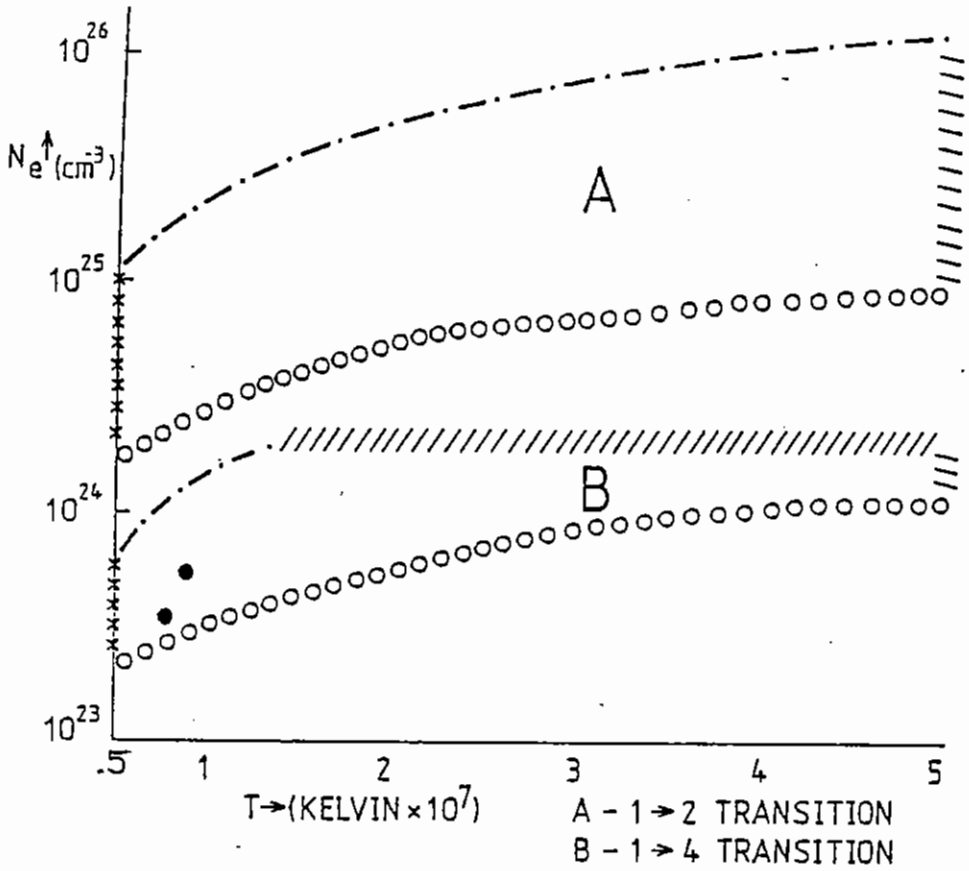

Figure 6.05 Plasma Temperature and Density of interest for Argon XVIII line shape studies. Origin of the constraint lines:

—·—·— = IP depression must be less than IP of upper state.

////// = N_e must be less than Inglis Teller limiting value.

OOOO = Stark width should be greater than Doppler width.

×××× = T_e should be at least on the order of lower ion stage IP.

\\\\\ = T_e should be less than IP of Hydrogenic species.

● = Some reported experimentally obtained plasma conditions,

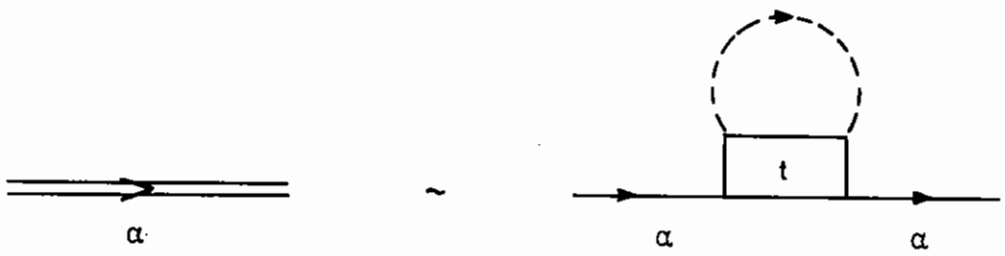

Figure 6.06 A graphical contribution of the two-body t-matrix to the single level shift and width operator for state ═══ level α propagator, ------ plasma propagator.

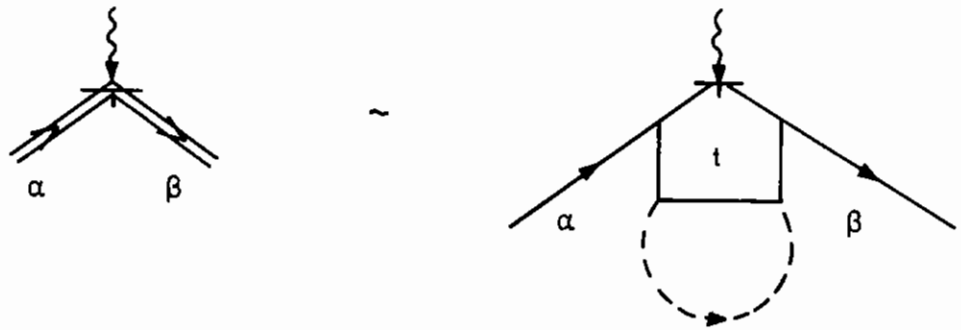

Figure 6.07 A graphical contribution to the vertex parts which couple the upper and lower level. ∿∿> is photon, ─┼─ is transition element, otherwise as Figure 6.06.

compression of ablatively driven multilayered targets.

In figure 6.08 is shown the level structure under consideration - the complexity is apparent. Further, the fact that 10 dipole allowed transitions are necessary for a complete study of the Lithium-like states is also apparent. These calculations required atomic structure data which was kindly provided by J Scofield of Lawrence Livermore Laboratory.

As an example of the result we show in figure 6.09 for the Br XXXIII n = 2 to some of the n = 3 transitions.

In the role as a diagnostic of the plasma density, and at times opacity, it is seen that the lines emitted from the Lithium-like ion have three important features for certain z emitters:

(a) isolated lines;

(b) pairs of allowed lines in same spectral region from same upper and lower state manifolds;

(c) dipole allowed and forbidden pairs.

Each of these features may be useful in separate situations and the addition of these to the standard hydrogenic and helium-like line profiles now used provides an important extension to the present diagnostic capability. Theoretically, the advantage of having another set of non-hydrogenic profiles to study gives one the opportunity to differentiate between errors in atomic structure and errors in the line broadening theory.

6.3.4 Simulation of the Effects of Gradients on the Spectral Emission Diagnostic in Laser Compressed Plasmas

A detailed analysis was performed of the effects of temperature and density gradients on the spectral output of the laser compressed cores as

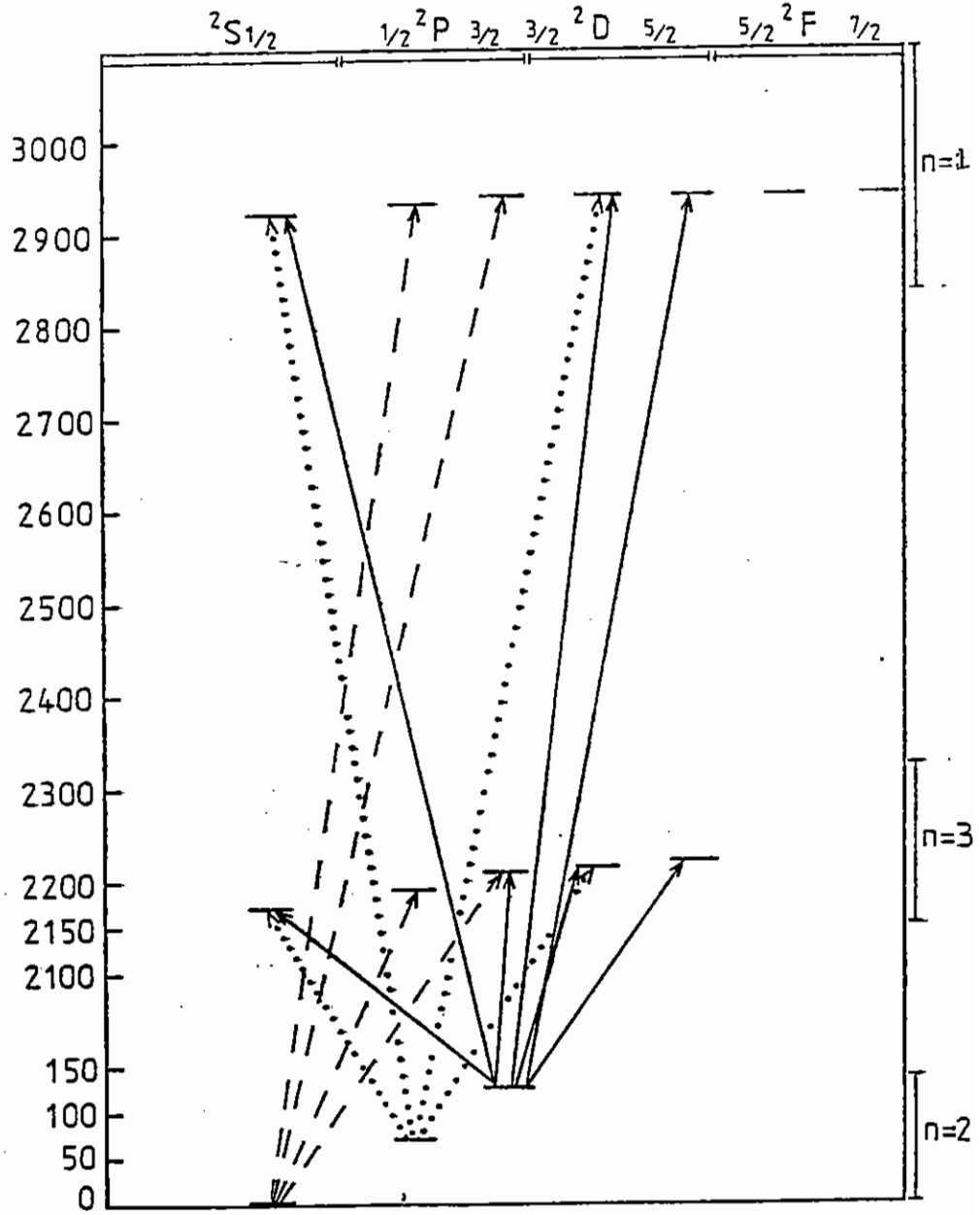

Figure 6.08 The energy level diagram for the Lithium-like transitions of interest. The dipole allowed lines calculated are denoted:- ------ indicates transitions from 2^2S; ——— indicates transition from $2^2P_{3/2}$; and ●●●● indicates transitions from $2^2P_{1/2}$.

these affect diagnostics. The method used was to introduce inward and/or output gradients in the temperature and density and then analyze the outputs as if these were 'experimental' data. This method provides us with a determination of the sensitivity of the diagnostic procedures and thus one obtains, in addition to the usual experimental and theoretical errors, a diagnostic error which arises from the assumptions inherent in the diagnostic method.

The following conclusions can be reached concerning the diagnosis of laser compressed plasma sources:

(a) These sources, although fully non-LTE and amenable to calculation using techniques developed for stellar atmospheres, are completely distinct in that they have small peak optical depths, no real thermalizationa and negligible interlocking effects on the lines below 15 Å.

(b) The accuracy of the diagnostics, which are all tested assuming small gradients, is never better than 50 %.

(c) The best diagnostic in test was the continuum edge determination; however, it suffered from complete failure when the edge, trough and peak becomes ill-defined. This is indeed what commonly occurs in experiment.

(d) The ratioing of the dielectronic satellites adjacent to the Lyman Ne X fails when the electron density is not in the region where the ratio is a sensitive function of the electron density.

(e) The optically thin line widths produce an electron density that is at least 50 % too high with these optimal conditions; while the optically thick lines produce a compensated ground state number density which is still 50 % in error even though it uses the optically thin line electron density determination.

(f) The reliability of the total diagnostic parameter is optimistically estimated as a factor of 2.

(g) Time dependent calculations are required to further improve the understanding of these diagnostics.

6.3.5 Study of the Role of Detailed Line Shapes in Simulation of Spectral Emission

There are many aspects of line shapes which affect the study of radiative transfer from plasmas. For the present limited discussion we will separate the effects into two general categories which are somewhat artificial but still serve to illustrate the importance of line profiles in the study of radiative transfer. These two categories are:

(a) The effect of the shape of the intrinsic (microscopic) profile on the macroscopic radiative properties of the plasma;

(b) The effect of the radiation transfer (RT) on the macroscopic line profile; ie the emitted line radiation is a function of the RT. (This is the most common case.)

For the two cases above we will attempt to show, by using a simple model, examples of these effects.

We will show results for the two effects (1 and 2 above) considered as deviations from a standard case. The standard case will be a compressed neon filled sphere which has a uniform temperature and mass density in LTE. The temperature is 3.5×10^6 Kelvin and the electron density, which is uniform in an LTE model, is 4.5×10^{22} cm^{-3} for a sphere of radius 10^{-3} cm.

In figure 6.10 we show the spectrum for a viewing angle along a diameter. Note the intensity is on a logarithmic scale to illustrate all the features and the wavelength scale is in Angstroms. The main features are the two resonance series of the Hydrogenic (Ne X) and the Helium-like (Ne IX) transitions and their continua. This can be thought of as a standard calculation which would be performed for diagnostics or 'opacity'

simulations. Note that it ignores Non-LTE (NLTE) effects but has the advantage that no iterative procedure is necessary to determine the spectrum so it is used in largescale RT calculation. This figure has some interesting features which are noteworthy:

(a) The ionization potential is depressed thus excluding the transition to level 5, ie Lyman δ is not there.

(b) The Lyman α and He-like 1^1S-2^1P lines are severly modified by optical depth: ($\tau_{Lyman} = 55$), ($\tau_{Helium} = 15$).

(c) The Lyman continuum edge is substantial but the He-like 1s np continuum edge is masked by the Lyman Beta transition.

(d) The dielectronic satellites on the red wing of Lyman alpha are intense.

Next the effects of NLTE RT on the line shape will be illustrated. We have seen the effects of LTE RT on the resonance lines with the 'usual' opacity effect in Figure 6.10. In Figure 6.11 we show the emission from the same sphere but here we have a calculated with the complete NLTE method outlined above. Note, in Figure 6.11 (which is labelled as figure 6.10), that two important effects occur. First, because the NLTE calculations include effects of radiation pumping, we have a marked decrease in opacity. This is due to the radiation intensity in the opaque lines being large enough to increase the population of the upper level of the transition by absorption, ie

$$n_1 B_{12} \bar{J} - n_2 B_{21} \bar{J}$$

the net radiative rate out of level 1 becomes large. Second, the NLTE calculation produces a gradient in the radiation field, such that there is a relative decrease in J towards the outer boundary, this produces a gradient in the population densities which is similar in its effect to a temperature gradient decreasing outward. Thus the appearance of 'self-reversal' even without a temperature gradient.

Next, to find if the line shape affects the RT, the role of the intrinsic profiles will be examined. To this end we have performed calculations for the same temperature and mass density sphere in the NLTE RT mode using Lorentzian line profiles. The widths of the Lorentzians are determined from the widths of the actual calculated Stark profiles so that the widths are substantially correct. In Figure 6.12, the results using the schematic line profiles are shown. Of course, the profiles are now all Lorentzian but the most important aspect is that the actual level populations are changed rather markedly from the case where the full profiles were used. This can best be illustrated by reference to Table 6.01, which shows the differences in the two calculations. Note that the profiles do affect the electron density (through the ability to pump population to higher levels). The relative importance of these line shapes on the electron density will of course increase with the ratio of the hydrogenic ion ground state to fully stripped ion populations. Thus the importance of the shape of the line profiles has been indicated.

6.3.6 A Diagnostic using Li-like Lines for Ablative Compression

Although the success of spectroscopic techniques as diagnostics of the plasma temperature and density has been well documented for laser compression experiments on exploding pusher targets (6.15, 6.16), the use of these techniques has been considered infeasible for ablative compression targets due to the thick glass shells used in these experiments (6.17). The difficulties arise because the ablative compression regime will produce lower compressed core temperatures and the thick glass shell will have a large opacity. The present comment shows that spectroscopic diagnostics can be employed on these targets with a judicious choice of atomic species seeded into the D-T filled microsphere.

In order to minimize the effects of the glass shell opacity on the spectral emission lines, the lines from the 2^2P to the 3^2D transitions of Lithium-like Bromine are studied. These lines are chosen for two reasons. First, as shown in Figure 6.13, these Bromine XXXIII lines have energies

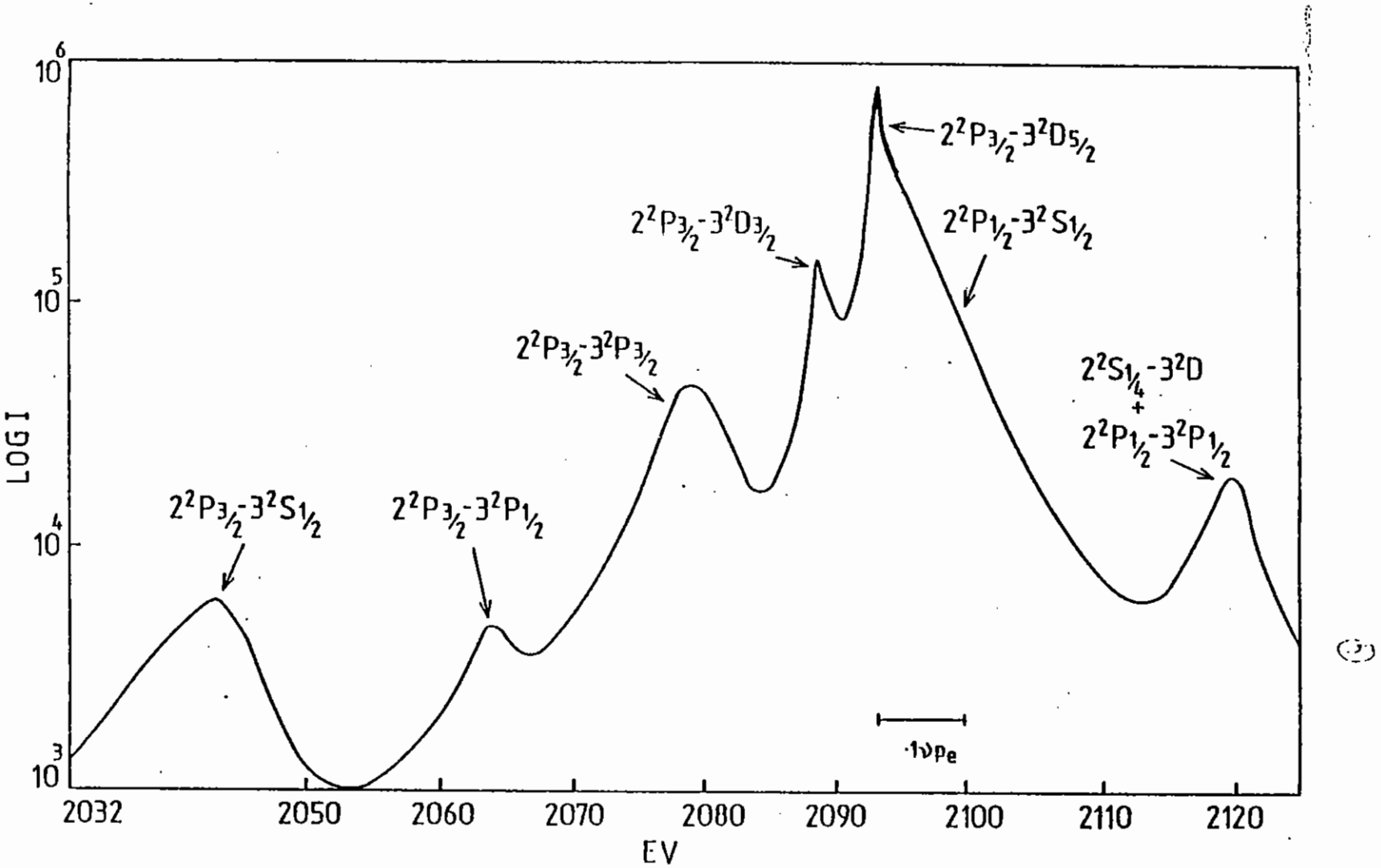

Figure 6.09 The two $1s^2 2p\ ^2P_{3/2}$-$1s^2 3d\ ^2D_{5/2,3/2}$ and other transitions of Br XXXIII for plasma temperature of 1000EV and electron density of 3.10^{24} cm^{-3}. The dipole forbidden lines are also indicated. The arrow $|\leftrightarrow|$ indicates 1/10 of the plasma frequency from $^2P_{3/2}$-$^2D_{5/2}$ line centre.

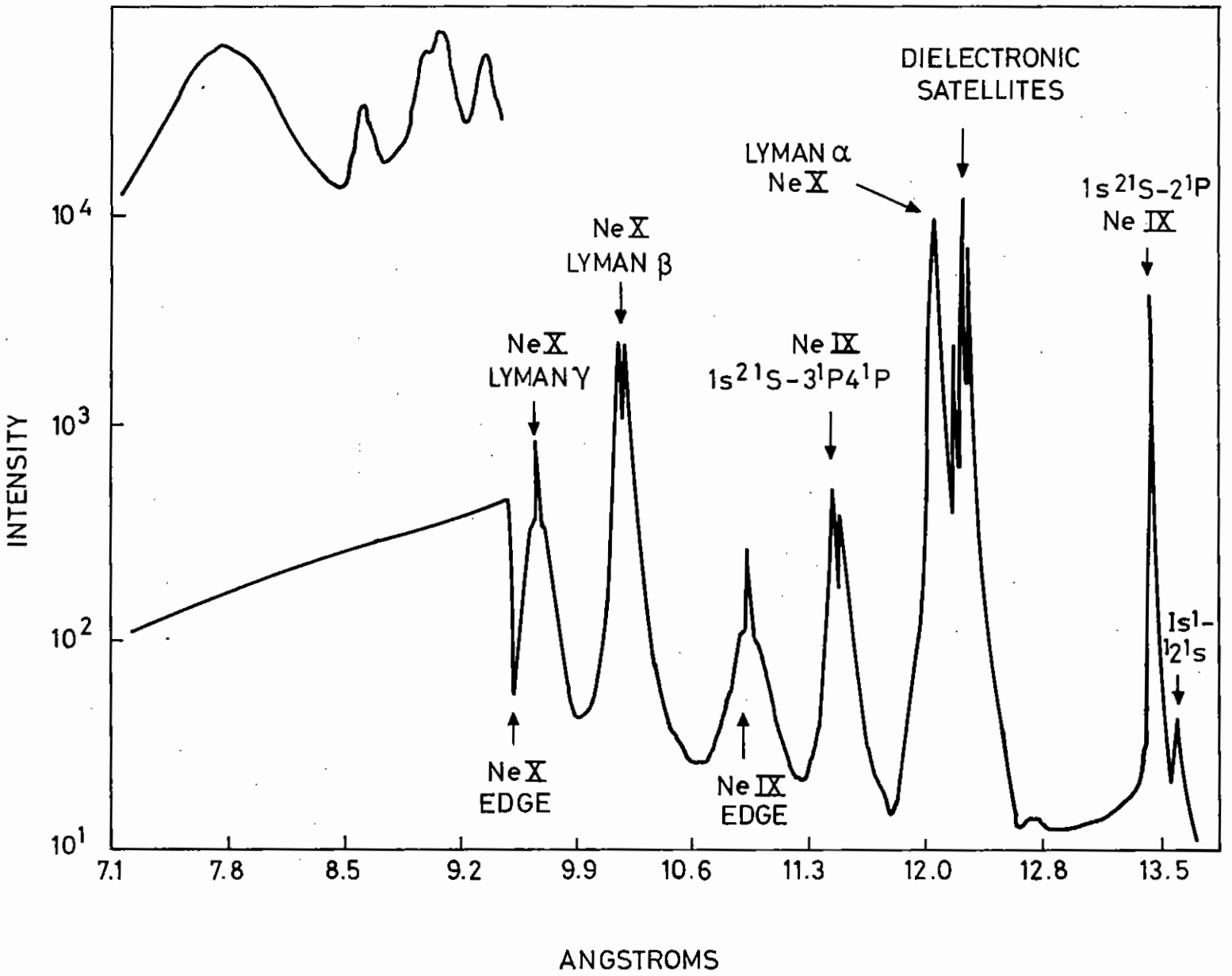

Figure 6.10 LTE calculation of the intensity viewed along a diameter of the Neon X and Neon IX resonance series emitted from a uniform sphere of radius 10 microns with a temperature equal to $3.5.10^6$ Kelvin and mass density of .2 gm/cm^3. The wavelength scale is in Angstroms and the intensity scale is logarithmic. The inset is an expanded scale of Lyman α plus dielectronic satellites.

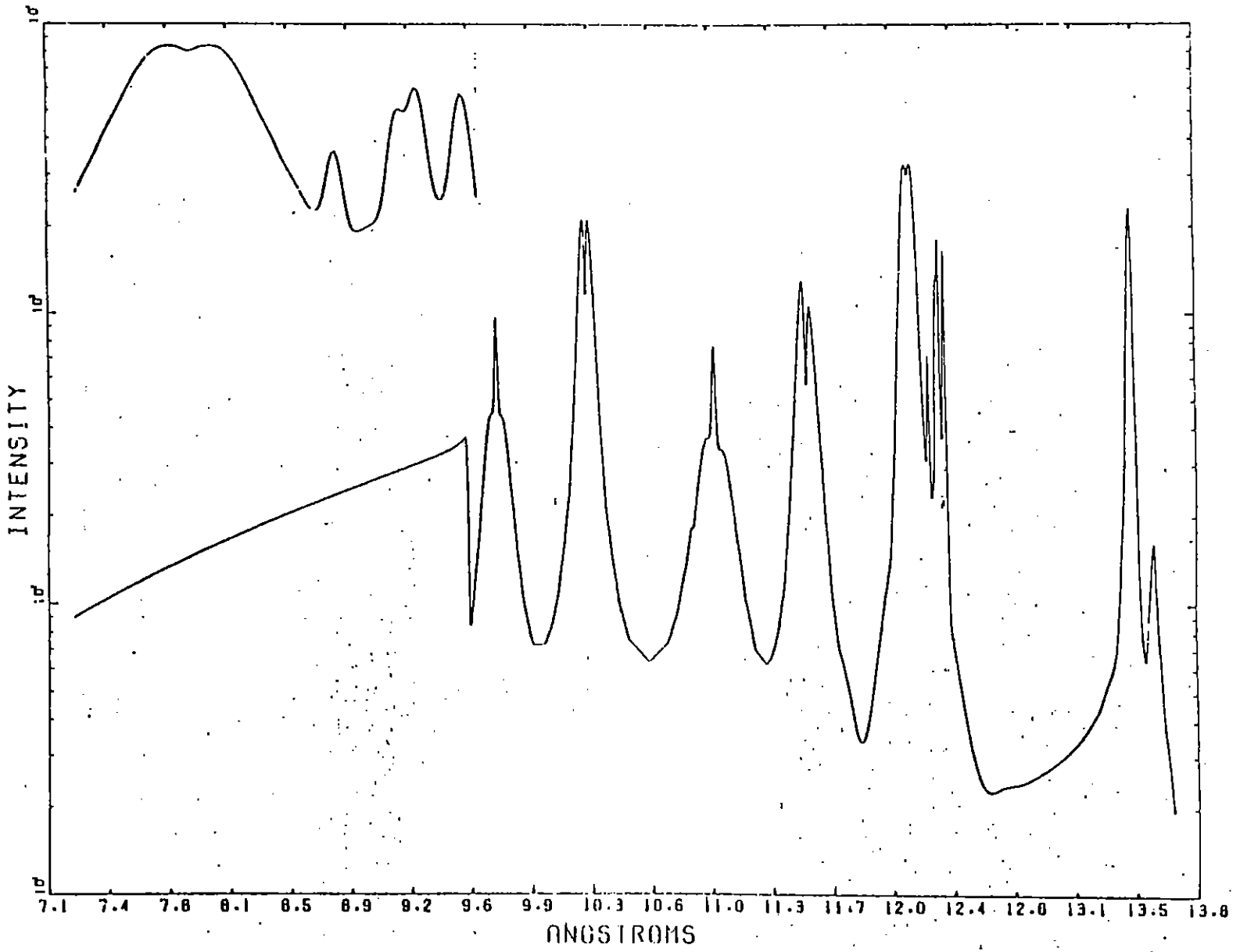

Figure 6.11 NLTE complete calculation - Otherwise as Figure 6.10.

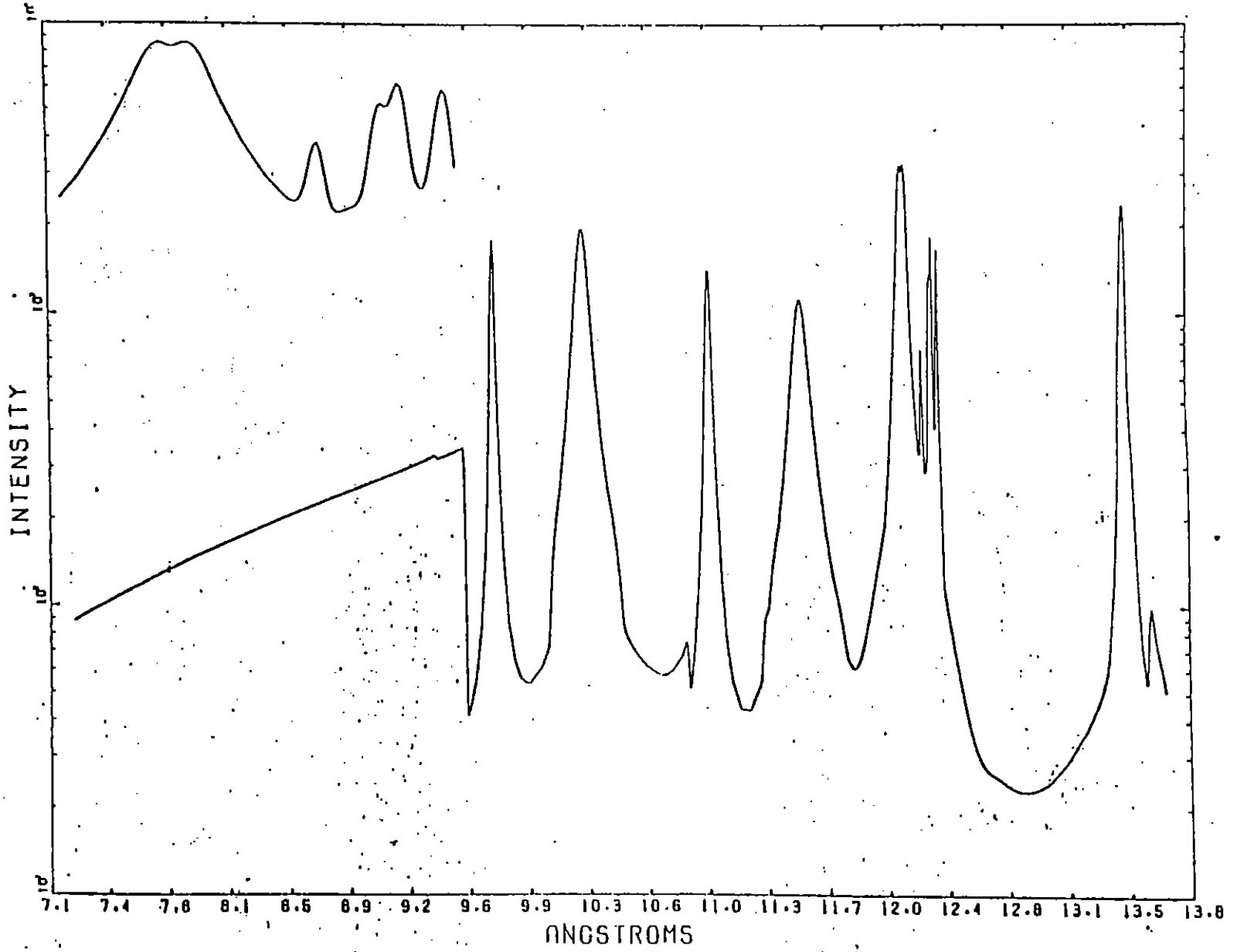

Figure 6.12 NLTE calculation with schematic Lorentzian profiles in place of detailed profiles. Otherwise as Figure 6.10.

TABLE 6.01

The Effects of the different calculations on Number Densities for the three cases shown in Figures 6.10 through 6.12

	LTE Fig.6.10	N LTE* Fig.6.11	N LTE-LORENTZ* Fig.6.12
Optical Depth Ly	26	55	62
Optical Depth He 1^1S-2^1P	4	14	16
$n_{Hydrogen\ ground}$	$4.3 \cdot 10^{20}$	$1.0 \cdot 10^{21}$	$1.2 \cdot 10^{21}$
$n_{Helium\ ground}$	$1.4 \cdot 10^{19}$	$1.4 \cdot 10^{20}$	$1.5 \cdot 10^{20}$
$n_{Fully\ stripped}$	$4.0 \cdot 10^{21}$	$3.1 \cdot 10^{21}$	$3.3 \cdot 10^{21}$

* The value for the level populations vary across the sphere, therefore these represent average values.

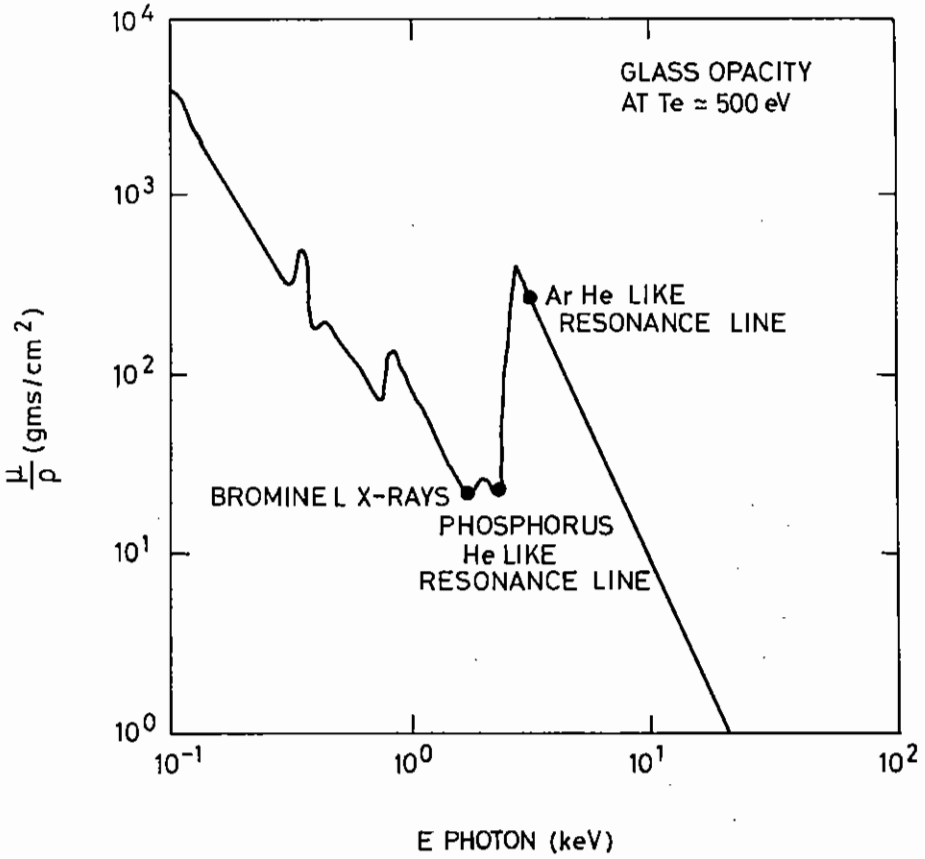

Figure 6.13 The opacity of Silicon versus energy in KeV. The placement of the Br XXXIII lines and the Argon XVIII lines are shown. Note the Br XXXIII lines are in the region below the Silicon

lower than the Silicon XIV contiuum edge. This indicates that the glass shell continuum will not affect the Bromine emission drastically. Further, these lines fall at higher energy than the resonance line of Si XIV Lyman α but below the lyman βline. Thus the lowering of the Silicon continuum edge will not affect these Bromine XXXIII lines since the shell densities will be less than the compressed core densities. Second, the ionization potential of Br XXXIII is 3.7 KeV so that for the temperatures predicted for ablative compression targets, ie between 0.5 and 1 KeV, these transitions should be observed. Moreover, the Bromine ionization potential compares favourably with the ionization potential of Ar XVII so that the Br XXXIII lines will be observable when Argon XVIII lines are observable, but these Argon lines will be obscured by the Silicon continuum (see Figure 6.13).

This method has been applied to compression experiments using the SHIVA laser system at Lawrence Livermore Laboratory.

6.3.7 Diagnostics using Argon XVII ^1S-2^1P, 2^1S, 2^3P

Using the techniques discussed by Kilkenny et al (6.16) to diagnose plasma density one particular experiment has been analysed which yields an electron density, from the compressed Argon core, of 10^{23} cm^{-3}. A novel feature of the Ar XVII 1^1S-2^1P transition is the appearance of the dipole-forbidden 1^1S-2^1S transition and the spin-forbidden 1^1S-2^1P transition which form a blend to the higher wavelength side of the resonance line (see figure 6.14). Analysis has been performed to estimate the intensity each line contributes to the blend, under the assumption that the collision rates are adequate to mix the singlet and triplet levels (this is possible due to the mixing of about 2 % in the singlet-triplet states). When this analysis is performed we find that the total line profile fits well and confirms the original diagnostic densities. This will be extremely useful in the future when time resolved spectra are performed on this transition since this one transition with its forbidden components and dielectronic satellites will provide three separate estimates of electron density and two separate estimates of

ground state number density.

6.3.8 Study of Methods used to Simulate Time-dependent Emission Spectra

A study was carried out to determine the efficacy of methods currently used to perform time dependent radiative transfer for laser compressed systems. The following conclusions were reached:

(a) The emphasis on ab initio time dependent radiative transfer calculations is not the correct way to proceed towards a better understanding of the problem. A semi-empirical approach which interacts with time resolved experiments should be developed and employed.

(b) The methods now employed to perform the time dependent radiative transfer calculations do not seem to satisfy the basic consideration of convergence in limiting cases.

(c) The use of time dependent radiation transfer to perform diagnostic and/or for energy balance equations are circumspect without more definite work on the validity of the models.

R W Lee, T A Stavrakas, D D Burgess, J D Kilkenny, J G Lunney, S Veats, A Shalom, D Matthews and J Scofield (Imp Coll)

6.4 Silicon Satellite Spectra from Laser-imploded Microballoons

The dielectronic satellite spectral lines, on the long wavelength side of the hydrogenic Si XIV Lyman-α line, have been observed in the space-resolved spectra from laser-imploded glass microballoons. In the electron density range 1×10^{22} to 2×10^{23} cm^{-3}, the intensities of the SiXIII $2s2p\ ^3P$ - $1s2s\ ^3S$ and $2p^2\ ^3P$ - $1s2p\ ^3P$ satellite lines increase with density in agreement with numerical modelling (6.18). These satellite lines are a promising density diagnostic for the imploded glass

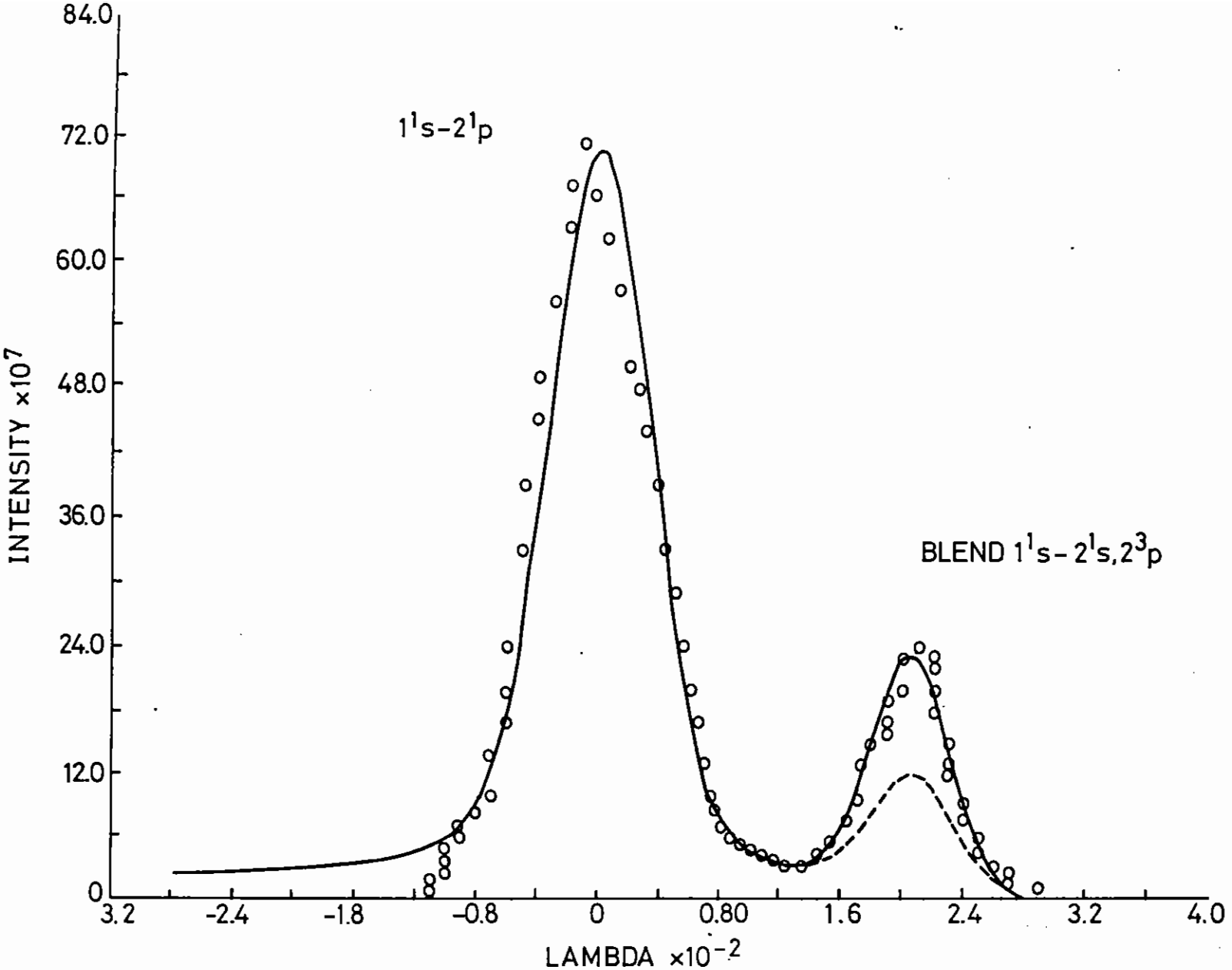

Figure 6.14 The Ar XVIII 1^1S-2^1P, and $1^1S-2^1S,2^3P$ Blend for the plasma diagnosed in Figure 3.

------ is contribution of 2^1S only.

——— is contribution of total profile.

ooooooo are experimental points

plasma. Advantages of this diagnostic technique are that the satellite lines are less susceptible to opacity effects, and the plasma parameters are obtained from the relative intensities of closely-spaced spectral lines. Time resolved x-ray spectroscopy (6.19) indicates that dielectronic satellite radiation is emitted only briefly from the hottest plasma region, whereas resonance radiation persists for a longer period of time in the cooler recombining plasma. Thus the satellite radiation is more characteristic of the hot, dense core region and is less affected by time averaging.

The SiXIV Lyman-α and satellite intensity distributions are obtained from the space resolved x-ray spectra from a series of two-beam laser implosions. The parameters for four representative laser shots are shown in Table 6.02. The diameter of the imploded silicon plasma is determined from the spatial extent of the SiXIV and SiXIII recombination continua. The electron temperature is calculated from the slopes of these recombination continua, and the electron density is determined from the Stark broadening of the SiXIV Lyman series lines, corrected for opacity (6.20). The parameter NR, the density of the hydrogenic SiXIV ground state multiplied by the optical path length, is obtained from the optically thick SiXIV Lyman-α line.

The silicon Lyman-α and satellite spectra from the ablation and implosion core plasmas of shot 328 are shown in Figure 6.15. The intensities of the $2s2p\ ^3P - 1s2s\ ^3S$ and $2p^2\ ^3P - 1s2p\ ^3P$ satellite lines, relative to the intensity of the $2p^2\ ^1D_2 - 1s2p\ ^1P_1$ satellite line, are stronger in the implosion core plasma (electron density 1.1×10^{23} cm^{-3}, 500 eV). The four core satellite spectra are shown in Figure 6.16, where the intensities of the triplet satellite lines increase with electron density. These spectra are recorded using a PET crystal and a 10 μm wide slit resulting in a 12 μm spatial resolution. The instrumental spectral line width, determined by the source size and the rocking curve of the crystal, is 4 mÅ.

The increase in intensity of the silicon triplet satellite lines with density is in agreement with numerical modelling of the satellite spectra.

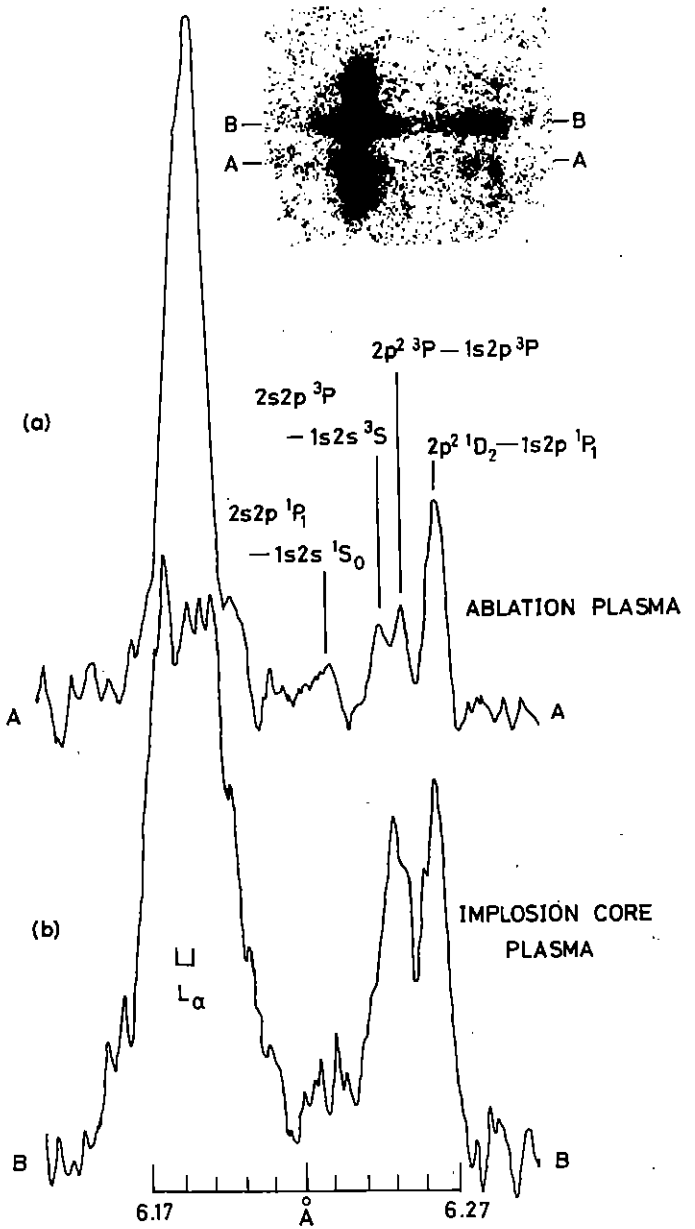

Figure 6.15 Densitometer tracings of the silicon Lyman-α and satellite lines from (a) the ablation plasma and (b) the implosion core plasma of shot 328. The densitometer tracings, as indicated on the photograph of the spectrum, are along line AA through the ablation region and BB through the core region.

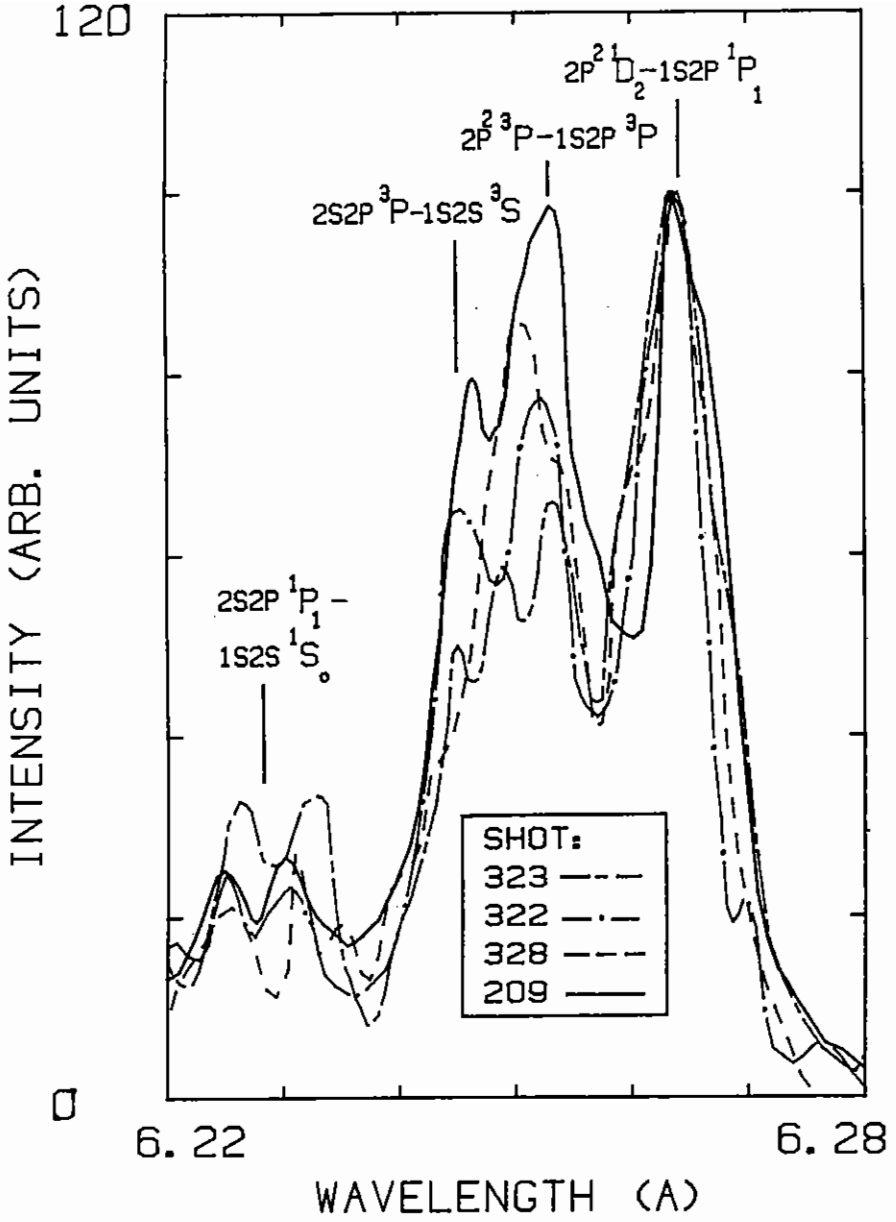

Figure 6.16 Relative intensities, determined from the Kodirex film calibration curve, of the silicon satellite lines from the implosion core plasmas of the four shots listed in Table 6.02. The intensities are normalized to the intensity of the $2p^2\ ^1D_2$ - $1s2p\ ^1P_1$ satellite line.

The steady-state rate equations for the ten 2ℓ2ℓ' levels, the three hydrogenic n = 2 levels, and the fully-stripped ionization stage are solved for the level populations relative to the hydrogenic ground state density. These levels are coupled by electron collisional processes (dielectronic recombination, collisional-radiative recombination, ionization, and excitation (6.21)) and by autoionization (6.22) and radiative decay where appropriate. The Lyman-α radiative rate is reduced by the frequency-dependent escape factor for an emitting-absorbing plasma (6.23). For NR < 10^{19} cm^{-2}, a condition that is well-satisfied in these implosions (see Table 6.02), satellite line opacity effects are negligible (6.24). From the intensity ratio of the SiXIII $^3F_1$ - $1s^2\ ^1S_o$ intercombination line to the 2s2p P -1s2s ^3S satellite line, typically equal to 4 for the core spectra, it may be shown that inner-shell excitation of the doubly-excited levels from the metastable levels of the He-like ion is negligible.

Having calculated the level populations, the spectral intensity distribution is simulated by summing the contributions, from each radiative transition, at particular wavelengths in the wavelength region that includes the Lyman-α and satellite lines. The Doppler, Stark, and 4 mÅ instrumental profiles are convolved, and the Lyman-α profile is further modified by opacity using the frequency-dependent escape factor for an emitting-absorbing plasma. The resulting calculated intensity distribution is a function of N_e, NR, and T_e. Since these plasma parameters are measured independently of the satellite lines, there are no free parameters in the numerical model.

The silicon satellite spectra, calculated using the plasma parameters listed in Table 6.02, are shown in Figure 6.17. The calculated satellite spectra are in good agreement with the experimental spectra. A more sophisticated radiation transport model could be used for the Lyman-α radiation, but since the temporal variations of the plasma parameters are unknown, the frequency-dependent escape factor approximation is adequate for the present analysis.

The calculated intensities of the SiXIII 2s2p ^3P - 1s2s ^3S and

TABLE 6.02 Parameters for the four shots

Shot number[a]	Laser power [TW]	Shell diameter [μm]	Shell thickness [μm]	Gas fill [bar]	SILICON IMPLOSION PLASMA D [μm]	T_e [eV]	N_e [cm^{-3}]	NR [cm^{-2}]
323	0.17	50	0.59	10 DT	34	580	2×10^{22}	1.8×10^{18}
322	0.15	50	0.60	10 DT	25	500	6×10^{22}	1.7×10^{18}
328	0.34	67	0.71	0.4 Ar	22	400	1.1×10^{23}	8.8×10^{17}
209	0.22	66	0.75	0.3 Ar	22	430	1.4×10^{23}	1.6×10^{18}

[a]The shot numbers, appearing in the table and in Fig 6.16, refer to the Rutherford Laboratory system of designating laser shots.

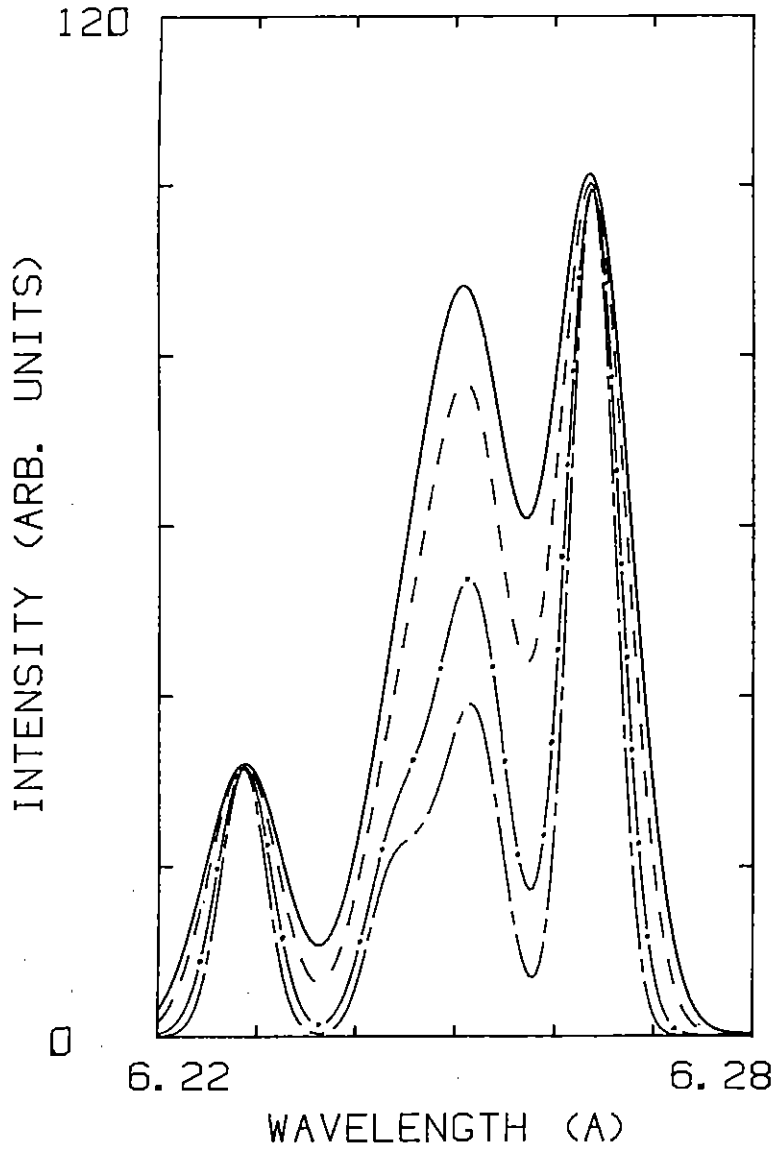

Figure 6.17 Calculated relative satellite intensities for the four shots listed in Table I. The four curves are identified by the legend in Figure 6.16.

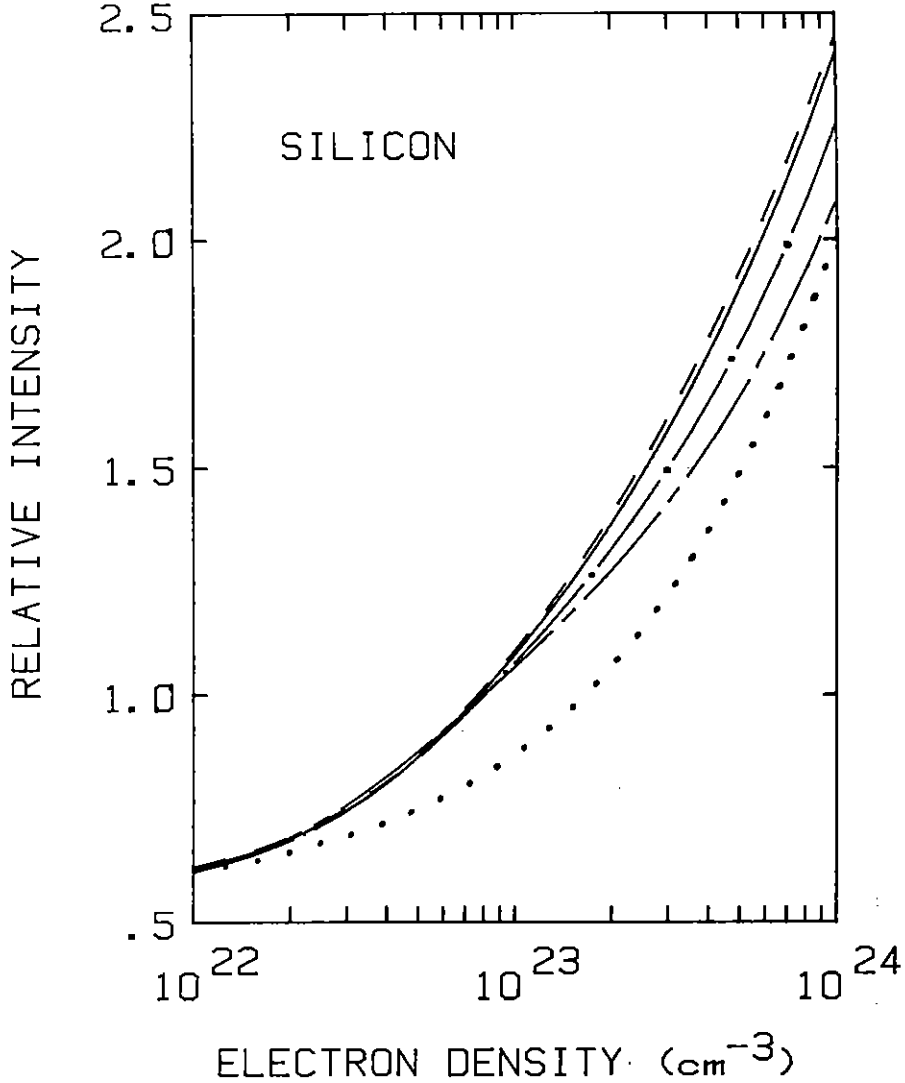

Figure 6.18 The calculated intensities of the SiXIII $2s2p\ ^3P - 1s2s\ ^3S$ and $2p^2\ ^3P - 1s2p\ ^3P$ satellite lines, with wavelengths 6.2432 Å to 6.2545 Å, relative to the intensity of the $2p^2\ ^1D_2 - 1s2p\ ^1P_1$ satellite line at 6.2637 Å. The dotted curve is for an electron temperature of 400 eV and an optically thin Lyman-α line. The upper four curves (see legend in Figure 6.16) are calculated using the parameters of the glass plasma listed in Table 6.02.

$2p^2\ ^3P$ - $1s2p\ ^3P$ satellite lines, relative to the intensity of the $2p^2\ ^1D_2$ - $1s2p\ ^1F_1$ satellite line, are shown in Figure 6.18 as functions of electron density. For electron density less than 10^{21} cm^{-3}, the $2\ell2\ell'$ levels are populated by dielectronic recombination, and the intensity ratio is constant and equal to 0.5. As the electron density increases, the $2s2p\ ^3P$ and $2p^2\ ^3P$ levels are populated by electron collisional excitation from the singlet doublet excited levels, and the intensity ratio increases to the value 2.7 in the limit of statistical occupation of the $2\ell2\ell'$ levels (dotted curve in Figure 6.18). The increase in the hydrogenic n = 2 population due to reabsorption of the Lyman-α radiation results in enhancement of the $2s2p\ ^3P$ and $2p^2\ ^3P$ populations by collisional recombination (upper four curves in Figure 6.18).

Extension of this diagnostic technique to higher electron densities should be possible by using the satellite lines of high Z impurities in the glass implosion of argon filled microballoons; and these are being analysed. The satellite spectra on the long wavelength side of the helium-like $1s2p\ ^1P_1$ - $1s^2\ ^1S_0$ line are also density dependent (6.26); and analysis of these spectra, for silicon and argon, is being carried out.

The work at the Naval Research Laboratory was partially supported by the US Department of Energy.

J G Lunney (TCD) and J F Seely (NRL)

REFERENCES CHAPTER 6

6.01 G J Pert, Phil Trans, accepted for publication

6.02 D Jacoby, G J Pert, L D Shorrock and G J Tallents, J Phys E, to be published

6.03 G J Tallents and L D Shorrock, J Phys E, 14 (1981)

6.04 J D Garcia and J E Mack, JOSA, 55, 654 (1965)

6.05 Rutherford Laboratory Annual Report to the Laser Facility Committee, RL-79-036 (1979)

6.06 R J Speer, Space Science Instrumentation, 2, 463 (1976)

6.07 R Hutcheon, Private Communication (1980)

6.08 M H Key, C L S Lewis and M J Lamb, Opt Comm, 28, 331 (1979)

6.09 Rutherford Laboratory Annual Report to the Laser Facility Committee, RL-80-026, section 1.6 (1980)

6.10 H R Grien, 'Spectral Line Broadening in Plasmas', Academic Press, New York (1974)

6.11 R L Green and J Cooper, JQSRT, 15, 1037 (1975)

6.12 U Fano, Phys Rev, 131, 259 (1963)

6.13 S Skupsky, Phys Rev A, 21, 1316 (1980)

6.14 E W Smith, J Cooper and C R Vidal, Ap J Suppl, 25, 37 (1973)

6.15 B Yaakobi et al, Phys REv A, 19, 1247 (1979)

6.16 J D Kilkenny, R W Lee, M H Key and J G Lunney, Phys Rev A, 22, 1275 (1980)

6.17 J M Auerbach et al, Phys Rev Lett, 44, 1672 (1980)

6.18 J G Lunney and J F Seely, Phys Rev Lett, 46, 342 (1981)

6.19 M H Key, C L S Lewis, J G Lunney, A Moore, J M Ward and R K Thareja, Phys Rev Lett, 44, 1669 (1980)

6.20 J D Kilkenny, R W Lee, M H Key, J G Lunney, Phys Rev A, 22 (1980)

6.21 D H Sampson, Private Communication (1980)

6.22 L A Vainshtein and U I Safronova, Atomic Data and Nuclear Data Tables, 21, 49 (1978)

6.23 B Yaakobi et al, Phys Rev A, 19, 1247 (1979)

6.24 D Duston and J Davis, Phys Rev A, 21, 932 (1980)

6.25 J F Seely, R H Dixon and R C Elton (unpublished)

6.26 V L Jacobs and M Blaha, Phys Rev A, 21, 525 (1980)

CHAPTER 7 THEORY AND COMPUTATION

INDEX

CHAPTER EDITOR: C J Webb

CHAPTER 7 Theory and Computation

7.1 Introduction

Returning to be the Convenor for the Theory and Computation group, I find that the work carried out over the past year has been increasingly useful to the experimental programme and also in some instances giving valuable explanation of new phenomena and guidance to experimenters for future experiments.

In compression studies a greater understanding of wavelength scaling and of the effects of non-uniform irradiation of the target have been found, whilst parametric processes in laser plasma interactions continue to be of much interest. Here we await the completion of the 2½ dimension particle-in-cell code HERMES in which a large investment of manpower has been made. Next year's report should contain some first results from this.

Perhaps it is in transport processes that the Theory Group has made its most distinctive contribution to the subject. A better appreciation of classical non-linear heat flow is emerging, but as yet can only account for a flux limiter of about 10 % of the free-streaming value. A new type of instability associated with heat flow has been proposed. This might explain the occurrence of fine scale plasma jets and filamentary structures found experimentally at the Rutherford Laboratory (see section 3.2). These instabilities could be more important as shorter wavelength lasers are employed, and their implication will be the subject of intensive study during the coming year.

M G Haines (Imp Coll)

7.2.1 Code Development at Hull

During the past year the code POLLUX, described below, has been developed by removing the self-generated magnetic fields from MAGT, and is now fully implemented on the ATLAS system. Minor improvement in the codes LAG2 and

MAGT have been made, and a regular update maintained in the Rutherford versions. The new version of LAG2 incorporating non-equilibrium ionisation physics is nearing completion, and a preliminary version has been installed on the ATLAS, for testing. A new code, ITEST, involving a novel hydrodynamic model with full ionisation physics has been developed, and is described below.

Modifications to LAG2

Further development of the extremum limited diffusion routine for two dimensional Lagrangian codes (7.01, 7.02) has resulted in the identification of a simple monotone condition which can be applied to the diffusion matrix. Numerical tests have shown that the modified algorithm using this test to avoid non-monotone matrix inversion when the time-step is small (by an explicit extremum limited flux of the anti-diffusion term) significantly improves the modelling on strongly distorted meshes, and avoids the spurious generation of negative energies.

Routines to model the atomic physics by a time dependent collisional-radiative mode have been incorporated into the two dimensional Lagrangian code LAG2. The advantage of a Lagrangian code to model ionisation processes due to the absence of convection between cells will be readily appreciated. The new code, LAG2I, has recently been implemented at the Rutherford Laboratory in a preliminary version, after an extensive series of trials performed at Hull and Manchester, including comparison with the existing code ITEST, used in a one dimensional Lagrangian mode. It is expected that the fully developed code will be released in the near future.

Modifications to MAGT

Further study has been carried out of the "unsatisfactory" behaviour of the cross product thermo-electric field term discussed in the previous year's report (7.01). Using the approach described there, several alternative versions of the routine were compared in which the value of the magnetic field B in the term $\beta_\wedge$ was differenced in various ways:

namely, upstream differencing, explicitly/implicitly, or centred differenced. The most satisfactory involved the least computational work, and a real solution was found to be that in which βn had the upstream/downstream explicit form:

$$\beta^{n+\frac{1}{2}}_{\wedge\, I+\frac{1}{2},J} = \beta^{1}_{\wedge\, I+\frac{1}{2},J} \begin{cases} B^{n}_{I+1,J} & \text{if } (\partial E/\partial Z)_{I+\frac{1}{2},J} > 0 \\ B^{n}_{I,J} & \text{otherwise} \end{cases}$$

subject to the constraint

$$\frac{\alpha c}{e}\left[\beta_{\wedge}\frac{\partial E}{\partial Z}\right]_{I+\frac{1}{2},J}\frac{Dt}{\Delta z} \leq 0.5$$

where Dt is the time-step, and Δz the mesh spacing.

The Code POLLUX

A two dimensional Eulerian code, POLLUX, has been constructed. This is based on MAGT but omits magnetic field generation and diffusion routines whilst retaining these treating the hydro, equation of state, thermal conduction and equilibration and laser energy deposition. This code has been implemented and used extensively at the Rutherford and more recently on the CRAY-1 at Daresbury by R G Evans in connection with studies of ablating foils.

In order to model more effectively the dynamics of laser irradiated thin foil targets in an Eulerian geometry, the existing algorithm in POLLUX dealing with mesh expansion during the fluid advection stage has been modified. Rezoning is performed in a quasi-Lagrangian manner independently along the two coordinated axes, R and Z, such that the mesh remains orthogonal. New values of the grid spacings, DZ_i and DR_j, along with the corresponding grid velocities, DU_i and DV_j, are computed at the end of each advection stage. These values are based on the change of mass in each column, i, or row, j, of cells during this advection in a manner similar to that proposed by Craxton and McCory (7.03). The new values are then used to move the mesh immediately prior to advection during the next iteration. This modification is being tested

at present and is hoped to be soon made available at Rutherford.

The Hybrid Model and the code ITEST

The existence of an exact solution of the equations of hydrodynamics involving a similarity flow into two dimensions, with a quasi one dimensional solution has been demonstrated and used to construct a three dimensional code to study the expansion of cylindrical targets under non-uniform laser heating. There exists a solution in which the density distribtuion in (xy) plane is Gaussian, with a uniform temperature, with variations in the z direction only. Conventional one dimensional fluid cell techniques may be used to integrate the flow in z direction. These may be either Eulerian or Lagrangian. For our purposes the Lagrangian formulation is particularly convenient, and a modified form of the von Neumann-Richtmyer algorithm works well.

An analysis of the stability conditions of the resultant finite difference operations shows that the solution is stable if the modified Courant-Friedrichs-Levy condition is upheld, namely:

$$C\Delta t \leq 1/\sqrt{\{1/\Delta z^2 + 1/2X^2 + 1/2Y^2\}}$$

where X and Y are the 1/e similarity radii, Δz the cell width, c the sound speed, and Δt the time-step.

As in the von Neumann-Richtmyer scheme it is necessary to introduce an artificial viscosity to treat shocks propagating in z properly. A suitable form in conformity with similarity conditions, is

$$q = \begin{cases} a^2\rho\,\dfrac{\partial(\Delta z)^2}{\partial t} & \text{if } \dfrac{\partial(\Delta z)}{\partial t} > 0 \\ 0 & \text{otherwise} \end{cases}$$

where a^2 is a constant ($\simeq 2.0$), ρ the density and Δz the cell width. This form has been found to work well in practice.

Thermal conduction in the direction z is readily included in the model.

In an extensive series of tests the model has been shown to work reliably provided the necessary physical conditions for its validity are upheld. Comparison with known analytic solutions of expanding flow has yielded results of accuracy comparable with, and in some cases better than, the equivalent similarity expansions (7.04).

The model has been used to construct the code ITEST in which the ionisation/recombination routines (7.05, 7.06) used in the earlier code GAIN are used to model the expansion of carbon fibres target in the XUV laser experiments.

We mmay remark on the value of this procedure using the similarity solutions to construct what is essentially a three dimensional Lagrangian code: an approach of wide application than considered here.

A J Bennett and G J Pert (Univ of Hull)

7.2.2 Hydrodynamic Simulation Codes

7.2.2(a) 1-D Simulations of Ablatively Accelerated Targets

A large number of MEDUSA simulations have been performed to study the changes in the ablation process with laser irradiance and wavelength. The absorption of laser energy is by classical inverse bremstrahlung and 20 % of the laser power actually penetrating to critical density is considered to be absorbed by collective effects. One half of this anomalously absorbed energy is used to heat the thermal electrons at critical density and one half is used to produce hot electrons with a temperature T_H calculated from $\phi\lambda^2$ at the critical density surface.

The computations are performed on a two dimensional 'grid' of irradiance and laser wavelength , the values of ϕ used are 10^{12}, 10^{13}, 10^{14}, 10^{15}, 10^{16} Wcm^{-2} and wavelengths 0.26 μm, 1.06 μm and 10.6 μm. The laser wavelengths are chosen to represent Nd doped glass lasers, and also the shortest and longest wavelengths of current interest.

The pellet for these runs is a hollow pellet of medium Z material, specifically Aluminium of density 2.5 g cm^{-3}, and thickness 20 μm, chosen large enough to stop most of the fast electrons. The laser pulse rises linearly from zero power at t = 0, to full power at $t = 1.0 \times 10^{-10}$ s, and thereafter remains constant. The simulation is nominally for a period of 3 ns but at the highest irradiances the target implodes in substantially less than this time.

For the standard runs the initial target radius is set to 100 μm and the free streaming limit on the heat flux is set to 0.03 times its classical value. The justification for this value of flux limit is simply that it has become the accepted value derived from the analysis of experimental data in many different laboratories (7.07, 7.08, 7.09). The choice of target radius is rather more arbitrary. There are compelling reasons for the choice of spherical rather than plane geometry since in plane geometry the amount of underdense plasma continually increases in time. This moves the absorption region to lower densities farther and farther from the ablation region, and the ablation pressure steadily decreases with time.

On the other hand in spherical geometry the divergence of the ablation flow allows a quasi steady state to be set up in which the separation of critical density and ablation surface is approximately constant. The choice of radius is rather arbitrary but 100 μm corresponds closely to present experimental conditions and for comparison we have also performed some simulations for a target radius of 1 mm.

In order to present the results of these standard simulations in an easily assimilable form we have chosen three representative parameters; the shock velocity through the solid, the peak pressure generated in the shell and the temperature at critical density. The last two quantities are measured after a simulation time of 500 ps but this is not critical.

In Figures 7.01, 7.02 and 7.03 we show these quantities as a function of incident laser irradiance with laser wavelength as a parameter. As expected the pressure and shock velocity data are very similar since for a perfect gas $v_s^2 = (\gamma-1)p/\rho$. The measurement of shock velocity is

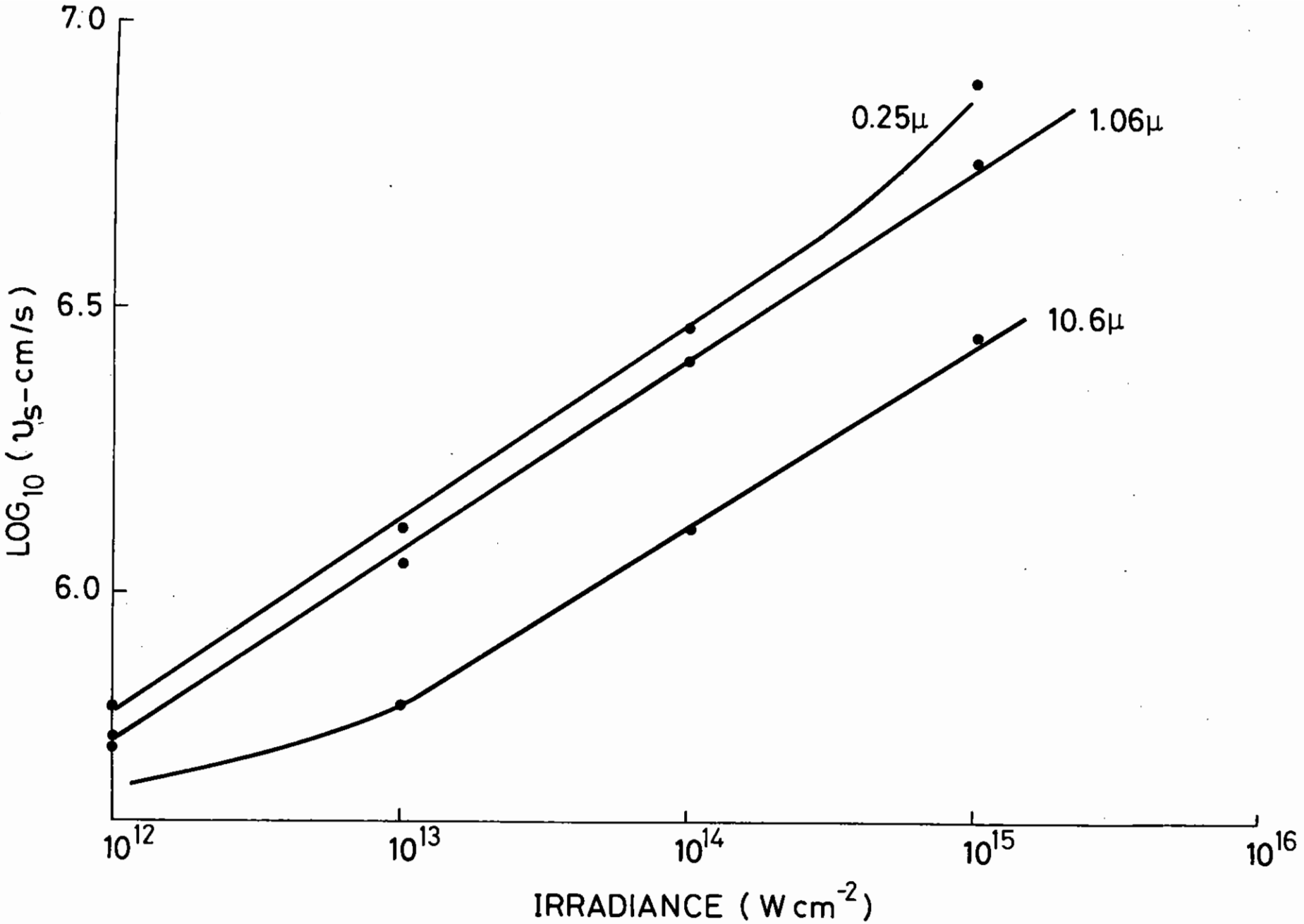

Figure 7.01 MEDUSA simulations of shock wave velocity as a function of laser irradiance and wavelength.

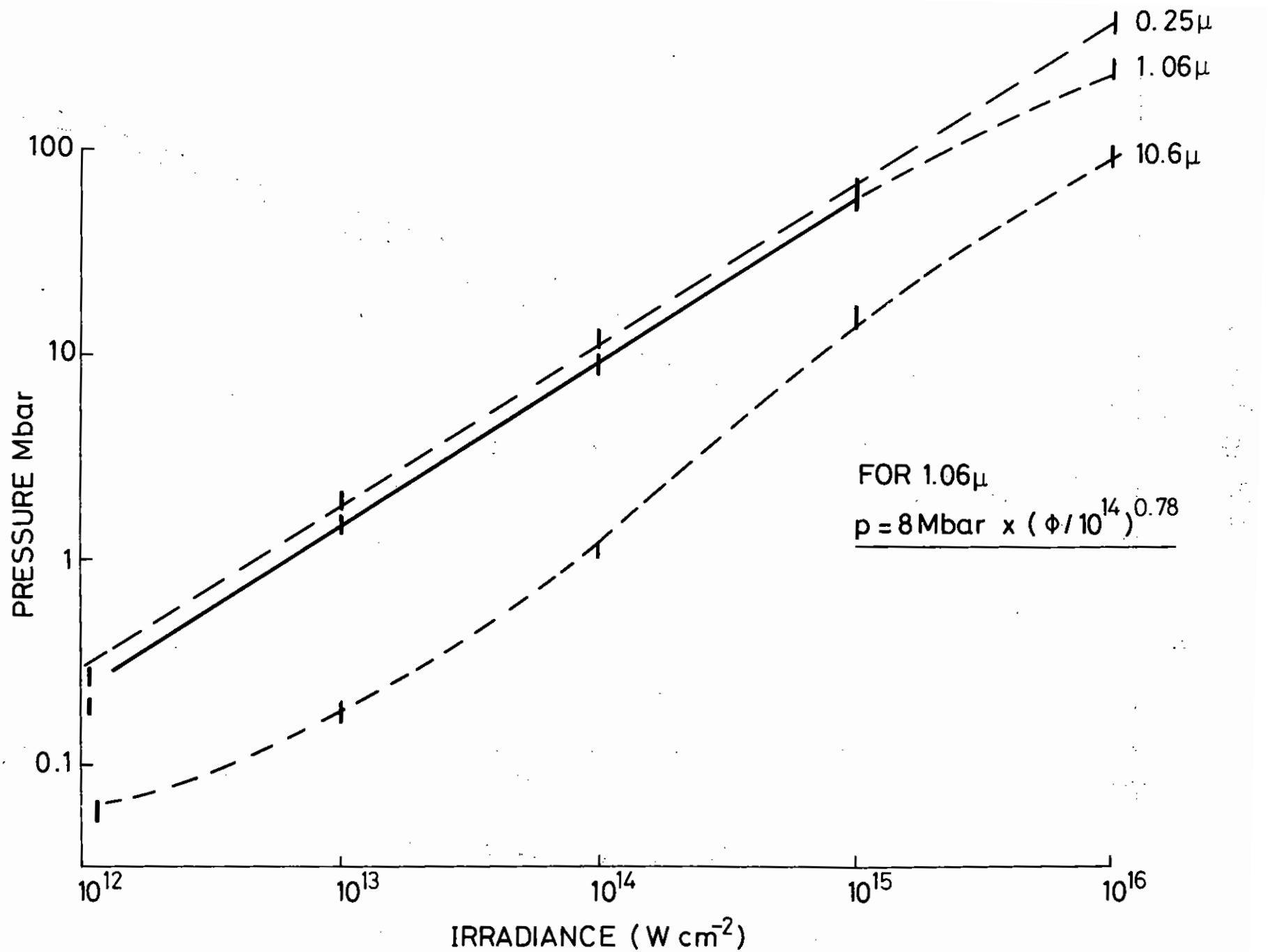

Figure 7.02 MEDUSA simulations of ablation pressure.

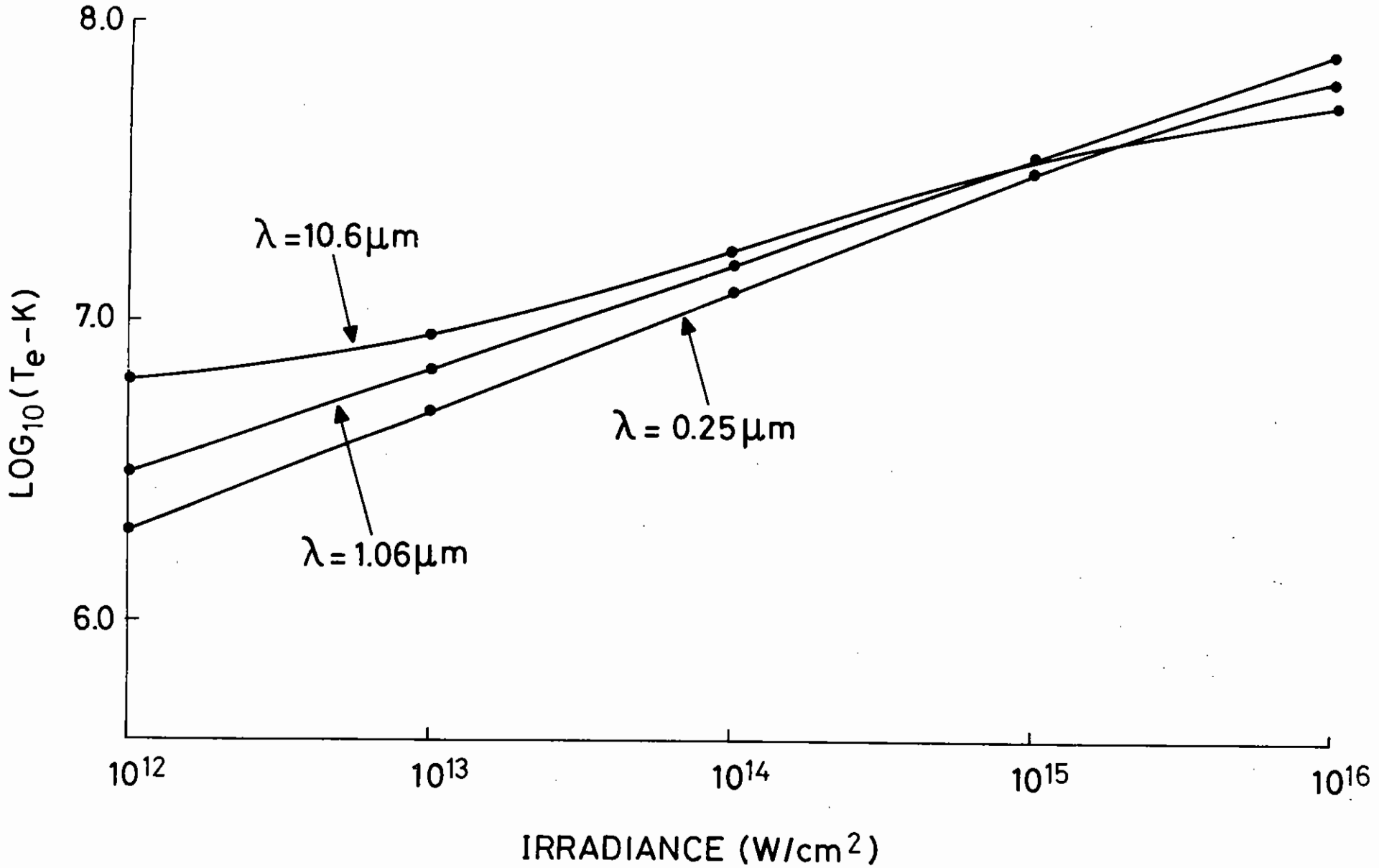

Figure 7.03 MEDUSA simulations of electron temperature in critical density region.

generally more precise than the measurement of pressure but at the highest irradiances the determination of shock velocity is confused by the preheating effect of the fast electrons.

Pressures and shock velocities are slightly higher for $\lambda = 0.25\mu$ than for $\lambda = 1.06\mu$ but $\lambda = 10.6\mu$ is definitely inferior in this respect. Conversely the ablation temperature is higher for the longer wavelength lasers, essentially because of the reduced heat capacity of the critical density plasma.

The simulations at $\lambda = 1.06$ μm and $\lambda = 0.25$ μm all have very large absorption fractions and typically in excess of 75 %, due to the neglect of all collective scattering phenomena. This is considerably larger than observed experimentally (7.07, 7.10, 7.11) and should be borne in mind in interpreting these results. A comparison of ablation pressures in terms of absorbed irradiance is made later in this paper.

Changing Target Radius

For $\lambda = 1.06$ μm we have repeated the above calculations for target radii of 1 mm and for plane geometry. In plane geometry there is the problem mentioned above that there is no steady state, but in analogy with the spherical target simulations we have taken the simulation results at $t = 500$ ps.

In Figure 7.04 we show the ablation pressure versus irradiance for $r = 100$ μm, $r = 1$ mm and $r = \infty$. The $r = 1$ mm calculations show a slightly higher pressure than at $r = 100$ μm. This is probably due to the reduced nozzle effect of the spherically diverging flow causing the sonic point to move to slightly higher densities. In plane geometry the pressures are higher at low irradiances for this same reason, but are reduced at high irradiances where the separation of critical density and the ablation surface becomes extreme.

Changing the Flux Limit

The general effect of reducing the free streaming limit on the electron heat flux is to reduce the heat conduction into the higher density plasma and hence to reduce the ablation pressure. Also the laser energy is more confined to the low density plasma and consequently the temperature there is higher. These effects tend to be more pronounced at higher irradiances where heat fluxes are larger.

In order to illustrate these effects we have repeated a subset of the standard runs ($\lambda = 1.06$ μm; $\lambda = 10.6$ μm; $\phi = 10^{13}$ W cm^{-2}; $\phi = 10^{14}$ W cm^{-2}; $\phi = 10^{15}$ W cm^{-2}) with the flux limiter first set to $f = 1.0$, ie the classical free streaming limit, and then to $f = 0.001$, ie a very severely limited heat flux. The effects on ablation pressure are not large and in order to show them more clearly we plot in Figure 7.05 the shock velocities, which are determined from the simulations with greater precision than is the ablation pressure. At an irradiance of 10^{13} W cm^{-2} the effect of changing the flux limiter is very small but increases at higher irradiances. In Figure 7.06 we show the corresponding variations in coronal temperature.

The effects of the flux limit are most pronounced at high irradiances when the transport of energy by superthermal electrons also becomes important and to some extent these simulations will be influenced by the exact treatment of the superthermal electrons. The integrated description of electron energy transport is an important area in which much work remains to be done.

Non Spherical Effects

It is not possible in a 1-D simulation such as MEDUSA to include explicitly non-spherical effects which may destroy the symmetry of the implosion. Lack of spherical symmetry may be induced by imperfections in the target pellet or in the illumination by the laser beams. Non-uniform illumination by the laser beams will produce a non-uniform drive pressure but this asymmetry may be reduced by lateral heat flow within the target

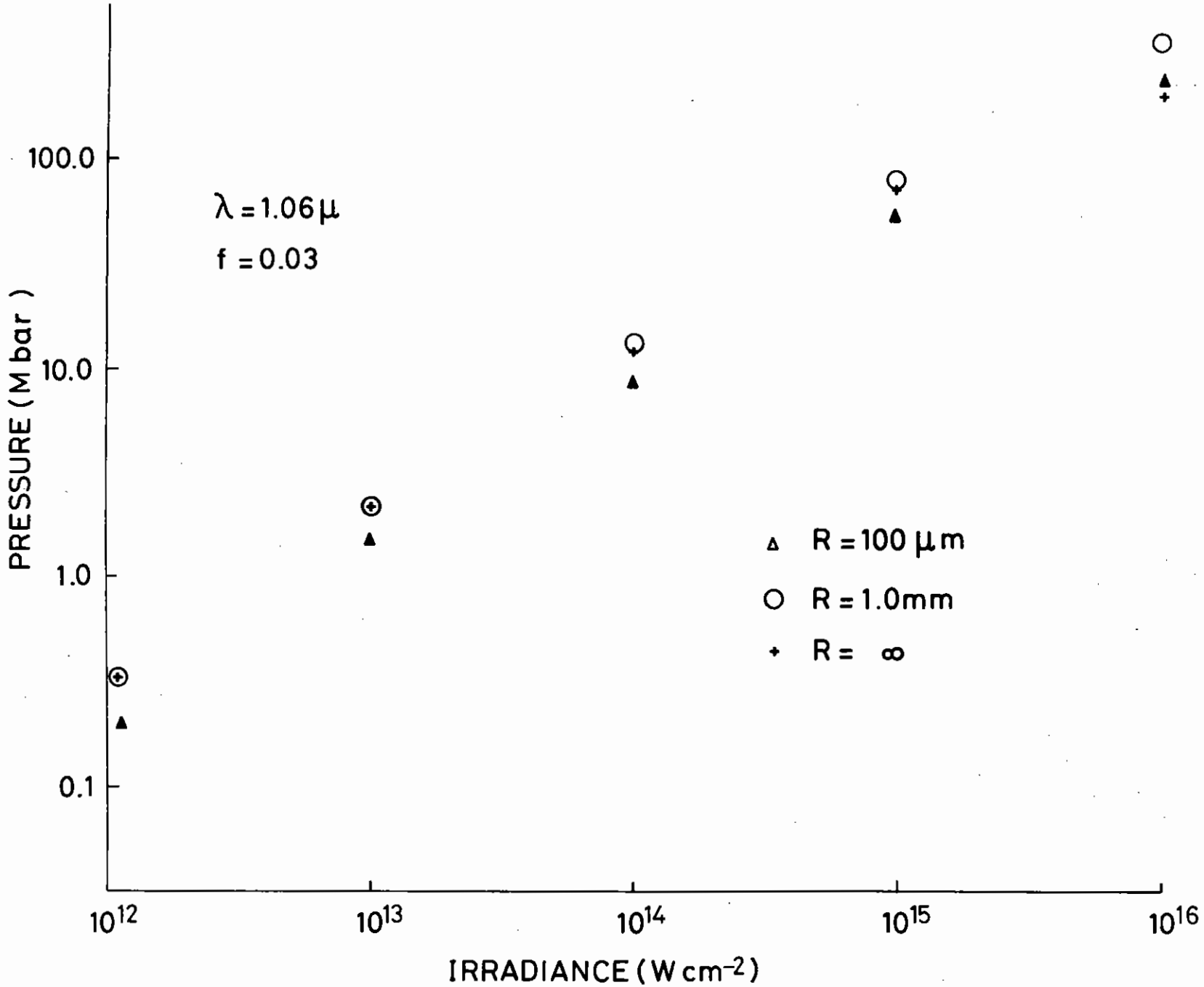

Figure 7.04 Dependence of ablation pressure on target geometry for λ = 1.06 μm, flux limit f = 0.03.

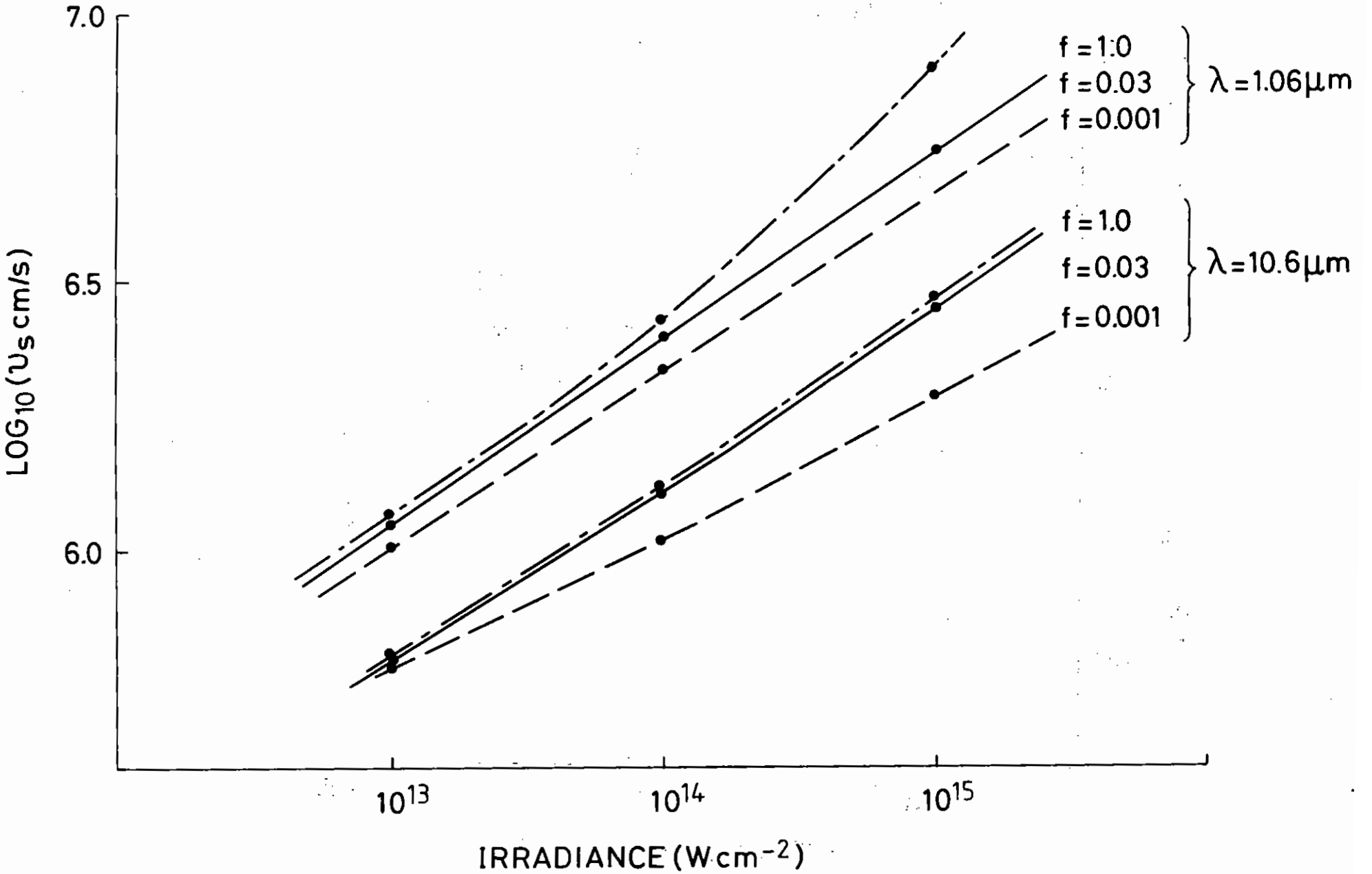

Figure 7.05. Variation of shock velocity with heat flux limit "f".

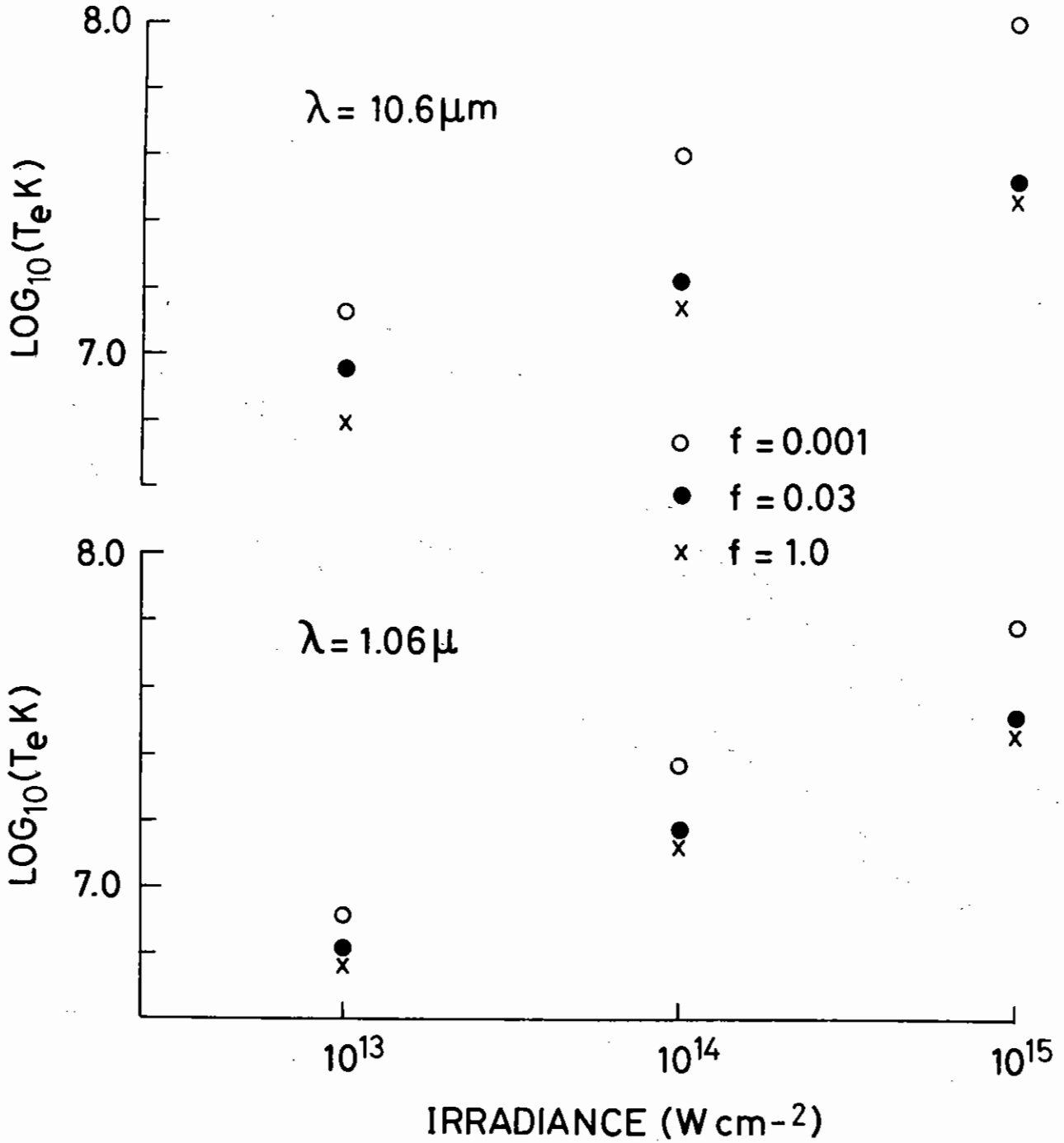

Figure 7.06 Variation of electron temperature in the critical density region with flux limit "f".

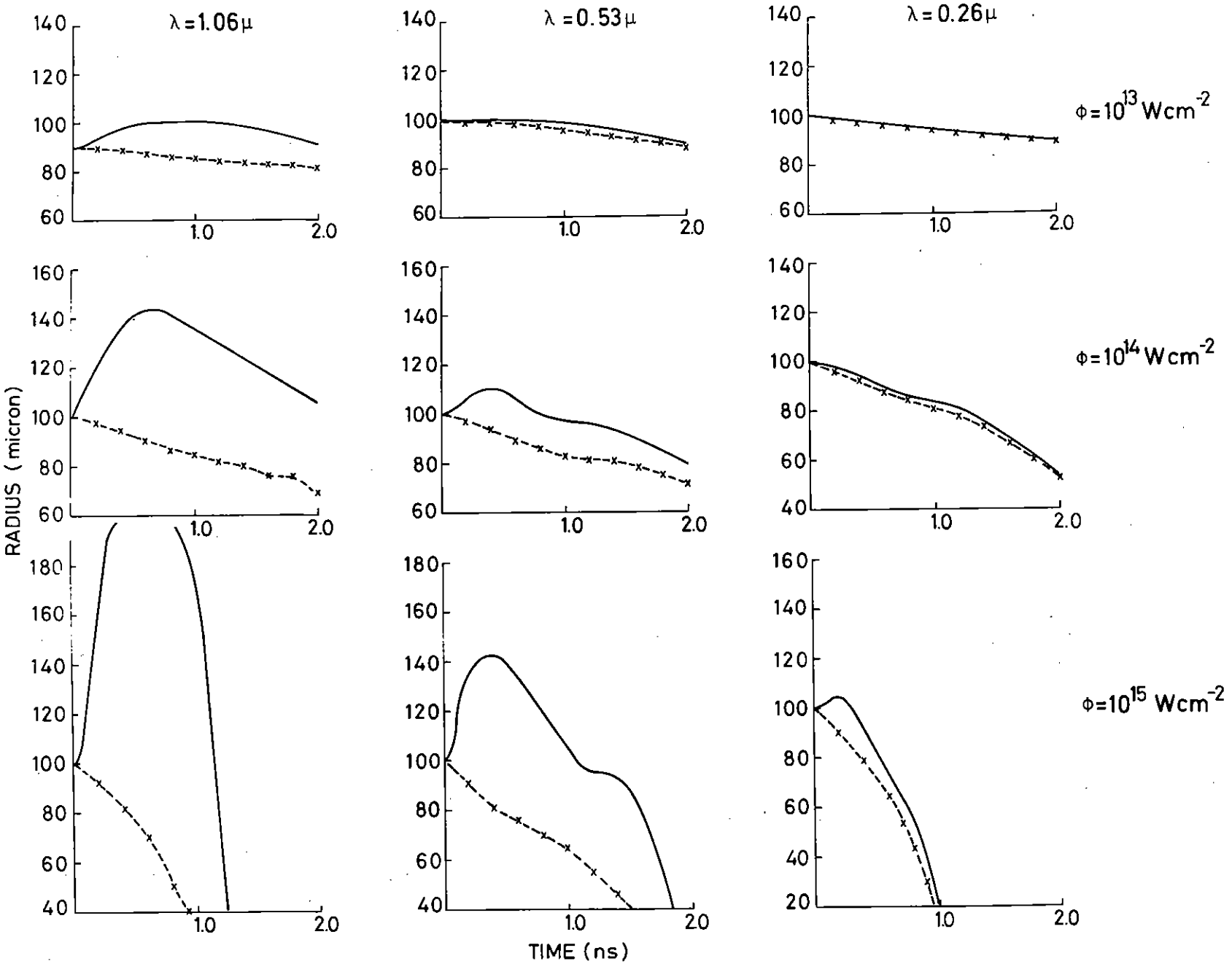

Figure 7.07 Relative motion of critical density and ablation surfaces as a function of laser wavelength and irradiance.

(7.12, 7.13). The relevant parameter is the separation between the critical density surface (where the light is absorbed) and the ablation surface, where the acceleration may be considered to be occuring. Very crudely it may be estimated that non-uniform illumination on a scale smaller than the separation of these two surfaces may largely be smoothed out by thermal conduction.

Since this effect may prove to be important for real laser systems we have plotted out the trajectories of critical density and ablation surfaces (defined as $v = 0$) for $\lambda = 1.06$ μm, 0.53 μm and 0.26 μm, and irradiances of $\phi = 10^{13}$ W cm^{-2}, 10^{14} W cm^{-2} and 10^{15} W cm^{-2} in Figure 7.07. The lowest and highest irradiances of the previous calculations have been ignored as being not of great practical interest. The case $\lambda = 10.6$ μm has been ignored since critical density is always well separated from the ablation surface, and we have included calculations at $\lambda = 0.53$ μm to give further information in the wavelength range of current interest.

The qualitative information contained in Figure 7.07 is clear, the separation of critical density and ablation surfaces increases with wavelength and with increasing irradiance. On a quantitative level it is very difficult to be precise since the required separation will depend on the spatial quality of individual laser beams. However we may guess that a separation of 10 μm would be the minimum for any significant thermal conduction smoothing, and hence we would deduce that $\lambda = 0.26$ μm is an uncomfortably short wavelength, at irradiances $\phi \lesssim 10^{15}$ W cm^{-2}.

The maximum usable irradiance is dependent on details of target design but crudely we may say $\phi\lambda^2 < 10^{14}$ W cm^{-2} μ^2 to avoid excessive production of hot electrons (7.14), and $\phi\lambda^3 < 10^{13}$ W cm^{-2} μ^3 to avoid excessive Brillouin scattering on large targets (7.15). The case of $\lambda = 0.53$ μm, $\phi = 10^{14}$ W cm^{-2} fulfills these requirements while also providing adequate thermal conduction smoothing.

Comparison with Analytic Models

Analytic models of laser driven ablation including spherical flow and

thermal conduction have been presented by Gitomer, Morse and Newberger (7.16), and by Max, McKee and Mead (7.17), this latter paper also includes flux limited thermal conduction. These analytic models are steady state (assuming that mass is continually created at $r = 0$), do not include hot electron effects, and assume that the absorption of laser energy occurs entirely at critical density. Despite these limitations of the analytic models it is valuable to compare them with the numerical simulations, and in particular we use the results of Max, McKee and Mead which are immediately comparable with the present numerical simulations.

Since the analytic calculations refer to absorbed irradiance we make the corresponding correction to the computed data and show the comparison of ablation pressures in Figure 7.08.

It is apparent that agreement is quite good at $\lambda = 1.06$ μm but poor at the longer and shorter wavelengths. In the case of $\lambda = 10.6$ μm the discrepancy between the simulations and the analytic model is clearly due to the neglect of superthermal electrons in the latter. Because they deposit their energy at high densities, the superthermal electrons generated at $\lambda = 10.6$ μm are particularly effective in generating ablation pressure, though they also produce unwanted preheating effects. In Figure 7.08 we see the 10.6 μm data rising very steeply at the lower irradiances as the range of the fast electrons increases. This increase of fast electron generated pressure at higher irradiances is also responsible for the $\lambda = 1.06$ μm simulations rising above the analytic predictions for $\phi > 10^{15}$ W cm^{-2}.

At $\lambda = 0.25$ μm the inverse bremsstrahlung absorption in the simulations is so large that an appreciable absorption takes place at densities much lower than critical whereas the analytic model assumes that all the absorption takes place at critical density. For this reason the simulation data at $\lambda = 0.25$ μm lies substantially below that predicted by the analytic theory. This discrepancy disappears if very small targets are used to reduce the amount of absorption below critical density. This is also the reason why the $\lambda = 1.06$ μm data falls below the analytic model at the lowest irradiance, $\phi \simeq 10^{12}$ W cm^{-2}, when inverse bremsstrahlung

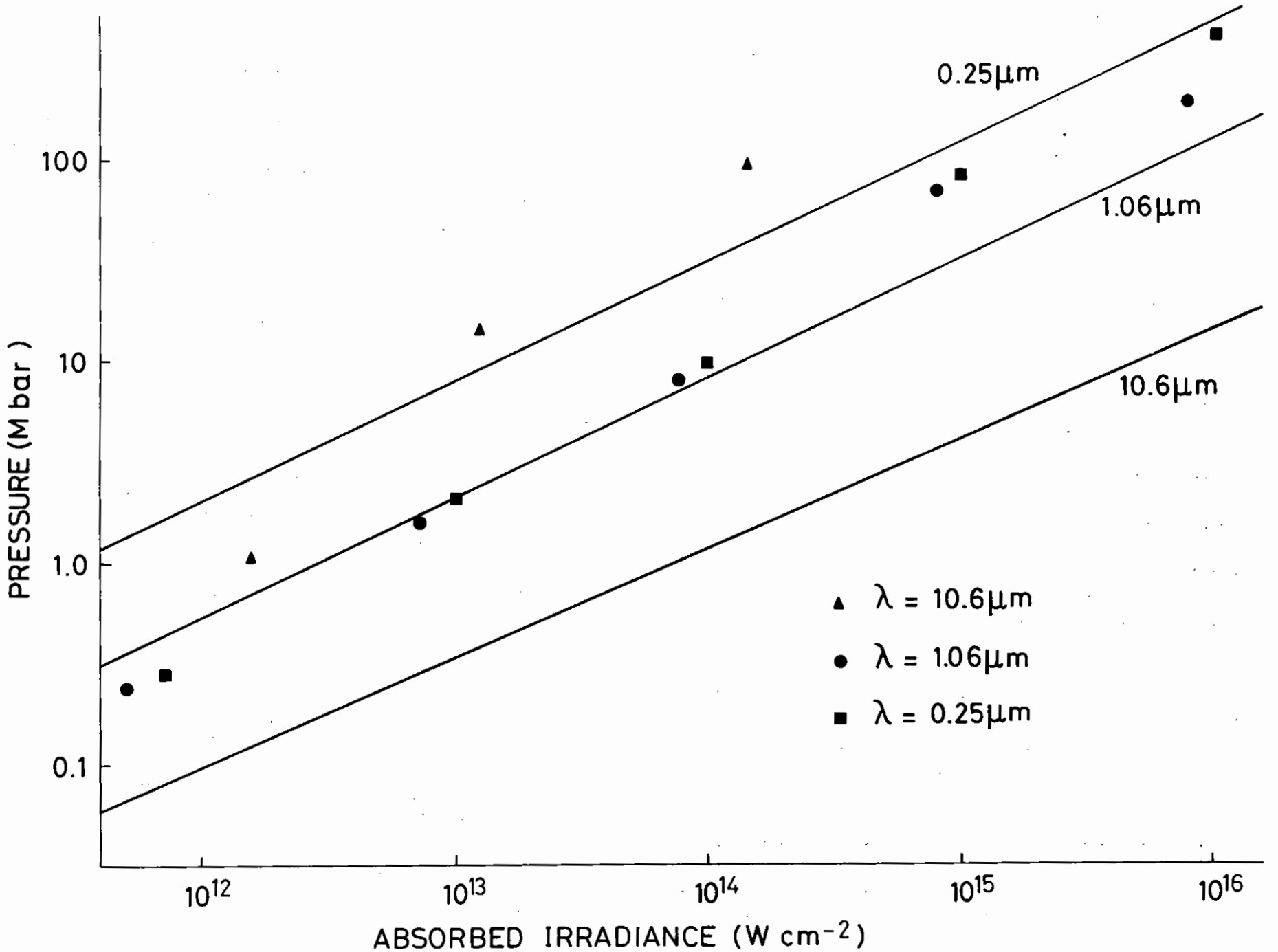

Figure 7.08 Comparison of the simulations (points) with the theory of Max, McKee and Mead (7.17) (full lines).

absorption increases with the reduced electron temperatures.

Over the rather limited range of irradiance and wavelength for which the model assumtions are valid the agreement with the numerical calculations is very good.

Conclusion

We have performed numerical simulations of laser driven ablation over a wide range of parameters. Short laser wavelengths provide higher ablation pressures at the expense of less smoothing by thermal conduction of non-uniformities in the laser illumination of the target. An optimum laser wavelength may exist, in the region of 0.5 μm to 0.3 μm, and a corresponding irradiance of $1 - 3 \times 10^{16}$ W cm^{-2}. Ablation pressures up to 30 bar may be produced with negligible fast electron preheat and stimulated Brillouin scattering.

R G Evans and A R Bell (RAL)

7.2.2(b) 2-D Simulations of Non Uniformly Irradiated Foils

A study is in progress of the effects of non-uniform target irradiation by lasers and ion beams. The 2-D fluid code developed at Hull and now named POLLUX has been implemented and partly vectorised on the CRAY-1 computer. The code POLLUX is further described in section 7.2.1.

The development of the density contours with time is shown in Figure 7.09 for a typical simulation. The laser is incident from the right of the figure and is modulated with two cycles of a sine wave of the form $P(r) = P_o(1 + 0.2 \cos k_\perp r)$, this being referred to as ± 20 % modulation. At time t = 0.0 the initial foil is shown, having a thickness of 12.5 μm and a density of 0.93 g cm^{-2}. At time t = 0.3 ns the appearance of the $\rho = 1$ contour shows the passage of the shock through the foil and the modulation of the left hand boundary of the contour shows the variation of shock velocity. At 0.6 ns the non-uniform acceleration is causing the foil to distort and at t = 0.8 ns there has been a significant

lateral flow of material resulting in islands of high density material being left behind as the foil is accelerated.

A summary of the results so far obtained is shown in Figure 7.10 where we plot the momentum modulation of the accelerated foil as a function of beam modulation, laser wavelength, and wavelength of the transverse beam modulation, all at an irradiance of $\phi = 5 \times 10^{13}$ W cm^{-2}.

As expected we see that shorter laser wavelengths produce larger modulations in the foil due to the reduced thermal conduction smoothing. The effect of changing the wavelength of the transverse modulation however is rather more interesting. With the 1.06 μm laser, changing from $\lambda_\perp = 50$ μm to $\lambda_\perp = 12.5$ μm results in a reduction of critical density and ablation surfaces being about 50 μm. On the other hand with the 0.26 μm laser the separation of critical density and ablation surfaces is very small, less than 5 μm so that neither $\lambda_\perp = 50$ μm or $\lambda_\perp = 12.5$ μm gives rise to appreciable thermal conduction smoothing. In this case the shorter modulation wavelength gives rise to larger modulations of the target since the transverse pressure gradients are larger. This is similar to the dependence of Rayleigh Taylor growth rate on wavenumber but it is most important to stress that these are not necessarily simulations of the Rayleigh Taylor instability since the resolution of the mesh is comparable to the width of the Rayleigh Taylor instable region.

It is premature to give any firm conclusions from this work but it appears that shorter laser wavlengths give rise to stricter requirements on the uniformity of illumination.

R G Evans (RAL), A J Bennett and G J Pert (Univ of Hull)

7.2.3 An Analytic Model for Laser Driven Ablative Implosions of Spherical Shell Targets

7.2.3(a) Introduction

The use of analytic models to describe the gross hydrodynamic features of

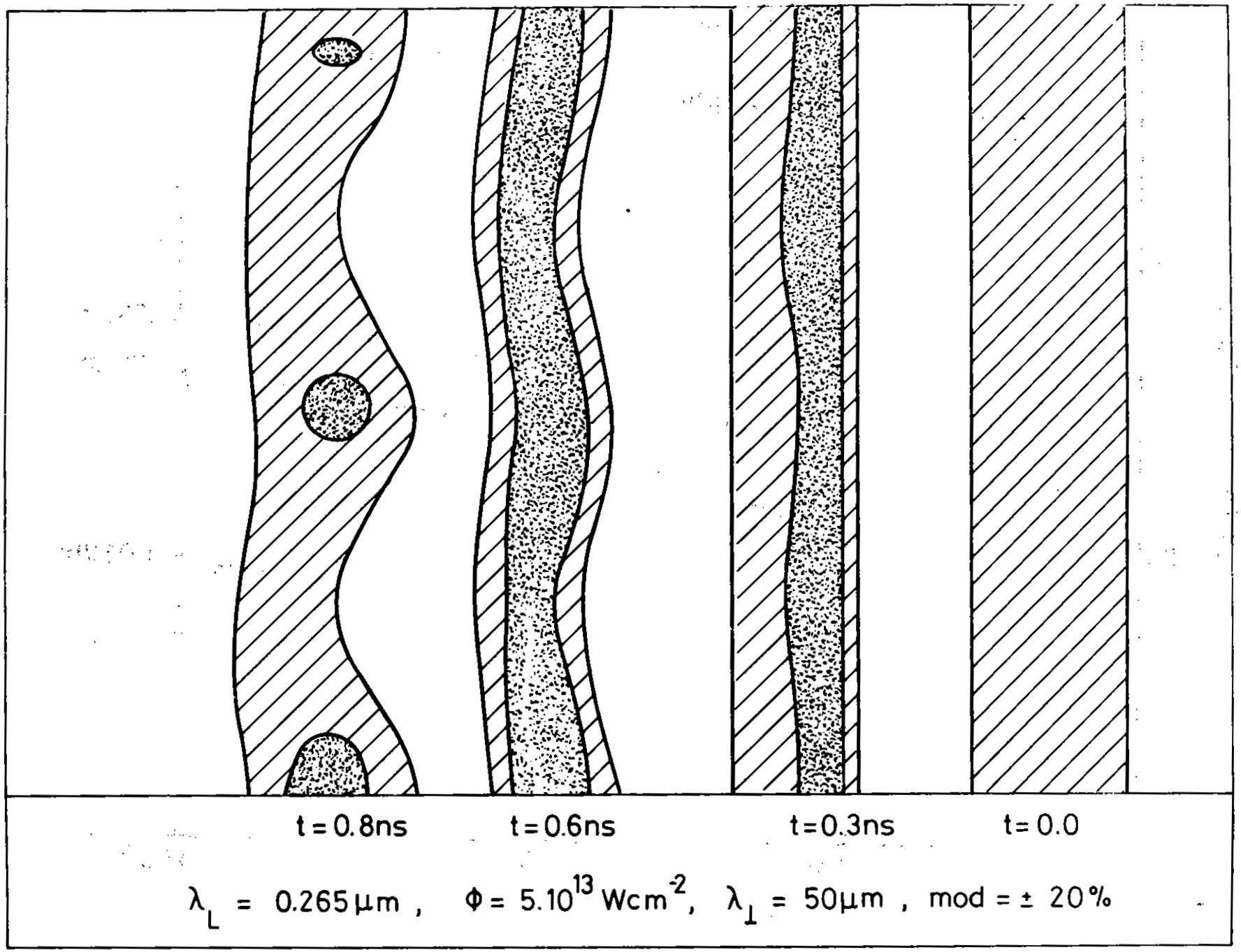

Figure 7.09 Development of density contours with time for a non-uniformly accelerated foil.

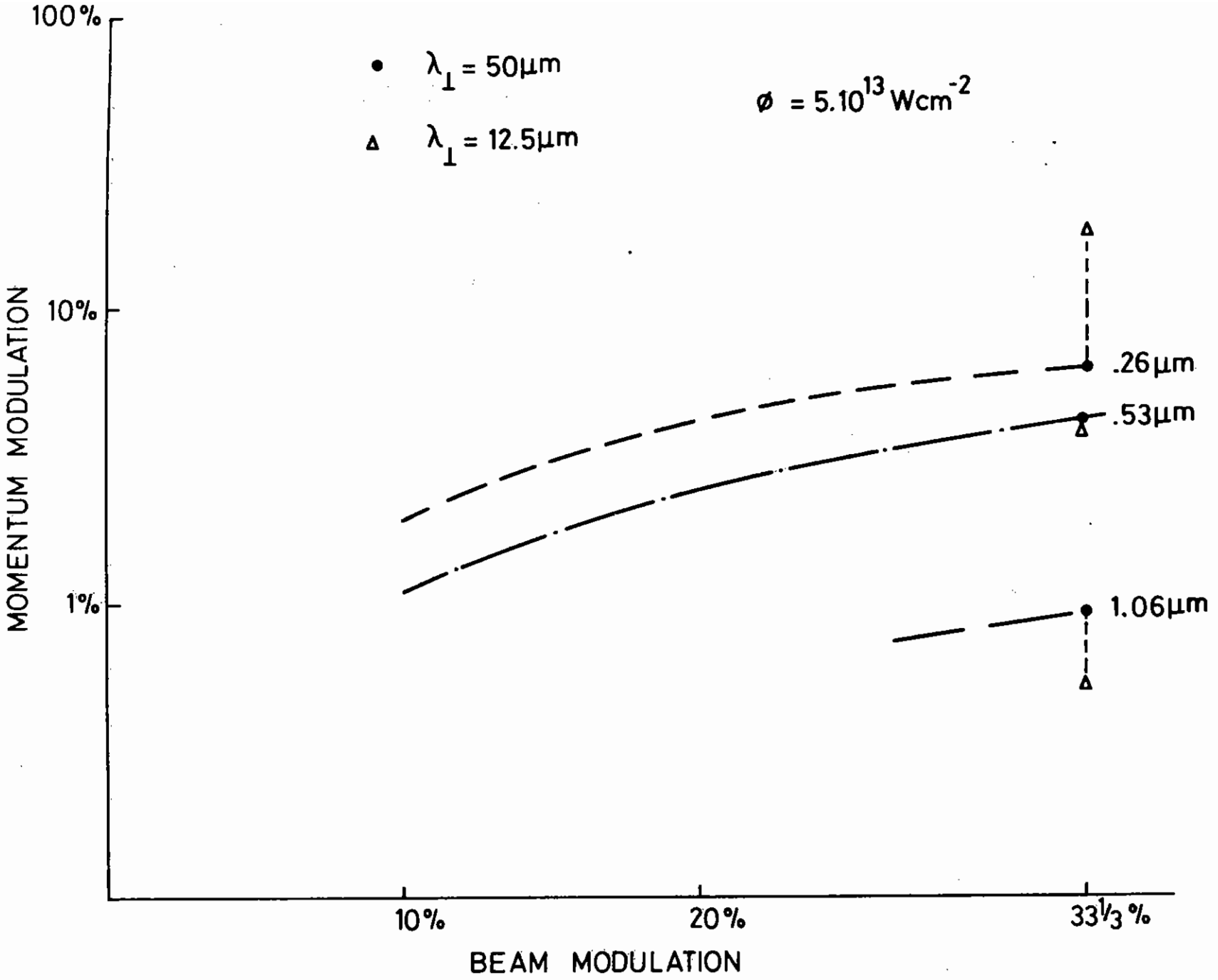

Figure 7.10 Variation of the modulation of the momentum of the foil with laser modulation, laser wavelength and wavelength of the transverse modulation.

the laser driven implosion of spherical (gas filled) solid shells has been discussed in earlier work both for 'exploding pusher' (7.18) and ablative (7.19) implosions.

These models described the hydrodynamics of compression of the gas in terms of an initial shock and a reflected shock followed by adiabatic compression, but used a treatment of spherical convergence which was accurate only for relatively small compression ratios. While this is satisfactory for 'exploding pusher' implosions where compression ratios are typically less than 100 it leads to inaccuracy in the case of ablative implosions where much larger compression ratios may be obtained.

A revision of the model description of ablative implosions incorporating an improved description of spherical convergence has been shown to give good quantitative agreement with numerical simulations and has been used to draw conclusions about the scaling behaviour of ablative implosions (7.20). A brief outline of this revised model and of some conclusions arising from it are presented below.

7.2.3(b) The Analytic Model

It is assumed as shown in Figure 7.11 that a solid spherical shell of radius r, thickness Δr and density ρ_s is driven radially inwards by an ablation pressure P_a which causes constant acceleration. The fraction of the shell mass lost by ablation is assumed to be small. A spherical shock wave driven by the pressure P_a traverses the shell and enters the gas fill of initial density ρ_1. It converges to the centre and reflects meeting the gas/shell contact surface at time t_2.

The density and pressure inside the reflected shock vary in space but approximate volume averaged values $\overline{\rho}_3$ and $\overline{P}_3$ can be obtained from a self similar solution for spherical shock waves (7.21) giving,

$$\left.\begin{aligned} \overline{\rho}_3 &= 2.7\,\frac{\gamma(\gamma+\gamma)}{(\gamma-1)^2}\,\rho_1 \\ \text{and} \qquad \overline{P}_3 &\quad 20\,\left(\frac{3\gamma-1}{\gamma-1}\right)\left(\frac{\rho_1}{\rho_1}\right)\,P_a \end{aligned}\right\} \qquad (1)$$

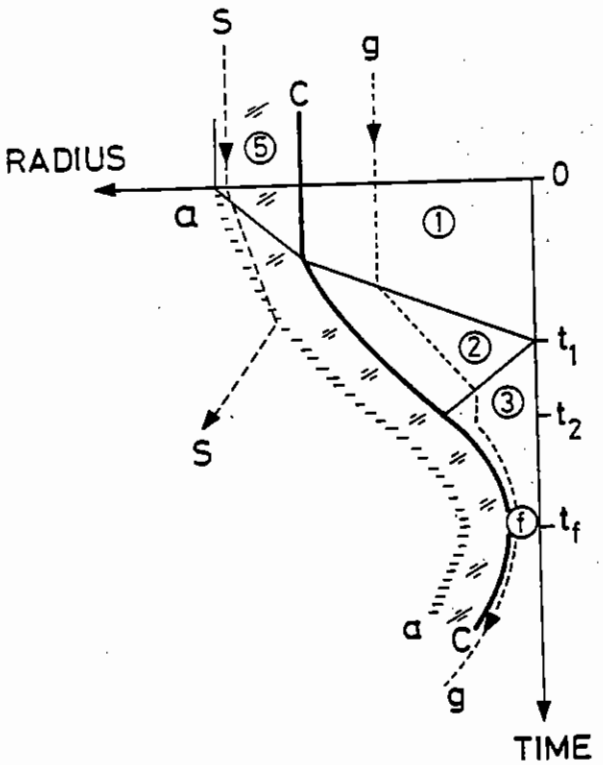

Figure 7.11 Schematic space-time characteristics of an ablative implosion. .... paths of fluid elements, in the shell, (s-s) and the gas, (g-g). The contact surface trajectory is (c-c) and the ablation front (a-a). S denotes the shell, 1 the undisturbed gas, 2 the gas after the passage of the first shock, 3 the gas after the reflected shock and f the gas at peak compression. The shocks are shown by the solid lines starting at t = 0 at the shell outer surfaces, reaching the centre at $t = t_1$, and meeting the contact surface after reflection at $t = t_2$.

It follows from equation (1) that the radius at time t_2 is approximately r/3. The shell accelerates at a constant rate without significant resistance from the gas upto this time. Thereafter the counter pressure of the gas decelerates the shell and the gas is compressed eventually isentropically because the shock strength becomes weak for $t > t_2$ after reflection at the shell/gas contact surface.

The compression terminates at time t_f when the radius is ρ_f, the density ρ_f and the pressure P_f.

The value of P_f, the stagnation pressure, is determined by the momentum flux density in the imploding shell. In the absence of spherical convergences it is $\tilde{\rho}_s v^2$ where $\tilde{\rho}_s$ is the average density of the imploding shell and v its velocity at time t_2. Spherical convergence enhances the pressure in approximately the ratio G of the contact surface area at t_2 to that at t_f since the shell is decelerated by pressure acting over a reducing area. Thus

$$P_f \approx G \bar{\rho}_s v^2 \tag{2}$$

where

$$G \approx \frac{I}{9} \left(\frac{\rho_f}{\rho_s}\right)^{2/3} \tag{3}$$

With the above simple descriptions of the effect of spherical convergence and proceeding as in earlier work to solve for the parameters t_f, ρ_f, $\rho_f r_f$, P_f and T_f (T_f being the temperature of the compressed gas), the following results are obtained (7.20).

$$t_f = \frac{3}{2}\left[1 - \left(\frac{\rho_1 \Delta r}{0.53 \rho_s r}\right)^{1/3}\right]\left[\frac{4}{3}\frac{\rho_s r \Delta r}{P_a}\right]^{1/2} \tag{4}$$

$$\rho_f = 0.53\ (r/\Delta r)\rho_s \tag{5}$$

$$\rho_f r_f = \rho_1 r[0.53(r/\Delta r)(\rho_s/\rho_1)]^{2/3} \tag{6}$$

$$P_f = \frac{8}{27}\left(\frac{\rho_f}{\rho_1}\right)^{2/3}\left(\frac{r}{\Delta r}\right) P_a \tag{7}$$

$$T_f/1\ \text{eV} = 0.76 \left[\frac{P_a/1\ \text{Mbar}}{\rho_1}\right]\left(\frac{\rho_1}{\rho_s}\right)^{1/3}\left(\frac{r}{\Delta r}\right)^{2/3} \tag{8}$$

These results give a useful scaling description of ablative implosions in which there is no steepening of the laser pulse so that the adiabat for the isentropic phase of compression of the gas has its starting point determined by shock heating resulting from the ablation pressure P_a acting as the outer surface of the shell.

7.2.3(c) Validity Criteria for the Model

The various assumptions in the model limit the parameter range of its applicability ie the values of the laser irradiance I and wavelength λ and the shell parameters r, Δr, ρ_s and ρ_1.

Analytic expression of these limits requires an analytic relationship between the ablation pressure P_a and mass ablation rate $\dot{m}$ and the laser parameters I and λ. The simplest such relationship is obtained from the assumption of sonic flow at the critical density (7.22). This gives the expressions

$$P_a = 13\ (\lambda/1\ \mu\text{m})^{-2/3}\ (I/10^{14}\ \text{W cm}^{-2})^{2/3}\ \text{Mbar} \tag{9}$$

$$\dot{m} = 1.7 \times 10^5\ (\lambda/1\ \mu\text{m})^{-1/3}\ (I/10^{14}\ \text{W cm}^{-2})^{1/3}\ \text{g cm}^{-2}\ \text{s}^{-1} \tag{10}$$

A more detailed model which includes the effect of thermal induction to densities greater than critical gives results that are qualitatively similar (7.17) eg

$$P_a = 7.2(\lambda/1\ \mu\text{m})^{-0.99}(I/10^{14}\ \text{W cm}^{-2})^{0.57}\ (Zr/0.1)^{0.07}\text{Mbar} \tag{11}$$

The model requires that the fractional loss of shell mass by ablation $\Delta M/M$ be small. It is interesting to note that the hydrodynamic efficiency, ε_h, relating energy in the accelerated shell to energy supplied to the ablation process is (7.20)

$$E_h \approx \Delta M/M$$

It follows from the model and equations (9) and (10) that,

$$r/\Delta r = 1.2\ \epsilon_n^{\ 2}\ (\rho_s/\rho_c) \tag{12}$$

where ρ_c is the critical density, which for a fully ionised plasma is given by

$$\rho_c = 3.3 \times 10^{-3}\ (\lambda/1\mu m)^{-2} \tag{13}$$

An upper limit on mass loss fraction or hydrodynamic efficiency therefore imposes an upper limit on aspect ratio $r/\Delta r$ (eq 12) and this upper limit is lower for shorter laser wavelengths (eq 3 and 1).

Another limit on the aspect ratio arises from the fact that the internal energy of the compressed gas U_g must be less than the maximum kinetic energy E_s of the imploding shell. If $U_g < 0.3\ E_s$

$$r/\Delta r < (\rho_s/\rho_1)^{1\ 2} \tag{14}$$

In addition the pressure $\bar{P}_3$ must be less than the pressure P_f in order that the model description of the gas compression be valid, giving the criterion

$$r/\Delta r > 46\ (\rho_1/\rho_s) \tag{15}$$

The temperature T_f and the enhancement of pressure G diverge in the limit $\rho_1 \to 0$ (eqs 3 and 8). This implies a minimum value of ρ_1 for validity of the model. Numerical simulations discussed below suggest that this is,

$$\rho_1 > 10^{-3}\ gcm^{-3} \tag{16}$$

At lower values radiation and heat conduction cool the small very hot gas volume giving lower values of T_f and P_f than predicted by the model,

which does not include these processes.

The assumption of an ideal gas equation of state requires that pressure in the compressed gas be higher than the Fermi degenerate electron pressure so that

$$P_a > 4.8\ \rho_s \rho_1^{2/3}\ Mbar \tag{17}$$

Conversely this criterion shows that under the assumed conditions a Fermi degenerate compression adiabat can be achieved only with low driving pressure because of shock preheating of the gas.

Preheating of the shell and gas by hot electrons generated in the laser plasma interaction process sets an upper limit to $I\lambda^2$. If it is assumed from experimental data that the hot electron temperature T_h is related to $I\lambda^2$ by (7)

$$kT_h\ /\ 1\ KeV = 5\left[(I/10^{14}\ W\ cm^{-2})\ (\lambda/1\ \mu m)^2\right]^{0.45} \tag{18}$$

and that the scale depth $(\rho\ell)_h$ of the experimentally measured approximately exponental energy deposition profile scales quadratically with electron energy (7.24) giving,

$$(\rho\ell)_h = 1.8 \times 10^{-4}\left[(I/10^{14} Wcm^{-2})(\lambda/1\mu m)^2\right]^{0.9} \tag{19}$$

then provided the fraction of the laser energy going into preheating by hot electrons η_h is known it is straight forward to write a criterion that shock preheating be greater than hot electron preheating. Experiments have shown $\eta_h \sim 0.06$ for 100 ps 1.06 μm laser pulses with $10^{15} = I\lambda^2 \sim 7 \times 10^{15}$ (7.24) and although it is a very crude assumption we take η_h to be a constant. It follows that

$$\exp\ \frac{-\rho_s \Delta r}{2(\rho\ell)_h} \leq \frac{5 \times 10^{-5}\ (I/10^{14}\ W\ cm^{-2})^{0.9}\ (\lambda/1\ \mu m)^{0.9}}{\rho_s r^{\frac{1}{2}}\ \Delta r^{\frac{1}{2}}} \tag{20}$$

in order that shock heating be dominant over hot electron preheating at time t_2 at the mid point of the shell wall.

For example where r = 50 μm Δr = 3 μm ρ_s = 2.5 this requires $I < 3 \times 10^{13}$ at > = 1 μm and $I < 8 \times 10^{14}$ at λ = 0.25 μm.

7.2.3(d) Comparison with Numerical Modelling

The accuracy of the model has been checked by comparison with numerical simulations of implosions. A one dimensional Lagrangian hydrodynamic code (MEDUSA) was used. It was assumed that the shell and gas had ideal gas equations of state and were fully ionized. Calculations were made for shells of radius r = 50 μm density ρ_s = 2.5 g cm^{-3} and ionic charge Z = 10. Shell thickness was varied from 1 to 10 μm. The gas had density ρ_1 from 10^{-4} to 10^{-1} g cm^{-3} and ionic charge Z = 1.

The code is expected to give an accurate description of shock and adiabatic compression, of spherical convergence and of heat conduction effects in the implosion of shells driven by an ablation pressure source confined to a relatively thin surface layer.

The code description of the ablation process itself was of more limited accuracy since detail of energy transport by hot and cold electrons cannot be accurately modelled without arbitrary assumptions. A simple prescription was used here in which laser energy was dumped at the critical density with 90 % of it going into a hot electron Maxwellian source with T_h related to $I\lambda^2$ and the energy deposition by the hot electrons modelled simply from classical range and energy loss results. Thermal conduction was classical, ie at the Spitzer value. This description gave ablation pressures which were in fair agreement with other sources for ablative conditions, particularly for short wavelengths (where inhibited thermal conduction is less important) and low $I\lambda^2$ (where hot electron range $(\rho\ell)_h$ is negligible).

For example for conditions used in simulations discussed below 10^{13} W cm^{-2} at λ = 0.25 μm gave an ablation pressure of 10 Mbar which is in fair agreement with 7.6 Mbar calculated from equation (11). Moreover equation (11) agrees reasonably with experimental data at λ = 0.53 μm as shown in Figure (7.12).

The sequence of events shown schematically in fig. 7.11 was observed in the simulations. Figure (7.13) shows for example the hydrodynamic situation when the initial shock, having broken out from the shell, is propagating through the gas.

The main purpose of the analytic calculation is to predict the conditions reached in the compresed gas and figure 7.14 compares ρ_f, P_f and t_f from the analytic model and from simulations with MEDUSA. The parameter varied is ρ_1 and the irradiation conditions are chosen to satisfy the main analytic model validity criteria of negligible preheating range, small mass ablation fraction ($\Delta M/M \sim 0.3$) and moderate aspect ratio ($r/\Delta r$ = 50/3). The results are in good agreement for $10^{-3} < \rho_1 < 10^{-1}$ where the analytic model is valid. For lower ρ_1 the compression ratio exceeds 10^4 and the temperature of the very small compression core becomes very high. The MEDUSA simulation which includes thermal conduction shows a lower pressure as heat conduction cools the core. The effect is not included in the analytic model which therefore over-estimates the pressure.

The limits of validity of the analytic model discussed above impose an upper limit on ρ_1 of 10^{-1}. The lower limit may be deduced from figure (7.14) to be around 10^{-3}.

In general comparisons with MEDUSA simulations suggest that where its validity criteria are met the analytic model gives a useful description of compressed plasma parameters and implosion time.

7.2.3(e) Scaling Conclusions

The analytic model may be used to assess the laser pulse characteristics needed to realise specific objectives.

The maximum ablation pressure available without violating the preheating constraint is readily estimated from equation (20) where to a first approximation $\rho_s \Delta r/(\rho\ell)_h$ = constant, and assuming in evaluating the 'constant' on the rhs of equation (20) that typically r = 100 μm, r = 6 μm,

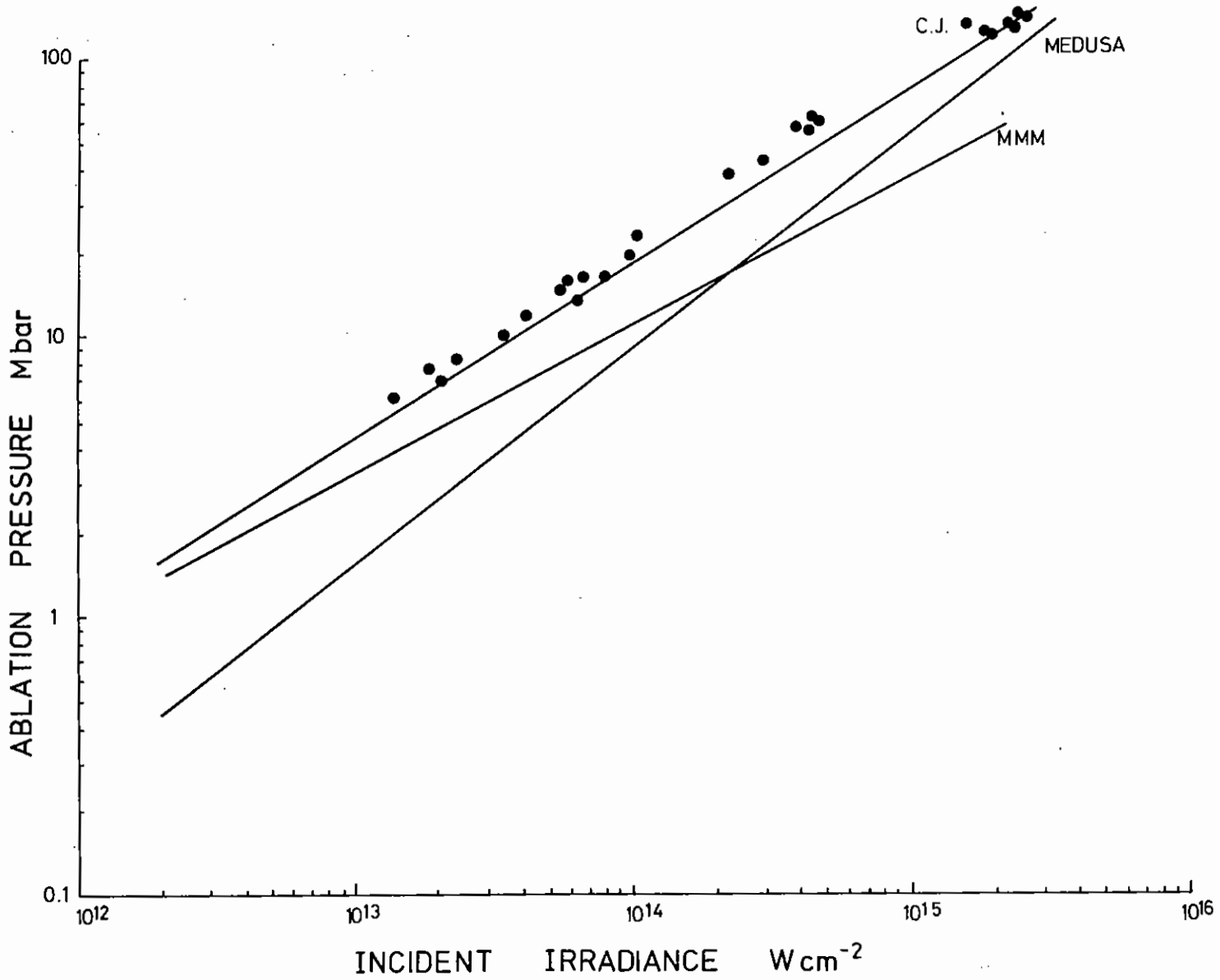

Figure 7.12 Variation of ablation pressure with incident irradiance at $\lambda = 0.53$ μm. Solid lines are CJ, equation 29, MMM, equation 30 and MEDUSA numerical calculations. Data are from experiments at the Rutherford Laboratory with a least squares fit shown as a dashed line.

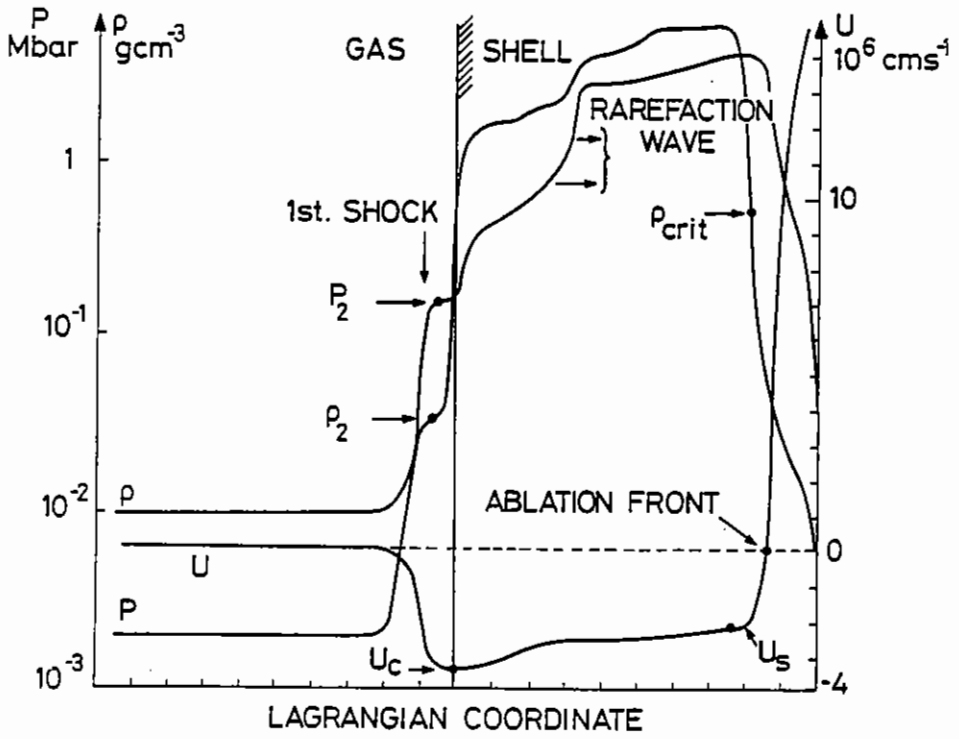

Figure 7.13 Profiles of pressure P density ρ and velocity u from numerical simulation at t = 0.28 ns during λ = 0.25 μm, 10^{13} W cm^{-2} irradiation of a shell with r = 50 μm, Δr = 3 μm, ρ_s = 2.5 and $\rho_1 = 10^{-2}$ g cm^{-3}. The break out of the first shock into the gas is seen with approximate values of u_c, u_s, P and ρ_2 indicated.

$\rho_s = 2.5$ gcm^{-2}, $I = 10^{14}$ Wcm^{-2}, $\lambda = 1$ μm it follows that the maximum irradiance is approximately,

$$I/10^{14} \text{ W cm}^{-2} \simeq 0.77\ (\lambda/1\ \mu\text{m})^{-2}\ (\Delta r/6\ \mu\text{m})^{1.11} \qquad (21)$$

so that the ablation pressure limit following equation (11) is

$$P_{am}/1 \text{ Mbar} = 6.2\ (\lambda/1\ \mu\text{m})^{-2.13}\ (\Delta r/6\ \mu\text{m})^{0.63} \qquad (22)$$

A more accurate result is obtained by solving the logarithmic equation (20) for I and then using equation (11) for P_a.

The significance of equations (21) and (22) is that the limiting ablation pressure is higher for shorter wavelength irradiation and that higher pressure may be used with thicker shells, ie with reduced aspect ratio at constant target size or with increased target size at constant aspect ratio.

The compressed plasma parameters (P_f, ρ_f, T_f, $\rho_f r_f$) with simple ablatively driven targets are given by equations (5) to (8). If may be useful to note that ρ_f is independent of the size of the target while P_f depends only weakly on size through the possibility of increased P_a with increased Δr discussed above. The compressed plasma can thus be formed at chosen density with a range of pressures from the Fermi-degenerate minimum up to a maximum determined by P_{am} and equation (7).

If it is required to study the hydrodynamics of ablative compression and the properties of dense high pressure plasmas it may be concluded from the previous discussion that target size need only be sufficient to permit diagnostic measurements of the smallest features of interest (eg the implosion core and fluid instabilities on the scale of the initial shell thickness Δr). A typical resolution limit for X-ray imaging is 5 μm so that a suitable target size is of the order r = 100 μm Δr = 6 μm assuming a moderate aspect ratio in the region of the maximum possible for adequate fluid stability.

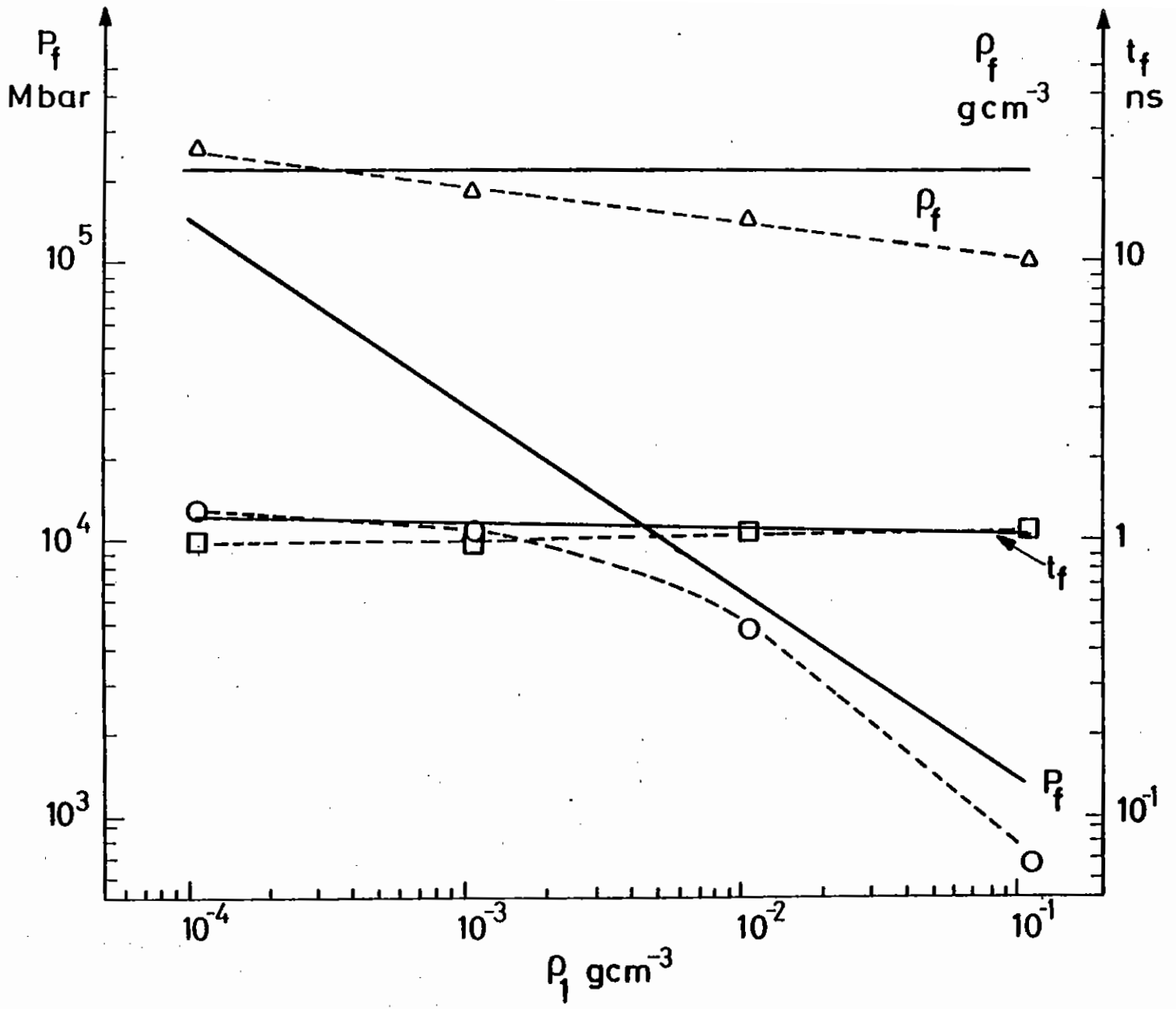

Figure 7.14 Parameters ρ_f, P_f and t_f as a function of ρ_1 in the implosion of a shell with r = 50 μm Δr = 3 μm, p_ρ = 2.5 g cm^{-2} driven by absorption of 10^{13} W cm^{-2} of λ = 0.25 μm radiation. Solid lines show values calculated from the model, dotted lines with data points show values from simulations with MEDUSA.

This 'typical target' may be used as a normalising example to show the requirements on the laser pulse to drive it and the accessible range of the plasma parameters. The maximum irradiance (solving equation (20)) is 4×10^{14} W cm^{-2} for $\lambda = 0.50$ λm and from equation (21) this scales with Δr approximately as 4×10^{14} $(\Delta r/6\ \mu m)^{1.11}$. The maximum ablation pressure given by equation (11) is 31 Mbar and this would scale approximately following equation (22) as $31(\lambda/0.5\ \mu m)^{-2.13}$ $(\Delta r/6\ \mu m)^{0.69}$ Mbar

The laser pulse requirements for constant preheating by hot electrons relative to shock preheating) can be expressed in a form showing scaling with λ and r at constant target aspect ratio ($r/\Delta r = 100/6$). A parameter α is introduced to represent the effect of the increased irradiance which may be used with increased shell thickness. Thus $\alpha = 0$ gives the scaling at irradiance $I = 4 \times 10^{14}$ $(\lambda/0.5\ \mu m)^{-2}$ W cm^{-2} which is the maximum irradiance for the chosen example with $\Delta r = 6$ μm. Setting $\alpha = 1$ gives the effect of increasing the irradiance with increasing shell thickness so that it has its maximum value
$I = 4 \times 10^{14}$ $(\lambda/0.5\ \mu m)^{-2}$ $(\Delta r/6\ \mu m)^{1.11}$ W cm^{-2} Thus the implosion time t_f for a shell of density 2.5 is

$$t_f/1\ ns = 1.2\ (\lambda/0.5\ \mu m)\ (r/100\ \mu m)^{1-0.32\alpha} \qquad (23)$$

The absorbed laser power is,

$$P_L/1\ TW = 0.5\ (\lambda/0.5\ \mu m)^{-2}\ (r/100\ \mu m)^{2\ +\ 1.11\alpha} \qquad (24)$$

The absorbed energy is,

$$E_L/1\ kJ = 0.6\ (\lambda/0.5\ \mu m)^{-1}\ (r/100\ \mu m)^{3\ +\ 0.74\alpha} \qquad (25)$$

The attainable compressed plasma parameters are

$$\rho_f = 22\ g\ cm^{-3} \qquad (26)$$

$$T_f/1\ KeV = 2.4\ (\lambda/0.5\ \mu m)^{-2.13}\ (\rho_1/0.01)^{-2/3}\ (r/100\ \mu m)^{0.63\alpha} \qquad (27)$$

$$P_f\ r_f = 1.7 \times 10^{-2}\ (\rho_1/0.01)^{1/3}\ (r/100\ \mu m) \qquad (28)$$

$$P_f/1Mbar = 2.6 \times 10^{4}(\lambda\ 0.5\mu m)^{-2.13}(\rho_i/0.01)^{-2/3}(r/100\mu m)^{0.63\alpha} \qquad (29)$$

Greater density at similar pressure is obtainable by suppressing shock preheating eg with a long slow build up to peak laser power. A rough estimate of the range of possibilities here is given by considering the Fermi degenerate density ρ_{fF} at the above pressure eq (29) which is,

$$\rho_{fF}/1gcm^{-3} = 218\ (\lambda 10.5\mu m)^{-1.28}(\rho_i/0.01)^{-2.15}(r/100\mu m)^{0.37\alpha} \qquad (30)$$

(neglecting any further pressure increase due to increased spherical convergence).

The size of the target is important for the inertial confinement parameter ρr. We have the scaling $\rho r \sim r$ and $E_L \sim (\rho r)^{3+0.74\alpha}$, (where the α dependence arises if I is increased with target size). The value of ρr needed for fusion ignition by reabsorption of DT α particles is $\rho r > 0.3$ g cm^{-2} and for high gain fusion burn $\rho r > 1$. The investigation of compression in this range of ρr needs much larger targets and laser power than are required for the basic physics studies discussed earlier. From equations (25) and (28) $E_L = 120$ MJ for $\rho_1 = 0.01$ $\rho_f r_f = 1$ at irradiance $I = 3 \times 10^{14}$ W cm^{-2} giving $T_f = 2.5$ KeV. This very large energy arises because kT_f is much above the Fermi energy.

The importance of compression close to the Fermi degenerate adiabat is illustrated by equation (30) which gives an estimate of $r_f = 66$ μm for $\rho_f r_f = 1$ which with equation (25) and assuming $\rho_1 = 0.01$ gives the much reduced energy requirement $E_L = 1.3$ MJ for an ideal isentropic compression to the same final pressure as in the previous calculation with shock preheating.

Figure (7.15) expresses this in another way by plotting the scale depth $(\rho\ell)_h$ for hot electron preheating together with the ablation pressure P_a as a function of irradiance I for $\lambda = 1$ μm and 0.5 μm. Since the size of the target is related to the energy of the laser pulse (eq 25) it

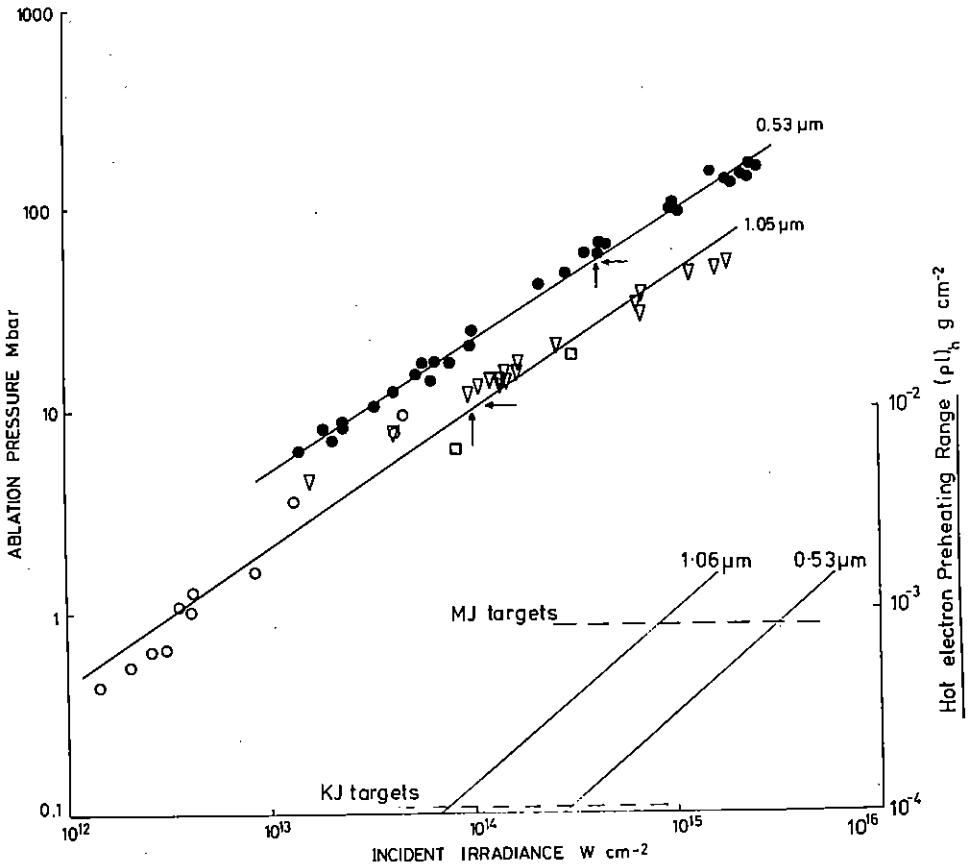

Figure 7.15 Ablation pressure as a function of incident irradiance at λ = 1.05 μm and 0.53 μm. Solid circles are 0.53 μm data from mass ablation rate measurements on plane targets. Open triangles are similar data at 1.05 μm; open squares are shock wave measurements; open circles are ion emission measurements. The range $(\rho\ell)_h$ of preheating by hot electrons estimated as discerned above is shown for λ = 1.05 μm and 0.53 μm and the dotted lines show the tolerable range for targets driven by kilojoule and megajoule laser energy. The arrows show the pressure obtainable at $I\lambda^2 = 10^{14}$ W cm^{-2} μm^2.

is possible to plot the hot electron preheat limit on the maximum irradiance for 1 KJ and 1 MJ laser energy, ie for typical present day laboratory experiments and possible laser fusion targets of the future. It is interesting to note that with λ = 0.5 μm the laser fusion could be driven at $P_a \sim 30$ Mb which is as high as is required for high gain target performance.

M H Key (RAL)

7.2.4 Thomas-Fermi Equations of State in MEDUSA

Equations of state based on the Thomas-Fermi theory have been used successfully in MEDUSA for more than a year. Further improvements have recently been made which make the routines more easily used by users who do not wish to pay close attention to the equations of state. It had been found that in certain situations when the plasma is strongly degerate at solid densities the routines could calculate a negative specific heat which led to MEDUSA failing to converge. Although these situations were avoidable by appropriate choice of the initial temperature it has been possible to make changes to the analytic approximations for pressure and energy such that the specific heat is always positive. In the case of the corrected Thomas-Fermi equation of state the temperature dependent terms in the quantum and exchange corrections have been discarded. As a result, the routines reproduce the corrections to the pressure and energy less accurately, but the error is only significant in a very limited regime in which the theory itself is inaccurate and a higher order theory would be more correct. Consequently, the new version is more satisfactory numerically without entailing any significant loss in accuracy.

A detailed description of the routines can be found in a laboratory report (7.25). The report includes graphs of pressure and energy, and compares the analytic approximations with data tabulated by McCarthy (7.26) for the Thomas-Fermi theory and with data from the Los Alamos Sesame Library (7.27).

A R Bell (RAL)

7.3.1 HERMES, a Particle in Cell Code

7.3.1(a) Simple Paging System

The last year has seen the completion of the 'simple paging' version of HERMES. The particles are held on disk and brought into core a page at a time, as required. The fields are, however, core resident. The amount of core available on the RL 360/195 computers restricts the size of mesh that can be handled. The field mesh was chosen to be 1628 mesh points to allow for future development of a 'full paging' system.

Energy calculations have been included. Poynting's vector ($\underline{E} \times \underline{B}$) is integrated to obtain the energy flow into the system, while an integral over $E^2 + B^2$ gives the potential energy stored. The kinetic energy of the particles is also calculated. The difference between the net flow of energy into the system and the rate of increase of the stored energy is called the energy balance. Ideally this should be zero but in practice it is a measure of the growth of noise in the simulation. The energy calculations are printed at present, graphical output will be provided at a later date.

7.3.1(b) Full Paging System

Increasing the mesh beyond the limits of the 'simple paging' program would make the code too large to run at the Rutherford Laboratory. The increase is achieved by paging the fields as well as the particles.

The computational field mesh is divided into 'slices', each slice being the same size as the simple paging mesh. These slices are held on disk and only one such page is brought into core at a time.

The particle paging is made much more complex by field paging. The paging dataset must be split into several parts, all the particles in a part of the dataset must lie in one slice. The movement of particles between slices must be handled.

Particle paging, either simple paging or full paging, results in a large amount of disk I/O. In this version of the code, the I/O is reduced by some 30 % by packing the particles before putting them on disk. This, and the unpacking, is done by an assembler routine to obtain fast execution. The rounding error introduced is less than the truncation error of the particle pusher.

A further major modification was the splitting off of the particle initialization into a separate program. The use of a preprocessor to create the particle coordinates has several advantages.

(a) It makes the creation of the particle datasets in HERMES simpler.

(b) The intermediate dataset between the preprocessor and HERMES may be kept. Similar problems may be run (eg changing the wavelength of the laser) without having to recreate the particles.

(c) HERMES will not now grow in size with every new method of initializing the particles.

(d) The preprocessor is small and simple in structure. It is easy to modify for a particular case, leaving HERMES unchanged from run to run.

All algorithms for this version have been written and the modifications to the 'simple paging' code made. The program is currently undergoing verification.

C J Webb (RAL) and D Cooke (Bangor)

7.3.2 Second Harmonic Emission

The dependence of the intensity of second harmonic emission on the angle of incidence of the laser light has been investigated for a plasma with a steep density gradient in the neighbourhood of the critical surface. Previous analytic (7.28, 7.29) and numerical (7.30) work assumes smooth

density gradients, whereas experimental results show density gradients near the critical surface which are such that the density goes from a fraction of critical to about twice critical in a distance of the order of one wavelength of the incident light. Under these conditions analytic methods based on WKB approximations and wavenumber matching conditions break down.

We consider plasma density profiles of the form shown in Figure 7.16 and calculate the second harmonic emission resulting from resonant absorption of a p-polarized wave. The equation describing second harmonic emission is (7.28)

$$\frac{d^2B_2}{d\xi^2} - \frac{d\ \ell n\ \varepsilon_2}{d\xi}\frac{dB_2}{d\xi} + 4\ [\varepsilon_2 - q^2]B_2 = -i\left\{iB\frac{dE_z}{d\xi} + E_x\frac{d\ E_z}{d\xi^2}\right.$$

$$\left. - \frac{d\ \ell n\ \varepsilon_2}{d\xi}E_x\frac{dE_z}{d\xi}\right\} - \left\{E_z\frac{dE_z}{d\xi}\,q + 2\frac{d\ \ell n\ \varepsilon_2}{d\xi}E_z{}^2\,q\right\} \qquad (1)$$

$$+ i\left\{2BE_x\,q + 3i\frac{d\ \ell n\ \varepsilon_2}{d\xi}E_x{}^2\,q\right\}$$

where the fields on the rhs are those at the fundamental frequency ω, $\varepsilon_2 = 1 - \omega p^2/4\omega^2$, $\xi = \omega z/c$, q is the sine of the angle of incidence and the electric and magnetic fields are in units of $m\omega c/e$ and $m\omega/e$ respectively. The terms of the rhs of equation (1) are found using the linear theory of resonant absorption, neglecting the effect of the second harmonic.

Some insight into the results obtained may be given by considering the Green's function solution for B_2 on the low density side of the critical surface ($\xi \to \infty$), viz

$$B_2 \simeq -\frac{u(\xi')f(\xi')}{W(\xi')}\,v(\xi)d\xi'. \qquad (2)$$

Here $f(\xi)$ is the rhs of (1), $u(\xi)$ is a solution of the homogeneous equation decaying as $\xi \to -\infty$, $v(\xi)$ is a solution representing an outgoing wave as $\xi \to +\infty$ and W is the Wronskian of these two solutions. The integral is taken over the region in which the driving term $f(\xi)$ is significant.

The dominant part of f arises from a product of plasma wave and em wave terms and the integral involves a product of these with a second harmonic solution. In shallow density gradients a WKB approximation may be used and the dominant term obtained from the point of stationary phase of the integrand giving a smooth dependence of the second harmonic on angle of incidence. For steep profiles f is only significant over a few wavelengths of u. There is no point at which wavenumber matching conditions are valid and the emission depends on the detailed interelation of the wave phases. As the angle of incidence varies this changes and oscillations in the intensity as a function of angle result. The function u consists of a superposition of outgoing and incoming waves and its structure depends on the density profile above critical and, in particular, on the position of the reflection point for the second harmonic wave.

Absorption coefficients and second harmonic emission are shown for different density profiles in Figures 7.17 and 7.18, the latter showing the complicated angular dependence anticipated above. In making experimental observations a rapid angle dependence (and a sensitive dependence on the density profile) might, in general, be expected to be smeared out. However, time and space resolved measurements (7.31) show short bursts of radiation from localised plasma regions, and it is interesting to speculate to what extent this may this may be connected with the fact that emission may be strongly dependent on the local angle of incidence. A more detailed account of this work may be found in (7.32).

R A Cairns (St Andrews)

7.3.3 Time dependence and saturation of Brillouin scattering

Estimates of the saturated values of Brillouin scattering from an underdense plasma have been given recently by Kruer (7.34) and Evans (7.35) using arguments based on the saturation of the instability owing to particle trapping, ion heating or a combination of these effects. Here we describe the extension of this work to a simple time-dependent model which

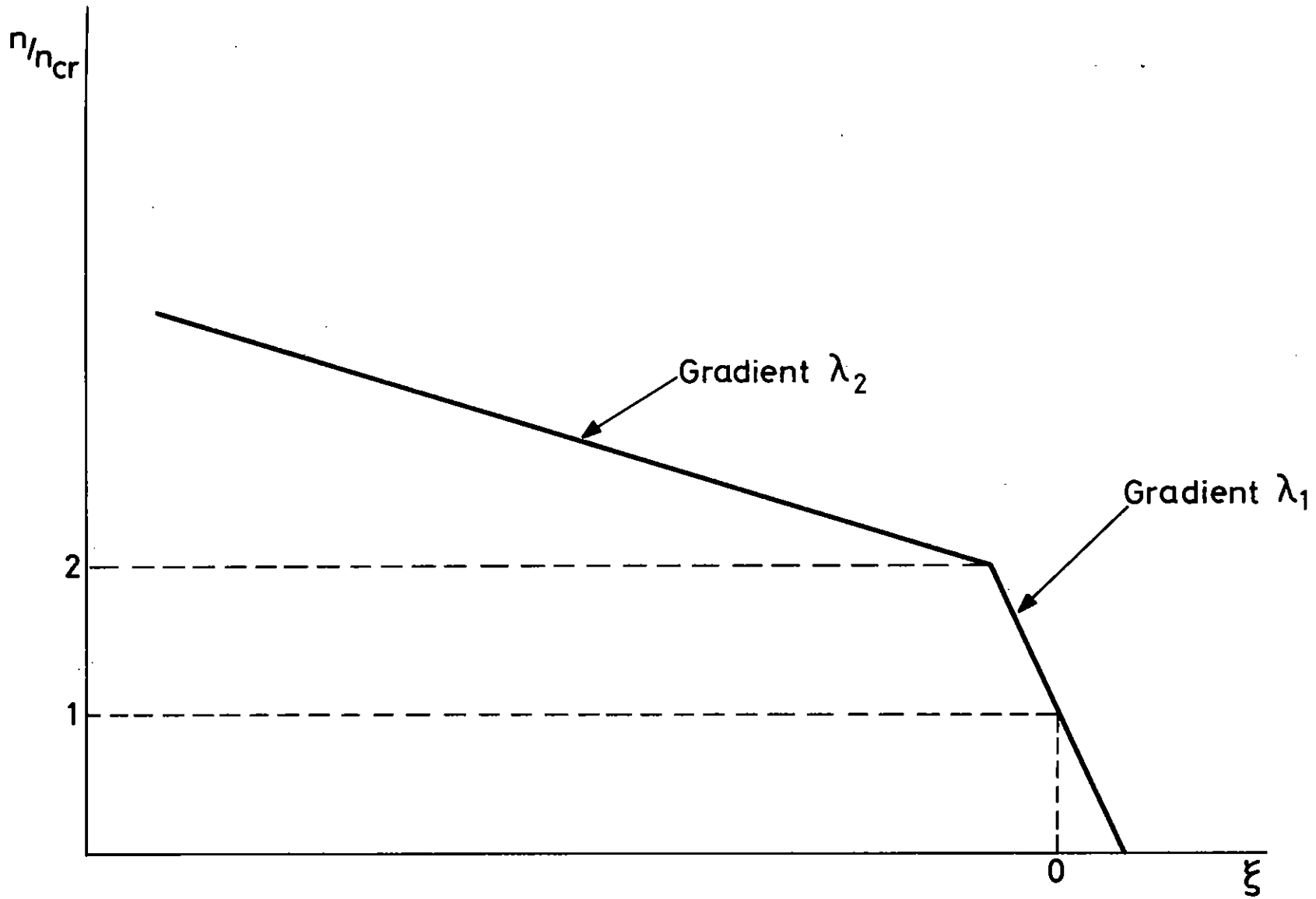

Figure 7.16 Form of the density profile used for the numerical calculations. These profiles were (a) $(\lambda_1,\lambda_2) = (0.2,0.02)$ (b) $(\lambda_1,\lambda_2) = (0.2,0.04)$ (c) $(\lambda_1,\lambda_2) = (0.4,0.02)$ (with λ_1,λ_2 in units of the vacuum wavenumber of the incident radiation).

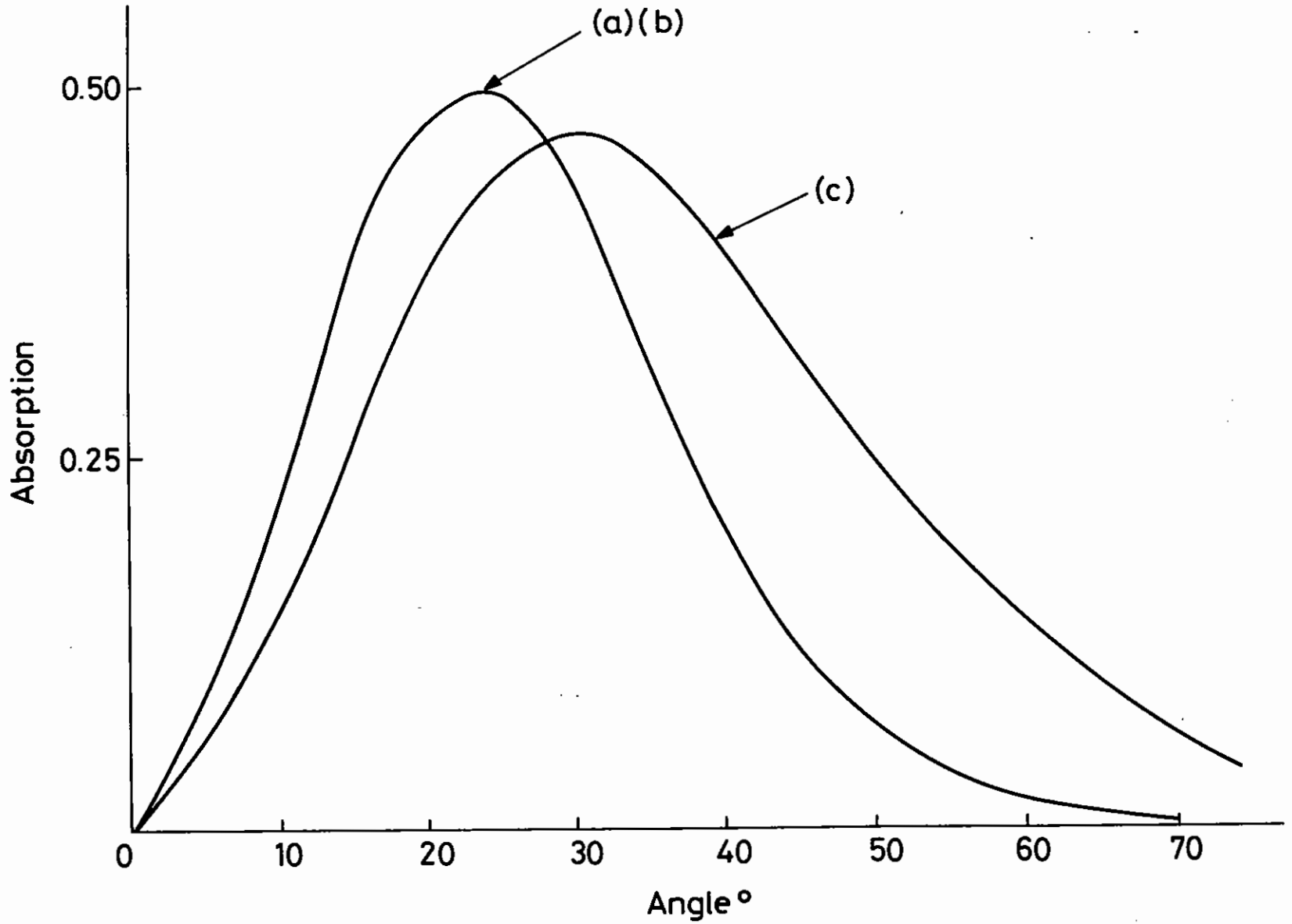

Figure 7.17 The absorption coefficient of the incident wave as a function of the angle of incidence for the profiles (a), (b), (c) described in the caption of Figure 7.16.

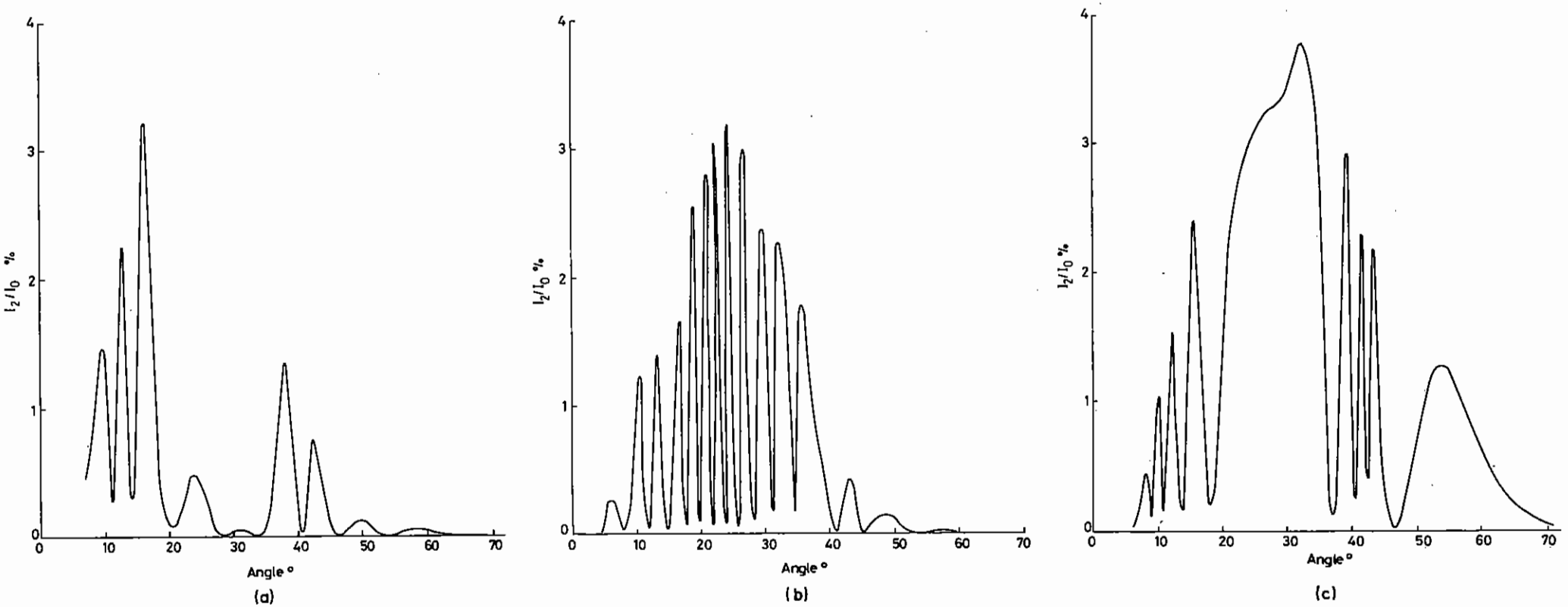

Figure 7.18 (a), (b), (c), Second harmonic emission as a function of angle for the corresponding profile. The intensity is expressed as a percentage of the incident intensity, the latter being such that $eE/m\omega c = 0.005$.

allows us to consider the effect of varying incident intensity. The equations describing Brillouin scattering are of the form (7.33)

$$\left(\frac{\partial}{\partial t} - c_1 \frac{\partial}{\partial x}\right) a_0 = -\frac{1}{4}\frac{\omega_p^2}{\omega_0}\frac{n}{n_0} a_1 \qquad (1)$$

$$\left(\frac{\partial}{\partial t} + c_1 \frac{\partial}{\partial x}\right) a_1 = \frac{1}{4}\frac{\omega_p^2}{\omega_0}\frac{n}{n_0} a_0 \qquad (2)$$

$$\left(\frac{\partial}{\partial t} - c_s \frac{\partial}{\partial x}\right) \frac{n}{n_0} = \frac{e^2 n_0 k^2}{2Mmc^2\omega} a_0 a_1 - \frac{\nu n}{n_0} \qquad (3)$$

where $c_1 = c\,(1 - \omega_p^2/\omega_0^2)^{\frac{1}{2}}$ and k and ω are the wavenumber and frequency of the ion sound wave.

The damping coefficient ν we take to be that due to linear Landau damping when n/n_0 is small, but when n/n_0 becomes larger an additional damping to take account of particle trapping is added. Kruer (7.34) has given the estimate

$$\frac{n}{n_0} \approx \frac{1}{2}\left((1 + 3T_i/T_e)^{\frac{1}{2}} - (3T_i/T_e)^{\frac{1}{2}}\right)$$

for the amplitude at which strong damping owing to trapping occurs. We include an ad hoc damping term which becomes comparable to ω when this amplitude is approached. It was found that the qualitative behaviour observed was the same regardless of exactly what form of this term was used.

Both Landau damping and trapping depend strongly on $\theta = \frac{T_i}{T_e}$ and self-consisted determination of θ was introduced through the equation

$$\frac{\partial\theta}{\partial t} + V\frac{\partial\theta}{\partial x} = \nu\left(\frac{n}{n_0}\right)^2 \qquad (4)$$

This assumes that damped energy goes into the ions, that ions are streaming outwards with velocity V and that ion energy transport is solely by convection.

Equations (1) - (4) have to be solved in a slab of length L with suitable

boundary conditions. it is convenient to rescale both dependent and independent variable by defining

$$T = c_1 t/L \qquad X = x/L$$

$$N = \frac{1}{4}\frac{\omega_p^2}{\omega_0}\frac{L}{c_1}\frac{n}{n_0}$$

$$A_{0,1} = \left(\frac{e^2k^2}{2Mmc^2\omega}\frac{1}{4}\frac{\omega_p^2}{\omega_0}\right)^{\frac{1}{2}}\left(\frac{L}{c_1}\right)a_{0,1}$$

in which case we obtain

$$\left(\frac{\partial}{\partial T} - \frac{\partial}{\partial X}\right) A_0 = -NA_1 \qquad (5)$$

$$\left(\frac{\partial}{\partial T} + \frac{\partial}{\partial X}\right) A_1 = NA_0 \qquad (6)$$

$$\left(\frac{\partial}{\partial T} - \frac{c_s}{c_1}\frac{\partial}{\partial X}\right) N = A_0A_1 - \nu_1 N \qquad (7)$$

$$\left(\frac{\partial}{\partial T} + \frac{V}{c_1}\frac{\partial}{\partial X}\right)\theta = \nu_2 N^2 \qquad (8)$$

to be solved in $0 \le X \le 1$.

After an initial period of growth of the instability A_0 and A_1 only change slowly, on a time scale governed by the rate of change of N and θ. In this regime we can neglect the time dependence in (5) and (6) and obtain the analytic solutions

$$A_1 = C \sinh \int_0^x N(x')dx'$$

$$A_0 = C \cosh \int_0^x N(x')dx'$$

This allows a much larger time step to be used in the numerical solution since the equations then appearing have much smaller propagation velocities associated with them.

For purposes of illustration numerical calculations were done for a

hydrogen plasma of thickness 100 μ, density one tenth critical and temperature 1 keV, irradiated with a laser of wavelength 1 μ. The scaled unit of time is then ∿ 0.35 ps and $A_0 = 1$ at the boundary represents an intensity of ∿ 2×10^{14} W cm^{-2}. Figure 7.19 shows the behaviour of the reflection coefficient with incident flux constant in time and boundary conditions on the ion sound wave and temperature equivalent to $n/n_o = 0.01$ at $x = L$ and $T_i/T_e = 0.1$ at $x = 0$. Figure 7.20 shows the effect of varying these latter conditions. In all cases an initial rapid growth in backscattered intensity is followed by a decrease as T_i/T_e increases. Figure 7.21 shows typical temperature and ion sound wave amplitude profiles after appreciable ion heating has occurred. It can be seen that the ion sound wave increases in a narrow boundary region near the end at which its boundary value is fixed and over most of the slab has a value determined by the balance between the driving electromagnetic waves and the damping. This probably explains the insensitivity of the reflection coefficient to the boundary value of the ion sound amplitude.

With this model the effect of a time-dependent incident amplitude can easily be examined and Figure 7.22 shows some results illustrating the way in which the shape of the backscattered pulse may be altered for various forms of the incident pulse. From these we see that for suitable incident pulse shapes the intensity of the backscatter may reach its peak before the incident amplitude does, and that the backscatter may decline then grow again. Behaviour with these qualitative features has been observed, and reported in Laser Facility Annual Reports over the last few years.

R Cairns (St Andrews)

7.4.1 Energy Flux Limitation

The severe limitation of the flow of absorbed laser energy from the subcritical plasma to the ablation front has been the subject of much investigation, a review of which has been given by Haines (7.36). More recent work by Bell et al (7.37), involving the numerical solution of the Fokker-Planck equation, has demonstrated that it is the collisional

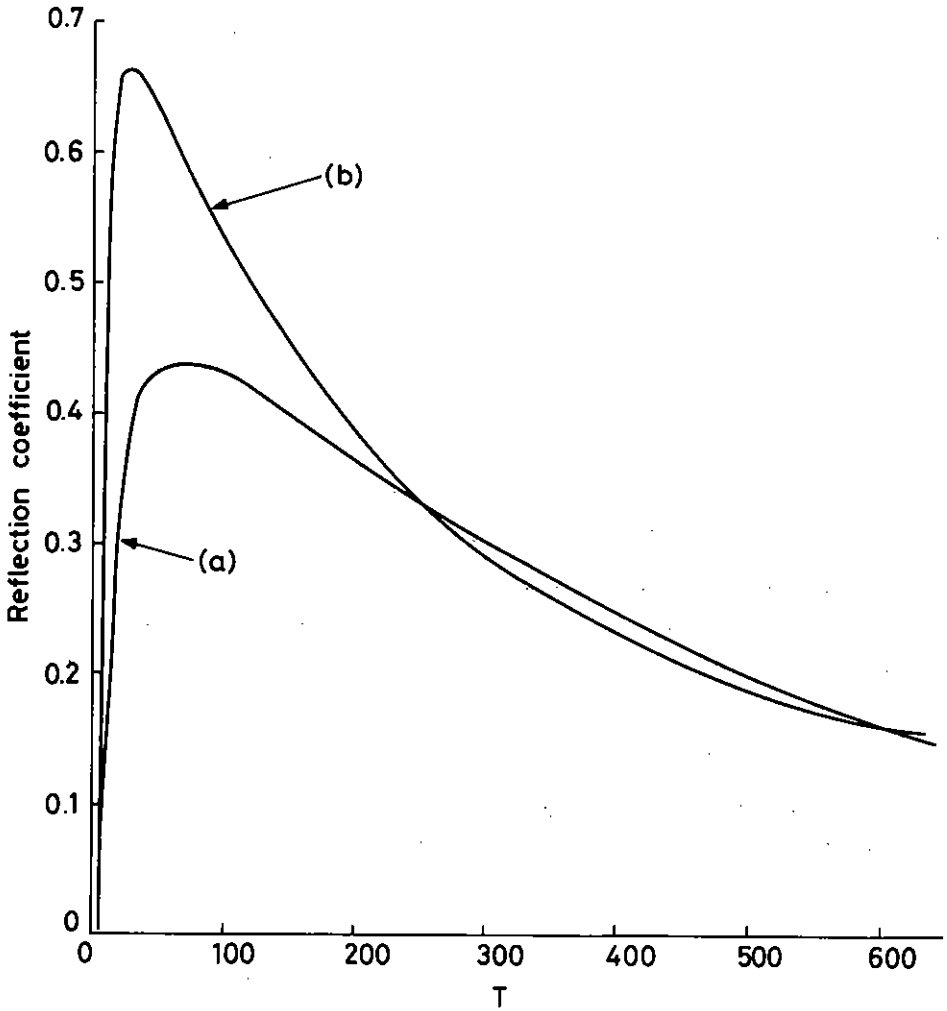

Figure 7.19 Reflection coefficient as a function of time with incident intensities (a) 0.25 (b) 1. The intensity is measured by A_o, where A_o is the dimensionless amplitude described in the text. Time is also scaled as described in the text.

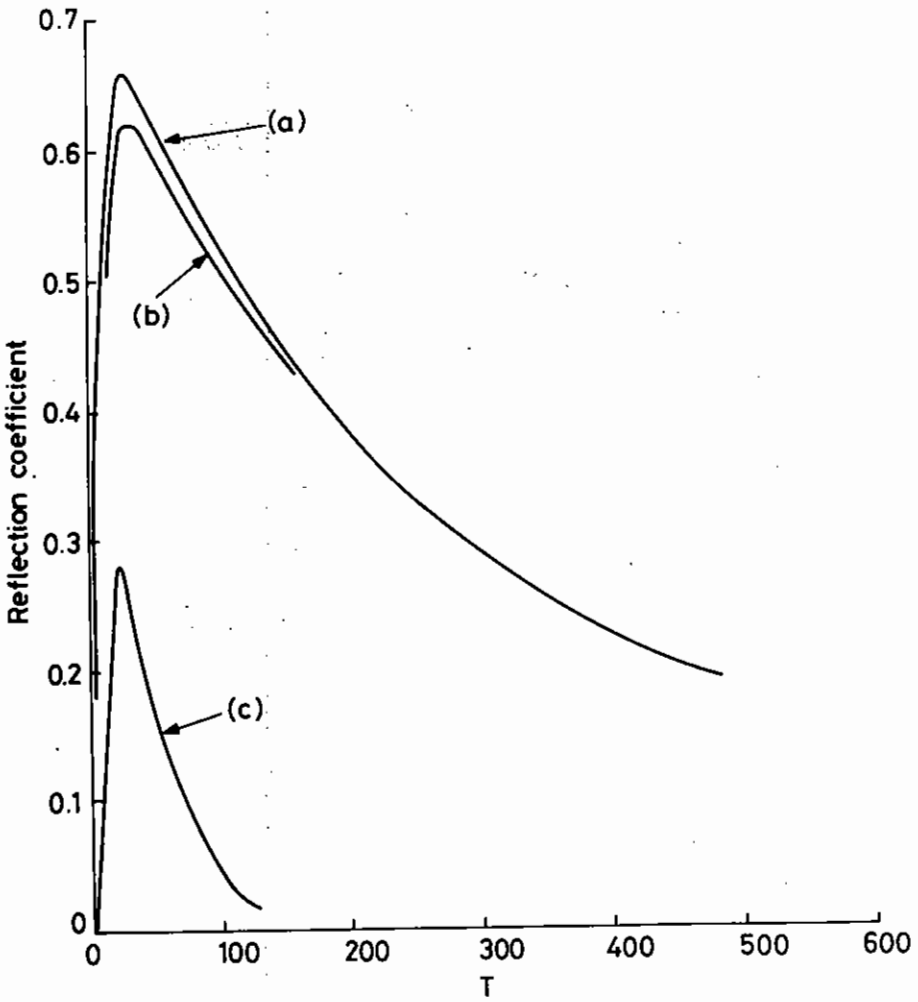

Figure 7.20 The effect on the reflection coefficient of changes in ion sound wave amplitude and temperature ratio at the boundaries. The incident intensity is 1 in all three cases and the boundary conditions are

(a) $n/n_o = 0.01$ at $X = 1$, $T_i/T_e = 0.1$ at $X = 0$,
(b) $n/n_o = 0.005$ at $X = 1$, $T_i/T_e = 0.1$ at $X = 0$,
(c) $n/n_o = 0.01$ at $X = 1$, $T_i/T_e = 0.2$ at $X = 0$.

resistance to the return cold current which is the essential limiting mechanism (cf the collisionless simulation of Evans (7.35)) since this, through quasi-neutrality, restricts the flow of hot electrons from critical surface to ablation front.

Here, a very simple model involving collisionless, hot, electrons, described by the Maxwell-Boltzmann distribution, and a collisional, cold electron fluid in a stationary, uniform ion background is solved in the steady-state, one dimensional case demonstrating substantial limitation of the energy flux. As is well-known, the free flow of the hot electrons sets up a potential which both reflects the slower, hot electrons and drives a return current of cold electrons. Each of these effects acts to reduce the net energy flux to the ablation surface.

Upon reflection a hot electron will flow back towards the critical surface with the cold electrons and in the simple model described here it is assumed that a reflected hot electron instantaneously becomes a cold electron. Reflection, therefore, is described by a hot electron sink term and an equal source term in the cold electron continuity equation. (This differs from the similar model proposed by Valeo and Bernstein (7.38), to explain fast ion generation, where hot and cold electrons retain their original identities and there are no sources or sink terms.)

Resistance to the return current is provided by the collisional interaction of the cold electrons with the stationary ions, described by a simple collision term in the cold electron momentum equation. Since, upon reflection, a hot electron has zero momentum in the direction of the ablation front there is no source term in this equation.

Taking the zero of the potential $\phi(x)$ at the critical surface ($x = 0$) and the distribution function, f_h, of the hot electrons there as the $v_x > 0$ half of the Maxwell distribution, with number density n_0 and temperature T_h, it follows that

$$f_h(x,v) = 2n_0 \left(\frac{m}{2\pi T_h} \right)^{3/2} \exp\left[-(\tfrac{1}{2}mv^2 + e\phi(x))/T_h\right] \quad (v_x > 0) \qquad (1)$$

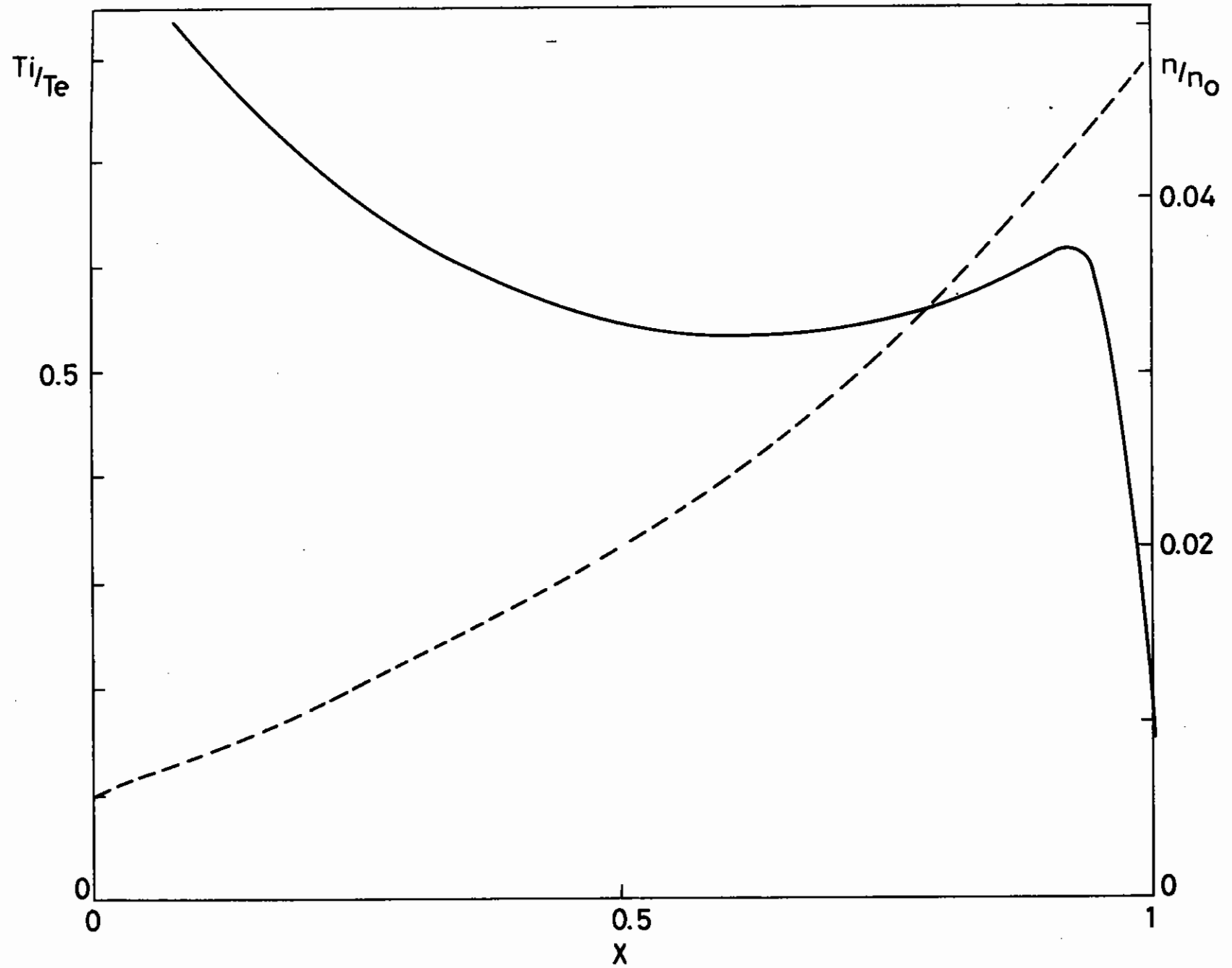

Figure 7.21 Typical ion sound wave amplitude —— and temperature ---- profiles after strong ion heating has occurred. (The case shown is with incident amplitude 1 at T = 300).

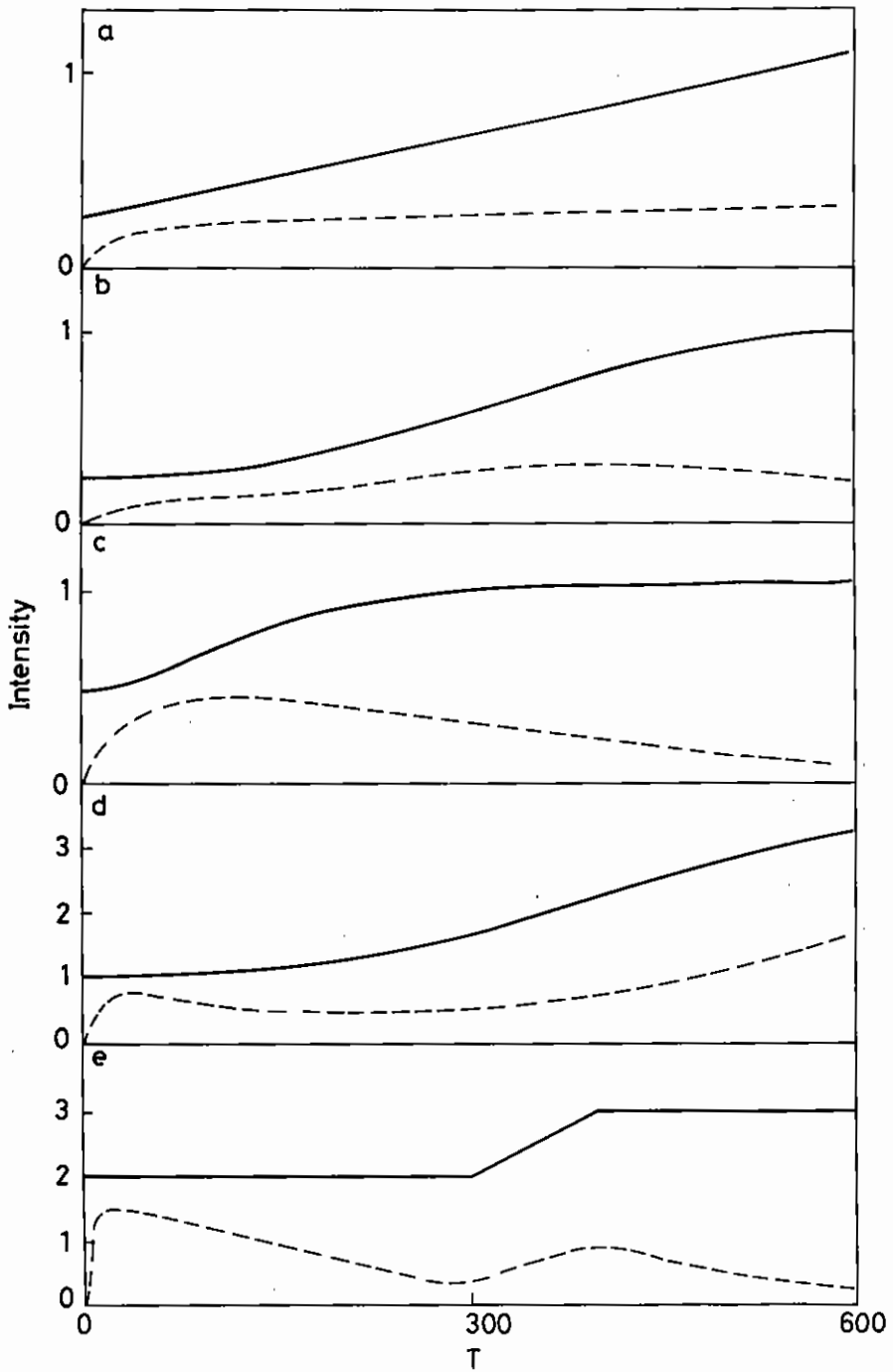

Figure 7.22 Backscattered intensities ---- for various shapes of

giving

$$n_h(x) = n_0 \exp(-e\phi(x)/T_h) \tag{2}$$

and

$$n_h(x)u_h(x) = \int_0^\infty v_x f_h d^3v = n\left(\frac{2T_h}{\pi m}\right)^{\frac{1}{2}} \exp(-e\phi(x)/T_h) \tag{3}$$

The steady-state, cold electron continuity and momentum equations are

$$\frac{d}{dx}(n_c u_c) = -\frac{d}{dx}(n_h u_h) \tag{4}$$

$$\frac{d}{dx}(n_c u_c^2) + \frac{en_c}{m}\frac{d\phi}{dx} = -\nu n_c u_c \tag{5}$$

and the quasi-neutrality condition

$$n_h + n_c = \text{const.} = N \tag{6}$$

completes the set. In these equations ν is the cold electron-ion collision frequency and all other symbols have an obvious interpretation.

Straightforward elimination of variables in equations (2) - (6) leaves a differential equation for $\phi(x)$ of the form

$$\left[\frac{2(2-y)}{\pi(1-y)^2} + \frac{1}{y} - \frac{1}{y^2}\right]\frac{dy}{dx'} = \sqrt{\frac{2}{\pi}} \tag{7}$$

in which

$$y = \alpha \exp(-\Phi)\ ,\ x' = \frac{\nu x}{v_h} = \frac{x}{\lambda_c}\sqrt{\frac{T_c}{T_h}} \tag{8}$$

where $\alpha = n_o/N$ is the initial fraction of hot electrons, $\Phi = e\phi/T_h$ is the dimensionless potential, and $v_h = (T_h/m)^{\frac{1}{2}}$. From its definition the dimensionless distance x' is measured in units of $(T_h/T_c)^{\frac{1}{2}}\lambda_c$, where λ_c is the cold electron mean free path.

Equation (7) is easily integrated giving (dropping the prime on x)

$$x\sqrt{\frac{2}{\pi}} = \frac{2}{\pi}\log\left[\frac{1-\alpha}{1-y}\right] + \frac{2(y-\alpha)}{\pi(1-\alpha)(1-y)} + \log\left[\frac{y}{\alpha}\right] + \left[\frac{\alpha-y}{\alpha y}\right] \qquad (9)$$

Since $0 < y \leq \alpha < 1$ the dominant term on the RHS of this equation is the last one; hence

$$y \approx \frac{\alpha}{1+(2/\pi)^{\frac{1}{2}}\alpha x} \qquad (10)$$

(Note that all the neglected terms in (9) are negative so that this approximation overestimates y.)

The net energy flux at distance x from the critical surface

$$q(x) = \frac{m}{2}\int v^2 v_x f_h \, d^3v + \frac{1}{2}mn_c u_c^3$$

$$= 2\sqrt{\frac{2}{\pi}}\, mn_o\, v_h^3\, e^{-\Phi}\left[1 - \frac{\alpha^2 e^{-2\Phi}}{2\pi(1-\alpha e^{-\Phi})^2}\right]$$

on using equations (1) - (4) and (6). Thus, the surviving fraction of the initial energy flux is

$$\frac{q}{q_o} = \frac{q(x)}{q(0)} = \frac{y(1-y^2/2\pi(1-y)^2)}{\alpha(1-\alpha^2/2\pi(1-\alpha)^2)} \qquad (11)$$

$$\approx \frac{y}{\alpha} = \frac{1}{1+(2/\pi)^{\frac{1}{2}}\alpha x} \qquad (12)$$

or $q/q_o = (1 + \alpha(2T_c/\pi T_h)^{\frac{1}{2}}(x/\lambda_c))^{-1}$ in dimensional variables. Here the neglected factor ≥ 1 so that this second approximation underestimates q/q_o. Rather fortuitously, these two systematic errors cancel each other to a remarkable degree so that equation (12) represents the correct q/q_o to within a few per cent over almost the whole range of α and x (at least up to several hundred mean free paths).
The exact q/q_o, obtained by substituting the exact solution of y(x) from (9) in (11), is shown in Figure 7.23 for several values of α, the initial fraction of hot electrons. All cases show a rapid decrease of the energy flux with x. For larger values of α this reduction is significant within tens of mean free paths and down to < 10 % within about a hundred mean free paths (assuming $T_h \sim 10\ T_c$).

It is perhaps worth pointing out, also, that

$$q_o = 2\sqrt{\frac{2}{\pi}}\, mNv_h^3 \quad \alpha(1-\alpha^2/2\pi(1-\alpha)^2)$$

a function which requires $\alpha \leq (2\pi)^{\frac{1}{2}}/(1 + (2\pi)^{\frac{1}{2}}) \approx 0.71$ for $q_o \geq 0$ and which takes its maximum value at $\alpha \approx 0.52$. However a more severe restriction on α arises from the behaviour of the differential equation (7). The coefficient of $\frac{dy}{dx}$, vanishes if $y \approx 0.43$ and only if α, the initial value of y, is less than this is a physically realistic solution, where Φ increases with x, obtained.

The error incurred in using the approximate analytic formula (12) is greatest for relatively large α and small x and is indicated for $\alpha = 0.4$ by the dashed curve. Even in this case it is everywhere < 20 % and < 10 % for $x \geq 15$.

From equation (10) it follows that the potential function has an approximately logarithmic dependence

$$\frac{e\phi(x)}{T_h} = \log[1 + \alpha(2T_c/\pi T_h)^{\frac{1}{2}}(x/\lambda_c)]$$

where we have again reverted to dimensional variables. It is the establishment of this potential, which slows down and reflects the hot electrons, in response to the cold current resistance which is essential in energy flux limitation. For example, in the above approximation $\phi \to 0$ as $\lambda_c \to \infty$ and, although quasi-neutrality ensures a return flux, a collisionless model does not result in significant flux limitation (7.35).

This simple model will be made somewhat more realistic by allowing for finite T_c. It is anticipated that this will further reduce the energy flux since the pressure term in the momentum equation will also act to resist the cold return current thus augmenting the potential $\phi(x)$. In addition, the residual kinetic energy of a reflected hot electron (which, in the model described here, simply disappears) will become a source of

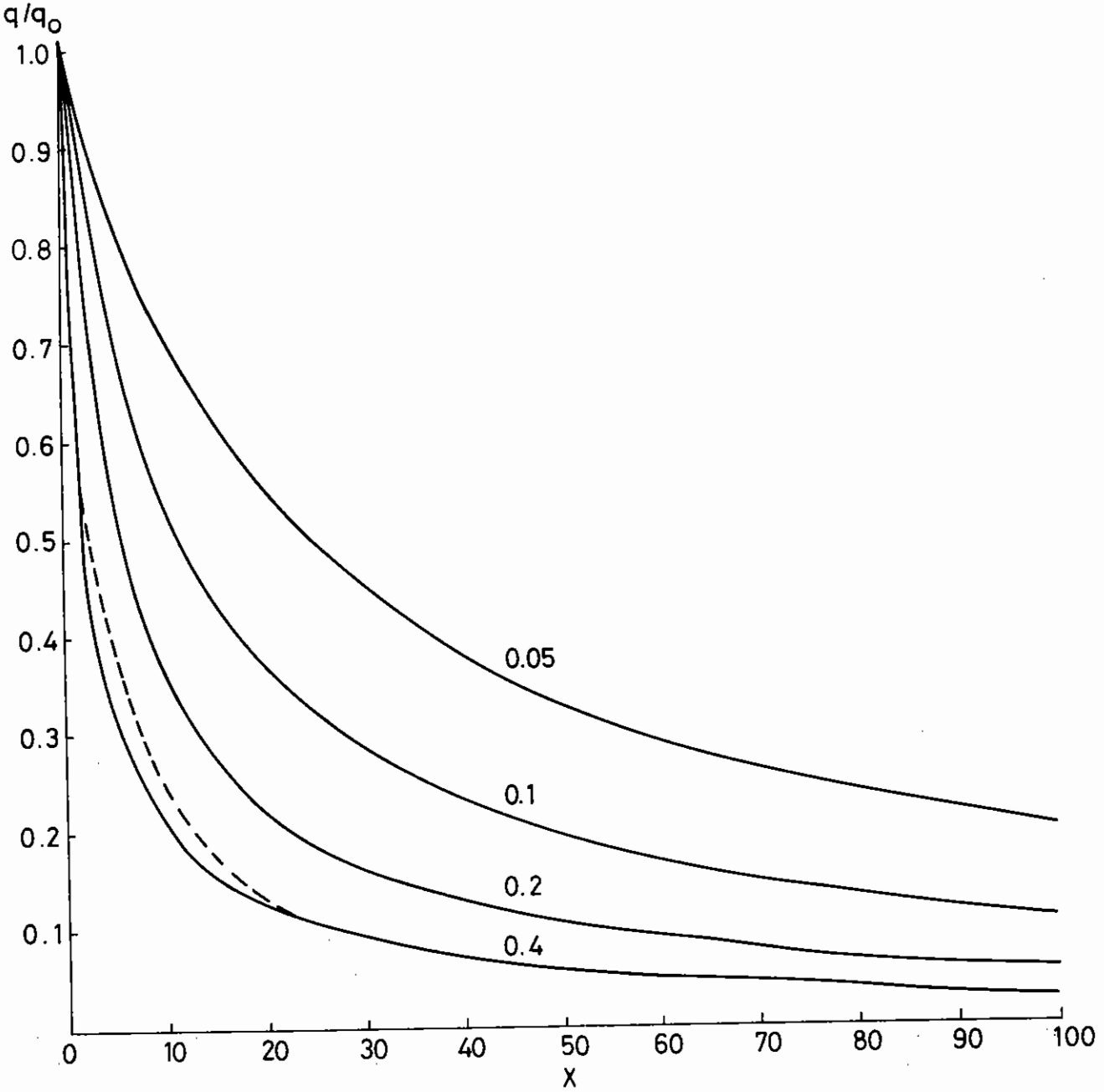

Figure 7.23 The solid curves show the fraction of the initial energy flux $q(x)/q_o$ as a function of x (measured in units of $\lambda_c(T_h/T_c)^{\frac{1}{2}}$) for various values of α, the initial fraction of hot electrons. For α = 0.4 the departure of the analytic solution, given by equation (12), from the exact solution is indicated by the dashed curve.

cold electron energy, thereby increasing the return energy flux.

R A Cairns and J J Sanderson (St Andrews)

7.4.2 Fokker-Planck Calculations of Thermal Transport

It was reported in the 1980 Annual Report to the Laser Facility Committee that the problem of thermal flux inhibition was being studied by numerical solution of the Fokker-Planck equation. Since that time the computer code has been fully tested, and the results have shown that the explanation of flux inhibition may indeed lie in correct evaluation of the heat flow down steep temperature gradients as determined by electron-electron and electron-ion collisions.

The program was tested as a complete unit by simulating three physical problems which have been solved elsewhere:

(a) The decay of Langmuir waves by Landau damping was simulated by switching off the collision terms. The computed oscillation period agreed with the expected value to within 0.2 %, and the decay rates agreed to an accuracy of 3 %.

(b) The relaxation of an isotropic non-Maxwellian distribution was compared with a numerical solution given by Dolinsky (7.39), and found to be in good agreement.

(c) The program was initialised to model very gentle temperature gradients and the conductivity calculated by Spitzer and Harm (7.40) in the limit of a small heat flow was reproduced to an accuracy of 10 %.

The heat flow down a steep temperature gradient was investigated by simulating a slab of plasma with $Z = 4$ which is initially uniform in temperature and density, but is quickly heated near one boundary to four times its initial temperature. The heated region of the plasma is supplied sufficient heat thereafter to maintain this temperature. Figure

7.24 is a graph of the spatial distribution of temperature $\langle v^2 \rangle$ and heat flow $\langle v^2 v_x \rangle$ at successive times. Time is in units of ω_{pe}^{-1} and distance in units of λ_D. The plasma is heated in the region $x < 350$. In dimensionless units the scattering time for an electron with velocity v is approximately $t_s(v) = 10.5\ v^3$. The high temperature extends progressively further into the unheated plasma as energy is conducted away from the heated region by heated electrons.

Figure 7.25 represents an attempt to reduce the data from the simulation in a meaningful way. It is a plot of heat flow Q divided by the 'free-streaming limit' $Q_f = nkT(kT/m)^{\frac{1}{2}}$ against the scalelength of the temperature gradient $L = T/\nabla T$ divided by the mean free path λ of an electron with energy $\frac{3}{2}kT$. All quantities (Q, Q_f, L and λ) are defined locally and each point on the plot represents a different place on the temperature distribution at one of the two times for which the points are plotted. There is one data point for each spatial grid-point. The Spitzer-Harm theory, valid for small temperature gradients, gives the relation $Q/Q_f = 3.64\ \lambda/L$, so a comparable plot in that case would show all points lying on the straight line indicated. Clearly, the situation is much more complicated in the steep temperature case since a single-valued function cannot be fitted to the points. Q/Q_f can take widely differing values for similar L/λ. This is because the heat flow at any point is no longer defined by the local plasma conditions. Most of the energy is carried by a small number of electrons on the tail of the velocity distribution, and since the electron mean free path is approximately proportional to v^4 these electrons are nearly collisionless and can cross the heat front without collision thus making the energy flow at any point dependent on what is happening elsewhere on the heat front.

The points in Figure 7.25 can be read from the bottom right where they relate to the hot end of the grid, following the line of points to the top left, corresponding to the top of the heat front, and then back to the right along the upper curves where they correspond to data at the bottom of the heat front at large x. The leftmost point always corresponds to the first grid-point immediately to the right of the heated region. Defined in this way, the thermal conductivity at the base of the heat

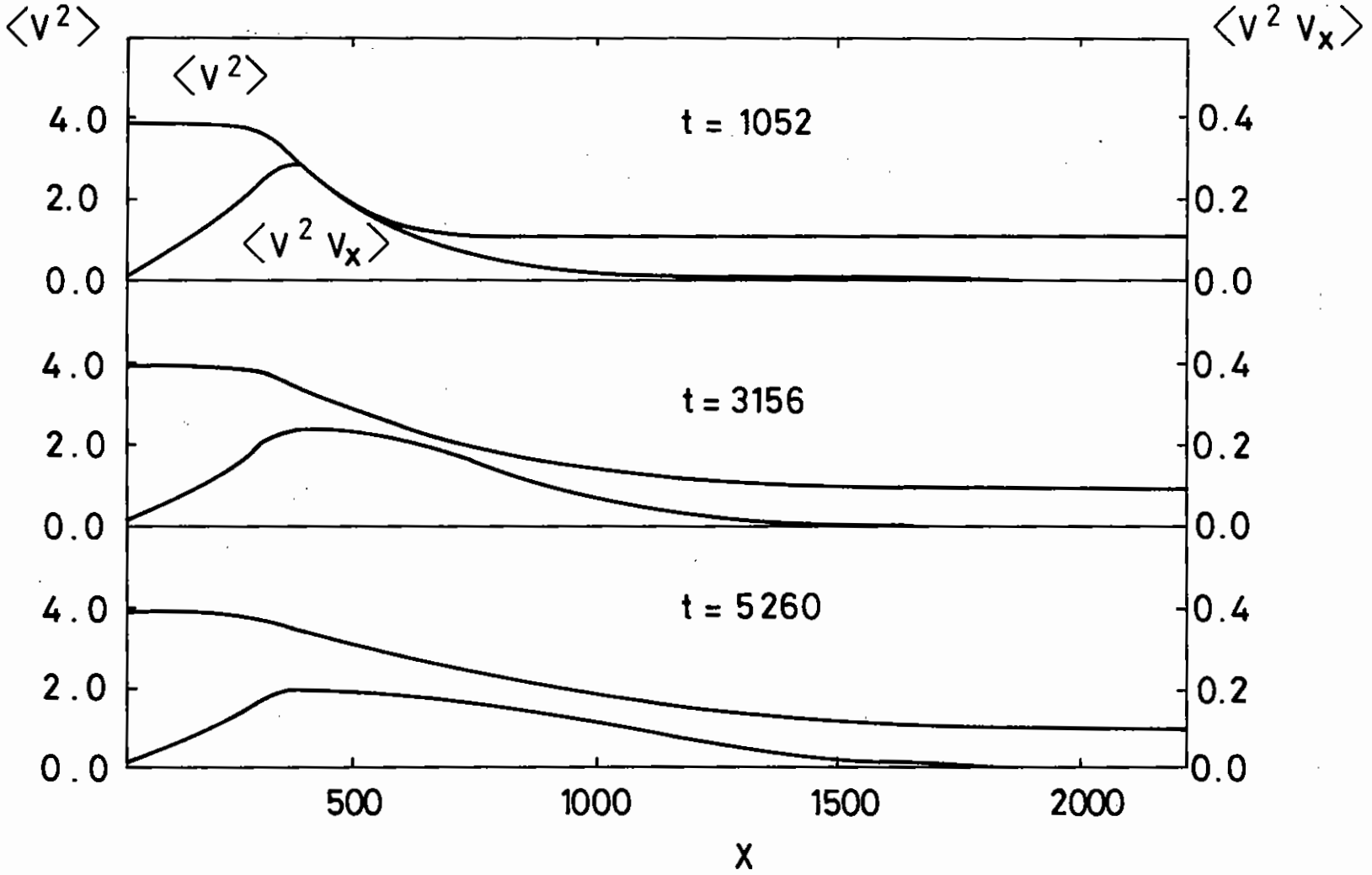

Figure 7.24 Plots of $\langle v^2 \rangle$ (temperature) and $\langle v^2 v_x \rangle$ (heat flow) as functions of x at times t=1052, 3156, and 5260. The plasma is heated in the region x<350.

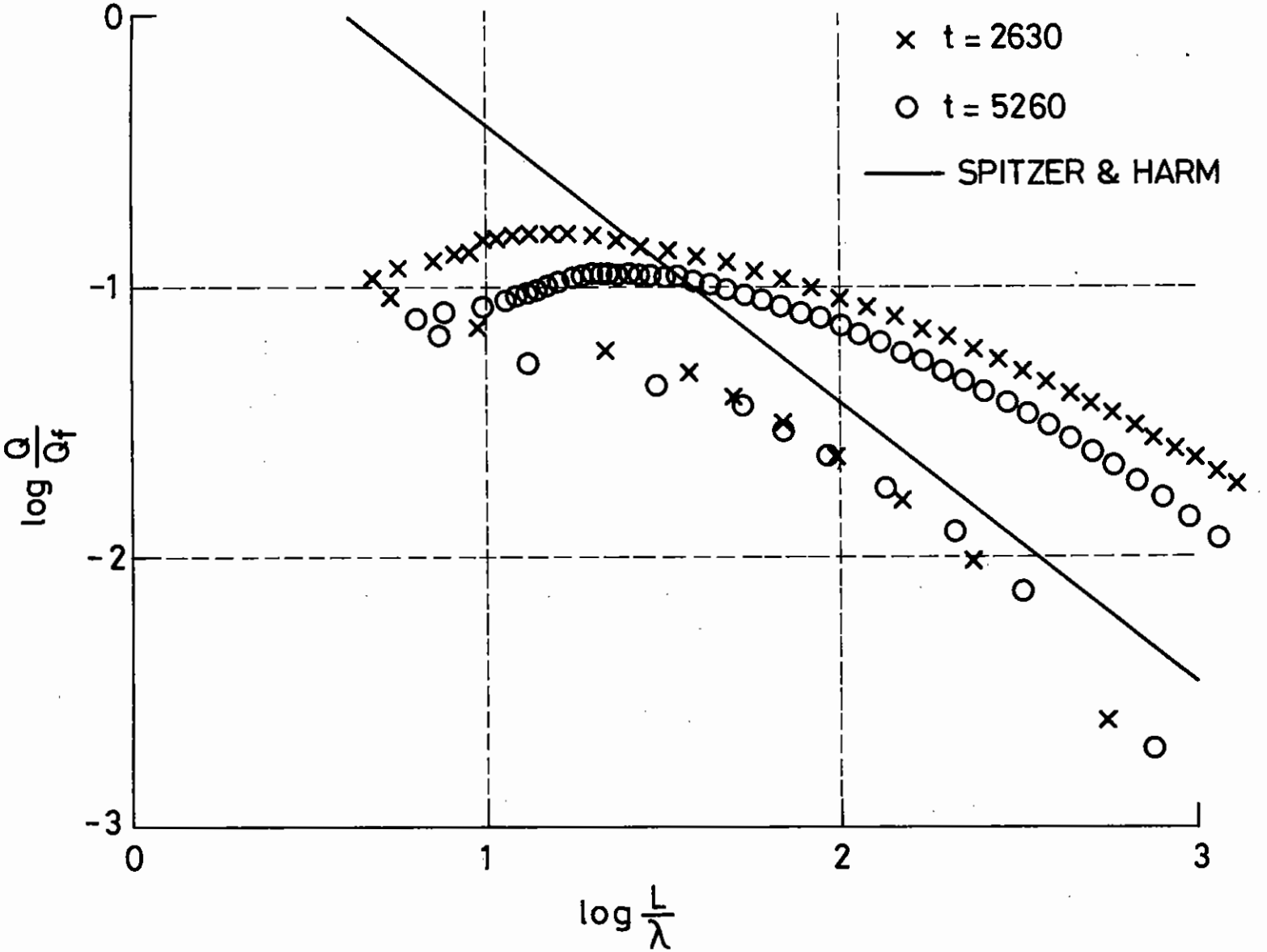

Figure 7.25 Plot of heat flow Q against inverse temperature gradient. $Q_f = nkT(kT/m)^{\frac{1}{2}}$, λ = mean free path of an electron with energy (3/2)kT, L=T/(dT/dx). All quantities are defined locally. The solid line gives the Spitzer-Harm conductivity for Z=4.

front exceeds the Spitzer-Harm conductivity. The large heat flow there is carried by hot, nearly collisionless, electrons streaming away from the top of the heat front while the free-streaming limit is determined by the initial population of unheated electrons. On the other hand, the values of Q/Q_f in the heated region (the lower line of points) are much lower than at the base of the front for similar values of L/λ. However, it is the heat flow on the main body of the heat front which determines its overall progress into the plasma, and this is given by the first few points on the left of Figure 7.25. The heat flow there is an order of magnitude less than the free-streaming limit. Hence we have evidence of 'flux inhibition' when the scale length of the temperature gradient is a few times the electron mean free path.

The reason for the low thermal conductivity becomes clear if we consider the velocity distribution calculated by Spitzer and Harm (7.40) which take the form $f(v,x,\theta) = f_o(v,x) + f_1(v,x) \cos\theta$. the heat flow is mainly carried by a small number of electrons on the tail of the Maxwellian distribution. As pointed out by Gray and Kilkenny (7.41) f_1/f_o exceeds unity at velocities for which the energy flux is large when λ/L is of the order of 0.01, and the linearised theory breaks down since f_1 is then negative. Figure 7.26 plots the ratio f_1/f_o as given by the simulation when t = 5260 at the point immediately to the right of the heated region where the heat flow is largest. f_1/f_o as given by the Spitzer-Harm theory is plotted for comparison and two major differences are apparent: (a) the simulation curve does not rise to values much larger than unity, (b) since f_1 is much lower at high velocities in the simulation, f_1 need not take such large negative values at low velocities to provide the return current. The limitation of f_1/f_o to around unity reduces the large heat flow which peaks at velocities around $4(kT/m)^{\frac{1}{2}}$ in the Spitzer-Harm theory thus reducing the overall heat flow by an order of magnitude.

The results indicate that flux inhibition may be a natural consequence of the Fokker-Planck theory. However, it has become apparent that there is no unique upper limit to the heat flow and we cannot derive a relationship between Q/Q_f and L/λ. The problem is non-local with the heat flow

depending on the plasma state over the whole of the heat front. This has a number of consequences:

(a) To derive results which are applicable to laser-plasma experiments we must include such features as density gradients and fluid flow.

(b) Hydrodynamic simulations of laser-plasmas calculate the heat flow from local plasma properties and it is difficult to reduce data from the Fokker-Planck simulation to provide meaningful parameters for a fluid code.

(c) The temperature profile calculated by a fluid code may not match that given by the more accurate Fokker-Planck treatment (7.42) and this may affect quantities such as the density profile, ablation velocity and driving pressure.

It appears that detailed evaluation of the Fokker-Planck account of flux inhibition requires solution of the self-consistent problem in which ion motions are determined by their interaction with an electron distribution treated by the Fokker-Planck theory and the resulting density and flow profiles then influence the electron distribution.

With these points in mind the simulation program has recently been developed further to include ion motions. The ions are treated as an adiabatic fluid, and thermal energy exchange between electrons and ions is ignored at present. Momentum transfer between electrons and ions is mediated both by collisions and by the electric field. The program can accommodate spatial grid-points at non-uniform intervals. The grid-points move with the ion fluid, and the electron distribution is calculated in the local ion rest frame. The program is being used to model the disassembly of a foil which is heated at subcritical densities by electron transport. Further program tests are needed before we can place confidence in the results.

A R Bell, R G Evans and D J Nicholas (RAL)

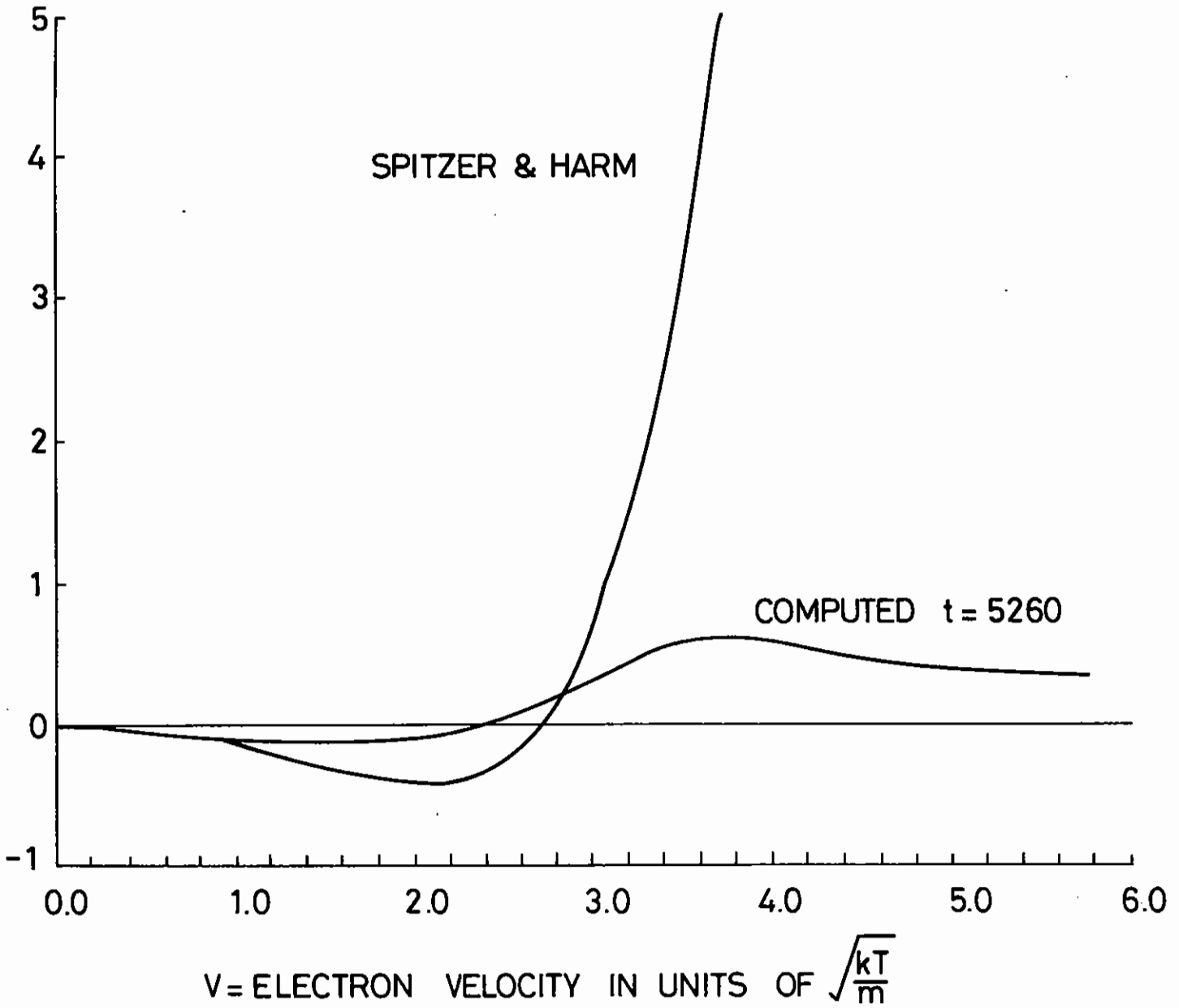

Figure 7.26 Comparison of the computed f_1/f_o with the curve given by Spitzer and Harm for the same temperature gradient. The distribution is plotted at time t=5260 and at the position immediately to the right of the heated region where the heat flow is at its maximum.

7.4.3 Nonlinear Thermal Transport

Two approaches are being employed to study the steady state heat flow in a plasma in the presence of a large temperature gradient.

(a) A method used by Lees (7.43) in gas dynamics has been applied to a plasma. Results with a simple Krook collision term have been derived (7.44). The method has now been extended to use a Fokker-Planck collision term. The dependence of the results on the choice of moment equations is being studied.

(b) Numerical calculations are being performed using a discrete ordinate code. The direction and energy meshes are chosen so that the motion of collisionless particles can be followed without need for redistribution. The linear characteristic method (7.45) is used for the spatial integration. A number of methods for accelerating the inner-iteration are being explored (7.46).

D J Bond and H Kho (Imp Coll)

7.4.4 Heat Flow Instability

Two models of instabilities arising from heat flow have been studied.

In the first, a homogeneous plasma in which heat flow is modelled as a current of hot relatively collisionless electrons balanced by an equal and opposite current of cold collisional electrons. It is shown that an electrothermal instability can be induced in the cold resistive plasma when the heat flow exceeds about 3 % of the free-streaming limit. This is non-convective if the cold plasma T is less than $0.2\ n_e^{\frac{1}{4}} Z^{\frac{1}{2}}\ ^0K$ (n_e m^{-3}). The hot and cold return currents are perturbed differently leading to a spatially oscillating net current with an associated magnetic field while inclusion of ion motion leads to density perturbations. For laser fusion conditions growth occurs on the ps time-scale and the optimum wavelength is about 10 μm. The instability could lead to filamentary structures in the ablation plasma, and also could have a deleterious effect on implosion

symmetry.

In the second model equilibrium temperature and density gradients are introduced but a linear tensor transport theory of Braginskii is employed which is probably only valid for low values of heat flow. Plasma flow and unequal electron and ion temperatures have been included. It is found that the simple criterion $\nabla n_0 . \nabla T_0 > 0$ for instability given by Tidman and Shanny (7.47) is modified by the inclusion of the thermoelectric term $\underline{\alpha} . \nabla T$ and ion motion or density perturbations. Similar but incomplete models have been published by Dolginov and Urpin (7.48) and Ogasawar et al (7.49). It is possible for the instability to grow with equilibrium temperature gradients only, and also if these are steep when $\nabla n_0 . \nabla T_0 < 0$.

M G Haines and E M Epperlein (Imp Coll)

7.4.5 Treatment of Radiation Transport in Laser-compression Simulations

We summarize the work done at Glasgow in collaboration with the Laser Division, Rutherford Laboratory, in the field of laser-plasma simulations during the past year. Our main interest was the numerical modelling of radiation transport in laser-produced plasmas. Our steady state, single temperature radiation diffusion model which we incorporated into MEDUSA previously (7.50) treats the electrons as a classical system. This model is valid for exploding pusher type of targets in which the final densities are low while the temperatures are very high. We have used this model to study the radiative preheat problem in targets of the above type, specifically thin glass microballoons filled with neon. Results are discussed in (7.51). In case of ablatively driven targets, on the other hand, we expect that the final target densities will be very high and the final temperatures relatively low. An appropriate equation of state is therefore required for the electrons in this case.

At present, we are incorporating our single temperature radiation physics package into the Rutherford Laboratory updated version of MEDUSA (7.52). This version of the code contains a corrected Thomas-Fermi equation of

state for the electrons and can therefore accurately model the ablative compression. It also contains suprathermal electron transport and it will thus allow a study of the relative importance of radiation and suprathermal transport in different types of target. This new package should be ready shortly.

Our steady state single temperature radiation model mentioned above is valid only in the optically thick core and is not applicable in the optically thin corona of the laser-target. In the latter case the radiation field cannot be described by a Planckian distribution but may be accurately represented by a multigroup scheme. In this scheme each group is assigned a temperature T_m and interacts with the electrons as a function of the local temperature difference $(T_e - T_m)$, where T_e is the electron temperature and m is the group number. The set of energy transport equations for the ions, electrons and various radiation groups must be solved numerically for their respective temperatures. The use of Gauss's elimination technique is not suitable in this case for two reasons. Firstly, in this model we have the order of twenty simultaneous differential equations to solve. If each of these equations were treated individually, it would involve a prohibitive amount of computer time. Secondly, the electron energy equation contains a large number of energy exchange terms. This equation therefore should be treated by a time splitting method which is inefficient as well as inaccurate. We propose instead to develop a numerical model to solve the electron energy equation together with the set of radiation energy equations in effect as a diffusion problem in the radial coordinate r and the energy variable E. Diffusion in real space will be treated by a flux limited transport model while diffusion in energy space will take place via electron-radiation energy exchange terms.

The efficiency of this package will be greatly enhanced by the use of ICCG numerical techniques (7.53). The ion energy equation will be treated separately using Gauss's elimination method. We shall develop this numerical package according to the Olympus format (7.54) so that it could be run as a self sufficient transport code. We shall incorporate this code into MEDUSA (7.55) to simulate radiative preheat effects in laser-compression experiments at the Central Laser Facility, Rutherford

Laboratory. The model is also relevant to heavy ion fusion studies. Details of this package are outlined in (7.56).

N A Tahir, E W Laing (Glasgow) and D J Nicholas (RAL)

7.4.6 Simulation of X-ray Line Emission Spectra from Laser Compressed Plasma

The analysis of x-ray line emission spectra has proved to be a powerful tool in the diagnosis of laser compressed plasmas (7.57). In the analysis of the time-integrated, space-integrated recorded spectra the plasma has been taken to be spatially homogeneous and the temperature and density were assumed to be constant during the time of emission; without these simplifications prohibitively long computer time would have been needed. A fuller calculation, however, is needed to clarify the validity of these simplifications, and is further motivated by the development of experiments recording time-resolved spectra (7.58). In the calculation reported here both spatial inhomogenity and time-evolution were taken into account.

The 1D hydrodynamics code MEDUSA was used to simulate the implosion of a glass balloon filled with neon, and the hydrodynamics data were used as an input into the radiation transport calculation. In a typical calculation, the radius of the balloon was taken as 100 μm, the thickness of the glass was 1 μm, and its density 2.5 g cm^{-3}. The initial density of the neon gas was taken to be 0.01 g cm^{-3}. The laser pulse was assumed to have a Gaussian shape with peak intensity of 10^{15} W cm^{-2}, and full width at half height of 60 ps. The peak density of the neon core was found to be 0.3 g cm^{-3} with temperatures of about 1 keV. In Figures (7.27) and (7.28) the electron temperature and density, respectively, of the 'middle' cell of neon are described as a function of time.

The radiation code employed (7.59), uses detailed line profiles. The radiation transport equation is solved, in the method developed by Hummer (7.60), along rays tangential to spherical shells at which plasma quantities are defined (by the hydrodynamics code). The population of

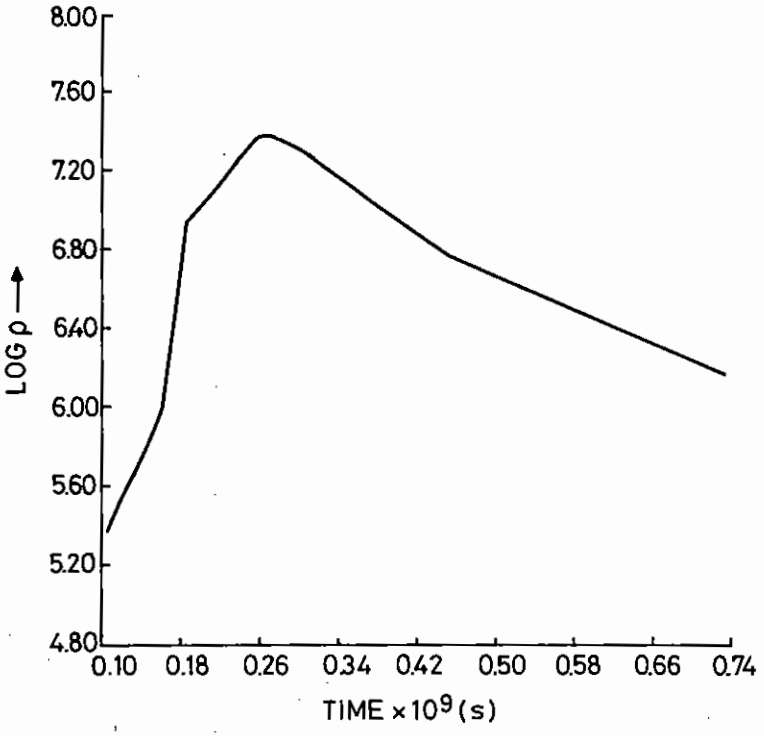

Figure 7.27 Log electron temperature vs time.

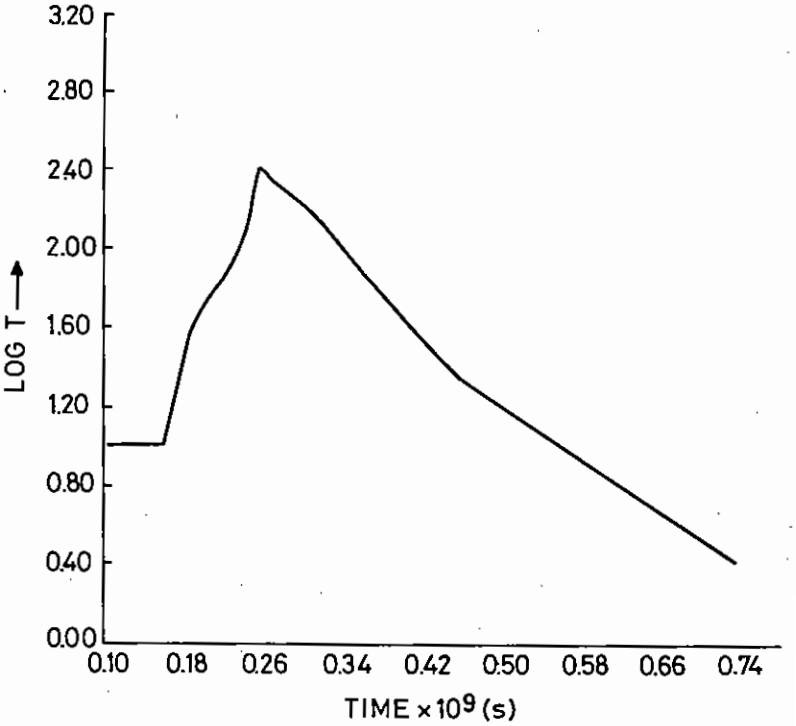

Figure 7.28 Log mass density vs time.

levels of hydrogen-like, helium-like, and lower ionisation stages (only the ground states for the latter), were assumed to obey steady state rate equations. The radiation transport and rate equations were solved consistently in an iterative method. The computer time needed by the radiation code to calculate the radiation field at a single hydrodynamics timestep equals the total computer-time needed for the simulation of the implosion by MEDUSA. It was, therefore, impracticable to apply the radiation code for each timestep and the following procedure was developed. The level populations, source functions and opacities were calculated at each timestep in a zeroth iteration whereby the reaction of the radiation field on the level population was neglected. The number density of ions in some levels is plotted as a function of hydrodynamics timestep number in Figure 7.29. These results were used to indicate the timesteps during which appreciable emission of hydrogen-like and helium-like lines takes place, and more particularly, where the emission intensity changes quickly with time.

The spectrum was calculated for a limited number of points, solving the full equations (with population of levels consistent with the radiation field). The points were selected to reflect the salient features of the implosion (cf Figures 7.27 and 7.28), and the zeroth order results (Figure 7.29), as explained. The time integrated spectrum is obtained simply by summing up the calculated spectra. Two examples of calculated spectra are shown in Figures 7.30 and 7.31. For Figure 7.30, t = 207 ps, for Figure 7.31 t = 278 ps, and the intensity is plotted for radiation emerging in the radial direction (for comparison with an experimental setup, integration over the relevent solid angle may be carried out). Figure 7.31 is for the time of maximum intensity of the Lyman α line (essentially, the time of maximum compression). A feature of the results is that the intensities of all lines do not evolve identically with time. This may have diagnostic potential in time-resolved experiments. As a first order check on the validity of time-independent simulations, let us introduce an 'effective' electron number density for a given spectral line

$$\langle n_e \rangle_\ell \equiv \int n_e(t) I_\ell(t) dt / \int I_\ell(t) dt$$

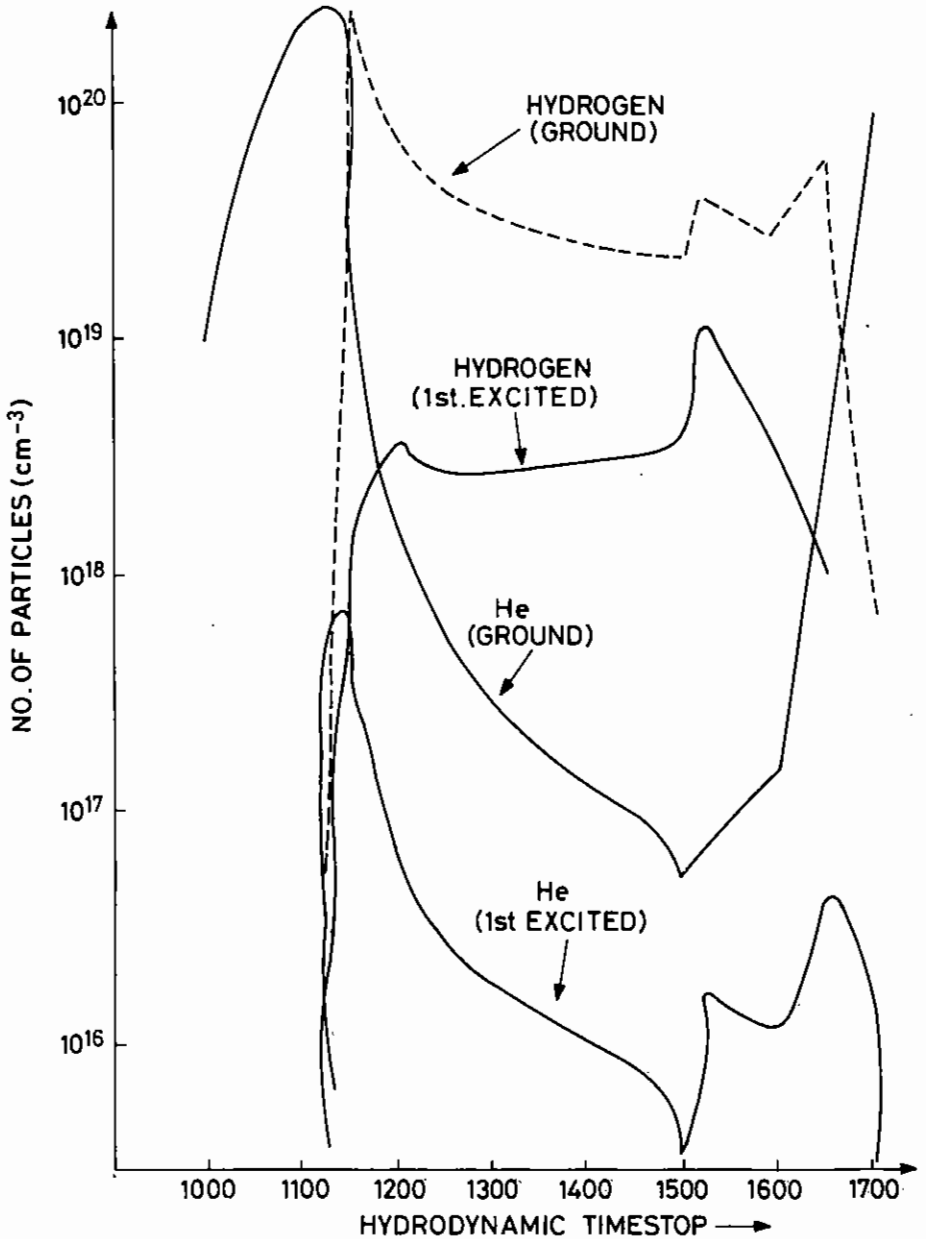

Figure 7.29 Population of levels (number/ cm^3) vs hydrodynamic time step.

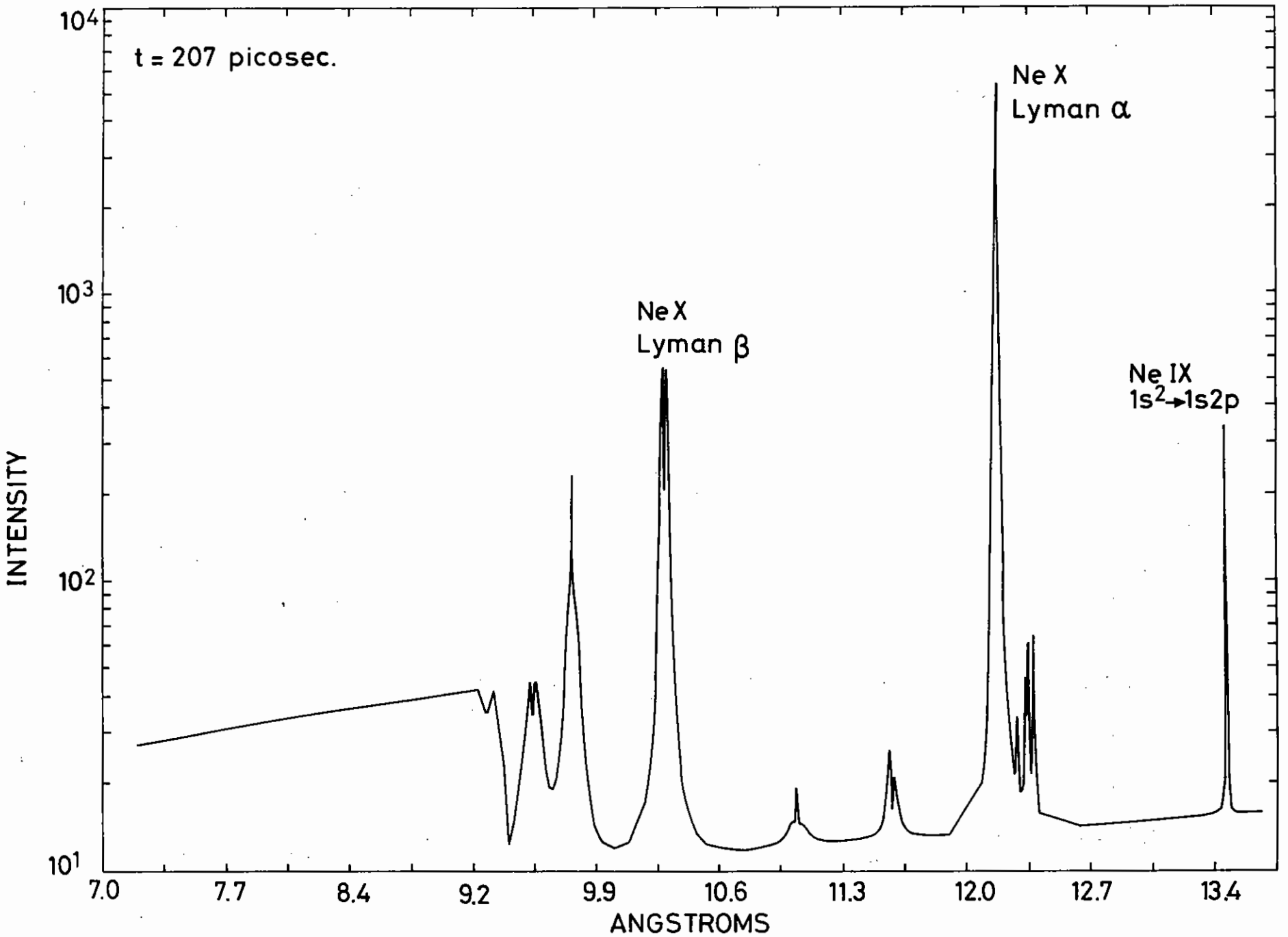

Figure 7.30 Spectrum at t = 207 picoseconds (hydrodynamic time step = 1300).

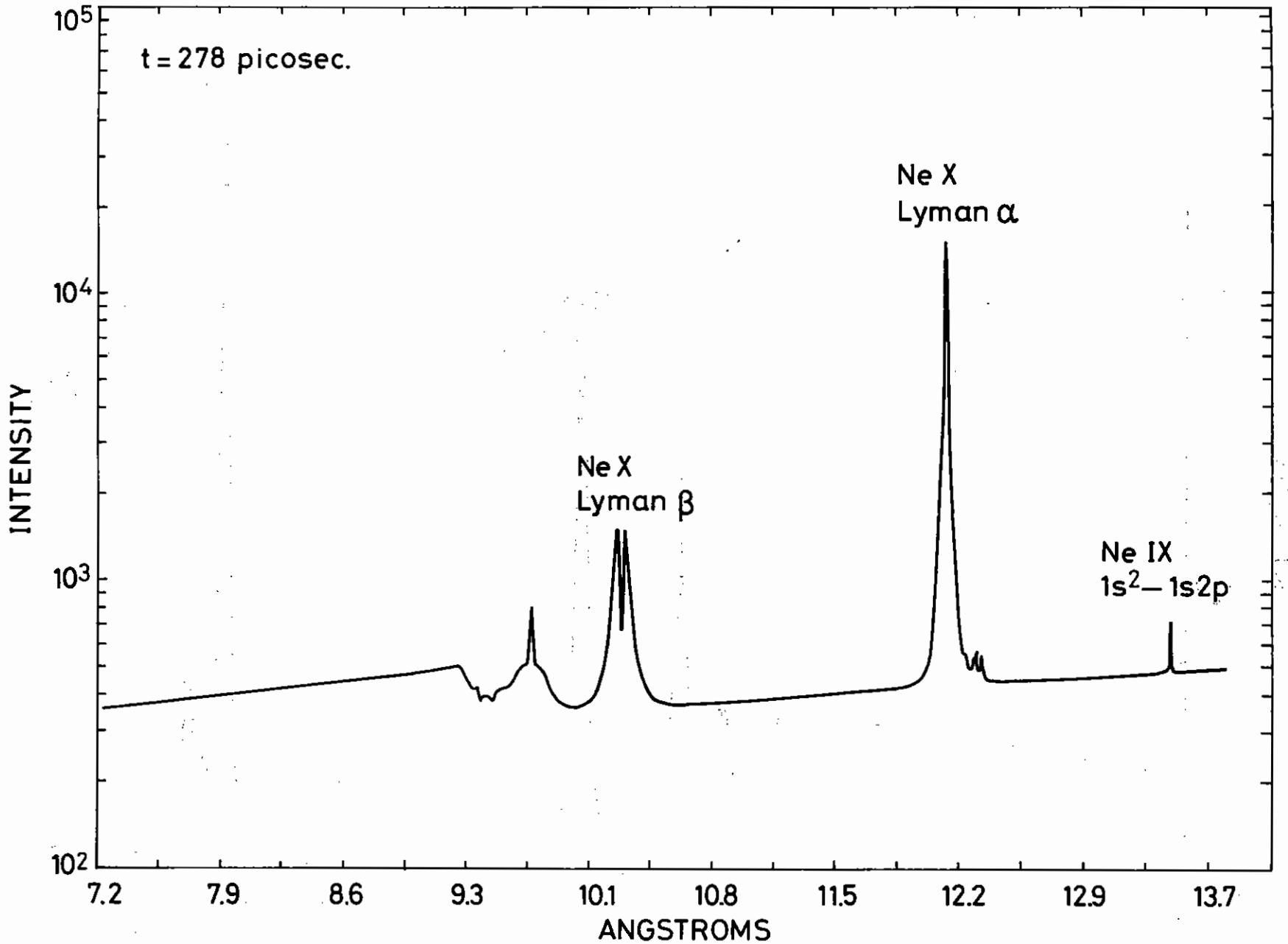

Figure 7.31 Spectrum at t = 287 picoseconds (hydrodynamic time step = 1520).

where $I_\ell(t)$ is the intensity of the line at time t, and similarly for electron temperature

$$\langle T_e \rangle_\ell \equiv \int T_e(t) I_\ell(t) dt / \int I_\ell(t) dt$$

Then, for Lyman α, Lyman β, and helium-like line ($1S^2 \leftarrow 1S2p$) the following is obtained

$$\langle n_e \rangle_\ell \simeq 6 \times 10^{22}/cm^3, \langle T_e \rangle_\ell \simeq 1.4 \times 10^7$$

while for Lyman δ, and helium-like ($1S^2 \leftarrow 1S3p$)

$$\langle n_e \rangle_\ell \simeq 8 \times 10^{22}/cm^3, \langle T_e \rangle_\ell \simeq 1.8 \times 10^7$$

The difference in these numbers is easily understood as the more highly excited levels are populated at higher points of the adiabat. The difference between the two pairs of numbers is smaller than the uncertainty in the fit of calculated and experimental spectra. This difference, however, contributes to a systematic error. Furthermore, the fine details of an experimental spectrum cannot be reproduced by simulated spectrum characterised by a single value of density and temperature.

The reported calculation have, in addition, supplied a wealth of information which may be useful in outlining the range of applicability of various models to laser compressed plasmas. One example is the data on the deviation of level populations from the LTE and coronal model approximations.

The results for line-radiation energy losses indicate that they are not completely negligible. Interactive radiation-hydrodynamics calculations, however, require exceedingly longer computer time.

A Shalom (Imp Coll)

7.4.7 Fast Electron Transport

Existing codes (7.61) have been used to study the effect of the density structure on the resistive inhibition of fast electrons by lower density gold targets. This is more fully described in section 4.2.

D J Bond (Imp Coll)

7.4.8 Ion Emission

Further work on ion emission has continued over the past year. The Lagrangian, hydrodynamic, plasma expansion code of Crow et al (7.62) has been adapted to incorporated both hot and cold electron populations with temperatures of T_h and T_c respectively. The main interest here is to incorporate space charge effects in the analysis of the localised singularities in the electric field that occur in the expansion of a quasineutral source plasma if $T_h/T_c > 5 + \sqrt{24}$ (Wickens et al (7.63), Bezzerides et al (7.64), Wickens and Allen (7.65)). Some modifications to the code are necessary to obtain convergence in the region of these large electric fields. In parallel with this computational study of the predicted singularities in the electric field an analytic investigation is underway using a two-electron-temperature version of the Korteneg de-Vries equation. This enables the time dependent nature of the plasma behaviour in the vicinity of the electric field singularity to be combined with space charge effects.

L M Wickens and J E Allen (Oxford)

7.5.1 Heavy Ion Fusion Target Studies

The HIF target studies programme is a collaborative effort between the Universities of Birmingham and Glasgow and the Rutherford and Appleton Laboratories. A Boltzmann equation treatment of radiation transport for bound-free and free-free processes is now fully working in conjunction with the one-dimensional Lagrangian hydrodynamics code MEDUSA. The code works in an arbitrary number of photon energy groups and can fully treat

any degree of anisotropy of the photon fluxes. Modelling of dE/dx for the ion-plasma interactions allows for variations of the density and temperature of the plasma and the effective charge state of the beam ion. Where measurements are available, good agreement with the theory is obtained.

A whole range of multi-layered target designs for various pulse shapes can now be routinely modelled, indicating that gains of 30-50 for about 5 mJ input should be obtainable. Significant progress has been made in developing computational techniques for charged particle transport in hot dense plasmas and work has started on a numerical study of time-dependent ionization and recombination rates in multi-level atoms in plasmas. Preliminary studies have been made on the numerical stability of a two-dimensional hydrodynamics code with the eventual aim of studying the effects of beam asymmetries on spherical targets. Nothing has been found which in any way questions the scientific feasibility of heavy-ion driven targets.

T D Beynon (Birmingham Univ)

7.5.2 Simulations of Ion Beam Heated Targets

The concept of intertial confinement fusion (7.66) requires that a hollow shell containing the Deuterium Tritium fuel be rapidly imploded by the absorption of energy from a laser or ion beam (7.67) driver. In order for the imploded fuel to reach the temperature needed to initiate thermonuclear reactions the velocity of implosion should be about 2×10^7 cm/s, and a density of about 200 g cm^{-3} is needed to obtain a reasonable fractional "burn" of fuel.

The ratio of the shell thickness Δr to its radius r_o is restricted by high driver power requirements for small values of $r_o/\Delta r$, and by possible hydrodynamic stability and symmetry requirements (7.68) for large values of $r_o/\Delta r$. Current target designs typically have $r_o/\Delta r$ in the range of 10 to 30.

We present here a set of numerical simulations of ion beam heated targets, with the intention of extracting the basic physical features of the targets, rather than attempting to optimise the gain.

The numerical simulations are performed using an improved version of the MEDUSA code which is fully described elsewhere (7.69, 7.70). The code assumes spherical symmetry, and calculates the heating, thermal transport and hydrodynamic motion of the target. A major omission in the code is an adequate treatment of the emission and transport of thermal radiation (ie soft X-rays) within the target. The ways in which this omission modifies the target behaviour will be described later.

Since the physical mechanisms of charged particle energy loss in hot dense plasma are incompletely understood we describe the ion beams by two parameters, namely the total range R g cm^{-2} and a "shape" parameter N which determines the form of the energy-loss relation for particles of initial energy E_o

$$\frac{1}{\rho E_o}\ \frac{dE}{dx} = \frac{N}{R}\left(\frac{E}{E_o}\right)^{\frac{N-1}{N}}$$

Putting N = ½ gives the classical Bragg peak at the end of the range and putting N = 1 makes dE/dx independent of E. The form N = ½ will be referred to as "light ions" and the case N = 1 as "heavy ions" since the accumulation of electrons by the heavy ions as they slow down will tend to eliminate the Bragg peak (7.71).

In order to illustrate the particle energies which are of interest a very approximate relationship between range and energy for protons and for ions of U^{238} is given in Table 7.01.

For the case of protons of 1 MeV energy the momentum of the beam ions begins to be important, as well as their energy, and would lead to an increase in the generated pressure by about 10 %. For the other cases the momentum of the beam ions is not significant and it has not been included in these simulations.

Table 7.01

Approximate Particle Ranges

R gm cm^{-2}	Protons	U^{238}
0.1	5 MeV	5.0 GeV
0.03	3 MeV	1.5 GeV
0.01	1 MeV	0.3 GeV

Simulation Results

The target for all the computations is a hollow aluminium shell of inside radius 2.5 mm and thickness 0.6 mm. The area mass density of this shell is 0.15 g cm^{-2} and particle ranges of R = 0.1, 0.03, and 0.01 g cm^{-2} have been used for both N = ½ and N = 1. The power density Φ on the targets was varied in decade steps between $\Phi = 10^{11}$ and $\Phi = 10^{15}$ W cm^{-2}, the beam power rising linearly to maximum at t = 100 psec and thereafter remaining constant.

In dealing with laser driven ablation (7.2.2) we were able to use the fact that a quasi steady state was set up to compare temperatures and pressures in different simulations. With ion beam heated targets however the situation is very different and on time scales of interest for inertial confinement fusion no quasi steady state is reached. The reason for this very marked difference is that the collisional absorption of laser energy is quadratic in the density of the absorbing material, and eventually a critical density is reached, beyond which the laser radiation cannot penetrate. For laser wavelengths $\lambda > 0.2$ μm this critical density is very much less than solid density and the laser energy is absorbed very much at the "surface" of the target and is transported inwards to higher densities by electron thermal conduction. The low density material outside the critical density surface has relatively little effect on the propagation of the laser energy.

In contrast the ion beam energy is initially absorbed in material of solid density, and as material is ablated the density at the end of the particle range steadily decreases. We can estimate the density at the end of the range in a steady state flow by a very simple argument.

Suppose that in the steady state the ablation flow velocity is everywhere constant, then the radial density profile will be the form

$$\rho = \rho_o \frac{r_o^2}{r^2}$$

where r_o and ρ_o are approximately the initial shell radius and

density. If the range of the beam particles is R then they will penetrate to a radius r′ given by

$$\int_{\infty}^{r'} \frac{\rho_o r_o^2}{r^2} \, dr = R$$

and the density at this point is

$$\rho\ (r') = \frac{R^2}{\rho_o r_o^2}$$

If the thickness of the shell is Δr, and we define the aspect ratio $A = r_o/\Delta r$ we can also write this as $\rho(r') = \rho_o\ \alpha^2/A^2$ where $\alpha = R/\rho\Delta r$ is the particle range divided by the area mass density of the shell. Since $\alpha < 1$ and $A \simeq 10$, the density at which the ion beam energy is absorbed will change by one or two orders of magnitude during the evolution to the steady state and this will markedly effect the pressure generated in the shell.

In order to understand the general behaviour of the ion beam heated shells it is convenient to take one particular simulation ($\Phi = 10^{13}$ W cm^{-2}, R = 0.1 g cm^{-2}, N = ½) and consider it in some detail. Afterwards we can examine how this behaviour is modified for different values of the parameters Φ, R and N.

In Figure 7.32 we show the motion of the Lagrangian mesh points in the simulation ie the trajectories of the fluid elements. A horizontal line corresponds to fluid at rest and in general the fluid velocity is equal to the gradient of the mesh trajectory. The passage of a shock wave through the material is evidenced by a discontinuous change in slope and the higher density material behind the shock front appears as a dark band where the Langrangian mesh lines are closer together. Figure 7.32 can be interpreted as an explosion of the shell with inward and outward propagating shock waves, each moving away from the initial position of the Bragg peak where the heating was strongest. Eventually the outward moving shock disappears after meeting the rarefaction wave moving in from the surface of the target.

This is in strong contrast to a laser heated target which we show in Figure 7.33. The steady ablation of material from the surface of the target is shown by the successive 'peeling-off' of the mesh lines. A shock wave moves inwards through the shell and subsequent to the passage of the shock wave the ablative acceleration of the shell appears as the increasing slope of the inwardly moving dark band.

From Figures 7.32 and 7.33 it is fairly clear that the ion beam has to heat up a large amount of initially cold material whereas the laser heats only a very thin surface layer which continually ablates away. The thermal time lag for the ion beams is considerable and in Figure 7.34 we show the temporal evolution of temperature and pressure in the simulation.

The temperature plotted is the maximum temperature in the shell which is always physically close to the Bragg peak, and this increases steadily with a time constant of several nanoseconds. The pressure (1 Mbar $\simeq 10^{12}$ dyne cm^{-2}) is plotted in two forms, firstly the maximum pressure in the shell and secondly the pressure at the ablation surface, defined as the point in the fluid where the velocity is zero.

In order to present the data on ablation pressure in a concise form we rather arbitrarily take the peak pressure measured at t = 5 nsec and plot this as a function of power density in Figure 7.35 and Figure 7.36. There now appears to be an optimum particle range for any given power density but to some extent this is an artifact of the time dependence of the pressure curves.

It is particularly useful to compare the pressure generated by ion beams with that generated by a laser of similar power density on target. We take the simulations of laser driven ablation from Evans and Bell (7.70) and choose a laser wavelength of $\lambda = 0.25$ μm which gives the highest pressures in that particular set of simulations. This comparison, which we show in Figure 7.37 clearly indicates that particle beams are markedly superior in generating pressure, the 0.25 μm laser requiring an order of magnitude more irradiance for the same pressure. The difference is entirely due to the ability of the particle beams, at least initially, to

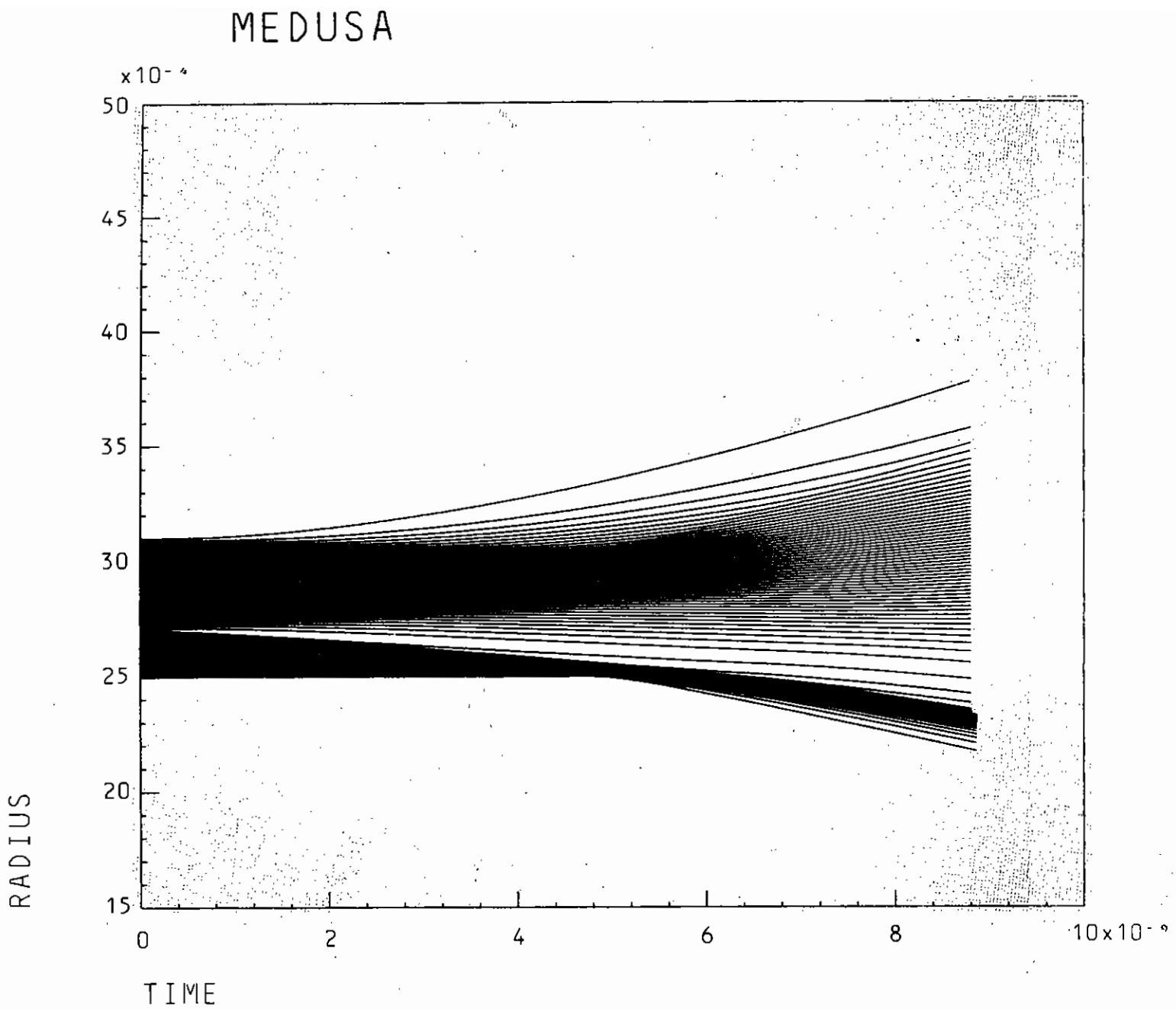

Figure 7.32 Motion of the Lagrangian mesh points in a simulation of an ion beam heated shell. ($\Phi = 10^{13}$ W cm^{-2}, R = 0.1 g cm^{-2}, N = $\frac{1}{2}$).

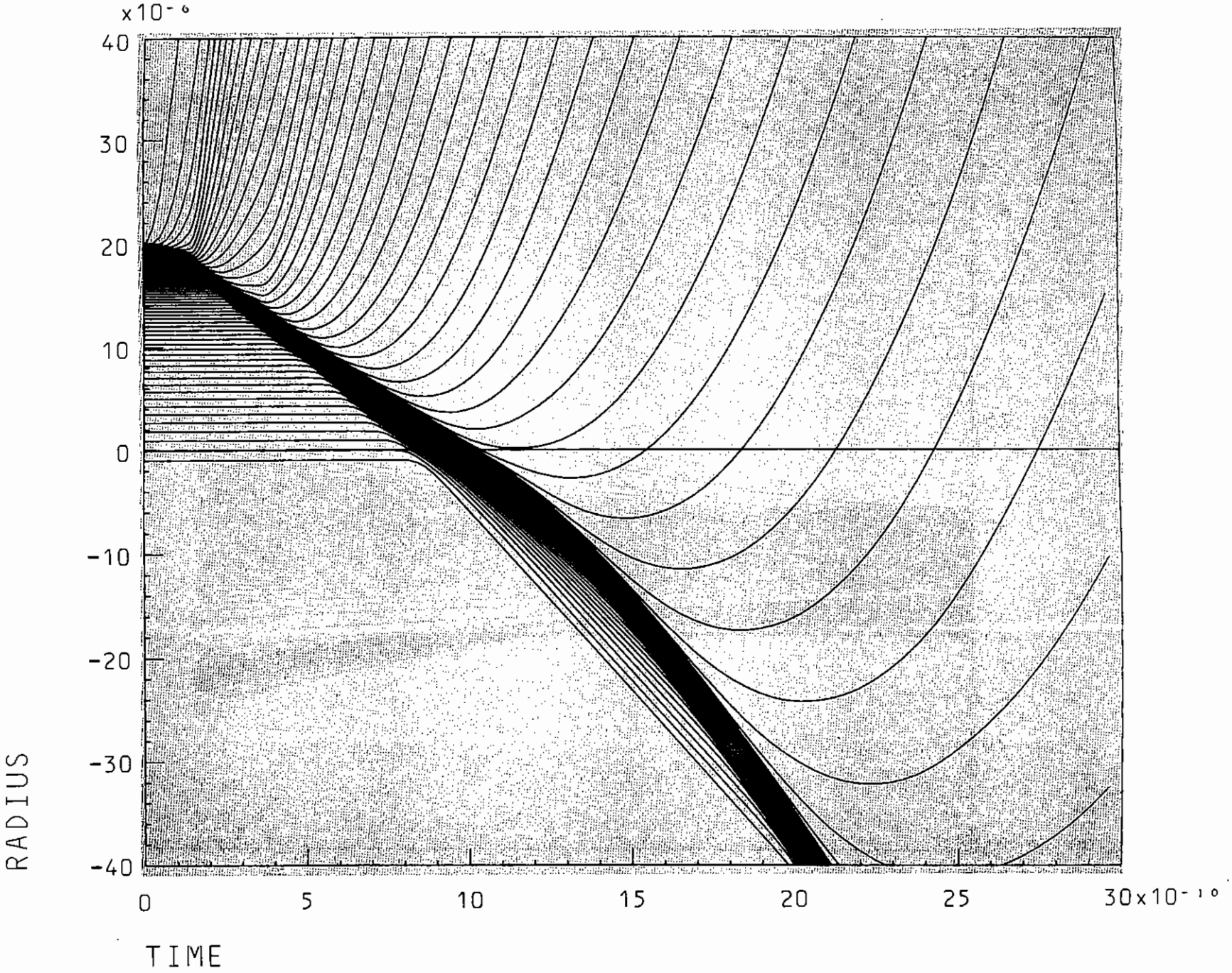

Figure 7.33 Motion of the Lagrangian mesh points in a simulation of a laser heated shell ($\Phi = 10^{14}$ W cm^{-2}, wavelength = 0.25 μm).

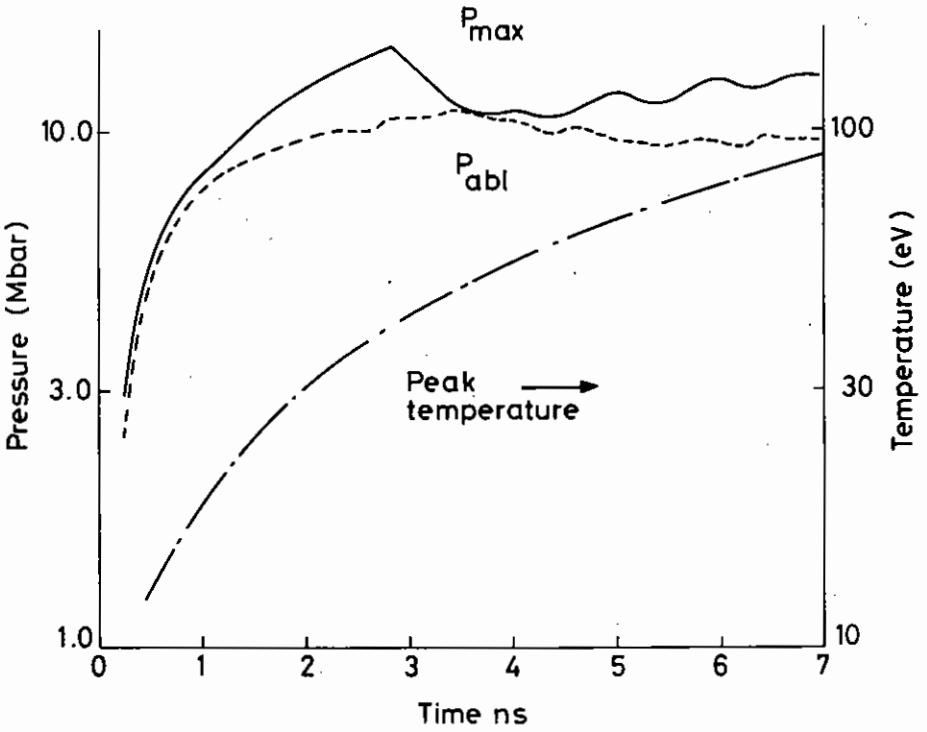

Figure 7.34 Temporal evolution of the temperature and density in the numerical simulation ($\Phi = 10^{13}$ W cm^{-2}, R = 0.1 g cm^{-2}, N = ½).

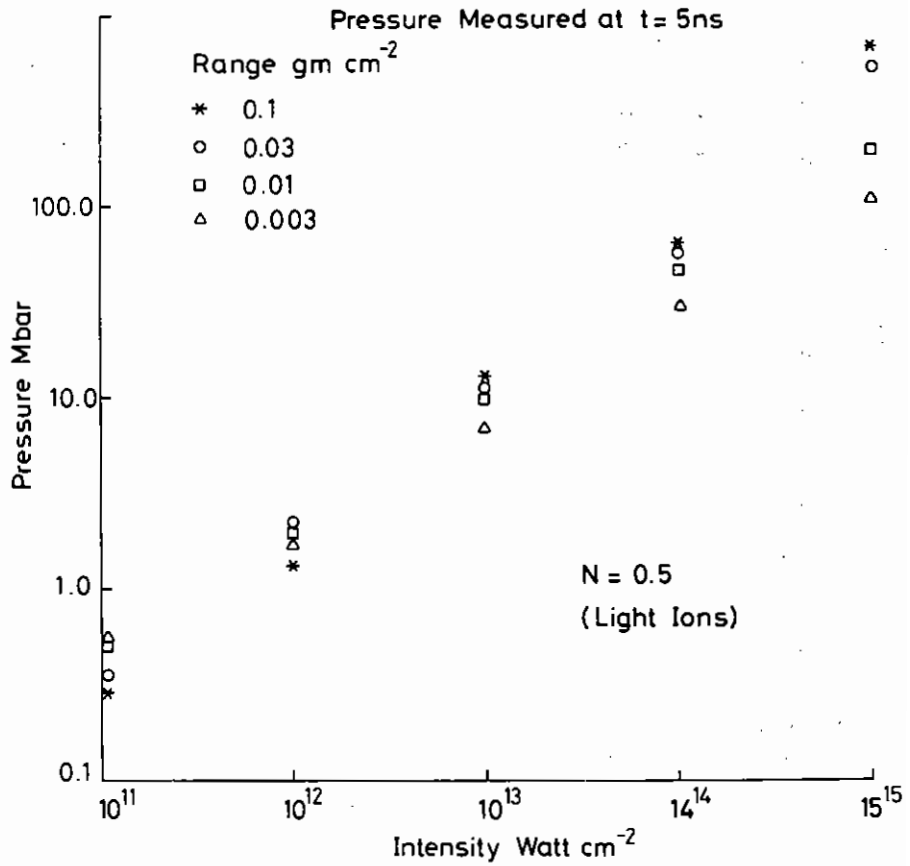

Figure 7.35 Peak pressure at t = 5 nsec for different values of range and power density (N = ½).

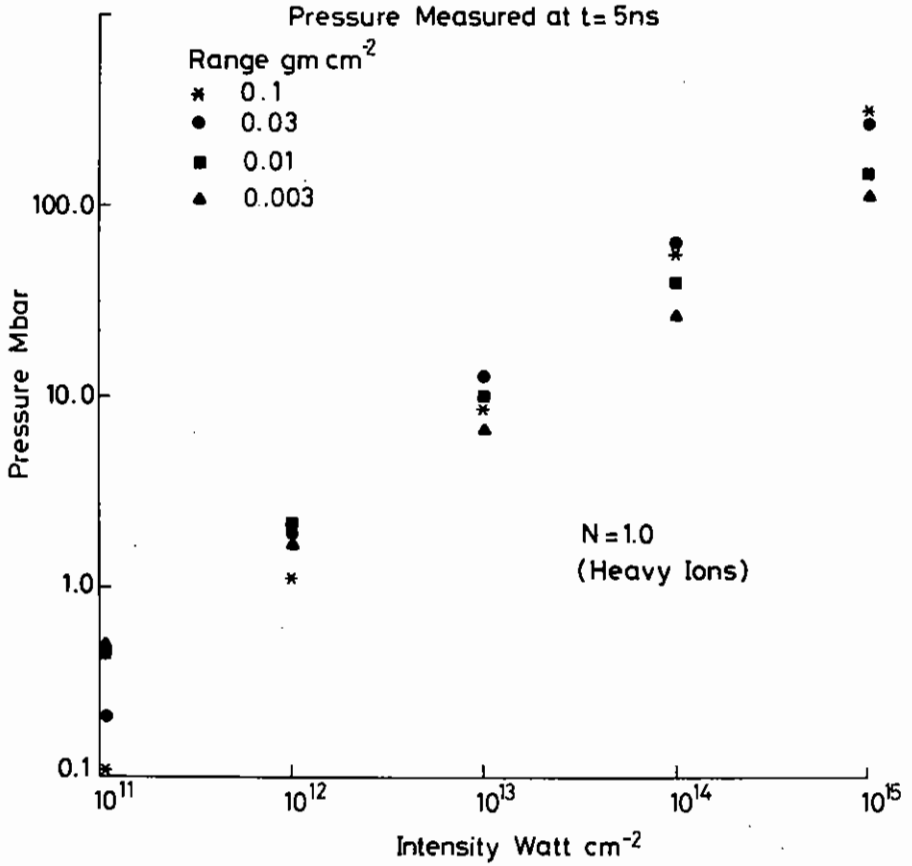

Figure 7.36 Peak pressure at t = 5 nsec for different values of range and power density (N = 1).

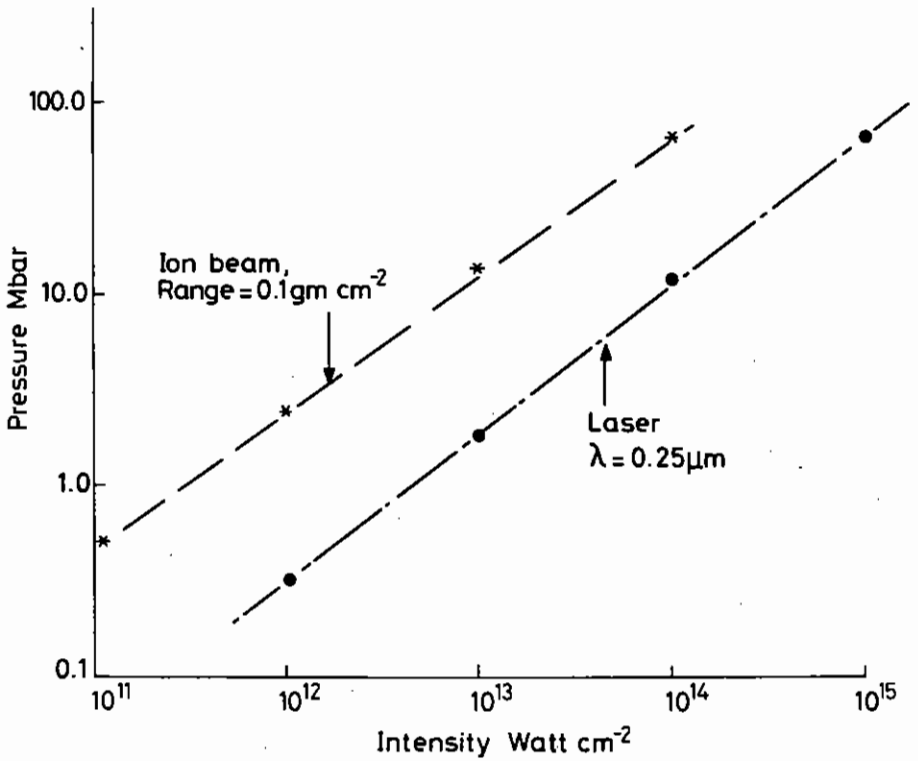

Figure 7.37 Comparison of pressure generated by ion beams (R = 0.1 g cm^{-2}, N = 1) and short wavelength lasers (wavelength λ = 0.25 μm).

deposit their energy at very high densities.

We can obtain a simple estimate of the pressures needed to drive a fusion pellet by considering a plane foil of thickness Δr, density ρ accelerated without loss of mass by a pressure p over a distance r. The terminal velocity is given by $v^2 = \frac{2pr}{\rho\Delta r}$ and if $v = 2 \times 10^7$ cm/s, as needed to achieve fusion temperatures in the compressed material, then $p = 200\ \rho\ \Delta r/r$ M bar. If $\Delta r/r \simeq 10$ and $\rho \gtrsim 1.0$ then $p \gtrsim 20$ Mbar which requires a power density of 3×10^{13} W cm^{-2} for ion beam drivers, or 3×10^{14} W cm^{-2} for laser drivers.

Validity of the Calculations

The major error in these simulations is the total neglect of energy transport and loss by thermal radiation. The effect of the ion beam is to heat material at a high density and this is an efficient means of producing soft X-rays. In order to model the effects of radiative transfer of energy it is necessary to calculate in some detail the atomic physics of the target in order to obtain radiative opacities and energy relaxation rates.

Since the radiation field cannot be more intense than a black body at the peak electron temperature in the target we can use this to place a rather crude upper limit on the rate of energy loss from the target.

In Figures 7.38 and 7.39 we have plotted the maximum temperature in the shell at t = 5 nsec as a function of power density.

The dashed line in these figures is obtained simply by using Stefan's Law to give the power radiated by a black body as a function of temperature. If the peak temperature in the simulations is below the black body line by a factor of 2 or more than radiative losses cannot be more than 1/16 of the incident power and are probably negligible.

When the peak temperature in the simulations is close to or above the black body line the situation is more complicated. The radiative losses

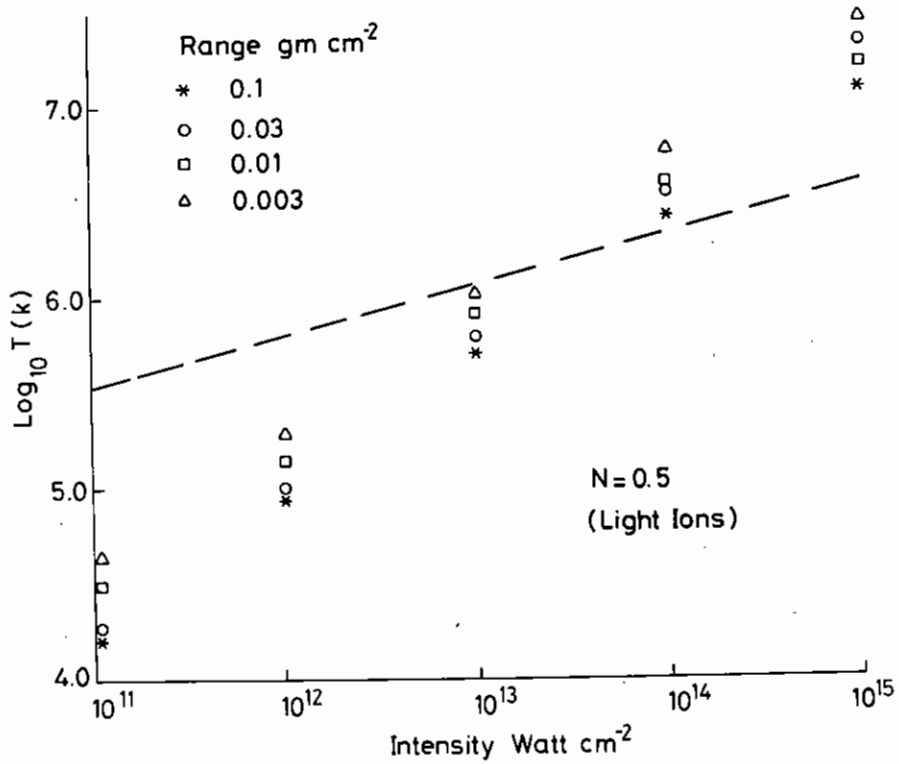

Figure 7.38 Maximum temperature at t = 5 nsec for different values of range and power density (N = ½). The dashed line represents the power density radiated by a black body.

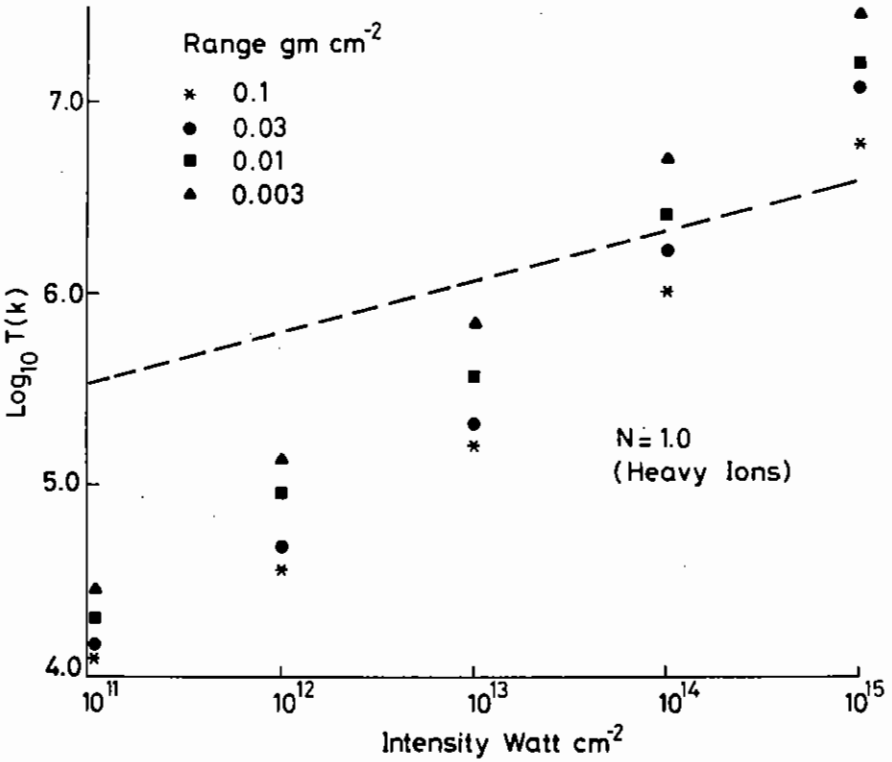

Figure 7.39 Maximum temperature at t = 5 nsec for different values of range and power density (N = 1). The dashed line represents the power radiated by a black body.

may be considered to emerge from a depth of one or two Planck mean free paths from the "surface" of the pellet and the temperature here may be considerably less than the peak temperature.

Clearly the situation is much more complicated when radiation transfer effects are included. It becomes desirable to structure the target materials for any particular form of the energy loss curve so as to maximise the tamping effect, to minimise the radiative losses to the outside, and to keep radiative preheat of the fuel at an acceptable level.

Conclusions

The simulations of ion beam accelerated hollow shells show that there is a marked contrast with laser accelerated shells. The ion beam simulations show a transient behaviour for several nanoseconds while the laser ablated shells rapidly reach a quasi steady state. In the transient phase the pressure generated by both light and heavy ion beams is almost an order of magnitude greater than that produced by the 'best' lasers. Moreover this transient phase may be less susceptible to Rayleigh Taylor instabilities than is the subsequent 'ablative' phase.

A more detailed study of the behaviour of these targets requires more precise calculations of the energy deposition from the beam ions and also of the transfer of thermal radiation within the target.

We note that since the ion beams deposit their energy at rather high densities, then they are very similar to short wavelength lasers and a very high degree of symmetry of irradiation is required, or else the target must be carefully shaped to correspond to the actual beam profiles of a proposed reactor system.

R G Evans (RAL)

CHAPTER 7 REFERENCES

7.01 Annual Report to LFC, RL-80-026, 7.26 (1980)

7.02 G J Pert, J Comp Phys, in press

7.03 R S Craxton and R L McCory, J Comp Phys, 33, 432 (1979)

7.04 G J Pert, J Fluid Mech, 100, 257 (1980)

7.05 G J Pert, J Comp Phys, 27, 241 (1978)

7.06 G J Pert, J Comp Phys, in press

7.07 F C Young, R R Whitlock, R Decoste, B H Ripin, D J Nagel, J A Stamper, J M McMahon and S E Bodner, Appl Phys Lett, 30, 45 (1977)

7.08 B Yaakobi and T C Bristow, Phys Rev Lett, 38, 350 (1977)

7.09 J S Pearlman and J P Anthes, Appl Phys Lett, 27, 581 (1975)

7.10 B H Ripin, P G Burkhalter, F C Young, J M McMahon, D G Colombant, S E Bodner, R R Whitlock, D J Nagel, D J Johnson, N K Winsor, C M Dozier, R D Bleach, J A Stamper and E A McLean, Phys Rev Lett, 34, 1313 (1974)

7.11 W C Mead, C D Orth, D S Bailey, G McLellan and K G Estabrook, University of California, Report UCRL 83163 (1979)

7.12 D B Henderson and R L Morse, Phys Rev Lett, 32, 7, 355 (1974)

7.13 R E Kidder, Nuclear Fusion, 16, 3 (1976)

7.14 J G Kephart, R P Godwin and G H McCall, Appl Phys Lett, 25, 108 (1974)

7.15 W L Kruer, Paper presented at the Tenth Conference on Anomalous Absorption of Electromagnetic Radiation, San Francisco, May 1980, unpublished.

7.16 S J Gitomer, R L Morse and B S Newberger, Phys Fluids, 20, 234 (1977)

7.17 C E Max, C F McKee and W C Mead, Phys Fluids, 23, 1620 (1980)

7.18 B Ahlborn and M H Key, Plasma Physics, 23 (1981) (in press)

7.19 B Ahlborn and M H Key, Annual Report to the LFC, RL-80-026, 7.2.1 (1980)

7.20 B Ahlborn, M H Key and A R Bell, Rutherford Lab Report RL-81-016 (1981)

7.21 E B Goldman, Plasma Phys, 15, 289 (1972)

7.22 C Fauquinon and F Floux, Phys Fluids, 13, 386 (1970)

7.23 F Amiranov, R Benattar, R Fabbro, E Fabre, C Garban and M Weinfeld, Bull APS, 24, 1054 (and Lab preprint)

7.24 J D Hares, H D Kilkenny, M H Key and J G Lunney, Phys Rev Lett, 42, 1216 (1979)

7.25 A R Bell, Rutherford and Appleton Lab Report RL-80-091 (1980)

7.26 B I Bennett, J D Johnson, G I Kerley and G T Rood, Los Alamos Lab Report LA 7130 (1978)

7.27 S L McCarthy, Lawrence Radiation Lab Report UCRL 14364 (1965)

7.28 G J Vinogradov & V V Pustovalov, Sov Phys JETP, 36, 492 (1973)

7.29 N S Erokhin, S S Moiseev & V V Mukhin, Nucl Fusion, 14, 333 (1974)

7.30 G Auer, K Sauer & K Baumgartel, Phys Rev Lett, 42, 1744 (1979)

7.31 P D Carter, S M L Sim & T P Hughes, Optics Comm, 27, 423 (1978)

7.32 R A Cairns, Plasma Phys (to be published)

7.33 D W Forslund, J M Kindel & E L Lindman, Phys Fluids, 18, 1002 (1975)

7.34 W L Kruer, Phys Fluids, 23, 1273 (1980)

7.35 R G Evans, Laser Facility Annual Report, RL-80-026, section 7.3.2 (1980)

7.36 M G Haines, "Coronal Region" in Laser-Plasma Interactions (Eds Cairns & Sanderson) SUSSP (1979)

7.37 A R Bell, R G Evans and D J Nicholas, Phys Rev Lett, 46, 243 (1981)

7.38 E J Valeo and I B Bernstein, Phys Fluids, 19, 1348 (1976)

7.39 A Dolinsky, Phys Fluids, 8, 436 (1965)

7.40 L Spitzer and R Harm, Phys Rev, 89, 977 (1953)

7.41 D R Gray and J D Kilkenny, Plasma Phys, 22, 81 (1980)

7.42 R J Mason, 'Suprathermal electron transport in laser produced plasmas'. Proc ANS/ENS meeting on 'Advances in Mathematical Methods for Nuclear Engineering Problems', Munich (1981)

7.43 L Lees and J Siam, Appl Math, 13, 278 (1968)

7.44 D J Bond, J Phys D (in press)

7.45 R E Alcouffe et al, Nuc Sci and Eng, 71, 111 (1979)

7.46 W F Miller, Nuc Sci and Eng, 65, 226 (1978)

7.47 D A Tidman and R A Shanny, Phys Fluids, 17, 1207 (1974)

7.48 A Z Dolginov and V A Urpin, JETP, 50, 912 (1979)

7.49 M Ogasawara et al, J Phys Soc Jap, 49, 322 (1980)

7.50 N A Tahir, E W Laing and D J Nicholas, Rutherford Lab Report RL-80-048 (1980)

7.51 N A Tahir and E W Laing, Phys Letts A, 77A, 6, 430 (1980)

7.52 A Bell and R G Evans, Private communication

7.53 D Kershaw, J Comp Phys, 26, 43 (1978)

7.54 J P Christiansen and K V Roberts, Comp Phys Comm, 7, 245 (1974)

7.55 J P Christiansen et al, Comp Phys Comm, 7, 271 (1974)

7.56 N A Tahir, E W Laing and D J Nicholas, Rutherford Lab Report RL-80-083 (1980)

7.57 J D Kilkenny et al, Phys Rev A, 22, 2746 (1980)

7.58 M H Key et al, Phys Rev Lett, 44, 1669 (1980)

7.59 R W Lee (to be published)

7.60 D G Hummer and G B Rybicki, Mon Nat R Astr Soc, 152, 1 (1971)
D G Hummer, C V Kunasz and P B Kunasz, Computer Phys Comm, 6, 38 (1973)

7.61 D J Bond, PhD Thesis, University of London (1980)

7.62 J E Crow, P L Auer and J E Allen, J Plasma Phys, 17, 393 (1975)

7.63 L M Wickens, J E Allen and P T Rumsby, Phys Rev Lett, 41, 243 (1978)

7.64 B Bezzerides, D W Forslund and E L Lindman, Phys Fluids, 21, 2179 (1978)

7.65 L M Wickens and J E Allen, J Plasma Phys, 22, 167 (1979)

7.66 J M Nuckolls, L Wood, A Thiessen and G Zimmerman, Nature, 239, 138 (1972)

7.67 M J Clauser, Phys Rev Lett, 35, 848 (1975)

7.68 R E Kidder, Nuclear Fusion, 16, 3 (1976)

7.69 D E T F Ashby, J P Christiansen and K V Roberts, Computer Phys Comm, 7, 271 (1974)

7.70 R G Evans and A R Bell, Rutherford Lab Report RL-80-085 (1980)

7.71 M D Brown and C D Moak, Phys Rev B, 6, 90 (1972)

APPENDIX

CENTRAL LASER FACILITY PUBLICATIONS 1980/81

RESEARCH PAPERS

B Ahlborn & M H Key
Scaling laws for laser driven exploding pusher targets
Plasma Phys (in press)

A R Bell, R G Evans & D J Nicholas
Electron energy transport in steep temperature gradients in laser produced plasmas
Phys Rev Letts, 46 243-6 (1981)

D J Bond, J D Hares & J D Kilkenny
Demonstration of resistive inhibition of fast electrons from laser produced plasmas in low density gold targets
Phys Rev Letts, 45 252 (1980)

N H Burnett, G Josin, B Ahlborn and R G Evans
Generation of shock waves by hot electron explosions by a CO_2 laser
Appl Phys Lett, 38 226-9 (1981)

R A Cairns
The intensity and angular dependence of second harmonic emission from a laser produced plasma
Plasma Physics (in press)

S S Chowdhury, R M Clement & H T Miles
Ion energy analyser for laser produced plasma
J Phys E: Sci Instrum, 13 1099-1105 (1980)

R M Clement, R A Davies, H T Miles & S K Sethuraman
Influence of charge transfer on energy measurements of ions expanding from laser-produced plasmas
J Phys D: Appl Phys, 13 1643-8 (1980)

A J Cole, J Murdoch, S M L Sim & R G Evans
Timer resolved studies of backscattered light from a plasma generated by a 0.52 m laser
Optics Comm, 36 51-7 (1981)

C Duncan, A Raven & P T Rumsby
Zone plate coded radiography of laser driven ablative implosions
Optics Comm, 35 384-7 (1980)

C B Edwards, F O'Neill & M J Shaw
60 ns e-beam excitation of rare-gas halide lasers
Appl Phys Lett, 36 617-620 (1980)

R G Evans
Saturation of Brillouin Scattering in a laser driven ablation plasma
Plasma Physics, 23 99-103 (1980)

A F Gibson & M F Kimmitt
Photon Drag Detection, 'Infra red and millimetre waves'
Editor K J Button, 3 181-217 (1981)

M C Gower
KrF laser-induced breakdown of gases
Optics Comm (in press0

M C Gower, A J Keasley & C E Webb
Photolysis of Se_2 by UV lasers: applications to kinetics of group VI laser systems
J Appl Phys, 50 5988 (1979)

M C Gower, A J Keasley & C E Webb
Group VI molecular photolytic dissociation studies using rare gas halide lasers, 'Laser-induced processes in molecules'
Eds K Komper & S D Smith, Springer-Berlag, Berlin (1979)

K T V Grattan, H R Hutchinson & E S Theocharous
Measurement of the wavelength-dependent photoionization cross section of Se* ('S) in the spectral region of 170-175 nm
IEEE J Quant Elect, 16 1170 (1980)

D R Gray, J Murdoch, S M L Sim, A J Cole, R G Evans & W Toner
Time resolved spectroscopic studies of laser produced plasmas
Plasma Physics, 22 967 (1980)

R J Hutcheon, L Cooke, M H Key, C L S Lewis & G E Bromage
Neon-like and fluorine-like X-ray emission spectra for elements from Cu to Sr
Physica Scripta, 21 89-97 (1980)

R Illingworth, R K Thareja, A Raven, P T Rumsby, J A Stamper & O Willi
Interferometric measurement of asymmetric electron density profiles of laser-created plasmas from composite plane targets
J Appl Phys, 51 1435 (1980)

R Illingworth & R K Thareja
Generalised coefficients for Abel inversion
J Phys E: Sci Instrum (in press) (1981)

M H Key, C L S Lewis, J G Lunney, A Moore, J M Ward & R K Thareja
Time resolved X-ray spectroscopy of laser produced plasmas
Phys Rev Lett, 44 1669 (1980)

M H Key, P T Rumsby, R G Evans, C L S Lewis, J M Ward & R L Cooke
A study of ablatively imploded spherical shell targets
Phys Rev Lett, 45 1801 (1980)

M H Key
Interactions of intense laser radiation with matter
Phil Trans Roy Soc (in press)

M H Key
Some topical issues in short pulse laser produced plasma research 'Ultra Short Laser Pulses'
Phil Trans Roy Soc, A298 141 (1980)

M H Key & R J Hutcheon
Spectroscopy of laser produced plasmas
Adv Atomic & Molecular Phys, 16 201-280 (1980)

J D Kilkenny, J D Hares, C L S Lewis & P T Rumsby
Search for Rayleigh Taylor instability in laser irradiated thin foil targets
J Phys D: Appl Phys, 13 L123 (1980)

J D Kilkenny, R W Lee, M H Key & J G Lunney
The X-ray spectroscopic diagnosis of laser produced plasmas, with emphasis on line broadening
Phys Rev A, 22 2746 (1980)

R W Lee & A J Freeman
The effects of different ion species on the shape of the hydrogenic n=4 to n=1 profiles of high z emitters in ultra-dense plasmas
JQSRT, 24 43 (1980)

Z Q Lin, O Willi and P T Rumsby
Evidence for beam self-focusing in the corona of laser irradiated spherical targets
J Phys D, 14 L35 (1981)

J G Lunney & J F Seely
Silicon satellite spectra from laser-imploded microballoons
Phys Rev Lett, 46 342-5 (1981)

M M Michaelis & P T Rumsby
Solaser Power
Sunworld, 4 28 (1980)

M M Michaelis & O Willi
Refractive fringe diagnostics of laser produced plasmas
Optics Comm, 36 153-7 (1981)

D J Nicholas & J E Boon
The generation of high precision aspherical surfaces in glass by CNC machining
J Phys D, 14 593-600 (1981)

M J Shaw, C B Edwards, F O'Neill, C Fotakis & R J Donovan
Efficient laser action on the 342 nm band of molecular iodine using ArF laser pumping
Appl Phys Lett, 37 346-348 (1980)

M J Shaw, M C Gower & S Rolt
Quantum yields for Se $^1S_0$, $^1D_2$ & $^3P_{0,1,2}$ atoms in ArF laser photolysis of OCSe
Chem Phys Letts, 73 478-482 (1980)

N A Tahir & E W Laing
Radiation effects in gas-filled microballoons
Phys Letts A, 77 430 (1980)

N A Tahir & E W Laing
Ionization effects in laser-produced plasmas
Phys Letts A, 79321 (1980)

N A Tahir & E W Laing
Radiation effects in laser compression simulations
Plasma Physics, 22 1113 (1980)

O Willi, R G Evans & A Raven
Time resolved density profiles of laser heated plasma
Phys Fluids, 23 2061 (1980)

O Willi, P T Rumsby and C Duncan
Megagauss magnetic fields on laser irradiated spherical targets
Optics Comm, 37 40 (1981)

O Willi and P T Rumsby
Filamentation on laser irradiated spherical targets
Optics Comm, 37 45 (1981)

O Willi, P T Rumsby and S Sartang
Optical probe observations of non-uniformities in laser produced plasmas
J Quant Elec (in press)

Papers published in the Proceedings of the 9th European Conference on Controlled Fusion and Plasma Physics, Oxford (1979)
Published by UKAEA Culham Laboratory, Oxford shire

J D Kilkenny, D J Bond, D R Gray, J D Hares, R G Evans, M H Key, W Toner & J G Lunney
Energy transport from 1.06 μm and 0.53 μm laser plasma interactions at 10^{15} W cm^{-2}

C L S Lewis, L Cooke, J G Lunney, A Moore, J M Ward, R G Evans, M H Key & T A Hall
Studies of laser driven implosions by time resolved shadowgraphy

Papers published in Laser Advances and Applications, editor B S Wherrett, J Wiley (1979)

A F Gibson
Lasers for plasma research (p191)

A R Bell & R G Evans
Improvements to the equation of state in the MEDUSA laser compression simulation (p197)

C L S Lewis, L Cooke, J G Lunney, A Moore, J M Ward, R G Evans, M H Key, P T Rumsby & T A Hall
Time resolved X-ray shadowgraphy of laser driven ablative implosions (p201)

J D Hares, J D Kilkenny, M H Key & J G Lunney
A parametric study of fast electron preheat in laser plasma interactions (p207)

D R Gray, J D Hares, J D Kilkenny, S A Veats, R G Evans & W Toner
X-ray diagnosis of the interaction of 0.53 μm radiation with layered targets at 5 x 10^{14} W cm^{-2} (p211)

T J M Boyd
Laser plasma interactions (p215)

D R Gray, J Murdoch, S M L Sim, A J Cole, R G Evans & W T Toner
Time resolved spectroscopy from laser produced plasmas (p221)

Papers to be published in the Proceedings of the Vth International Conference on Spectral Line Shapes, Berlin, 1980, to be published by W de Gruyter, Berlin

D D Burgess, D Everett & N J Peacock
Doppler profiles of XUV emission from dense plasmas

R W Lee
Line-shapes in high density plasmas

R W Lee
Radiative transfer simulation of spectral line simulation

R W Lee, J Kilkenny, S Veats & A Shalom
Emission spectra from six beam laser compression experiments

Other Conference Papers

T J M Boyd
Proceedings of the International Symposium on Plasma Physics
Basic processes in the physics of laser generated plasmas
Indian National Academy of Sciences, p11 (1980)

T J M Boyd & H C Barr
Proceedings of the International Conference on Plasma Physics, Nagoya
Saturation levels of ion acoustic turbulence
Fusion Research Association of Japan, 1 44 (1980)

M C Gower
12th Atomic and Molecular Physics Conference 1980
Potential new laser media using laser switched collisions

J D Kilkenny et al
Proceedings of the Vth Workshop on Laser Interaction with Matter
Recent progress in laser interaction and ablative compression experiments at the Rutherford Laboratory
Plenum Press (1980)

R W Lee, J D Kilkenny, J G Lunney, J Hares & M H Key
Proceedings of the Xth Conference on Laser-Plasma Interaction
Progress in Laser Compression Experiments
Editors Shwarz and Hora, Academic Press (1980)

D J Nicholas & J E Boon
The production of an aspheric surface for an F31 focussing lens by CNC machining
Proc Int Seminar on Aspheric Optics SPIE 164 (1980)

D J Nicholas & I N Ross
Beam propogation studies in high powered laser systems
Proceeding Int Seminar on Optical Systems and Applications SPIE 172 (1980)

A Raven
Proceedings of the International Conference on Plasma Physics, Nagoya
High Resolution Diagnostics
Fusion Research Association of Japan, 2 370 (1980)